Journal of Nanomaterials

The Potential of Nanomaterials for Drug Delivery, Cell Tracking, and Regenerative Medicine

Guest Editors: Krasimir Vasilev, Haifeng Chen, and Patricia Murray

The Potential of Nanomaterials for Drug Delivery, Cell Tracking, and Regenerative Medicine

Journal of Nanomaterials

The Potential of Nanomaterials for Drug Delivery, Cell Tracking, and Regenerative Medicine

Guest Editors: Krasimir Vasilev, Haifeng Chen, and Patricia Murray

Editorial Board

Contents

Hindawi Publishing Corporation
Journal of Nanomaterials
Volume 2012, Article ID 206582, 2 pages
doi:10.1155/2012/206582

Editorial

The Potential of Nanomaterials for Drug Delivery, Cell Tracking, and Regenerative Medicine

Krasimir Vasilev,[1,2] Haifeng Chen,[3] and Patricia Murray[4]

[1] *Mawson Institute, University of South Australia, Mawson Lakes, SA 5095, Australia*
[2] *School of Advanced Manufacturing, University of South Australia, Mawson Lakes, SA 5095, Australia*
[3] *Department of Biomedical Engineering, College of Engineering, Peking University, Beijing 100871, China*
[4] *School of Biological Sciences, University of Liverpool, Liverpool L69 7ZB, UK*

Correspondence should be addressed to Krasimir Vasilev, krasimir.vasilev@unisa.edu.au

Received 27 May 2012; Accepted 27 May 2012

Recent progress in bio- and nanotechnology has led to the development of a rich variety of novel materials, precisely engineered at the nanoscale, which hold great potential to revolutionize traditional medical treatments and therapies. This special issue brings together and highlights the latest advances in the use of nanomaterials in biomedical technologies, such as drug delivery, cell tracking, imaging, and regenerative medicine as a whole. Regenerative medicine has been a rapidly developing field which is forecast to gain further momentum through growing government and commercial investments in R&D and new technologies. Although emerging therapies need to undergo the inevitable regulatory approval processes, recent market reports suggest that, in the next five years, regenerative medicine will occupy a significant share of the biomedical space. Undoubtedly, the success of regenerative medicine would not have been possible without novel nanomaterials, including, but not limited to the following: nanoparticles, nanotubes, nanoengineered scaffolds, and nanoscale surface modifications. One of the aims of this special issue is to highlight the current challenges and obstacles which lie on the path to fully integrating these promising nanomaterial-based technologies in medicine. Further, this special issue aims to provide guidance to researchers in the field of bionanotechnology and to inform the research, medical, and industry communities of the current and future directions of the field.

This special issue is a collection of quality contributions from established laboratories around the world. It contains instructive review articles and original research articles dealing with diverse areas of regenerative medicine.

Seven excellent reviews published in this special issue present a critical overview of recent progress in the corresponding field of regenerative medicine and the authors' view for their future directions. Two of the reviews focus on drug delivery through hydrogels and porous silicon. A review article by S. Dey and T. K. Maiti discusses gene silencing though superparamagnetic nanoparticles. The progress and challenges of cell tracking and imaging with nanocrystals and nanoparticles used in magnetic resonance are discussed in two separate reviews. A paper by the group of K. Ostrikov draws the reader's attention to potential toxicity of novel nanomaterials such as grapheme and carbon nanotubes which hold great promise in many advanced applications including medicine. Recent advances in microfluidic platforms for evaluation of nanobiomaterials have also been brought to the attention of the readers of this special issue.

The special issue also contains 18 original research articles which make substantial contributions to various areas of regenerative medicine. These areas include the delivery of therapeutics, such as proteins and genes, through nanomaterials or biocarriers, to stem cells for tissue repair, or for tumour targeting. Several papers deal with cell tracking and imaging facilitated by superparamagnetic nanoparticles, luminescent nanocrystals, or titanium dioxide nanoparticles for dual mode enhancement of computed tomography. Another important area of regenerative medicine that is well presented in this special issue is the development of tissue engineering scaffolds. A paper by X. Wang et al. demonstrates the potential of titania-based nanostructured ceramic scaffolds to drive cell differentiation and create

an osteogenic environment for bone tissue engineering. Novel gradient technology for high-throughput screening is proposed by A. Michelmore et al. Nanomaterials offer great promises; however, many potential health hazards are not yet understood. This special issue provides insight in this area such as the cytotoxicity of carbon nanotubes to microphages. When medical treatments are implemented (both traditional and new), infections are always a significant problem. Through a paper by L. Ploux and coworkers focused on the antibacterial properties of silver-loaded plasma polymer coatings, the special issue makes a contribution in this area too.

Acknowledgments

The editorial team would like to thank all authors for their excellent contributions. This special issue would not have been of such quality without the constructive criticism of the reviewers. We gratefully acknowledge all colleagues who contributed to the peer review process. We also acknowledge the great support and assistance of the publishing team of the Journal of Nanomaterials. K. Vasilev would also like to thank the Australian Research Council for fellowship FT100100292 which allowed him the time to edit this special issue. H. Chen thanks the support from the Ministry of Science and Technology of China (Grant 2012CB933903). P. Murray acknowledges support from the UK Engineering and Physical Sciences Research Council (EP/H046143/1).

Krasimir Vasilev
Haifeng Chen
Patricia Murray

Hindawi Publishing Corporation
Journal of Nanomaterials
Volume 2012, Article ID 830503, 15 pages
doi:10.1155/2012/830503

Review Article

Nanoporous Silicon as Drug Delivery Systems for Cancer Therapies

Sazan M. Haidary,[1] Emma P. Córcoles,[1] and Nihad K. Ali[2,3]

[1] *Faculty of Health Science and Biomedical Engineering, Universiti Teknologi Malaysia, 81310 Johor, Skudai, Malaysia*
[2] *Material Innovations and Nanoelectronics Research Group, Faculty of Electrical Engineering, Universiti Teknologi Malaysia, 81310 Johor, Skudai, Malaysia*
[3] *Ibnu Sina Institute for Fundamental Science Studies, Universiti Teknologi Malaysia, 81310 Johor, Skudai, Malaysia*

Correspondence should be addressed to Emma P. Córcoles, emma@biomedical.utm.my

Received 13 January 2012; Revised 10 May 2012; Accepted 18 May 2012

Academic Editor: Krasimir Vasilev

Porous silicon nanoparticles have been established as excellent candidates for medical applications as drug delivery devices, due to their excellent biocompatibility, biodegradability, and high surface area. The simple fabrication method by electrochemical anodization of silicon and its photoluminescent properties are some of the merits that have contributed to the increasing interest given to porous silicon. This paper presents the methods of fabrication, which can be customized to control the pore size, various chemical treatments used for the modification of silicon surfaces, and the characterization and pore morphology of silicon structures. Different approaches used for drug loading and the variety of coatings used for the controlled released are revised. The monitoring of the toxicity of silicon degradation products and the in vivo release of a drug in a specific site are described taking into account its significance on medical applications, specifically on cancer therapy.

1. Introduction

Nanotechnology has revolutionized engineering designs in a range of materials and applications. Biotechnology, pharmaceutics, food technology, and semiconductors among others are some of the various scientific fields that have benefitted from this technology.

Among some of the numerous applications, the fabrication of nanostructures has been envisioned as drug delivery systems. These have the potential of reducing side effects by delivering the exact amount of drugs into a specific site rather than the common systemic delivery, which diffuses across tissues and organs [1–3]. Special efforts are required on the design and development of a new drug delivery system. Identification of the target and management of the release over time are important issues to consider in order to achieve maximum treatment. Nanoporous structures with pore size of less than 100 nm have been fabricated in different materials such as titanium oxide (TiO_2), aluminum oxide (Al_2O_3), and silicon (Si) [4, 5]. Porous silicon (pSi) has been and still being investigated in both bulk crystalline and as nanostructure for applications as diverse as optics [6–8], chemical sensors [9–11] and biosensors [12–16], radiotherapy [17], tissue engineering [18], cell culture [19], biotechnology, gas separation, catalyst and microelectronics [20]. pSi with pore size 2–50 nm has played a significant role as a carrier in pharmaceutical technology for its drug loading and controlled release properties [1, 2, 21–23].

Uhlir first discovered pSi in the Bell laboratories in 1950s when cleaning and polishing Si surfaces [24], and interest in pSi increased during 1970s–1980s due to its high surface area, which made it useful as a model in spectroscopic studies [25, 26]. During the 1990s, after its photoluminescence properties were discovered, pSi fascination increased and it was used later as a biomaterial, when covered with hydroxyapatite [27]. pSi pore dimensions can be precisely controlled depending on fabrication parameters. This useful feature enables a range of bioactive species to be loaded and the desired rate of drug release to be easily obtained [28]. Additionally, pSi presents properties such as a high surface area

(400–1000 m^2/g) [29], and the ability to degrade completely in aqueous solutions into nontoxic silicic acid, the major silicon form in the human body [27]. Silicic acid is known to be absorbed by the gastrointestinal tract and then secreted through the urine [30, 31]. However, other results have found pSi to be bioinert, bioactive or biodegradable depending on the porosity and pore size [32]. Subcutaneous injection of mesoporous silicates in rats showed no toxicity effects, but intraperitoneal and intravenous injections resulted in death or euthanasia. This was reported as a consequence of the formation of thrombus and hence further modifications of the structures were suggested [28]. Pore sizes together with surface treatments have been considered to play a major role in cell-particle interactions and hence determine toxicity of the material [33]. In an in vitro cytotoxicity study, the smallest particles were reported to be the most toxic, and the surface chemistry treatment the key factor regarding the toxicity aspect [34]. Nevertheless, there is still a need for more reports in cytotoxicity or biocompatibility of silicon structures for biotechnological applications.

Microfabricated pSi particles as drug delivery systems have shown to enhance paracellular delivery of insulin [21] and the permeability of griseofulvin [35] across intestinal Caco-2 cell monolayers. They have also been used as excellent carriers of clorgyline across the blood brain barrier as a treatment for central nervous system diseases such as Parkinson and Alzheimer [36]. Loading and release of various drugs have been investigated in vitro such as common oral drugs (antipyrine, ibuprofen, griseofulvin, ranitidine, and furosemide) [37, 38] or dexamethasone for cancer treatment [39]. The capability of pSi to carry up to 80% excess of load has been demonstrated in various studies with protein [40], anticancer drugs [41], and other types of drugs [37, 39].

The scope of this paper is to review the fabrication and characterization of pSi nanoparticles for application as drug delivery devices. With that in mind, surface modification, drug loading and controlled release methods are also revised. A special interest is given to these structures for application in cancer therapies.

2. Fabrication of Porous Silicon

Silicon is a biomaterial, one of the most frequent elements in the earth's crust [42]. A range of methods can be applied for the fabrication of porous Si, chemical stain etching, chemical vapor etching, laser-induced etching, metal-assisted etching, spark processing and reactive ion (plasma) etching. However, the most recurrent methods are electrochemical anodization and stain etching. A recent review discusses the various Si porosification methods and the numerous parameters (electrolyte composition and pH, current density, etching time, temperature, wafer doping and orientation, lighting, magnetic field, and ultrasonic agitation) that influence the process [43].

2.1. Electrochemical Anodization. PSi can be prepared by electrochemical anodization of a single crystalline silicon wafer using a solution of hydrofluoric acid (HF) [44]. The method itself does not present any complication, but a tight control of the porous structures is challenging since it depends on several factors. Current density, concentration of hydrofluoric acid, electrolyte stirring, type of dopant (*p*-type and *n*-type), orientation of the crystalline Si, resistivity and temperature, the etching time and the illumination and wavelength during the etching process are key factors that affect the outcome of the Si nanoporous structures [45].

Typically, the electrochemical anodization consists in applying a constant current between two electrodes immersed in an electrochemical cell containing an aqueous solution of hydrofluoric acid and ethanol, where ethanol acts as surfactant to reduce hydrogen bubble formation [44, 46] (Figure 1). Other methods present some variants such as the use of H_2O_2 in the wet etching bath, with a high etching current [47] or by means of pulsed current anodic etching [48] and the use of ultrasound to further enhance the electrochemical etching [49].

A constant current is applied between the anode (Si wafer) and the cathode (platinum electrode) immersed in an electrochemical aqueous solution of hydrofluoric acid, where the following reactions take place:

$$\text{Pt} : 2H^+ + 2e^- \longrightarrow H_2 \tag{1}$$

$$\text{Si} : \text{Si} + 6F^- + 2H^+ + 2e^- \longrightarrow {SiF_6}^{2-} + H_2 \tag{2}$$

Pore formation in the Si wafer follows the mechanism shown in Figure 2, where (1) due to the low polarization between the hydrogen and silicon atoms, the fluoride ion of the HF-based electrolyte solution attacks the hydrogen-saturated silicon surface as long as there is absence of electron holes; (2) Si–F bond is formed by nucleophilic attack on a Si–H by a fluoride ion if a hole reaches the surface; (3) the polarization due to Si–F bond influences the second fluoride ion attack, replacing the remaining hydrogen bond and injecting two hydrogen atoms of one electron into the substrate; (4) after polarization, the Si-F bonds reduce the electron density of the Si–Si back bonds, and these make it liable to be attacked by HF or H_2O; (5) the highly stable SiF_6 fluoroanion is the reaction product of the tetrafluoride molecule with HF [50].

The porosity of Si structures can be defined as a percentage of empty hole volume, ranging between 20% and 80%, causing the difference in morphology. Pore morphology depends on the type of substrate and other anodization conditions. Increasing the etching time increases the overall size and thickness of the pSi layer [51].

In order to separate the porous layer from the substrate, an electropolishing process or lift-off method at a critical value of current density is required following the formation of pSi. Electropolishing processes occur at potentials higher than the peak potential of pSi formation. Pore diameter increases, in general, with increasing potential and decreasing HF concentration, while the amount of chemical dissolution increases with immersion time and decreasing HF concentration [52]. Hence, the etched Si is immersed in a different HF electrolyte solution, and secondary current pulses are applied [53]. During lower concentration of HF electrolyte, it is considered that the process occurs under

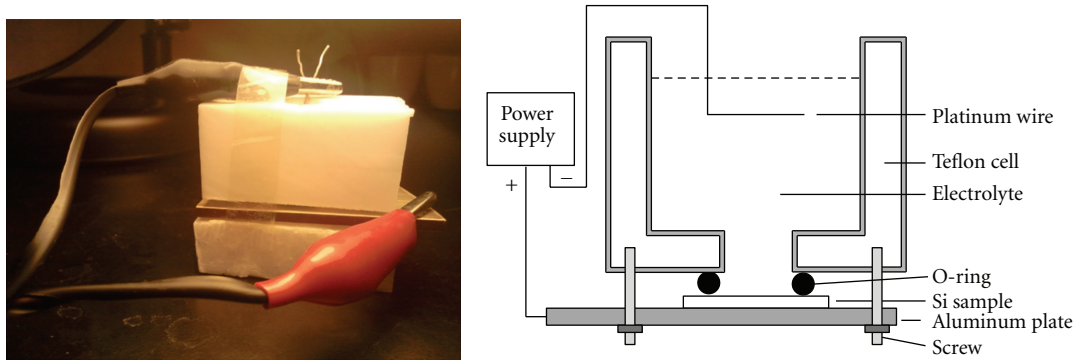

Figure 1: Setup for electrochemical etching of porous silicon. (a) Teflon cell containing the silicon wafer (anode) and the platinum wire (cathode). (b) Sketch of the Teflon cell illustrating the components of the setup.

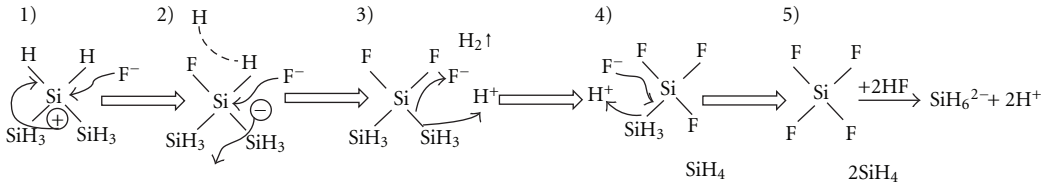

Figure 2: Mechanism of pore formation. (1) F ion attacks the hydrogen saturated silicon surface; (2) Si–F bond is formed by nucleophilic attack on a Si–H by a F ion; (3) the second F ion attack replaces the remaining hydrogen bond; (4) HF or H_2O attacks the Si–Si back bond due to the reduced the electron density; (5) the tetrafluoride molecule reacts with HF producing the highly stable SiF_6 fluoroanion.

diffusion-limited conditions and the propagation of pores is slower than the removal of Si from the interface between Si substrate and pSi layer [54]. However, the HF concentration, current densities, and immersion time have been found to vary among groups [36, 55], which suggests that an accurate balance between immersion time, HF concentration and current pulses is required. Once the porous layer is released from the Si substrate, it can be converted to microparticles using ultrasonic fracture (Figure 3).

2.2. Stain Etching. Unlike electrochemical anodization, stain etching, which gets this name due to the brownish or reddish color formed on the surface of the Si, is a simpler method [56, 57]. It depends on the chemical reaction, and no addition of current is needed. Typically, HNO_3 and HF are used and the product of the cathodic reaction (NO) serves as a hole injector, enabling Si to dissolve [44, 58]. The disadvantage of this method is that the etching outline is not uniform, presenting both cathodic and anodic sites randomly but constantly distributed on the Si surface. Reproducibility and the pSi layer formed are quite limited in stain etching compared with anodization [44]. More recently, other aqueous solutions have been used producing brilliantly luminescent pSi and reproducible homogeneous thick films compared with those of nitrate/nitrite-based methods [59–61].

3. Morphology of Porous Si

The IUPAC defines a pore as a cavity, channel, or interstice with depth exceeding its width. pSi is classified into three types in terms of its pore size: microporous silicon ≤ 2 nm, mesoporous silicon 2–50 nm, and macroporous silicon ≥ 50 nm (IUPAC classification of pore size). The porosity, pore size and volume, thickness and shape of the porous layer determine the optical properties of pSi, making the material interesting for a range of applications in the biomedical field, especially controlled drug delivery devices [45, 62]. The control over all these characteristics depends on the various fabrication factors stated before. The diverse types of pSi have been classified into three groups: (1) space-charge layer control, (2) substrate resistance control, and (3) photocarrier control. The first extends to all pSi formed, except the macropores formed from *p*-type, and the micropores formed under illumination. The second involves macroporous Si formed in low-doped *p* type Si, and the third covers all micropores formed under illumination [63, 64]. Doping type, HF concentration, and applied voltage determine the size and geometry of the pores. In general, smoothness and pores size increase by decreasing the concentration of the electrochemical solution, using ethanol as a diluting agent or by increasing the current density [54]. However, increasing the pore size decreases the interpore connection and the degree of branching [44]. For the development of nanoporous materials, it is necessary to control the pore size, shape, and distribution, since the rate of degradation increases with the porosity of the material. An excellent summary of all manifestations of pores in silicon is reviewed by Föll et al., where pores from 1 to 10 nm are reported to be the typical dimension of the sponge-like perfection and cylindrical face morphology [65]. In addition, samples

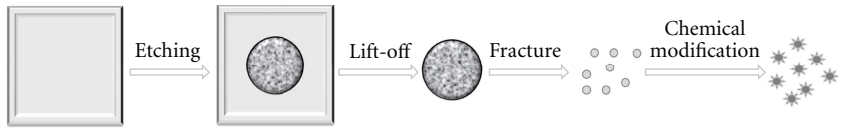

Figure 3: Schematic representation of the fabrication of pSi. Following the electrochemical anodization of the silicon wafer, the porous layer can be separated from the substrate by a secondary current pulse. Ultrasonic fracture is the common method for the conversion of the pSi layer in microparticles that can then be subsequently treated by chemical modification methods.

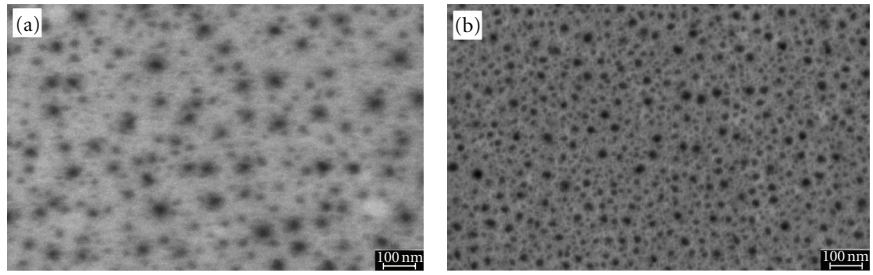

(a) (b)

Figure 4: Field emission-scanning electron microscopy images of porous silicon samples following anodization with current densities of (a) 5 mA and (b) 10 mA.

with higher porosity have shown to possess higher surface area and consequently cover larger groups of Si-Hx [66]. Morphology and pore size of Si structures are typically characterized by field emission-scanning electron microscopy (FE-SEM) as shown in Figure 4.

4. Porous Si Surface Modification

Surface chemistry of silicon is an area of strong interest, not only for the possibility of exciting technological application but also from a basic perspective. pSi bulk crystalline and nanostructure forms are used in a range of biomedical applications such as tissue engineering, cell culture, biosensing and as drug delivery device. The material's surface plays an important role during the degradation of this in vivo. As such, the stability of porous Si in aqueous medias is affected by the surface chemistry, its compatibility with tissue, and its affinity for different biomolecular species [18]. The development of the concept of pSi surface modification occurred as it became evident that the material's surface was unstable without any chemical adjustment [67]. Typically pSi is oxidized in normal conditions of humidity, temperature, and composition of ambient air. The oxidation process changes the pSi surface from hydrophobic to hydrophilic due to the formation of an oxide monolayer [68]. At physiological pH and temperature, oxidation process is enhanced increasing further the formation of the silicon oxide monolayer. This property has been used to study the oxidation-induced release of attached fluorophore molecules such as the anticancer drug doxorubicin [69]. The semiconducting silicon matrix typically quenches the fluorescence of this drug, but the fluorescence intensity increases with the growth of the insulating silicon oxide layer (oxidation of silicon). The recovery of fluorescence and the molecule released can then be monitored in real time by fluorescence microscopy. Nevertheless, pSi surface modification is usually required in order to control pSi degradation rate and to increase stability and optical properties at the same time as modifying the character hydrophobic and hydrophilic of the surface [70–73].

Following electrochemical anodization, the surface of pSi presents hydrogen-terminated compounds (Si-H, Si-H_2, and Si-H_3) [74], fluorine species, and oxygen impurities from the storage in ambient air [32]. pSi surfaces are typically modified by oxidation in gas phase [75, 76], hydrosilylation [77], thermal carbonization [78], and grafting [18]. These have shown to significantly improve the capabilities of pSi as a controlled and localized drug delivery device [79]. Few reviews have covered extensively the surface modification of pSi [32, 54, 80].

4.1. Oxidation. Typically during oxidation, the hydrogen atoms are replaced by oxygen atoms, and the surface character changes from hydrophobic to hydrophilic. This newer attraction for water provides a more convenient environment for substances dissolved in water such as drugs, converting porous Si in an ideal drug delivery device under physiological conditions [44].

Both thermal and chemical oxidations are common methods. Typically, thermal oxidation produces Si–O bonds following oxidation for few hours at 300°C, and pSi appears completely oxidized at around 750–800°C [18]. Chemical oxidation is also used for surface stabilization, using reagents that contain nitrogen such as nitric acid and pyridine [75, 81, 82] or other reagents like ozone hydrogen peroxide, halogen and dimethyl sulfoxide (DMSO) [83, 84]. DMSO is employed for slow oxidation of pSi at room temperature (Figure 5), which generates a stable oxide layer, and to

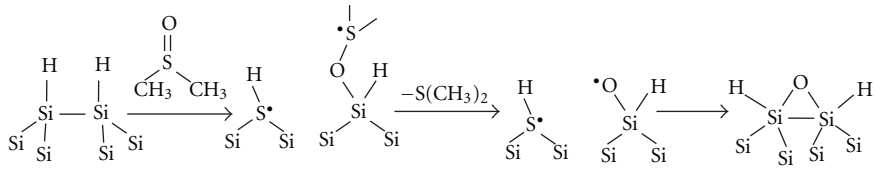

Figure 5: Mechanism of oxidation of pSi by dimethyl sulfoxide. The nucleophilic attack of the sulfoxide occurs at the most reactive Si–Si bonds, forming two radical structures that then react with each other forming a more stable Si–O bond.

expand the porous for loading dexamethasone [39]. Anodic oxidation and photonic oxidation are also sometimes used, but thermal and chemical oxidation are more easily implemented [44].

Oxidation of pSi has been investigated at different temperatures and during exposure to humid and dry air, water, vapors with pyridine and other solutions. Thermal oxidation is a simple method since no chemicals are required. Several groups have shown the suitability of thermal treatments for drug delivery devices, where the stability is increased [85], chemical reactions with the load prevented [29], and cell damage reduced [34] without significant effects on the electrical properties [9]. However, chemical oxidation confers a further improved stability against environmental aging and a good electronic surface passivation to allow chemical functionalization [82]. Other surface chemical treatments include thermally hydrocarbonized [34, 86] and carbonized with acetylene [87]. Few studies have investigated in vitro the effect of surface chemical treatment. Santos et al. used with this purpose a human colon carcinoma cell line [34]. Thermally carbonized pSi was found to enhance the kinetics of furosemide release and to decrease the pH dependence of dissolution behavior [38]. Others have investigated the amount of ibuprofen loaded on pSi to observe the effect of surface treatment by thermal oxidation and thermal carbonization during different periods of storage at 30°C [33].

4.2. Hydrosilylation. Hydrosilylation of pSi was first demonstrated by Buriak et al. [88] and extensively studied since then [89–91]. Long hydrophobic alkynes and alkenes attack the hydride terminated pSi surfaces to produce Si–C bonds by either photochemical reaction, mediated by excitation [92], or by chemical reaction, catalyzed by Lewis acid [88]. The low electronegativity of C confers a greater stability to Si–C bonds compared with Si–O, which is easily attacked by nucleophiles. Freshly prepared pSi (with abundant Si–H bonds) must be used during hydrosilylation methods, and Schlenk tubes and vacuum techniques are required to eliminate the formation of Si–O bonds by oxidation of the surface [54]. In the effort to develop a chemical method that provides stabilization of the pSi without significant loss of the photoemissive properties, Stewart and Buriak succeeded using a white light-promoted reaction that enabled the hydrosilylation [92]. De Smet et al. proposed a mechanism of the formation of Si–C bonded monolayers on silicon by reaction of alkenes with hydrogen-terminated pSi surfaces, via the same radical chain process as at single-crystal surfaces [93].

Alternatively, microwave irradiation has been used to chemically modify hydrogen-terminated pSi in an attempt to simplify common hydrosilylation methods, typically performed in the Schlenk tube under vacuum conditions for up to 1 hour. The microwave technique not only produces highly stable organic monolayers, but also allows the introduction of different functional groups and greatly reduced reaction times (approximately 10 minutes). Furthermore, the rate of the hydrosilylation reaction was increased, and a higher surface coverage obtained with the use of microwaves as an energy source [94]. Common organic compounds used during hydrosilylation techniques are dodecene, undecylenic, methoxy, trimethylsiloxy, and folate [76, 95–97].

4.3. Chemical or Electrochemical Grafting of Si–C Bonds. Grafting by covalent attachment is another way for chemically modifying the surface using Grignard, alkyl, or aryl lithium reagents [98]. Dense monolayers are prepared on the silicon surface by 1-alkene or 1-alkynes and diacylperoxides [99], followed by oligoethyleneglycol (OEG), polyethylene glycol (PEG), or other chemical species employed to graft the pSi surface. Activated ester monolayers have also been covalently attached to modify pSi surfaces [100]. OEG has been grafted on pSi surface through thermal hydrosylilation reaction with different alkenes species [84, 91]. PEG can be covalently attached onto pSi by Si–C bonds, increasing the hydrophilic character of the Si surfaces [54, 101]. Higher hydrophilic character has shown a stronger ability of the Si surface to admit sucrose and bovine serum albumin (BSA) [101], or other species such as drugs [102].

Typically, two steps are involved in the modification by covalent attachment of Si surfaces, the production of an intermediate surface, which acts as an attachment site for another molecule and the attachment of the molecule itself [103, 104].

In general, surface modification establishes the surface chemistry at the same time that it provides the exact chemical structure required [88]. Electroluminescent properties of pSi were stabilized using thermal oxidation treatments, where the Si–H bonds on the Si surface were replaced by more stable silicon-carbon (Si–C) and silicon-oxygen (Si–O–C) bonds [9].

5. Biocompatibility and Biodegradability

Nanostructures, capable of circulating in the body, are potentially the ideal solution for many diagnostic and therapeutic applications. Nontoxic, noncarcinogenic, nonantigenic

and nonmutagenic are the requirements of biocompatible materials [5]. pSi has exhibited extraordinary qualities for application in biological field as a drug delivery system due to its biocompatibility and biodegradability [78], low toxicity and solubility [54]. Nanomaterials for medical application require inoffensive disposal from the body, once they have reached their diagnostic or treatment goal, following a reasonable time after implantation [78, 86]. Biocompatibility, the ability of a biomaterial to remain in the human body without causing any undesirable effect, is one of the main advantages of pSi, together with its bioresorbability [39]. Safe intravenous administration of Si nanoparticles was reported with no change in plasma levels of renal and hepatic biomarkers as well as 23 plasma cytokines [106]. Orthosilicic acid ($Si(OH)_4$), a nontoxic, soluble silicon degradation product, is naturally found in numerous tissues and can be absorbed by the human body [79]. Some studies reported an excess of silica acid in urine samples excreted from the subjects monitored [41, 78, 107]. The complete dissolution and nontoxicity of a Si-implanted structure was investigated in vivo in the eye of a living rabbit as intraocular drug delivery device [74]. The low toxicity of Si structures was also reported in human colon carcinoma and murine microphage cells, suggesting these to be a suitable candidate for oral drug delivery application [76]. The slow degradation of Si in physiological fluid and the capability of this to be controlled with the porosity of the Si structure (biodegradable with porosity >70% and bioactive with porosity <70%) explain the extremely low concentration of silicic acid during in vivo studies [44]. Lumeniscent pSi nanostructures in a mouse model self-destructed into particles that could be cleared by the kidneys in relatively short period and without causing any toxicity effect [78]. This is extremely important for chronic use, where unlike most of the optically active materials (carbon nanotubes, gold nanoparticles and quantum dots), that cannot be metabolized or self-destructed, there is no need for excretion or surgical removal after their administration.

Alternatively, a purification procedure has recently been reported, capable of reducing the concentration of residual impurities to levels acceptable for biomedical applications while preserving the required photoactivity of the Si particles [108]. Wesselinova has discussed further some of the toxicity features in a recent review [109].

6. Drug Loading with Porous Silicon

Drugs loaded into pSi nanostructures have the potential to deliver the appropriate concentration at the appropriate location to minimize side effects. In general, the process of loading the drug in the nanoporous structure is performed through capillary action by dropping the drug solution on the device surface or by immersing the device in the drug solution [5, 21, 110]. Typically, sonication of the solution is required to enhance the intake of the drug by the device. The three most common methods for loading drugs into pSi implant are described in this section: covalent attachment, physical trapping, and spontaneous adsorption.

6.1. Covalent Attachment. Covalent attachment is the most robust approach for loading drugs into porous matrix. Typically, organic molecules that contain carboxyl species on the distal end of terminal alkenes are used during grafting. The hydrosilylation reaction between the end of alkenes and Si surface leaves the carboxyl terminal free, where the drug payload can be directly attached, or alternatively, this is attached via the PEG linker [91, 101]. Typically, acid and succinimidyl functional groups are added on the porous Si surface. The reaction of hydrogen-terminated surface with undecylenic acid under thermal condition results in an organic monolayer covalently joined to the surface through Si–C bonds and terminal COOH functional group [91]. The pSi surface modified by thermal hydrosilylation promotes the attachment of different-size molecule such as proteins and enzyme to the surface [111, 112]. Aminoacids and anticancer drugs such as doxorubicin, covalently attached onto pSi matrix, have been investigated in vitro [69, 113, 114]. While this method arguably presents the strongest attachment, the release of the drug requires breaking the covalent bonds or degrading the porous matrix. Hence, it is necessary to perform activity assays to ensure that the active principle of the drug is still effective following the disentanglement process [54].

6.2. Physical Trapping by Oxidation. The oxidation process causes Si to expand to accommodate the extra volume of O atoms and hence the pores shrink, trapping the drug molecules inside those. In recent years, the oxidation of pSi has been the subject of extensive studies since deliberated oxidation increases the stability of pSi surface [82]. Oxidation of freshly prepared Si surfaces has been induced by a range of solutions such as ammonia and pyridine [82, 115]. IR-spectroscopy and photoluminescence have been used to study the influence of the etching of the oxide matrix of porous nanocomposite Si/SiOx structures by HF vapors, which cause a significant decrease in the volume of a film and a partial additional oxidation of its surface [116].

6.3. Spontaneous Adsorption. Spontaneous adsorption of the drug molecules into the matrix pores consists of a simple immersion of the porous Si structure into the drug solution. Loading of drug molecules such as ibuprofen, gentamicin, and BSA onto mesoporous silicon has been investigated [37, 40]. pSi isoelectric point is found at pH of 2, so it is generally negatively charged with most of the solutions used [117]. At the appropriate pH, pSi spontaneously adsorbs various positively charged molecules such as immunoglobulin G (IgH) [118] and protein A [119]. The hydrophobic surface can be extremely advantageous for the adsorption and delivery of small hydrophobic molecules such as doxorubicin [41], dexamethasone [39], porphyrins [120], or BSA [40]. The surface chemistry can control the affinity of pSi particles for a particular molecule, and hence the amount of drug loaded and the rate of release. Adsorption is recognized as an optimal technique for drug loading since it does not require high mechanical energy [120]. This can be performed at room temperature without exposing the drug to harsh chemical conditions, and the nanoparticles are recovered

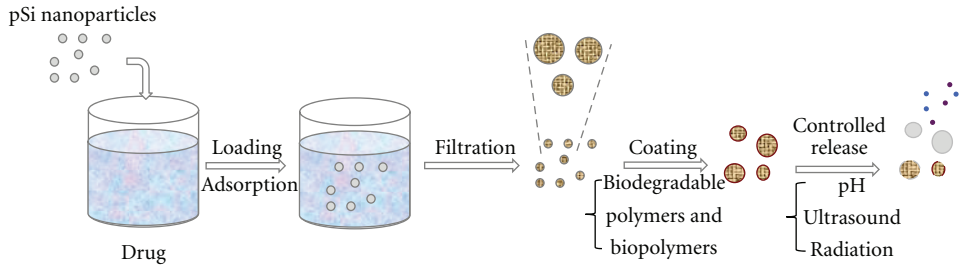

Figure 6: Schematic representation of drug loading and coating of pSi. Spontaneous adsorption of the drug molecules into the matrix pores consists of a simple immersion of the pSi structure into the drug solution. The particles are then recovered by filtration and coated with a range of biodegradable polymers for controlled release.

with basic filtration procedures [121] (Figure 6). However, it is not feasible for long release periods, since the attachment is weaker than covalent or physical trapping. Electrostatic adsorption is typically used when rapid drug delivery rates are required as this increases with time at alkaline pH and temperatures of 37°C [122]. However, in a recent review a monoclonal antibody bevacizumab (Avastin), spontaneously adsorbed on the nanostructure, provided a sustained release over a period of one month, and the electrostatic adsorption allowed bevacizumab to be concentrated [123].

7. Coating Nanoporous Silicon for Drug Release Control

Surface coatings offer an effective method to control the drug release from porous materials. These materials can be coated with films that surround the drug and control its release rate due to the diffusion process of the drug through the film [22]. In general, nanoparticles as drug delivery devices are coated with hydrophilic polymers/surfactants and biodegradable copolymers with hydrophilic segments [5]. Some of the materials used for coating are polyethylene glycol, polyethylene oxide, poloxamer, and poloxamine, polysorbate and lauryl ethers [124, 125]. Porous layers oxidize rapidly and degrade in short time, hence coating increases the stability of the material and improves the drug release [126]. Hydroxyapatite coatings have shown to increase the bioactivity of pSi [127]. Silica gel has been used for coating pSi substrates, which enhances the photoluminescence properties, and can then be used for in vivo monitoring of the delivery systems [128]. Silica xerogel coatings proved to be easy, flexible, and an efficient way for the controlled release of vitamin B1 from mesoporous silicon structures [22]. Other studies demonstrated the benefits of silica xerogel as controlled release material for the treatment of bone infection [129], and recently, it has been suggested as a coating for metallic implantable materials [130]. Other coatings used for in vitro studies include polymeric matrix of dextran for the release in vitro of two types of anticancer drugs, dacarbazine and bleomycin [105], chitosan polysaccharides to slow down the release of insulin [120] and BSA for capping the antibiotic vancomycin from pSi [131]. The use of biopolymers that are cleaved by specific proteases such as zein (derived from maize) can be potentially used as a highly selective drug delivery system for specific tissues or organs (Figure 6) [124, 132, 133].

Alternatively, since pores size can be controlled by varying fabrication factors, pSi has been used as a template for other materials. pSi composites have shown to improve the mechanical stability and the control release rate [124]. Polymers selected to form the Si composite must be biocompatible and biodegradable. In some cases the composite itself is used as a carrier [125], whereas in others only the polymer (formed with Si template, which is then removed) is the drug delivery system [124]. Some of the polymers used are polycaprolactone and poly(N-Isopropylacrylamide) [134]. Metals or metal oxides encapsulated into pSi have also been used, typically to generate a potential magnetic resonance imaging contrast agent [114, 135–138].

For controlled release, approaches such as pH-value-responsive release due to electrostatic interactions [136, 139] ultrasound to fracture and remove the porous layer [53, 140], and microwave radiation [141], are some of the current investigations. When porous Si matrix is oxidized, the release is also induced; however, these methods are limited to in vitro studies [69]. In general, drug release can easily be adjusted by changing pore properties [142].

8. Characterization and In Vivo Monitoring

Development of nanotechnology requires a high-quality characterization approach. Parameters such as pore distribution, diameter, and geometric shape of the pores determine the properties of pSi. In general, Si structures are characterized by imaging techniques, scanning electron microscopy (SEM), atomic force microscopy (AFM) [143–147], transmission Fourier transform infrared (FTIR) spectroscopy [148, 149], X-ray photoelectron spectroscopy (XPS), and contact angle measurements [18, 150, 151]. However, other techniques are required for monitoring drug loading and release.

Raman spectroscopy has been used during different steps of functionalization and protein grafting [112], while electrochemical impedance spectroscopy (EIS) and cyclic voltammetry measurements have been carried out to detect the electrochemical behavior of etched silicon surfaces [61, 113]. Drug loading has been monitored by optical interferometric measurements [123], differential scanning calorimetry

(DSC) [152] and high-pressure liquid chromatography (HPLC) which also determines the chemical purity of the loaded porous particles [105, 121].

During the etching process of Si, the optical properties can be adjusted with the variation of current density, tailoring in this way the refractive index of the nanostructures [102, 153]. The chemical treatment of Si surface also causes a change in optical properties, such as the strong decrease of the absorption in the visible spectrum observed in oxidized samples compared with nonoxidized ones. The excitons bound on these new Si–O bonds formed due to the oxidation are related to radiative transitions that can be measured by photoluminiscence [8]. The medium used also has been shown to affect the photoluminescence of nanoporous Si [154]. pSi have been long envisioned as integrated optoelectronic devices. The tunable light emission and room-temperature quantum efficiencies have led to the production of quantum dots structures that can display fluorescence [155]. This provides an advantage over other nanoparticles for in vivo sensing and therapeutic applications. Detailed description of the optical properties of pSi can be found elsewhere [156, 157], but basically consist of changes of refractivity and reflectivity index of the pSi layer. Spectrometers and interferometers are used to measure the reflectivity spectrum that can be resolved by fitting the reflectivity data by fast Fourier transform (FFT). Photonic crystals can be prepared by forming multiple pSi layers, known as rugate filters, which at predetermined wavelengths provides an intensive reflectivity peak to the pSi particles. A shift in the FFT peaks may indicate the loading or release of various biomolecules [119].

Degradation and drug delivery can also be monitored by digital imaging or spectroscopic techniques. Spectroscopic ellipsometry has been used during studies of adsorption of oxidized pSi [158]. Wu et al. used ultraviolet absorption spectroscopy to monitor the release of daunorubicin. The strong reflectivity peak generated by the pSi photonic crystal provides a distinctive color to the particles that evolved as the drug was released [159]. Others have followed in vitro antibody bevacizumab (Avastin) drug release profiles by enzyme-linked immunosorbent assay (ELISA), confirming that the antibody was released in its active, VEGF-binding form [123].

In case of in vivo studies, other techniques are required depending on the tissue itself. For example, the stability and toxicity of different chemically modified pSi particles injected into rabbit vitreous were studied by indirect ophthalmoscopy, biomicroscopy, tonometry, electroretinography and histology and showed no toxicity effects for a period up to 4 months [140]. Accumulation and degradation of luminescent pSi nanoparticles carrying a drug payload could be monitored in vivo in a mouse model due to the intrinsic near-infrared photoluminescence of these particles [78]. The near-infrared region of pSi reflectivity spectrum was used for the surveillance of the particles up to thickness of 1 mm through human tissues, which accounts for the advantage of these nanoparticles as in vivo self-reporting systems [124]. Alternatively, Fe_3O_4 nanoparticle, radiolabels or particles with intrinsic luminescence are embedded in pSi nanoparticles to be able to track them by near-infrared photoluminescence or positron emission tomography [53, 78, 114, 135, 160]. Nevertheless, there is still a need for further studies to overcome the physical barrier presented by the body such as blood vessel walls, organs' physical entrapment and phagocytic cells removal. Ideally, nanoparticles for drug delivery should not only overcome these barriers, but also allow real-time visualization, detection, and selectivity as well as rapid accumulation at damaged tissue and effective therapy [161].

9. Application in Cancer Therapies

Nanoscale devices are smaller than human cells, but similar in size to large biomolecules such as enzymes and receptors. Devices smaller than 50 nm can easily enter most of the cells, and when smaller than 20 nm they can move out of blood vessels while circulating through the human body [162]. This tissue accessibility is one of the most advantageous factors of nanomaterials in biomedical application. Nanoparticles for cancer therapies are particularly advantageous for their intrinsic properties as contrast agents, which can significantly improve diagnosis at the same time as delivering treatment agents [163]. Moreover, particles of certain size tend to accumulate more in cancer tissues than in normal tissues due to the leaky blood cells in tumors [164]. Approaches to deliver the nanoparticles specifically to the tumor site can be physical or mechanical, such as loading the nanoparticles with magnetic agents that can be directed by an external magnetic field (Figure 7). Chemical and biological approaches use molecules such as antibodies and enzymes that recognize the tumor cells since these express molecules on their surface that distinguishes them from normal cells [165]. This brings the possibility of delivering higher doses for longer periods of time, which allows the selective destruction of cancer cells without damaging the surrounding healthy cells.

Si nanoparticles optoelectronic properties are the reason for its use as biological interfaced devices [166]. This has made possible the incorporation of anticancer drugs in pSi devices for the specific release in tumor sites. Cisplatin combined with layers of hydroxyapatite on a pSi delivery device was tested in simulated body fluid for treatment of bone cancer [167] and the delivery of doxorubicin into human colon showed cytotoxic effects towards the carcinoma cells [41]. Chondroitin sulphate (a sulphated glycosaminoglycan), lactoferrin (globular protein with antimicrobial activity), and N-butyldeoxynojirimycin (an iminosugar that inhibits the growth of the CT-2A brain tumour) showed a significant decrease in tumoral cells density [114]. A recent study demonstrated the remarkable capability of a single drug-loaded porous nanoparticle modified with a targeting peptide that specifically binds to human hepatocellular carcinoma to kill a drug-resistant human carcinoma [168]. Superparamagnetic iron oxide nanoparticles and the anticancer drug doxorubicin loaded in pSi microparticles were delivered under the guidance of a magnetic field to in vitro human cervical cancer cells [53]. Particle sizes and magnetic properties have shown the ability to enhance the oncolytic

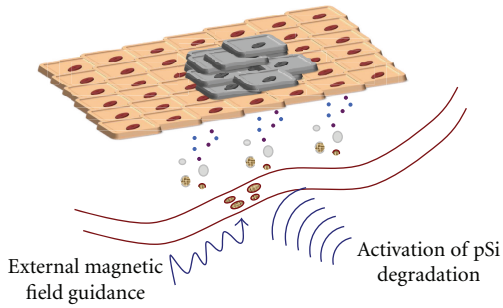

Figure 7: Schematic representation of targeted release on tumor cells. The pSi nanoparticles loaded with magnetic agents can be guided by external magnetic fields to the specific site and the drug released via photothermal activation.

potency of adenovirus [138] and magnetic mesoporous nanocomposites to produce magnetic hyperthermia, a very promising result for application as thermoseeds for cancer treatment [137].

The photothermal capacity of pSi nanoparticles in combination with a near-infrared laser has been employed to efficiently destroy cancer cells selectively without damaging the surrounding healthy cells during in vivo animal studies [169–171]. This same property has allowed researchers to treat cancer cells with pSi prepared as photosensitizers, exhibiting a 45% cell death rate compared with 10% in control experiments [172]. The inhibition of the proliferation of cancer cells when placed on pSi with 10–100 nm nanostructures and the complete destruction of these during additional ultrasonic exposure was demonstrated [173], leading to new possibilities for the application of Si as photo- and sono-sensitizers for cancer therapy [174] (Figure 7). The attachment and long-term viability of the three types of human cancer cell lines onto nanostructured oxidized pSi substrates are also being investigated [175]. A synergistic effect of combined chemo- and photo-thermotherapy was found at moderate power intensity of near-infrared irradiation based on the doxorubicin release and the photothermal effect of gold magnetic core/mesoporous silica shell nanostructure [136].

Other studies showed the endocytosis process of Si nanoparticles releasing their content into the cells in response to lysosomal acidity during in vitro human pancreatic carcinoma studies [176] and the therapeutic efficacy of liposomal encapsulated silicon-RNA [177]. Fluorescent polymers encapsulated inside silica-shell and recovered with folic acid have recently shown to enhance significantly the uptake by breast cancer cells, conferring a great potential for early detection of cancer [178].

10. Future Trends

pSi has shown its superiority in a wide range of technological applications over the last 50 years. More recently Si nanoparticles have been proposed for applications in biomedical and pharmaceutical fields as drug delivery and sensing systems. The simplicity of its fabrication and surface modification methods, its low cytotoxicity and its optical properties have put these at the forefront of implantable drug delivery devices [179]. The optical properties of porous Si provides an advantage over other nanoparticles, since these can be detected in vivo with imaging techniques, without the need for a label. Furthermore, its optical reflectivity can be used for the development of sensing devices. In fact, Si has been used extensively for electronics and micro- and nanochips have been fabricated for biosensign applications [80, 132, 180]. Biocompatibility issues with the biorecognition molecule and the metals of some of the components of the sensors are currently slowing down the implementation of this in vivo. Membranes that impart permeability and decrease biofouling of the electrodes are investigated and porous Si provides again an interesting solution [181, 182]. Microfluidic devices to deliver small volumes of fluids have also seen the advantageous properties of porous Si [183]. Aptamer-incorporated nanoparticles have been envisioned as delivery systems where the drug release is controlled via aptamer molecular gates [184]. With the advance of science and technology, closed-loop systems are seen as the next generation of therapeutic devices, where sensing mechanisms would trigger and control the release of the drug at a specific site or when reaching a certain threshold.

The diversity of pSi allows the combination of microfluidics, microarray biosensors, drug delivery [185], and high-resolution imaging techniques that can provide detailed images of cancerous cells and lesions [186], thus creating systems with incredible synergetic capabilities for therapeutic and diagnosis applications.

Acknowledgments

The authors acknowledge the support of the Material Innovations and Nano-Electronics (MINE) and Biosignal Processing (BSP) Research Groups and the financial funding of Ministry of Higher Education of Malaysia and Universiti Teknologi Malaysia for this paper.

References

[1] K. Khosravi-Darani, A. Pardakhty, H. Honarpisheh, V. S. N. M. Rao, and M. R. Mozafari, "The role of high-resolution imaging in the evaluation of nanosystems for bioactive encapsulation and targeted nanotherapy," *Micron*, vol. 38, no. 8, pp. 804–818, 2007.

[2] D. S. Kumar, D. Banji, B. B. Madhavi, V. Bodanapu, S. Dondapati, and A. P. Sri, "Nanostructured porous silicon—a novel biomaterial for drug delivery," *International Journal of Pharmacy and Pharmaceutical Sciences*, no. 2, pp. 8–16, 2009.

[3] A. E. Garcia-Bennett, "Synthesis, toxicology and potential of ordered mesoporous materials in nanomedicine," *Nanomedicine*, vol. 6, no. 5, pp. 867–877, 2011.

[4] D. Losic and S. Simovic, "Self-ordered nanopore and nanotube platforms for drug delivery applications," *Expert Opinion on Drug Delivery*, vol. 6, no. 12, pp. 1363–1381, 2009.

[5] E. Gultepe, D. Nagesha, S. Sridhar, and M. Amiji, "Nanoporous inorganic membranes or coatings for sustained drug delivery in implantable devices," *Advanced Drug Delivery Reviews*, vol. 62, no. 3, pp. 305–315, 2010.

[6] D. J. Lockwood, A. Wang, and B. Bryskiewicz, "Optical absorption evidence for quantum confinement effects in porous silicon," *Solid State Communications*, vol. 89, no. 7, pp. 587–589, 1994.

[7] S. M. Weiss and P. M. Fauchet, "Porous silicon one-dimensional photonic crystals for optical signal modulation," *IEEE Journal on Selected Topics in Quantum Electronics*, vol. 12, no. 6, pp. 1514–1519, 2006.

[8] A. V. Pavlikov, A. V. Lartsev, I. A. Gayduchenko, and V. Yu Timoshenko, "Optical properties of materials based on oxidized porous silicon and their applications for UV protection," *Microelectronic Engineering*, vol. 90, pp. 96–98, 2012.

[9] B. Gelloz, H. Sano, R. Boukherroub, D. D. M. Wayner, D. J. Lockwood, and N. Koshida, "Stabilization of porous silicon electroluminescence by surface passivation with controlled covalent bonds," *Applied Physics Letters*, vol. 83, no. 12, pp. 2342–2344, 2003.

[10] N. Gabouze, S. Belhousse, H. Cheraga et al., "CO_2 and H_2 detection with a CH_x/porous silicon-based sensor," *Vacuum*, vol. 80, no. 9, pp. 986–989, 2006.

[11] B. Mahmoudi, N. Gabouze, M. Haddadi et al., "The effect of annealing on the sensing properties of porous silicon gas sensor: use of screen-printed contacts," *Sensors and Actuators B*, vol. 123, no. 2, pp. 680–684, 2007.

[12] J. J. Saarinen, S. M. Weiss, P. M. Fauchet, and J. E. Sipe, "Optical sensor based on resonant porous silicon structures," *Optics Express*, vol. 13, no. 10, pp. 3754–3764, 2005.

[13] M. Lee and P. M. Fauchet, "Two-dimensional silicon photonic crystal based biosensing platform for protein detection," *Optics Express*, vol. 15, no. 8, pp. 4530–4535, 2007.

[14] S. Kim, T. Rim, K. Kim et al., "Silicon nanowire ion sensitive field effect transistor with integrated Ag/AgCl electrode: PH sensing and noise characteristics," *Analyst*, vol. 136, no. 23, pp. 5012–5016, 2011.

[15] P. J. Ko, R. Ishikawa, T. Takamura et al., "Porous-silicon photonic-crystal platform for the rapid detection of nanosized superparamagnetic beads for biosensing applications," *Nanoscience and Nanotechnology Letters*, vol. 3, no. 5, pp. 612–616, 2011.

[16] M. J. Jawad, M. R. Hashim, and N. K. Ali, "Synthesis, structural, and optical properties of electrochemically deposited GeO2 on porous silicon," *Electrochemical and Solid-State Letters*, vol. 14, no. 2, pp. D17–D19, 2011.

[17] C. Talamonti, M. Bruzzi, L. Marrazzo, D. Menichelli, M. Scaringella, and M. Bucciolini, "Bidimensional silicon dosimeter: development and characterization," *Nuclear Instruments and Methods in Physics Research, Section A*, vol. 658, no. 1, pp. 84–89, 2011.

[18] S. D. Alvarez, A. M. Derfus, M. P. Schwartz, S. N. Bhatia, and M. J. Sailor, "The compatibility of hepatocytes with chemically modified porous silicon with reference to in vitro biosensors," *Biomaterials*, vol. 30, no. 1, pp. 26–34, 2009.

[19] A. A. Agrawal, B. J. Nehilla, K. V. Reisig et al., "Porous nanocrystalline silicon membranes as highly permeable and molecularly thin substrates for cell culture," *Biomaterials*, vol. 31, no. 20, pp. 5408–5417, 2010.

[20] W. Bogaerts, P. de Heyn, T. van Vaerenbergh et al., "Silicon microring resonators," *Laser and Photonics Reviews*, vol. 6, no. 1, pp. 47–73, 2012.

[21] A. B. Foraker, R. J. Walczak, M. H. Cohen, T. A. Boiarski, C. F. Grove, and P. W. Swaan, "Microfabricated porous silicon particles enhance paracellular delivery of insulin across intestinal caco-2 cell monolayers," *Pharmaceutical Research*, vol. 20, no. 1, pp. 110–116, 2003.

[22] Z. Wu, Y. Jiang, T. Kim, and K. Lee, "Effects of surface coating on the controlled release of vitamin B1 from mesoporous silica tablets," *Journal of Controlled Release*, vol. 119, no. 2, pp. 215–221, 2007.

[23] I. M. Kempson, T. J. Barnes, and C. A. Prestidge, "Use of TOF-SIMS to study adsorption and loading behavior of methylene blue and papain in a nano-porous silicon layer," *Journal of the American Society for Mass Spectrometry*, vol. 21, no. 2, pp. 254–260, 2010.

[24] A. Uhlir, "Electrolytic shaping of Germanium and silicon," *The Bell System Technical*, pp. 333–347, 1956.

[25] Y. Watanabe, Y. Arita, T. Yokoyama, and Y. Igarashi, "Formation and properites of porous silicon and its application," *Journal of the Electrochemical Society*, vol. 122, no. 10, pp. 1351–1355, 1975.

[26] K. Imai, "A new dielectric isolation method using porous silicon," *Solid State Electronics*, vol. 24, no. 2, pp. 159–164, 1981.

[27] L. T. Canham, "Bioactive silicon structure fabrication through nanoetching techniques," *Advanced Materials*, vol. 7, no. 12, pp. 1033–1037, 1995.

[28] S. P. Hudson, R. F. Padera, R. Langer, and D. S. Kohane, "The biocompatibility of mesoporous silicates," *Biomaterials*, vol. 29, no. 30, pp. 4045–4055, 2008.

[29] M. Kilpeläinen, J. Riikonen, M. A. Vlasova et al., "In vivo delivery of a peptide, ghrelin antagonist, with mesoporous silicon microparticles," *Journal of Controlled Release*, vol. 137, no. 2, pp. 166–170, 2009.

[30] D. M. Reffitt, R. Jugdaohsingh, R. P. H. Thompson, and J. J. Powell, "Silicic acid: its gastrointestinal uptake and urinary excretion in man and effects on aluminium excretion," *Journal of Inorganic Biochemistry*, vol. 76, no. 2, pp. 141–147, 1999.

[31] S. P. Low, K. A. Williams, L. T. Canham, and N. H. Voelcker, "Evaluation of mammalian cell adhesion on surface-modified porous silicon," *Biomaterials*, vol. 27, no. 26, pp. 4538–4546, 2006.

[32] J. Salonen, A. M. Kaukonen, J. Hirvonen, and V. P. Lehto, "Mesoporous silicon in drug delivery applications," *Journal of Pharmaceutical Sciences*, vol. 97, no. 2, pp. 632–653, 2008.

[33] T. Limnell, J. Riikonen, J. Salonen et al., "Surface chemistry and pore size affect carrier properties of mesoporous silicon microparticles," *International Journal of Pharmaceutics*, vol. 343, no. 1-2, pp. 141–147, 2007.

[34] H. A. Santos, J. Riikonen, J. Salonen et al., "In vitro cytotoxicity of porous silicon microparticles: effect of the particle concentration, surface chemistry and size," *Acta Biomaterialia*, vol. 6, no. 7, pp. 2721–2731, 2010.

[35] L. M. Bimbo, E. Mäkilä, T. Laaksonen et al., "Drug permeation across intestinal epithelial cells using porous silicon nanoparticles," *Biomaterials*, vol. 32, no. 10, pp. 2625–2633, 2011.

[36] M. Pradeepa, P. Venkatesan, E. Menaka, K. Rajendran, and S. Kumaran, "Fabrication of porous siliconnanoparticles to attach clorgyline for drug delivery," in *Proceedings of the International Conference of Bioscience, Biochemistry and Bioinformatics (IPCBEE '11)*, IACSIT Press, Singapore, 2011.

[37] J. Salonen, L. Laitinen, A. M. Kaukonen et al., "Mesoporous silicon microparticles for oral drug delivery: loading and release of five model drugs," *Journal of Controlled Release*, vol. 108, no. 2-3, pp. 362–374, 2005.

[38] A. M. Kaukonen, L. Laitinen, J. Salonen et al., "Enhanced in vitro permeation of furosemide loaded into thermally carbonized mesoporous silicon (TCPSi) microparticles," *European Journal of Pharmaceutics and Biopharmaceutics*, vol. 66, no. 3, pp. 348–356, 2007.

[39] E. J. Anglin, M. P. Schwartz, V. P. Ng, L. A. Perelman, and M. J. Sailor, "Engineering the chemistry and nanostructure of porous silicon fabry-pérot films for loading and release of a steroid," *Langmuir*, vol. 20, no. 25, pp. 11264–11269, 2004.

[40] L. Tay, N. L. Rowell, D. Poitras, J. W. Fraser, D. J. Lockwood, and R. Boukherroub, "Bovine serum albumin adsorption on passivated porous silicon layers," *Canadian Journal of Chemistry*, vol. 82, no. 10, pp. 1545–1553, 2004.

[41] L. Vaccari, D. Canton, N. Zaffaroni, R. Villa, M. Tormen, and E. di Fabrizio, "Porous silicon as drug carrier for controlled delivery of doxorubicin anticancer agent," *Microelectronic Engineering*, vol. 83, no. 4-9, pp. 1598–1601, 2006.

[42] W. Lai, J. Garino, and P. Ducheyne, "Silicon excretion from bioactive glass implanted in rabbit bone," *Biomaterials*, vol. 23, no. 1, pp. 213–217, 2002.

[43] G. Korotcenkov and B. K. Cho, "Silicon porosification: state of the art," *Critical Reviews in Solid State and Materials Sciences*, vol. 35, no. 3, pp. 153–260, 2010.

[44] J. Salonen and V. P. Lehto, "Fabrication and chemical surface modification of mesoporous silicon for biomedical applications," *Chemical Engineering Journal*, vol. 137, no. 1, pp. 162–172, 2008.

[45] P. Kumar, "Effect of silicon crystal size on photoluminescence appearance in porous silicon," *ISRN Nanotechnology*, vol. 2011, Article ID 163168, 6 pages, 2011.

[46] T. Dittrich, S. Rauscher, V. Y. Timoshenko et al., "Ultrathin luminescent nanoporous silicon on n-Si:pH dependent preparation in aqueous NH4F solutions," *Applied Physics Letters*, vol. 67, p. 1134, 1995.

[47] N. K. Ali, M. D. R. Hashim, and A. Abdul Aziz, "Fabrication and characterization of uniform quantum size porous silicon," *Materials Science Forum*, vol. 517, pp. 232–236, 2006.

[48] N. K. Ali, M. R. Hashim, A. Abdul Aziz, and I. Hamammu, "Method of controlling spontaneous emission from porous silicon fabricated using pulsed current etching," *Solid-State Electronics*, vol. 52, no. 2, pp. 249–254, 2008.

[49] Y. Liu, Z. H. Xiong, Y. Liu et al., "A novel method of fabricating porous silicon material: ultrasonically enhanced anodic electrochemical etching," *Solid State Communications*, vol. 127, no. 8, pp. 583–588, 2003.

[50] V. Lehmann and U. Gösele, "Porous silicon formation: a quantum wire effect," *Applied Physics Letters*, vol. 58, no. 8, pp. 856–858, 1991.

[51] M. Hajj-Hassan, M. C. Cheung, and V. P. Chodavarapu, "Ultra-thin porous silicon membranes fabricated using dry etching," *Micro and Nano Letters*, vol. 6, no. 4, pp. 226–228, 2011.

[52] G. X. Zhang, "Porous silicon: morphology and formation mechanisms," in *Modern Aspects of Electrochemistry*, C. G. Vayenas, R. E. White, and M. E. Gamboa-Adelco, Eds., pp. 65–133, Springer, 2006.

[53] L. Gu, J. H. Park, K. H. Duong, E. Ruoslahti, and M. J. Sailor, "Magnetic luminescent porous silicon microparticles for localized delivery of molecular drug payloads," *Small*, vol. 6, no. 22, pp. 2546–2552, 2010.

[54] E. J. Anglin, L. Cheng, W. R. Freeman, and M. J. Sailor, "Porous silicon in drug delivery devices and materials," *Advanced Drug Delivery Reviews*, vol. 60, no. 11, pp. 1266–1277, 2008.

[55] A. E. Pap, K. Kordás, J. Vähäkangas, and A. Uusimäki, "Optical properties and applications of porous silicon," in *Proceedings of the IEEE/LEOS Optical MEMS: International Conference on Optical MEMS and Their Applications*, pp. 139–140, August 2005.

[56] R. J. Archer, "Stain films on silicon," *Journal of Physics and Chemistry of Solids*, vol. 14, pp. 104–110, 1960.

[57] K. H. Beckmann, "Investigation of the chemical properties of stain films on silicon by means of infrared spectroscopy," *Surface Science*, vol. 3, no. 4, pp. 314–332, 1965.

[58] S. Shih, K. H. Jung, T. Y. Hsieh, J. Sarathy, J. C. Campbell, and D. L. Kwong, "Photoluminescence and formation mechanism of chemically etched silicon," *Applied Physics Letters*, vol. 60, no. 15, pp. 1863–1865, 1992.

[59] S. Litvinenko, S. Alekseev, V. Lysenko et al., "Hydrogen production from nano-porous Si powder formed by stain etching," *International Journal of Hydrogen Energy*, vol. 35, no. 13, pp. 6773–6778, 2010.

[60] K. W. Kolasinski, "Charge transfer and nanostructure formation during electroless etching of silicon," *Journal of Physical Chemistry C*, vol. 114, no. 50, pp. 22098–22105, 2010.

[61] A. S. Mogoda, Y. H. Ahmad, and W. A. Badawy, "Characterization of stain etched p-type silicon in aqueous HF solutions containing HNO_3 or $KMnO_4$," *Materials Chemistry and Physics*, vol. 126, no. 3, pp. 676–684, 2011.

[62] T. Karacali, B. Cakmak, and H. Efeoglu, "Aging of porous silicon and the origin of blue shift," *Optics Express*, vol. 11, no. 10, pp. 1237–1242, 2003.

[63] C. Lévy-Clément, "Macro porous micro structures including silicon," in *Semiconductor Electrodes and Photoelectrochemistry*, S. Licht, Ed., WILEY-VCH, Weinheim, Germany, 2002.

[64] X. G. Zhang, "Morphology and formation mechanisms of porous silicon," *Journal of the Electrochemical Society*, vol. 151, no. 1, pp. C69–C80, 2004.

[65] H. Föll, M. Christophersen, J. Carstensen, and G. Hasse, "Formation and application of porous silicon," *Materials Science and Engineering R*, vol. 39, no. 4, 2002.

[66] V. Lysenko, J. Vitiello, B. Remaki, D. Barbier, and V. Skryshevsky, "Nanoscale morphology dependent hydrogen coverage of meso-porous silicon," *Applied Surface Science*, vol. 230, no. 1-4, pp. 425–430, 2004.

[67] E. A. Petrova, K. N. Bogoslovskaya, L. A. Balagurov, and G. I. Kochoradze, "Room temperature oxidation of porous silicon in air," *Materials Science and Engineering B*, vol. 69, pp. 152–156, 2000.

[68] R. B. Bjorklund, S. Zangooie, and H. Arwin, "Adsorption of surfactants in porous silicon films," *Langmuir*, vol. 13, no. 6, pp. 1440–1445, 1997.

[69] E. C. Wu, J. H. Park, J. Park, E. Segal, F. Cunin, and M. J. Sailor, "Oxidation-triggered release of fluorescent molecules or drugs from mesoporous Si microparticles," *ACS Nano*, vol. 2, no. 11, pp. 2401–2409, 2008.

[70] N. K. Ali, M. R. Hashim, and A. A. Aziz, "Effects of surface passivation in porous silicon as H_2 gas sensor," *Solid-State Electronics*, vol. 52, no. 7, pp. 1071–1074, 2008.

[71] N. K. Ali, M. R. Hashim, and A. Abdul Aziz, "Pulse current electrochemical deposition of silicon for porous silicon capping to improve hardness and stability," *Electrochemical and Solid-State Letters*, vol. 12, no. 3, pp. D11–D14, 2009.

[72] J. Mönkäre, J. Riikonen, E. Rauma, J. Salonen, V. P. Lehto, and K. Järvinen, "In vitro dissolution methods for hydrophilic and hydrophobic porous silicon microparticles," *Pharmaceutics*, vol. 3, no. 2, pp. 315–325, 2011.

[73] C. M. Thompson, A. M. Ruminski, A. Garcia Sega, M. J. Sailor, and G. M. Miskelly, "Preparation and characterization of pore-wall modification gradients generated on porous silicon photonic crystals using diazonium salts," *Langmuir*, vol. 27, no. 14, pp. 8967–8973, 2011.

[74] K. L. Jarvis, T. J. Barnes, and C. A. Prestidge, "Surface chemical modification to control molecular interactions with porous silicon," *Journal of Colloid and Interface Science*, vol. 363, no. 1, pp. 327–333, 2011.

[75] J. Tuura, M. Björkqvist, J. Salonen, and V. P. Lehto, "Electrically isolated thermally carbonized porous silicon layer for humidity sensing purposes," *Sensors and Actuators B*, vol. 131, no. 2, pp. 627–632, 2008.

[76] L. M. Bimbo, M. Sarparanta, H. A. Santos et al., "Biocompatibility of thermally hydrocarbonized porous silicon nanoparticles and their biodistribution in rats," *ACS Nano*, vol. 4, no. 6, pp. 3023–3032, 2010.

[77] E. V. Rogozhina, D. A. Eckhoff, E. Gratton, and P. V. Braun, "Carboxyl functionalization of ultrasmall luminescent silicon nanoparticles through thermal hydrosilylation," *Journal of Materials Chemistry*, vol. 16, no. 15, pp. 1421–1430, 2006.

[78] J. H. Park, L. Gu, G. Von Maltzahn, E. Ruoslahti, S. N. Bhatia, and M. J. Sailor, "Biodegradable luminescent porous silicon nanoparticles for in vivo applications," *Nature Materials*, vol. 8, no. 4, pp. 331–336, 2009.

[79] R. B. Vasani, S. J. P. McInnes, M. A. Cole, A. M. M. Jani, A. V. Ellis, and N. H. Voelcker, "Stimulus-responsiveness and drug release from porous silicon films ATRP-grafted with poly(N-isopropylacrylamide)," *Langmuir*, vol. 27, no. 12, pp. 7843–7853, 2011.

[80] M. J. Sailor and E. C. Wu, "Photoluminescence-based sensing with porous silicon films, microparticles, and nanoparticles," *Advanced Functional Materials*, vol. 19, no. 20, pp. 3195–3208, 2009.

[81] J. H. Song and M. J. Sailor, "Chemical modification of crystalline porous silicon surfaces," *Comments on Inorganic Chemistry*, vol. 21, no. 1-3, pp. 69–84, 1999.

[82] G. Mattei, V. Valentini, and V. A. Yakovlev, "An FTIR study of porous silicon layers exposed to humid air with and without pyridine vapors at room temperature," *Surface Science*, vol. 502-503, pp. 58–62, 2002.

[83] J. H. Song and M. J. Sailor, "Dimethyl sulfoxide as a mild oxidizing agent for porous silicon and its effect on photoluminescence," *Inorganic Chemistry*, vol. 37, no. 13, pp. 3355–3360, 1998.

[84] M. J. Sweetman, F. J. Harding, S. D. Graney, and N. H. Voelcker, "Effect of oligoethylene glycol moieties in porous silicon surface functionalisation on protein adsorption and cell attachment," *Applied Surface Science*, vol. 257, no. 15, pp. 6768–6775, 2011.

[85] E. Pastor, J. Salonen, V. P. Lehto, and E. Matveeva, "Electrochemically induced bioactivity of porous silicon functionalized by acetylene," *Physica Status Solidi (A)*, vol. 206, no. 6, pp. 1333–1338, 2009.

[86] P. Kinnari, E. Mäkilä, T. Heikkilä, J. Salonen, J. Hirvonen, and H. A. Santos, "Comparison of mesoporous silicon and non-ordered mesoporous silica materials as drug carriers for itraconazole," *International Journal of Pharmaceutics*, vol. 414, no. 1-2, pp. 148–156, 2011.

[87] J. Salonen, M. Björkqvist, and J. Paski, "Temperature-dependent electrical conductivity in thermally carbonized porous silicon," *Sensors and Actuators A*, vol. 116, no. 3, pp. 438–441, 2004.

[88] J. M. Buriak, M. P. Stewart, T. W. Geders et al., "Lewis acid mediated hydrosilylation on porous silicon surfaces," *Journal of the American Chemical Society*, vol. 121, no. 49, pp. 11491–11502, 1999.

[89] A. B. Sieval, A. L. Demirel, J. W. M. Nissink et al., "Highly stable Si-C linked functionalized monolayers on the silicon (100) surface," *Langmuir*, vol. 14, no. 7, pp. 1759–1768, 1998.

[90] J. M. Schmeltzer, L. A. Porter, M. P. Stewart, and J. M. Buriak, "Hydride, abstraction initiated hydrosilylation of terminal alkenes and alkynes on porous silicon," *Langmuir*, vol. 18, no. 8, pp. 2971–2974, 2002.

[91] R. Boukherroub, J. T. C. Wojtyk, D. D. M. Wayner, and D. J. Lockwood, "Thermal hydrosilylation of undecylenic acid with porous silicon," *Journal of the Electrochemical Society*, vol. 149, no. 2, pp. H59–H63, 2002.

[92] M. P. Stewart and J. M. Buriak, "Exciton-mediated hydrosilylation on photoluminescent nanocrystalline silicon," *Journal of the American Chemical Society*, vol. 123, no. 32, pp. 7821–7830, 2001.

[93] L. C. P. M. De Smet, H. Zuilhof, E. J. R. Sudhölter, L. H. Lie, A. Houlton, and B. R. Horrocks, "Mechanism of the hydrosilylation reaction of alkenes at porous silicon: experimental and computational deuterium labeling studies," *Journal of Physical Chemistry B*, vol. 109, no. 24, pp. 12020–12031, 2005.

[94] R. Boukherroub, A. Petit, A. Loupy, J. N. Chazalviel, and F. Ozanam, "Microwave-assisted chemical functionalization of hydrogen-terminated porous silicon surfaces," *Journal of Physical Chemistry B*, vol. 107, no. 48, pp. 13459–13462, 2003.

[95] M. Warntjes, C. Vieillard, F. Ozanam, and J. N. Chazalviel, "Electrochemical methoxylation of porous silicon surface," *Journal of the Electrochemical Society*, vol. 142, no. 12, pp. 4138–4142, 1995.

[96] V. M. Dubin, C. Vieillard, F. Ozanam, and J. N. Chazalviel, "Preparation and characterization of surface-modified luminescent porous silicon," *Physica Status Solidi (B)*, vol. 190, no. 1, pp. 47–52, 1995.

[97] F. Erogbogbo, K. T. Yong, I. Roy, G. X. Xu, P. N. Prasad, and M. T. Swihart, "Biocompatible luminescent silicon quantum dots for imaging of cancer cells," *ACS Nano*, vol. 2, no. 5, pp. 873–878, 2008.

[98] N. Y. Kim and P. E. Laibinis, "Derivatization of porous silicon by grignard reagents at room temperature," *Journal of the American Chemical Society*, vol. 120, no. 18, pp. 4516–4517, 1998.

[99] M. R. Linford, P. Fenter, P. M. Eisenberger, and C. E. D. Chidsey, "Alkyl monolayers on silicon prepared from 1-alkenes and hydrogen-terminated silicon," *Journal of the American Chemical Society*, vol. 117, no. 11, pp. 3145–3155, 1995.

[100] J. T. C. Wojtyk, K. A. Morin, R. Boukherroub, and D. D. M. Wayner, "Modification of porous silicon surfaces with activated ester monolayers," *Langmuir*, vol. 18, no. 16, pp. 6081–6087, 2002.

[101] M. P. Schwartz, F. Cunin, R. W. Cheung, and M. J. Sailor, "Chemical modification of silicon surfaces for biological applications," *Physica Status Solidi (A)*, vol. 202, no. 8, pp. 1380–1384, 2005.

[102] K. A. Kilian, T. Böcking, K. Gaus, M. Gal, and J. J. Gooding, "Si-C linked oligo(ethylene glycol) layers in silicon-based photonic crystals: optimization for implantable optical materials," *Biomaterials*, vol. 28, no. 20, pp. 3055–3062, 2007.

[103] H. Jiang, S. Yuan, G. Liu, and Q. Wang, "Theoretical study on reactions of alkene molecules on H-terminated Si(1 1 1):

density functional theory and ab initio molecular dynamics," *Chemical Physics Letters*, vol. 438, no. 1-3, pp. 53–58, 2007.

[104] N. Chiboub, R. Boukherroub, N. Gabouze et al., "Covalent grafting of polyaniline onto aniline-terminated porous silicon," *Optical Materials*, vol. 32, no. 7, pp. 748–752, 2010.

[105] A. Bragaru, M. Kusko, M. Simion et al., "Fabrication and in vitro testing of porous silicon microcarriers," *Proceedings of the International Semiconductor Conference*, vol. 1, Article ID 6095730, pp. 117–120, 2011.

[106] T. Tanaka, B. Godin, R. Bhavane et al., "In vivo evaluation of safety of nanoporous silicon carriers following single and multiple dose intravenous administrations in mice," *International Journal of Pharmaceutics*, vol. 402, no. 1-2, pp. 190–197, 2010.

[107] J. F. Popplewell, S. J. King, J. P. Day et al., "Kinetics of uptake and elimination of silicic acid by a human subject: a novel application of 32Si and accelerator mass spectrometry," *Journal of Inorganic Biochemistry*, vol. 69, no. 3, pp. 177–180, 1998.

[108] S. Koynov, R. N. Pereira, I. Crnolatac et al., "Purification of nano-porous silicon for biomedical applications," *Advanced Engineering Materials*, vol. 13, no. 6, pp. B225–B233, 2011.

[109] D. Wesselinova, "Current major cancer targets for nanoparticle systems," *Current Cancer Drug Targets*, vol. 11, no. 2, pp. 164–183, 2011.

[110] A. A. Ayon, M. Cantu, K. Chava et al., "Drug loading of nanoporous TiO2 films," *Biomedical Materials*, vol. 1, no. 4, article no. L01, pp. L11–L15, 2006.

[111] B. R. Hart, S. E. Létant, S. R. Kane, M. Z. Hadi, S. J. Shields, and J. G. Reynolds, "New method for attachment of biomolecules to porous silicon," *Chemical Communications*, no. 3, pp. 322–323, 2003.

[112] M. Hiraoui, M. Guendouz, N. Lorrain, A. Moadhen, L. Haji, and M. Oueslati, "Spectroscopy studies of functionalized oxidized porous silicon surface for biosensing applications," *Materials Chemistry and Physics*, vol. 128, no. 1-2, pp. 151–156, 2011.

[113] S. Sam, J. N. Chazalviel, A. C. Gouget-Laemmel et al., "Covalent immobilization of amino acids on the porous silicon surface," *Surface and Interface Analysis*, vol. 42, no. 6-7, pp. 515–518, 2010.

[114] I. Kleps, T. Ignat, M. Miu et al., "Nanostructured Silicon particles for medical applications," *Journal of Nanoscience and Nanotechnology*, vol. 10, no. 4, pp. 2694–2700, 2010.

[115] J. R. Dorvee, A. M. Derfus, S. N. Bhatia, and M. J. Sailor, "Manipulation of liquid droplets using amphiphilic, magnetic one-dimensional photonic crystal chaperones," *Nature Materials*, vol. 3, no. 12, pp. 896–899, 2004.

[116] V. A. Dan'ko, S. O. Zlobin, I. Z. Indutnyi et al., "Influence of the HF vapor treatment on the structure and luminescence properties of porous si/siox nanocomposites," *Ukrainian Journal of Physics*, vol. 55, no. 9, pp. 1038–1044, 2010.

[117] G. A. Parks, "The isoelectric points of solid oxides, solid hydroxides, and aqueous hydroxo complex systems," *Chemical Reviews*, vol. 65, no. 2, pp. 177–198, 1965.

[118] M. P. Schwartz, C. Yu, S. D. Alvarez et al., "Using an oxidized porous silicon interferometer for determination of relative protein binding affinity through non-covalent capture probe immobilization," *Physica Status Solidi (A)*, vol. 204, no. 5, pp. 1444–1448, 2007.

[119] C. Pacholski, M. Sartor, M. J. Sailor, F. Cunin, and G. M. Miskelly, "Biosensing using porous silicon double-layer interferometers: reflective interferometric fourier transform spectroscopy," *Journal of the American Chemical Society*, vol. 127, no. 33, pp. 11636–11645, 2005.

[120] E. Pastor, E. Matveeva, A. Valle-Gallego, F. M. Goycoolea, and M. Garcia-Fuentes, "Protein delivery based on uncoated and chitosan-coated mesoporous silicon microparticles," *Colloids and Surfaces B*, vol. 88, no. 2, pp. 601–609, 2011.

[121] J. Hirvonen, T. Laaksonen, L. Peltonen, H. Santos et al., "Feasibility of silicon-based mesoporous materials for oral drug delivery applications," *Dosis*, vol. 24, no. 2, pp. 129–149, 2008.

[122] S. H. C. Anderson, H. Elliott, D. J. Wallis, L. T. Canham, and J. J. Powell, "Dissolution of different forms of partially porous silicon wafers under simulated physiological conditions," *Physica Status Solidi (A)*, vol. 197, no. 2, pp. 331–335, 2003.

[123] J. S. Andrew, E. J. Anglin, E. C. Wu et al., "Sustained release of a monoclonal antibody from electrochemically prepared mesoporous silicon oxide," *Advanced Functional Materials*, vol. 20, no. 23, pp. 4168–4174, 2010.

[124] Y. Y. Li, F. Cunin, J. R. Link et al., "Polymer replicas of photonic porous silicon for sensing and drug delivery applications," *Science*, vol. 299, no. 5615, pp. 2045–2047, 2003.

[125] K. S. Soppimath, T. M. Aminabhavi, A. R. Kulkarni, and W. E. Rudzinski, "Biodegradable polymeric nanoparticles as drug delivery devices," *Journal of Controlled Release*, vol. 70, no. 1-2, pp. 1–20, 2001.

[126] T. Islam, D. D. Saha, P. M. Z. Hasan, and S. S. Islam, "γ-Al_2O_3-coated porous silicon for trace moisture detection," *IEEE Sensors Journal*, vol. 11, no. 4, pp. 882–887, 2011.

[127] C. Shaoqiang, Z. Ziqiang, Z. Jianzhong et al., "Hydroxyapatite coating on porous silicon substrate obtained by precipitation process," *Applied Surface Science*, vol. 230, no. 1-4, pp. 418–424, 2004.

[128] Y. Posada, L. F. Fonseca, P. Vallejo, L. S. Miguel, O. Resto, and I. Balberg, "Enhancement of the photoluminescence properties of porous silicon by silica gel coating," *Journal of Applied Physics*, vol. 99, no. 11, Article ID 114313, 2006.

[129] S. Radin, G. El-Bassyouni, E. J. Vresilovic, E. Schepers, and P. Ducheyne, "In vivo tissue response to resorbable silica xerogels as controlled-release materials," *Biomaterials*, vol. 26, no. 9, pp. 1043–1052, 2005.

[130] C. M. Han, E. J. Lee, H. E. Kim, Y. H. Koh, and J. H. Jang, "Porous TiO2 films on Ti implants for controlled release of tetracycline-hydrochloride (TCH)," *Thin Solid Films*, 2011.

[131] L. A. Perelman, C. Pacholski, Y. Y. Li, M. S. Van Nieuwenhz, and M. J. Sailor, "pH-triggered release of vancomycin from protein-capped porous silicon films," *Nanomedicine*, vol. 3, no. 1, pp. 31–43, 2008.

[132] M. M. Orosco, C. Pacholski, and M. J. Sailor, "Real-time monitoring of enzyme activity in a mesoporous silicon double layer," *Nature Nanotechnology*, vol. 4, no. 4, pp. 255–258, 2009.

[133] J. Tang, I. I. Slowing, Y. Huang et al., "Poly(lactic acid)-coated mesoporous silica nanosphere for controlled release of venlafaxine," *Journal of Colloid and Interface Science*, vol. 360, no. 2, pp. 488–496, 2011.

[134] P. Mukherjee, M. A. Whitehead, R. A. Senter, D. Fan, J. L. Coffer, and L. T. Canham, "Biorelevant mesoporous silicon/polymer composites: directed assembly, disassembly, and controlled release," *Biomedical Microdevices*, vol. 8, no. 1, pp. 9–15, 2006.

[135] J. M. Kinsella, S. Ananda, J. S. Andrew et al., "Enhanced magnetic resonance contrast of Fe_3O_4 nanoparticles trapped in a porous silicon nanoparticle host," *Advanced Materials*, vol. 23, no. 36, pp. H248–H253, 2011.

[136] M. Ma, H. Chen, Y. Chen et al., "Au capped magnetic core/mesoporous silica shell nanoparticles for combined photothermo-/chemo-therapy and multimodal imaging," *Biomaterials*, vol. 33, no. 3, pp. 989–998, 2012.

[137] D. Arcos, V. Fal-Miyar, E. Ruiz-Hernández et al., "Supramolecular mechanisms in the synthesis of mesoporous magnetic nanospheres for hyperthermia," *Journal of Materials Chemistry*, vol. 22, no. 1, pp. 64–72, 2012.

[138] N. Tresilwised, P. Pithayanukul, P. S. Holm et al., "Effects of nanoparticle coatings on the activity of oncolytic adenovirus-magnetic nanoparticle complexes," *Biomaterials*, vol. 33, no. 1, pp. 256–269, 2012.

[139] L. A. Perelman, *Biosensing and Composites*, 2008.

[140] L. Cheng, E. Anglin, F. Cunin et al., "Intravitreal properties of porous silicon photonic crystals: a potential self-reporting intraocular drug-delivery vehicle," *British Journal of Ophthalmology*, vol. 92, no. 5, pp. 705–711, 2008.

[141] X. X. Zhang, H. Y. Sang, J. X. Shi, M. L. Gong, J. Y. Zhou, and Z. R. Qiu, "A novel approach for infrared optical activation of neodymium-doped porous silicon using microwave radiation," *Journal of Materials Chemistry*, vol. 11, no. 2, pp. 696–698, 2001.

[142] J. Roine, M. Murtomaa, and J. Salonen, "Electroencapsulation of mesoporous silicon particles for controlled oral drug delivery," in *Proceedings of the ESA Annual Meeting on Electrostatics*, vol. 12, pp. 1–6, 2010.

[143] G. Craciun, A. Dafinei, C. Vrinceanu, E. Vasile, and C. Flueraru, "On the morphology of porous silicon layers obtained by electrochemical method," in *Proceedings of the 1995 International Semiconductor Conference, CAS'95*, pp. 331–334, October 1995.

[144] J. Jakubowicz, "Study of surface morphology of electrochemically etched n-Si (111) electrodes at different anodic potentials," *Crystal Research and Technology*, vol. 38, no. 3-5, pp. 313–319, 2003.

[145] A. S. Al Dwayyan, M. N. Khan, M. S. Al Salhi et al., "Properties of luminescent silicon nanocrystallines doped sol gel for laser applications," *Journal of Materials Science and Engineering*, vol. 3, no. 12, pp. 44–52, 2009.

[146] A. K. Patel, "Use of electrochemically machined porous silicon to trap protein molecule," *Research Journal of Applied Sciences, Engineering and Technology*, vol. 2, no. 3, pp. 208–215, 2010.

[147] H. Wanyika, E. Gatebe, P. Kioni, Z. Tang, and Y. Gao, "Synthesis and characterization of ordered mesoporous silica nanoparticles with tunable physical properties by varying molar composition of reagents," *African Journal of Pharmacy and Pharmacology*, vol. 5, no. 21, pp. 2402–2410, 2011.

[148] D. B. Mawhinney, J. A. Glass, and J. T. Yates, "FTIR study of the oxidation of porous silicon," *Journal of Physical Chemistry B*, vol. 101, no. 7, pp. 1202–1206, 1997.

[149] W. J. Salcedo, F. J. Ramirez Fernandez, and E. Galeazzo, "Structural characterization of photoluminescent porous silicon with FTIR spectroscopy," *Brazilian Journal of Physics*, vol. 27, no. 4, pp. 158–161, 1997.

[150] D. J. Guo, J. Wang, W. Tan, S. J. Xiao, and Z. D. Dai, "Macroporous silicon templated from silicon nanocrystallite and functionalized Si(single bond)H reactive group for grafting organic monolayer," *Journal of Colloid and Interface Science*, vol. 336, no. 2, pp. 723–729, 2009.

[151] Y. Xia, B. Liu, S. Zhong, and C. Li, "X-ray photoelectron spectroscopic studies of black silicon for solar cell," *Journal of Electron Spectroscopy and Related Phenomena*, vol. 184, no. 11-12, pp. 589–592, 2012.

[152] J. Salonen, J. Paski, K. Vähä-Heikkilä, T. Heikkilä, M. Björkqvist, and V. P. Lehto, "Determination of drug load in porous silicon microparticles by calorimetry," *Physica Status Solidi (A)*, vol. 202, no. 8, pp. 1629–1633, 2005.

[153] B. Sciacca, E. Secret, S. Pace et al., "Chitosan-functionalized porous silicon optical transducer for the detection of carboxylic acid-containing drugs in water," *Journal of Materials Chemistry*, vol. 21, no. 7, pp. 2294–2302, 2011.

[154] A. S. Al Dwayyan, M. Naziruddin Khan, and M. S. Al Salhi, "Optical characterization of chemically etched nanoporous silicon embedded in sol-gel matrix," *Journal of Nanomaterials*, no. 7, Article ID 713203, 2012.

[155] R. T. Collins, P. M. Fauchet, and M. A. Tischler, "Porous silicon: from luminescence to leds," *Physics Today*, vol. 50, no. 1, pp. 24–31, 1997.

[156] D. J. Lockwood, "Optical properties of porous silicon," *Solid State Communications*, vol. 92, no. 1-2, pp. 101–112, 1994.

[157] W. Theiß, "Optical properties of porous silicon," *Surface Science Reports*, vol. 29, no. 3-4, pp. 91–192, 1997.

[158] S. Zangooie, M. Schubert, C. Trimble, D. W. Thompson, and J. A. Woollam, "Infrared ellipsometry characterization of porous silicon Bragg reflectors," *Applied Optics*, vol. 40, no. 6, pp. 906–912, 2001.

[159] E. C. Wu, J. S. Andrew, L. Cheng, W. R. Freeman, L. Pearson, and M. J. Sailor, "Real-time monitoring of sustained drug release using the optical properties of porous silicon photonic crystal particles," *Biomaterials*, vol. 32, no. 7, pp. 1957–1966, 2011.

[160] M. Sarparanta, E. Mäkilä, T. Heikkilä, J. Salonen et al., "18F-labeled modified porous silicon particles for investigation of drug delivery carrier distribution in vivo with positron emission tomography," *Molecular Pharmaceutics*, vol. 8, no. 5, pp. 1799–1806, 2011.

[161] M. T. Neves-Petersen, G. P. Gajula, and S. B. Petersen, "UV light effects on proteins: from photochemistry to nanomedicine," in *Molecular Photochemistry—Various Aspects*, S. Saha, Ed., pp. 125–158, InTech, 2012.

[162] M. S. Arayne and N. Sultana, "Review: nanoparticles in drug delivery for the treatment of cancer," *Pakistan Journal of Pharmaceutical Sciences*, vol. 19, no. 3, pp. 258–268, 2006.

[163] L. Smith, Z. Kuncic, K. Ostrikov, and S. Kumar, "Nanoparticles in cancer imaging and therapy," *Journal of Nanomaterials*, vol. 2012, Article ID 891318, 7 pages, 2012.

[164] D. Peer, J. M. Karp, S. Hong, O. C. Farokhzad, R. Margalit, and R. Langer, "Nanocarriers as an emerging platform for cancer therapy," *Nature Nanotechnology*, vol. 2, no. 12, pp. 751–760, 2007.

[165] N. S. Barakat, D. BinTaleb, and A. S. Al Salehi, "Target nanoparticles: an appealing drug delivery platform," *Journal of Nanomedicine & Nanotechnology*, vol. 3, no. 3, pp. 1–9, 2012.

[166] A. H. Mayne, S. C. Bayliss, P. Barr, M. Tobin, and L. D. Buckberry, "Biologically interfaced porous silicon devices," *Physica Status Solidi (A)*, vol. 182, no. 1, pp. 505–513, 2000.

[167] X. Li, J. L. Coffer, Y. Chen, R. F. Pinizzotto, J. Newey, and L. T. Canham, "Transition metal complex-doped hydroxyapatite layers on porous silicon," *Journal of the American Chemical Society*, vol. 120, no. 45, pp. 11706–11709, 1998.

[168] C. E. Ashley, E. C. Carnes, G. K. Phillips et al., "The targeted delivery of multicomponent cargos to cancer cells by nanoporous particle-supported lipid bilayers," *Nature Materials*, vol. 10, no. 5, pp. 389–397, 2011.

[169] C. Hong, J. Lee, M. Son, S. S. Hong, and C. Lee, "In-vivo cancer cell destruction using porous silicon nanoparticles," *Anti-Cancer Drugs*, vol. 22, no. 10, pp. 971–977, 2011.

[170] C. Hong, J. Lee, H. Zheng, S. S. Hong, and C. Lee, "Porous silicon nanoparticles for cancer photothermotherapy," *Nanoscale Research Letters*, vol. 6, no. 1, pp. 1–8, 2011.

[171] C. Lee, C. Hong, J. Lee, M. Son, and S. S. Hong, "Comparison of oxidized porous silicon with bare porous silicon as a photothermal agent for cancer cell destruction based on in vitro cell test results," *Lasers in Medical Science*. In press.

[172] L. Xiao, L. Gu, S. B. Howell, and M. J. Sailor, "Porous silicon nanoparticle photosensitizers for singlet oxygen and their phototoxicity against cancer cells," *ACS Nano*, vol. 5, no. 5, pp. 3651–3659, 2011.

[173] L. A. Osminkina, E. N. Luckyanova, M. B. Gongalsky et al., "Effects of nanostructurized silicon on proliferation of stem and cancer cell," *Bulletin of Experimental Biology and Medicine*, pp. 1–5, 2011.

[174] L. A. Osminkina, M. B. Gongalsky, A. V. Motuzuk, V. Y. Timoshenko, and A. A. Kudryavtsev, "Silicon nanocrystals as photo- and sono-sensitizers for biomedical applications," *Applied Physics B*, pp. 1–4, 2011.

[175] T. Zeidman, R. Parush, N. Massad, and E. Segal, "Compatibility of cancer cells with nanostructured oxidized porous silicon substrates," *Physica Status Solidi (C)*, vol. 8, no. 6, pp. 1903–1907, 2011.

[176] M. Xue, X. Zhong, Z. Shaposhnik et al., "PH-operated mechanized porous silicon nanoparticles," *Journal of the American Chemical Society*, vol. 133, no. 23, pp. 8798–8801, 2011.

[177] R. E. Serda, B. Godin, E. Blanco, C. Chiappini, and M. Ferrari, "Multi-stage delivery nano-particle systems for therapeutic applications," *Biochimica et Biophysica Acta*, vol. 1810, no. 3, pp. 317–329, 2011.

[178] H. Tan, Y. Zhang, M. Wang et al., "Silica-shell cross-linked micelles encapsulating fluorescent conjugated polymers for targeted cellular imaging," *Biomaterials*, vol. 33, no. 1, pp. 237–246, 2012.

[179] P. Gardner, "Microfabricated nanochannel implantable drug delivery devices: trends, limitations and possibilities," *Expert Opinion on Drug Delivery*, vol. 3, no. 4, pp. 479–487, 2006.

[180] A. M. Giovannozzi, V. E. V. Ferrero, F. Pennecchi, S. J. Sadeghi, G. Gilardi, and A. M. Rossi, "P450-based porous silicon biosensor for arachidonic acid detection," *Biosensors and Bioelectronics*, 2011.

[181] T. A. Desai, D. J. Hansford, L. Leoni, M. Essenpreis, and M. Ferrari, "Nanoporous anti-fouling silicon membranes for biosensor applications," *Biosensors and Bioelectronics*, vol. 15, no. 9-10, pp. 453–462, 2000.

[182] L. M. Bonanno and E. Segal, "Nanostructured porous silicon-polymer-based hybrids: from biosensing to drug delivery," *Nanomedicine*, vol. 6, no. 10, pp. 1755–1770, 2011.

[183] J. Liu, X. Du, and X. Zhang, "Enzyme-inspired controlled release of cucurbit[7]uril nanovalves by using magnetic mesoporous silica," *Chemistry*, vol. 17, no. 3, pp. 810–815, 2011.

[184] V. C. Ozalp, F. Eyidogan, and H. A. Oktem, "Aptamer-gated nanoparticles for smart drug delivery," *Pharmaceuticals*, vol. 4, no. 8, pp. 1137–1157, 2011.

[185] Z. B. Liu, Y. Zhang, J. J. Yu, A. F. T. Mak, Y. Li, and M. Yang, "A microfluidic chip with poly(ethylene glycol) hydrogel microarray on nanoporous alumina membrane for cell patterning and drug testing," *Sensors and Actuators B*, vol. 143, no. 2, pp. 776–783, 2010.

[186] H. Xing, W. Bu, S. Zhang et al., "Multifunctional nanoprobes for upconversion fluorescence, MR and CT trimodal imaging," *Biomaterials*, vol. 33, no. 4, pp. 1079–1089, 2012.

Hindawi Publishing Corporation
Journal of Nanomaterials
Volume 2012, Article ID 715838, 7 pages
doi:10.1155/2012/715838

Research Article

Cytotoxicity of Carbon Nanotubes on J774 Macrophages Is a Purification-Dependent Effect

Silvia Lorena Montes-Fonseca,[1] Erasmo Orrantia-Borunda,[1] Alberto Duarte-Möller,[1] Antonia Luna-Velasco,[1] Manuel Román-Aguirre,[1] Carmen González Horta,[2] and Blanca Sánchez-Ramírez[2]

[1] *Departamento de Energías Renovables y Protección al Medio Ambiente, Centro de Investigación en Materiales Avanzados (CIMAV), Miguel de Cervantes 120, Complejo Industrial Chihuahua, 31109 Chihuahua, CHIH, Mexico*
[2] *Departamento de Biotecnología, Facultad de Ciencias Químicas, Universidad Autónoma de Chihuahua, 31125 Chihuahua, CHIH, Mexico*

Correspondence should be addressed to Erasmo Orrantia-Borunda, erasmo.orrantia@cimav.edu.mx

Received 16 February 2012; Revised 3 May 2012; Accepted 8 May 2012

Academic Editor: Krasimir Vasilev

The cytotoxicity of the carbon nanotubes (CNTs) is an important factor for the manufacture of nanovaccines. The aim of this work was to evaluate the relationship of the purification method of CNTs in cellular toxicity using macrophages (MOs) from the J774 cell line. Viability test was performed with MTT assays at 24 h of exposure at concentrations of 0.06, 0.6, and 6 mg/L of unpurified (UP-CNTs) or purified (P-CNTs) CNTs by two different methods: (1) reflux with 3M HNO_3 and (2) sonication in H_2SO_4/HNO_3. Characterization and COOH content of CNTs was performed using scanning electron microscopy, raman spectroscopy, and titration with $NaHCO_3$. P-$CNTs_1$ had lengths >100 μm and 2.76% COOH content, while P-$CNTs_2$ had lengths >1 μm and 7% COOH content. This last particle showed a lower toxic effect. The results suggest that the lenght and COOH content are important factors in the toxicity of the CNTs.

1. Introduction

Carbon nanotubes (CNTs) are cylindrical nanoparticles, which have unique structure and fascinating physical and chemical properties allowing them to be used in biotechnological applications [1, 2]. Due to their ability to penetrate plasmatic membrane [3], CNTs may be used as particulate substances carriers in biological systems [4, 5], as well as in biosensors to detect cellular tumors [6], and for nanovaccine production [7, 8]. Nevertheless, these applications are limited by the high insolubility of CNTs, which conduct to generate CNTs deposition in cells, organs, and tissues, causing toxic effects [9]. Several studies have demonstrated that CNTs provoke cellular apoptosis and a decrease in viability in lung tumor cells [10], human fibroblasts [11], human T lymphocytes [12], and umbilical vein endothelial cells [13]. It has also been observed that CNTs induce the production of reactive oxygen species in human epidermal keratinocytes (HEKs) [14] and macrophages cells [15, 16]. Some authors attribute these effects to the hydrophobic nature of the CNTs, fabrication residues, and high surface area and size [17]. According to this last point, many authors converge with the notion that the length of CNTs is an additional factor for cellular toxicity. Poland et al. [18] found that intraperitoneal exposure of mice to multiwall CNTs with length of 20 μm or longer resulted in asbestosis-like pathology.

Some authors recommend to purify the CNTs previous to test in a biological system, in order to eliminate the fabrication residues. Saito et al. [19] performed a purification technique using a mixture of concentrated H_2SO_4/HNO_3 3 : 1 v/v and sonication in a water bath for 22 h. They obtained shortened CNTs with length <1 μm and found that these can be easily dispersed in polar solvents such as ethanol, dimethyl sulfoxide, and dimethyl formamide. In addition, acid-treated CNTs are excellent candidates for functionalization with amino compounds [19] to be used in

biomedical applications. However, studies about toxicity of these particles in biological systems have not been done. Therefore, the aim of this work was to evaluate the relationship of the purification method of CNTs in cellular toxicity using macrophages (MOs) from the J774 cell line.

2. Methods

2.1. Synthesis and Purification of CNTs. CNTs were synthesized by spray pyrolysis, using toluene and ferrocene as the carbon source and the catalyst, respectively [20]. For the first group of CNTs ($CNTs_1$) the synthesis time was 20 min and the purification was carried out with 0.1 g of unpurified CNTs ($UP\text{-}CNTs_1$) and 150 mL of HNO_3 3 M. The mixture was dispersed by sonication for 90 min and refluxed for 24 h. Purified CNTs of the first group ($P\text{-}CNTs_1$) were filtered and washed with distilled water in an oven at 90°C for 8 h. For the second group of CNTs ($CNTs_2$) the synthesis time was 2 min and the purification method was as follows: 0.2 g of $UP\text{-}CNTs_2$ was suspended in 400 mL of a mixture of concentrated H_2SO_4 (90%)/HNO_3 (70%) 3 : 1 v/v and sonicated in a water bath for 48 h. The resultant $P\text{-}CNTs_2$ were collected with a polytetrafluoroenthylene filter with 450 nm pore size and washed four times with water and methanol, respectively. Finally, the $P\text{-}CNTs_2$ were dried at room temperature [19].

2.2. Characterization of CNTs. The CNTs were characterized by scanning electronic microscopy (SEM) in a JEOL SEM, model JSM-5800 LV equipped with an energy dispersive X-ray analyzer (for elemental analysis). The quality of the structure of CNTs was measured by Raman spectroscopy using a micro-Raman LabRAM HR, Horiba Jobn Yvon, coupled to Olympus BX-4 microscope. The laser line used to excite the sample was 632.8 nm and all measurements were performed at room temperature. The carboxyl groups (COOH) in the P-CNTs were measured by titration with $NaHCO_3$ base on a method established by Hu et al. [21], modified as follows: 0.1 g of $P\text{-}NTC_1$ and $P\text{-}NTC_2$ was stirred in 50 mL of 0.05 N $NaHCO_3$ aqueous solution. The mixture was then filtered through a membrane (pore size of 0.45 μm). The P-NTCs collected on the membrane were washed with deionized water to remove the $NaHCO_3$ residues. The combined filtrate and washings were added to 50 mL of 0.05 N aqueous HCl solution and boiled for 20 min to degas the CO_2 of the solution. After cooling to room temperature, the excess HCl in the solution was titrated with 0.05 N aqueous NaOH solution to reach a neutral pH 7.00 [21].

2.3. Viability Tests in J774 MOs Cell Line. Cell viability was determined using 3-(4,5-dimethylthiozol-2-yl)-2,5-diphenyltetrazolium bromide (MTT) assays (Sigma, St. Louis MI, USA) in 96-well plates, as described previously [22]. Briefly, 10^5 cells were cultivated in DMEM-HG supplemented with 10% heat-inactivated bovine fetal serum, 100 IU/mL of penicillin, 100 μm/mL of streptomycin, and 2 mM L-glutamine; MOs were interacted with $UP\text{-}CNTs_1$, $P\text{-}CNTs_1$, $UP\text{-}CNTs_2$, and $P\text{-}CNTs_2$ in supplemented DMEM-HG at concentrations of 0.06, 0.6, and 6 mg/L and sonicated for 30 min previous to cell interaction. Cultures were incubated for 24 h at 37°C in humid atmosphere at 5% CO_2. MOs without stimulus were used as control. At 20 h of cultivation time, 0.1 mg of MTT dissolved in sterile phosphate-buffered saline was added to each well and incubated for 4 h more. Cells were lyzed with acidified isopropanol and absorbances at 590 nm were quantified using a BioRad ELISA microreader.

Table 1: Analysis of elements found in unpurified (UP) or purified (P) samples of CNT_1 and CNT_2.

	$CNTs_1$% weight*		$CNTs_2$% weight*	
Element	$UP\text{-}CNTs_1$	$P\text{-}CNTs_1$	$UP\text{-}CNTs_2$	$P\text{-}CNTs_2$
C	94.83	93.23	95.56	75.98
O	1.26	4.26	1.22	22.21
Fe	3.89	1.12	3.23	1.81
Total	100	100	100	100

*Element content was determined by semiquantitative analysis of elemental composition.

2.4. Statistical Analysis. Statistical analysis was carried out through the Minitab software and using a one-way ANOVA in order to determine the difference between the MOs interactions with different CNTs at all the concentrations used.

3. Results and Discussion

3.1. Characterization of CNTs. The different groups of CNTs were characterized by SEM (Figure 1). The dimensions obtained for $UP\text{-}CNTs_1$ averaged 20 to 100 nm in diameter and 120 μm in length (Figures 1(a) and 1(c)). The $P\text{-}CNTs_1$ obtained by reflux with HNO_3 3 M showed better particle dispersion than $UP\text{-}CNTs_1$. Also open-end formations were favored in $P\text{-}CNTs_1$, but length was similar than for $UP\text{-}CNTs_1$. Semiquantitative analysis of elemental composition (Table 1) showed a 2.77% decrease in Fe content between unpurified and purified samples, as well a slight increase in O content from 1.26 to 4.26%. On other hand, the dimensions for $UP\text{-}CNTs_2$ averaged 20–40 nm in diameter and 30 μm in length (Figures 1(b) and 1(d)). $P\text{-}CNTs_2$ obtained by sonication with H_2SO_4/HNO_3 3 : 1 v/v showed a considerable decrease of their length from 30 μm to <1 μm (Figure 1(f)). Likewise, the semiquantitative analysis of elemental composition showed a 1.42% decrease in Fe content and an increase in O content from 1.22 to 22.21%, in $P\text{-}CNTs_2$ (Table 1).

These results indicates that both purification techniques encourage to an effective removal of Fe from the surface of the UP-CNTs. However, the length and the O content are quite different between $P\text{-}CNTs_1$ and $P\text{-}CNTs_2$. Although $P\text{-}CNTs_1$ showed an increase in O content, $P\text{-}CNTs_2$ had an increase of fivefold, indicating a greater addition of oxidized groups (COOH, OH, CO) on the surface of the CNTs [19, 23].

In order to confirm that the O content on the surface of the P-CNTs was related with the addition of COOH groups, these last were measured by tritration with $NaHCO_3$ as was indicated in the methodology section. The tritration results clearly showed that $P\text{-}CNTs_2$ had a higher percentage of

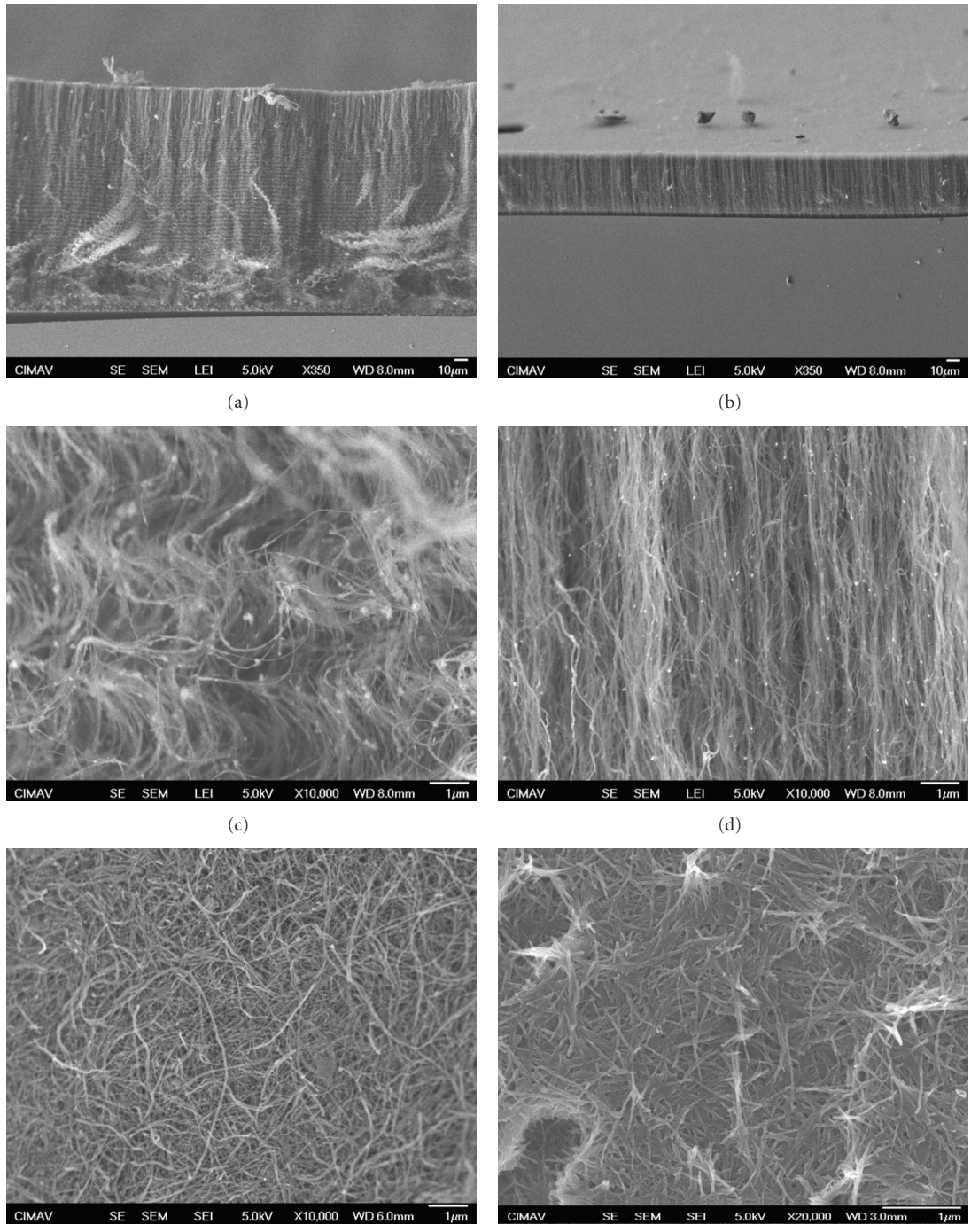

Figure 1: Photomicrophotographs of UP-CNTs and P-CNTs obtained by SEM. Microphotographs show length for UP-$CNTs_1$ and UP-$CNTs_2$ ((a), (b) resp.) and diameter for UP-$CNTs_1$ and UP-$CNTs_2$ ((c), (d) resp.). (e) and (f) are shown characteristics of P-$CNTs_1$ and P-$CNTs_2$ respectively.

COOH groups (7%) than in P-$CNTs_1$ (2.76%). This indicates that the acid purification process combined with sonication (used for P-$CNTs_2$) increased the formation of acid groups on the surface of P-CNTs due to the strong interaction of CNTs allowing open-end formations and promoting the oxidation of exposed carbon atoms [24].

On the other hand, the quality of the CNTs structures was determined by Raman spectroscopy. Figure 2 shows the raman spectra for UP-$CNTs_1$, UP-$CNTs_2$, P-$CNTs_1$, and P-$CNTs_2$. Each of them consists of two characteristic bands, namely, D-band at 1338 cm^{-1} and G-band at 1600 cm^{-1}. The G-band is a characteristic feature of the graphitic layers

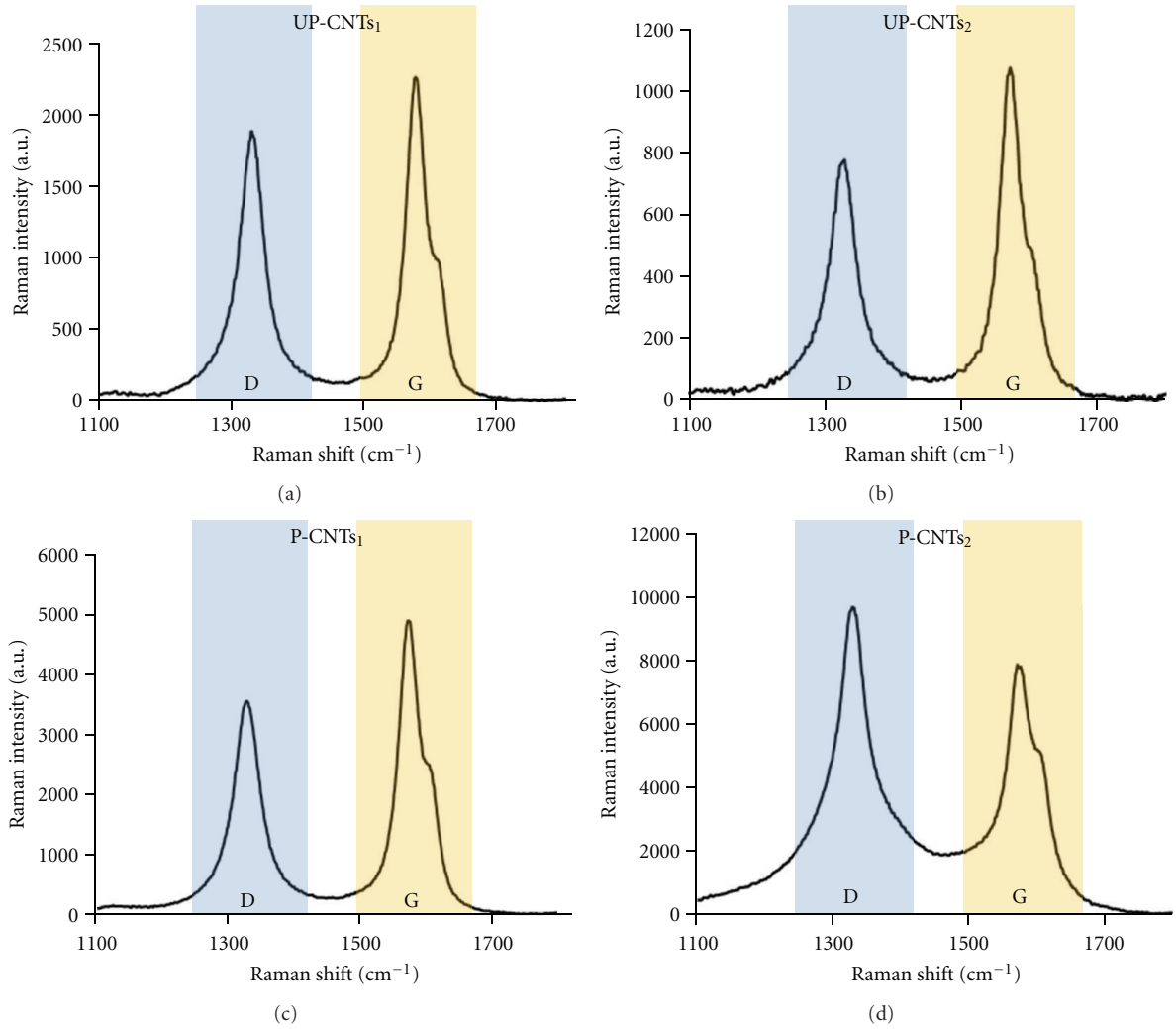

Figure 2: Raman spectra of CNTs samples. Different Raman spectra obtained from UP-CNTs$_1$ (a), UP-CNTs$_2$ (b), P-CNTs$_1$, (c) and P-CNTs (d). In each figure are shown the D-band at 1338 cm^{-1} and the G-band at 1600 cm^{-1} (laser excitation 632.8 nm).

and corresponds to the tangential vibration of the carbon atoms, while the D-band is a typical sign for defective graphitic structures and is usually attributed to the presence of amorphous or disordered carbon in the CNTs samples. The comparison of the ratios of these two peaks intensities (I_G/I_D) gives a measure of the quality of the samples. If bands have similar intensity this indicates a high quantity of structural defects [25, 26].

Based on the Raman spectra obtained for CNTs, it was observed that the UP-CNTs$_1$ had a D-band intensity higher than that obtained for UP-CNTs$_2$, and I_G/I_D ratio obtained for UP-CNTs$_1$ (1.19) was lower than ratio observed for UP-CNTs$_2$ (1.38). These data indicate that UP-CNTs$_2$ had better structural quality than UP-CNTs$_1$. In the case of the P-CNTs, a lower D-band intensity was obtained for P-CNTs$_1$; however I_G/I_D ratio (1.37) was higher compared with ratio obtained for P-CNTs$_2$ (I_G/I_D ratio =0.81). These results suggest that reflux purification process increases the structure quality of CNTs. These results agree with the observation that P-CNTs$_2$ had more open-end formations than P-CNTs$_1$.

3.2. Cell Viability of J774 MQ Cell Line. Viability results of MOs that interacted with UP-CNTs and P-CNTs at concentration of 0.06, 0.6 and 6 mg/L during 24 h are shown in Figures 3 and 4. MOs that interacted with UP-CNTs$_1$ showed a significant decrease to 40% of cell viability independent of the dose of UP-CNTs$_1$ tested, as reported recently by our investigation group [27]. In MOs that interacted with UP-CNTs$_2$ a dose-dependent toxic effect was observed, no significant cytotoxic effect was observed at 0.06 and 0.6 mg/L concentration, whereas cells that interacted with 6 mg/L had a significant decrease in cellular viability, when compared to control (Figure 3). These results indicate that length and quality structure of the CNTs contributes to cellular toxicity. The toxic effect was greater with UP-CNT$_1$ which were longer and more defectuous than UP-CNT$_2$. These results agree with Yamashita et al. [28], who demonstrated that long and thick CNTs cause DNA damage and severe inflammatory effects. Similarly Sato et al. [29] observed that CNTs of 825 nm of length were more toxic than shorter CNTs. On the other hand, MOs that interacted with both groups of P-CNTs

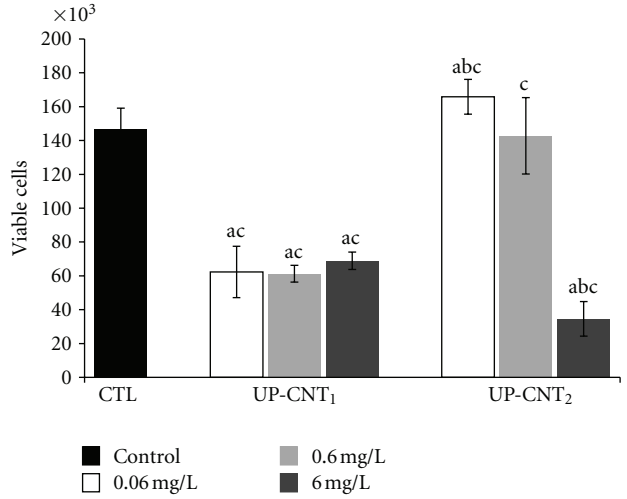

Figure 3: Viability of MOs that interacted with UP-CNTs at different concentration at 24 h. Each bar represents mean ± SD of two experiments done in triplicates ($n = 6$). a, $P < 0.01$ denotes significant differences between mean values measured in the indicated group as compared to control without stimulus (CTL); b, $P < 0.01$ denotes differences between mean values for CNTs at different concentration; c, $P < 0.01$ denotes differences between mean values for a particular concentration among different CNTs.

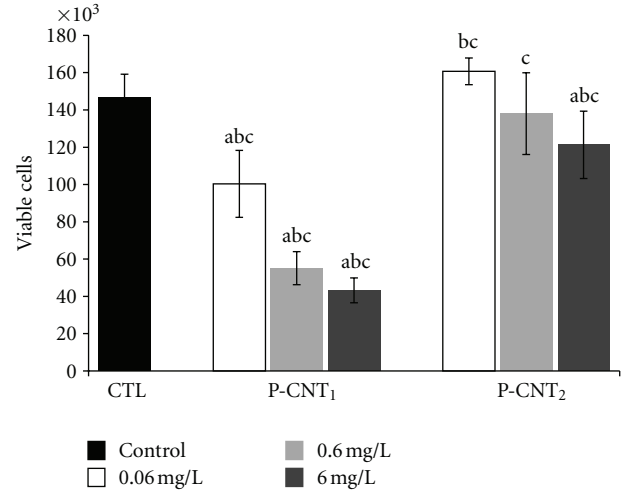

Figure 4: Viability of MOs that interacted with P-CNTs at different concentration at 24 h. Each bar represents mean ± SD of two experiments done in triplicates ($n = 6$). a, $P < 0.01$ denotes significant differences between mean values measured in the indicated group as compared to control without stimulus (CTL); b, $P < 0.01$ denotes differences between mean values for CNTs at different concentration; c, $P < 0.01$ denotes differences between mean values for a particular concentration among different CNTs.

had a dose-dependent toxic effect. However, cell viability had a significant decrease in MOs that interacted with P-CNTs$_1$ at all concentration tested compared with control cultures (Figure 4). In the case of MOs that interacted with P-CNTs$_2$, a significant decrease in cellular viability was detected only with 6 mg/L, and lower concentrations had no significant effect (Figure 4).

Some authors have reported that CNTs interact with MTT and avoid salt metabolism, blocking formazan formation, a colored compound that is detected at 590 nm [30, 31]. In this study we incubated NP-CNTs and/or P-CNTS with MTT, and no interference or nonspecific reduction of MTT was detected (data not shown).

Several works have reported that the purification process eliminates residues present on the CNTs superface and that additionally introduces certain charged groups on their surface, allowing higher stability in aqueous solution and decreasing the toxic effect [10, 12]. Nevertheless, the purification procedure could also contribute to CNT toxicity. Many studies have found that P-CNTs or acid-treated CNTs had greater toxic effect than UP-CNTs [31, 32]. Some authors attribute this behavior to the COOH groups, which may be causing a stress on cells [10, 12]. On the contrary, works such as reported by Pulskamp et al. [30] showed that P-CNTs are less toxic than UP-CNT. These contradictory results could be related with the purification methodology used in those studies, since acid treatment modifies chemical and structural CNTs characteristics. Indeed, there are scarce cytoxicity studies in which purification and structural nanoparticle characteristics are considered and that is probably one reason why it has been hard to identify the origin of toxicity. In our work, we found that the toxic effect of CNTs was dependent of length and COOH content. P-CNTs$_2$ whose length was <1 μm and COOH percentage was 7% were less toxic compared with P-CNTs$_1$ (length >100 μm and 2.76% of COOH). The relationship of COOH groups with the toxicity of CNTs on cellular cultures is not clear yet, since in most of the studies COOH groups are not quantified. However, the effect of O content has been reported in some toxicity studies, where a greater toxicity of P-CNTs was found with low content of O [27, 30], and P-CNTs with O content above 20% decreased notably the cytotoxicity [31, 33]. Considering that the O content is associated with the COOH groups in the P-CNTs, our results agree with those in which P-CNTs have high O content. However the COOH quantification is desirable to make a direct toxicity comparison.

In addition to chemical and structural properties, the aggregation differences between CNTs could be related with cytotoxicity variations [33–35]. In our study, treatment with 3 : 1 H_2SO_4/HNO_3 and sonication for 48 h allowed to obtain CNTs shorter and with a higher content of COOH groups, which were more soluble in aqueous medium. Moreover, increase of COOH groups in the surface of the CNTs is indispensable to favour nanoparticle functionalization with drugs or peptides, a relevant process for nanocarriers or nanovaccines production.

4. Conclusion

Results obtained in this work demonstrated that purification methodology is a key event for P-CNTs production for their use in nanobiotechnology; acid treatment with 3 : 1 H_2SO_4/HNO_3 and sonication was highly effective to remove

Fe and permits us to obtain P-CNTs with low cytotoxicity on MOs of J774A cell line. Cytotoxic effect was related to the length and COOH content of P-CNTs. This finding is of great importance for generation of nanobiotechnological products such as nanocarriers or nanovaccines, in which CNTs exhibit minimal toxicity and high expectations in the future.

Acknowledgments

This work was partially supported by FOMIX-Chihuahua-CONACyT (CHIH-2008-C01-92074). S. L. Montes-Fonseca was the recipient of a Ph.D. scholarship from CONACyT (reg. 213778). The authors have no other relevant affiliations or financial involvement with any organization or entity with a financial interest in or financial conflict with the subject matter or materials discussed in the paper apart from those disclosed.

References

[1] N. Tagmatarchis and M. Prato, "Carbon-based materials: from fullerene nanostructures to functionalized carbon nanotubes," *Pure and Applied Chemistry*, vol. 77, no. 10, pp. 1675–1684, 2005.

[2] X. Zhao and R. Liu, "Recent progress and perspectives on the toxicity of carbon nanotubes at organism, organ, cell, and biomacromolecule levels," *Environment International*, vol. 40, no. 1, pp. 244–255, 2012.

[3] R. Singh, D. Pantarotto, L. Lacerda et al., "Tissue biodistribution and blood clearance rates of intravenously administered carbon nanotube radiotracers," *Proceedings of the National Academy of Sciences of the United States of America*, vol. 103, no. 9, pp. 3357–3362, 2006.

[4] S. S. Wong, E. Joselevich, A. T. Woolley, C. L. Cheung, and C. M. Lieber, "Covalently functionalized nanotubes as nanometresized probes in chemistry and biology," *Nature*, vol. 394, no. 6688, pp. 52–55, 1998.

[5] A. Hirsch, "Functionalization of single-walled carbon nanotubes," *Angewandte Chemie - International Edition*, vol. 41, no. 11, pp. 1853–1859, 2002.

[6] S. E. McNeil, "Nanotechnology for the biologist," *Journal of Leukocyte Biology*, vol. 78, no. 3, pp. 585–594, 2005.

[7] T. Fifis, A. Gamvrellis, B. Crimeen-Irwin et al., "Size-dependent immunogenicity: therapeutic and protective properties of nano-vaccines against tumors," *Journal of Immunology*, vol. 173, no. 5, pp. 3148–3154, 2004.

[8] D. Pantarotto, C. D. Partidos, R. Graff et al., "Synthesis, structural characterization, and immunological properties of carbon nanotubes functionalized with peptides," *Journal of the American Chemical Society*, vol. 125, no. 20, pp. 6160–6164, 2003.

[9] V. L. Colvin, "The potential environmental impact of engineered nanomaterials," *Nature Biotechnology*, vol. 21, no. 10, pp. 1166–1170, 2003.

[10] A. Magrez, S. Kasas, V. Salicio et al., "Cellular toxicity of carbon-based nanomaterials," *Nano Letters*, vol. 6, no. 6, pp. 1121–1125, 2006.

[11] L. Ding, J. Stilwell, T. Zhang et al., "Molecular characterization of the cytotoxic mechanism of multiwall carbon nanotubes and nano-onions on human skin fibroblast," *Nano Letters*, vol. 5, no. 12, pp. 2448–2464, 2005.

[12] M. Bottini, S. Bruckner, K. Nika et al., "Multi-walled carbon nanotubes induce T lymphocyte apoptosis," *Toxicology Letters*, vol. 160, no. 2, pp. 121–126, 2006.

[13] Y. Y. Guo, J. Zhang, Y. F. Zheng, J. Yang, and X. Q. Zhu, "Cytotoxic and genotoxic effects of multi-wall carbon nanotubes on human umbilical vein endothelial cells in vitro," *Mutation Research - Genetic Toxicology and Environmental Mutagenesis*, vol. 721, no. 2, pp. 184–191, 2011.

[14] N. A. Monteiro-Riviere, R. J. Nemanich, A. O. Inman, Y. Y. Wang, and J. E. Riviere, "Multi-walled carbon nanotube interactions with human epidermal keratinocytes," *Toxicology Letters*, vol. 155, no. 3, pp. 377–384, 2005.

[15] C. Cheng, K. H. Müller, K. K. K. Koziol et al., "Toxicity and imaging of multi-walled carbon nanotubes in human macrophage cells," *Biomaterials*, vol. 30, no. 25, pp. 4152–4160, 2009.

[16] M. L. Di Giorgio, S. D. Bucchianico, A. M. Ragnelli, P. Aimola, S. Santucci, and A. Poma, "Effects of single and multi walled carbon nanotubes on macrophages: cyto and genotoxicity and electron microscopy," *Mutation Research - Genetic Toxicology and Environmental Mutagenesis*, vol. 722, no. 1, pp. 20–31, 2011.

[17] G. V. Letsou, J. H. Connelly, R. M. Delgado et al., "Is native aortic valve commissural fusion in patients with long-term left ventricular assist devices associated with clinically important aortic insufficiency?" *Journal of Heart and Lung Transplantation*, vol. 25, no. 4, pp. 395–399, 2006.

[18] C. A. Poland, R. Duffin, I. Kinloch et al., "Carbon nanotubes introduced into the abdominal cavity of mice show asbestos-like pathogenicity in a pilot study," *Nature Nanotechnology*, vol. 3, no. 7, pp. 423–428, 2008.

[19] T. Saito, K. Matsushige, and K. Tanaka, "Chemical treatment and modification of multi-walled carbon nanotubes," *Physica B*, vol. 323, no. 1-4, pp. 280–283, 2002.

[20] A. Aguilar-Elguézabal, W. Antúnez, G. Alonso, F. P. Delgado, F. Espinosa, and M. Miki-Yoshida, "Study of carbon nanotubes synthesis by spray pyrolysis and model of growth," *Diamond and Related Materials*, vol. 15, no. 9, pp. 1329–1335, 2006.

[21] H. Hu, P. Bhowmik, B. Zhao, M. A. Hamon, M. E. Itkis, and R. C. Haddon, "Determination of the acidic sites of purified single-walled carbon nanotubes by acid-base titration," *Chemical Physics Letters*, vol. 345, no. 1-2, pp. 25–28, 2001.

[22] T. Mosmann, "Rapid colorimetric assay for cellular growth and survival: application to proliferation and cytotoxicity assays," *Journal of Immunological Methods*, vol. 65, no. 1-2, pp. 55–63, 1983.

[23] C. Cheng, K. H. Müller, K. K. K. Koziol et al., "Toxicity and imaging of multi-walled carbon nanotubes in human macrophage cells," *Biomaterials*, vol. 30, no. 25, pp. 4152–4160, 2009.

[24] J. Zhang, H. Zou, Q. Qing et al., "Effect of chemical oxidation on the structure of single-walled carbon nanotubes," *Journal of Physical Chemistry B*, vol. 107, no. 16, pp. 3712–3718, 2003.

[25] A. M. Keszler, L. Nemes, S. R. Ahmad, and X. Fang, "Characterisation of carbon nanotube materials by Raman spectroscopy and microscopy - A case study of multiwalled and singlewalled samples," *Journal of Optoelectronics and Advanced Materials*, vol. 6, no. 4, pp. 1269–1274, 2004.

[26] V. Datsyuk, M. Kalyva, K. Papagelis et al., "Chemical oxidation of multiwalled carbon nanotubes," *Carbon*, vol. 46, no. 6, pp. 833–840, 2008.

[27] S. L. Montes-Fonseca, E. Orrantia-Borunda, A. Aguilar-Elguezabal, C. G. Horta, P. Talamás-Rohana, and B. Sánchez-Ramirez, "Cytotoxicity of functionalized carbon nanotubes in J774A macrophages," *Nanomedicine: Nanotechnology, Biology and Medicine*. In press.

[28] K. Yamashita, Y. Yoshioka, K. Higashisaka et al., "Carbon nanotubes elicit DNA damage and inflammatory response relative to their size and shape," *Inflammation*, vol. 33, no. 4, pp. 276–280, 2010.

[29] Y. Sato, A. Yokoyama, K. I. Shibata et al., "Influence of length on cytotoxicity of multi-walled carbon nanotubes against human acute monocytic leukemia cell line THP-1 in vitro and subcutaneous tissue of rats in vivo," *Molecular BioSystems*, vol. 1, no. 2, pp. 176–182, 2005.

[30] K. Pulskamp, S. Diabaté, and H. F. Krug, "Carbon nanotubes show no sign of acute toxicity but induce intracellular reactive oxygen species in dependence on contaminants," *Toxicology Letters*, vol. 168, no. 1, pp. 58–74, 2007.

[31] T. Coccini, E. Roda, D. A. Sarigiannis et al., "Effects of water-soluble functionalized multi-walled carbon nanotubes examined by different cytotoxicity methods in human astrocyte D384 and lung A549 cells," *Toxicology*, vol. 269, no. 1, pp. 41–53, 2010.

[32] O. Vittorio, V. Raffa, and A. Cuschieri, "Influence of purity and surface oxidation on cytotoxicity of multiwalled carbon nanotubes with human neuroblastoma cells," *Nanomedicine: Nanotechnology, Biology, and Medicine*, vol. 5, no. 4, pp. 424–431, 2009.

[33] D. M. Brown, I. A. Kinloch, U. Bangert et al., "An in vitro study of the potential of carbon nanotubes and nanofibres to induce inflammatory mediators and frustrated phagocytosis," *Carbon*, vol. 45, no. 9, pp. 1743–1756, 2007.

[34] P. M. V. Raja, J. Connolley, G. P. Ganesan et al., "Impact of carbon nanotube exposure, dosage and aggregation on smooth muscle cells," *Toxicology Letters*, vol. 169, no. 1, pp. 51–63, 2007.

[35] P. Wick, P. Manser, L. K. Limbach et al., "The degree and kind of agglomeration affect carbon nanotube cytotoxicity," *Toxicology Letters*, vol. 168, no. 2, pp. 121–131, 2007.

Hindawi Publishing Corporation
Journal of Nanomaterials
Volume 2012, Article ID 863704, 8 pages
doi:10.1155/2012/863704

Research Article

Immunocytes as a Biocarrier to Delivery Therapeutic and Imaging Contrast Agents to Tumors

Jinhyang Choi,[1] Ha-Na Woo,[1] Eun Jin Ju,[1] Joohee Jung,[1,2] Hye-Kyung Chung,[3] Jaesook Park,[1] Seok Soon Park,[1] Seol Hwa Shin,[3] Hye Ji Park,[3] Jin Seong Lee,[4] Si Yeol Song,[1,5] Seong-Yun Jeong,[1] and Eun Kyung Choi[1,3,5]

[1] *Institute for Innovative Cancer Research, Asan Medical Center, University of Ulsan College of Medicine, Seoul 138-736, Republic of Korea*
[2] *College of Pharmacy, Duksung Women's University, Seoul 132-714, Republic of Korea*
[3] *Center for Development and Commercialization of Anti-Cancer Therapeutics, Asan Medical Center, Seoul 138-736, Republic of Korea*
[4] *Department of Radiology and Research Institute of Radiology, Asan Medical Center, University of Ulsan College of Medicine, Seoul 138-736, Republic of Korea*
[5] *Department of Radiation Oncology, Asan Medical Center, University of Ulsan College of Medicine, Seoul 138-736, Republic of Korea*

Correspondence should be addressed to Seong-Yun Jeong, syj@amc.seoul.kr and Eun Kyung Choi, ekchoi@amc.seoul.kr

Received 13 February 2012; Revised 10 May 2012; Accepted 13 May 2012

Academic Editor: Patricia Murray

Radiotherapy for cancer treatment has been used for primary or adjuvant treatment in many types of cancer, and approximately half of all cancer patients are undergoing radiation. However, ionizing radiation exposure induces genetic alterations in cancer cells and results in recruitment of monocytes/macrophages by triggering signals released from these cells. Using this characteristic of monocytes/macrophages, we have attempted to develop a biocarrier loading radiosensitizing anticancer agents that can lead to enhance the therapeutic effect of radiation in cancer treatment. The aim of this study is to demonstrate the proof of this concept. THP-1 labeled with Qdot 800 or iron oxide (IO) effectively migrated into tumors of subcutaneous mouse model and increased recruitment after ionizing radiation. Functionalized liposomes carrying a radiosensitizing anticancer agent, doxorubicin, are successfully loaded in THP-1 (THP-1-LP-Dox) with reduced cytotoxicity, and THP-1-LP-Dox also was observed in tumors after intravenous administration. Here, we report that monocytes/macrophages as a biocarrier can be used as a selective tool for amplification of the therapeutic effects on radiotherapy for human cancer treatment.

1. Introduction

Nearly half of all cancer patients receive radiotherapy, either alone or in combination with other treatment modalities such as surgery or chemotherapy [1]. Although radiotherapy alone or with other treatments reaches a successive survival rates in treated patients with some cancers (e.g., early stage larynx cancer and non-small-cell lung cancer), for many other sites (e.g., glioblastomas, sarcomas, and advanced non-small-cell lung cancer), it shows low survival rates or the other chronic health problems such as second primary cancers and aggressive metastatic cancers to other organs [1, 2].

One of the reasons which reduce or neglect the therapeutic effect of radiotherapy is hypoxia in solid tumors. Hypoxia is a common feature in solid tumors and implicated in resistance to ionizing radiation and chemotherapy through multiple mechanisms caused by genetic or metabolic alterations in cancer cells [3]. Hypoxic tumor cells are significantly less responsive to radiotherapy and chemotherapy than well-oxygenated counterparts because of reduction or absence of the oxygen-derived free radicals that are needed to enhance DNA damage induced by ionizing radiation and nonproliferative hypoxic cells. The effect of these resistances brings increased invasiveness and metastatic potential, loss of apoptosis, and chaotic angiogenesis [4].

The accumulation of monocytes/macrophages from the blood circulation is a hallmark feature of cancers. As a result of release of a bunch of chemoattractants from altered tumor cells, monocytes are recruited into malignant tumors and differentiate into tumor-associated macrophages (TAMs) that facilitate tumor growth and survival [5]. The level of TAM numbers often correlates with aggressiveness and poor prognosis in human tumors and, in particular, appears to be affected by hypoxia [5]. TAMs are recruited to hypoxic sites by the release of macrophage chemoattractants (e.g., VEGF, endothelin-2, and EMAPLL) from hypoxic cells or by direct inhibition of the modality of TAMs [4]. These recruited and entrapped TAMs play an important role part in promoting tumor growth and progression by releasing many cytokines and growth factors such as VEGF and FGF2 [5].

The consequences of these complicated correlations among a limitation of radiotherapy, the presence of widespread hypoxia, and the accumulation of macrophages bring out a big hurdle in effective cancer treatments. Despite having difficulties in selecting a target for a cancer therapy, we focused on monocytes/macrophages that predominantly accumulate into tumors that resulted from radiotherapy and hypoxia. We postulated that monocytes/macrophages can be used as a biocarrier that loads anticancer agents to potentiate therapeutic effects based on cell-mediated drug delivery. Recently, one study reported a trial of the use of macrophages, acting as a Trojan Horse, in nanoparticle delivery and therapeutic system [6]. The efficient migration of Au-nanoshell laden macrophage toward T47D breast cancer spheroid and Au-nanoshell laden macrophage death induced by the near-infrared (NIR) irradiation in the hypoxic regions of a tumor spheroid was demonstrated.

The aim of this study is to verify our idea that monocytes/macrophages loading imaging or therapeutic agents can be used, either alone or in combination with radiotherapy, to treat cancer.

2. Materials and Methods

2.1. Preparation of THP-1. THP-1 (human acute monocytic leukemia cell line; ATCC, VA, USA) was cultured and maintained in RMPI 1640 medium (Gibco, NJ, USA) supplemented with 2-mercaptoethanol to a final concentration of 0.05 mM, 10% (v/v) heat-inactivated FBS plus 100 units/mL penicillin and 100 μg/mL streptomycin. For experiments, THP-1 was pretreated with 20 nM phorbol-12-myristate-13-acetate (PMA; CalBiochem, Merk KGaA, Darmstadt, Germany) for 16 hrs.

2.2. Development of Mouse Models. A549 (ATCC, VA, USA) was cultured and maintained in F12K nutrient mixture (Kaighn's modification, Invitrogen, NY, USA) containing 10% FBS plus 100 units/mL penicillin and 100 μg/mL streptomycin, respectively. Male Balb/c nude mice (5 weeks old) were purchased from SLC (Shizuoka, Japan) for generating subcutaneous mouse model. All experiments were performed following the protocol approved by Institutional Animal Care and Use Committee of ASAN Institute for Life Science. 5×10^5 human non-small-cell lung cancer A549 cells in 100 μL of PBS were injected into the subcutaneous tissue of the hind limb of each Balb/c nude mouse, after collecting cells by trypsinizing. When tumors grew to 100 mm^3, mice were treated with THP-1 cell containing liposomal doxorubicin or free doxorubicin. For an irradiation (2 or 10 Gy), tumors were irradiated using 6 MV photon beam linear accelerator (CL/1800, Varian, CA).

2.3. Labeling THP-1 and Imaging. For labeling THP-1 cells, attached THP-1 on a plate was incubated with Qdot 800 (Qtracker 800; Molecular Probes, Inc., Eugene, OR) following the manufacturer's protocol. After labeling with Qdot 800, 2×10^6 cells suspended in 200 μL of PBS were injected through the tail vein of a xenograft mouse model bearing subcutaneous A549 tumor. *In vivo* optical imaging was taken using an IVIS spectrum imaging system (Caliper Life Science Inc.). The imaging was taken with a combination of a 430 nm excitation filter and a 780 nm emission filter. Gray scale photographic images and fluorescence color images were processed using living image V.3.2 (Caliper Life Science Inc.). Fluorescence signals are expressed as total flux (i.e., p/s).

THP-1 (1×10^7 cells per 10 cm dish) was labeled with iron oxide (IO; 112 μg/mL; Rezovist; Bayer AG, Zurich, Swiss) by incubation for 24 h at 37°C and 5% CO_2. After removing excessive IO by washing with PBS, THP-1 cells were collected by trypsinizing. In order to observe the migration of macrophages labeled with IO, 2×10^6 cells suspended in 200 μL of PBS were injected through the tail vein of a xenograft mouse model bearing subcutaneous A549 tumor. MR images were taken prior to irradiation and 5 days after irradiation. The tumors were imaged with a 4.7-T Bruker Biospin imager (Bruker Medical Systems, Karlsruhe, Germany) prior to an injection for baseline and on days 2 and 5. All animals were anesthetized (1.5% isoflurane in a 1 : 2 mixture of O_2/N_2O) before imaging. The imaging protocol included a T2*-weighted, gradient-echo sequence (repetition time msec/echo time msec, 356.5/10.3; flip angle, 30°). A transverse (orthogonal to tibia) section orientation was chosen for anatomic reproducibility of the image position and correlation with histological sections. The spatial resolution was 256 × 256 matrix; field of view, 2.18 × 2.06 cm; section thickness, 0.67 mm; section gap, 0.33 mm; number of sections, 16. All animals were scarified for histopathological evaluation after MR imaging.

2.4. Prussian Blue Staining. All animals were sacrificed by means of administration of inhalable pure CO_2. The hind legs including a tumor were dissected, ex-articulated, fixed in 4% paraformaldehyde, and embedded in paraffin for staining. Paraffin sections of 5 μm were prepared transversely. All slides were deparaffinized and rehydrated by sequenced sinking in xylene and ethanol. Prussian blue staining was performed using a mixture of 10% aqueous solution of potassium ferrocyanide and 20% aqueous solution of hydrochloric acid. After incubation for 20 minutes, the slides were washed at least 3 times in distilled water and counterstained with nuclear fast red for 5 minutes. After dehydration

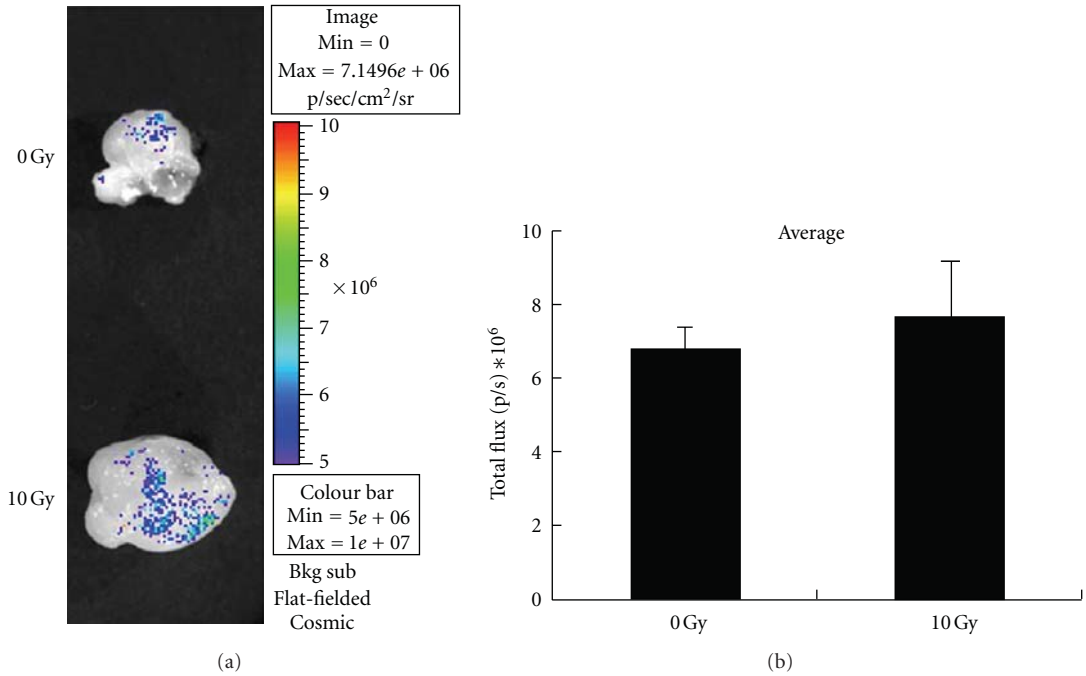

Figure 1: *In vivo* migration of THP-1-Qdot 800. IVIS images of A549 subcutaneous tumors after an injection of THP-1-Qdot 800 intravenously. (a) The fluorescence of Qdot was observed in tumors, and the intensity of fluorescence was increased after irradiation. (b) The total flux also shows slight increase after irradiation.

and clearing in ethanol and xylene, sections were evaluated using a microscope to determine the efficiency of labeling. Any cells that showed blue particles inside were considered labeled.

2.5. Preparation and Characterization of Liposomal Doxorubicin (LP-Dox). Unilamellar liposomes of approximately 150 nm diameter were prepared by the extrusion method employing a laboratory extruder. Briefly, the lipid composition was based on 15 : 15 : 30 : 40 molar ratio of DPPC (dipalmitoylphosphatidylcholine, Nof Corporation, Tokyo, Japan): DPPE (dipalmitoylphosphatidylethanolamine, Sigma-Aldrich Co., MO, USA): DPPG-Na (dipalmitoylphosphatidylglycerol, Nof Corporation, Tokyo, Japan): Cholesterol (Wako Pure Chemical Industries. Ltd., Osaka, Japan). The lipids were dissolved and mixed in chloroform/methanol (4 : 1 v/v) to assure a homogeneous mixture of lipids. The lipid film was thoroughly dried to remove residual organic solvent by placing the flask on a vacuum pump overnight. Then, the suspension obtained in 5 mL of hydration buffer (pH 4.0, 10 mM of HEPES and 120 mM Ammonium Sulfate) was extruded through polycarbonate filters with 800, 400, 200, and twice of 100 nm pore size for a size control. The average concentration of liposome was 5 mg/mL calculated with a cholesterol quantitation kit (BioVision incorporated, CA, USA) following a manufacturer's protocol. Encapsulation of doxorubicin hydrochloride (doxorubicin; Dox; Sigma-Aldrich, MO, USA) into the liposomal core was performed at 60°C in a water bath for 30 min after the pH exchange of buffer (pH 7.4, 10 mM of HEPES, 100 mM Sodium chloride, and 100 mM Sucrose) in Sephadex G25 column (GE Healthcare Life Sciences, NJ, USA). The ratio of added doxorubicin to liposome is 1.8 mg : 15 mg. Removal of nonencapsulated doxorubicin was achieved by size exclusion chromatography using Sephadex G25. The encapsulate doxorubicin concentration was determined by a measurement of the fluorescence intensity (excitation at 537 nm and emission at 584 nm) with an Enspire 2300 multilabel reader (Perkin Elmer, MA, USA). The average concentration of doxorubicin in LP-Dox was 0.6 mg/mL. For the size determination of liposome, a Zetasizer (Nano-ZS, Malvern instruments, Malvern, UK) was used.

2.6. THP-1-LP-Dox Viability and Uptake. 5×10^3 THP-1 cells in 100 μL medium were plated in each well of a 96-well plate. Then, Dox or LP-Dox was added by concentration gradients, 1, 2, 10, or 20 μg/mL. Macrophages with Dox or LP-Dox were additionally incubated for 3, 6, or 24 hours. At the end of incubation time point, Dox or LP-Dox was removed by medium changing and washing. For a viability assay, macrophages were incubated with 100 μL of fresh medium containing 10 μL of the CCK8 solution (Dojindo Laboratories, Kumamoto, Japan) for 3 hours at 37°C in 5% CO_2. The absorbance was measured at 450 nm using an Enspire 2300 multilabel reader (Perkin Elmer).

To determine the concentration of Dox uptaken by macrophages, the survived cells were lysed at the end point of an incubation time, mixed with methanol to melt liposomes, and then measured fluorescence intensity.

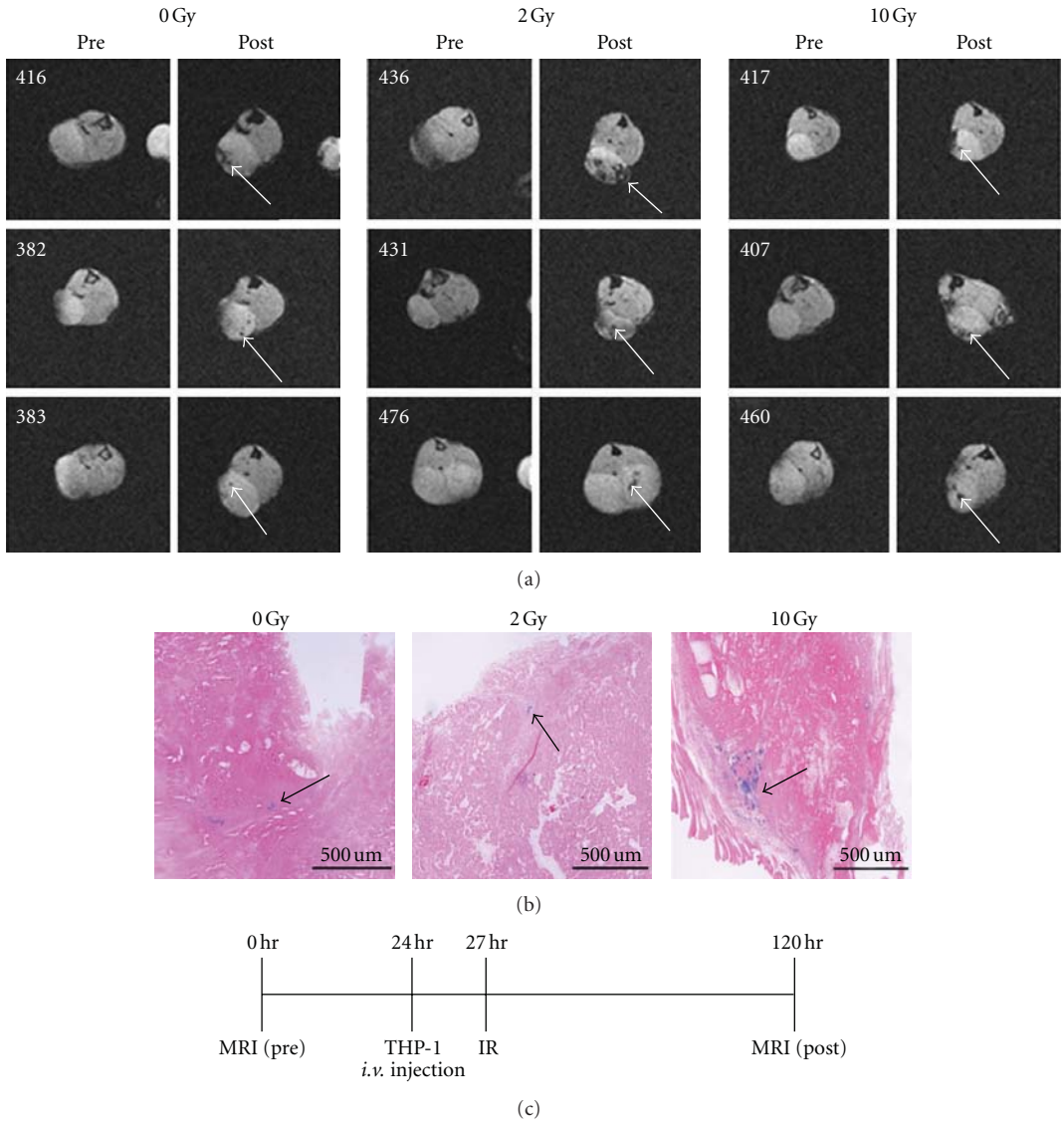

Figure 2: *In vivo* migration of THP-1-IO. MR images of A549 subcutaneous tumors after an injection of THP-1-IO intravenously. (a) Tumors contained IO, and the volume of IO detected was gradually increased followed with an increasing dose of irradiation. Numbers indicate individual samples. (b) IO was detected by Prussian blue staining (arrows) in a tumor from mice injected THP-IO. (c) The time frame indicates MR imaging schedule. Calibration bar = 500 μm.

2.7. THP-1-LP-Dox Imaging. The plate-adherent THP-1 cells (approximately 5×10^6 cells per a 6 cm dish) were incubated with LP-Dox containing 20 μg/mL of Dox for 6 hours. After removing the remained LP-Dox in medium by washing with PBS, live THP-1 was harvested and counted. To determine the concentration of Dox uptaken by THP-1, 5×10^6 cells were lysed, mixed with methanol to melt liposomes, and then measured fluorescence intensity. For a test of delivery of macrophages-LP-Dox in subcutaneous or metastasis mouse models, 60 μg of Dox loaded THP-1-LP-Dox (approximately 10^6 cells) in 100 μL of PBS was administrated into a mouse through the tail vein, when a tumor volume was reached at 100 mm^3 in a subcutaneous model. Tumors were collected at 24 hours postinjection and subjected to fluorescence microscopic analysis. In order to collect tumors from each mouse at the end point of an experiment, mice were euthanized with CO_2 inhalation. Tumors collected were fixed in 4% paraformaldehyde and embedded in paraffin for staining. Paraffin sections of 5 μm were prepared and stained with DAPI (VECTASHIELD Mounting Media with DAPI, Vector Laboratories, Inc., CA) after deparaffinization and dehydration. Images were captured and processed with a fluorescence microscope (Bx53; Olympus, Tokyo, Japan) equipped with a cooled CCD camera (ORCA-R2; Hamamtsu Photonics K.K., Hamamatsu, Japan).

2.8. Statistical Analysis. All data expressed as mean ±SD are representative of at least three different experiments. Comparisons between individual points were performed by a Student's *t*-test using Prism statistical software (GraphPad,

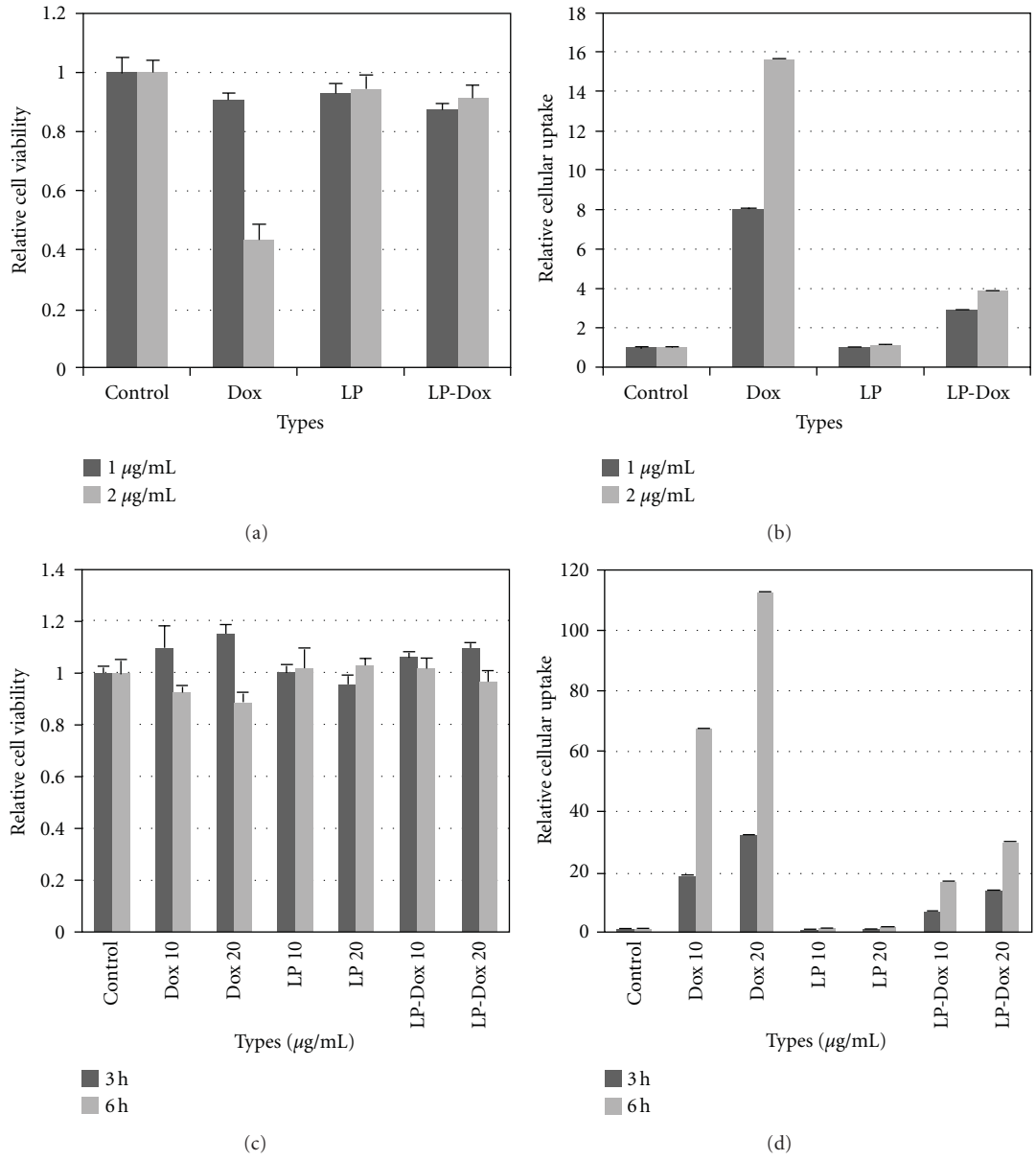

Figure 3: Conditions for incubating THP-1 with LP-Dox. (a) THP-1 viability after 24 h incubation of Dox, LP, or LP-Dox. (b) The uptake volume of Dox in THP-1 after 24 h incubation of Dox, LP, or LP-Dox. (c) THP-1 viability after 3 or 6 h incubation of Dox, LP, or LP-Dox. (d) The uptake volume of Dox in THP-1 after 3 or 6 h incubation of Dox, LP, or LP-Dox.

CA, USA). P values less than 0.05 were considered statistically significant.

3. Results

3.1. In Vivo Migration of THP-1 Labeled with Qdot 800 in a Xenograft Mouse Model. In order to demonstrate our hypothesis, we first needed to verify the migration ability of macrophages toward tumors *in vivo*. We tested the *in vivo* migration and infiltration ability of THP-1 using a xenograft mouse model bearing a subcutaneous A549 tumor. For long-term tracking or *in vivo* imaging easily, THP-1 cells were labeled with Qdot 800 which supports the intense fluorescence under various biological conditions and less autofluorescence in tissues. After 5 days postinjection of labeled THP-1 cells through tail vein, we imaged tumors with IVIS spectrum imaging system. Fluorescence located in tumors was apparently observed (Figure 1(a)). In order to observe the radiation effect on the migration of macrophages, we irradiated tumors with 10 Gy after THP-1 injection. Interestingly, we observed increased intensity of fluorescence in tumors after 10 Gy of radiation (Figures 1(a) and 1(b)), compared to nonirradiated tumors.

3.2. In Vivo Migration of THP-1 Labeled with IO in a Xenograft Mouse Model. In addition to Qdot, we also attempted to

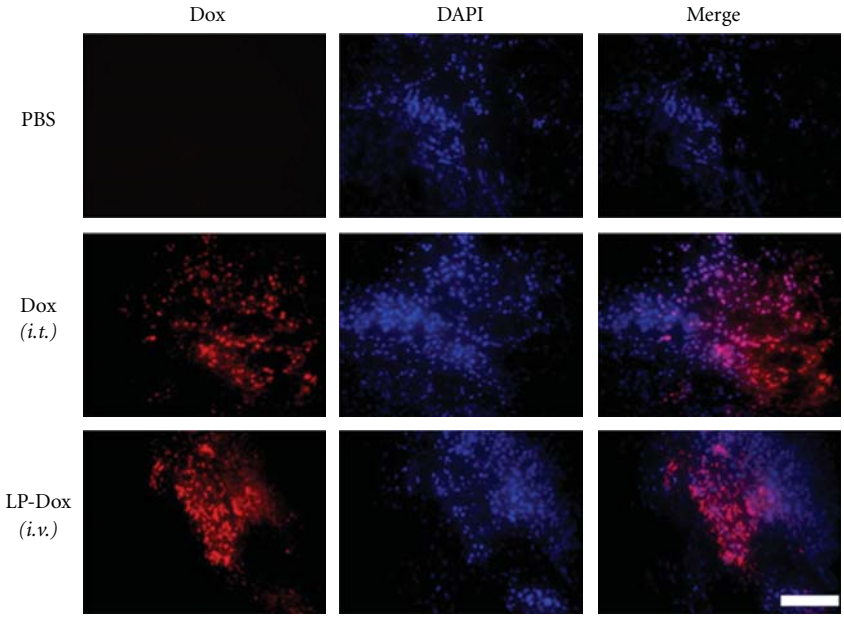

Figure 4: Distinct fluorescent expressions of Dox or LP-Dox (red) in tumors at 24 h postinjection of THP-1-LP-Dox. DAPI (blue) was used for a counter staining. Calibration bar = 50 μm.

label THP-1 cells with IO to expand to other labeling methods. Like results with Qdots, distinct IO expressions in tumors after intravenous (*i.v.*) injection were observed in MR imaging and the expression was enhanced after radiation (Figure 2(a)). We confirmed this result with blue stained IO in tumors with a Prussian blue staining (Figure 2(b)). We observed a large number of blue stained IO spread in a deep side of a tumor from a mouse injected macrophages IO (Figure 2(b)). We gave radiation with different doses, 2 and 10 Gy, if the radiation dose affects the migration ability of macrophages. Interestingly, we observed increased intensity of IO expression gradually followed with increased dose of radiation (Figures 2(a) and 2(b)).

These results led to open our hypothesis that macrophage can be used as a biocarrier, such as imaging or anticancer agents, to deliver into tumors with assistance of radiation or not.

3.3. Development of THP-1-LP-Dox. Next, we asked to approach the way to load anticancer agents to THP-1 cells. The majority of anticancer agents has overt cytotoxicity. In order to use macrophages as a biocarrier for an anticancer agent, we needed to protect macrophages from a direct toxicity of a selected agent, Dox, as a cargo until they can reach tumors alive. We chose liposomes for encapsulating drugs to release slowly. Liposomes, nature biomolecules, have the ability to carry a greater amount of drugs while minimizing the risk associated with premature leakage. Dox was chosen as an anticancer drug in our experiment because of its unique fluorescence characteristic in excitation at 537 nm and emission at 584 nm which has the easy accesses to monitor their action. We successfully encapsulated Dox with liposome (approximately 150 nm diameter) composed of DPPC : DPPE : DPPG-Na : Cholesterol = 15 : 15 : 30 : 40 molar ratio followed by our regular protocol.

We then tested a toxicity of LP-Dox to THP-1 by CCK8 assay compared with free Dox as a control. With relatively long-term incubation (24 h), LP-Dox showed almost no cytotoxicity in our given concentrations compared to free Dox (Figure 3(a)), although the total volume of cellular uptake of LP-Dox was much less than free Dox, which was not enough to our expectation (Figure 3(b)). Therefore, we multiplied a concentration of LP-Dox into cells and reduced an incubation time to increase loading efficacy of LP-Dox in cells without any cytotoxicity. With short-time incubations (3 and 6 h), we observed only slight cytotoxicity in free Dox with a high concentration (Figure 3(c)). The total volume of cellular uptake of LP-Dox was increased with the 10 times higher concentration as we added (20 μg/mL) without any effects on cell viability (Figure 3(d)). We chose this concentration of LP-Dox (20 μg/mL) and an incubation time (6 h) for conditions of the next *in vivo* experiment.

3.4. In Vivo Migration of THP-1-LP-Dox in a Xenograft Mouse Model. Although we previously observed the migration by using THP-1 labeled with Qdot or IO toward tumor site *in vivo*, we needed to confirm the migration of THP-1-LP-Dox into the tumor site *in vivo*. With an established subcutaneous mouse model that developed A549 tumor on the right thigh, we attempted to verify the migration of THP-1-LP-Dox after *i.v.* injection through tail vein. We collected tumors from each mouse at 24 hours postinjection of THP-1-LP-Dox and observed fluorescence on tumor tissues after DAPI counterstaining. Compared with a tumor which showed widespread Dox expression in the tumor after an intratumoral (*i.t.*) injection of free Dox, we observed similar

amount of Dox expression infiltrated in the tumor from the group of THP-1-LP-Dox (Figure 4). Unlike free Dox, Dox in these tumors was observed in the cells between tumor cells. These results indicated that macrophages effectively carried LP-Dox into the tumor site and could be used as a valuable tool for carrying anticancer agents.

4. Discussion

This study is to prove the concept of our idea that macrophages/monocytes can be used for a valuable tool for drug delivery into specific tumor sites. The unique characteristics of macrophages offered their potential as a target-specific drug carrier. Macrophages are immunocytes that migrate across the blood-tumor barriers to the tumor and can be collected easily from the blood. And their innate phagocytic capability provides an easy access of loading with therapeutic nanoparticles.

As a first trial in this study, we used THP-1 cells, which are originated from human acute monocytic leukemia cells, for a drug carrier. Although these cells loading with imaging or anticancer agents showed an active targeting and migrating ability towards tumors in our study, they should be considered more carefully as a carrier. THP-1 cells are cancer cells which can bring a chance of the second tumorigenesis and an immune rejection reaction in the body. Our final goal of the study is engaged on applying autoimplantation of monocytes/macrophages isolated from a cancer patient, as a biocarrier for chemotherapeutic anticancer agents not only to improve their therapeutic efficacy but also to eliminate an immune rejection response.

Recently, several studies using human or mouse macrophages as a delivery for nanoparticles or viruses have been reported [6–9]. Notably, macrophages were served as a "Trojan Horse" delivery vector for nanoparticle therapeutics into inaccessible tumor regions, such as a hypoxic area. Choi et al. [6] demonstrated a study of using Trojan Horse nanoparticle delivery and therapeutics within their several critical steps that are the efficient phagocytosis of gold nanoshells by macrophages, photoinduced ablation of gold nanoshells laden macrophages, tumor recruitment, and photoinduced cell death of a human breast tumor spheroid. In another study, similar to our study, macrophages carrying 5-fluorouracil (5-FU) encapsulated in oligomannose-coated liposomes (OML) were used for drug delivery in a mouse intraperitoneal (*i.p.*) metastasis model [7]. The controlled tumor development by coadministration of OML-encased 5-FU and OML-encased magnetic nanoparticles, followed by treatment with an alternating magnetic field, was demonstrated in their study. Although these works were well demonstrated macrophages as a biocarrier, it was not proved whether the *in vivo* systemic approach was accessible.

Cell-mediated drug delivery using immunocytes, mononuclear phagocytes, and stem cells, and so forth offers targeted drug transfer to specific tumor sites with reduced drug immunogenicity and cytotoxicity [10]. Despite the advantages, this field of study is still considered an unexplored area with several limitations including high drug loading volume in cells to be enough to affect tumor cell death, active migration ability and time-controlled drug release at the desirable site without any leakage of drugs, and the improvement of safe and relatively stable drug formulation to be loaded in cells.

In this study, we showed the effective migration of THP-1 loading imaging agents or anticancer agents encapsulating liposomes into tumor sites *in vivo*. Also, increased accumulation of THP-1 cells in tumors was observed after radiation. These results suggest macrophage-mediated liposome-encapsulated drug delivery system alone or with a combination with a radiation is a new potential therapeutic system to amplify an efficacy in cancer treatment. However, in order to approach this, there are many views to be demonstrated further; when drug release is performed at the right sites in the body, how the drug loading volume in cells can be increased with any toxicity, how can we improve more sophisticated time-control release of drugs into the desired sites, and there is an efficient and obvious therapeutic effect we can recognize after a treatment.

Conflict of Interest

The authors declare no conflict of interest.

Acknowledgments

This work was supported by a grant of the Nuclear R&D program through the Korea Science and Engineering Foundation funded by the Ministry of Education, Science and Technology of Korea (2008-03876), the Korean Health Technology R&D Project, Ministry for Health and Welfare, Republic of Korea (A062254 and A102059), and the Basic Science Research Program through the National Research Foundation of Korea (NRF) funded by the Ministry of Education, Science and Technology (KRF-2008-313E00444).

References

[1] A. C. Begg, F. A. Stewart, and C. Vens, "Strategies to improve radiotherapy with targeted drugs," *Nature Reviews Cancer*, vol. 11, no. 4, pp. 239–253, 2011.

[2] W. D. Newhauser and M. Durante, "Assessing the risk of second malignancies after modern radiotherapy," *Nature Reviews Cancer*, vol. 11, no. 6, pp. 438–448, 2011.

[3] W. R. Wilson and M. P. Hay, "Targeting hypoxia in cancer therapy," *Nature Reviews Cancer*, vol. 11, no. 6, pp. 393–410, 2011.

[4] C. Murdoch and C. E. Lewis, "Macrophage migration and gene expression in response to tumor hypoxia," *International Journal of Cancer*, vol. 117, no. 5, pp. 701–708, 2005.

[5] C. Lewis and C. Murdoch, "Macrophage responses to hypoxia: implications for tumor progression and anti-cancer therapies," *American Journal of Pathology*, vol. 167, no. 3, pp. 627–635, 2005.

[6] M. R. Choi, K. J. Stanton-Maxey, J. K. Stanley et al., "A cellular trojan horse for delivery of therapeutic nanoparticles into tumors," *Nano Letters*, vol. 7, no. 12, pp. 3759–3765, 2007.

[7] Y. Ikehara, T. Niwa, L. Biao et al., "A carbohydrate recognition-based drug delivery and controlled release system using

intraperitoneal macrophages as a cellular vehicle," *Cancer Research*, vol. 66, no. 17, pp. 8740–8748, 2006.

[8] R. F. Bressani, A. S. Nowacek, and S. Singh, "Pharmacotoxicology of monocyte-macrophage nanoformulated antiretroviral drug uptake and carriage," *Nanotoxicology*, vol. 5, pp. 592–605, 2011.

[9] S. J. Madsen, S. K. Baek, A. R. Makkouk, T. Krasieva, and H. Hirschberg, "Macrophages as cell-based delivery systems for nanoshells in photothermal therapy," *Annals of Biomedical Engineering*, vol. 40, no. 2, pp. 507–515, 2012.

[10] E. V. Batrakova, H. E. Gendelman, and A. V. Kabanov, "Cell-mediated drug delivery," *Expert Opinion on Drug Delivery*, vol. 8, no. 4, pp. 415–433, 2011.

Hindawi Publishing Corporation
Journal of Nanomaterials
Volume 2012, Article ID 789841, 14 pages
doi:10.1155/2012/789841

Review Article

Microfluidic Platforms for Evaluation of Nanobiomaterials: A Review

Venkataraman Giridharan,[1] YeoHeung Yun,[1] Peter Hajdu,[2] Laura Conforti,[2] Boyce Collins,[1] Yongseok Jang,[1] and Jagannathan Sankar[1]

[1] *Engineering Research Center, North Carolina A&T State University, Greensboro, NC 27411, USA*
[2] *College of Medicine, University of Cincinnati, Cincinnati, OH 45267, USA*

Correspondence should be addressed to Jagannathan Sankar, sankar@ncat.edu

Received 18 February 2012; Accepted 19 April 2012

Academic Editor: Haifeng Chen

Biomaterials, especially those based on nanomaterials, have emerged as critical tools in biomedical applications. The applications encompass a wide range such as implantable devices, tissue regeneration, drug delivery, diagnostic systems, and molecular printing. The type of materials used also covers a wide range: metals (permanent and degradable), polymers (permanent and degradable), carbon nanotubes, and lipid nanoparticles. This paper explores the use of microfluidic platforms as a high-throughput research tool for the evaluation of nanobiomaterials. Typical screening of such materials involves cell/tissue cultures to determine attributes such as cell adhesion, proliferation, differentiation, as well as biocompatibility. In addition to this, other areas such as drug delivery and toxicity can also be evaluated via microfluidics. Traditional approach for screening of such materials is very time-consuming, and a lot of animals should be sacrificed since it involves one material and a single composition or concentration for a single test. The microfluidics approach has the advantage of using multiple types of drugs and their concentration gradients to simultaneously study the effect on the nanobiomaterial and its interaction with cell/tissue. In addition to this, microfluidics provides a unique environment to study the effect of cell-to-extracellular interaction and cell-to-cell communication in the presence of the nanobiomaterials.

1. Introduction

The field of microfluidics has seen great advances in the past decade. Two important application areas of microfluidics have been the use of it as a platform for medical diagnostics and biosensing. Microfluidic platforms like lab-on-a-chip have the advantage of using very small quantities of reagents, typically in the nanoliter to microliter range. This feature is very valuable in medical diagnoses like cell-based assays, drug screening, and screening for diseases [1–9]. Microfluidic devices are especially useful for cell-based assays because of the comparable scale of microfluidic channels and cells. In addition to this, the scale of the devices allows for things like growth factors to accumulate and form a stable environment for cell culture. Microfluidics also presents the potential to influence stem cell research, particularly for high-throughput analysis of signals that affect stem cells [4]. In light of this potential, one of the leading areas for microfluidics research will be its use as a platform for nanobiomaterials-based cell cultures [1–6, 10–20]. Such a high-throughput method will be a key factor in the future in enabling more realistic predictions of nanobiomaterial behavior in relation to cell toxicity, cell proliferation, and differentiation. This predictive capability is very important for preclinical methods since this has a direct impact on improving the attrition rates of candidate materials during clinical testing [21, 22].

This paper reviews the use of microfluidics as a high-throughput analysis platform for evaluation of nanobiomaterials. First, we provide a brief overview of microfluidic devices and their advantages over traditional cell culture technology. The following section discusses nanobiomaterials and some of their biomedical applications. Section 3 discusses the advances in microfluidic technology and how it is being applied as a high-throughput method in areas such

as material screening, toxicity testing, and drug discovery. Finally, Section 4 reviews research performed in evaluating nanobiomaterials using microfluidics. We conclude the paper with suggestions for next steps in specific areas.

2. Overview of Nanobiomaterials and Their Applications

Nanomaterials can provide the cells with the desired matrices that mimic the native environment of the cells. Usage of these materials includes hip replacements, fracture plates, bioresorbable sutures, tissue engineering scaffolds, and drug delivery devices [24–35]. Nanomaterials which mimic the matrix composition of the body are important regulator of stem cell differentiation towards specific cell lineages. These materials provide sites for cell adhesion and initiation of matrix-generated signal transduction pathways.

A nanobiomaterial can be defined as a biomaterial substrate composed of nanometer scale components. One example of a naturally occurring nanobiomaterial is inorganic bone matrix which is composed of hydroxyapatite crystals. Significant property changes can occur at the nanoscale, especially related to surface energy and reactivity. There are more atoms at the surface of nanostructured biomaterials which results in a marked increase in surface area to volume ratio when compared to micron scale biomaterials. Correlations of surface properties with stability, toxicity, and biodistributions are essential for *in vivo* applications [36]. This is very important considering that, for example, cell adhesion, proliferation, and migration during tissue repair are dependent on protein adsorption on the surface of implanted biomaterials.

The application potential of nanobiomaterials varies widely from tissue engineering to biosensing and diagnostics to drug delivery and disease therapy. Examples of some such applications are (a) nanohydroxyapatite for orthopedic implants and drug carriers for bone diseases, (b) carbon nanotubes and nanofibers as novel drug delivery devices, (c) gold nanoparticles for cancer diagnostics, and (d) quantum dots as biological sensors [37–43]. The use of carbon nanotubes and various types of nanoparticles in medicine is very prevalent in research and hence described in separate sections here.

2.1. Carbon Nanotubes in Medicine. Carbon nanomaterials are being used to develop the next generation of biomaterials for applications in therapeutics and regenerative medicine. Carbon nanomaterials, mainly in the form of nanotubes and graphene, have become the focus of intensive research because of their unique physical and chemical properties such as their hollow structure, their high surface area-to-volume ratio, electrical conductance, thermal conductivity, mechanical stiffness, and the possibilities of functionalizing them to change their intrinsic properties. Functionalization can increase their solubility and biocompatibility under physiological conditions. The nanomaterials can be further conjugated with specific biomolecules such as polymers, peptides, proteins, nucleic acids, and other therapeutic agents, which can target specific types of cells, tissue, and organs.

Carbon nanomaterials demonstrate several significant features that have promise for use in nervous system repair. Carbon nanomaterials have the type of nanosurface features that have been demonstrated to encourage nervous tissue regeneration, including the physical shape (a linear geometry), the nanoscale surface topology, and the high aspect ratio of nanomolecules or larger structures made from carbon nanotubes, like carbon nanotube thread. These closely resemble the microenvironment that nerve fibers migrate along during embryonic development and regeneration. Carbon nanomaterials also offer high mechanical strength to support process outgrowth and flexibility to avoid further damage of soft surrounding tissues during movement. Two applications of carbon nanomaterials of especial interest to neurobiologists are discussed here, their use in scaffolds to repair damaged nervous tissues, and their use as biocompatible electrodes for recording from or stimulating nervous tissues.

2.2. Nanoparticles in Medicine. Naturally occurring nanoparticles (NPs; such as LDL, HDL, and VDL), which are endogenously produced in developed organism, are utilized in transportation of hydrophobic molecules such as cholesterol and triglycerides into various parts of the body via the circulation. In the past twenty years, several groups started to develop various nanoparticles that can be an appropriate tool in diagnostics as well as cell/tissue-specific therapy. At present, nanoparticles are applied in several field of medicine: cancer treatment, high-resolution imaging, siRNA-based gene therapy and so forth. In this section, we give a brief summary on the up-to-date knowledge on NPs used in medicine.

At the dawn of the application of nanometer-sized particles, liposomes, which encapsulated highly hydrophobic anticancer agents (doxorubicin, daunorubicin), were used to deliver these compounds via circulation to the tumor cells. Due to passive distribution of these lipid vesicles in the body, toxic side-effect might occur causing arrhythmia, which could lead to heart failure. To overcome this problem, active targeting of lipid vehicles has been extensively studied and advanced: antibodies or their fragments, oligopeptides, nucleic acids (aptamers), small molecules, or others (vitamins or carbohydrates) are conjugated to the surface of nanoparticles [45].

In the presence of malignant tumors, hypocholesterolemia may arise due to the enhanced LDL uptake of cancerous cells. Thus, LDL vesicles, as naturally targeted lipoprotein vesicles, have been studied in diagnostics and treatment of cancer for several years: (1) LDL particles loaded/conjugated with photosensitizers are applied in photodynamic therapy; (2) ^{99m}Tc, ^{131}I, ^{125}I, or ^{68}Ga/^{111}. In labeled LDLs were used in *in vivo* tumor detection with gamma camera or PET (positron emission tomography) in animal models, respectively; (3) with the help of Gd or iron-loaded LDL vesicles could adequately image the boundary of the tumor with MRI [46–52]. It was also demonstrated that HDL

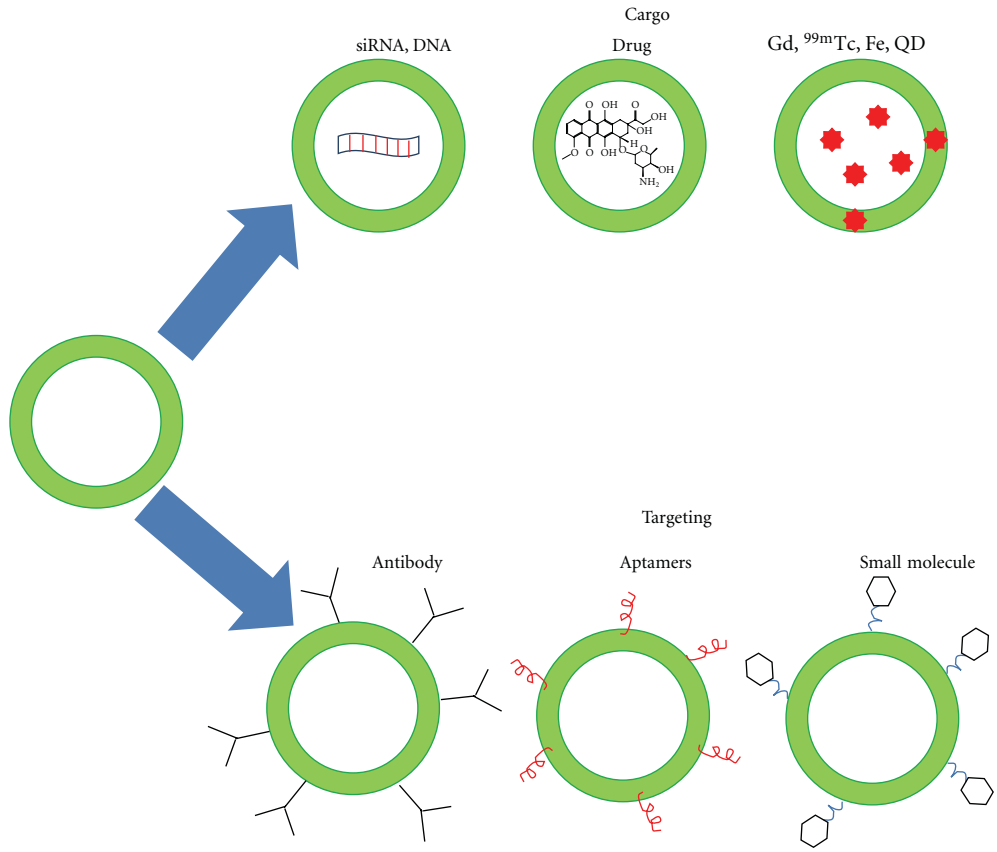

Figure 1: Classification of lipid-based nanovesicles mainly used in medicine.

cholesterol level was lower in certain malignancies, which can be also attributed to increased cholesterol consumption of cancer cells. Since several cancer cell lines express scavenger receptor class B type I (SR-BI), which is responsible for HDL uptake, anticancer agent loaded HDL or HDL mimicking, targeted lipid-protein vesicles can be used to deliver their cargo the tumor cells [53–55]. Furthermore, nanovesicles can also be applied to boost the immune system: injections of anticancer liposome vaccine resulted in hindered E.G7-OVE tumor progression in mice, and, in a clinical study, the survival time of patients with nonsmall cell lung cancer was longer compared to control group [56–58].

Atherosclerosis is the chief risk factor in the onset of cardiovascular diseases, which is a leading cause of death in the adult population and characterized by a complex etiology. In a recent paper, Lewis et al. reviewed several novel, nanometer-sized particle approaches on the therapy and detection of atherosclerotic plaques in model system or in human (Figure 1) [59].

2.3. TiO_2 Photocatalyst in Medicine. Biomedical research applications of titania (TiO_2) have primarily focused on harnessing its potential as a photocatalyst, specifically its ability to perform oxidative or reductive chemistry under illumination of UV light [61, 62]. Recent advances in doping, nanoparticle assembly, and dye conjugation have extended this photochemistry into the visible [63, 64]. Applications in biomedical field are becoming more routine due in part to the use of titania as an implant material and a desire to modify the surface of the titanium and make the implant "smarter." For example, photolysis of TiO_2 and nanotube TiO_2 with X-ray radiation was performed to demonstrate a possible drug release methodology [65]. In another study, precursors to hydroxyapatite formation were embedded in TiO_2 nanotubes and shown to influence bone formation in adult pig model [66]. Titania particles have also been used in disinfection applications and the killing of cancer cells [67, 68]. The ability to vary TiO_2 properties, morphology, and surface functionalities as a result of years of materials research allows for a wide range of possible medical benefits.

3. Microfluidics Devices for High-Throughput Analysis of Nanobiomaterials

There are numerous parameters of nanobiomaterials that can affect cellular behavior. The complexity of interacting parameters is one of the main motivations for the high-throughput screening of nanobiomaterials.

3.1. Introduction to Microfluidics. Microfluidic devices that enable high-throughput analysis have typically been produced using photoassisted and soft lithography techniques.

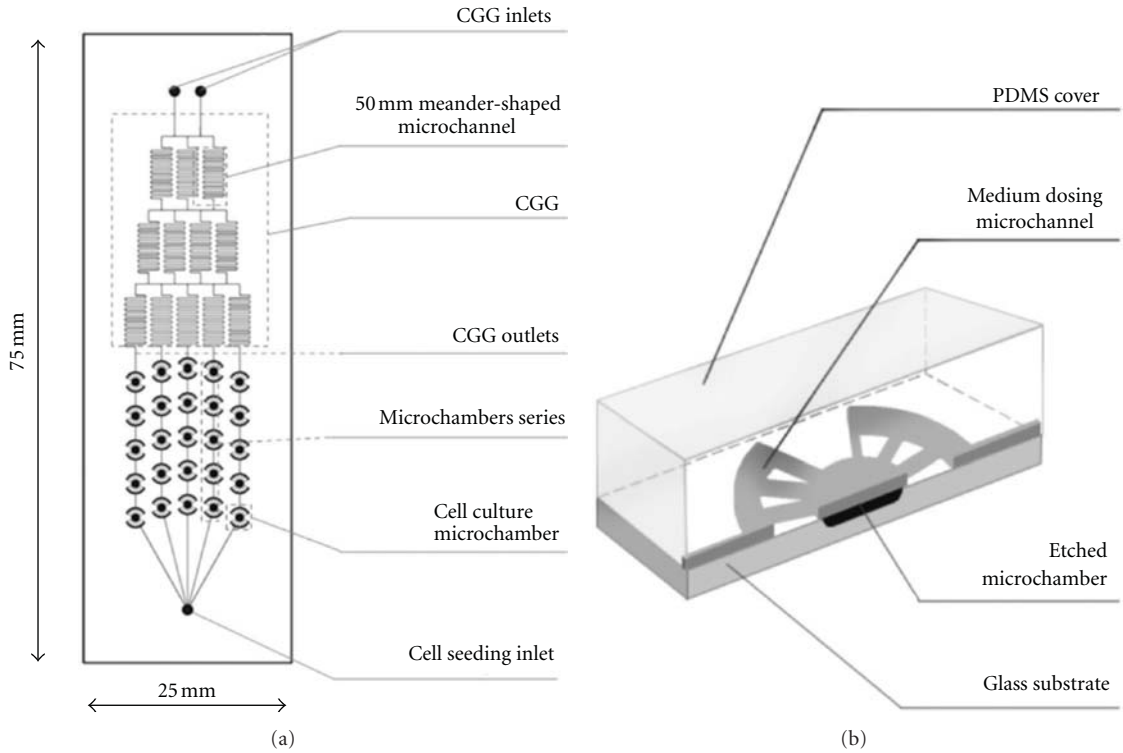

Figure 2: (a) The geometry of a microfluidic cell culture array for high-throughput analysis, (b) cross-section of cell culture microchamber [23] (reprinted from [23]).

An increasing demand for fully automated and quantitative cell culture technology has resulted in the development of microfluidic chip-based arrays. Compared to traditional culture tools, microfluidic platforms provide much greater control over cell microenvironment and rapid optimization of media composition using relatively small numbers of cells. Because a group of cells can more easily maintain a local environment within microchannels than in traditional culture flasks, cells grow significantly slower in microchannels than cells in traditional culture flasks [23, 70]. Figure 2 shows a typical microfluidic cell culture array for high-throughput analysis. The bonded PDMS cell culture microchambers provide a stable and uniform microenvironment for the cells [23].

3.2. Microfluidic Assays for Implant Material Screening. Recent advances in microfluidic techniques have increased the potential of high-throughput biochemical assays on individual mammalian cells. A microfluidic assay for bacterial chemotaxis was developed, in which a gradient of chemoeffectors was established inside a microchannel via diffusion between parallel streams of liquid in laminar flow [19, 71]. Bacterial adhesion often occurs in implant surgeries. Biomaterial-related infection starts with the adhesion of infectious bacteria, which is considered as one of the main causes of failure in implant surgery. Bacterial adhesion to surfaces is usually present in aqueous flows since such flows can promote the transport of microorganisms to surfaces. Considering that nanomaterial surfaces can be extremely reactive, the problem of bacterial adhesion becomes even more important. A microfluidic flow system was utilized to investigate the behaviors of biological cells under various flow conditions. This system offers precise kinetic control of the cellular microenvironment [20]. Microfluidics can also be applied for high-throughput and combinatorial electrochemistry where numerous channels operating in parallel can provide for synthesis of large arrays of materials and subsequently characterized for corrosion properties [44]. Figure 3 shows examples of such systems.

Microfluidic biochips offer the advantage of being able to include a whole new set of technologies that can preserve cellular function *in vitro* over a long period of time. This in turn would allow the proposal of relevant and alternative models to reduce the animal experimentation and their costs. They offer the possibility of dynamic cultures and kinetic studies on microengineered tissues simulating the cellular organizations that are found *in vivo*. This would minimize animal use as well as offer assays more relevant than traditional techniques [73].

3.3. Microfluidics Screening in Tissue Engineering. Applications of microfluidic systems based on cell and tissue culture are now emerging, as platforms for high-throughput screening, drug discovery, and toxicity testing. A new generation of microfluidics-based approaches are designed for specific tissue and organ applications, incorporating microvascular

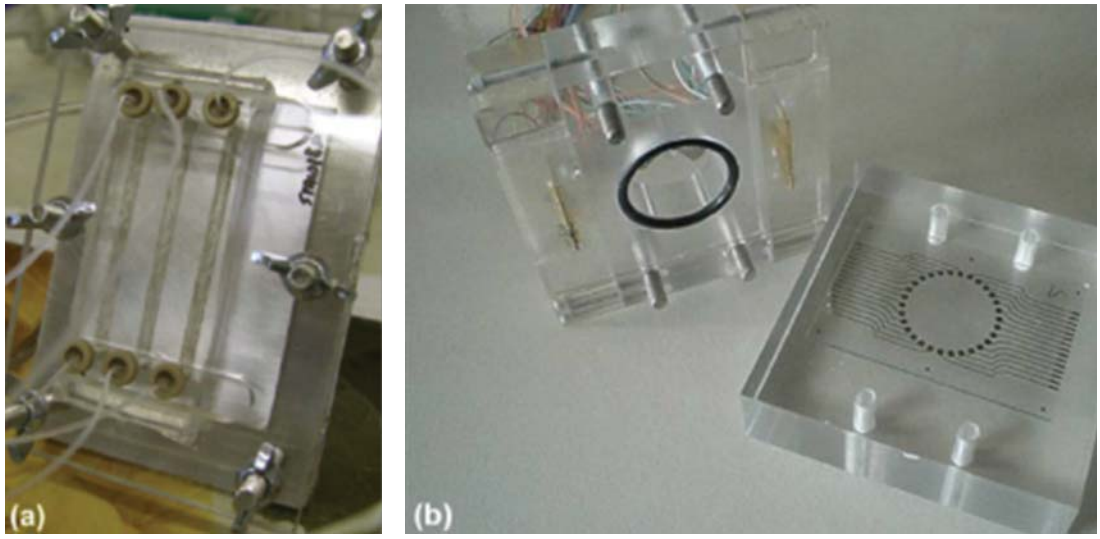

(a) (b)

Figure 3: (a) Microfluidic assembly for high-throughput corrosion experiments, (b) multielectrode electrochemical testing cell [44] (reprinted [44]).

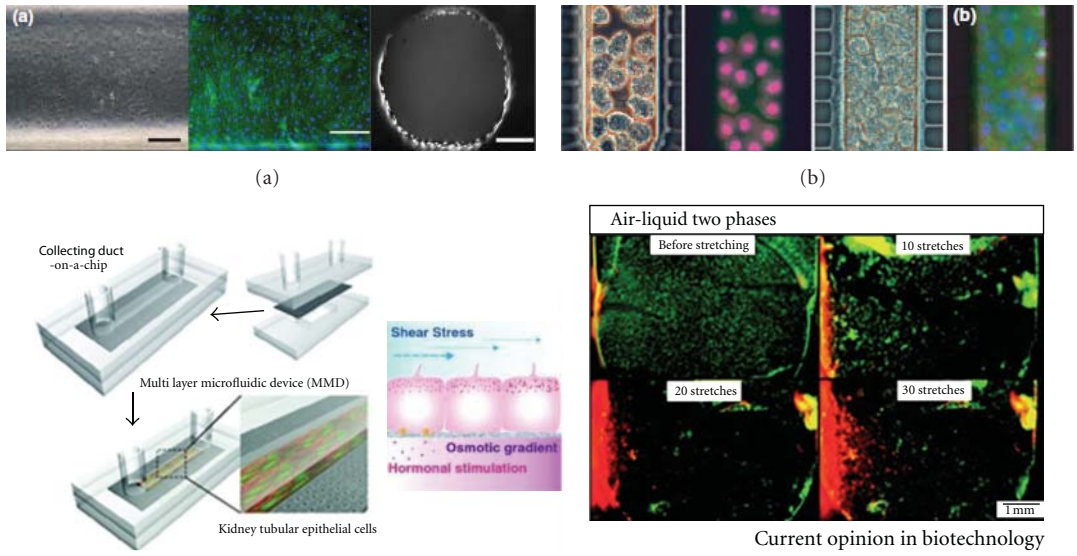

Figure 4: Organ-specific tissue-engineered microfluidic devices: (a) vasculature, (b) liver sinusoid, (c) renal tubule, and (d) alveolar fluid-liquid interface [16] (reprinted from [16]).

networks, structures for transport and filtration, and a three-dimensional microenvironment suitable for supporting phenotypic cell behavior, tissue function, and implantation, and host integration [16]. Figure 4 shows a range of such devices.

Microvascular networks are key sites for many of cell-cell and particle-cell interactions during physiological and/or pathological processes. Advances in targeted drug delivery to the microvasculature often involve encapsulating drugs in delivery vehicles ranging from microparticles to nanoparticles. Development of *in vitro* microfluidic devices to mimic these microcirculatory processes has been a critical step forward in our understanding of the inflammatory process, developing of nanoparticulate drug carriers, and developing realistic *in vitro* models of the microvasculature and its surrounding tissue [17].

3.4. Microfluidics with Microarrays for High-Throughput Multiplexing. A microarray consists of a support onto which hundreds to thousands of different molecular reporter probes are attached or immobilized at fixed locations in

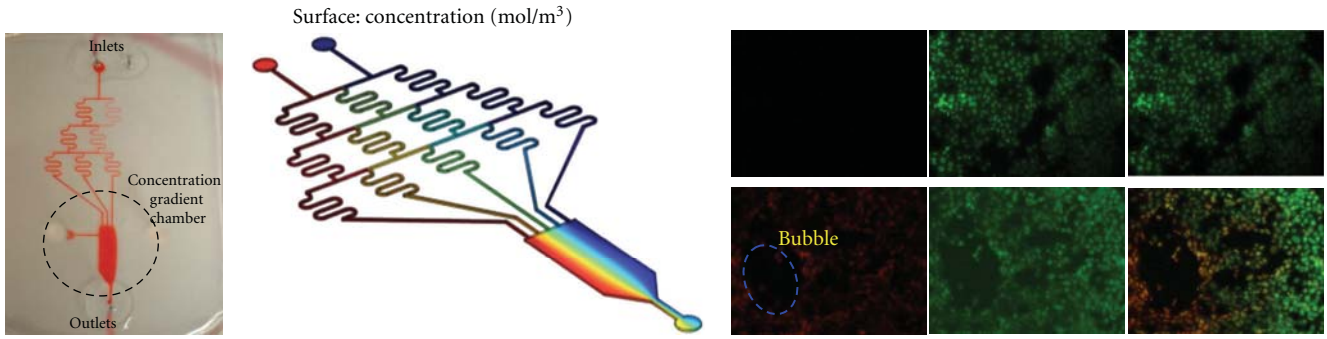

Figure 5: (a) Layout of microfluidic gradient mixer used to generate a linear concentration gradient. (b) Linear concentration gradient obtained from a three-dimensional numerical simulation using COMSOL. (c) Osteoblast cell live/dead assay using the microfluidic network shown above.

either a two-dimensional or three-dimensional format. The multiplexing capabilities of microarray-based assays are produced by spatially encoding the array, in which each location on the array is used as a reporter of a specific analyte. For conventional microarrays, shortcomings include (a) the analyte binding process on supports requires long incubation times to produce the optimal signal due to slow diffusional kinetics and (b) consumption of large amounts of precious sample material for interrogating the array due to the large area occupied by high-density arrays. The use of microfluidic platforms can directly address these issues as well as offer the potential for parallel processing of multiple samples [5].

Chemotaxis is the directional migration of cells in response to chemical gradients of molecules called chemoattractants. The process is crucial in numerous biological processes. Most of the traditional methods (e.g., different types of chambers or puffer pipettes) are nonideal in that the generated gradients are created in macroscopic environments, are nonlinear, and change with time in an uncontrolled manner. By making use of microfluidic gradient generators, chemotaxis studies can be carried out with precise spatial and temporal control of the chemical environment around cells [6, 76]. Figure 5 shows an osteoblast cell live/dead assay using a microfluidic gradient generator. Such a setup can be used for screening of cell interaction with nanomaterials in the presence of growth factors.

4. Evaluation of Nanobiomaterials Using Microfluidics

4.1. Combinatorial Screening. The application of combinatorial approaches to the discovery of new nanomaterials provides exciting opportunities to produce materials designed to give optimal performance for specific applications. This process has been facilitated by the development of the automated fabrication and analysis of polymer microarrays, produced largely by contact or ink-jet printing. Studies have focused on the discovery of materials that support cell attachment for particular cell types. In addition to applications of microarrays in screening for desirable material properties, the size of the sample set provides enormous potential to be able to elucidate key underlying principles that govern biological-material interactions [2, 77–79]. As mentioned previously in Section 2, the use of microfluidics in conjunction with microarrays enables a high-throughput mode for screening of nanomaterials and their interactions with the cell environment.

Cell-based assays are currently considered central to toxicity testing and biomaterials testing [6, 16, 81–86]. Despite the frequent lack of correlation between *in vivo* models and *in vivo* observations, cell models still seek validation as a useful screening bridge between materials quality analysis and *in vivo* deployment. Advances in high-throughput methods using microfluidics allow for toxicity and efficacy screening of multiple nanomaterials at multiple concentrations with multiple cell lines, simultaneously. By assaying numerous material types/functionalizations and material concentrations on numerous cell types, all in parallel, complex interactions between materials and cells may be ascertained through data analysis [87]. Nanomaterials for biomedical applications exhibit extremely high specific surface areas exposed to physiological environments. Due to the extremely reactive nature of nanomaterials surfaces, extensive characterization and correlation of nanophase surface properties with their stability, toxicity, and distributions are essential for *in vivo* applications [36, 60].

One such study used surface chemistry, nanostructures, and microfluidics to create a set of tools applicable for problems ranging from molecular to cellular analysis. Microfluidics allows the precise manipulation of fluids down to the nanoliter scale, and this is important since most biochemical processes take place in the aqueous phase. Surface gradients with arbitrary shapes from virtually any type of biomolecules can be formed by transferring the gradients in solution to a surface by adsorption as shown in Figure 6 below. One example presented in this study is that of axon specification during differentiation of neuritis into axons and dendrites. Microfluidic gradient generators similar to the one shown in Figure 6 were used to generate gradients of laminin in solution and transferred to the substrate by physical adsorption. The study indicates that

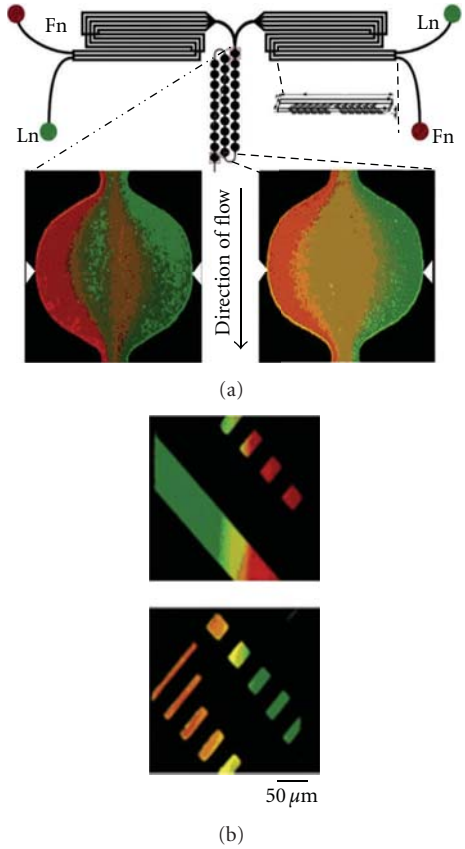

Figure 6: (a) Generation of complex gradients in solution by combining two microfluidic generators. (b) Transferring the gradient in solution into a gradient on surfaces through adsorption [60] (reprinted from [60]).

axon specification orients in the direction of increasing laminin surface density [60].

4.2. Microfluidic Evaluation in Tissue Engineering. A microfluidic 3D tissue model was used to evaluate the efficacy of PLGA micropatterns for promoting osteogenic development by osteoblasts and preventing biofilm formation. This study demonstrated the tremendous efficiency of the tissue model approach by significantly reducing the number of samples and experiments required to assess the *in vitro* efficacy of the micropatterns by conventional biofilm and cell culture experiments. This approach provided an ability to directly monitor how the 3D tissue development was positively influenced by the presence of biphasic calcium phosphate nanoparticles in the micropattern [15, 89]. Another study looked at biofilm-related infection of orthopedic implants in physiologically relevant microenvironments using a multichannel microfluidic device. It was used to observe in real time the development of osteoblasts into three-dimensional (3D) tissue-like structures how this development was influenced by phenotypes of a specific bacteria [90]. The microfluidics approach has also been used to build a three-dimensional heterogeneous multilayer tissue-like structure inside microchannels. Patterning of biological structures can be achieved not only on the surface but also over the thickness of the construct. The tissue formed from different types of cells and biopolymer components can be engineered to model layered *in vivo* living systems. This approach provides a novel solution to fabricate hybrid biopolymers and hierarchical tissue structures for tissue engineering and basic cell biology [91]. One of the keys to tissue engineering and cell therapy is the ability to identify materials that support cell adhesion, proliferation, and differentiation.

One such study utilizes microfluidics for nanoliter-scale synthesis of materials and simultaneous characterization of their interaction with embryonic stem cells using this high-throughput approach. This study simultaneously characterizes over 1700 embryonic stem cell material interactions. The identification of materials that selectively support the growth of specific cell types could be useful for the creation of complex tissue-engineered constructs. The proof-of-concept study was carried out with hES cells, and it identified polymers that allow for varying levels of hES cell attachment and spreading, cell-type specific growth, and growth factor-specific proliferation [92]. There are other studies that discuss the characterization of biomaterial interaction with stem cells using microfluidic approaches [3, 13, 93]. These approaches can be adopted for characterization of nanobiomaterials as well.

Another study describes a highly parallel cell-based microfluidic device where biomolecules are transported via mobile substrates, like micro/nano beads or cells. Such dynamic microarrays present several advantages over static microarrays like the ability to mix and match the beads or the cells to cater for the type of screening to be performed and introduce them into the microarray on demand. The beads or cells can be replaced, thus resulting in a reusable format that greatly reduces the cost of operation. The reaction on beads tends to be faster compared to conventional planar surfaces, as micro/nano beads have increased surface area to volume ratio and hence higher binding capacity. Combining such a device with automation will allow for high-throughput screening in an environment that closely mimics cell-cell interactions found in animals [69]. Figure 7 shows the potential contribution of MEMS and nanobiotechnology to society.

4.3. Nanobiomaterials Evaluation for Diagnostics and Sensors. A number of studies have focused on microfluidic and nanofluidic devices as diagnostic tools for cancer and other infectious diseases [29, 72, 94–97]. Inorganic nanoparticles, semiconductor quantum dots (QDs), carbon nanotubes, polymeric nanoparticles, as well as cantilevers and nanochips, all have the potential to be useful in the design of sensitive pathogen diagnostics [98]. The fabrication of nanodevices as probes is complex, most likely the assembly of building blocks including nanoparticles, nanowires, nanotubes, and substrates. Typical examples of nanodevices are nanofluidic arrays and protein nanobiochips. One of the most promising uses of nanofluidic devices is isolation and analysis of individual biomolecules, such as DNA, which could lead to new detection schemes for cancer. Devices

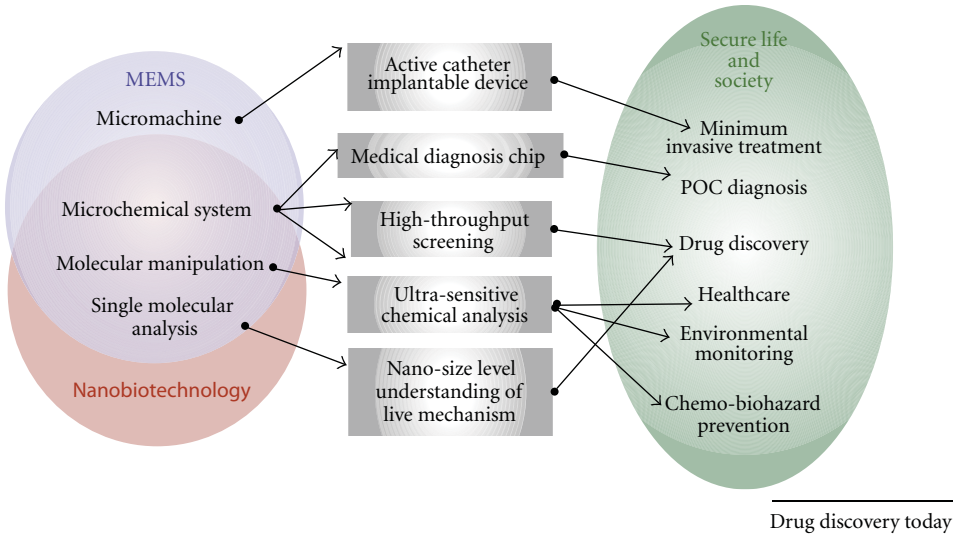

Figure 7: Contribution of MEMS and nanobiotechnology to the quality of life for society in the future through medical and pharmacological applications [69] (reprinted from [69]).

based on nanowires are emerging as a powerful and general platform for ultrasensitive, direct electrical detection of biological and chemical species [95]. Nanowire sensors may be formed into dense circuits which can be constructed within microfluidics environments, creating very dense sensor libraries. These enable measurements of many different genes and proteins from very small tissue samples or even single cells [97]. Nano/microfluidic diagnostic technologies are potentially applicable to global health applications, since they are disposable, inexpensive, portable, and easy-to-use for detection of infectious diseases. Nano/microfluidic technologies have been successfully integrated with current POC devices for on-chip diagnosis and monitoring of infectious diseases at resource-limited settings [72, 96]. Figure 8 shows a microfluidic NMR biosensor combined with magnetic nanoparticles.

Another study used microfluidics as an *in vitro* assessment of the cytotoxicity potential of quantum dots. A multicompartmental device was integrated with a syringe pump to establish a flow exposure system. This study enabled the exposure of cell cultures to variable concentrations of QDs simultaneously. The controlled flow conditions mimicked *in vivo* physiological conditions very closely. The results were compared to those from static exposure conditions. Both static and flow conditions are illustrated in Figure 9 below. The static exposure of cells to QDs resulted in a higher percentage of cell death and an increased number of detached and deformed cells. This study demonstrated the efficient utilization of microfluidic technology in nanotoxicity research [74].

Another QD study involved tracking the mechanism of nerve growth factor (NGF) signal propagation from the axon terminal to cell body. Axonal transport of NGF signals is critical to survival, differentiation, and maintenance of peripheral sympathetic and sensory neurons. One set of hypotheses for retrograde axonal transport of NGF states that NGF and its signaling proteins are transported in complex vesicles such as multivesicular bodies, lysosomes, or macropinosomes. To study this, dorsal root ganglion (DRG) neurons were cultured in a microfluidic chamber (shown in Figure 10 below) and treated with quantum dot-labeled NGF (QD-NGF). The conclusion from this study was that small vesicles (50–150 nm) are responsible for most retrograde axonal transport of QD-NGF in DRG axons [75].

In a third study involving QDs, an integrated microfluidic device capable of screening an anticancer drug has been presented by analyzing apoptotic cells using biofunctionalized QDs. The cell immobilizing structures and gradient-generating channels were integrated within the device. The technique utilizes Annexin V conjugated quantum dots as apoptosis detection probes as shown in Figure 11. This technique can bridge the gap between the quantum dots based *in vitro* cell imaging, and the analysis of individual apoptotic cell in a microfluidic system allows an easy operating protocol to screen some clinically available anticancer drugs [80].

Liposome nanoparticles have been evaluated for formulation composition and stability using a microfluidic biochip. Changes in size and surface chemistry of these nanoparticles are important since they can significantly alter *in vivo* distributions of these nanoparticles which affect therapeutic outcomes. The biochip was embedded with dielectric microsensors which enabled quantitative measurements of formulation using unique electrical properties of liposomes [99]. In another study, microfluidics has been used as a platform for monitoring lipid vesicle membrane permeability to tetracyclines. This approach allows for use of artificial nanovesicles to study the influence on permeability. Liposomes are immobilized onto the glass surface in a stripe pattern via an avidin-biotin bond. The biggest advantage provided by microfluidics in this case is the ability to reliably resemble an *in vivo* environment. The fluid flow provides

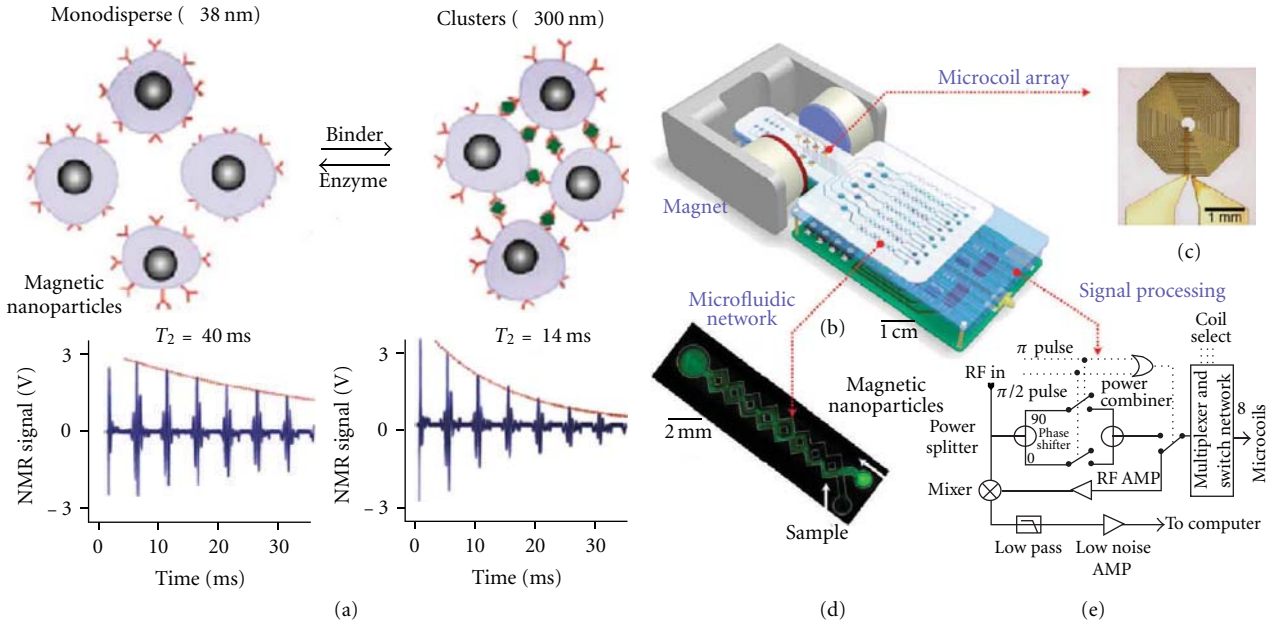

Figure 8: Microfluidic NMR biosensor combined with magnetic nanoparticles for potential applications of TB testing in resource-limited settings [72] (reprinted from [72]).

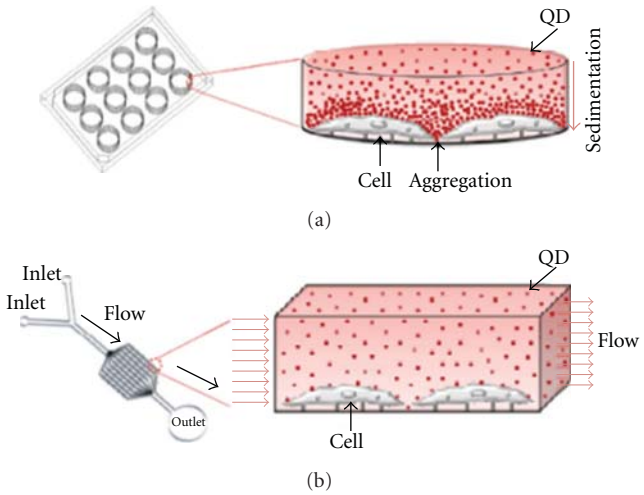

Figure 9: Schematic illustration of (a) static exposure resulting in sedimentation of quantum dots and (b) flow exposure resulting in homogeneous distribution of quantum dots [74] (reprinted from [74]).

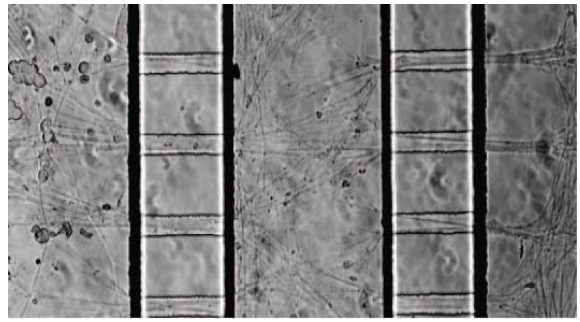

Figure 10: A representative image of DRG neurons cultured inside a microfluidic device. Axons were able to extend across two columns of microgrooves into the distal axon chamber [75] (reprinted from [75]).

a constant concentration profile and thereby resembles the drug transport via blood in the human body. Additionally, many different drug concentrations and pH conditions can be investigated in parallel with this approach. It allows the measurements of slow and fast kinetics with a good temporal resolution, requires only short measuring times, consumes very small volumes of drug solution and vesicle suspension, and allows sensitive detection at low concentrations using TIRF microscopy [88]. Figure 12 shows the setup used in this study.

Synthesis of nanoscale lipid vesicles using microfluidic channels has been studied where the device geometry and flow rate have been used to influence the vesicle size. This method enables a reliable control over vesicle size and homogeneity when compared to bulk liquid synthesis techniques [100].

5. Conclusions and Future Work

In summary, the use of microfluidics as a platform for biomedical research and applications is very widespread. The specific use of microfluidic devices in conjunction with nanobiomaterials is becoming an established method for fast-throughput analysis in biomedical engineering. The usage covers cell-based assays for toxicity and biocompatibility screening of materials, tissue engineering and cell therapy,

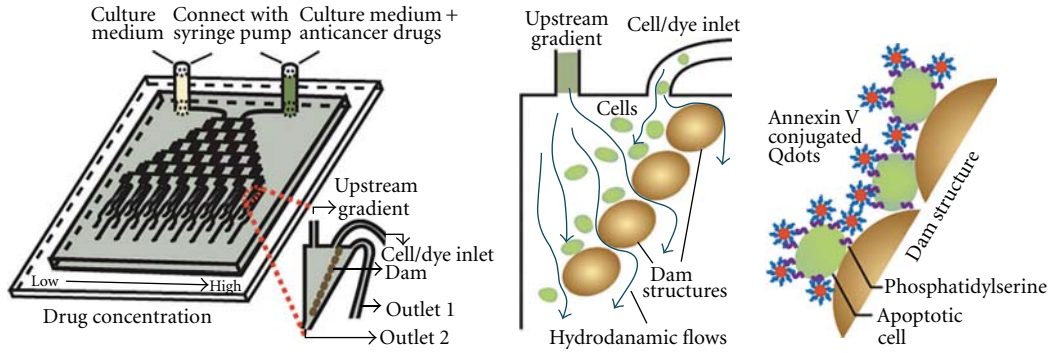

FIGURE 11: Schematic drawing of (a) microfluidic gradient generator, (b) cell trapping on sand-bag structures, and (c) detection of apoptotic cells immobilized on dam structures using Annexin V conjugated QDs [80] (reprinted from [80]).

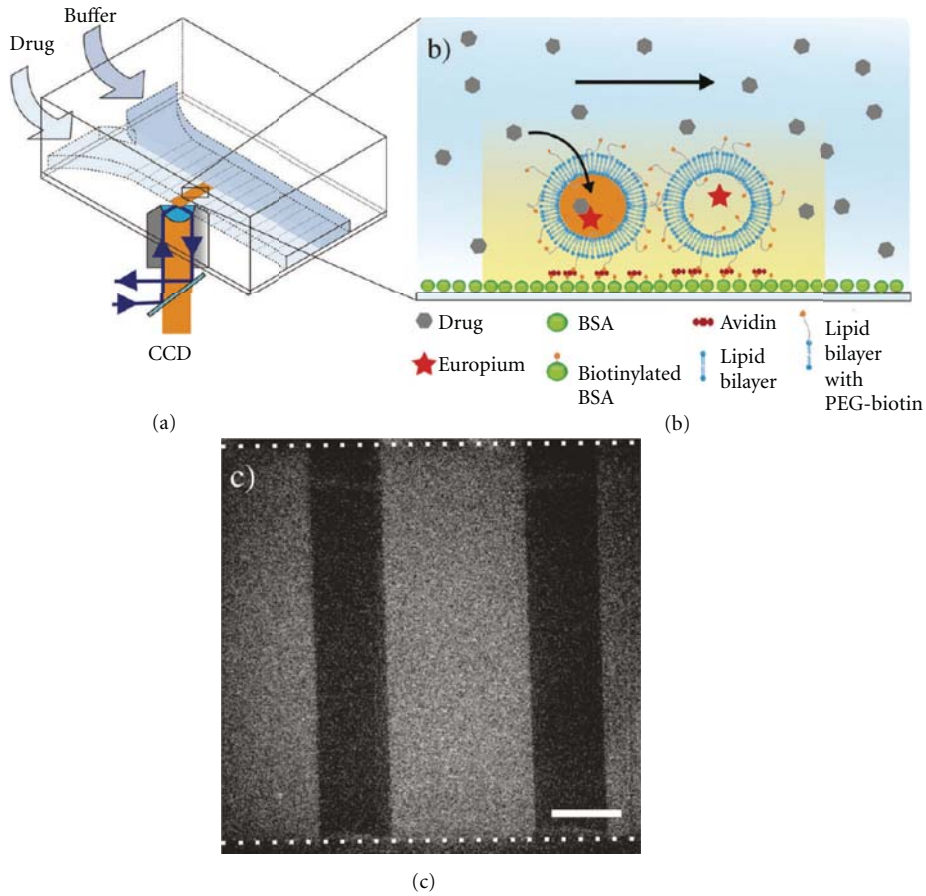

FIGURE 12: A microfluidic chip, mounted on a TIRF microscope, is used to supply buffer and tetracyclines through a microchannel to vesicles immobilized on the bottom glass slide. (b) Scheme of the detection assay. (c) Micrograph of the stripe pattern. Dotted lines indicate the channel walls [88] (reprinted from [88]).

nerve regeneration, diagnostics and sensing for infectious diseases and cancer biomarkers, and drug discovery. The nanomaterials used in the microfluidic environments present a challenge to characterization due to their unique properties and reactive nature, and this should be noted while performing future research. These microfluidic platforms have great potential for integration into lab-on-a-chip type of devices and providing point-of-care solutions.

Future work in this area by the authors will focus on using microfluidics as an assessment tool for nanobiomaterials in emerging research on degradable metallic biomaterials. The target applications for such materials include

craniofacial and orthopedic implants, nerve regeneration, bone and bone-ligament fixation, and airway stents. One of the objectives of the research will be to use computational tools to complement experimental efforts in microfluidics. For example, computational models can be used to predict distribution of species such as growth factors in cell culture chambers as a result of concentration gradient generation in microfluidic networks. Additionally, these models can be used to simulate various microenvironments in cell cultures which in turn mimic *in vivo* conditions. Finally, microfluidic platforms can be used to assess the effect of growth factors on nanobiomaterial-cell interactions, and the high-throughput capability can result in simultaneous assessment of multiple concentrations in conjunction with various biomaterial compositions.

Acknowledgments

This work was sponsored by the NSF ERC for Revolutionizing Metallic Biomaterials, http://erc.ncat.edu/. This project was supported in part by NIH Grant (1R21AR060966), Korea Grant (Project no. 00042172-1), and ONR Grant (N00014-11-1-0315).

References

[1] A. Astashkina, B. Mann, and D. W. Grainger, "A critical evaluation of *in vitro* cell culture models for high-throughput drug screening and toxicity," *Pharmacology & Therapeutics*, vol. 134, no. 1, pp. 82–106, 2012.

[2] A. L. Hook, D. G. Anderson, R. Langer, P. Williams, M. C. Davies, and M. R. Alexander, "High throughput methods applied in biomaterial development and discovery," *Biomaterials*, vol. 31, no. 2, pp. 187–198, 2010.

[3] T. G. Fernandes, M. M. Diogo, D. S. Clark, J. S. Dordick, and J. M. S. Cabral, "High-throughput cellular microarray platforms: applications in drug discovery, toxicology and stem cell research," *Trends in Biotechnology*, vol. 27, no. 6, pp. 342–349, 2009.

[4] M. Yliperttula, B. G. Chung, A. Navaladi, A. Manbachi, and A. Urtti, "High-throughput screening of cell responses to biomaterials," *European Journal of Pharmaceutical Sciences*, vol. 35, no. 3, pp. 151–160, 2008.

[5] C. Situma, M. Hashimoto, and S. A. Soper, "Merging microfluidics with microarray-based bioassays," *Biomolecular Engineering*, vol. 23, no. 5, pp. 213–231, 2006.

[6] J. Pihl, J. Sinclair, M. Karlsson, and O. Orwar, "Microfluidics for cell-based assays," *Materials Today*, vol. 8, no. 12, pp. 46–51, 2005.

[7] C. Rivet, H. Lee, A. Hirsch, S. Hamilton, and H. Lu, "Microfluidics for medical diagnostics and biosensors," *Chemical Engineering Science*, vol. 66, no. 7, pp. 1490–1507, 2011.

[8] S. le Gac and A. van den Berg, "Single cells as experimentation units in lab-on-a-chip devices," *Trends in Biotechnology*, vol. 28, no. 2, pp. 55–62, 2010.

[9] W. Siyan, Y. Feng, Z. Lichuan et al., "Application of microfluidic gradient chip in the analysis of lung cancer chemotherapy resistance," *Journal of Pharmaceutical and Biomedical Analysis*, vol. 49, no. 3, pp. 806–810, 2009.

[10] P. G. Gross, E. P. Kartalov, A. Scherer, and L. P. Weiner, "Applications of microfluidics for neuronal studies," *Journal of the Neurological Sciences*, vol. 252, no. 2, pp. 135–143, 2007.

[11] S. Kim, H. J. Kim, and N. L. Jeon, "Biological applications of microfluidic gradient devices," *Integrative Biology*, vol. 2, no. 11-12, pp. 584–603, 2010.

[12] J. M. Klostranec, Q. Xiang, G. A. Farcas et al., "Convergence of quantum dot barcodes with microfluidics and signal processing for multiplexed high-throughput infectious disease diagnostics," *Nano Letters*, vol. 7, no. 9, pp. 2812–2818, 2007.

[13] A. Ranga and M. P. Lutolf, "High-throughput approaches for the analysis of extrinsic regulators of stem cell fate," *Current Opinion in Cell Biology*, vol. 24, pp. 1–9, 2012.

[14] Kshitiz, D. H. Kim, D. J. Beebe, and A. Levchenko, "Micro- and nanoengineering for stem cell biology: the promise with a caution," *Trends in Biotechnology*, vol. 29, no. 8, pp. 399–408, 2011.

[15] J.-H. Lee, Y. Gu, H. Wang, and W. Y. Lee, "Microfluidic 3D bone tissue model for high-throughput evaluation of wound-healing and infection-preventing biomaterials," *Biomaterials*, vol. 33, no. 4, pp. 999–1006, 2012.

[16] N. K. Inamdar and J. T. Borenstein, "Microfluidic cell culture models for tissue engineering," *Current Opinion in Biotechnology*, vol. 22, pp. 681–689, 2011.

[17] B. Prabhakarpandian, M. C. Shen, K. Pant, and M. F. Kiani, "Microfluidic devices for modeling cell-cell and particle-cell interactions in the microvasculature," *Microvascular Research*, vol. 82, pp. 210–220, 2011.

[18] A. Schober, C. Augspurger, U. Fernekorn et al., "Microfluidics and biosensors as tools for NanoBioSystems research with applications in the 'Life Science'," *Materials Science and Engineering B*, vol. 169, no. 1–3, pp. 174–181, 2010.

[19] C. Yi, C. W. Li, S. Ji, and M. Yang, "Microfluidics technology for manipulation and analysis of biological cells," *Analytica Chimica Acta*, vol. 560, no. 1-2, pp. 1–23, 2006.

[20] Y. Liu, J.-C. Wang, L. Ren et al., "Microfluidics-based assay on the effects of microenvironmental geometry and aqueous flow on bacterial adhesion behaviors," *Journal of Pharmaceutical Analysis*, vol. 1, no. 3, pp. 175–183, 2011.

[21] A. L. van de Ven, J. H. Sakamoto, B. Godin et al., "Enabling individualized therapy through nanotechnology," *Pharmacological Research*, vol. 62, no. 2, pp. 57–89, 2010.

[22] J. S. Murday, R. W. Siegel, J. Stein, and J. F. Wright, "Translational nanomedicine: status assessment and opportunities," *Nanomedicine*, vol. 5, no. 3, pp. 251–273, 2009.

[23] K. Ziolkowska, E. Jedrych, R. Kwapiszewski, J. Lopacinska, M. Skolimowski, and M. Chudy, "PDMS/glass microfluidic cell culture system for cytotoxicity tests and cells passage," *Sensors and Actuators B*, vol. 145, no. 1, pp. 533–542, 2010.

[24] S. Kobel and M. P. Lutolf, "Biomaterials meet microfluidics: building the next generation of artificial niches," *Current Opinion in Biotechnology*, vol. 22, pp. 690–697, 2011.

[25] A. Muralimohan, Y. J. Eun, B. Bhattacharyya, and D. B. Weibel, "Dissecting microbiological systems using materials science," *Trends in Microbiology*, vol. 17, no. 3, pp. 100–108, 2009.

[26] Y. Wang, J. D. Byrne, M. E. Napiera, and J. M. DeSimonea, "Engineering nanomedicines using stimuli-responsive biomaterials," *Advanced Drug Delivery Reviews*. In press.

[27] A. Seidi, M. Ramalingam, I. Elloumi-Hannachi, S. Ostrovidov, and A. Khademhosseini, "Gradient biomaterials for soft-to-hard interface tissue engineering," *Acta Biomaterialia*, vol. 7, no. 4, pp. 1441–1451, 2011.

[28] A. Kunze, M. Giugliano, A. Valero, and P. Renaud, "Micropatterning neural cell cultures in 3D with a multi-layered scaffold," *Biomaterials*, vol. 32, no. 8, pp. 2088–2098, 2011.

[29] J. V. Jokerst, A. Raamanathan, N. Christodoulides et al., "Nano-bio-chips for high performance multiplexed protein detection: determinations of cancer biomarkers in serum and saliva using quantum dot bioconjugate labels," *Biosensors and Bioelectronics*, vol. 24, no. 12, pp. 3622–3629, 2009.

[30] D. F. Williams, "On the nature of biomaterials," *Biomaterials*, vol. 30, no. 30, pp. 5897–5909, 2009.

[31] D. Chow, M. L. Nunalee, D. W. Lim, A. J. Simnick, and A. Chilkoti, "Peptide-based biopolymers in biomedicine and biotechnology," *Materials Science and Engineering R*, vol. 62, no. 4, pp. 125–155, 2008.

[32] A. A. Agrawal, B. J. Nehilla, K. V. Reisig et al., "Porous nanocrystalline silicon membranes as highly permeable and molecularly thin substrates for cell culture," *Biomaterials*, vol. 31, no. 20, pp. 5408–5417, 2010.

[33] H. Chen, C. Jiang, C. Yu, S. Zhang, B. Liu, and J. Kong, "Protein chips and nanomaterials for application in tumor marker immunoassays," *Biosensors and Bioelectronics*, vol. 24, no. 12, pp. 3399–3411, 2009.

[34] M. E. Furth, A. Atala, and M. E. V. Dyke, "Smart biomaterials design for tissue engineering and regenerative medicine," *Biomaterials*, vol. 28, no. 34, pp. 5068–5073, 2007.

[35] R. Langer and D. A. Tirrell, "Designing materials for biology and medicine," *Nature*, vol. 428, no. 6982, pp. 487–492, 2004.

[36] D. W. Grainger and D. G. Castner, "Nanobiomaterials and nanoanalysis: opportunities for improving the science to benefit biomedical technologies," *Advanced Materials*, vol. 20, no. 5, pp. 867–877, 2008.

[37] H. Liu and T. J. Webster, "Nanomedicine for implants: a review of studies and necessary experimental tools," *Biomaterials*, vol. 28, no. 2, pp. 354–369, 2007.

[38] E. Engel, A. Michiardi, M. Navarro, D. Lacroix, and J. A. Planell, "Nanotechnology in regenerative medicine: the materials side," *Trends in Biotechnology*, vol. 26, no. 1, pp. 39–47, 2008.

[39] R. P. Singh, "Prospects of nanobiomaterials for biosensing," *International Journal of Electrochemistry*, vol. 2011, pp. 1–30, 2011.

[40] L. Yildirimer, N. T. K. Thanh, M. Loizidou, and A. M. Seifalian, "Toxicology and clinical potential of nanoparticles," *Nano Today*, vol. 6, no. 6, pp. 583–607, 2011.

[41] F. Gelain, "Novel opportunities and challenges offered by nanobiomaterials in tissue engineering," *International Journal of Nanomedicine*, vol. 3, no. 4, pp. 415–424, 2008.

[42] W. Hu and C. M. Li, "Nanomaterial-based advanced immunoassays," *Wiley Interdisciplinary Reviews*, vol. 3, no. 2, pp. 119–133, 2011.

[43] B. G. Chung, L. Kang, and A. Khademhosseini, "Micro- and nanoscale technologies for tissue engineering and drug discovery applications," *Expert Opinion on Drug Discovery*, vol. 2, no. 12, pp. 1653–1668, 2007.

[44] T. H. Muster, A. Trinchi, T. A. Markley et al., "A review of high throughput and combinatorial electrochemistry," *Electrochimica Acta*, vol. 56, no. 27, pp. 9679–9699, 2011.

[45] M. K. Yu, J. Park, and S. Jon, "Targeting strategies for multifunctional nanoparticles in cancer imaging and therapy," *Theranostics*, vol. 2, no. 1, pp. 43–44, 2012.

[46] I. R. Corbin, H. Li, J. Chen et al., "Low-density lipoprotein nanoparticles as magnetic resonance imaging contrast agents," *Neoplasia*, vol. 8, no. 6, pp. 488–498, 2006.

[47] R. A. Firestone, "Low-density lipoprotein as a vehicle for targeting antitumor compounds to cancer cells," *Bioconjugate Chemistry*, vol. 5, no. 2, pp. 105–113, 1994.

[48] D. Kessel, "Porphyrin-lipoprotein association as a factor in porphyrin localization," *Cancer Letters*, vol. 33, no. 2, pp. 183–188, 1986.

[49] S. M. Moerlein, A. Daugherty, B. E. Sobel, and M. J. Welch, "Metabolic imaging with gallium-68- and indium-111-labeled low-density lipoprotein," *Journal of Nuclear Medicine*, vol. 32, no. 2, pp. 300–307, 1991.

[50] E. Ponty, G. Favre, R. Benaniba et al., "Biodistribution study of 99mTc-labeled LDL in B16-melanoma-bearing mice. Visualization of a preferential uptake by the tumor," *International Journal of Cancer*, vol. 54, no. 3, pp. 411–417, 1993.

[51] P. C. N. Rensen, R. L. A. de Vrueh, J. Kuiper, M. K. Bijsterbosch, E. A. L. Biessen, and T. J. C. van Berkel, "Recombinant lipoproteins: lipoprotein-like lipid particles for drug targeting," *Advanced Drug Delivery Reviews*, vol. 47, no. 2-3, pp. 251–276, 2001.

[52] G. Zheng, H. Li, M. Zhang, S. Lund-Katz, B. Chance, and J. D. Glickson, "Low-density lipoprotein reconstituted by pyropheophorbide cholesteryl oleate as target-specific photosensitizer," *Bioconjugate Chemistry*, vol. 13, no. 3, pp. 392–396, 2002.

[53] S. Acton, A. Rigotti, K. T. Landschulz, S. Xu, H. H. Hobbs, and M. Kriegert, "Identification of scavenger receptor SR-BI as a high density lipoprotein receptor," *Science*, vol. 271, no. 5248, pp. 518–520, 1996.

[54] Z. Zhang, J. Chen, L. Ding et al., "HDL-mimicking peptide-lipid nanoparticles with improved tumor targeting," *Small*, vol. 6, no. 3, pp. 430–437, 2010.

[55] W. J. McConathy, M. P. Nair, S. Paranjape, L. Mooberry, and A. G. Lacko, "Evaluation of synthetic/reconstituted high-density lipoproteins as delivery vehicles for paclitaxel," *Anti-Cancer Drugs*, vol. 19, no. 2, pp. 183–188, 2008.

[56] C. Butts, N. Murray, A. Maksymiuk et al., "Randomized phase IIB trial of BLP25 liposome vaccine in stage IIIB and IV non-small-cell lung cancer," *Journal of Clinical Oncology*, vol. 23, no. 27, pp. 6674–6681, 2005.

[57] N. Kojima, L. Biao, T. Nakayama, M. Ishii, Y. Ikehara, and K. Tsujimura, "Oligomannose-coated liposomes as a therapeutic antigen-delivery and an adjuvant vehicle for induction of *in vivo* tumor immunity," *Journal of Controlled Release*, vol. 129, no. 1, pp. 26–32, 2008.

[58] J. Neidhart, K. O. Allen, D. L. Barlow et al., "Immunization of colorectal cancer patients with recombinant baculovirus-derived *KSA* (Ep-CAM) formulated with monophosphoryl lipid a in liposomal emulsion, with and without granulocyte-macrophage colony-stimulating factor," *Vaccine*, vol. 22, no. 5-6, pp. 773–780, 2004.

[59] D. R. Lewis, K. Kamisoglu, A. W. York, and P. V. Moghe, "Polymer-based therapeutics: nanoassemblies and nanoparticles for management of atherosclerosis," *Wiley Interdisciplinary Reviews*, vol. 3, no. 4, pp. 400–420, 2011.

[60] Y. Sun, Y. Liu, W. Qu, and X. Jiang, "Combining nanosurface chemistry and microfluidics for molecular analysis and cell biology," *Analytica Chimica Acta*, vol. 650, no. 1, pp. 98–105, 2009.

[61] A. Fujishima and K. Honda, "Electrochemical photolysis of water at a semiconductor electrode," *Nature*, vol. 238, no. 5358, pp. 37–38, 1972.

[62] A. Fujishima and X. Zhang, "Titanium dioxide photocatalysis: present situation and future approaches," *Comptes Rendus Chimie*, vol. 9, no. 5-6, pp. 750–760, 2006.

[63] A. Zaleska, "Doped-TiO_2: a review," *Recent Patents on Engineering*, vol. 2, no. 3, pp. 157–164, 2008.

[64] S. G. Kumar and L. G. Devi, "Review of modified TiO_2 photocatalyst under UV/Visible light: selected results and related mechanisms on interfacial charge carrier dynamics," *The Journal of Physical Chemistry A*, vol. 115, pp. 13211–13241, 2011.

[65] F. Schmidt-Stein, R. Hahn, J. F. Gnichwitz et al., "X-ray induced photocatalysis on TiO_2 and TiO_2 nanotubes: degradation of organics and drug release," *Electrochemistry Communications*, vol. 11, no. 11, pp. 2077–2080, 2009.

[66] C. V. Wilmowsky, S. Bauer, R. Lutz et al., "*In Vivo* evaluation of anodic TiO_2 nanotubes; an experimental study in the pig," *Journal of Biomedical Materials Research*, vol. 89, no. 1, pp. 165–171, 2009.

[67] D. M. Blake, P. C. Maness, Z. Huang, E. J. Wolfrum, J. Huang, and W. A. Jacoby, "Application of the photocatalytic chemistry of titanium dioxide to disinfection and the killing of cancer cells," *Separation and Purification Methods*, vol. 28, no. 1, pp. 1–50, 1999.

[68] Y. Kubota, T. Shuin, C. Kawasaki et al., "Photokilling of T-24 human bladder cancer cells with titanium dioxide," *British Journal of Cancer*, vol. 70, no. 6, pp. 1107–1111, 1994.

[69] D. Collard, S. Takeuchi, and H. Fujita, "MEMS technology for nanobio research," *Drug Discovery Today*, vol. 13, no. 21-22, pp. 989–996, 2008.

[70] M. Huang, S. Fan, W. Xing, and C. Liu, "Microfluidic cell culture system studies and computational fluid dynamics," *Mathematical and Computer Modelling*, vol. 52, no. 11-12, pp. 2036–2042, 2010.

[71] J. P. Shelby, J. White, K. Ganesan, P. K. Rathod, and D. T. Chiu, "A microfluidic model for single-cell capillary obstruction by Plasmodium falciparum-infected erythrocytes," *Proceedings of the National Academy of Sciences of the United States of America*, vol. 100, no. 25, pp. 14618–14622, 2003.

[72] W. G. Lee, Y. G. Kim, B. G. Chung, U. Demirci, and A. Khademhosseini, "Nano/Microfluidics for diagnosis of infectious diseases in developing countries," *Advanced Drug Delivery Reviews*, vol. 62, no. 4-5, pp. 449–457, 2010.

[73] R. Baudoin, A. Corlu, L. Griscom, C. Legallais, and E. Leclerc, "Trends in the development of microfluidic cell biochips for *in vitro* hepatotoxicity," *Toxicology in Vitro*, vol. 21, no. 4, pp. 535–544, 2007.

[74] S. K. Mahto, T. H. Yoon, and S. W. Rhee, "A new perspective on *in vitro* assessment method for evaluating quantum dot toxicity by using microfluidics technology," *Biomicrofluidics*, vol. 4, no. 3, pp. 1–8, 2010.

[75] B. Cui, C. Wu, L. Chen et al., "One at a time, live tracking of NGF axonal transport using quantum dots," *Proceedings of the National Academy of Sciences of the United States of America*, vol. 104, no. 34, pp. 13666–13671, 2007.

[76] C. Beta and E. Bodenschatz, "Microfluidic tools for quantitative studies of eukaryotic chemotaxis," *European Journal of Cell Biology*, vol. 90, no. 10, pp. 811–816, 2011.

[77] M. Taylor, A. J. Urquhart, D. G. Anderson et al., "A methodology for investigating protein adhesion and adsorption to microarrayed combinatorial polymers," *Macromolecular Rapid Communications*, vol. 29, no. 15, pp. 1298–1302, 2008.

[78] C. G. Simon Jr., N. Eidelman, S. B. Kennedy, A. Sehgal, C. A. Khatri, and N. R. Washburn, "Combinatorial screening of cell proliferation on poly(L-lactic acid)/poly(D,L-lactic acid) blends," *Biomaterials*, vol. 26, no. 34, pp. 6906–6915, 2005.

[79] S. Heungsoo, "Fabrication methods of an engineered microenvironment for analysis of cell-biomaterial interactions," *Biomaterials*, vol. 28, no. 2, pp. 126–133, 2007.

[80] L. Zhao, P. Cheng, J. Li et al., "Analysis of nonadherent apoptotic cells by a quantum dots probe in a microfluidic device for drug screening," *Analytical Chemistry*, vol. 81, no. 16, pp. 7075–7080, 2009.

[81] S. M. Ong, C. Zhang, Y. C. Toh et al., "A gel-free 3D microfluidic cell culture system," *Biomaterials*, vol. 29, no. 22, pp. 3237–3244, 2008.

[82] K. Anselme, P. Davidson, A. M. Popa, M. Giazzon, M. Liley, and L. Ploux, "The interaction of cells and bacteria with surfaces structured at the nanometre scale," *Acta Biomaterialia*, vol. 6, no. 10, pp. 3824–3846, 2010.

[83] W. H. Huang, F. Ai, Z. L. Wang, and J. K. Cheng, "Recent advances in single-cell analysis using capillary electrophoresis and microfluidic devices," *Journal of Chromatography B*, vol. 866, no. 1-2, pp. 104–122, 2008.

[84] D. Falconnet, G. Csucs, H. Michelle Grandin, and M. Textor, "Surface engineering approaches to micropattern surfaces for cell-based assays," *Biomaterials*, vol. 27, no. 16, pp. 3044–3063, 2006.

[85] H. Dan-Qun, Z. Liu, C. J. Hou et al., "Recent advances on optical detection methods and techniques for cell-based microfluidic systems," *Chinese Journal of Analytical Chemistry*, vol. 38, no. 9, pp. 1357–1365, 2010.

[86] A. Kunzmann, B. Andersson, T. Thurnherr, H. Krug, A. Scheynius, and B. Fadeel, "Toxicology of engineered nanomaterials: focus on biocompatibility, biodistribution and biodegradation," *Biochimica Et Biophysica Acta*, vol. 1810, no. 3, pp. 361–373, 2011.

[87] C. F. Jones and D. W. Grainger, "*In vitro* assessments of nanomaterial toxicity," *Advanced Drug Delivery Reviews*, vol. 61, no. 6, pp. 438–456, 2009.

[88] P. Kuhn, K. Eyer, S. Allner, D. Lombardi, and P. S. Dittrich, "A microfluidic vesicle screening platform: monitoring the lipid membrane permeability of tetracyclines," *Analytical Chemistry*, vol. 83, no. 23, pp. 8877–8885, 2011.

[89] H. V. D. Andersson and A. Berg, "Microfabrication and microfluidics for tissue engineering: state of the art and future opportunities," *Lab on a Chip*, vol. 4, no. 2, pp. 98–103, 2004.

[90] J.-H. Lee, H. Wang, J. B. Kaplan, and W. Y. Lee, "Microfluidic approach to create three-dimensional tissue models for biofilm-related infection of orthopaedic implants," *Tissue Engineering*, vol. 17, no. 1, pp. 39–48, 2011.

[91] W. Tan and T. A. Desai, "Layer-by-layer microfluidics for biomimetic three-dimensional structures," *Biomaterials*, vol. 25, no. 7-8, pp. 1355–1364, 2004.

[92] D. G. Anderson, S. Levenberg, and R. Langer, "Nanoliter-scale synthesis of arrayed biomaterials and application to human embryonic stem cells," *Nature Biotechnology*, vol. 22, no. 7, pp. 863–866, 2004.

[93] N. S. Hwang, S. Varghese, and J. Elisseeff, "Controlled differentiation of stem cells," *Advanced Drug Delivery Reviews*, vol. 60, no. 2, pp. 199–214, 2008.

[94] P. Boisseau and B. Loubaton, "Nanomedicine, nanotechnology in medicine," *Comptes Rendus Physique*, vol. 12, pp. 620–636, 2011.

[95] X. Chi, D. Huang, Z. Zhao, Z. Zhou, Z. Yin, and J. Gao, "Nanoprobes for *in vitro* diagnostics of cancer and infectious diseases," *Biomaterials*, vol. 33, no. 1, pp. 189–206, 2012.

[96] T. S. Hauck, S. Giri, Y. Gao, and W. C. W. Chan, "Nanotechnology diagnostics for infectious diseases prevalent in developing countries," *Advanced Drug Delivery Reviews*, vol. 62, no. 4-5, pp. 438–448, 2010.

[97] A. Pope-Harman, M. M. C. Cheng, F. Robertson, J. Sakamoto, and M. Ferrari, "Biomedical nanotechnology for cancer," *Medical Clinics of North America*, vol. 91, no. 5, pp. 899–927, 2007.

[98] C. Kaittanis, S. Santra, and J. M. Perez, "Emerging nanotechnology-based strategies for the identification of microbial pathogenesis," *Advanced Drug Delivery Reviews*, vol. 62, no. 4-5, pp. 408–423, 2010.

[99] G. Birnbaumer, S. Küpcü, C. Jungreuthmayer et al., "Rapid liposome quality assessment using a lab-on-a-chip," *Lab on a Chip*, vol. 11, no. 16, pp. 2753–2762, 2011.

[100] A. Jahn, S. M. Stavis, J. S. Hong, W. N. Vreeland, D. L. Devoe, and M. Gaitan, "Microfluidic mixing and the formation of nanoscale lipid vesicles," *ACS Nano*, vol. 4, no. 4, pp. 2077–2087, 2010.

Hindawi Publishing Corporation
Journal of Nanomaterials
Volume 2012, Article ID 193704, 6 pages
doi:10.1155/2012/193704

Research Article

Therapeutic Angiogenesis of PLGA-Heparin Nanoparticle in Mouse Ischemic Limb

Lishan Lian, Feng Tang, Jing Yang, Changwei Liu, and Yongjun Li

Department of Vascular Surgery, Peking Union Medical College Hospital, Peking Union Medical College, Chinese Academy of Medical Science, Beijing 100730, China

Correspondence should be addressed to Yongjun Li, yongj_93@hotmail.com

Received 11 January 2012; Revised 12 April 2012; Accepted 13 April 2012

Academic Editor: Haifeng Chen

Objective. To evaluate the possibility and efficacy of the nanoparticle encapsulating heparin as a novel delivery system to treat ischemic disease. *Methods*. Firstly, to synthesize the PLGA heparin and test the surface morphology, the average diameter, the loading efficiency, and the release time in vitro, then inject the PLGA heparin into mouse ischemic limbs to observe the perfusion recovery with LDPI at the time of postischemic 7, 14, 21, and 28 days, and, finally, test the expression of VEGF and HGF, the number of the neovessels and record the necrotic score of ischemic limbs. *Results*. The surface morphology of the PLGA heparin was smooth, the average diameter was 297 nm, the loading efficiency was 5.35%, and the release period maintained for 14 days. In animal experiment, the perfusion recovery, HGF expression level, and capillary density in PLGA-heparin group were significantly higher than that in control group, and this was consistent with less ischemic limb necrosis. *Conclusion*. Nanoparticle encapsulating heparin could be successful and efficient in ischemic disease. The therapeutic angiogenesis of PLGA heparin might be due to the prolongation of its biological effects with stimulating growth factor expression.

1. Introduction

Ischemic diseases are major cause of morbidity and mortality [1]. Though pharmacology, stents, and bypass have been advantageously developed in this area, some of the patients, with diabetes, hyperlipidemia, or hypertension, are poorer clinical outcomes as well as poorer responses to pharmacology and not eligible or poor candidates for revascularization [2]. There are currently no medical therapies available to improve perfusion and thereby alter the poor prognosis [3].

Angiogenesis is the growth and proliferation of new blood vessels from existing vascular structures [4]. Therapeutic angiogenesis seeks to employ this phenomenon for the treatment of disorders of inadequate tissue perfusion.

Currently, a lot of growth factors and stem cells have been tried as an angiogenic promoter. However, their clinical effects on patients are not as exciting as experimental results in animal models. Originally, heparin is a basic anticoagulant for the prevention and treatment of arterial and venous thromboembolic diseases [5–7]. The anticoagulant activity of heparin depends on a unique pentasaccharide which binds to antithrombin III (AT III), potentiates the inhibition of thrombin, and activates factor X (Xa) [8–10]. Heparin has also a number of other effects, including stimulating the expression of tissue factor pathway inhibitor, binding to numerous plasma and platelet proteins, acting with endothelial cells, and leukocytes, suppressing of platelet function, and improving vascular permeability. More importantly, heparin has been proved to improve angiogenesis in clinic [8]. However, heparin has pharmacokinetic and biological limitation of its short half-life. To maintain its function needs recurrent injection or continuous intravenous infusion.

Polymeric nanoparticles formulated from biodegradable copolymer, poly lactic-coglycolic acid (PLGA), have been extensively investigated in drug and gene delivery [11–14]. PLGA nanoparticles have advantages such as a controlled release of drug delivery, high stability, being easily uptaken into the cells by endocytosis, and targeting ability to specific tissue or organ by adsorption or coating with ligand materials at the surface of spheres. In addition, PLGA has good biocompatibility and has been approved by Food and Drug Administration for certain human clinical uses [15–17].

In this study, we evaluated the possibility and efficiency of PLGA nanoparticles encapsulating unfractionated heparin as a novel drug delivery system to prolong heparin release and investigated the therapeutic angiogenesis efficacy in ischemic limbs of mice.

2. Materials and Methods

2.1. Preparation of PLGA-Heparin Nanoparticles. Double emulsion-solvent evaporation method was used to synthesize PLGA-heparin nanoparticles [18]. Briefly, 2 mL unfractionated heparin solution (12500 IU) was emulsified in 10 mL of PLGA solution (5% w/v in methylene chloride), using homogenizer for 3 min in ice bath. The water-in-oil emulsion was further emulsified in 50 mL of a 2% (w/v) aqueous solution of polyvinyl alcohol (PVA, MW 30,000–70,000) for 3 min to form a water-in-oil-in-water (w/o/w) multiple emulsion. The emulsion was stirred to remove the methylene chloride above 2 h. The PLGA-heparin nanoparticles were recovered by ultracentrifugation (23,000 rpm for 20 min, Beckman, USA), washed 3 times to remove PVA, and then lyophilized to obtain a dry powder.

2.2. Characteristics of PLGA-Heparin Nanoparticles. A Submicro Laser Defractometer (PCS Brookhaven Co. USA, BI-9000AT Correlator, BI200SM Photometer) was used to assess the size distribution. The particle morphology was observed by scanning electron microscopy. Freeze-dried nanoparticles were spread on the sticky surface of an aluminum stub. The nanoparticle surface was coated with gold before being viewed under the microscope.

The amount of heparin entrapped within PLGA nanoparticles was determined by extracting the heparin using distilled water after dissolving the PLGA with a chloroform solution. Heparin concentration in the aqueous solution was assayed by spectrophotometer.

In vitro heparin release from the nanoparticles was performed in distilled water at 37°C utilizing double-chamber diffusion cell. A Millipore hydrophilic polyvinylidene fluoride membrane was placed between the two chambers. The receiver buffer was replaced with fresh distilled water at predetermined intervals. Heparin concentration in the aqueous solution was assayed by spectrophotometer.

2.3. Mouse Hindlimb Ischemic Model. C57BL/6J mice at 4 weeks of age (15–18 g body weight, from Laboratory Animals Center, Chinese Academy of Medical Sciences, China) were obtained. Hindlimb ischemic mouse model was surgically induced according to procedures described previously [19]. Briefly, mice underwent surgically induced unilateral hindlimb ischemia with ligation and excision of the femoral artery from its origin just above the inguinal ligament to its bifurcation at the origin of the saphenous and popliteal arteries under general anesthesia. The above-mentioned arteries from the opposite limb were not ligated and were used as an internal control to calculate perfusion recovery.

The extent of necrosis, if any, in ischemic hindlimb was recorded once between days 3 and 5 after surgery. The scores of necrosis were described as follows: grade 0, no necrosis in ischemic limb; grade I, necrosis limited to toes; grade II, necrosis extending to dorsum pedis; grade III, necrosis extending to curs; grade IV, necrosis extending to thigh.

Totally, 40 hindlimb ischemic mice were assigned to two groups: PLGA-heparin group ($n = 20$) and control group ($n = 20$). PLGA heparin (300 μL was equivalent to 6 IU heparin; this dosage of heparin was equivalent to 300 IU/kg in clinic) was intramuscular injected into the ischemic limb (6 points) of each mouse right after the femoral artery was ligated and excised. Same amount of saline was intramuscular injected into the ischemic limb as we did in treatment group.

Blood flow recovery was monitored with Laser Doppler Perfusion Image (LDPI, PERIMED, Stockholm, Sweden). Briefly, mice were anesthetized and placed on a heating pad to maintain a constant temperature. Hair was removed with an electric shaver followed by a depilatory cream. LDPI was used to estimate dermal blood flow in the calf and foot before, immediately after procedures, and on days 7, 14, 21, and 28 after hindlimb ischemia. Ratio of the operated/nonoperated limb was calculated to minimize the potential differences between ambient temperature and lighting.

2.4. Histological Examination, ELISA, and Western Blot

2.4.1. Preparation of Tissue Samples. Mice were sacrificed after LDPI at day 28 after-operation, and the gastrocnemius and tibialis anterior muscles from the right and left sides were harvested and weighed. The distal part of the muscle was frozen and embedded for histology study, and the proximal part was used either to detect vascular endothelial growth factor (VEGF) level with enzyme-linked immunosorbent assay (ELISA) or to determine hepatocyte growth factor (HGF) expression with Western blot.

2.4.2. Endothelial Phosphate Alkaline Staining for Capillary Density. Immunohistochemistry was performed on muscle sections of the gastrocnemius and tibialis anterior. Capillary per muscle fiber ratio was determined by endothelial phosphate alkaline staining; blue dots indicated capillaries. Capillary density was measured by counting six random high-power (magnification ×200) fields or a minimum of 200 fibers from each ischemic and nonischemic limb on an inverted light microscope.

2.4.3. Expression of VEGF and HGF. Available ELISA for VEGF was performed on homogenized muscle samples as the manufacturer's instructions (R&D Systems, USA). Briefly, leg muscle harvested from sacrificed mice was snap frozen in liquid nitrogen and pulverized by using a prechilled mortar and pestle on dry ice. Approximately 100 mg of each muscle was homogenized in 1.5 mL NP-40 lysis buffer containing protease inhibitors. Muscle homogenates were centrifuged at 13000 rpm. The surface lipid layer was removed, and

the supernatant was saved at −80°C for ELISA and protein assay. Protein concentration was measured by using a 1 : 500 dilution of the supernatant in the microtiter plate by micro-BCA protein assay (Pierce, Rockford, USA). Supernatant dilutions of 1 : 6 were used for the VEGF ELISA assays.

Protein samples were separated on SDS-polyacrylamide gels and then transferred to a polyvinylidene difluoride membranes which were treated with blocking buffer (5% skim milk). An anti-HGF antibody (Santa Cruz Biotechnologies, CA) was used as the primary antibody followed by incubation with an anti-mouse horseradish peroxidase-conjugated secondary antibody. Immune reactivity was visualized using ECL plus system. Quantification of results was performed by densitometry (Image J, NIH, USA), comparing the density of identically sized areas (corresponding to immunoreactive bands) and results analyzed as total integrated density (arbitrary units).

2.5. Statistical Analysis. Results were expressed as mean ± standard deviation (SD). For comparison of mean data on PLGA-heparin treatment versus control, at one time point (i.e., VEGF HGF expression, capillary density), statistical significance was evaluated by use of 2-tailed Student's paired t test. To determine the perfusion ratio over time, a standard variance ANOVA repeated measure was performed. Probability values <0.05 were considered to be significant.

3. Results

3.1. Characteristics of PLGA-Heparin Nanoparticles. A scanning electron microphotograph of heparin nanoparticles showed that the nanoparticles were spherical and discrete particles without aggregation and that they were smooth in surface morphology (Figure 1(a)). The average diameter of the nanoparticles was 297 nm (Figure 1(b)).

The loading efficiency of heparin in the nanoparticles was 5.35%. The heparin release from nanoparticles in vitro was 40% in day 1 and 85% in day 3 and sustained over 14 days (Figure 2).

3.2. PLAG Heparin Improved Blood Flow Restoration and Prevented Limb Necrosis. The recovery of perfusion in PLGA-heparin group was similar to that of control group on day 7 (0.500 ± 0.084 versus 0.485 ± 0.095). However, perfusion ratio was significantly increased on day 14 (0.623 ± 0.077 versus 0.536 ± 0.086, $P < 0.05$), day 21 (0.684 ± 0.068 versus 0.588 ± 0.082, $P < 0.01$), and day 28 (0.733 ± 0.093 versus 0.606 ± 0.079, $P < 0.01$) (Figure 3).

Immunohistochemical staining showed that capillary density was richer in PLGA-heparin group compared to that of in control group (in gastrocnemius, 0.19 ± 0.08 versus 0.30 ± 0.08, $P < 0.05$; in tibialis anterior 0.22 ± 0.11 versus 0.33 ± 0.04, $P < 0.05$). Capillary density was represented as capillaries per muscle fiber (Figure 4).

The results of necrotic scores were consistent with the blood flow recovery and capillary density. With more capillaries formation and more blood flow restoration, the limb necrosis was much less in PLGA-heparin treated group.

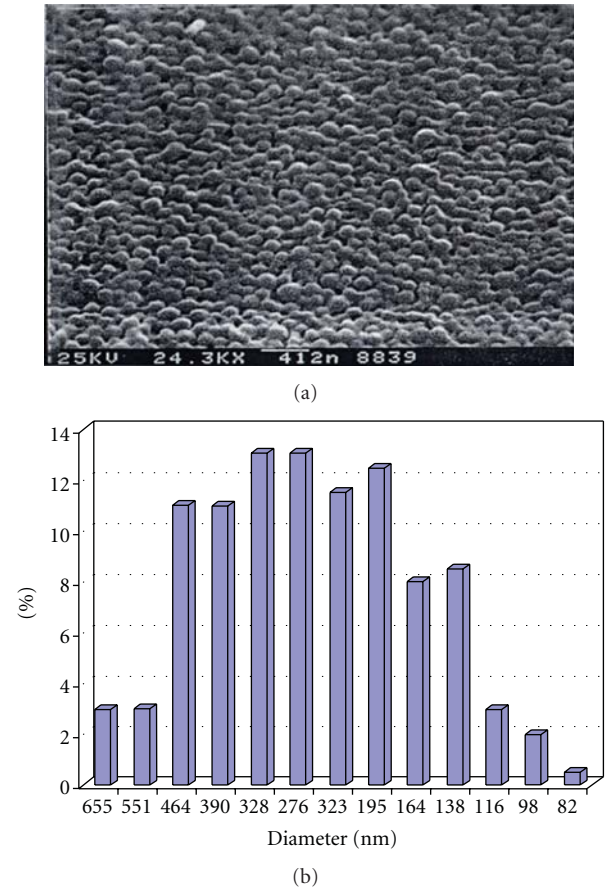

Figure 1: (a) A scanning electron microphotograph of heparin nanoparticles. (b) Size distribution of heparin nanoparticles.

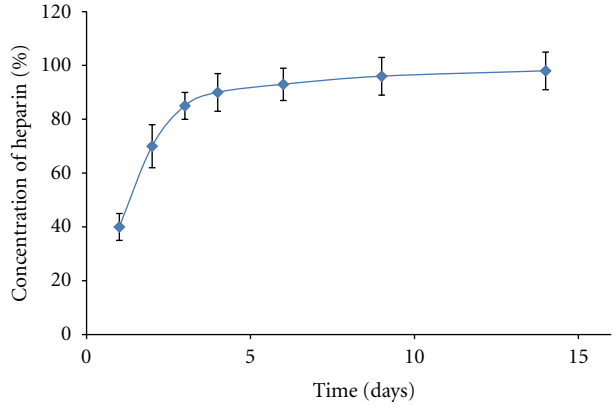

Figure 2: Cumulative release profile (% of amount loaded) of heparin from nanoparticles.

Only 5% mice showed grade I necrosis. However, in control group, 20% mice presented limb necrosis, and they were grade I (10.0%), II (5.0%), and III (5.0%).

3.3. PLGA Heparin Upregulated the Expression of HGF. VEGF concentration was evaluated with ELISA. With ischemic injury stimulation, the VEGF level was increased

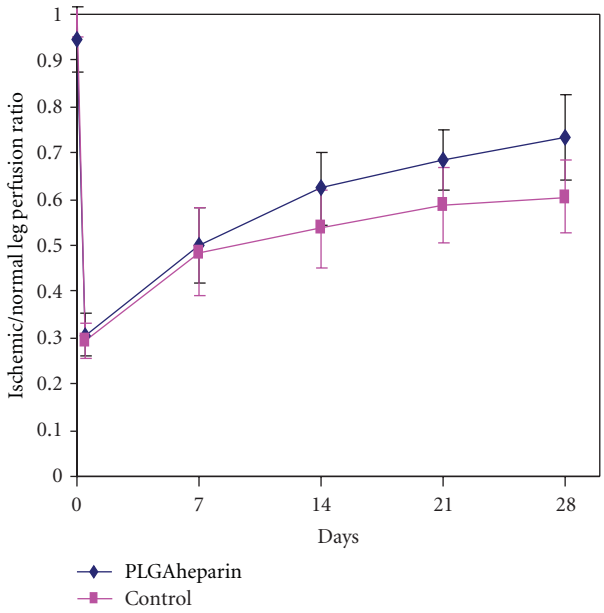

Figure 3: Perfusion recovery after surgical-induced hindlimb ischemia.

in both PLGA-heparin group and control group (20.6% and 20.2% increased, respectively, $P > 0.05$). There was no significant difference between these 2 groups.

However, western blot showed more expression of HGF in PLGA-heparin group than that in control group. Quantitative analysis with Image J showed the HGF/Tubulin ratio was significantly increased with PLGA-heparin versus control treatment, 0.43 ± 0.02 versus 0.20 ± 0.06, $P < 0.05$, (integrated density) (Figure 5).

4. Discussion

Heparin is a typical anticoagulant and has been used to prevent and treat thromboembolic ischemic diseases such as coronary artery disease and peripheral arterial occlusion disease which imperil people's life or survive lower extremity limbs. However, a short half-life and the need for recurrent injection have limited its use for chronic ischemic disease. In this study, we attempt to use nanoparticle techniques to overcome this disadvantage and encapsulate heparin with PLGA to prolong its biological effect. To the best of our knowledge, this paper is the first to investigate the therapeutic efficiency of PLGA heparin in a preclinical hindlimb ischemic model. The major findings of our study were the following: (a) heparin could be encapsulated with PLGA and controlled release for at least 14 days; (b) PLGA heparin improved blood flow restoration with more capillaries formation and prevented limb necrosis; (c) the potential therapeutic angiogenesis of PLGA heparin might be due to interaction with growth factors.

According to our results, PLGA heparin nanoparticles formulated by double emulsion solvent evaporation technique were smooth and spherical in shape with a loading efficiency of 5.35%. The average diameter of PLGA heparin was 297 nm, with a range of 82 nm to 655 nm. The heterogeneity in particular size might relate to the homogenization method. The concentration of PVA and the speed of homogenization had been reported to affect the particle size of PLGA nanoparticles [20, 21]. The smaller particle size might have better potential effects of controlled release. The method of double-chamber diffusion was adopted for heparin release determination [22]. Result showed that heparin released from nanoparticles in vitro was 40% in day 1, 85% in day 3, and sustained over at least 14 days. Even though 90% of heparin was released from nanoparticle in the earlier 7 days, PLGA heparin did prolong the existence of heparin and made it possible to sustain the biological effects of heparin.

The controlled release of heparin from PLGA nanoparticles may offer the advantage of sustaining therapeutic effect in the target cells or tissues. A sustained drug release may be more important in the treatment of chronic disease such as critical limb ischemia and myocardial infarction. It also has the advantages that prolong the injection intermission for the convenience of clinic use and the improvement of patient compliance.

Our data showed that sustained heparin release from PLGA nanoparticles could be feasible and effective in therapeutic angiogenesis of mice in the setting of hindlimb ischemia. First of all, we detected the blood flow recovery with LDPI. Following surgical-induced hindlimb ischemia, the restoration of limb perfusion was spontaneous recovery over time, with one dosage of PLGA-heparin treatment; the restoration was accelerated. The differences demonstrated on day 14 following operation and lasted for 28 days. This finding was consistent with histological examination, with more capillaries formation in the PLGA-heparin treatment limbs. For clinical interest, less happening of necrosis on limbs confirmed the benefit of PLGA-heparin treatment.

We then sought to investigate the mechanisms of therapeutic angiogenesis of PLGA heparin. The vascular endothelial growth factor family is perhaps the most extensively studied angiogenic growth factor. VEGF is a key angiogenic factor that induces the proliferation, migration, and survival of endothelia cells and promotes angiogenesis [23]. We found an increase of VEGF expression during the recovery period after surgical-induced hindlimb ischemia. However, there was not distinct difference between the PLGA-heparin treatment and the saline control groups. That implied that there might be other mechanisms for promoting angiogenesis.

In this study, we found that PLGA heparin could upregulate the expression of HGF. HGF plays important roles in wound healing, tissue and organ regeneration, morphogenesis, and angiogenesis [24]. HGF and its specific receptor, c-met, have been expressed in the blood vessels, including endothelial cells and vascular smooth muscle cells. HGF had been confirmed as a novel angiogenic growth factor in models of hindlimb ischemia and myocardial infarction [25]. Moreover, clinical trials which are based on those bench works are on the way [26].

Taking all this information together, we conclude that it is a feasible and effective method to encapsulate the heparin

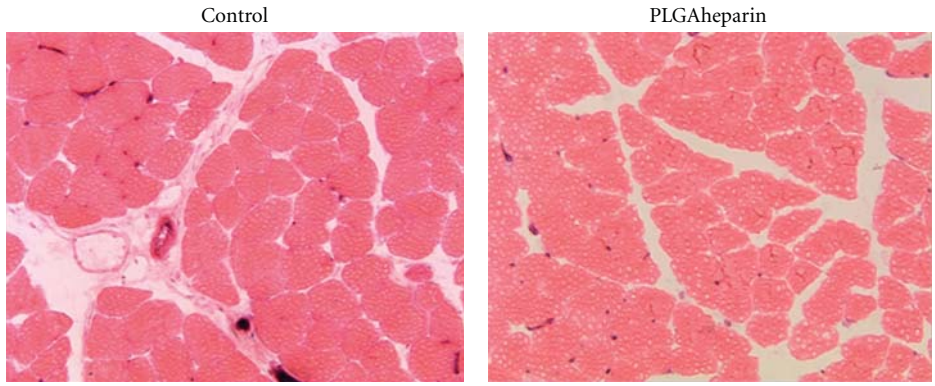

Figure 4: Endothelial phosphate alkaline staining for capillaries. The pictures represented staining of endothelial phosphate alkaline; blue dots indicated capillaries (original magnification ×200).

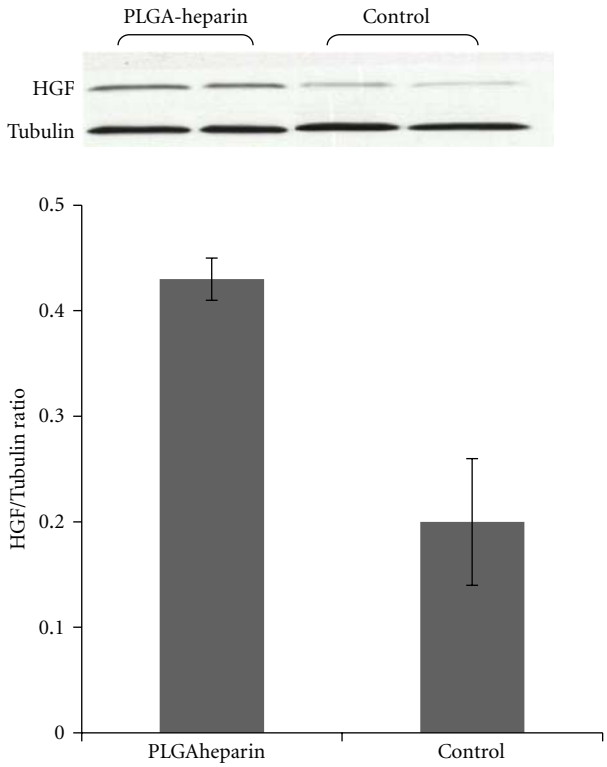

Figure 5: Western blot for HGF. Quantitative analysis with integrated density showed significantly more expression of HGF in PLGA-heparin group than that in control group.

into PLGA, and with controlled release of heparin, PLGA-heparin can promote therapeutic angiogenesis in hindlimb ischemic mouse model. The potential mechanisms may be due to the upregulation of angiogenic factors.

Acknowledgment

This paper was supported by the National Natural Science Foundation of China (Grant no. 30772114).

References

[1] Y. He, Y. Jiang, J. Wang, L. Fan, X. Li, and F. B. Hu, "Prevalence of peripheral arterial disease and its association with smoking in a population-based study in Beijing, China," *Journal of Vascular Surgery*, vol. 44, no. 2, pp. 333–338, 2006.

[2] Y. H. Kusumanto, V. Van Weel, N. H. Mulder et al., "Treatment with intramuscular vascular endothelial growth factor gene compared with placebo for patients with diabetes mellitus and critical limb ischemia: a double-blind randomized trial," *Human Gene Therapy*, vol. 17, no. 6, pp. 683–691, 2006.

[3] B. Cristofaro, O. A. Stone, A. Caporali et al., "Neurotrophin-3 is a novel angiogenic factor capable of therapeutic neovascularization in a mouse model of limb ischemia," *Arteriosclerosis, Thrombosis, and Vascular Biology*, vol. 30, no. 6, pp. 1143–1150, 2010.

[4] H. Zhou, Y. H. Yang, N. O. Binmadi et al., "The hypoxia-inducible factor-responsive proteins semaphorin 4D and vascular endothelial growth factor promote tumor growth and angiogenesis in oral squamous cell carcinoma," *Experimental Cell Research*. In press.

[5] M. Sobel and R. Verhaeghe, "Antithrombotic therapy for peripheral artery occlusive disease: American College of Chest Physicians evidence-based clinical practice guidelines (8th edition)," *Chest*, vol. 133, no. 6, pp. 815S–843S, 2008.

[6] C. Kearon, S. R. Kahn, G. Agnelli, S. Goldhaber, G. E. Raskob, and A. J. Comerota, "Antithrombotic therapy for venous thromboembolic disease: American College of Chest Physicians evidence-based clinical practice guidelines (8th edition)," *Chest*, vol. 133, no. 6, pp. 454S–545S, 2008.

[7] L. Norgren, W. R. Hiatt, J. A. Dormandy, M. R. Nehler, K. A. Harris, and F. G. R. Fowkes, "Inter-Society consensus for the management of peripheral arterial disease (TASC II)," *European Journal of Vascular and Endovascular Surgery*, vol. 33, pp. S32–S53, 2007.

[8] D. A. Lane, "Heparin binding and neutralizing protein," in *Heparin: Chemical and Biological Properties, Clinical Applications*, D. A. Lane and U. Lindahl, Eds., pp. 363–391, CRC Press, Boca Raton, Fla, USA, 1989.

[9] R. D. Rosenberg and L. Lam, "Correlation between structure and function of heparin," *Proceedings of the National Academy of Sciences of the United States of America*, vol. 76, no. 3, pp. 1218–1222, 1979.

[10] J. Hirsh, T. E. Warkentin, S. G. Shaugnessy et al., "Heparin and low-molecular-weight heparin: mechanisms of action, pharmacokinetics, dosing considerations, monitoring, efficacy and safety," *Chest*, vol. 119, supplement, pp. 64S–94S, 2001.

[11] M. Stern, K. Ulrich, D. M. Geddes, and E. W. F. W. Alton, "Poly (D, L-lactide-co-glycolide)/DNA microspheres to facilitate prolonged transgene expression in airway epithelium in vitro, ex vivo and in vivo," *Gene Therapy*, vol. 10, no. 16, pp. 1282–1288, 2003.

[12] S. W. Kang, H. W. Lim, S. W. Seo, O. Jeon, M. Lee, and B. S. Kim, "Nanosphere-mediated delivery of vascular endothelial growth factor gene for therapeutic angiogenesis in mouse ischemic limbs," *Biomaterials*, vol. 29, no. 8, pp. 1109–1117, 2008.

[13] O. Jeon, S. W. Kang, H. W. Lim, J. Hyung Chung, and B. S. Kim, "Long-term and zero-order release of basic fibroblast growth factor from heparin-conjugated poly(L-lactide-co-glycolide) nanospheres and fibrin gel," *Biomaterials*, vol. 27, no. 8, pp. 1598–1607, 2006.

[14] J. Yang, C. Song, Y. Li et al., "Polymeric Particles with therapeutic gene for gene therapy: preparation and in vivo gene transfer study," *BioMedical Engineering*, vol. 22, no. 3, pp. 438–442, 2005.

[15] Y. Lemmouchi, E. Schacht, P. Kageruka et al., "Biodegradable polyesters for controlled release of trypanocidal drugs: in vitro and in vivo studies," *Biomaterials*, vol. 19, no. 20, pp. 1827–1837, 1998.

[16] R. A. Jain, "The manufacturing techniques of various drug loaded biodegradable poly(lactide-co-glycolide) (PLGA) devices," *Biomaterials*, vol. 21, no. 23, pp. 2475–2490, 2000.

[17] X. Liu, J. Yang, C. Zhou et al., "Constructing hybrid films of conjugated oligomers and gold nanoparticles for efficient photoeletronic properties," *Physical Chemistry Chemical Physics*, vol. 13, no. 6, pp. 1984–1989, 2011.

[18] A. Lamprecht, N. Ubrich, M. Hombreiro Pérez, C. M. Lehr, M. Hoffman, and P. Maincent, "Biodegradable monodispersed nanoparticles prepared by pressure homogenization-emulsification," *International Journal of Pharmaceutics*, vol. 184, no. 1, pp. 97–105, 1999.

[19] T. Couffinhal, M. Silver, L. P. Zheng, M. Kearney, B. Witzenbichler, and J. M. Isner, "Mouse model of angiogenesis," *American Journal of Pathology*, vol. 152, no. 6, pp. 1667–1679, 1998.

[20] D. R. Kalaria, G. Sharma, V. Beniwal, and M. N. V. Ravi Kumar, "Design of biodegradable nanoparticles for oral delivery of doxorubicin: in vivo pharmacokinetics and toxicity studies in rats," *Pharmaceutical Research*, vol. 26, no. 3, pp. 492–501, 2009.

[21] J. Sameni, N. I. Bukhari, N. A. Azlan, T. Julianto, and A. B. A. Majeed, "The effect of preparation parameters on the size and morphology of PLGA-based nanoparticles," in *Proceedings of the IEEE Symposium on Industrial Electronics and Applications (ISIEA '09)*, pp. 700–704, Kuala Lumpur, Malaysia, October 2009.

[22] J. Lv, Y. Zhao, G. Li et al., "Aggregation-enhanced emission in gold nanoparticles protected by tetradentate perylene derivative," *Langmuir*, vol. 25, no. 19, pp. 11351–11357, 2009.

[23] T. T. Rissanen, I. Vajanto, M. O. Hiltunen et al., "Expression of vascular endothelial growth factor and vascular endothelial growth factor receptor-2 (KDR/Fik-1) in ischemic skeletal muscle and its regeneration," *American Journal of Pathology*, vol. 160, no. 4, pp. 1393–1403, 2002.

[24] R. Zarnegar and G. K. Michalopoulos, "The many faces of hepatocyte growth factor: from hepatopoiesis to hematopoiesis," *Journal of Cell Biology*, vol. 129, no. 5, pp. 1177–1180, 1995.

[25] R. Madonna, C. Cevik, M. Nasser et al., "Hepatocyte growth factor: molecular biomarker and player in cardioprotection and cardiovascular regeneration," *Thrombosis and Haemostasis*, vol. 107, no. 4, pp. 656–661, 2012.

[26] R. Morishita, H. Makino, M. Aoki et al., "Phase I/IIa clinical trial of therapeutic angiogenesis using hepatocyte growth factor gene transfer to treat critical limb ischemia," *Arteriosclerosis, Thrombosis, and Vascular Biology*, vol. 31, no. 3, pp. 713–720, 2011.

Hindawi Publishing Corporation
Journal of Nanomaterials
Volume 2012, Article ID 959578, 7 pages
doi:10.1155/2012/959578

Research Article

Evaluation of the Morphology and Osteogenic Potential of Titania-Based Electrospun Nanofibers

Xiaokun Wang,[1] Jingxian Zhu,[2] Ling Yin,[1] Shize Liu,[1] Xin Zhang,[2] Yingfang Ao,[2] and Haifeng Chen[1]

[1] *Department of Biomedical Engineering, College of Engineering, Peking University, No. 5 Yiheyuan Road, Haidian District, Beijing 100871, China*
[2] *Institute of Sports Medicine, Peking University Third Hospital, 49 North Garden Road, Haidian District, Beijing 100191, China*

Correspondence should be addressed to Haifeng Chen, haifeng.chen@pku.edu.cn

Received 8 February 2012; Accepted 3 April 2012

Academic Editor: Krasimir Vasilev

Submicron-scale titania-based ceramic fibers with various compositions have been prepared by electrospinning. The as-prepared nanofibers were heat-treated at 700°C for 3 h to obtain pure inorganic fiber meshes. The results show that the diameter and morphology of the nanofibers are affected by starting polymer concentration and sol-gel composition. The titania and titania-silica nanofibers had the average diameter about 100–300 nm. The crystal phase varied from high-crystallized rutile-anatase mixed crystal to low-crystallized anatase with adding the silica addition. The morphology and crystal phase were evaluated by SEM and XRD. Bone-marrow-derived mesenchymal stem cells were seeded on titania-silica 50/50 fiber meshes. Cell number and early differentiation marker expressions were analyzed, and the results indicated osteogenic potential of the titania-silica 50/50 fiber meshes.

1. Introduction

The design and preparation of nanoscale fine structures have attracted great attention because of their potential unique properties and applications. The electrospinning technique has been reported to be a simple and versatile method to produce fibrous structure with nanoscale to microscale dimensions from synthetic and natural polymers [1–5]. Moreover, the principles of electrospinning technique have been expanded to the ceramic and metal oxide systems [6–9]. The morphology and properties of the nanofibers depend on the concentration of polymer solutions, solvent, applied electric field strength, and deposition distance [10–12].

There are many studies focusing on applying electrospun fibrous scaffolds to bone tissue engineering [13, 14]. Most of the electrospun scaffolds are made of polymers or polymer-ceramic nanoparticle composite, and a few studies have been done on pure ceramic scaffolds [15–18]. Titania is well known as biocompatible surface of titanium implants, and, as the major component of bioglass, silica is also considered to have good biology performance. A number of methods have been applied to produce titania-silica nanostructures, including the sol-gel process [19], plasma-spraying [20], and chemical vapor deposition [21]. Many previous studies of nanostructured titania-silica materials focus on their optical properties, high thermal stability, and high surface area properties, and this material has been widely used as optical chemical sensors [22], supporting materials [23], and catalysts [24]. In the aspect of their biology performance, most of the applications of nanostructured titania-silica materials in the field of biomedical engineering are using titania-silica as coating material or fillers for composite scaffolds [25–29].

Recent research has showed that electrospun titania nanofibers have the osteoinductive potentials, and the effects of surface roughness on MG63 osteoblast-like cells were also discussed [30]. However, few researches are available that give an insight into how titania-silica nanofibers influence cell responses. Therefore, the aim of this study is to characterize the morphology of electrospun titania-based fibers and evaluate bone-derived mesenchymal stem cell (MSC) responses and osteoinductivity of titania-silica fibers

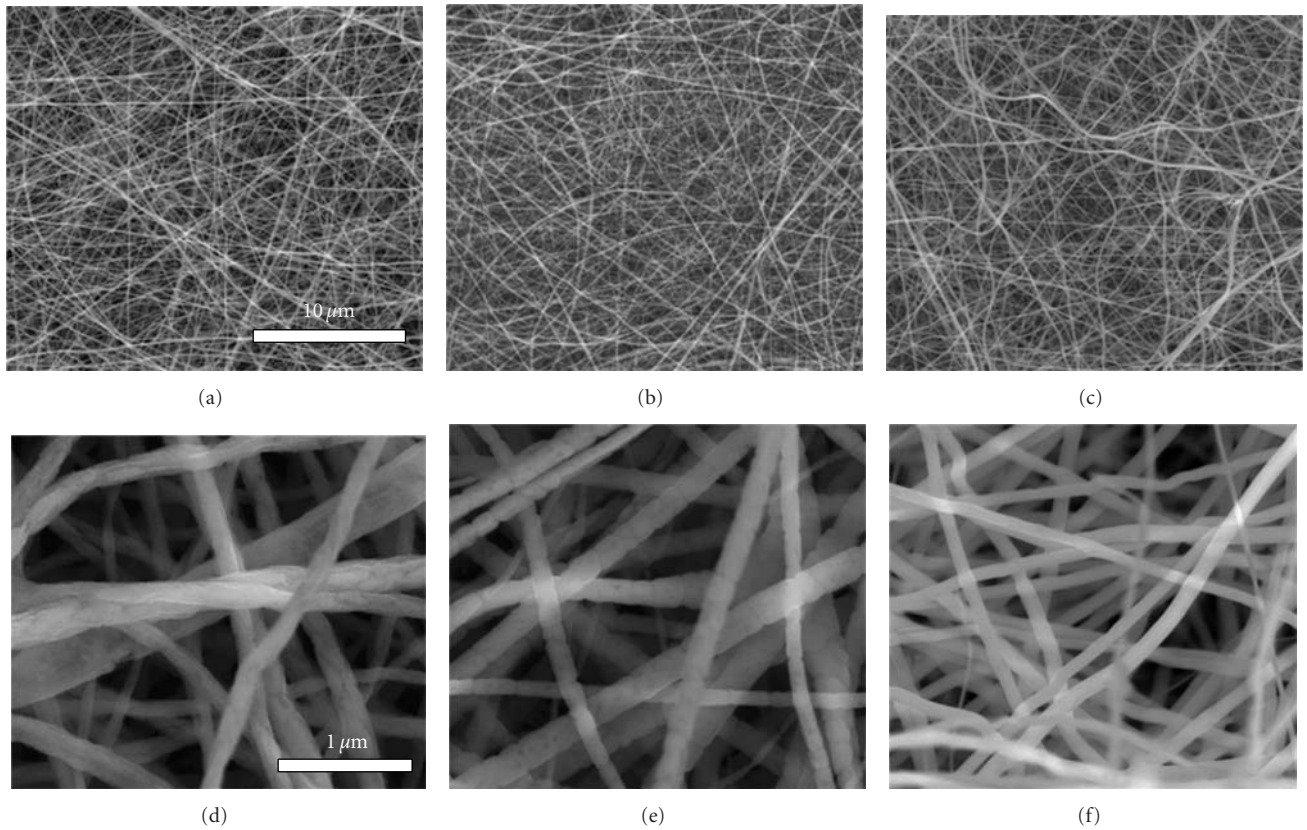

Figure 1: SEM images and analysis of the morphology of the electrospun nanofiber meshes produced with ((a),(d)) 6% PVP TiO_2, ((b),(e)) 10% PVP TiO_2, ((c),(f)) 10% PVP TiO_2-SiO_2 50/50.

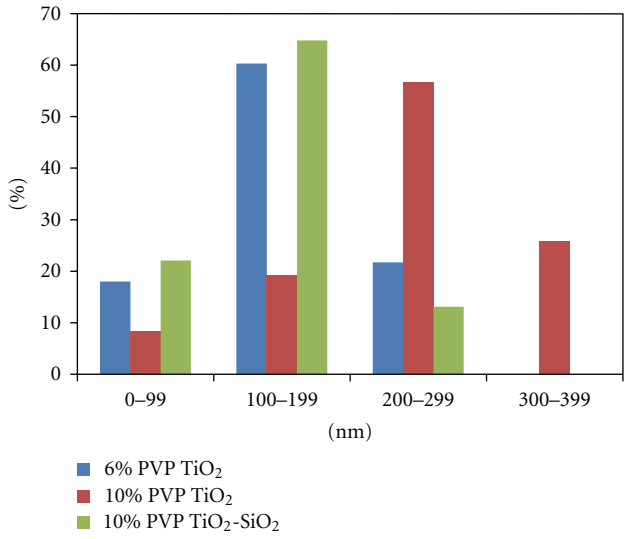

Figure 2: Histogram of diameter distribution of nanofibers on the meshes.

to determine their potential application as a scaffold material for bone tissue engineering.

2. Materials and Methods

2.1. Fabrication of Titania and Titania-Silica Nanofibers. The titania and titania-silica fibrous meshes were prepared from titanium(IV) isopropoxide (TiP), tetraethyl orthosilicate (TEOS), poly(vinyl pyrrolidone) (PVP, $M_w \approx 1\,300\,000$), and acetic acid. In a typical procedure, 0.5 mL of TiP was mixed with 0.5 mL ethanol and 0.5 mL acetic acid. After 10 min stirring, the sol was added to 1.5 mL 6% and 10% PVP ethanol solution, followed by magnetic stirring for 30 min. The starting solution of titania-silica fibers was made of sol containing 0.25 mL of TiP and 0.25 mL TEOS mixed with 0.5 mL ethanol and 0.5 mL acetic acid. Then the sol was added to 1.5 mL 10% PVP ethanol solution. In the electrospinning setup, the collection distance was 10 cm, and the applied voltage was 8 kV. The electrospun fibers were collected on the flat plate. Finally, the PVP was removed from these fibers by heating them in air at 700°C for 3 h.

Sample topography and cell morphology were examined by scanning electron microscopy (Hitachi S-4800) using a 15 kV accelerating voltage. Fiber diameter distribution was evaluated by image analysis software (ImageJ, NIH software) from three SEM images of at least two different samples. Fiber diameter was evaluated from at least 150 fibers at 16,000x magnification.

The chemical composition of the scaffolds was examined by XPS (Axis Ultra by Kratos Analytical Ltd.) of at least two different samples with 3 spots per sample. Additionally, crystal structure X-ray diffraction (XRD) was investigated by RAPID-S (Rigaku Denkico Co., Ltd.)

2.2. Cell Culture. Bone-derived mesenchymal stem cells were extracted from two lower extremities of a Wistar rat with approval of the animal ethics committee of the Peking University Third Hospital. Briefly, the adherent soft tissues of bones were cleaned, and epiphyses were removed with a scissor. The marrow was harvested by inserting a syringe needle (16-gauge) into each end of the bone and flushing repeatedly with phosphate-buffered saline (PBS) supplemented with 100 U/mL penicillin and streptomycin into a 100 mm culture dish. Cell suspension was obtained by drawing the marrow into a 20 mL syringe through 22-gauge needles. The cells were then centrifuged, counted, seeded at a density of 1×10^6 in 8 mL of α-MEM (Minimal Essential Medium) with 10% fetal bovine serum (FBS), 100 U/mL penicillin, and streptomycin per 100 mm culture dish, and cultured at 37°C in a humidified atmosphere of 95% air and 5% CO_2. Nonadherent cells were removed at 3 days after seeding by changing the medium; thereafter, the medium was changed every 3 days. Cells of the 3rd to the 5th passage were used for further study.

For cell culture on the titania-silica 50/50 meshes, MSCs were cultured in osteogenic media, containing Dulbecco's modified Eagle medium, containing 10% fetal bovine serum (FBS) and 1% penicillin and streptomycin, 0.1 μmol/L dexamethasone, 10 mmol/L β-sodium glycero-phosphate, and 50 μmol/L ascorbic acid phosphate, at 37°C in 5% CO_2 and 100% humidity. Cells were grown on 12-well plate tissue culture polystyrene and titania-silica 50/50 meshes, at a density of 10,000 cells/cm^2. MSCs were fed every 48 h and harvested at Day 3 and Day 7. RNA was extracted by using Qiagen's RNeasy Mini Kit and reverse-transcribed by using the Qiagen-Omniscript RT kit as per the manufacturer's directions. RT-PCR and Real time PCR were performed for Runx2 (NCBI accession no. NM_009820.2) and ALP (NCBI accession no. NM_007431). Optimal oligonucleotide primers were designed by using Primer Express 2.0 software and purchased from Sigma-Geosys. Data were normalized to the endogenous reference gene GAPDH (NCBI accession no. NM_008084).

3. Results

Figure 1 shows the SEM images of electrospun fibers. These images reveal that fibers have diameters varying from around 100 nm to 300 nm. Under lower magnification (Figures 1(a), 1(c), and 1(e)), fibers in each group were evenly distributed in general, and higher-magnification images (Figures 1(b), 1(d), and 1(f)) revealed more detailed structures of the fiber. Comparing Figures 1(b) and 1(d), it is observed that the average diameter of fibers increases with the increasing starting polymer concentration. Also, even using the same concentration of starting polymer, pure titania meshes have thicker fibers than titania-silica 50/50 hybrid meshes (Figures 1(d) and 1(f)). Beside the diameter, the existence of silica also has influences on fiber surface morphology. Figure 1(d) shows that pure titania fibers form of titania crystal clusters and the titania-silica 50/50 fibers (Figure 1(f)) have smoother surfaces.

Table 1: Elemental composition ± standard deviation (SD) of electrospun meshes analyzed by XPS.

	Ti	Si	O	C
6% PVP-TiO_2	21.4 ± 0.8	2.5 ± 1.1	61.2 ± 3.1	13.8 ± 1.1
10% PVP-TiO_2	22.5 ± 1.2	2.3 ± 0.9	63.4 ± 2.3	12.7 ± 1.8
10% PVP-TiO_2-SiO_2	15.3 ± 0.4	14.6 ± 0.9	60.1 ± 2.1	9.9 ± 1.3

Figure 2 shows the diameter distribution of calcined fibers analyzed by ImageJ. It confirms the observation of SEM images, which is 6% PVP titania fibers, and 10% PVP titania-silica 50/50 fibers have thinner diameter than 10% PVP titania fibers.

Chemical analysis by XPS (Table 1) showed no N, indicating PVP was removed thoroughly by the heat treatment. 6% PVP and 10% PVP titania fiber meshes were generally composed by Ti, O, and small amount of silica as well. The titania-silica 50/50 fiber mesh has Ti, Si, and O, and the ratio of Ti to Si was 1 : 1, consistent with the initial molar ratio of TiP to TEOS.

Typical XRD patterns of titania fibers and titania-silica 50/50 fibers with heat treatment are shown in Figure 3. Two groups of titania fibers have similar spectra, which is presented in Figure 3(a). The peaks of rutile and anatase crystal structures were found in the two groups of pure titania fibers. For titania-silica 50/50 fibers, only the peaks of anatase were found and the peak intensity of hybrid fibers was also weaker than that of pure titania fibers.

MSC morphology on titania-silica 50/50 fiber meshes was observed by SEM and confocal microscope. The cells grew throughout the surfaces with elongated morphology (Figures 4(a) and 4(b)). Cell number on fibrous mesh groups was lower than that on TCPs. However, Runx2 and alkaline phosphatase gene expressions were affected in the opposite way, with cells on the hybrid mesh groups having the higher level of relative gene expression (Figures 5(a)–5(c)). In general, the cell behavior was sensitive to the fibrous surface.

4. Discussion

In this study, pure titania and titania-silica 50/50 ceramic fibrous meshes were made by electrospinning process, and MSC responses on titania-silica fibers were evaluated.

Factors which can influence the fiber diameter and fiber morphology of electrospun nanofibers were discussed in previous studies [10, 11]. The concentration of starting polymer solution is the most commonly used method to adjust the electrospun fiber diameter. Generally, increasing polymer concentration is one of the major methods to increase electrospun fiber diameter [11]. For the pure ceramic electrospun fibers which need heat treatment to

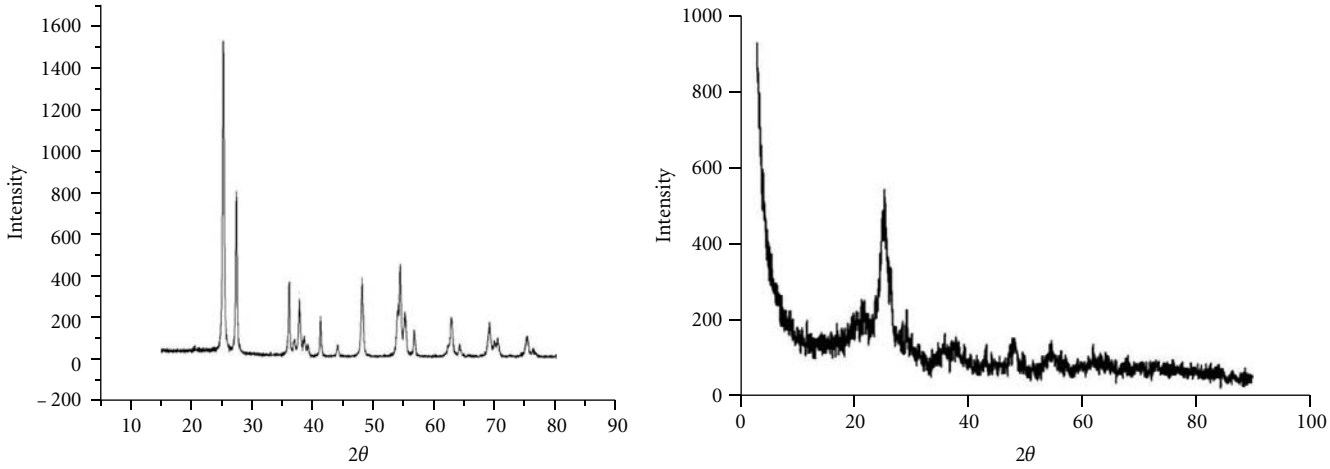

Figure 3: XRD spectra of (a) TiO_2 meshes and (b) titania-silica 50/50 meshes. Respective rutile (^) and anatase (*) reference peaks are marked according to JCPDS database.

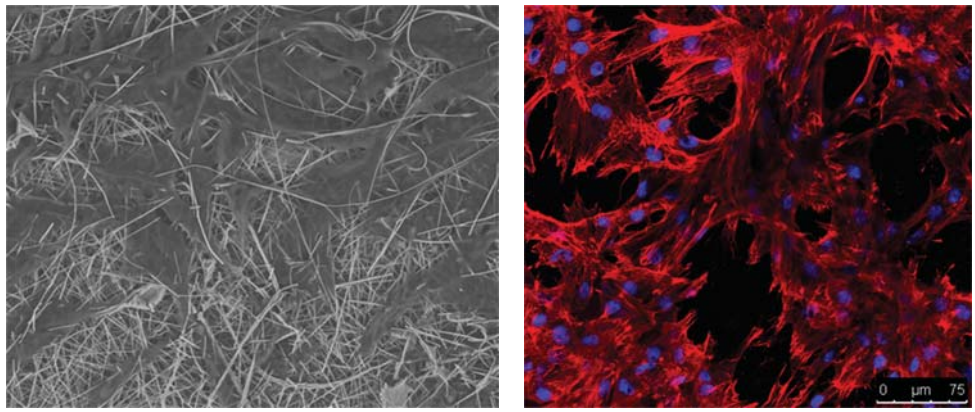

Figure 4: SEM (a) and confocal microscope (b) images of the morphology of MSCs cultured on the titania-silica 50/50 meshes.

remove the polymer component, the sol-gel content and calcination temperature can also contribute to fiber morphology [31]. SEM images show that 10% PVP titania meshes have thicker fiber diameter than 6% PVP titania meshes; the result is consistent with previous study [30]. When silica is added into the sol-gel system, even with the same concentration of starting polymer and same gel content, the fiber diameter is thinner than pure titania fibers. In addition, the addition of silica had influence on fiber surface morphology, too. The surface of titania-silica fiber is smoother than that of pure titania fiber. This result is further supported by XRD spectrum, which shows that titania-silica has lower degree of crystallization under the same calcination temperature. After heating up to 700°C for 3 h, two groups of pure titania fibers formed rutile-anatase mixed crystals while titania-silica 50/50 fibers formed not well-crystalized anatase crystals. Similar results were reported by heating the mixture of silica and titania nanoparticles [32], which shows that the addition of silica affects crystal phase transformation of titania-silica particles. XPS results with the lack of N support the point that PVP was removed during calcination and the substrates are composed of silica and titania. The small amount of silica in titania fibers may be caused by calcining the fiber meshes on a silicon wafer.

Cell number on the meshes was affected by the fibrous structure of the titania-silica meshes, which had lower cell number than TCPs. This effect of fibrous surfaces and rough surfaces on cell number has been previously reported by many studies for Ti/TiO_2 surfaces that promote osteoblast or MSCs differentiation toward osteoblast [30, 33, 34]. Beside cell number, the differentiation of MSCs was also affected by surface structure. Runx2, a transcription factor belonging to the Runx family, determines the osteoblast lineage from multipotent MSCs. Runx2 induces osteoblastic differentiation at early stage [35]. The relative gene expression of Runx2 of this study is significantly higher than control. Also alkaline-phosphatase-specific activity, which is also an early marker of osteogenic differentiation, was significantly higher

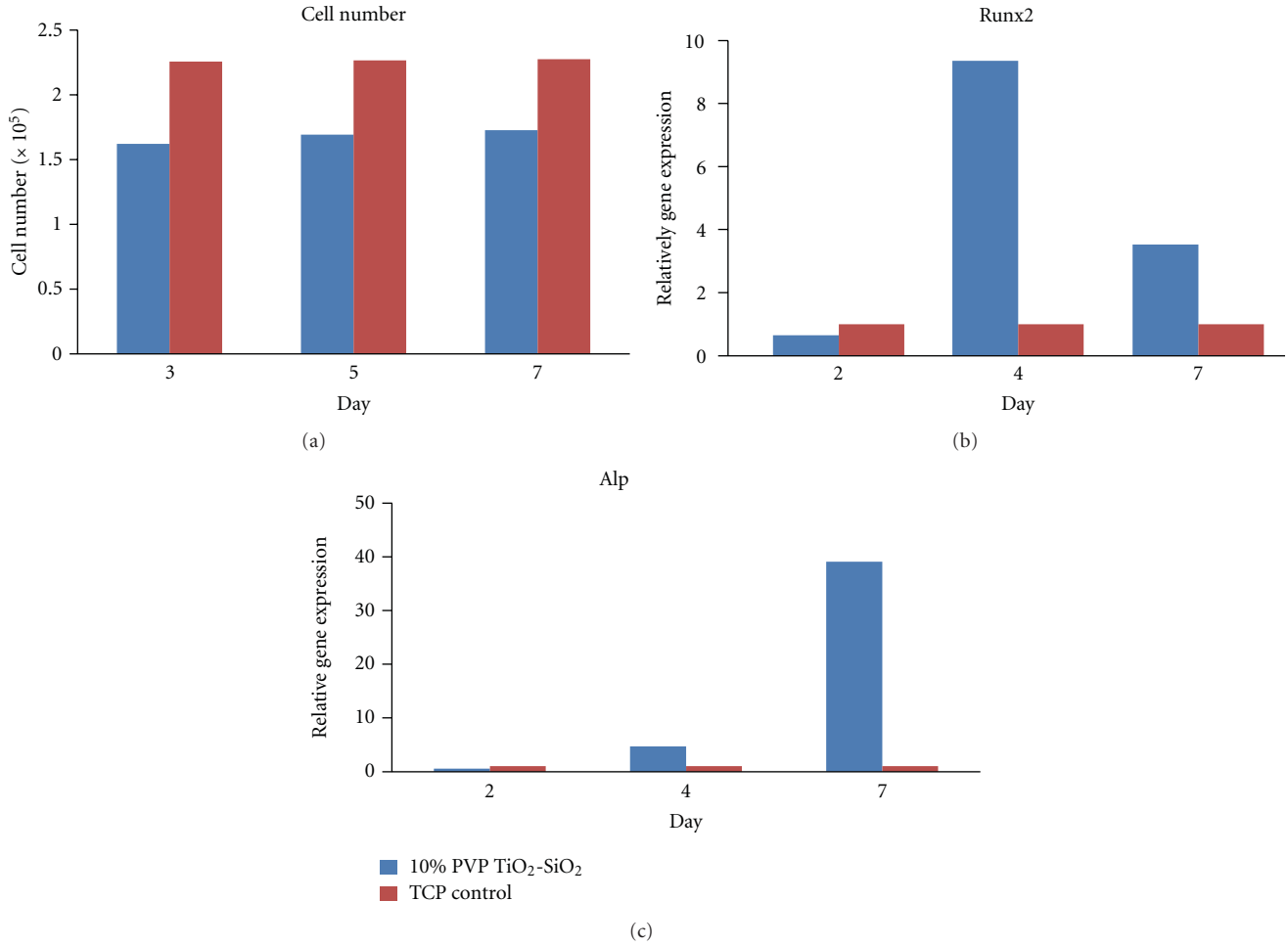

Figure 5: Effects of titania-silica 50/50 nanofibers on cell number and mRNA expression in MSCs. (a) Cell number, (b) Runx2, (c) alkaline phosphatase.

in titania-silica 50/50 when compared to the TCP control. The cell results show that titania-silica 50/50 fiber meshes have osteogenic potential.

5. Conclusion

In this study, submicron-scale composite fiber titania-based ceramics with various compositions have been prepared by electrospinning. Pure ceramic fibers were obtained by heat treatment at 700°C for 3 h. SEM images showed that the diameter and morphology of the nanofibers were influenced by starting polymer concentration and sol composition. The titania and titania-silica nanofibers have the average diameter around 100~300 nm. The fiber surface morphology and crystal phase were influenced by silica content. Bone-marrow-derived MSCs were seeded on titania-silica 50/50 fiber meshes. Cell number and early differentiation marker expressions were analyzed, and the results indicate osteogenic potential of the titania-silica 50/50 fiber meshes. In conclusion, the present work has shown that both the morphology and crystal phase of titania-based electrospun nanofibers are able to be controlled by starting polymer concentration and chemical composition. And these titania-based electrospun nanofibers may have potential use as a new scaffold material for bone tissue engineering.

Acknowledgments

The work is supported by the Ministry of Science and Technology of China (Grants 2012CB933903, 2011AA030102) and the Wallace H. Coulter Foundation.

References

[1] B. Ding, H. Y. Kim, S. C. Lee et al., "Preparation and characterization of a nanoscale poly(vinyl alcohol) fiber aggregate produced by an electrospinning method," *Journal of Polymer Science, Part B*, vol. 40, no. 13, pp. 1261–1268, 2002.

[2] Y. Z. Zhang, J. Venugopal, Z. M. Huang, C. T. Lim, and S. Ramakrishna, "Crosslinking of the electrospun gelatin nanofibers," *Polymer*, vol. 47, no. 8, pp. 2911–2917, 2006.

[3] M. T. Hunley and T. E. Long, "Electrospinning functional nanoscale fibers: a perspective for the future," *Polymer International*, vol. 57, no. 3, pp. 385–389, 2008.

[4] I. Keun Kwon, S. Kidoaki, and T. Matsuda, "Electrospun nano- to microfiber fabrics made of biodegradable copolyesters: structural characteristics, mechanical properties and cell adhesion potential," *Biomaterials*, vol. 26, no. 18, pp. 3929–3939, 2005.

[5] F. Yang, R. Murugan, S. Wang, and S. Ramakrishna, "Electrospinning of nano/micro scale poly(l-lactic acid) aligned fibers and their potential in neural tissue engineering," *Biomaterials*, vol. 26, no. 15, pp. 2603–2610, 2005.

[6] D. Li, Y. Wang, and Y. Xia, "Electrospinning of polymeric and ceramic nanofibers as uniaxially aligned arrays," *Nano Letters*, vol. 3, no. 8, pp. 1167–1171, 2003.

[7] R. Ramaseshan, S. Sundarrajan, R. Jose, and S. Ramakrishna, "Nanostructured ceramics by electrospinning," *Journal of Applied Physics*, vol. 102, no. 11, pp. 1063–1080, 2007.

[8] M. Macías, A. Chacko, J. P. Ferraris, and K. J. Balkus Jr., "Electrospun mesoporous metal oxide fibers," *Microporous and Mesoporous Materials*, vol. 86, no. 1–3, pp. 1–13, 2005.

[9] X. Wang, C. Drew, S. H. Lee, K. J. Senecal, J. Kumar, and L. A. Samuelson, "Electrospun nanofibrous membranes for highly sensitive optical sensors," *Nano Letters*, vol. 2, no. 11, pp. 1273–1275, 2002.

[10] J. Doshi and D. H. Reneker, "Electrospinning process and applications of electrospun fibers," *Journal of Electrostatics*, vol. 35, no. 2-3, pp. 151–160, 1995.

[11] W. K. Son, J. H. Youk, T. S. Lee, and W. H. Park, "The effects of solution properties and polyelectrolyte on electrospinning of ultrafine poly(ethylene oxide) fibers," *Polymer*, vol. 45, no. 9, pp. 2959–2966, 2004.

[12] P. Gupta, C. Elkins, T. E. Long, and G. L. Wilkes, "Electrospinning of linear homopolymers of poly(methyl methacrylate): exploring relationships between fiber formation, viscosity, molecular weight and concentration in a good solvent," *Polymer*, vol. 46, no. 13, pp. 4799–4810, 2005.

[13] C. Li, C. Vepari, H. J. Jin, H. J. Kim, and D. L. Kaplan, "Electrospun silk-BMP-2 scaffolds for bone tissue engineering," *Biomaterials*, vol. 27, no. 16, pp. 3115–3124, 2006.

[14] W. J. Li, C. T. Laurencin, E. J. Caterson, R. S. Tuan, and F. K. Ko, "Electrospun nanofibrous structure: a novel scaffold for tissue engineering," *Journal of Biomedical Materials Research*, vol. 60, no. 4, pp. 613–621, 2002.

[15] S. R. Bhattarai, N. Bhattarai, H. K. Yi, P. H. Hwang, D. I. Cha, and H. Y. Kim, "Novel biodegradable electrospun membrane: scaffold for tissue engineering," *Biomaterials*, vol. 25, no. 13, pp. 2595–2602, 2004.

[16] Y. Zhang, J. R. Venugopal, A. El-Turki, S. Ramakrishna, B. Su, and C. T. Lim, "Electrospun biomimetic nanocomposite nanofibers of hydroxyapatite/chitosan for bone tissue engineering," *Biomaterials*, vol. 29, no. 32, pp. 4314–4322, 2008.

[17] Y. Ito, H. Hasuda, M. Kamitakahara et al., "A composite of hydroxyapatite with electrospun biodegradable nanofibers as a tissue engineering material," *Journal of Bioscience and Bioengineering*, vol. 100, no. 1, pp. 43–49, 2005.

[18] S. Sakai, Y. Yamada, T. Yamaguchi, and K. Kawakami, "Prospective use of electrospun ultra-fine silicate fibers for bone tissue engineering," *Biotechnology Journal*, vol. 1, no. 9, pp. 958–962, 2006.

[19] S. Z. Chu, S. Inoue, K. Wada, D. Li, H. Haneda, and S. Awatsu, "Highly porous $(TiO_2$-SiO_2-$TeO_2)/Al_2O_3/TiO_2$ composite nanostructures on glass with enhanced photocatalysis fabricated by anodization and sol-gel process," *Journal of Physical Chemistry B*, vol. 107, no. 27, pp. 6586–6589, 2003.

[20] M. F. Morks, "Plasma spraying of zirconia-titania-silica bioceramic composite coating for implant application," *Materials Letters*, vol. 64, no. 18, pp. 1968–1971, 2010.

[21] R. Leboda, V. V. Turov, M. Marciniak, A. A. Malygin, and A. A. Malkov, "Characteristics of the hydration layer structure in porous titania-silica obtained by the chemical vapor deposition method," *Langmuir*, vol. 15, no. 24, pp. 8441–8446, 1999.

[22] T. H. Tran-Thi, R. Dagnelie, S. Crunaire, and L. Nicole, "Optical chemical sensors based on hybrid organic-inorganic sol-gel nanoreactors," *Chemical Society Reviews*, vol. 40, no. 2, pp. 621–639, 2011.

[23] K. M. S. Khalil, A. A. Elsamahy, and M. S. Elanany, "Formation and characterization of high surface area thermally stabilized titania/silica composite materials via hydrolysis of titanium(IV) tetra-isopropoxide in sols of spherical silica particles," *Journal of Colloid and Interface Science*, vol. 249, no. 2, pp. 359–365, 2002.

[24] X. Zhang, F. Zhang, and K. Y. Chan, "Synthesis of titania-silica mixed oxide mesoporous materials, characterization and photocatalytic properties," *Applied Catalysis A*, vol. 284, no. 1-2, pp. 193–198, 2005.

[25] V. Ääritalo, S. Areva, M. Jokinen, M. Lindén, and T. Peltola, "Sol-gel-derived TiO_2-SiO_2 implant coatings for direct tissue attachment. Part I: design, preparation and characterization," *Journal of Materials Science*, vol. 18, no. 9, pp. 1863–1873, 2007.

[26] V. V. Meretoja, A. E. De Ruijter, T. O. Peltola, J. A. Jansen, and T. O. Narhi, "Osteoblast differentiation with titania and titania-silica-coated titanium fiber meshes," *Tissue Engineering*, vol. 11, no. 9-10, pp. 1489–1497, 2005.

[27] V. Muhonen, S. Kujala, A. Vuotikka et al., "Biocompatibility of sol-gel-derived titania-silica coated intramedullary NiTi nails," *Acta Biomaterialia*, vol. 5, no. 2, pp. 785–793, 2009.

[28] V. V. Meretoja, T. Tirri, V. Ääritalo, X. F. Walboomers, J. A. Jansen, and T. O. Närhi, "Titania and titania-silica coatings for titanium: comparison of ectopic bone formation within cell-seeded scaffolds," *Tissue Engineering*, vol. 13, no. 4, pp. 855–863, 2007.

[29] J. J. Yoo and S. H. Rhee, "Evaluations of bioactivity and mechanical properties of poly (ε-caprolactone)/silica nanocomposite following heat treatment," *Journal of Biomedical Materials Research—Part A*, vol. 68, no. 3, pp. 401–410, 2004.

[30] X. Wang, R.A. Gittens, R. Song et al., "Effects of structural properties of electrospun TiO_2 nanofiber meshes on their osteogenic potential," *Acta Biomaterialia*, vol. 8, no. 2, pp. 878–885, 2012.

[31] B. Ding, H. Kim, C. Kim, M. Khil, and S. Park, "Morphology and crystalline phase study of electrospun TiO_2-SiO_2 nanofibres," *Nanotechnology*, vol. 14, no. 5, pp. 532–537, 2003.

[32] H. Chang, S. K. Kim, H. D. Jang, and S. W. Cho, "Effect of SiO_2 nanoparticles on the phase transformation of TiO_2 in micron-sized porous TiO_2-SiO_2 mixed particles," *Materials Letters*, vol. 65, no. 21-22, pp. 3272–3274, 2011.

[33] D. D. Deligianni, N. Katsala, S. Ladas, D. Sotiropoulou, J. Amedee, and Y. F. Missirlis, "Effect of surface roughness of the titanium alloy Ti-6Al-4V on human bone marrow cell response and on protein adsorption," *Biomaterials*, vol. 22, no. 11, pp. 1241–1251, 2001.

[34] S. P. Xavier, P. S. P. Carvalho, M. M. Beloti, and A. L. Rosa, "Response of rat bone marrow cells to commercially pure

titanium submitted to different surface treatments," *Journal of Dentistry*, vol. 31, no. 3, pp. 173–180, 2003.

[35] T. Fujita, Y. Azuma, R. Fukuyama et al., "Runx2 induces osteoblast and chondrocyte differentiation and enhances their migration by coupling with PI3K-Akt signaling," *Journal of Cell Biology*, vol. 166, no. 1, pp. 85–95, 2004.

Hindawi Publishing Corporation
Journal of Nanomaterials
Volume 2012, Article ID 987938, 7 pages
doi:10.1155/2012/987938

Research Article

Interlayer Structure of Bioactive Molecule, 2-Aminoethanesulfonate, Intercalated into Calcium-Containing Layered Double Hydroxides

Tae-Hyun Kim, Hyoung Jun Kim, and Jae-Min Oh

Department of Chemistry & Medical Chemistry, College of Science & Technology, Yonsei University, Wonju, Gangwon-do 220-710, Republic of Korea

Correspondence should be addressed to Jae-Min Oh, jaemin.oh@yonsei.ac.kr

Received 14 February 2012; Accepted 5 April 2012

Academic Editor: Krasimir Vasilev

We have successfully intercalated 2-aminoethanesulfonate, a well-known biomolecule taurine, into calcium-containing layered double hydroxides via optimized solid phase intercalation. According to X-ray diffraction patterns and infrared spectroscopy, it was revealed that the intercalated taurine molecules were each directly coordinated to other calcium cation and arranged in a zig-zag pattern. Scanning electron microscopy showed that the particle size and morphology of the LDHs were not affected by the solid phase intercalation, and the surface of intercalates was covered by organic moieties. From ninhydrin amine detection tests, we confirmed that most of the taurine molecules were well stabilized between the calcium-containing LDH layers.

1. Introduction

Drug delivery systems are now a major concern in nanoscience and nanotechnology [1–5], and the two-dimensional nanomaterial layered double hydroxide (LDH) is attracting increasing interest in the field. LDHs have a general chemical formula of $[M(II)_{1-x}M(III)_x(OH)_2]^{x+}$ $(A^{n-})_{x/n}\cdot mH_2O$ (M(II), M(III): metal ions, A^{n-} anionic species). They are composed of positively charged layers and exchangeable interlayer anions along water molecules [6]. Their crystal structure evolves from electrically neutral brucite-($Mg(OH)_2$-) like layers in which $M(II)(OH)_6$ octahedrons are connected in the *xy*-plane direction by sharing their edges. The isomorphic substitution of M(II) with M(III) causes a positive charge on the layers, and the anionic species between the layers compensate and produce charge neutrality. The interlayer anions, which can be a number of diverse things from small molecules to drugs or DNA strands, can acquire stabilization energy through electrostatic interaction with the layers [7–9].

For decades, LDH nanomaterials, have been widely studied as antacids, catalytic supports, polymer stabilizers, adsorbents and others [6, 10–12]. The last ten years, however, have been more devoted to studying LDHs for biomedical applications due to their tailored properties as drug delivery nanocarriers, ability to stabilize interlayer anions from external harsh conditions [7, 13], high rate of cellular uptake via clathrin-mediated endocytosis [14, 15], low toxicity due to dissolution physiological pH [16, 17], and easily modifiable surface for additional functionality [18].

The intercalation of biologically active substances such as anticancer or anti-inflammatory drugs and therapeutic genes into LDHs has been reported to dramatically enhance the curative efficacy as well as to release the drug molecules in sustained manner [9, 19].

Among the various types of LDHs with different metal compositions, LDHs containing calcium are unique in their structure and expected to be highly biocompatible. As reported, biological systems, especially human bodies, have abundant calcium moieties for the formation of skeletal structure and for the cell signaling [20], so it follows that LDHs with Ca/Al or Ca/Fe compositions should be highly biocompatible as well. The structure of calcium-containing LDHs (abbreviated as CaM-LDHs) is different from others

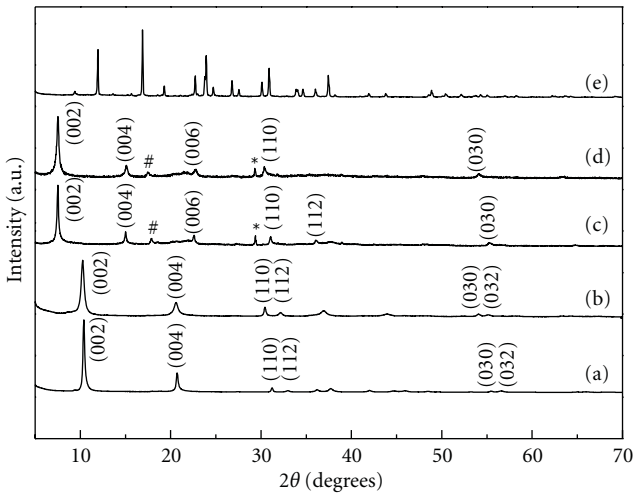

Figure 1: X-ray diffraction patterns for (a) CaAl-LDH, (b) CaFe-LDH, (c) CaAl-Tau-LDH, (d) CaFe-Tau-LDH, and (e) Na^+-taurine salt. (*: $NaNO_3$, #: undetermined impurity).

due to the large size of the Ca^{2+} ions. Heptacoordinated calcium hydroxide decahedrons and hexacoordinated trivalent metal hydroxide octahedrons are arranged in a 2-dimensional lattice by sharing their edges, however, the seventh coordination on calcium is usually occupied by interlayer anions or water molecules [21].

Despite the expected advantages in drug delivery applications, there have only been a few reports on the intercalation of biologically active molecules into CaM-LDHs. The possible bond between metal cations and anions during the synthesis may prevent the formation of anion-intercalated LDH in coprecipitation, which is the most well-known synthesis method for LDH. In ion exchange reactions, the dissolution of layers rather than intercalation may occur due to the dissolution properties of CaM-LDHs in neutral pH.

In this study, we successfully intercalated the bioactive organic acid taurine (2-aminoethanesulfonate) into CaAl- or CaFe-LDHs via solid phase reaction. Taurine (Tau) is a well-known bile product that acts in antioxidation and osmoregulation [22] and recently has been attracting gaining interest for drug delivery systems [23]. We demonstrate systematic approaches for solid phase intercalation of taurine molecules into CaM-LDHs as an alternative for coprecipitation and ion exchange routes. The structural analyses of taurine-intercalated CaM-LDHs are described in terms of interlayer structure and bonding nature.

2. Experimental and Procedures

2.1. Materials. $Ca(NO_3)_2 \cdot 4H_2O$ was purchased from Junsei Chemical Co., Ltd., (Tokyo, Japan); $Al(NO_3)_3 \cdot 9H_2O$, $Fe(NO_3)_3 \cdot 9H_2O$, and 2% ninhydrin solution were purchased from Sigma-Aldrich Co., Ltd. (USA); NaOH pellets were obtained from Daejung Chemicals & Metals Co., Ltd., (Gyonggido, Korea) and used without further purification. Taurine (2-aminoethanesulfonate) was purchased from Sigma-Aldrich Co., Ltd., (USA), and Na^+-taurine salt was prepared by mixing taurine and NaOH solution with 1 : 1 molar ratio followed by drying with a rotary evaporator.

2.2. Synthesis of Pristine CaM-LDHs and Solid Phase Intercalation. For the preparation of CaAl- and CaFe-LDHs mixed metal nitrate solutions (0.315 M of Ca^{2+} and 0.158 M of M^{3+} (Al^{3+} or Fe^{3+})) were prepared and titrated with NaOH solution until the pH reached ~11.5 and ~13.0, respectively. The precipitates were aged for 24 hours under N_2 atmosphere with vigorous stirring. The products were filtered and washed with decarbonated water and dried in vacuum at 40°C. Pristine LDHs (0.2 g) were mixed with taurine salts (0.0802 g for CaAl- and 0.0762 g for CaFe-LDH to achieve a 1 : 1 molar ratio between taurine and M^{3+}) and ground in a mortar for 5 min with various amounts of water added (0, 5, 10, 20, 30, and 40 μL). After grinding, the products were dried for 12 hours in vacuum at 40°C.

2.3. Characterization. Powder X-ray diffraction patterns were obtained with a Bruker AXS D2 Phaser with degree and time step increments of 0.02° and 1 sec/step, respectively. Fourier transform infrared (FT-IR; Perkin Elmer, spectrum one B.v5.0) spectroscopy was performed with conventional KBr methods. The particle size and morphology of the CaM-LDHs and corresponding intercalates were investigated with scanning electron microscopy (SEM) on a Quanta 250 FEG at Yonsei University in Wonju. The chemical compositions of both LDHs were evaluated with inductively coupled plasma-atomic emission spectroscopy (ICP-AES: Perkin Elmer Optima-4300 DV) and elemental analysis (EA: EA 1110).

2.4. Primary Amine Detection (Ninhydrin Test). For ninhydrin test, CaAl-, CaFe-LDHs, taurine salt, CaAl-Tau-, and CaFe-Tau-LDHs were dispersed in 2% ninhydrin solution and diluted with ethanol at four-times the volume. After vortexing for 1 min, aliquot was gathered and redispersed in ethanol for UV-Vis spectroscopy (UV-1800; SHZMADZU) and photographs.

3. Result and Discussion

In order to intercalate taurine molecules into CaM-LDH, we first tried the most widely utilized intercalation routes, coprecipitation and ion exchange reactions. As indicated in the X-ray diffraction patterns (see Figure S1 in Supplementary material available online at doi: 10.1155/2012/987938), coprecipitation was determined not to be effective for the preparation of taurine intercalated CaM-LDHs (CaM-Tau-LDHs). In the coprecipitation reaction system, there were 7-times as much nitrate as taurine molecules; therefore, nitrate ion is favored for intercalation. The ion exchange was also proven not to be adaptable for the intercalation of taurine into CaM-LDHs, although there were 1.5-times more taurine molecules than nitrate (data not shown). Studies on intercalation utilizing CaM-LDHs through coprecipitation and ion exchange have been less reported compared with general LDHs, and different types of intercalation such as

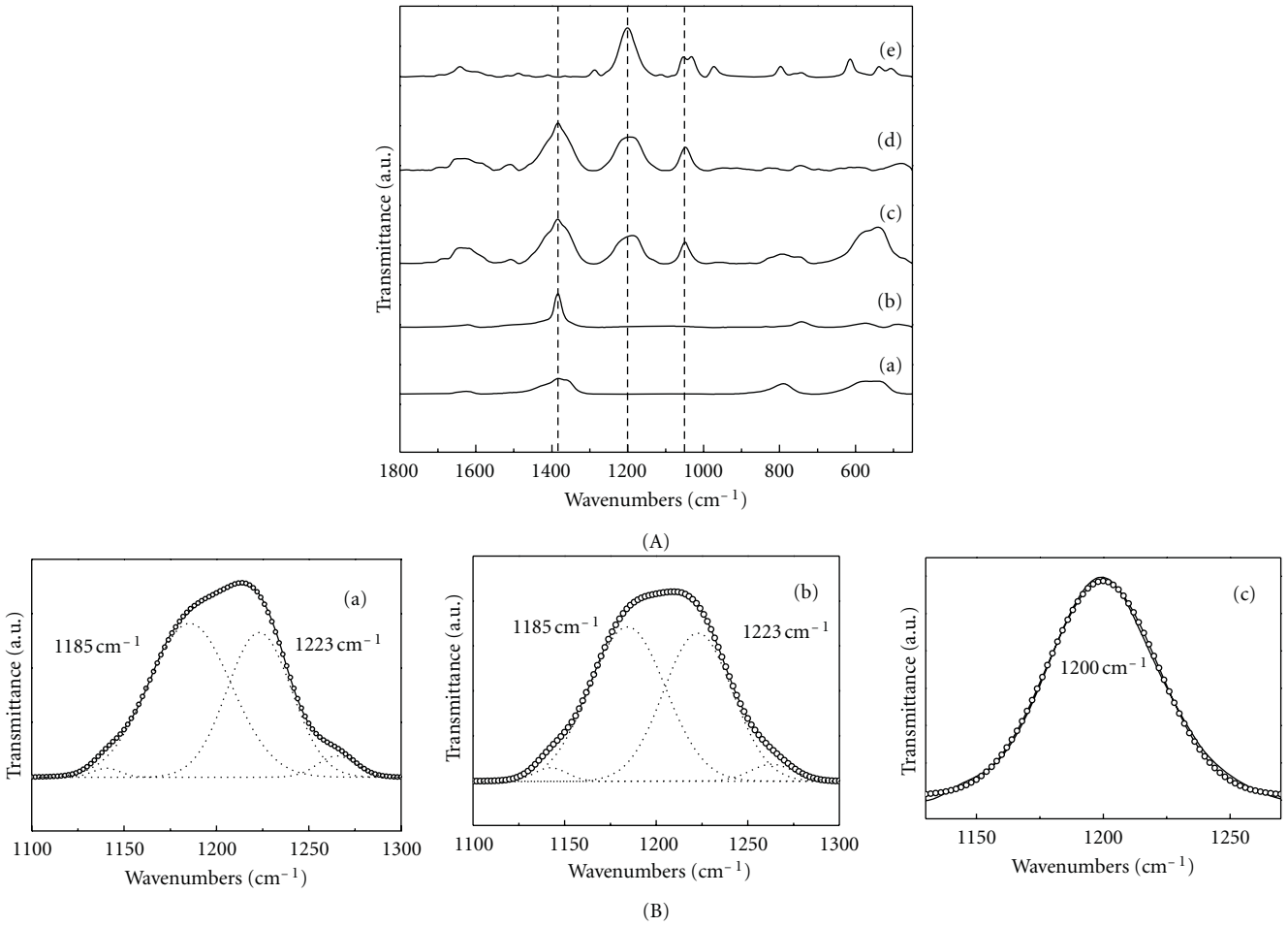

Figure 2: (A) Fourier transform infrared spectra for (a) CaAl-LDH, (b) CaFe-LDH, (c) CaAl-Tau-LDH, (d) CaFe-Tau-LDH, and (e) Na^+-taurine salt. (B) The magnified and multipeak fitted $\nu_{asym}(SO_3^-)$: (a) CaAl-Tau-LDH, (b) CaFe-Tau-LDH, and (c) Na^+-taurine salt. (Solid line: observed peak, dotted line: fitted peaks, open circle: summation of fitted peaks).

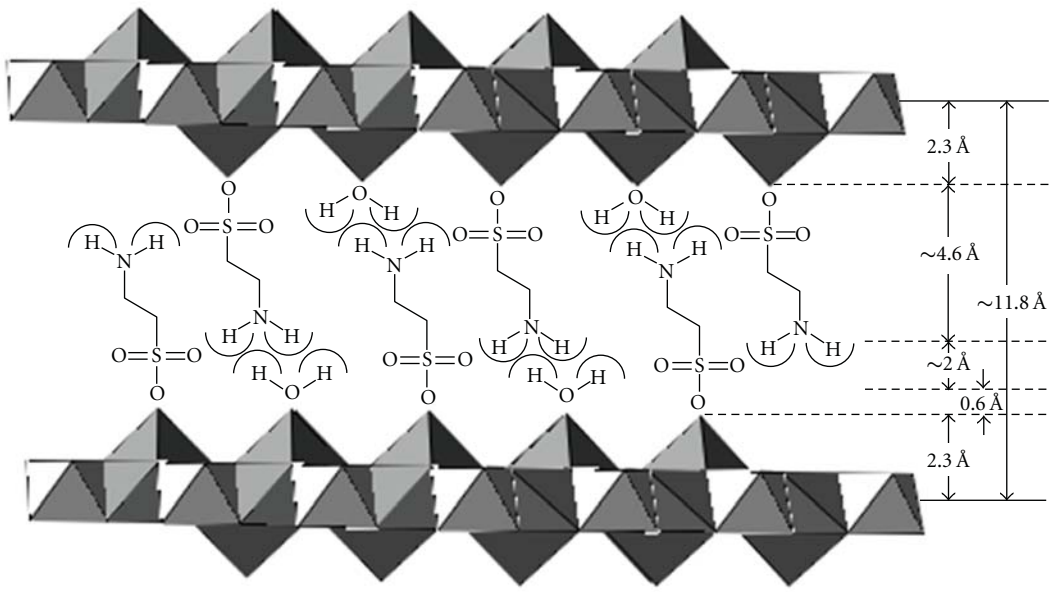

Figure 3: Schematic diagram for the possible orientation of interlayer taurin molecules in the CaM-Tau-LDH hybrid.

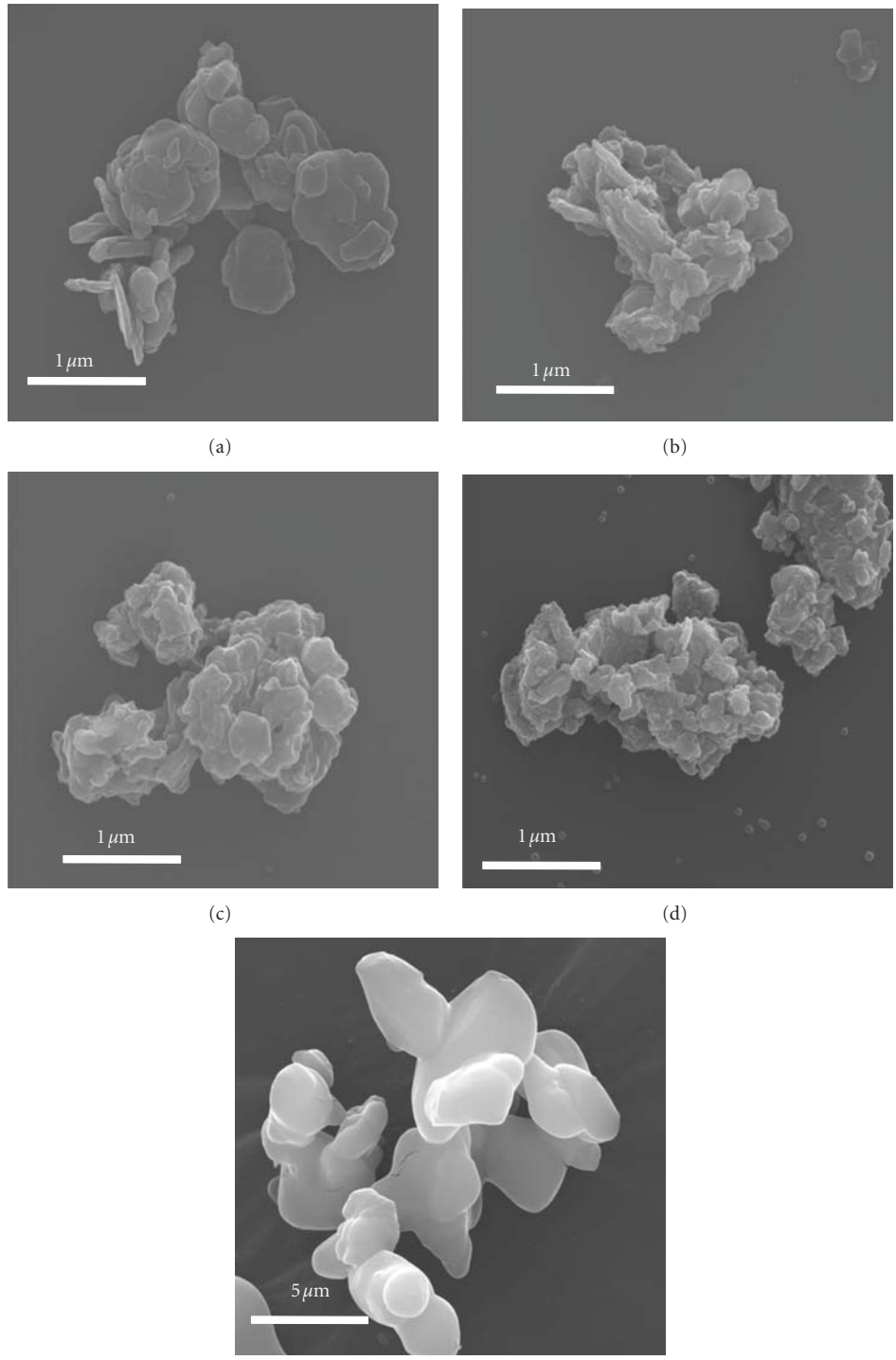

Figure 4: Scanning electron microscopic images for (a) CaAl-LDH, (b) CaFe-LDH, (c) CaAl-Tau-LDH, (d) CaFe-Tau-LDH, and (e) Na^+-taurine salt.

induced-hydrolysis-based reactions have been studied by Plank and von Hoessel [24].

The best synthetic strategy intercalation of taurine into CaM-LDHs was solid phase intercalation, in which both pristine LDHs and anion molecules are homogeneously ground in mortars with only a small amount of water. Since the amount of water is a key synthetic condition in this solid phase intercalation [25], various amounts of water were added to find an optimum condition (Figures S2 and S3). Although a phase transformation correlation with

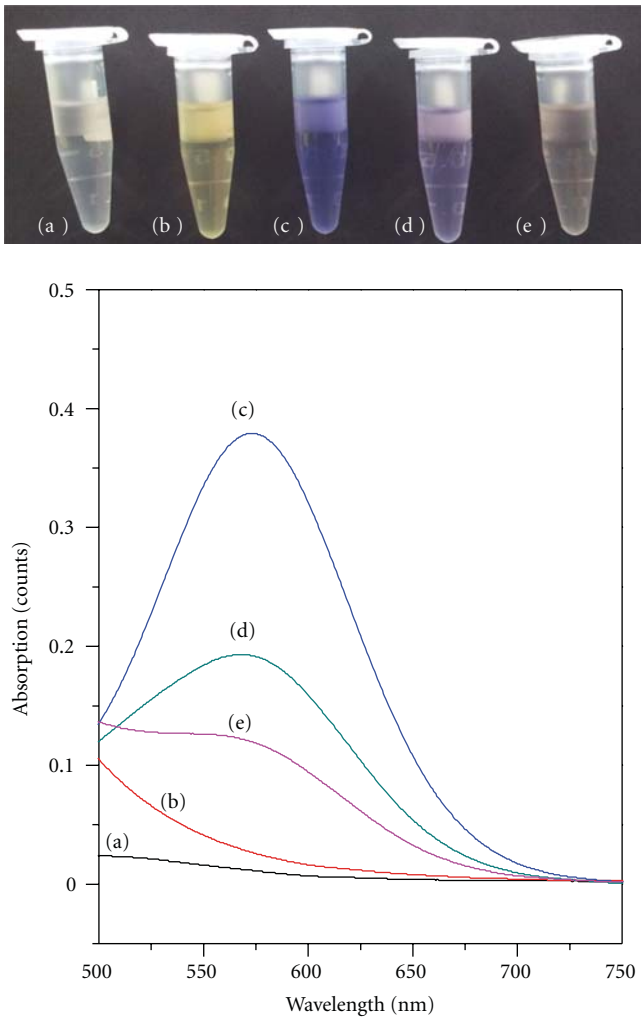

Figure 5: UV-Vis spectra for ninhydrin-treated (a) CaAl-LDH, (b) CaFe-LDH, (c) Na^+-taurine salt, (d) CaAl-Tau-LDH, and (e) CaFe-Tau-LDHs. The inset shows photographs for ninhydrin-treated (a′) CaAl-LDH, (b′) CaFe-LDH, (c′) Na^+-taurine salt, (d′) CaAl-Tau-LDH, and (e′) CaFe-Tau-LDHs.

increasing amounts of water added could not be found, it was determined that the addition of 10 μL water to 0.2 g CaM-LDH and ~0.08 g Na^+-taurine salt is the optimum synthetic condition.

Figure 1 shows the X-ray diffraction patterns for the CaM-LDHs and their taurine intercalates. The diffraction patterns for the pristine LDHs corresponded well with previously reported results (Figure 1) [21, 26]. After intercalation, the (00l) peaks shift to the lower 2-theta region, revealing lattice expansion from ~8.5 to ~11.8 Å along the *z*-axis (layer stacking direction). The lattice parameters *a* and *c* in the hexagonal crystal system for pristine material and intercalates were calculated based on the (*hkl*) indexing results. The *c* values increase from 17.12 and 17.25 to 23.58 and 23.44 after intercalation for CaAl- and CaFe-LDHs, respectively, while the *a* values remain almost constant at ~ 5.74 and ~5.87 Å. This result revealed that the 2-dimensional lattice structures of the LDHs were neither decomposed nor dissolved during the intercalation. The asterisks indicate the diffraction patterns for $NaNO_3$ salt which may have resulted from the disintercalated nitrates.

In order to verify the preservation of functional groups in taurine as well as the bonding nature between taurine and the LDHs, Fourier transform infrared (FT-IR) spectroscopic studies were performed (Figure 2). In the spectra for pristine material and intercalates, the peaks at 1380 and below 600 cm^{-1} are attributed to the $\nu(NO_3^-)$ and ν(M-O) modes. Symmetric and asymmetric stretching modes of sulfonates could be observed at around 1054 and 1200 cm^{-1}, respectively, in the spectra of both Na^+-taurine salt and CaM-Tau-LDH intercalates. It is worthy to note that $\nu_{asym}(SO_3^-)$ splits into two peaks at 1185 and 1223 cm^{-1} after intercalation (Figure 2(b)). Similar splitting of $\nu_{asym}(SO_3^-)$ was reported in the infrared spectra of sulfonates coordinated to metal cations [27]. It is therefore concluded that the taurine molecules were stabilized in the interlayer space of CaM-LDHs via coordination bonds between sulfonate and calcium cation.

From the X-ray diffraction patterns, FT-IR spectra and chemical formulae, we could suggest the possibility of an interlayer structure of taurine in an ideal case (Figure 3). According to the ICP-AES and CHNS elemental analysis, the chemical formulae of both CaM-Tau-LDHs were determined to be $[Ca_{1.99}Al(OH)_6(Tau)_{0.97}\cdot 5H_2O]$ and $[Ca_{1.91}Fe(OH)_6(Tau)_{1.19}\cdot 5H_2O]$, respectively. Since the amount of taurine molecules existing in the hybrids is almost the same compared to the ideal composition, $Ca_{1.99}Al(OH)_{5.98}(Tau)\cdot 5H_2O$ and $Ca_{1.91}Fe(OH)_{5.82}(Tau)\cdot 5H_2O$, we could propose a schematic diagram of interlayer taurine orientation as shown in Figure 3.

In a previous study [26], we reported that the bond distance between calcium and the seventh coordinated nitrate is approximately 2.3 Å. The molecular dimensions along the *z*-axis for taurine (distance from outermost sulfate oxygen to amine hydrogen) and water are approximately 4.6 and 0.6 Å, respectively. Considering the van der Waals radii of hydrogen, the distance between the facing hydrogens is about 2 Å. For the summation of bond length Ca-O, the molecular dimensions along the *z*-axis and van der Waals interactions distance give ~11.8 Å, which corresponds well to the basal spacing of CaM-Tau-LDHs determined by X-ray diffraction patterns. As suggested in Figure 3, the taurine and water molecules are arranged in a zig-zag pattern to be effectively stabilized in the interlayer space.

The particle size and morphology of pristine LDHs, intercalates, and Na^+-taurine salts were investigated with scanning electron microscopy (Figure 4). Both CaM-LDHs before and after intercalation showed plate-like morphology with particle size distributed from 200 to 600 nm, while Na^+-taurine salt morphology was undetermined, with particle sizes larger than 2 μm. In Figures 4(c) and 4(d), the surface of CaM-Tau-LDHs seems to be covered with organic moieties which may have resulted from the surface-attached taurine molecules. It is worthy to note that the average particle size and morphology of the LDHs were not significantly altered

after intercalation, which was also confirmed by the X-ray diffraction result showing similar crystallinity for CaM-LDHs and their intercalates (Figure 1).

It was also verified by the ninhydrin test that most of the taurine molecules were stabilized in the interlayer space of the CaM-LDHs. Ninhydrin molecules form deep-purple chromophores when they encounter primary amines. Figure 5 shows the UV-vis spectra and photographs of ninhydrin-treated Na^+-taurine salt and CaM-Tau-LDHs. It should be noted that the amount of taurine in salt and intercalate was set at the same amount for quantitative analysis. As shown in the UV-vis spectra, the absorbance at λ_{max} = 575 nm in intercalates was much lower than that of taurine salt, indicating that most of the taurine molecules did not react with the ninhydrin due to the stabilization of the LDH layers. The slightly brown color in the CaFe-Tau-LDH (Figure 5(e′)) can be explained by the partial dissolution of Fe^{3+}, which was also observed in the pristine CaFe-LDH treated with ninhydrin (Figure 5(b′)).

4. Conclusion

We have successfully intercalated the biologically active molecule taurine into two different kinds of calcium-containing LDHs, CaAl- and CaFe-LDHs. Since coprecipitation and anionic exchange were determined to be not effective for the intercalation, we optimized the reaction conditions of a solid phase intercalation method. Structural analyses including X-ray diffraction patterns, infrared spectroscopy, microscopic study, ICP-AES, and ninhydrin tests showed that the taurine molecules were well stabilized between the LDH layers by forming direct coordination bonds with calcium cations.

Acknowledgments

This paper was financially supported by a National Research Foundation of Korea grant funded by the Korean Government (2010-0001488) and partly the Herbal Crop Research Project (PJ006921) of RDA, Republic of Korea.

References

[1] S. J. Choi, G. E. Choi, J. M. Oh, Y. J. Oh, M. C. Park, and J. H. Choy, "Anticancer drug encapsulated in inorganic lattice can overcome drug resistance," *Journal of Materials Chemistry*, vol. 20, no. 42, pp. 9463–9469, 2010.

[2] X. M. Jiang, Y. S. Cheng, and H. D. C. Smyth, "Nanostructured aerosol particles: fabrication, pulmonary drug delivery, and controlled release," *Journal of Nanomaterials*, vol. 2011, Article ID 198792, 2 pages, 2011.

[3] J. M. Oh, T. T. Biswick, and J. H. Choy, "Layered nanomaterials for green materials," *Journal of Materials Chemistry*, vol. 19, no. 17, pp. 2553–2563, 2009.

[4] E. Ruiz-Hernández, A. Baeza, and M. Vallet-Regí, "Smart drug delivery through DNA/magnetic nanoparticle gates," *ACS Nano*, vol. 5, no. 2, pp. 1259–1266, 2011.

[5] L. X. Zhao, A. C. Liu, M. Sun et al., "Enhancement of oral bioavailability of puerarin by polybutylcyanoacrylate nanoparticles," *Journal of Nanomaterials*, vol. 2011, Article ID 126562, 8 pages, 2011.

[6] A. Vaccari, "Preparation and catalytic properties of cationic and anionic clays," *Catalysis Today*, vol. 41, no. 1-3, pp. 53–71, 1998.

[7] J. H. Choy, J. S. Jung, J. M. Oh et al., "Layered double hydroxide as an efficient drug reservoir for folate derivatives," *Biomaterials*, vol. 25, no. 15, pp. 3059–3064, 2004.

[8] J. H. Choy, S. Y. Kwak, J. S. Park, Y. J. Jeong, and J. Portier, "Intercalative nanohybrids of nucleoside monophosphates and DNA in layered metal hydroxide," *Journal of the American Chemical Society*, vol. 121, no. 6, pp. 1399–1400, 1999.

[9] J. M. Oh, M. Park, S. T. Kim, J. Y. Jung, Y. G. Kang, and J. H. Choy, "Efficient delivery of anticancer drug MTX through MTX-LDH nanohybrid system," *Journal of Physics and Chemistry of Solids*, vol. 67, no. 5-6, pp. 1024–1027, 2006.

[10] L. van der Ven, M. L. M. van Gemert, L. F. Batenburg et al., "On the action of hydrotalcite-like clay materials as stabilizers in polyvinylchloride," *Applied Clay Science*, vol. 17, no. 1-2, pp. 25–34, 2000.

[11] K. M. Kim, C. B. Park, A. J. Choi, J. H. Choy, and J. M. Oh, "Selective DNA adsorption on layered double hydroxide nanoparticles," *Bulletin of the Korean Chemical Society*, vol. 32, no. 7, pp. 2217–2221, 2011.

[12] W. Kagunya, Z. Hassan, and W. Jones, "Catalytic properties of layered double hydroxides and their calcined derivatives," *Inorganic Chemistry*, vol. 35, no. 21, pp. 5970–5974, 1996.

[13] J. M. Oh, S. Y. Kwak, and J. H. Choy, "Intracrystalline structure of DNA molecules stabilized in the layered double hydroxide," *Journal of Physics and Chemistry of Solids*, vol. 67, no. 5-6, pp. 1028–1031, 2006.

[14] J. M. Oh, S. J. Choi, G. E. Lee, J. E. Kim, and J. H. Choy, "Inorganic metal hydroxide nanoparticles for targeted cellular uptake through clathrin-mediated endocytosis," *Chemistry*, vol. 4, no. 1, pp. 67–73, 2009.

[15] J. M. Oh, S. J. Choi, S. T. Kim, and J. H. Choy, "Cellular uptake mechanism of an inorganic nanovehicle and its drug conjugates: enhanced efficacy due to clathrin-mediated endocytosis," *Bioconjugate Chemistry*, vol. 17, no. 6, pp. 1411–1417, 2006.

[16] S. J. Choi, J. M. Oh, and J. H. Choy, "Toxicological effects of inorganic nanoparticles on human lung cancer A549 cells," *Journal of Inorganic Biochemistry*, vol. 103, no. 3, pp. 463–471, 2009.

[17] S. J. Choi, J. M. Oh, and J. H. Choy, "Biocompatible ceramic nanocarrier for drug delivery with high efficiency," *Journal of the Ceramic Society of Japan*, vol. 117, no. 1365, pp. 543–549, 2009.

[18] J. M. Oh, S. J. Choi, G. E. Lee, S. H. Han, and J. H. Choy, "Inorganic drug-delivery nanovehicle conjugated with cancer-cell-specific ligand," *Advanced Functional Materials*, vol. 19, no. 10, pp. 1617–1624, 2009.

[19] V. Ambrogi, G. Fardella, G. Grandolini, and L. Perioli, "Intercalation compounds of hydrotalcite-like anionic clays with antiinflammatory agents—I. Intercalation and in vitro release of ibuprofen," *International Journal of Pharmaceutics*, vol. 220, no. 1-2, pp. 23–32, 2001.

[20] S. J. Lippard and J. M. Berg, *Princlples of Bioinorganic Chemistry*, University Science Book, Mill Valley, Calif, USA, 1994.

[21] G. Renaudin and M. François, "The lamellar double-hydroxide (LDH) compound with composition 3CaO·Al2O3·Ca(NO3)2·10H2O," *Acta Crystallographica Section C*, vol. 55, no. 6, pp. 835–838, 1999.

[22] T. R. Green, J. H. Fellman, A. L. Eicher, and K. L. Pratt, "Antioxidant role and subcellular location of hypotaurine and taurine in human neutrophils," *Biochimica et Biophysica Acta*, vol. 1073, no. 1, pp. 91–97, 1991.

[23] N. Ozmeric, G. Ozcan, C. M. Haytac, E. E. Alaaddinoglu, M. F. Sargon, and S. Senel, "Chitosan film enriched with an antioxidant agent, taurine, in fenestration defects," *Journal of Biomedical Materials Research*, vol. 51, pp. 500–503, 2000.

[24] J. Plank and F. von Hoessle, "Formation of an inorganic-organic host-guest material by intercalation of acetone formaldehyde sulfite polycondensate into a hydrocalumite structure," *Zeitschrift fur Anorganische und Allgemeine Chemie*, vol. 636, no. 8, pp. 1533–1537, 2010.

[25] A. Hayashi and H. Nakayama, "Simple intercalation reaction of layered double hydroxide with sodium valproate under solid conditions," *Chemistry Letters*, vol. 39, no. 10, pp. 1060–1062, 2010.

[26] T. H. Kim, I. Heo, C. B. Park et al., "Layered metal hydroxides containing calcium and their structural analysis," *Bulletin of the Korean Chemical Society*, vol. 33, no. 6, pp. 1845–1850, 2012.

[27] B. Sun, Y. Zhao, J. G. Wu, Q. C. Yang, and G. X. Xu, "Crystal structure and FT-IR study of cesium 4-methylbenzenesulfonate," *Journal of Molecular Structure*, vol. 471, no. 1–3, pp. 63–66, 1998.

Hindawi Publishing Corporation
Journal of Nanomaterials
Volume 2012, Article ID 706134, 9 pages
doi:10.1155/2012/706134

Review Article

Intra/Inter-Particle Energy Transfer of Luminescence Nanocrystals for Biomedical Applications

Ching-Ping Liu,[1] Shih-Hsun Cheng,[1] Nai-Tzu Chen,[1,2] and Leu-Wei Lo[1]

[1] *Division of Medical Engineering Research, National Health Research Institutes, Zhunan 350, Taiwan*
[2] *Department of Chemistry, National Taiwan University, Taipei 106, Taiwan*

Correspondence should be addressed to Leu-Wei Lo, lwlo@nhri.org.tw

Received 17 February 2012; Accepted 11 April 2012

Academic Editor: Patricia Murray

Elaborate design of energy transfer systems in luminescent nanocrystals revealed tremendous advantages in nanotechnology, especially in biosensing and drug delivery systems. Recently, upconversion nanoparticles have been discussed as promising probes as labels in biological assays and imaging. This article reviews the works performed in the recent years using quantum dot- and rare-earth doped nanoparticle-based energy transfer systems for biomedical applications.

1. Introduction

Luminescence nanocrystals offer great promise in numerous biomedical applications from early diagnosis to cancer therapy. Quantum dots (QDs) have unique photophysical properties offering significant advantages as optical labels for biosensing. Unlike molecular fluorophores capable of the narrow excitation range, QDs have broad absorbance bands, which allow the excitation of various sizes QDs at a common wavelength. Owing to their bright and stable fluorescence, QDs improve sensitivity in their use as optical labels. However, the major concerns about potential toxicity of QDs have limited their use in biological applications. Therefore, searching different types of nanoparticles with better biocompatibility is emerging with considerable interest. Recently, rare-earth-doped nanoparticles were demonstrated with an appearing potential in biological applications because of their optical properties and low cytotoxicity [1–3]. Rare-earth doped nanoparticles such as upconversion nanoparticles (UCNPs) have attractive features as the following: high photostability, high light penetration depth in tissue, easy separation of the narrow emission bands from stray light, good biocompatibility, and weak autofluorescence background generated by near-infrared (NIR) excitation [4]. The synthesis and investigation of UCNPs were reviewed recently by Haase and Schäfer [5], and their biological applications were reviewed by Wang et al. [4] and Zhou et al. [6].

In this paper, we present the current use of QD- and rare-earth doped nanoparticle-based energy transfer systems for biological applications. Extensive efforts are also dedicated to the research involving certain luminescence nanocrystals possessing unique properties to exploit mechanisms of intra/inter particle energy transfer in nanometer scale. To be different from those reviews focus on synthesis and development of luminescence nanocrystals, this current review put emphasis on their biological applications that deploy elaborate design of energy transfer systems such as Förster/fluorescence resonance energy transfer (FRET), bioluminescence resonance energy transfer (BRET), and luminescence resonance energy transfer (LRET) as well as photoinduced cleavage for drug release and photoactivation of drugs. The QDs for biosensing and the rare-earth-doped nanoparticles for cancer therapy are hereof reviewed in detail in attempt to reveal the advances of NIR and X-ray sensitized nanoparticles for potential deep cancer diagnostics and therapy.

2. Luminescence-Nanocrystal-Based Energy Transfer Systems

2.1. Quantum Dots. Quantum dot (QD) serves as a great candidate for nanodelivery and nanosensor in biological application. QDs have many advantages such as highly

photostability and brightness as well as resistance of photobleaching as compared to conventional organic fluorophores [7–10]. Therefore, the large extinction coefficients and wide absorption wavelength ranges of QDs allow excitation of different QDs by a single excitation source. These nanosizes of QDs result in size-tunable absorption and emission wavelengths by their quantum mechanical behaviors [7, 8]. Owing to these advantages, QDs suggest they are ideally suitable for long-term biosensors for multiple biomolecules tracking. For the photoluminescence properties of broad absorption and narrow emission (few spectral cross-talk), QDs have been wildy exploited as efficient Forster resonance energy transfer (FRET) donors to make the selection of acceptor easy. There were many scientists have designed specific peptide and protein-based conjugations of QDs and utilized FRET to sense biological behaviors and mechanisms *in vitro* and *in vivo*. In another approach, a number of reports used QD as the drug carrier and monitored the dynamics of drug release from QD using FRET [8, 11–13].

2.1.1. Biosensing. In previous reports, QDs have been used in biosensing with diverse energy transfer designs of single-step FERT system (see Figure 1) and multiple-step FRET system (see the Figure 2). For DNA detection, Leong's group developed a single-step quantum-dot-mediated system (QD-FRET) to investigate the structural composition and dynamic behavior of plasmid DNA hybrid nanostructure *in vitro* [14]. The QD-FRET system was developed with 605 nm QD as the donor and the plasmid DNA (pDNA), whereas Cy5 was conjugated as the acceptor for energy transfer. The ultrasensitive system reveals the dynamic release of DNA vectors from the hybrid nanostructure. The FRET signal was abrogated as pDNA releases into the cytosol. The protection of pDNA from potential enzymatic barriers such as nuclease-mediated DNA degradation depended on the stability of nanocarriers. By using QD-FRET system, both pDNA release and subsequent degradation could be simultaneously monitored (as shown in Figure 1(a)).

Choi et al. demonstrated a QD-peptide probe which was prepared simply from one step electrostatic interaction for detecting HIV-1 protease (HIV-1 PR) activity *in vitro* and in live cells (see Figure 1(b)) [15]. The peptide with HIV-1 PR recognition site SQNYPIVQ was conjugated to the negative charged QDs. It was specifically cleavable when expose to HIV-PR and such a peptide-QD system could render the detection sensitivity of HIV-PR in the range of picomol. Lee et al. also designed a positively charged compact QD–DNA complex for detection of nucleic acids [16]. The fluorescence of the QD is quenched up to 90% by complexion with 5′-carboxytetramethylrhodamine- (TAMRA-) modified oligonucleotide through FRET. The present QD-DNA probe shows the capability to detect the 200 nm H5N1 influenza virus oligonucleotide. QD-based molecule also designed to unveil the detailed information of DNA microenvironment via FRET. Shaheen et al. developed a *de novo* method for quantifying the decondensation of pDNA in heterochromatin and euchromatin separately by means of a QD-FRET technique [17]. In this system, FRET between QD-labeled pDNA as a donor and rhodamine-labeled polycation as an acceptor was measured for visualizing and quantifying nuclear decondensation in specified nuclear subdomains via the use of an artificial DNA condenser. Chen's Group developed a new QD-aptamer (QD-apt) beacon that acts by folding-induced dissociation of a DNA intercalating dye, BOBO-3, is demonstrated with label-free thrombin detection [18]. The beacon is constructed by (1) coupling of a single-stranded thrombin aptamer to Qdot 565 via EDC/Sulfo-NHS chemistry and (2) staining the duplex regions of the aptamer on QD with excess BOBO-3 before thrombin binding. When mixing a thrombin sample with the QD-apt beacon, BOBO-3 is competed away from the beacon due to target-induced aptamer folding, which then caused a decrease in QD FRET-mediated BOBO-3 emission and achieved thrombin quantitation.

With the mechanism as shown in Figure 2(a), Rogach's Group fabricated the hybrid nanostructure of CdTe-conjugated polymers, which can use the light harvesting and FRET donor properties of QD for DNA hybridization detection [19]. The conjugated polymer: Poly[9,9-bis(3′-((N,N-dimethyl)-N-ethylammonium)-propyl)-2,7-fluorene-alt-1,4-phenylene] dibromide (PDFD) plays two key roles in the detection function. First, PDFD is a light harvesting antenna to enhance the emission of QD by the first level FRET (FRET 1). The other is that PDFD provides a positive-charged surface to allow negative-charged dye-labeled DNA to interact with. This second FRET (FRET 2) from QD to IRD700 (infrared fluorescence-emitting dye) labeled on the DNA probe provides a sensing platform discriminating between complementary and noncomplementary DNA. Owing to the higher local charge density of ds-DNA, the unambiguous detection is allowed by a stronger electrostatic binding to the PDFD/QD complex. Therefore, the DNA hybridization could be quantified by the ratio of emission intensity of IRD700 dye to that of QD.

Recently, Chen et al. demonstrated a two-step FRET system (see Figure 2(b)) which was constructed from the QD donor to the first acceptor of a nuclear dye (ND, First energy transfer, E12), and ND served as a relay donor to the second acceptor Cy5 (second energy transfer, E23) [20, 21]. For stable compact nanocomplexes, the QD donor drives energy transfers through the ND which acted as a relay to Cy5 conjugated on the polymeric gene carrier (E12 and E23 were "on"). While the nanocomplex begins to unpack and release intact pDNA, the E23 was off (Emission of Cy5 was diminished) and only the ND was "on." Finally, the E12 was "off" due to the degradation of free pDNA. By monitoring the combinations of FRET-mediated emission from the ND and Cy5 with this two-step QD-FRET system, both polyplex dissociation and pDNA degradation within cells were sensed simultaneously.

Medintz's group has previously reported the use of metal-affinity coordination between His_n residues and the ZnS shell of CdSe/ZnS QDs. The His_n residues have strong binding affinities for conjugating proteins, peptides, and even modified DNA sequences to the nanocrystals to sense nutrients, explosives, DNA, and enzymatic activity via FRET [22, 23]. Authors used this concept to design

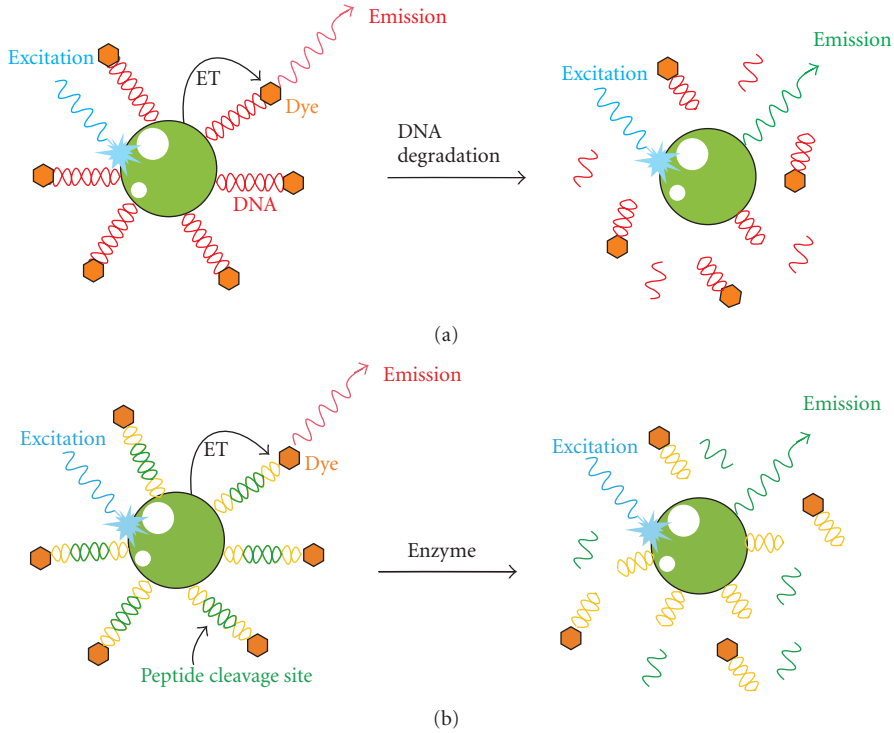

Figure 1: Single-step FRET-based QD biosensors designed to probe DNA degradation and protein. (a) The dsDNA (labeled with fluorescent dyes) degraded from QD surface compromises the FRET between dsDNA and QD. (b) The fluorescently labeled peptides, each with an enzyme-specific cleavage site, are bound to a QD and construct FRET. The FRET becomes decreasing as the enzyme starts to cleave the peptide into fragments.

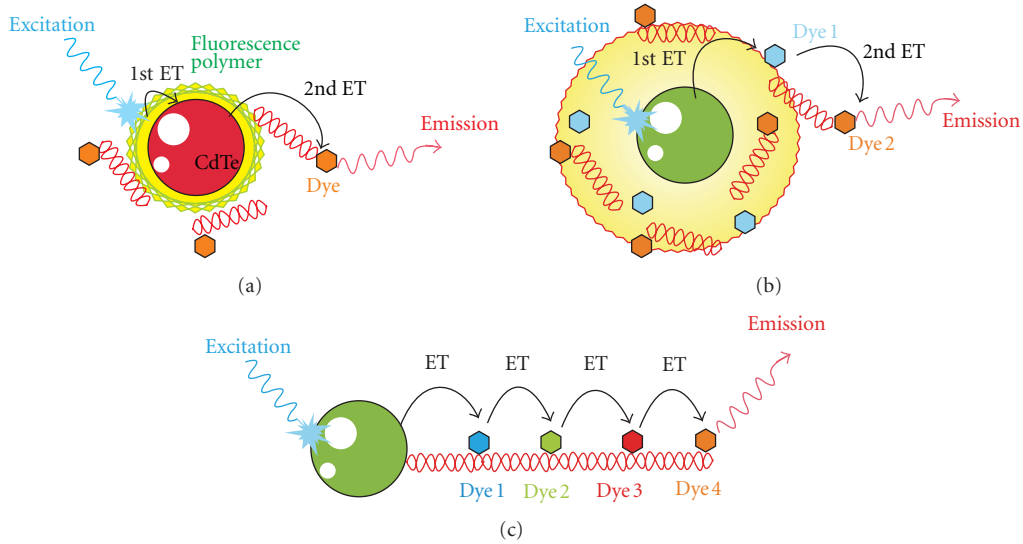

Figure 2: Multiple-step FRET-based QD biosensors. (a) The hybrid nanostructure of CdTe conjugated fluorescence polymers, which exploits the light harvesting and FRET donor properties of QD for detection of DNA hybridization. (b) The two-step QD-FRET system, where the first energy transfer occurs from QD to Dye 1 in polymeric matrix, followed by the second energy transfer from Dye 1 to DNA-labeling Dye 2. Thus both the polymer and DNA degradation in cells can be assessed by the combination of FRET-mediated emission. (c) The multiple dye-labeled DNA symmetrically arrays on the surface of QD. By excitation of the central QD donor, the energy transfer is relayed through the sequentially aligned dye-acceptors which emit from the visible to NIR portion of the spectrum.

QD-fluorescence protein assemblies for sensing caspase-3 activity [24]. The QD-fluorescent protein sensor is developed as the fluorescence protein: mCherry expressing the caspase-3 cleavage site self-assembled to the surface of CdSe-ZnS Dihydrolipoic acid- (DHLA-) functionalized QDs, resulting in FRET quenching of the QD and sensitized emission from the mCherry acceptor. While caspase-3 cleaves the linker, it reduces the FRET efficiency.

Based on the [25], Medintz et al. demonstrated the Ni^{2+}-supplemented 565 nm ITK-COOH QDs resulting in His_6-driven protein coordination to the Ni^{2+}-COOH QD surfaces in mCherry-His_6 expressing cells. They used FRET-sensitized emission from QD to mCherry to confirm the intracellular protein assembly. Recently, the same group demonstrated the hybrid multifluorophore DNA-photonic wires that both self-assemble around QDs and QDs function as UV energy harvesting to drive FRET cascades through the DNA wires with emission which approach near-infrared (see Figure 2(c)) [26]. The peptide portion facilitated metal-affinity coordination of multiple hybridized DNA-dye structures to a central QD completing the final nanocrystal-DNA photonic wire structure. They conjugated multiple copies of DNA hybridized with 4-sequentially arranged acceptor dyes on the central QD and demonstrated 4-consecutive energy transfer steps monitored with both steady-state and time-resolved spectroscopy. Additionally, Medintz's group investigated the use of QD-peptide FRET sensor to monitor the activity of the Botulinum neurotoxins (BoNT) serotype A light chain protease (LcA) [27]. They designed modular LcA peptide substrate with Cy3 acceptor and the terminal oligohistidine that allowed for peptide-QD-selfassembly. The 350 pM LcA limit of detection was demonstrated with indirect preexposure of peptide to LcA prior to QD assembly. Rao's group demonstrated that carboxylated polymer modified QDs could coordinate His_6-tagged luciferase enzymes to create protease sensors via bioluminescence resonance energy transfer (BRET) [28]. While excess Ni^{2+} was added to the QDs, His_6-luciferase binding and BRET interactions were significantly increased.

Freeman et al. reported Nile-Blue- (NB-) functionalized QDs revealed the luminescence quenching of the QDs via FRET mechanism [29]. The FRET process triggering by QDs is prohibited by colorless NBH2 units yielded by the reduction of the NB-units by 1,4-dihydronic-otineamide adenine dinucleotide (phosphate), NAD(P)H. This process could be used to detect the NAD(P)H cofactors, and a series of NAD(P)+-dependent enzymes and their substrates. Moreover, authors used the modified QDs to follow intracellular metabolism for anticancer drugs screening, for example, the anticancer drug: Taxol which is known to inhibit the metabolic processes. They demonstrated the QD fluorescence increased by the NAD(P)H cofactors in the Taxol-treated cells.

Skajaa et al. developed a lipoprotein-based nanoparticle that consists of a quantum dot (QD) core and Cy5.5 labeled lipidic coating to study of lipoprotein-lipoprotein interaction [30]. They judiciously tuned QD/Cy5.5 ratio to optimize the FRET between QD and Cy5.5 coating. The dynamics of lipid exchange influenced by apolipoproteins is monitored via FRET process. Moreover, authors have studied high density lipoprotein- (HDL-) cell interactions and exploit FRET to visualize HDL association with live macrophage cells.

2.1.2. Drug Delivery and Therapy. In another approach, QDs were introduced as a traceable marker and a nanocarrier for drug delivery. Bagalkot et al. reported the multifunctional QD-Apt delivery system for simultaneous imaging and therapeutic uses [31]. The multifunctional QD-Apt was conjugated with the targeting modality of RNA aptamer. The RNA aptamers serve for both targeting and therapy functions. For targeting, RNA aptamers pinpoint the prostate-specific membrane antigen (PSMA) expressed in LNCaP cells; and for therapy, anticancer drug, doxorubicin (Dox), was intercalated on aptamers. In this bi-FRET (dual donor-quencher) system, the QD fluorescence was quenched by Dox and the fluorescence of Dox was quenched by the RNA aptamers. When the Dox was loading, both QD and Dox fluorescence were turned "OFF" through bi-FRET. While the QD-Apt complex was uptaken by prostate cancer cells and Dox was gradually released, both QD and Dox fluorescence switched to "ON." This multifunctional QD-Apt-Dox delivered Dox to PSMA-expressing LNCaP cells more efficiently compared to nontargeted PC3 cells, and the delivery efficiency of Dox was monitored by FRET spontaneously.

2.2. Rare-Earth-Doped Nanoparticles. Rare-earth-doped nanoparticles usually include a host/matrix as light absorber and the rare earth ions are doped into a host of high intrinsic transparency and low vibrational energy. The rare-earth-doped nanoparticles can be either excited on the domain of host/matrix by ultraviolet (UV) light followed by the subsequent energy transfer to the rare-earth ions or using direct excitation of the rare-earth ion responsible for the emission. In the case of codoping such as Ce and Tb, it is able to transfer energy from Ce^{3+} to the emitting ion of Tb^{3+}. In some cases, such as UCNPs, they display the unique property of converting low-energy NIR light to high-energy UV or visible light. This process is based on sequential multiphoton absorption and energy transfer steps involving real metastable, long-lived states [32]. The intraparticle energy transfer between two doping lanthanide ions in the excited states leads to short wavelength emission.

2.2.1. Bioimaging. UCNPs conjugated with biological molecules are investigated as fluorescent markers for biological imaging due to their attractive optical properties as mentioned in Section 1. Following significant progress in techniques, UCNPs have been introduced for cell and animal imaging [33–39]. Recently, multimodal imaging and imaging combined therapies have become a new trend [40–42]. $NaGdF_4$ codoped $Tm^{3+}/Er^{3+}/Yb^{3+}$ upconversion nanophosphors were used to demonstrate the dual-modality of NIR-to-NIR upconversion luminescence (UCL) together with MRI for *in vivo* imaging of the whole-body animal [43]. The Gd^{3+} introduced in the synthesis of UCNPs enhanced the contract of MRI, whereas the NIR-to-NIR UCL enables imaging of the target inside the tissues due to both excitation

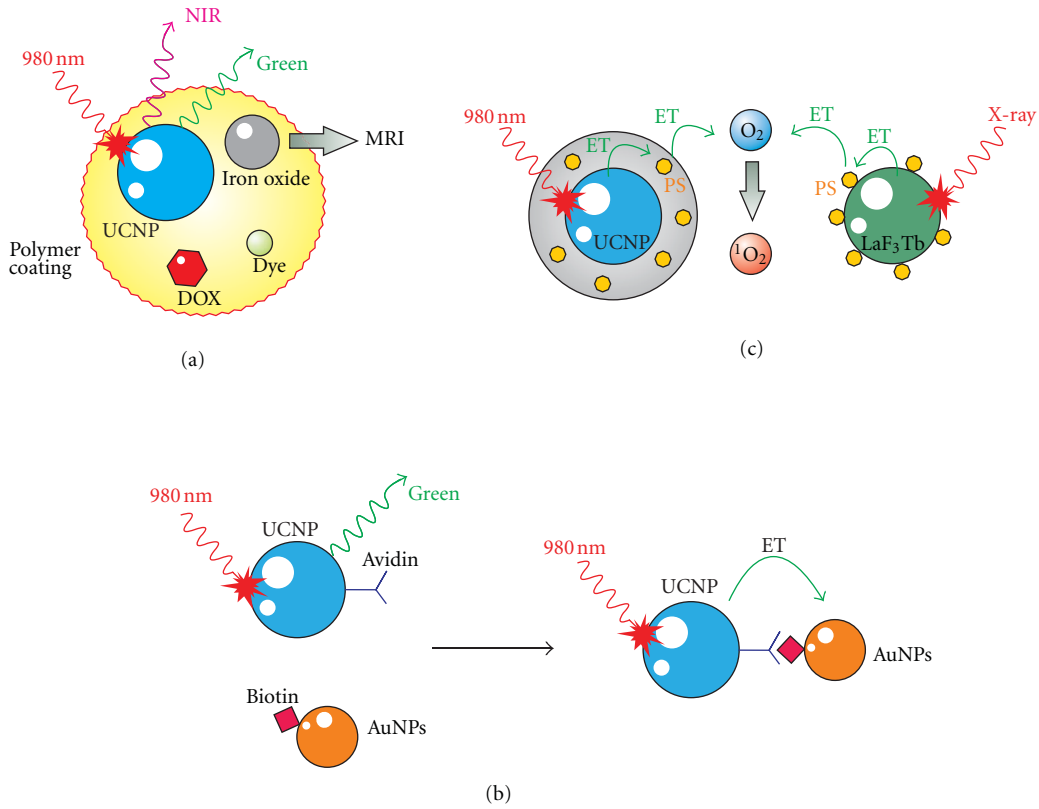

Figure 3: Different UCNP nanocomposites and applications. (a) Triple-modal UCL/FL/MRI nanocomposite: UCNPs for UCL, dye for FL, and iron oxide for MRI; DOX for therapeutic drug. (b) The biotin-avidin affinity system modulates FRET via the quench of UCNPs emission by gold nanoparticles. (c) Photodynamic therapy in deep tissue: both NIR excitation of UCNPs and X-ray irradiation of scintillation nanoparticles can generate visible light, which further synergistically activates photosensitizers in proximity to generate cytotoxic singlet oxygen for cancer treatment.

and emission light can penetrate deep into/from tissues. Their results showed high contrast in both NIR-to-NIR and NIR-to-visible luminescence imaging as well as MRI, which can serve as a platform technology for the next generation of probes for *in vivo* bioimaging.

In Figure 3(a), polymer encapsulated UCNPs and iron oxide as a nanocopmposite can be further loaded fluorescent dye and anticancer drug for triple-modal UCL/downconversion fluorescence(FL)/MRI *in vitro* and *in vivo* as well as the imaging-guided and magnetic-targeted drug delivery [44]. The Squaraine (SQ) fluorescent dye-loaded nanocomposite was used for the whole-body animal imaging of nude mice. Both strong UCL signals from UCNPs and FL from the SQ dye were observed predominately in the liver as well as a dramatic darkening effect from MRI, indicating the high uptake of the nanocomposite in the liver. On the other hand, for doxorubicin (DOX) loaded into the nanocomposite, the saturated maximal DOX loading efficiency was obtained ca. 8% (w/w) and nearly 45% of DOX was released in the acidic condition (at pH 5.0). The multimodal UCL/FL/MR imaging can enhance sensitivity and improve tissue penetration compared to each single imaging tool. In addition, the imaging-guided magnetic targeted drug delivery is specific and selective to localized regions, which can be extended to the delivery of NIR-light induced UCNP-based photothermal therapy as reported by the same group [45].

2.2.2. FRET-Based Biosensing. Organic dyes and QDs have been already known for some drawbacks as applied for *in vitro* or *in vivo* FRET assays due to the strong autofluorescence from cell and biomolecules. Depending on different dopants of lanthanide ions, rare-earth-doped nanoparticles typically function as energy donors, can provide tunable emission to fit any accepters in energy transfer nanocomposites. For DNA-sensitive study, Wang et al. have developed a novel DNA fluorescence detection method based on the polymer-coated rare-earth-doped nanoparticles [46]. The fluorescence originated from Tb^{3+} transitions of LaF_3:Ce^{3+}, Tb^{3+} nanoparticles can be quenched by the presence of nucleic acids such as DNA. They proposed two possible fluorescent quenching mechanisms: (1) the formation of hydrogen bonds between DNA and carboxylic acids outside of nanocomposites enables energy transfer from the excited Tb^{3+} to DNA; (2) the generation of a nonfluorescent or weakly fluorescent compound which is a fluorophore-quenching ternary complex involves the LaF_3 and DNA. Due to that, the concentration of DNA can be determined by measuring the fluorescence intensity of LaF_3:Ce^{3+}, Tb^{3+} nanoparticles.

UCNPs also have an appearing potential as donors in FRET-based application [47–51]. The UCNPs as donors can greatly improve the sensitivity and efficiency of FRET assays because most biological materials do not absorb

NIR light thus to reduce the background interference. In addition, the extremely narrow and sharp emission bands of lanthanide ions are also helpful for the separation of cell background fluorescence and direct acceptor excitation in FRET experiments. Li's Group developed an upconversion biosensor based on the FRET between bioconjugated UCNPs and gold NPs, which is the first example of using the FRET technique for a bioassay based on UCNPs [52]. In this case, the emission band of the biotinylated $NaYF_4$:Yb, Er UCNPs overlaps well with the absorption band of the biotinylated AuNPs, thereby quenching occurs in close proximity of both nanoparticles. Consequently, quantitative analysis of avidin could be achieved since the luminescence excited by NIR light was gradually quenched with increasing amounts of avidin. Another biotin-avidin affinity system based on the interaction of two types of nanoparticles was reported by Saleh et al. [53]. By labeling the UCNPs with avidin and the AuNPs with biotin (see Figure 3(b)), they established a model system for a self referenced affinity system by ratioing two emission bands from UCNPs.

The fluorescence-based imaging modality with the aid of FRET is an efficient tool for tracking dynamics of therapeutic drug release. Jiang and Zhang developed the FRET-based UCNPs/siRNA-BOBO3 complex system, which energy is transferred from the donor (UCNPs) to the acceptor (BOBO-3) upon NIR excitation [54]. BOBO-3 is a siRNA staining dye performed by imaging of siRNA. The intracellular changes of siRNA and UCNPs in live cell were observed by FRET between the UCNPs and BOBO-3 in close proximity.

2.2.3. Drug Release. The photoinduced release systems have been suffered from some drawbacks, like they require high-energy UV or visible light as the trigger. However, UV excitation is not optimal for applications in living cells or organisms due to its short penetration depth in biological systems. UCNPs capable of excitation with NIR light and conversion to emit UV light can provide the need of UV light activation in the photolysis and compromise the shortage of UV excitation. Carling et al. developed the remote-control release system by using the decoration of UCNPs with 3′,5′-di(carboxymethoxy)benzoin cage [55]. The rationale behind the choice of $NaYF_4$:Yb, Tm nanoparticles and the photocage is based on the absorption band of 3′,5′-di(carboxymethoxy)benzoin acetate ($\lambda = 282$ nm) partially overlapping the emission band of the UCNPs ($\lambda = 290$ nm). The $NaYF_4$:Yb, Tm nanoparticles provided UV light when irradiated with 980 nm laser followed byenergy transfer to trigger the uncaging in a remote-control process.

2.2.4. Therapy. Most available photosensitizers have absorption bands at wavelengths shorter than 700 nm. Such a photosensitization approach is suitable to treat only superficial tumors due to limited penetration of visible light. For this reason, light delivery is still a challenging issue for deep cancer treatment by PDT. UCNPs can be opted for photosensiters of PDT targeted in tumor at depth in tissue (see Figure 3(c)), owing to the weak tissue absorption of NIR photons which thus can penetrate a few centimeters of tissue. Zhang et al. doped photosensitizer, Merocyanine 540 (MC540) into the thin silica surface of NaY_4:Yb, Er and conjugated with a targeted mouse monoclonal antibody (anti-MUC1/episialin), which was specific to MCF-7 breast cancer cells [56]. The singlet oxygen generated from the UCNP of NaY_4:Yb, Er/MC540 upon irradiation with NIR light of 974 nm was profiled using the compound of 9,10-anthracenedipropionic acid (ADPA). This is the first report exploiting UCNP combined with photosensitizer for PDT with NIR excitation. With a further design, Chatterjee et al. synthesized a polyethylenimine- (PEI-) coated UCNP on which the photosensitizer zinc phthalocyanine (ZnPc) could be electrostatically attached [57]. NaY_4:Yb, Er was also used to transfer the emitted visible light ($\lambda = 670$ nm) to excite the attached ZnPc photosensitizers to generate singlet oxygen upon NIR 980 nm excitation. Their results show that the treatment of NaY_4:Yb, Er/PEI/ZnPc can induce effective phototoxicity of HT29 human colonic cells. In order to enhance solubility and increase the efficiency of energy transfer between UCNPs and photosensitizer, the same group synthesized the $NaYF_4$ composite with a mesoporous silica shell encapsulating ZnPc [58]. In the experiments with MB49 bladder cancer cells pretreated with $NaYF_4$:Yb, Er/ZnPc, 5-minute exposure of NIR light was sufficient to activate the energy transfer for generation of abundant singlet oxygen followed by significant cytotoxicity.

Chen and Zhang proposed a novel approach that radiotherapy and PDT are combined and activated synergistically by employing scintillating nanoparticles, and thus the tumor destruction will be more efficient [59]. In this new concept, the photosensitizers such as porphyrins conjugated to X-ray luminescent nanoscintillators are targeted to the tumor. The nanoscintillators convert high-energy X-rays into visible light, which then activates the photosensitizers via energy transfer for PDT. The pilot studies have demonstrated that LaF_3:Tb^{3+} is an efficient nanoscintillator to activate photosensitizers generating singlet oxygen for PDT [60] (see Figure 3(c)). The energy transfer from LaF_3:Tb^{3+} nanoparticles to meso-tetra(4-carboxyphenyl) porphine (MTCP) was estimated by the fluorescence quenching technique measured over the lifetime changes. With such an energy transfer mechanism, singlet oxygen was generated from LaF_3:Tb^{3+}-MTCP conjugates upon X-ray irradiation at a low-energy dose of 13.2 Gy. In addition, the targeting ligands of folic acid conjugated onto the LaF_3:Tb^{3+}/MTCP have shown no effect on the singlet oxygen generation.

In the hypoxic environments associated with many tumors, the utility of reactive oxygen species- (ROS-) dependent therapy is limited. To circumvent this problem, Scaffidi et al. have recently developed the anticancer drugs in which scintillating nanoparticles (nanoscintillators) can be used to activate psoralen in deep tissue [61]. Psoralen was bound to a fragment of the HIV-1 TAT cell-penetrating/nuclear targeting peptide anchored to UVA-emitting Y_2O_3 nanoscintillators. When X-ray radiation is absorbed by the Y_2O_3, the emitted UVA light activates psoralen to cross-link adenine and thymine residues in DNA. Although preliminary attempts in the PC-3 human prostate cancer cell line yielded only modest *in vitro* reductions in cell

number, their results represent the first evidence of drug-associated, X-ray-activated cell killing or growth inhibition for psoralen-functionalized nanoscintillators.

2.2.5. Others. Rare-earth cerium oxide (CeO_2) nanoparticles (nanoceria) have shown great potential as antioxidant and radioprotective agents for applications in cancer therapy [62–66]. The autoregenerative reaction involving redox cycles $Ce^{3+} \leftrightarrow Ce^{4+}$ oxidation states allows nanoceria to react catalytically with superoxide and hydrogen peroxide, mimicking the behavior of superoxide dismutase and catalase. For this reason, nanoceria can potentially reduce the amount of intracellular ROS and scavenge free radicals produced by radiation, preventing human health from radiation-induced damage. Animal studies by Colon et al. demonstrated that CeO_2 nanoparticles protect against radiation-induced pneuminits in animals exposed to high doses of radiation and are well tolerated by living animals [62].

Seal's Group recently synthesized rare earth codoped cerium oxide nanoparticles with a sensitizer Yb^{3+} and an emitter Er^{3+} having NIR to visible upconversion fluorescence [67]. The codoped nanoceria exhibited strong upcoverting luminescence with lifetime of 10.6 μs compared to about 3 ms of typical UCNPs with fluoride hosts. Although the significant fluorescence quenching occurred on the codoped nanoceria, the intensity is sufficient to use as potential biomarkers. The codoped nanoceria were found to kill lung cancer cells (CRL-5803) as evidenced by determining cell viability and measuring the activation of caspase-3/7. Redox-active codoped nanoceria may induce apoptosis in cancerous cells by producing ROS and oxidative stress, however, the mechanism is still under investigation. Nevertheless, this work demonstrated an example of the potential using codoped nanoceria for biomedical imaging and therapeutics.

3. Conclusion

Different sensing schemes have been developed in which QDs were typically used as FRET donors. To improve the FRET efficiency, how to avoid the aggregation of QDs *in vivo* is an important issue for their practical use in biology and medicine. In addition, the biocompatibility of QDs remains as a major challenge in advance of their biomedical applications. The development of new class of QDs with low toxicity will be crucial for more versatile applications in biological systems other than optical beacons for *in vitro* diagnostics (IVDs) and biosensing. The possibility to use rare-earth-doped nanoparticles has been demonstrated in many different biological applications due to their unique optical property and relatively low toxicity. UCNPs can be easily applied in a variety of assay formats including bioimaging, sensing, drug delivery, and cancer therapy. UCNPs offer an alternative with minimal photodamage and autofluorescence due to NIR excitation, which enhances their prospects as optical biolabels. Literatures support the possibility of using scintillating nanoparticles combined with X-ray for self-lighting photodynamic therapy [59]. However, this reported work only demonstrated the capability of scintillating nanoparticles in generation of singlet oxygen in solutions, no cells study was implemented. It is, therefore, particularly interested in further demonstration of the utility of X-ray/PDT combined therapy with *in vitro* cancer cell lines or even *in vivo* animal pathological models in the near future. Some efforts have focused on exploring new types of UCNPs conjugated with PS for deep cancer treatment. NIR excitation of such UCNPs to activate photosensitizers also needs further investigation to profile their photodynamic effects in use of cancer therapy *in vivo*.

Acknowledgment

This study was prepared with the support of the Grants MED-099-PP-04 and MED-100-PP-04 from the National Health Research Institutes of Taiwan and NSC 99–2113-M-400-001-MY3 from the National Science Council of Taiwan.

References

[1] C. Bouzigues and T. G. Alexandrou, "Biomedical applications of rare-earth based nanoparticles," *ACS Nano*, vol. 5, no. 11, pp. 8488–8505, 2011.

[2] H. S. Mader, P. Kele, S. M. Saleh, and O. S. Wolfbeis, "Upconverting luminescent nanoparticles for use in bioconjugation and bioimaging," *Current Opinion in Chemical Biology*, vol. 14, no. 5, pp. 582–596, 2010.

[3] D. K. Chatterjee, M. K. Gnanasammandhan, and Y. Zhang, "Small upconverting fluorescent nanoparticles for biomedical applications," *Small*, vol. 6, no. 24, pp. 2781–2795, 2010.

[4] F. Wang, D. Banerjee, Y. Liu, X. Chen, and X. Liu, "Upconversion nanoparticles in biological labeling, imaging, and therapy," *Analyst*, vol. 135, no. 8, pp. 1839–1854, 2010.

[5] M. Haase and H. Schäfer, "Upconverting nanoparticles," *Angewandte Chemie International Edition*, vol. 50, no. 26, pp. 5808–5829, 2011.

[6] J. Zhou, Z. Liu, and F. Y. Li, "Upconversion nanophosphors for small-animal imaging," *Chemical Society Reviews*, vol. 41, no. 3, pp. 1323–1349, 2012.

[7] P. Reiss, M. Protière, and L. Li, "Core/shell semiconductor nanocrystals," *Small*, vol. 5, no. 2, pp. 154–168, 2009.

[8] U. Resch-Genger, M. Grabolle, S. Cavaliere-Jaricot, R. Nitschke, and T. Nann, "Quantum dots versus organic dyes as fluorescent labels," *Nature Methods*, vol. 5, no. 9, pp. 763–775, 2008.

[9] I. L. Medintz, H. T. Uyeda, E. R. Goldman, and H. Mattoussi, "Quantum dot bioconjugates for imaging, labelling and sensing," *Nature Materials*, vol. 4, no. 6, pp. 435–446, 2005.

[10] C. Y. Zhang, H. C. Yeh, M. T. Kuroki, and T. H. Wang, "Single-quantum-dot-based DNA nanosensor," *Nature Materials*, vol. 4, no. 11, pp. 826–831, 2005.

[11] R. Gill, M. Zayats, and I. Willner, "Semiconductor quantum dots for bioanalysis," *Angewandte Chemie International Edition*, vol. 47, no. 40, pp. 7602–7625, 2008.

[12] P. Zrazhevskiy, M. Sena, and X. H. Gao, "Designing multifunctional quantum dots for bioimaging, detection, and drug delivery," *Chemical Society Reviews*, vol. 39, no. 11, pp. 4326–4354, 2010.

[13] N. Hildebrandt, "Biofunctional quantum dots: controlled conjugation for multiplexed biosensors," *ACS Nano*, vol. 5, no. 7, pp. 5286–5290, 2011.

[14] Y. P. Ho, H. H. Chen, K. W. Leong, and T. H. Wang, "Evaluating the intracellular stability and unpacking of DNA nanocomplexes by quantum dots-FRET," *Journal of Controlled Release*, vol. 116, no. 1, pp. 83–89, 2006.

[15] Y. Choi, J. Lee, K. Kim, H. Kim, P. Sommer, and R. Song, "Fluorogenic assay and live cell imaging of HIV-1 protease activity using acid-stable quantum dot-peptide complex," *Chemical Communications*, vol. 46, no. 48, pp. 9146–9148, 2010.

[16] J. Lee, Y. Choi, J. Kim, E. Park, and R. Song, "Positively charged compact quantum Dot-DNA complexes for detection of nucleic acids," *ChemPhysChem*, vol. 10, no. 5, pp. 806–811, 2009.

[17] S. M. Shaheen, H. Akita, A. Yamashita et al., "Quantitative analysis of condensation/decondensation status of pDNA in the nuclear sub-domains by QD-FRET," *Nucleic Acids Research*, vol. 39, no. 7, article e48, 2011.

[18] C. W. Chi, Y. H. Lao, Y. S. Li, and L. C. Chen, "A quantum dot-aptamer beacon using a DNA intercalating dye as the FRET reporter: application to label-free thrombin detection," *Biosensors and Bioelectronics*, vol. 26, no. 7, pp. 3346–3352, 2011.

[19] G. Jiang, A. S. Susha, A. A. Lutich, F. D. Stefani, J. Feldmann, and A. L. Rogach, "Cascaded FRET in conjugated polymer/quantum dot/dye-labeled DNA complexes for DNA hybridization detection," *ACS Nano*, vol. 3, no. 12, pp. 4127–4131, 2009.

[20] H. H. Chen, Y. P. Ho, X. Jiang, H. Q. Mao, T. H. Wang, and K. W. Leong, "Quantitative comparison of intracellular unpacking kinetics of polyplexes by a model constructed from quantum Dot-FRET," *Molecular Therapy*, vol. 16, no. 2, pp. 324–332, 2008.

[21] H. H. Chen, Y. P. Ho, X. Jiang, H. Q. Mao, T. H. Wang, and K. W. Leong, "Simultaneous non-invasive analysis of DNA condensation and stability by two-step QD-FRET," *Nano Today*, vol. 4, no. 2, pp. 125–134, 2009.

[22] I. L. Medintz, J. H. Konnert, A. R. Clapp et al., "A fluorescence resonance energy transfer-derived structure of a quantum dot-protein bioconjugate nanoassembly," *Proceedings of the National Academy of Sciences of the United States of America*, vol. 101, no. 26, pp. 9612–9617, 2004.

[23] J. B. Delehanty, K. Boeneman, C. E. Bradburne, K. Robertson, and I. L. Medintz, "Quantum dots: a powerful tool for understanding the intricacies of nanoparticle-mediated drug delivery," *Expert Opinion on Drug Delivery*, vol. 6, no. 10, pp. 1091–1112, 2009.

[24] K. Boeneman, B. C. Mei, A. M. Dennis et al., "Sensing caspase 3 activity with quantum dot-fluorescent protein assemblies," *Journal of the American Chemical Society*, vol. 131, no. 11, pp. 3828–3829, 2009.

[25] K. Boeneman, J. B. Delehanty, K. Susumu, M. H. Stewart, and I. L. Medintz, "Intracellular bioconjugation of targeted proteins with semiconductor quantum dots," *Journal of the American Chemical Society*, vol. 132, no. 17, pp. 5975–5977, 2010.

[26] K. Boeneman, D. E. Prasuhn, J. B. Blanco-Canosa et al., "Self-assembled quantum dot-sensitized multivalent DNA photonic wires," *Journal of the American Chemical Society*, vol. 132, no. 51, pp. 18177–18190, 2010.

[27] K. E. Sapsford, J. Granek, J. R. Deschamps et al., "Monitoring botulinum neurotoxin a activity with peptide-functionalized quantum dot resonance energy transfer sensors," *ACS Nano*, vol. 5, no. 4, pp. 2687–2699, 2011.

[28] H. Yao, Y. Zhang, F. Xiao, Z. Xia, and J. Rao, "Quantum dot/bioluminescence resonance energy transfer based highly sensitive detection of proteases," *Angewandte Chemie International Edition*, vol. 46, no. 23, pp. 4346–4349, 2007.

[29] R. Freeman, R. Gill, I. Shweky, M. Kotler, U. Banin, and I. Willner, "Biosensing and probing of intracellular metabolic pathways by NADH-sensitive quantum dots," *Angewandte Chemie International Edition*, vol. 48, no. 2, pp. 309–313, 2009.

[30] T. Skajaa, Y. Zhao, D. J. van den Heuvel et al., "Quantum dot and Cy5.5 labeled nanoparticles to investigate lipoprotein biointeractions via förster resonance energy transfer," *Nano Letters*, vol. 10, no. 12, pp. 5131–5138, 2010.

[31] V. Bagalkot, L. Zhang, E. Levy-Nissenbaum et al., "Quantum dot-aptamer conjugates for synchronous cancer imaging, therapy, and sensing of drug delivery based on bi-fluorescence resonance energy transfer," *Nano Letters*, vol. 7, no. 10, pp. 3065–3070, 2007.

[32] F. Auzel, "Upconversion and anti-stokes processes with f and d ions in solids," *Chemical Reviews*, vol. 104, no. 1, pp. 139–173, 2004.

[33] D. K. Chatterjee, A. J. Rufaihah, and Y. Zhang, "Upconversion fluorescence imaging of cells and small animals using lanthanide doped nanocrystals," *Biomaterials*, vol. 29, no. 7, pp. 937–943, 2008.

[34] R. A. Jalil and Y. Zhang, "Biocompatibility of silica coated $NaYF_4$ upconversion fluorescent nanocrystals," *Biomaterials*, vol. 29, no. 30, pp. 4122–4128, 2008.

[35] M. Nyk, R. Kumar, T. Y. Ohulchanskyy, E. J. Bergey, and P. N. Prasad, "High contrast in vitro and in vivo photoluminescence bioimaging using near infrared to near infrared up-conversion in Tm^{3+} and Yb^{3+} doped fluoride nanophosphors," *Nano Letters*, vol. 8, no. 11, pp. 3834–3838, 2008.

[36] L. Q. Xiong, Z. G. Chen, M. X. Yu, F. Y. Li, C. Liu, and C. H. Huang, "Synthesis, characterization, and *in vivo* targeted imaging of amine-functionalized rare-earth up-converting nanophosphors," *Biomaterials*, vol. 30, no. 29, pp. 5592–5600, 2009.

[37] L. Xiong, Z. Chen, Q. Tian, T. Cao, C. Xu, and F. Li, "High contrast upconversion luminescence targeted imaging in vivo using peptide-labeled nanophosphors," *Analytical Chemistry*, vol. 81, no. 21, pp. 8687–8694, 2009.

[38] X.-F. Yu, M. Li, M. Y. Xie, L. D. Chen, Y. Li, and Q.-Q. Wang, "Dopant-controlled synthesis of water-soluble hexagonal $NaYF_4$ nanorods with efficient upconversion fluorescence for multicolor bioimaging," *Nano Research*, vol. 3, no. 1, pp. 51–60, 2010.

[39] X.-F. Yu, Z. Sun, M. Li et al., "Neurotoxin-conjugated upconversion nanoprobes for direct visualization of tumors under near-infrared irradiation," *Biomaterials*, vol. 31, no. 33, pp. 8724–8731, 2010.

[40] F. Chen, S. Zhang, W. Bu et al., "A neck-formation strategy for an antiquenching magnetic/upconversion fluorescent bimodal cancer probe," *Chemistry*, vol. 16, no. 37, pp. 11254–11260, 2010.

[41] S. Gai, P. Yang, C. Li et al., "Synthesis of magnetic, up-conversion luminescent, and mesoporous core-shell-structured nanocomposites as drug carriers," *Advanced Functional Materials*, vol. 20, no. 7, pp. 1166–1172, 2010.

[42] G. Zhang, Y. L. Liu, Q. H. Yuan, C. H. Zong, J. H. Liu, and L. H. Lu, "Dual modal *in vivo* imaging using upconversion luminescence and enhanced computed tomography properties," *Nanoscale*, vol. 3, no. 10, pp. 4365–4371, 2011.

[43] J. Zhou, Y. Sun, X. X. Du, L. Q. Xiong, H. Hu, and F. Y. Li, "Dual-modality *in vivo* imaging using rare-earth nanocrystals

with near-infrared to near-infrared (NIR-to-NIR) upconversion luminescence and magnetic resonance properties," *Biomaterials*, vol. 31, no. 12, pp. 3287–3295, 2010.

[44] H. Xu, L. Cheng, C. Wang, X. X. Ma, Y. G. Li, and Z. Liu, "Polymer encapsulated upconversion nanoparticle/iron oxide nanocomposites for multimodal imaging and magnetic targeted drug delivery," *Biomaterials*, vol. 32, no. 35, pp. 9364–9373, 2011.

[45] L. Cheng, K. Yang, Y. Li et al., "Facile preparation of multifunctional upconversion nanoprobes for multimodal imaging and dual-targeted photothermal therapy," *Angewandte Chemie International Edition*, vol. 50, no. 32, pp. 7385–7390, 2011.

[46] L. Wang, P. Li, and L. Wang, "Luminescent and hydrophilic LaF_3-polymer nanocomposite for DNA detection," *Luminescence*, vol. 24, no. 1, pp. 39–44, 2009.

[47] K. Kuningas, T. Rantanen, T. Ukonaho, T. Lövgren, and T. Soukka, "Homogeneous assay technology based on upconverting phosphors," *Analytical Chemistry*, vol. 77, no. 22, pp. 7348–7355, 2005.

[48] K. Kuningas, T. Ukonaho, H. Päkkilä et al., "Upconversion fluorescence resonance energy transfer in a homogeneous immunoassay for estradiol," *Analytical Chemistry*, vol. 78, no. 13, pp. 4690–4696, 2006.

[49] K. Kuningas, H. Päkkilä, T. Ukonaho, T. Rantanen, T. Lövgren, and T. Soukka, "Upconversion fluorescence enables homogeneous immunoassay in whole blood," *Clinical Chemistry*, vol. 53, no. 1, pp. 145–146, 2007.

[50] T. Rantanen, M. L. Järvenpää, J. Vuojola, K. Kuningas, and T. Soukka, "Fluorescence-quenching-based enzyme-activity assay by using photon upconversion," *Angewandte Chemie International Edition*, vol. 47, no. 20, pp. 3811–3813, 2008.

[51] F. Vetrone, R. Naccache, C. G. Morgan, and J. A. Capobianco, "Luminescence resonance energy transfer from an upconverting nanoparticle to a fluorescent phycobiliprotein," *Nanoscale*, vol. 2, no. 7, pp. 1185–1189, 2010.

[52] L. Wang, R. Yan, Z. Huo et al., "Fluorescence resonant energy transfer biosensor based on upconversion-luminescent nanoparticles," *Angewandte Chemie International Edition*, vol. 44, no. 37, pp. 6054–6057, 2005.

[53] S. M. Saleh, R. Ali, T. Hirsch, and O. S. Wolfbeis, "Detection of biotin-avidin affinity binding by exploiting a self-referenced system composed of upconverting luminescent nanoparticles and gold nanoparticles," *Journal of Nanoparticle Research*, vol. 13, no. 10, pp. 4603–4611, 2011.

[54] S. Jiang and Y. Zhang, "Upconversion nanoparticle-based FRET system for study of siRNA in live cells," *Langmuir*, vol. 26, no. 9, pp. 6689–6694, 2010.

[55] C.-J. Carling, F. Nourmohammadian, J.-C. Boyer, and N. R. Branda, "Remote-control photorelease of caged compounds using near-infrared light and upconverting nanoparticles," *Angewandte Chemie International Edition*, vol. 49, no. 22, pp. 3782–3785, 2010.

[56] P. Zhang, W. Steelant, M. Kumar, and M. Scholfield, "Versatile photosensitizers for photodynamic therapy at infrared excitation," *Journal of the American Chemical Society*, vol. 129, no. 15, pp. 4526–4527, 2007.

[57] D. K. Chatterjee and Z. Yong, "Upconverting nanoparticles as nanotransducers for photodynamic therapy in cancer cells," *Nanomedicine*, vol. 3, no. 1, pp. 73–82, 2008.

[58] H. S. Qian, H. C. Guo, P. C. L. Ho, R. Mahendran, and Y. Zhang, "Mesoporous-silica-coated up-conversion fluorescent nanoparticles for photodynamic therapy," *Small*, vol. 5, no. 20, pp. 2285–2290, 2009.

[59] W. Chen and J. Zhang, "Using nanoparticles to enable simultaneous radiation and photodynamic therapies for cancer treatment," *Journal of Nanoscience and Nanotechnology*, vol. 6, no. 4, pp. 1159–1166, 2006.

[60] Y. Liu, W. Chen, S. Wang, and A. G. Joly, "Investigation of water-soluble x-ray luminescence nanoparticles for photodynamic activation," *Applied Physics Letters*, vol. 92, no. 4, pp. 043901–043903, 2008.

[61] J. P. Scaffidi, M. K. Gregas, B. Lauly, Y. Zhang, and T. Vo-Dinh, "Activity of psoralen-functionalized nanoscintillators against cancer cells upon X-ray excitation," *ACS Nano*, vol. 5, no. 6, pp. 4679–4687, 2011.

[62] J. Colon, L. Herrera, J. Smith et al., "Protection from radiation-induced pneumonitis using cerium oxide nanoparticles," *Nanomedicine*, vol. 5, no. 2, pp. 225–231, 2009.

[63] R. W. Tarnuzzer, J. Colon, S. Patil, and S. Seal, "Vacancy engineered ceria nanostructures for protection from radiation-induced cellular damage," *Nano Letters*, vol. 5, no. 12, pp. 2573–2577, 2005.

[64] C. Korsvik, S. Patil, S. Seal, and W. T. Self, "Superoxide dismutase mimetic properties exhibited by vacancy engineered ceria nanoparticles," *Chemical Communications*, no. 10, pp. 1056–1058, 2007.

[65] S. Bhattacharyya, R. A. Kudgus, R. Bhattacharya, and P. Mukherjee, "Inorganic nanoparticles in cancer therapy," *Pharmaceutical Research*, vol. 28, no. 2, pp. 237–259, 2011.

[66] I. Celardo, J. Z. Pedersen, E. Traversa, and L. Ghibelli, "Pharmacological potential of cerium oxide nanoparticles," *Nanoscale*, vol. 3, no. 4, pp. 1411–1420, 2011.

[67] S. Babu, J.-H. Cho, J. M. Dowding et al., "Multicolored redox active upconverter cerium oxide nanoparticle for bio-imaging and therapeutics," *Chemical Communications*, vol. 46, no. 37, pp. 6915–6917, 2010.

Hindawi Publishing Corporation
Journal of Nanomaterials
Volume 2012, Article ID 129107, 15 pages
doi:10.1155/2012/129107

Review Article

Superparamagnetic Nanoparticles and RNAi-Mediated Gene Silencing: Evolving Class of Cancer Diagnostics and Therapeutics

Sanchareeka Dey and Tapas K. Maiti

Biotechnology Department, Indian Institute of Technology, Kharagpur 721302, India

Correspondence should be addressed to Tapas K. Maiti, maititapask@gmail.com

Received 13 February 2012; Accepted 23 April 2012

Academic Editor: Haifeng Chen

The ever increasing death of patients affected by various types of fatal cancers is of concern worldwide. Curative attempts by radiation/chemotherapy and surgery are often a failure in the long run. Moreover, adverse side effects of such treatments burden the patients with painful survival at the last phase of their life. The failure of early diagnosis is one of the root causes of the problem. Intensive research activities are being pursued in reputed laboratories across the globe to find superior diagnostics and therapeutics. Over the last decade, a number of publications have highlighted RNA interference based silencing of cancer-related gene expression as a promising technology to tackle the aforesaid problems. Superparamagnetic iron oxide nanoparticles (SPIONs) are reported to be excellent vehicles for short-interfering RNA (siRNA). The SPION-siRNA conjugate is biocompatible, stable, and amenable to specific targeting and can cross the blood brain barrier. The issues related to their synthesis, surface properties, delivery, tracking, imaging in relevance to cancer diagnostic and therapeutic, and so forth demand an extensive review, and we have addressed these aspects in this paper. The future prospects of the technology have also been traced.

1. Introduction

The number of patients suffering from various fatal types of cancers (lung, breast, prostate, etc.) has been increasing worldwide, irrespective of the countries that are developed or developing. Several nonspecific treatments include radiation therapy and chemotherapy. The treatment failure continues to be very high, and multidrug resistance is known.

The adverse side effects of drugs and drug formulation vehicles are of serious concern [1]. Capecitabine, the oral prodrug for fluorouracil, for example, given to ovarian, prostate and pancreatic cancer patients develop systemic toxicity [2] including neutropenia, stomatitis, and so forth [3]. Similarly, breast cancer patients treated with anthracyclines and taxanes as well as antibody therapies (anti-HER2 drug herceptin) exhibit long-term cardiotoxicity. The blood brain barrier (BBB) is a major obstacle in the treatment of brain cancer through intravascular drug application because only a small fraction of the drug actually reaches tumor, and most local delivery methods bring neurotoxicity [4]. As a result of such healthcare complications in cancer patients receiving prolonged treatments, only palliative treatments are prescribed in many cases at the last phase of their survival. Targeted drug delivery systems (liposomes, micelles, polymer drug conjugates, etc.) have short comings of drug leakage *in vivo*, packaging limitations, reduced potency, and so forth.

In the last decade, several exciting articles on RNAi have been published on their potential in suppressing oncogenes by silencing. The 20–30 nucleotides double-stranded small or micro-RNAs (siRNAs or miRNAs) cause natural post-transcriptional gene silencing in eukaryotic cells [5]. The delivery of siRNAs was experimented by conjugating with natural or synthetic polymers and using nanoparticles as a vehicle. The last one are the most important because of their nontoxicity, effectiveness due to large surface area, and ability to cross tight junction of endothelial cells in blood brain barrier. Superparamagnetic nanoparticles can act as agents for effective treatment of cancers, especially brain tumor. Superparamagnetic iron oxide nanoparticles (SPIONs) have interesting properties such as biocompatibility, stability in body fluids, nonimmunogenicity, and amenability to coating/conjugation for cell-specific targeting

and imaging/tracking. Overall, SPIONs could be designed into a multifunctional unit [6–8].

A recent article on the possibility of gene delivery by SPIONs in three-dimensional cell cultures underscores the amazing potential for this promising technology. In this paper, we review the usefulness of the versatile SPIONs with regard to their superiority as a vehicle for RNAi-mediated gene silencing. We present here their importance as an evolving new class of cancer diagnostics and therapeutics.

2. SPION Synthesis for Biomedical Application

When the material dimension is reduced to nanoscale, the enhanced magnetic property is superparamagnetism. Ferro- or ferri-magnetic materials at sizes on the order of tens of nanometers become a single magnetic domain and maintain one large magnetic moment. At sufficiently high temperatures (i.e., blocking temperature TB), free rotation of the particle is however induced resulting in a loss of net magnetization (i.e., their magnetization appears to be in average zero, and they are said to be in the superparamagnetic state) in the absence of an external field [42]. SPIONs are the most commonly used superparamagnetic nanoparticles for biomedical applications (i.e., immunoassays, magnetic resonance imaging, magnetic cell separation, magnetic oligonucleotide and nucleic acid separation, drug delivery, etc.). There has been intense investigations by chemists and material scientists over the synthesis of SPIONs.

SPIONs can be synthesized by either chemical or mechanical approaches. Chemical synthesis is however more suitable for the production of SPIONs of uniform size and composition [43]. A variety of synthetic processes have been adopted for the production of iron oxide nanoparticles ranging from the more conventional wet chemistry solution-based methods to more fascinating techniques such as laser pyrolysis. The two most commonly employed methods for SPION synthesis for biomedical application include alkaline coprecipitation and microemulsion of Fe 2+ and Fe 3+ salts [44, 45].

2.1. Coprecipitation. Coprecipitation is the most commonly followed synthetic route for SPION synthesis because it is the simplest and most efficient pathway [6, 45–47]. Iron salts are coprecipitated with a strong base under aqueous conditions to yield the core of the SPION [48]. During nanoparticle formation, conditions are optimized to yield a short nucleation event followed by a slower growth phase. The end product obtained has good monodispersity [49]. The SPION core has two fates. One is the direct conjugation of the core with surface coatings, while the other is the purification and dispersion in a multistep procedure followed by surface coating [44]. The major advantage of coprecipitation is the quantity of nanoparticles that can be synthesized [50]. Another advantage is that the size and magnetic quality of the nanoparticle can be controlled by manipulating factors like ionic strength of the solution, pH, and stoichiometry of the reactants [44]. Controlling the crystal growth step is inevitable for producing SPIONs of sub nm size [45]. In order to improve the uniformity and stability of SPIONs, modifications of the standard coprecipitation approach have been investigated. Synthesis of SPIONs by alkaline coprecipitation of ferric (0.086 M) and ferrous (0.043 M) salts has been reported [11]. SPION synthesis by coprecipitation of $FeCl_2$, $FeCl_3$, and 2, 2 (ethylenedioxy)bis(ethylamine) (EDEA) in the presence of PEG has also been reported [21].

2.2. Microemulsion. This method of SPION synthesis is relatively new. Microemulsion is a thermodynamically stable, isotropic dispersion of two immiscible liquids. For water-in-oil (water in oil: W/O) microemulsions, water droplets behave as nanoreactors in a continuous phase (oil), stabilized by a monolayer of surfactant, at the interface of the two liquids [45–47]. Unlike coprecipitation method, little control of particle size and shape has been achieved by controlling factors like pH and reactants stoichiometry but is generally more controlled with respect to size distribution. SPIONs synthesized by microemulsion technique also suffer from poor crystallinity. This situation can, however, be handled by annealing [44, 45]. The overall hydrodynamic radius is a critical factor in determining the particle diffusion.

Other methods for SPION preparation that are reported in the literature include thermal decomposition [6, 46, 49, 51], sol-gel method [43, 45, 50], hydrothermal method [43, 47, 50, 51], polyol method, and so forth [43, 50]. Despite the difficulty faced in controlling the nanoparticle dynamics with respect to size and crystallinity, they have been used extensively for biomedical applications. The main advantages of using SPIONs for biomedical applications are (i) they aggregate only in the presence of a strong external magnetic field over an extended period of time which facilitates the particles to maintain their colloidal stability and avoid aggregation, (ii) they have greater surface area to volume ratio due to their small size, which improves its binding kinetics [52], (iii) SPIONs attached with a drug can be injected and guided through the body to target sites (i.e., tumour) by the application of an external magnetic field [45], (iv) they can be visualized by magnetic resonance imaging (MRI) [25, 37, 46, 49, 52–54], and (v) they can be heated to provide hyperthermia for cancer therapy [53]. They also have magnetic susceptibilities much higher than paramagnetic materials [52]. Hence, there are several aspects for the application of SPIONs including diagnostic molecular imaging [52], delivery of drug and gene and targeted therapy [37, 45, 49, 52, 55].

3. Commonly Used SPIONs and Their Surface Properties

SPIONs mainly include magnetite (Fe_3O_4), maghemite (γ-Fe_2O_3), and hematite (α-Fe_2O_3). Ferrites (oxides of iron mixed with other transition metal ions) have also been reported to be superparamagnetic. Fe_3O_4 and γ-Fe_2O_3 are however apparently, most commonly employed for biomedical applications [21, 42, 45, 47]. SPION consists of an iron oxide core coated with a biocompatible polymer. It has a huge potential as carriers for biomolecules like proteins, antibodies, enzymes, and nucleic acids. SPIONs

have low toxicity and great biocompatibility and are hence well tolerated by the biological system. Their size is similar to biomacromolecules and is therefore ideal scaffolds to produce nanobioconjugates. The different categories of SPIO, based on their overall diameter (including iron oxide core and coating), are oral SPIO (diameter ~ 300 nm −3.5 μm); standard SPIO (SSPIO) (diameter ~ 60–150 nm); ultrasmall SPIO (USPIO) (diameter ~ 10–40 nm); monocrystalline iron oxide nanoparticles (MION) (diameter ~ 10–30 nm) very small superparamagnetic iron oxide nanoparticles (VSOP) (diameter < 10 nm) [6, 8, 26, 56, 57]. A typical SPION consists of a magnetically active core with a stable core coating to which targeting ligands, imaging modalities, and therapeutic agents are anchored (see Figure 1). The function of surface coatings is to (i) prevent agglomeration of iron oxide core, (ii) enable conjugation of drug molecules, targeting ligands, imaging modalities, and so forth, to the surface, (iii) limit nonspecific cell interactions and (iv) prevent toxic elements to leach into the body during *in vivo* application [49]. There are many choices of coating materials like silica, gold, natural polymers (carbohydrates (e.g., dextran; starch), proteins (e.g., albumin, RGD), and lipids), and synthetic organic polymers [poly(ethyleneglycol) (PEG), and polyvinyl alcohol (PVA), polyethyleneimine (PEI)] [49, 55]. A list of biomolecules for matrix coating and their corresponding application in biomedicine has been reported [53, 55].

The surface of the SPIONs needs to be modified in order to attach biomolecules to the surface. Otherwise biomolecules may not bind, or bound biomolecules may interact poorly with the surface of the nanoparticles resulting in the instant release of these biomolecules during delivery. Modification through organic linkers is the preferred option as it provides a wide range of surface properties to suit biomolecules in various conditions. For example, when applying for gene and drug delivery, the most suitable surface is a positively charged one whereas to bind proteins like lysozyme and antibodies, negatively charged surface is favored. Organic linkers include amine (–NH_2, –NHR, –NR_2), carboxylic acid (–COOH), aldehyde (–CHO), and thiol (–SH) [49, 55]. For successful application, SPIONs need to be engineered carefully with respect to its size, shape, coating, and surface modifications to specifically target damaged tissue. Each of these design parameters must be thoroughly evaluated to produce a NP that can overcome biological barriers and carry out its function efficiently. A number of chemical approaches have been used for the conjugation of targeting, therapeutic, and imaging reporter molecules with NP surfaces [49, 58]. These can be categorized as covalent linkage strategies (direct nanoparticle conjugation; click chemistry; covalent linker chemistry) and physical interactions (electrostatic; hydrophilic/hydrophobic; affinity interactions).

The choice of chemistry depends on the chemical properties of the SPION and the functional groups of the coating and ligand to be linked. SPIONs can be coated by a number of approaches (i) end-grafted polymer-coated MNP: polymers are generally anchored to the NP surface by polymer end groups resulting in brush-like extensions, (ii) SPION fully encapsulated in polymer coating: the NP core is uniformly encapsulated by the coating by *in situ* and postsynthesis modification with polysaccharides and copolymers, (iii) Liposome encapsulated MNP: a shell is created around the SPION core by micelle forming molecules liposomes [49, 52] (see Figure 2).

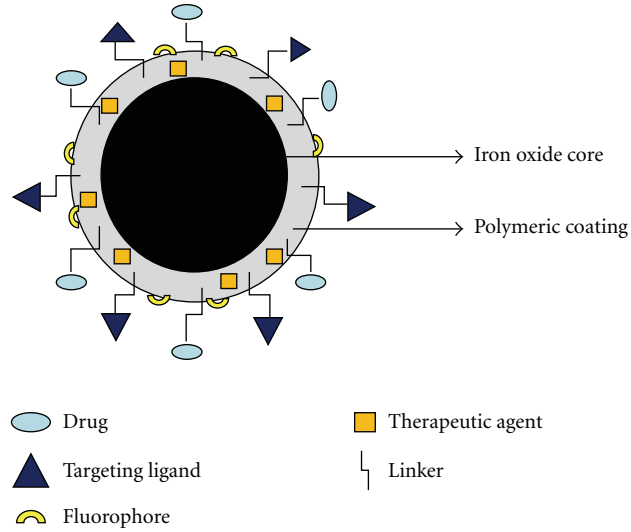

Figure 1: Surface modification of SPIONs. (a) Drug, (b) targeting ligand, (c) fluorophore, (d) therapeutic agent, and (e) linker.

4. SPIONs for Cancer (Drug Delivery and Imaging)

SPIONs have attracted a great deal of interest in biomedical research and clinical applications over the past decades specially for targeted drug delivery combined with magnetic resonance imaging (MRI) for non-invasive, early cancer detection, and treatment. Surface properties, specifically designed for cell targeting are required for this purpose. The general strategy involves creating a biocompatible polymeric or nonpolymeric coating and subsequently conjugating bioactive molecules to it. Since SPIONs only exhibit magnetic properties in the presence of an applied magnetic field, they have the advantage of being used in both *in vitro* as well as *in vivo* applications such as hyperthermia [59], magnetic drug targeting (MDT), magnetic resonance imaging (MRI), gene delivery and wide range of applications in the detection, diagnosis, and treatment of cancer. SPIONs have shown clinical efficacy in cancer drug delivery and imaging. Some formulations are now FDA-approved for use in the clinic. Some SPION formulations designed for cancer therapy have been listed in Table 1.

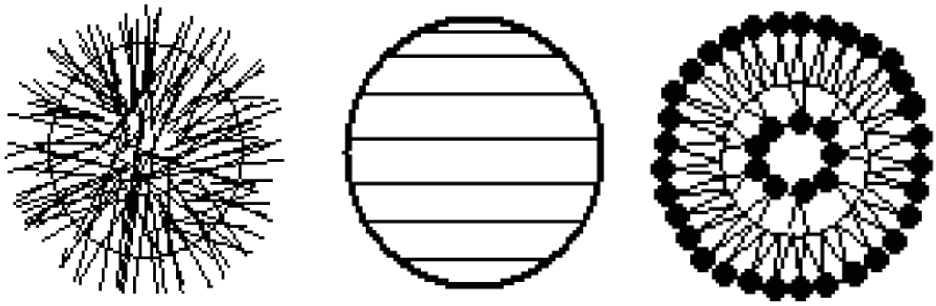

(a) (b) (c)

Figure 2: MNP structures and coating schemes. (a) End-grafted polymer coated MNP. (b) MNP fully encapsulated in polymer coating. (c) Liposome-encapsulated MNP.

4.1. Drug Delivery

4.1.1. Chemotherapeutic Drugs. Targeted drug delivery systems (DDSs) for cancerous cells maximize the efficiency of chemotherapy and radiotherapy and reduce its side effects as well as dosage and cost [46].

In MDT, SPIONs loaded with anticancer drugs are administrated either intravenously or intra-arterially and randomly circulated in the blood stream. When an external high-gradient magnetic field is applied at the desired site, the drug/carrier complex is accumulated at that site. Later, the drug is released via enzymatic cleavage or changes in physiological conditions, such as pH, osmolality or temperatures. Another advantage of using SPIONs is that the success of MDT in distributing and capturing these particles can be traced by MRI. The criteria for SPIONs to be used as carriers for MDT includes a size range of 10–100 nm to avoid renal clearance and extravasation by the reticuloendothelial system, a strong magnetic force to overcome the drag forces from blood flow, hydrophilic surfaces to maximize blood circulation and reduce absorption by plasma proteins [46]. Conventional drugs such as mitoxantrone, doxorubicin, and methotrexate can be either attached or encapsulated in SPIONs for the treatment of tumors [9, 25, 60–63]. Carriers can be specifically designed to enhance the efficacy of these therapeutic agents. It is also possible to engineer characteristics such as loading capacities and drug release profiles by controlling structural and chemical features within the SPION conjugate.

4.1.2. Proteins and Peptides. Peptides and proteins constitute a new generation of drugs. Chlorotoxin (Cltx), a peptide with high affinity for a variety of tumors, is currently being evaluated for applications in cancer imaging and therapy. In addition to serving as a targeting agent, Cltx also exhibits the ability to inhibit tumor invasion, which is particularly useful in the treatment of highly invasive brain tumors such as gliomas [21, 64]. The biggest barrier in using protein drugs for therapy is however its transportation across the tissue [65]. SPIONs of narrow size ranges are easily produced and coupled to proteins, enabling its easy delivery into the cell. A number of SPION formulations have been investigated as carriers of therapeutic proteins and peptides [10, 19, 21, 26, 56].

4.1.3. DNA and siRNA. Antisense and gene therapy have been areas of intense research due to their vast potential in medicine. Most of the efforts in gene therapy currently aim at cancer. For the *in vivo* application of DNA and siRNA, it should be efficiently and stably transferred across the cell membrane, should have a convenient blood half-life, and must be available to the tissue in optimum quantity [39]. Hence, there should be a way to deliver them noninvasively to tissues of interest. Also to conceive and optimize the delivery and treatment strategies, using clinically relevant imaging paradigms is needed. SPIONs may be designed to serve as new dual-purpose probe for the simultaneous noninvasive imaging and delivery of DNA and siRNAs to tumors (magnetofection). This technique has been successfully applied for *in vitro* transfection and is presently being optimized for *in vivo* applications [37, 49].

4.1.4. Targeting Ligands. A promising approach toward increasing the local accumulation of SPIONs in diseased tissue is specific targeting of cancer cells by the conjugation of targeting molecules to SPIONs that possess high affinity toward unique molecular signatures found on malignant cells. By integrating cancer cell-specific ligands, these multifunctional MNPs can serve strictly as a vehicle for drug delivery [41].

4.1.5. Magnetic Fluid Hyperthermia (MFH) Therapy. Cancerous cells are more sensitive to temperature than normal cells. Hence, Hyperthermia is a very promising treatment for cancer. Heating devices for hyperthermia include ultrasound, microwaves, laser fibers, and so forth. SPIONs can act as transducers to the tumor cells by converting AC electromagnetic energy into heat which targets only the SPION-loaded cells [67]. The use of SPIONs facilitates hyperthermia treatment because (i) they are nano-sized (they have greater specific absorption rates than micrometer-sized particles), (ii) magnetic (they can be localized and

Table 1: SPIO-based formulation used for cancer therapy.

SPIO preparation	SPIO coating	Cell line	Aim	REF
(1) Thermal decomposition	PEG-PLA, cRGD ligand, and doxorubicin	SLK	Ligand targeted drug delivery and MRI	[9]
(2) Coprecipitation	LHRH; LH/CG	MDA-MB-435S	Ligand targeted drug delivery and MRI	[10]
(3) Coprecipitation	Dextran/PVA; Cy5.5/Cy3.5	Brain-derived endothelial cells; microglial cells	MDT and MRI	[11]
(4) Coprecipitation	Poly(TMSMA-*r*-PEGMA)	LLC in mice	MRI	[12]
(5) Coprecipitation	DMSA ligand, rhodamine B, and fluorescein diacetate maleimide	HeLa	Fluorescent and magnetic cell labeling	[13]
(6) Thermal cross-linking	Poly(3-(trimethoxysilyl)propyl methacrylate-r-PEG methyl ether, methacrylate-r-N-acryloxysuccinimide), and Cy5.5	LLC	Dual-imaging probe	[14]
(7) SPIONs purchased from (model Resovist, Schering AG, Germany)	Hydrogel	CT-26 mice cancer cells	Hyperthermia cancer therapy	[15]
(8) SPIONs purchased from (SHU 555 A, Resovist; Schering, Berlin, Germany)	Carboxy dextran	CCL185	R2 and R2* mapping	[16]
(9) Thermal decomposition	Poly(amidoamine) dendrimers, 6-TAMRA fluorescent dye, and folic acid molecules	KB, UM-SCC-38	MRI	[17]
(10) Thermal cross-linking	Doxorubicin	LLC cells	MDT and MRI	[18]
(11) Coprecipitation	Amine-functionalized PEG silane, Alexa Fluor 680 (AF680) fluorochrome, and CTX	C6	Ligand targeted drug delivery	[19]
(12) Coprecipitation	Glycerol monooleate, antibody HER2, paclitaxel, and rapamycin	MCF7	Ligand targeted drug delivery	[20]
(13) Coprecipitation	PEG, CTX, and Cy5.5	Mouse bearing 9L gliosarcoma cells	Ligand targeted drug delivery and MRI	[21]
(14) Cross-linking	Dextran, cRGD, epichlorohydrin, ammonia, and Cy5.5	BT-20 tumor cells	Ligand targeted drug delivery and MRI	[22]
(15) Cross-linking	Dextran, bombesin, epichlorohydrin, ammonia, and Cy5.5	MIA-PaCa 2	MRI	[23]
(16) Coprecipitation	Paclitaxel	OECM1	MDT	[24]
(17) Coprecipitation	Oleic acid, pluronic, doxorubicin, and paclitaxel	MCF-7 breast cancer cells	MDT and MRI	[25]
(18) Coprecipitation	3-aminopropyltrimethoxysilane (APTMS), Arg-Gly-Asp, and (RGD) peptides	HaCaTras-A-5RT3, A431 tumors	Ligand targeted drug delivery and MRI	[26]

controlled in deep tissues enabling efficient heating), and (iii) their surface can be modified for high cellular selectivity [46].

4.2. Imaging. Nanobiotechnology plays an important role in molecular imaging of cancer cells for diagnostic purpose, particularly magnetic resonance imaging (MRI) and computed tomography (CT). Significant efforts have been made in recent years to develop SPIONs for target-specific MRI contrast agents (Table 1) because of their unique paramagnetic properties, which generate significant susceptibility effects resulting in strong T2 and T^*2 contrast, as well as T1 effects at very low concentrations [42, 48, 68, 69]. SPION can provide critically important insights into the rate of tumor growth, degree of tumor angiogenesis, effectiveness of the treatment, and condition of normal cells by imaging proliferating cells *in vivo*. Researchers have recently demonstrated the use of SPIONs to image neovasculature in glioma of animal models *in vitro* and *in vivo*. FDA has approved several SPION formulations for clinical application as contrast agents in MRI. Most of the SPION preparations on sale are in a size range from 60 nm to some micrometers. When SPIONs are injected intravenously, they are quickly engulfed by the reticulo-endothelial system (RES) and accumulate in the liver and spleen [70]. Due to such accumulation, SPIONs have been exploited for the detection of lesions and tumors in the liver. USPIO nanoparticles, because they are much smaller than the SPIONs, do not accumulate in the RES system and are characterized by

longer blood circulating times. Several forms of SPIONs have proven to be safe for human use [71, 72]. SPIONs can be internalized by various cell lines, which allows for magnetic labeling of the targeted cells [71]. All these features give SPIONs huge advantage for *in vivo* tumor imaging and drug delivery compared with other types of nanoparticles. Another advantage is the early detection of metastases which plays an important role in the management of metastatic cancer. Patients with prostate cancer who undergo surgical lymph node resection or biopsy, MRI with lymphotropic superparamagnetic nanoparticles is an alternative since it can correctly identify all patients with nodal metastases. This diagnosis is not possible with conventional MRI alone. Zhang et al. reported the fabrication of USPIO nanoparticles that exhibited a strong T^*2 contrast enhancement in gelatin gels when incubated with HUVECs *in vitro* in the phantom imaging experiments to access the angiogenic profiles of tumor [26].

5. siRNA in Cancer Therapy

RNA interference (RNAi)—the silencing of gene expression by double-stranded RNA molecules was first discovered by Andrew Fire, Craig Mello and colleagues in 1998 in nematode worms *C. elegans* [5]. The different stages where gene silencing can be induced by dsRNA have been depicted in Figure 3. RNAi is triggered when a cell encounters a long double-stranded RNA (dsRNA), which might have been produced by the introduction of a transgene, a viral intruder or a rogue genetic element.

RNA molecules that are a part of the RNAi mechanism include

(i) siRNA (short-interfering RNA, short 21-22 nucleotides long dsRNA);

(ii) miRNA (microRNAs, short 19–25-nucleotide long ssRNA);

(iii) tncRNA (tiny noncoding, 20–22-nucleotide long RNAs in *C. elegans*);

(iv) smRNA (small modulatory RNA, short dsRNA in mice) [5].

RNAi technology has been widely employed for the manipulation of gene expression in mammalian and human cells to elucidate signal pathways and to identify the function of a particular gene in the genome. Many pharmaceutical companies are interested in the commercialization of RNAi-based drugs for various diseases, especially in cancers. Alterations in cancer-susceptibility genes (oncogenes and tumor suppressor genes) are involved in different stages of tumor genesis like tumor initiation, progression, angiogenesis, and metastasis [73]. RNA-mediated gene-silencing is a powerful tool for identifying genes critical for the growth, differentiation, death of cells, and so forth (see Table 2). These genomic functional RNA molecules can be targeted with small fragments of their cognate sequences as the most ideal drug.

The two types of RNA molecules that are central to RNA interference are miRNA and siRNA. Here we focus mainly on siRNA. siRNA is generated by the cleavage of long double-stranded RNA sequences by Dicer. After cleavage, the "sense" strand is removed, leaving a single-stranded siRNA (antisense strand) lodged inside RNA-induced silencing complex (RISC). The antisense strand is then used by RISC to guide it to the target mRNA transcript [5, 74].

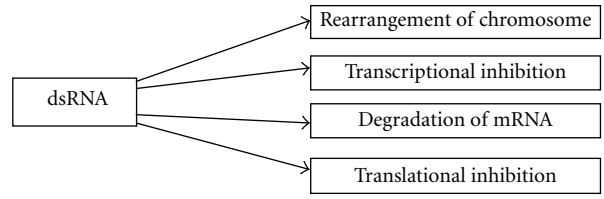

Figure 3: Mechanisms of selective gene silencing induced by dsRNA [78].

Mammalian RNAi was first described in mouse embryos using long dsRNA. The siRNAs are emerging as new generation biodrugs because of their specific and potent triggering activity. siRNAs offer several advantages as potential new drugs since (i) siRNA does not interfere with DNA transcription which reduces concerns about possible adverse gene manipulation that might result from DNA-based gene therapy, (ii) The interaction of siRNA with mRNA rather than proteins, makes it possible to reduce the production of harmful proteins, (iii) SiRNA-based drug can target any mRNA of interest, irrespective of its cellular location, (iv) only a few siRNA molecules per cell are required to produce the desired gene silencing effect, and (v) the identification of appropriate drug candidates using siRNA is simpler compared to traditional pharmaceuticals. Despite the several advantages of using siRNAs as potential new drugs, there are also challenges that need to be overcome in future research. (i) the silencing of nontarget genes may lead to problems in interpretation of data and potential toxicity. (ii) siRNA may result in the activation of innate immune responses upon its uncontrolled introduction inside the cell leading to several non specific events. (iii) SiRNAs are unable to enter cells by passive diffusion mechanisms since they are anionic and hydrophilic in nature [75]. Synthetically prepared siRNAs have gained wide acceptance as a laboratory tool for the validation of a target. siRNAs are highly efficient for the knockdown of gene (see Table 2) messages *in vitro* and *in vivo* that are pivotal for tumor cell growth, metastasis, angiogenesis, and chemoresistance, leading to tumor growth suppression [76]. Chemically synthesized siRNAs can be introduced into the cell either directly or by the use of plasmid and viral vectors encoding for siRNA [77].

6. Delivery and Tracking of siRNA with SMNPS

6.1. Delivery. Not surprisingly, genetically modified viruses (viral vectors) are the most efficient shuttles that are currently used for introducing nucleic acids into cells. For various reasons, including the possibility of biological risks, practicability, and the costs of manufacturing, researchers have however focused on synthetically designed alternatives

Table 2: Development of siRNA in cancer therapy.

S. no. Cell Line	Target	Result	REF
(1) PC-3 and DU 145	hTERT	Downregulation of hTERT inhibited cell proliferation	[27]
(2) HT144	RRM2	Downregulation of RRM2 inhibited cell proliferation	[28]
(3) H1299 and MDA-MB-468	Ran,TPX2, SCD1	Reduced survival of human tumor cell lines	[29]
(4) H1299	PTTG	Decreasing PTTG expression reduced tumor growth *in vivo* and *in vitro*	[30]
(5) Panc-1, PCI-19, PAN-03-JCK, and so forth	S100A4	Knockdown of S100A4 suppressed cell growth, induced apoptosis, and decreased cell migration	[31]
(6) MDA-MB-231 and ZR751	uPA	Downregulation of decreased tumor invasion, angiogenesis, and growth	[32]
(7) A549 and H460	Nrf2	Silencing inhibited tumor growth, and increasing efficacy of chemotherapy	[33]
(8) Cx1, HCT8, HT29, HCT15, and so forth.	CDCA1 and KNTC2	Knockdown suppressed cell proliferation and induced apoptosis	[34]
(9) A549 PC9	Wild type p53 Surviving	Inhibition of wildtype p53 upregulated antiapoptotic survin expression. Inhibition of surviving with mutated p53 depressed cell proliferation	[35]
(10) Ten HNSCC cell lines from one nasal cavity cancer (RPMI12650)	IGF2	Upregulation acquired resistance for RDDP in human head and neck squamous cell carcinoma	[36]

to viruses as nucleic acid shuttles. Moreover, the delivery via viral or synthetic vectors is diffusion-limited one irrespective of the size of the nucleic acid constructs. In other words, the time required by vectors to encounter their target cells by simple diffusion and bind to their surface constitutes a major limitation for the successful delivery of nucleic acids. This limitation is even more prominent *in vivo* (living animals or patients) where vectors are inactivated by opsonization, immune system and degradative processes and can be purged from the target tissue by the blood stream even upon local administration. The local confinement of nucleic acid delivery is particularly an important requirement *in vivo* to achieve an effective dose at a target site and reduce side effects at nontarget sites. Hence, for the successful application of siRNAs in cancer treatment, the following points should be taken into consideration: size limit, to avoid difficulty in membrane penetration, degradation by exonucleases within the cell, trafficking into the appropriate cell compartment, and proper folding of the siRNA in the cell [79, 80]. In this background, the principles of magnetic drug targeting (or magnetofection) to nucleic acid delivery using magnetic nanoparticles have been adapted. The fundamental principle of magnetofection is simple. It involves the formulation of a magnetic carrier to which the siRNA is attached, adding this to the cell culture medium or injecting it systemically via the blood stream or applying it to the target tissue, and applying a magnetic field to direct the vector towards the target cells [81]. It has been reported that the driving force for increased transfection efficiency when complexed with magnetic vectors is accelerated sedimentation of nucleic acids. About 78% and 66% GFP downregulation were observed at siRNA concentrations of 32 and 8 nM, respectively, when transfected with duplexes of PEI-25Br-Mag material and anti-GFP siRNA at Fe-to-DNA ratio of 1 : 1 [82]. Effective delivery of siRNA was achieved with LipoMag, consisting of an oleic acid-coated iron oxide core and cationic lipid shells, in mice gastric tumor models [83]. SPIONs generally consist of a magnetic iron-oxide core either encapsulated within a polymer or metallic shell or dispersed within a polymer matrix—such as silica, PVA, or dextran. The shell is then functionalized by attaching carboxyl groups, streptavidin, antibodies, and so forth. For *in vitro* magnetofection, the particles are usually coated with PEI, binding the nucleic acids to the surface of the SPION via charge interactions [84]. It is generally believed that positively charged nanoparticles are most efficient for siRNA delivery. *In vitro* magnetofection kits which utilize cationic polymer-coated MNPs are commercially available for routine laboratory use. *In vivo* delivery of siRNA with SPION particles is also being investigated. The role of siRNA nanoparticles as multifunctional siRNA delivery agents for effective cancer therapy has been demonstrated [40]. It would also enable real-time monitoring of the therapeutic outcome of siRNA therapy. The ability of SPIONs and poly(propyleneimine) generation 5 dendrimers (PPI G5) to enhance siRNA complexation in order to develop a multifunctional siRNA delivery system for targeted cancer therapy was investigated. The incorporation of poly(ethylene glycol) (PEG) coating and cancer-specific targeting moiety (LHRH peptide) into SPIO-PPI G5-siRNA increased the serum stability and selective internalization by cancer cells and increased the efficiency of targeted gene suppression *in vitro* [40]. A TAT-conjugated PEGylated magnetic polymeric liposome (TAT-PEG-MPLs) with superparamagnetic nanoparticles was successfully designed and evaluated *in vitro* and *in vivo* by [85]. Cell penetration tests were performed through fluorescein isothiocyanate

(FITC) labeling. Results indicated that the uptake of TAT-PEG-MPLs by MCF-7 cells was greater than that of PEG-MPLs. *In vivo* animal experiment, MRI, histological analysis, and atomic absorption spectrophotometry also revealed significant accumulation of TAT-PEG-MPLs nanoparticles around the target site [85].

6.2. Cellular Tracking. In spite of the successful delivery of siRNA using various nanomaterials, tracking their delivery and monitoring their transfection efficiency is an essential requirement and is difficult without a suitable tracking agent or marker [86]. The aim is to develop nanoparticles, which would not only enable cancer-specific targeting, effectively deliver sufficient dose of siRNA to target cells to induce gene silencing, but also provide the capability of carrier monitoring [49]. Recently, several strategies to track the gene delivery using nanoparticles of imaging modality have been reported [51]. SPIONs have been widely explored for this purpose (see Table 3). They are particularly useful for viewing the location and trafficking of siRNA, for *in vivo* applications [66].

7. Targeting Cancer Cells with siRNA-SMNPS

The objective of an efficient delivery system is to discharge their payloads specifically at the diseased tissue. Two approaches to serve this purpose are "passive" and "active" targeting. Passive targeting involves homing of the carriers to infected tissues, whereas active targeting relies on specific recognition of the ligands attached to the delivery vehicles by cell surface receptors on the diseased tissue [53, 68, 87, 88].

7.1. Passive Targeting. Passive targeting involves the specific migration of the nanoparticle to the target tissue mediated by the predetermined physicochemical properties of a given NP [89]. The phenomenon is based on the fact that tissues possess "leaky" vasculature allowing the extravasation and accumulation of the nanobioconjugate in the tissue more readily. Moreover, inefficient lymphatic drainage results in poor clearance of these agents, leading to selective accumulation [49, 52, 90]. With the development of long-circulating magnetic nanoparticles, exploiting the structural abnormalities in the vasculature of particular pathologies, such as tumors, has become easier. Passive targeting has been demonstrated with nanoparticles ranging from 10 to 500 nm in diameter [52]. SPIO probes lacking molecular specificity have been well documented for imaging biological systems via naturally directed physiological process. For passive targeting, the most important parameter is the hydrodynamic radius and the surface charge of the SPIO coating material. These parameters control the time of circulation of the nanoparticles, its accessibility to tissues, opsonization, and rate of uptake by the cell [6, 90]. Passive targeting is available for only certain *in vivo* applications and does not necessarily guarantee the uptake of the SPIONs by targeted cells. Hence, they can be additionally modified with molecular targeting ligands to employ active cell targeting. SPIONs are now being designed such that they are conjugated with targeting molecules, complementary to unique receptors on target cells, to actively target only diseased tissue.

7.2. Active Targeting. The 2 major goals in the development of therapeutic agents or imaging contrast formulations are greater target selectivity and better delivery efficiency. Ideally, a therapeutic drug must be selectively enriched in the tumor lesions causing minimal damage to normal tissues [68, 91]. Several approaches to improve the selective toxicity of anticancer therapeutics are being pursued presently of which the most commonly used method is the ligand-mediated targeting of anticancer therapeutics. The basic principle that underlies ligand-targeted therapeutics is that the drug molecules are precisely associated with other antibody/ligand molecules that bind to antigens/receptors, uniquely expressed or over-expressed on target cells compared with normal tissues [68]. Cancer biomarkers include a variety of molecules such as mutant genes, RNAs, proteins, lipids, carbohydrate, and small metabolite molecules. Their altered expression or presentation on the cell surface is related to a biological change expressed as neoplasia. Identifying these cancer biomarkers could enhance the possibility to diagnose the patient's cancer molecular profile, leading to personalised and predictive medicine [92]. By coating nanoparticles with drug conjugates that contain a ligand recognized by a receptor on the target cell the selective delivery of drugs to cancer cells or cancer-associated tissues such as tumor vasculature, can be achieved [93]. Multifunctional nanoparticles can combine different functionalities including small organic molecules [37, 49, 58, 94], proteins [20, 94, 95], antibodies [58, 96–98], aptamers [49, 58, 94], and peptides [9, 10, 21, 26, 56, 58, 94, 95, 99] in a single stable construct. A number of SPION systems have implemented this strategy into their design with varying success. These sophisticated multifunctional nanoparticle probes can successfully deliver itself into deep tissue, target specific cell types, and generate contrast based on target-specific clustering. In order to target cells *in vivo*, it is essential to graft high-affinity ligands on the nanoparticles surface to favor specific interactions and to prevent the interactions with serum protein and subsequent capture by the RES [100, 101]. Also to generate sufficient contrast for MR detection, adequate levels of SPION should be localized at a disease site. With this goal in mind, several approaches have been evaluated to improve the site-specific accumulation of SPION and enhance MR sensitivity. Active targeting is preferred to passive targeting as it could allow the early detection as well as more accurate staging of cancer. Numerous studies have already established the active targeting strategies to identify early cancer biomarkers [6].

siRNA "targeted" therapeutics for sequence-specific gene inhibition promise the ultimate level of precision in cancer therapy, but the hindrance lies in the poor intracellular uptake, limited blood stability, and nonspecific immune stimulation. To address these problems, sterically stabilized nanoparticles with targeting ligands have been adapted for siRNA therapeutics. Self-assembling nanoparticles have been fabricated, carrying siRNA and with Arg-Gly-Asp (RGD) peptide ligand attached at the distal end of the polyethylene

Table 3: SPION formulation for the delivery and tracking/imaging siRNA in cancer cells.

S. no. SPION preparation	Coating	Targeting ligands	Imaging of internalized SPION	Cell line	Target	siRNA sequence	REF
(1) Coprecipitation	Chitosan, PEG, and PEI	CTX peptide	MRI Flow cytometry of Dy547-labelled siRNA	C6 rat glioma cells	GFP expression	5′GAACUUCAGGGUCAGCUUGCUU3′ sense and 5′GCAAGCUGACCCUGAAGUUCUU3′ antisense	[37]
(2) Thermal decomposition	Oleic acid, PEI, and PEG	CTX peptide	MRI ferrozine-based assay	C6 cells	GFP	5′GAACUUCAGGGUCAGCUUGCUU3′ sense and 5′GCAAGCUGACCCUGAAGUUCUU3′ antisense,	[38]
(3) Dextran coated iron oxide colloid crosslinked with epichlorohydrin, and treated with ammonia	Dextran	MPAP peptide	MRI optical imaging of Cy5.5-labelled SPIONs	LS174T and 9L	GFP	5′-GCA AGC TGA CCC TGA AGT TC-3′	[39]
(4) Thermal decomposition	PEG, and PPI G5	LHRH peptide	MRI FAM-labeled siRNA complexes analyzed by fluorescence and confocal microscopes	A549 and SKOV-3	BCL2 and β2-microglobulin	GGA TTG TGG CCT TCT TTG AG sense, CCA AAC TGA GCA GAG TCT TC antisense and ACC CCC ACTGAA AAA GAT GA sense, ATC TTC AAA CCT CCATGA TG antisense.	[40]

glycol (PEG) [102]. The intravenous administration of this nanovector into tumor-bearing mice targeted tumor neovasculature expressing integrins, gave selective tumor uptake, siRNA sequence-specific inhibition of vascular endothelial growth factor receptor-2 (VEGF R2) protein expression and inhibition of both tumor angiogenesis and growth rate. Hence, the results suggest achievement at two levels of targeting: tumor tissue selective delivery via the targeting ligand and gene pathway selectivity via the siRNA [102]. The possibility of utilizing TCL-SPIONs in distinct ways to develop combined therapeutic and diagnostic modalities by incorporating siRNA and small-molecular anticancer drugs have been reported [18]. A patient has completed the first successful dosing cycle with small-interfering RNA (siRNA) for the treatment of cancer in a clinical trial. The patient was administered with four doses of Calando's CALAA-01, a targeted siRNA nanoparticle, over a two-week period [92, 103].

8. Three-Dimensional Cell Culture, Tissue Engineering, Regenerative Medicine, and Applications of SPIONs in Three- Dimensional Self-Assembly

Animal cell culture in 3D architecture with abilities of cell adhesion, proliferation, and differentiation is an exciting area of research in simulating in vivo conditions. Various scaffolds have been described as promising in engineering tissues to achieve the aforesaid cell/tissue properties. Neural, skeletal, and cardiovascular cells/tissues are being engineered for the purpose. The flow of liquid and gaseous ingredients carrying nutrients, drugs and cell tracking/imaging molecules assume great significance to study cell/tissue behavior in 3D architecture.

Polyethylenimine (PEI)-coated superparamagnetic nanoparticles (SPMNs) were shown to deliver interfering RNA and green fluorescent protein (GFP) plasmids through a collagen gel matrix into 3D cell cultures driven by an external magnetic field. PEI-coated SPMNs silenced the GFP expression with 82% efficiency [104]. These nanoparticles can also deliver small molecules and macromolecules with reduced mass transfer resistance.

Nanofiber-scaffold-mediated delivery of small-interfering RNA (siRNA) provided biomimicking topographical signals and enhanced gene silencing effects to seeded cells [105]. The feasibility of encapsulating siRNA and transfection reagent complexes was demonstrated within nanofibers comprising of a copolymer of caprolactone and ethyl ethylene phosphate. Sustained release of bioactive naked siRNA was obtained for about a month.

A few recent articles described fascinating possibilities of using SPIONs in tissue engineering and also in creating 3D cell-dense construct by manipulating their magnetic properties. Poly (L-lactide-co-glycolide) SPION fibrous bundles were fabricated through electrospinning technique [106]. They demonstrate 3D self-assembly of these fibrous bundles in 3D architecture by applying an external magnetic field. C2C12 myoblasts cell rods were formed (similar to those of native skeletal muscle tissues), and in differentiation medium they formed multinucleated myotubes.

9. Future Prospects

The siRNAs regulate almost all aspects of cancer (i.e., proliferation, apoptosis, metastasis, etc.) and are therefore versatile tools in cancer theragnosis. Using SPIONs as vehicle, their entry in cells/tissue, passage within cells, and the molecular mechanisms of their interactions could be well monitored.

The precise synthesis of siRNA molecules enables perfect inactivation of target mRNAs. In addition, their ability of crossing blood brain barrier will help understand brain tumor-related events which are otherwise not reachable now. As the siRNAs have the ability to silence diverse gene functions, the overall understanding of the events related to cancer diagnosis and therapy would evolve a systems biology approach in cancer treatment.

All these achievements in targeted cancer therapy using SPIONs conjugated with siRNA and targeting ligands suggest that for the first time it may be possible to tackle cancer management needs and individualize therapies by developing personalized treatments. Clinical laboratories have started using nanotechnology-based assays to detect tumor biomarkers of each patient as well as formulate the nanoparticles using the same biomarkers, carrying the specific genetic drug (i.e., siRNA) designed to knock down the biomarker protein related to that tumor. Some SPION formulations approved clinically include Feridex IV and Endorem for liver and spleen imaging, Ferumoxytol for iron replacement therapy, Combidex for imaging lymph node metastases, and Lumiren and Gastromark for bowel imaging [45, 49, 52, 107]. Ferumoxtran-10 is a commercially available USPIO [108–110].

Targeted-specific immune cells in detecting metastatic liver *in vivo* by tagging β-glucan with SPION and accumulation in Kupffer cells were confirmed by MRI [111]. The further possibility of real-time study of *in vivo* migration and differentiation of stem cells is likely to enable imaging of all aspects of differentiation and development continuously [112]. A recent publication [113] on the achievement of delivering both hydrophilic and hydrophobic drugs by oligo-/multil-amellar hybrid SPION-liposome nanostructures based on phosphatidylcholine indicates the more versatile nature of SPION-mediated drug delivery. The encapsulation of the SPION inside multi-lamellar structure helped stabilize them against aggregation and sedimentation for 3 months. The vistas of SPION-siRNA diagnosis and therapy are depicted in Figure 4.

10. Conclusion

(i) microRNAs (miRNAs) are nonprotein-coding RNAs that control diverse gene targets and can induce silencing of many genes. Short-interfering RNAs (siRNAs) are 21-22 nucleotide long dsRNAs generated by dicer cleavage of long dsRNAs and can bind to nontranslated region of mRNAs resulting in degradation of target mRNAs. Chemically synthesized siRNAs could be used as biodrugs, for treatment of cancer;

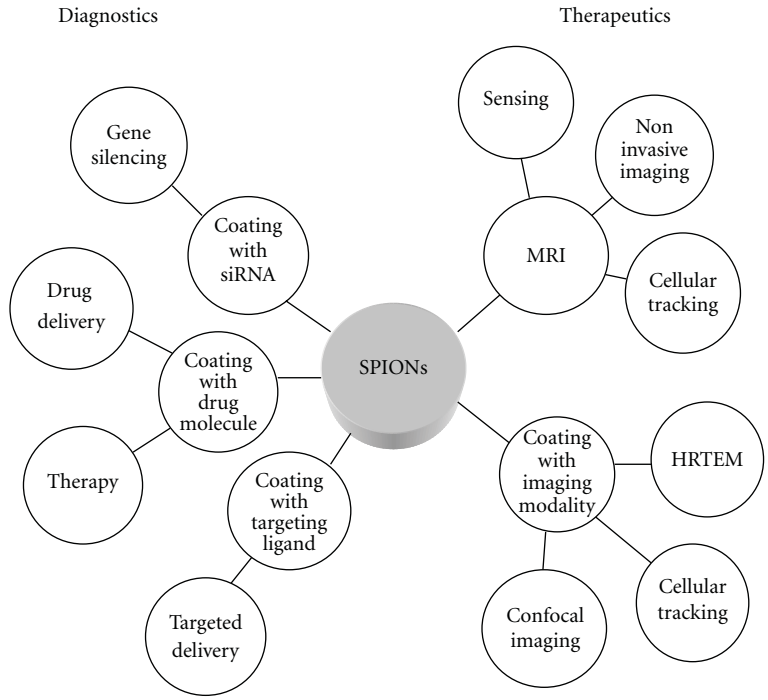

Figure 4: Prospects of diagnosis and therapy using SPION-siRNA conjugate.

(ii) superparamagnetic nanoparticles are excellent biocompatible vehicles for siRNA and can cross blood brain barrier. Superparamagnetic iron oxide (magnetite, maghemite, etc.) nanoparticles (SPIONs), coated with suitable linker molecules, can conjugate with a variety of target biomolecules including fluorophore for non-invasive imaging and siRNAs for gene silencing. SPIONs have also been used as cancer drug delivery systems;

(iii) SPIONs could commonly be synthesized by coprecipitation and microemulsification techniques, and the former is proved to be superior;

(iv) SPIONs have also been used in magnetic fluid hyperthermia (MFH) therapy for cancer by employing them as transducers for converting AC electromagnetic energy to heat in target cancer cells, that are more sensitive to heat than normal cells;

(v) commercial products like Combidex and Endorem have already been used in Europe for the early detection of metastases;

(vi) the possibility of achieving 3D tissue architecture in SPION-coated biomaterial fibers is an exciting incentive in research in simulating *in vivo* conditions *in vitro*.

References

[1] A. J. Tije, J. Verweij, W. J. Loos, and A. Sparreboom, "Pharmacological effects of formulation vehicles: implications for cancer chemotherapy," *Clinical Pharmacokinetics*, vol. 42, no. 7, pp. 665–685, 2003.

[2] C. M. Walko and C. Lindley, "Capecitabine: a review," *Clinical Therapeutics*, vol. 27, no. 1, pp. 23–44, 2005.

[3] L. J. M. Oostendorp, P. F. M. Stalmeier, A. R. T. Donders, W. T. A. van der Graaf, and P. B. Ottevanger, "Efficacy and safety of palliative chemotherapy for patients with advanced breast cancer pretreated with anthracyclines and taxanes: a systematic review," *The Lancet Oncology*, vol. 12, no. 11, pp. 1053–1061, 2011.

[4] D. R. Groothuis, "The blood-brain and blood-tumor barriers: a review of strategies for increasing drug delivery," *Neuro-Oncology*, vol. 2, no. 1, pp. 45–49, 2000.

[5] C. D. Novina and P. A. Sharp, "The RNAi revolution," *Nature*, vol. 430, no. 6996, pp. 161–164, 2004.

[6] D. L. J. Thorek, A. K. Chen, J. Czupryna, and A. Tsourkas, "Superparamagnetic iron oxide nanoparticle probes for molecular imaging," *Annals of Biomedical Engineering*, vol. 34, no. 1, pp. 23–38, 2006.

[7] K. K. Jain, "Application of nanobiotechnology in cancer therapeutics," in *Pharmaceutical Perspectives of Cancer Therapeutics*, Y. Lu and R. I. Mahato, Eds., pp. 245–268, Springer, New York, NY, USA, 2009.

[8] Z. Liu, F. Kiessling, and J. Gätjens, "Advanced nanomaterials in multimodal imaging: design, functionalization, and biomedical applications," *Journal of Nanomaterials*, vol. 2010, Article ID 894303, 2010.

[9] N. Nasongkla, E. Bey, J. Ren et al., "Multifunctional polymeric micelles as cancer-targeted, MRI-ultrasensitive drug delivery systems," *Nano Letters*, vol. 6, no. 11, pp. 2427–2430, 2006.

[10] C. Leuschner, C. S. S. R. Kumar, W. Hansel, W. Soboyejo, J. Zhou, and J. Hormes, "LHRH-conjugated magnetic iron oxide nanoparticles for detection of breast cancer metastases," *Breast Cancer Research and Treatment*, vol. 99, no. 2, pp. 163–176, 2006.

[11] F. Cengelli, D. Maysinger, F. T. Monnet et al., "Interaction of functionalized superparamagnetic iron oxide nanoparticles with brain structures," *Journal of Pharmacology and Experimental Therapeutics*, vol. 318, no. 1, pp. 108–116, 2006.

[12] H. Lee, E. Lee, D. K. Kim, N. K. Jang, Y. Y. Jeong, and S. Jon, "Antibiofouling polymer-coated superparamagnetic iron oxide nanoparticles as potential magnetic resonance contrast agents for *in vivo* cancer imaging," *Journal of the American Chemical Society*, vol. 128, no. 22, pp. 7383–7389, 2006.

[13] F. Bertorelle, C. Wilhelm, J. Roger, F. Gazeau, C. Ménager, and V. Cabuil, "Fluorescence-modified superparamagnetic nanoparticles: intracellular uptake and use in cellular imaging," *Langmuir*, vol. 22, no. 12, pp. 5385–5391, 2006.

[14] H. Lee, M. K. Yu, S. Park et al., "Thermally cross-linked superparamagnetic iron oxide nanoparticles: synthesis and application as a dual imaging probe for cancer *in vivo*," *Journal of the American Chemical Society*, vol. 129, no. 42, pp. 12739–12745, 2007.

[15] H. Y. Tseng, C. Y. Lee, Y. H. Shih, X. Z. Lin, and G. B. Lee, "Hyperthermia cancer therapy utilizing superparamagnetic nanoparticles," in *Proceedings of the IEEE International Conference on Nano/Micro Engineered and Molecular Systems (NEMS '07)*, vol. 19, pp. 163–166, January 2007.

[16] R. Kuhlpeter, H. Dahnke, L. Matuszewski et al., "R2 and R2* mapping for sensing cell-bound superparamagnetic nanoparticles: *in vitro* and murine *in vivo* testing," *Radiology*, vol. 245, no. 2, pp. 449–457, 2007.

[17] K. J. Landmark, S. D. Maggio, J. Ward et al., "Synthesis, characterization, and *in vitro* testing of superparamagnetic iron oxide nanoparticles targeted using folic acid-conjugated dendrimers," *American Chemical Society Nano*, vol. 2, no. 4, pp. 773–783, 2008.

[18] M. K. Yu, Y. Y. Jeong, J. Park et al., "Drug-loaded superparamagnetic iron oxide nanoparticles for combined cancer imaging and therapy *in vivo*," *Angewandte Chemie - International Edition*, vol. 47, no. 29, pp. 5362–5365, 2008.

[19] O. Veiseh, J. W. Gunn, F. M. Kievit et al., "Inhibition of tumor-cell invasion with chlorotoxin-bound superparamagnetic nanoparticles," *Small*, vol. 5, no. 2, pp. 256–264, 2009.

[20] F. Dilnawaz, A. Singh, C. Mohanty, and S. K. Sahoo, "Dual drug loaded superparamagnetic iron oxide nanoparticles for targeted cancer therapy," *Biomaterials*, vol. 31, no. 13, pp. 3694–3706, 2010.

[21] C. Sun, K. Du, C. Fang et al., "PEG-mediated synthesis of highly dispersive multifunctional superparamagnetic nanoparticles: their physicochemical properties and function *in vivo*," *American Chemical Society Nano*, vol. 4, no. 4, pp. 2402–2410, 2010.

[22] X. Montet, K. Montet-Abou, F. Reynolds, R. Weissleder, and L. Josephson, "Nanoparticle imaging of integrins on tumor cells," *Neoplasia*, vol. 8, no. 3, pp. 214–222, 2006.

[23] X. Montet, R. Weissleder, and L. Josephson, "Imaging pancreatic cancer with a peptide-nanoparticle conjugate targeted to normal pancreas," *Bioconjugate Chemistry*, vol. 17, no. 4, pp. 905–911, 2006.

[24] J. R. Hwu, Y. S. Lin, T. Josephrajan et al., "Targeted paclitaxel by conjugation to iron oxide and gold nanoparticles," *Journal of the American Chemical Society*, vol. 131, no. 1, pp. 66–68, 2009.

[25] T. K. Jain, J. Richey, M. Strand, D. L. L. Pelecky, C. A. Flask, and V. Labhasetwar, "Magnetic nanoparticles with dual functional properties: drug delivery and magnetic resonance imaging," *Biomaterials*, vol. 29, no. 29, pp. 4012–4021, 2008.

[26] C. Zhang, M. Jugold, E. C. Woenne et al., "Specific targeting of tumor angiogenesis by RGD-conjugated ultrasmall superparamagnetic iron oxide particles using a clinical 1.5-T magnetic resonance scanner," *Cancer Research*, vol. 67, no. 4, pp. 1555–1562, 2007.

[27] P. Gandellini, M. Folini, R. Bandiera et al., "Down-regulation of human telomerase reverse transcriptase through specific activation of RNAi pathway quickly results in cancer cell growth impairment," *Biochemical Pharmacology*, vol. 73, no. 11, pp. 1703–1714, 2007.

[28] M. E. Davis, J. E. Zuckerman, C. H. J. Choi et al., "Evidence of RNAi in humans from systemically administered siRNA via targeted nanoparticles," *Nature*, vol. 464, no. 7291, pp. 1067–1070, 2010.

[29] S. E. Morgan-Lappe, L. A. Tucker, X. Huang et al., "Identification of Ras-related nuclear protein, targeting protein for Xenopus kinesin-like protein 2, and stearoyl-CoA desaturase 1 as promising cancer targets from an RNAi-based screen," *Cancer Research*, vol. 67, no. 9, pp. 4390–4398, 2007.

[30] S. S. Kakar and M. T. Malik, "Suppression of lung cancer with siRNA targeting PTTG," *International Journal of Oncology*, vol. 29, no. 2, pp. 387–395, 2006.

[31] T. Tabata, N. Tsukamoto, A. A. I. Fooladi et al., "RNA interference targeting against S100A4 suppresses cell growth and motility and induces apoptosis in human pancreatic cancer cells," *Biochemical and Biophysical Research Communications*, vol. 390, no. 3, pp. 475–480, 2009.

[32] S. Kunigal, S. S. Lakka, C. S. Gondi, N. Estes, and J. S. Rao, "RNAi-mediated downregulation of urokinase plasminogen activator receptor and matrix metalloprotease-9 in human breast cancer cells results in decreased tumor invasion, angiogenesis and growth," *International Journal of Cancer*, vol. 121, no. 10, pp. 2307–2316, 2007.

[33] A. Singh, S. B. Adamsky, R. K. Thimmulappa et al., "RNAi-mediated silencing of nuclear factor erythroid-2-related factor 2 gene expression in non-small cell lung cancer inhibits tumor growth and increases efficacy of chemotherapy," *Cancer Research*, vol. 68, no. 19, pp. 7975–7984, 2008.

[34] N. Kaneko, K. Miura, Z. Gu et al., "siRNA-mediated knockdown against *CDCA1* and *KNTC2*, both frequently overexpressed in colorectal and gastric cancers, suppresses cell proliferation and induces apoptosis," *Biochemical and Biophysical Research Communications*, vol. 390, no. 4, pp. 1235–1240, 2009.

[35] K. Yonesaka, K. Tamura, T. Kurata et al., "Small interfering RNA targeting survivin sensitizes lung cancer cell with mutant p53 to adriamycin," *International Journal of Cancer*, vol. 118, no. 4, pp. 812–820, 2006.

[36] T. Ogawa, K. Ogawa, K. Shiga et al., "Upregulation of *IGF2* is associated with an acquired resistance for cis-diamminedichloroplatinum in human head and neck squamous cell carcinoma," *European Archives of Oto-Rhino-Laryngology*, vol. 267, no. 10, pp. 1599–1606, 2010.

[37] O. Veiseh, F. M. Kievit, C. Fang et al., "Chlorotoxin bound magnetic nanovector tailored for cancer cell targeting, imaging, and siRNA delivery," *Biomaterials*, vol. 31, no. 31, pp. 8032–8042, 2010.

[38] H. Mok, O. Veiseh, C. Fang et al., "PH-sensitive siRNA nanovector for targeted gene silencing and cytotoxic effect in cancer cells," *Molecular Pharmaceutics*, vol. 7, no. 6, pp. 1930–1939, 2010.

[39] Z. Medarova, W. Pham, C. Farrar, V. Petkova, and A. Moore, "*In vivo* imaging of siRNA delivery and silencing in tumors," *Nature Medicine*, vol. 13, no. 3, pp. 372–377, 2007.

[40] O. Taratula, O. Garbuzenko, R. Savla, Y. A. Wang, H. He, and T. Minko, "Multifunctional nanomedicine platform for cancer specific delivery of sirna by superparamagnetic iron oxide nanoparticles-dendrimer complexes," *Current Drug Delivery*, vol. 8, no. 1, pp. 59–69, 2011.

[41] J. H. Zhou, L. Huang, W. W. Wang et al., "Prostate cancer targeted MRI nanoprobe based on superparamagnetic iron oxide and copolymer of poly(ethylene glycol) and polyethyleneimin," *Chinese Science Bulletin*, vol. 54, pp. 3137–3146, 2009.

[42] Q. A. Pankhurst, J. Connolly, S. K. Jones, and J. Dobson, "Applications of magnetic nanoparticles in biomedicine," *Journal of Physics D*, vol. 36, no. 13, pp. R167–R181, 2003.

[43] M. A. Willard, L. K. Kurihara, E. E. Carpenter, S. Calvin, and V. G. Harris, "Chemically prepared magnetic nanoparticles," *International Materials Reviews*, vol. 49, no. 3-4, pp. 125–170, 2004.

[44] S. R. Dave and X. Gao, "Monodisperse magnetic nanoparticles for biodetection, imaging, and drug delivery: a versatile and evolving technology," in *Nanomedicine and Nanobiotechnology*, J. R. Baker, Ed., vol. 1, pp. 583–609, John Wiley & Sons, Hoboken, NJ, USA, 2009.

[45] M. Mahmoudi, S. Sant, B. Wang, S. Laurent, and T. Sen, "Superparamagnetic iron oxide nanoparticles (SPIONs): development, surface modification and applications in chemotherapy," *Advanced Drug Delivery Reviews*, vol. 63, no. 1-2, pp. 24–46, 2011.

[46] M. M. Lin, D. K. Kim, A. J. E. Haj, and J. Dobson, "Development of superparamagnetic iron oxide nanoparticles (SPIONS) for translation to clinical applications," *IEEE Transactions on Nanobioscience*, vol. 7, no. 4, pp. 298–305, 2008.

[47] A. Figuerola, R. D. Corato, L. Manna, and T. Pellegrino, "From iron oxide nanoparticles towards advanced iron-based inorganic materials designed for biomedical applications," *Pharmacological Research*, vol. 62, no. 2, pp. 126–143, 2010.

[48] M. H. Amtenbrink, B. V. Rechenberg, and H. Hofmann, "Superparamagnetic nanoparticles for biomedical applications," in *Nanostructured Materials for Biomedical Applications*, M. C. Tan, G. M. Chow, and L. Ren, Eds., chapter 5, pp. 119–148, Transworld Research Network, Trivandrum, India, 2009.

[49] O. Veiseh, J. W. Gunn, and M. Zhang, "Design and fabrication of magnetic nanoparticles for targeted drug delivery and imaging," *Advanced Drug Delivery Reviews*, vol. 62, no. 3, pp. 284–304, 2010.

[50] S. Laurent, D. Forge, M. Port et al., "Magnetic iron oxide nanoparticles: synthesis, stabilization, vectorization, physicochemical characterizations and biological applications," *Chemical Reviews*, vol. 108, no. 6, pp. 2064–2110, 2008.

[51] J. Kim, Y. Piao, and T. Hyeon, "Multifunctional nanostructured materials for multimodal imaging, and simultaneous imaging and therapy," *Chemical Society Reviews*, vol. 38, no. 2, pp. 372–390, 2009.

[52] C. Sun, J. S. H. Lee, and M. Zhang, "Magnetic nanoparticles in MR imaging and drug delivery," *Advanced Drug Delivery Reviews*, vol. 60, no. 11, pp. 1252–1265, 2008.

[53] T. Neuberger, B. Schöpf, H. Hofmann, M. Hofmann, and B. von Rechenberg, "Superparamagnetic nanoparticles for biomedical applications: possibilities and limitations of a new drug delivery system," *Journal of Magnetism and Magnetic Materials*, vol. 293, no. 1, pp. 483–496, 2005.

[54] C. W. Lu, Y. Hung, J. K. Hsiao et al., "Bifunctional magnetic silica nanoparticles for highly efficient human stem cell labeling," *Nano Letters*, vol. 7, no. 1, pp. 149–154, 2007.

[55] S. C. McBain, H. H. P. Yiu, and J. Dobson, "Magnetic nanoparticles for gene and drug delivery," *International Journal of Nanomedicine*, vol. 3, no. 2, pp. 169–180, 2008.

[56] C. Zhang, B. Wängler, B. Morgenstern et al., "Silica—and alkoxysilane—coated ultrasmall superparamagnetic iron oxide particles: a promising tool to label cells for magnetic resonance imaging," *Langmuir*, vol. 23, no. 3, pp. 1427–1434, 2007.

[57] D. Högemann, L. Josephson, R. Weissleder, and J. P. Basilion, "Improvement of MRI probes to allow efficient detection of gene expression," *Bioconjugate Chemistry*, vol. 11, no. 6, pp. 941–946, 2000.

[58] J. R. McCarthy and R. Weissleder, "Multifunctional magnetic nanoparticles for targeted imaging and therapy," *Advanced Drug Delivery Reviews*, vol. 60, no. 11, pp. 1241–1251, 2008.

[59] F. Sonvico, S. Mornet, S. Vasseur et al., "Folate-conjugated iron oxide nanoparticles for solid tumor targeting as potential specific magnetic hyperthermia mediators: synthesis, physicochemical characterization, and *in vitro* experiments," *Bioconjugate Chemistry*, vol. 16, no. 5, pp. 1181–1188, 2005.

[60] C. Alexiou, R. Jurgons, C. Seliger, O. Brunke, H. Iro, and S. Odenbach, "Delivery of superparamagnetic nanoparticles for local chemotherapy after intraarterial infusion and magnetic drug targeting," *Anticancer Research*, vol. 27, no. 4, pp. 2019–2022, 2007.

[61] F. M. Kievit, F. Y. Wang, C. Fang et al., "Doxorubicin loaded iron oxide nanoparticles overcome multidrug resistance in cancer *in vitro*," *Journal of Controlled Release*, vol. 152, no. 1, pp. 76–83, 2011.

[62] N. Kohler, C. Sun, J. Wang, and M. Zhang, "Methotrexate-modified superparamagnetic nanoparticles and their intracellular uptake into human cancer cells," *Langmuir*, vol. 21, no. 19, pp. 8858–8864, 2005.

[63] C. Alexiou, R. Jurgons, R. Schmid et al., "*In vitro* and *in vivo* investigations of targeted chemotherapy with magnetic nanoparticles," *Journal of Magnetism and Magnetic Materials*, vol. 293, no. 1, pp. 389–393, 2005.

[64] J. Deshane, C. C. Garner, and H. Sontheimer, "Chlorotoxin inhibits glioma cell invasion via matrix metalloproteinase-2," *Journal of Biological Chemistry*, vol. 278, no. 6, pp. 4135–4144, 2003.

[65] R. Solaro, F. Chiellini, and A. Battisti, "Targeted delivery of protein drugs by nanocarriers," *Materials*, vol. 3, pp. 1928–1980, 2010.

[66] J. H. Lee, K. Lee, S. H. Moon, Y. Lee, T. G. Park, and J. Cheon, "All-in-One target-cell-specific magnetic nanoparticles for simultaneous molecular imaging and siRNA delivery," *Angewandte Chemie*, vol. 48, no. 23, pp. 4174–4179, 2009.

[67] J. L. Phillips, "A topical review of magnetic fluid hyperthermia," *Journal of Science and Health at the University of Alabama*, pp. 14–28, 2005.

[68] X. Wang, L. Yang, Z. Chen, and D. M. Shin, "Application of nanotechnology in cancer therapy and imaging," *CA: A Cancer Journal for Clinicians*, vol. 58, no. 2, pp. 97–110, 2008.

[69] C. E. Sjögren, C. Johansson, A. Naevestad, P. C. Sontum, K. Briley-Saebø, and A. K. Fahlvik, "Crystal size and properties of superparamagnetic iron oxide (SPIO) particles," *Magnetic Resonance Imaging*, vol. 15, no. 1, pp. 55–67, 1997.

[70] C. C. Berry and A. S. G. Curtis, "Functionalisation of magnetic nanoparticles for applications in biomedicine," *Journal of Physics D*, vol. 36, no. 13, pp. R198–R206, 2003.

[71] M. F. Kircher, J. R. Allport, E. E. Graves et al., "*In vivo* high resolution three-dimensional imaging of antigen-specific cytotoxic T-lymphocyte trafficking to tumors," *Cancer Research*, vol. 63, no. 20, pp. 6838–6846, 2003.

[72] K. M. Hauff, R. Rothe, R. Scholz et al., "Intracranial thermotherapy using magnetic nanoparticles combined with external beam radiotherapy: results of a feasibility study on patients with glioblastoma multiforme," *Journal of Neuro-Oncology*, vol. 81, no. 1, pp. 53–60, 2007.

[73] F. L. Tan and J. Q. Yin, "Application of RNAi to cancer research and therapy," *Frontiers in Bioscience*, vol. 10, no. 2, pp. 1946–1960, 2005.

[74] Y. Tomaru and Y. Hayashizaki, "Cancer research with non-coding RNA," *Cancer Science*, vol. 97, no. 12, pp. 1285–1290, 2006.

[75] Y. K. Oh and T. G. Park, "siRNA delivery systems for cancer treatment," *Advanced Drug Delivery Reviews*, vol. 61, no. 10, pp. 850–862, 2009.

[76] A. W. Tong, Y. A. Zhang, and J. Nemunaitis, "Small interfering RNA for experimental cancer therapy," *Current Opinion in Molecular Therapeutics*, vol. 7, no. 2, pp. 114–124, 2005.

[77] M. Masiero, G. Nardo, S. Indraccolo, and E. Favaro, "RNA interference: implications for cancer treatment," *Molecular Aspects of Medicine*, vol. 28, no. 1, pp. 143–166, 2007.

[78] R. Agami, "RNAi and related mechanisms and their potential use for therapy," *Current Opinion in Chemical Biology*, vol. 6, no. 6, pp. 829–834, 2002.

[79] A. Khaled, S. Guo, F. Li, and P. Guo, "Controllable self-assembly of nanoparticles for specific delivery of multiple therapeutic molecules to cancer cells using RNA nanotechnology," *Nano Letters*, vol. 5, no. 9, pp. 1797–1808, 2005.

[80] L. Huang and J. Li, "Targeted delivery of RNAi therapeutics for cancer therapy," *Nanomedicine*, vol. 5, no. 10, pp. 1483–1486, 2010.

[81] U. Schillinger, T. Brill, C. Rudolph et al., "Advances in magnetofection—magnetically guided nucleic acid delivery," *Journal of Magnetism and Magnetic Materials*, vol. 293, no. 1, pp. 501–508, 2005.

[82] O. Mykhaylyk, D. Vlaskou, N. Tresilwised, P. Pithayanukul, W. Möller, and C. Plank, "Magnetic nanoparticle formulations for DNA and siRNA delivery," *Journal of Magnetism and Magnetic Materials*, vol. 311, no. 1, pp. 275–281, 2007.

[83] Y. Namiki, T. Namiki, H. Yoshida et al., "A novel magnetic crystal-lipid nanostructure for magnetically guided *in vivo* gene delivery," *Nature Nanotechnology*, vol. 4, no. 9, pp. 598–606, 2009.

[84] J. Dobson, "Gene therapy progress and prospects: magnetic nanoparticle-based gene delivery," *Gene Therapy*, vol. 13, no. 4, pp. 283–287, 2006.

[85] H. Wang, S. Zhang, Z. Liao et al., "PEGlated magnetic polymeric liposome anchored with TAT for delivery of drugs across the blood-spinal cord barrier," *Biomaterials*, vol. 31, no. 25, pp. 6589–6596, 2010.

[86] S. S. Suri, H. Fenniri, and B. Singh, "Nanotechnology-based drug delivery systems," *Journal of Occupational Medicine and Toxicology*, vol. 2, 16 pages, 2007.

[87] M. De, P. S. Ghosh, and V. M. Rotello, "Applications of nanoparticles in biology," *Advanced Materials*, vol. 20, no. 22, pp. 4225–4241, 2008.

[88] F. M. Kievit and M. Zhang, "Surface engineering of iron oxide nanoparticles for targeted cancer therapy," *Accounts of Chemical Research*, vol. 44, no. 10, pp. 853–862, 2011.

[89] H. Maeda, J. Wu, T. Sawa, Y. Matsumura, and K. Hori, "Tumor vascular permeability and the EPR effect in macromolecular therapeutics: a review," *Journal of Controlled Release*, vol. 65, no. 1-2, pp. 271–284, 2000.

[90] R. Sinha, G. J. Kim, S. Nie, and D. M. Shin, "Nanotechnology in cancer therapeutics: bioconjugated nanoparticles for drug delivery," *Molecular Cancer Therapeutics*, vol. 5, no. 8, pp. 1909–1917, 2006.

[91] Y. Gao, X. L. Liu, and X. R. Li, "Research progress on siRNA delivery with nonviral carriers," *International Journal of Nanomedicine*, vol. 6, pp. 1017–1025, 2011.

[92] M. Wang and M. Thanou, "Targeting nanoparticles to cancer," *Pharmacological Research*, vol. 62, no. 2, pp. 90–99, 2010.

[93] Y. Liu, H. Miyoshi, and M. Nakamura, "Nanomedicine for drug delivery and imaging: a promising avenue for cancer therapy and diagnosis using targeted functional nanoparticles," *International Journal of Cancer*, vol. 120, no. 12, pp. 2527–2537, 2007.

[94] N. Sanvicens and M. P. Marco, "Multifunctional nanoparticles—properties and prospects for their use in human medicine," *Trends in Biotechnology*, vol. 26, no. 8, pp. 425–433, 2008.

[95] O. Veiseh, C. Sun, J. Gunn et al., "Optical and MRI multifunctional nanoprobe for targeting gliomas," *Nano Letters*, vol. 5, no. 6, pp. 1003–1008, 2005.

[96] Y. Zhang, N. Kohler, and M. Zhang, "Surface modification of superparamagnetic magnetite nanoparticles and their intracellular uptake," *Biomaterials*, vol. 23, no. 7, pp. 1553–1561, 2002.

[97] Y. M. Huh, Y. W. Jun, H. T. Song et al., "*In vivo* magnetic resonance detection of cancer by using multifunctional magnetic nanocrystals," *Journal of the American Chemical Society*, vol. 127, no. 35, pp. 12387–12391, 2005.

[98] F. Hu, L. Wei, Z. Zhou, Y. Ran, Z. Li, and M. Gao, "Preparation of biocompatible magnetite nanocrystals for *in vivo* magnetic resonance detection of cancer," *Advanced Materials*, vol. 18, no. 19, pp. 2553–2556, 2006.

[99] A. Moore, Z. Medarova, A. Potthast, and G. Dai, "*In vivo* targeting of underglycosylated MUC-1 tumor antigen using a multimodal imaging probe," *Cancer Research*, vol. 64, no. 5, pp. 1821–1827, 2004.

[100] C. Wilhelm, C. Billotey, J. Roger, J. N. Pons, J. C. Bacri, and F. Gazeau, "Intracellular uptake of anionic superparamagnetic nanoparticles as a function of their surface coating," *Biomaterials*, vol. 24, no. 6, pp. 1001–1011, 2003.

[101] A. K. Gupta, C. Berry, M. Gupta, and A. Curtis, "Receptor-mediated targeting of magnetic nanoparticles using insulin as a surface ligand to prevent endocytosis," *IEEE Transactions on Nanobioscience*, vol. 2, no. 4, pp. 255–261, 2003.

[102] R. M. Schiffelers, A. Ansari, J. Xu et al., "Cancer siRNA therapy by tumor selective delivery with ligand-targeted sterically stabilized nanoparticle," *Nucleic Acids Research*, vol. 32, no. 192, p. 10, 2004.

[103] O. C. Farokhzad and R. Langer, "Impact of nanotechnology on drug delivery," *American Chemical Society Nano*, vol. 3, pp. 16–20, 2010.

[104] H. Zhang, M. Y. Lee, M. G. Hogg, J. S. Dordick, and S. T. Sharfstein, "Gene delivery in three-dimensional cell cultures by superparamagnetic nanoparticles," *American Chemical Society Nano*, vol. 4, no. 8, pp. 4733–4743, 2010.

[105] P. O. Rujitanaroj, Y. C. Wang, J. Wang, and S. Y. Chew, "Nanofiber-mediated controlled release of siRNA complexes

for long term gene-silencing applications," *Biomaterials*, vol. 32, no. 25, pp. 5915–5923, 2011.

[106] W. Y. Lee, W. Y. Cheng, Y. C. Yeh et al., "Magnetically directed self-assembly of electrospun superparamagnetic fibrous bundles to form three-dimensional tissues with a highly ordered architecture," *Tissue Engineering*, vol. 17, no. 6, pp. 651–661, 2011.

[107] D. J. Bharali and S. A. Mousa, "Emerging nanomedicines for early cancer detection and improved treatment: current perspective and future promise," *Pharmacology & Therapeutics*, vol. 128, no. 2, pp. 324–335, 2010.

[108] M. G. Harisinghani, M. A. Saksena, P. F. Hahn et al., "Ferumoxtran-10-enhanced MR lymphangiography: does contrast-enhanced imaging alone suffice for accurate lymph node characterization?" *American Journal of Roentgenology*, vol. 186, no. 1, pp. 144–148, 2006.

[109] R. Sharma, S. Saini, P. R. Ros et al., "Safety profile of ultrasmall superparamagnetic iron oxide ferumoxtran-10: phase II clinical trial data," *Journal of Magnetic Resonance Imaging*, vol. 9, no. 2, pp. 291–294, 1999.

[110] W. M. L. L. G. Deserno, M. G. Harisinghani, M. Taupitz et al., "Urinary bladder cancer: preoperative nodal staging with ferumoxtran-10-enhanced MR imaging," *Radiology*, vol. 233, no. 2, pp. 449–456, 2004.

[111] H. Vu-Quang, H. Muthiah, H. J. Lee et al., "Immune cell-specific delivery of beta-glucan-coated iron oxide nanoparticles for diagnosing liver metastasis by MR imaging," *Carbohydrate Polymers*, vol. 87, pp. 1159–1168, 2012.

[112] S. Haque and G. R. Fuhr, "New system for real time study of *in vivo* migration and differentiation of stem cells," *Microsystem Technologies*, vol. 17, no. 1, pp. 47–58, 2011.

[113] A. Floris, A. Ardu, A. Musinu et al., "SPION@liposomes hybrid nanoarchitectures with high density SPION association," *Soft Matter*, vol. 7, no. 13, pp. 6239–6247, 2011.

Hindawi Publishing Corporation
Journal of Nanomaterials
Volume 2012, Article ID 469372, 7 pages
doi:10.1155/2012/469372

Research Article

Effect of Orally Administered Glutathione-Montmorillonite Hybrid Systems on Tissue Distribution

Miri Baek and Soo-Jin Choi

Department of Food Science and Technology, Seoul Women's University, Seoul 139-774, Republic of Korea

Correspondence should be addressed to Soo-Jin Choi, sjchoi@swu.ac.kr

Received 13 February 2012; Accepted 12 April 2012

Academic Editor: Haifeng Chen

An ubiquitous tripeptide, glutathione (GSH), is assigned a role in detoxification, activation of immune system, intermediary metabolism, transport, and protection of cells against free radicals or reactive oxygen species. However, instability of orally administered GSH in gastrointestinal (GI) tract leads to low absorption and low bioavailability in tissues. In this study, we attempted to synthesize GSH-montmorillonite (MMT) hybrid systems by intercalating GSH into the interlayers of a cationic clay delivery carrier, MMT, to improve GSH bioavailability at the systemic level. Polymer coating of the hybrid with polyvinylacetal diethylaminoacetate (AEA) was further performed to obtain better stability. Synthetic condition of both GSH-MMT and AEA-GSH-MMT hybrids was optimized, and then GSH-delivery efficiency was evaluated in various organs after oral administration in normal as well as GSH-deficient mice. The present GSH-MMT hybrids remarkably enhanced GSH concentration in the plasma, heart, kidney, and liver, especially when AEA-GSH-MMT hybrid was administered under GSH-deficient condition. Moreover, both hybrids did not induce acute oral toxicity up to 2000 mg/kg, suggesting their great potential for pharmaceutical application.

1. Introduction

GSH (L-glutamyl-L-cysteinylglycine) is the most abundant low molecular thiol compound widely present in living plants and animals [1]. GSH is an important substance involved in a wide range of biological functions such as metabolism, catalysis, amino acid transport, cysteine-reservoir, detoxification, and removal of free radicals [2, 3]. It also plays a role in many cellular events by modulating redox-regulated cellular signal transduction and regulating cell proliferation, protein/gene expression, and immune response via thiol-disulfide exchange reaction [4–6]. It was also suggested that GSH may be implicated in cancer prevention [7]. Thus, GSH deficiency induces oxidative stress, which is implicated in the pathogenesis of many diseases including Alzheimer', Parkinson's, acute respiratory, ocular and liver diseases, AIDS, and heart attack. In particular, GSH depletion was reported to be closely associated with increased virus replication in HIV-positive patients [8–10]. GSH can be absorbed intact from the intestinal lumen, taken up by enterocytes and finally released into the blood stream [11]. However, most of orally ingested GSH tends to be rapidly degraded to free amino acids by both chemical and enzymatic hydrolysis such as γ-glutamyl-transpeptidase and γ-glutamyl-cyclotransferase, leading to low absorption rate during GI transit [12, 13]. Moreover, the thiol group of GSH can be easily oxidized both enzymatically and nonenzymatically under intestinal condition, forming glutathione disulfide (GSSG) which is devoid of antioxidant activity [14].

The aim of this study was, therefore, to enhance the bioavailability of oral GSH *in vivo* by developing a novel delivery system in which GSH was intercalated into the layers of a cationic clay, MMT. It is a type of smectite clay mineral composed of structural units of silica tetrahedral sheets with a central alumina octahedral sheet. Its unique structure gives rise to having large specific surface area, adsorption ability, cation exchange capacity (CEC), and adhesive ability, which are attractive properties as a delivery carrier, leading to intercalate labile molecule into the interlayer spaces via ion

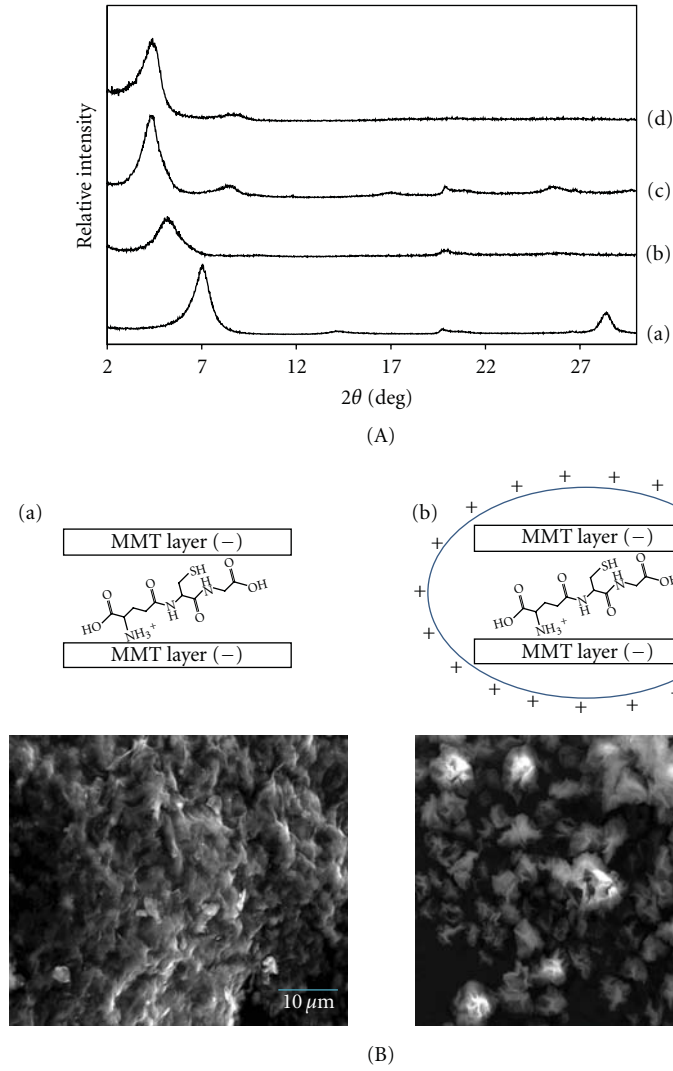

Figure 1: PXRD patterns (A) of pristine MMT, (a) GSH-MMT hybrid (CEC1), (b) GSH-MMT hybrid (CEC2), and (c) GSH-MMT hybrid (CEC3). (d) Schematic diagram and SEM images (B) of GSH-MMT hybrid (a) and AEA-GSH-MMT hybrid (b).

exchange reaction [15]. It was also reported that MMT has low toxicity and favorable kinetic behaviors in terms of no accumulation into specific tissues and rapid clearance from the body [16]. In our previous study, we were successful to develop both GSH-MMT and AEA-GSH-MMT hybrid systems [17]. The latter was obtained by polymer coating of the former with positively charged AEA for better stability at the systemic level, demonstrating that the latter significantly enhanced pharmacokinetic behaviors of GSH in mice by enhancing absorption amount and prolonging circulation time [17].

In the present study, we optimized the synthetic condition and evaluated the efficacy of GSH-MMT and AEA-GSH-MMT hybrids, focusing on tissue distribution in normal as well as GSH-deficient mice. Moreover, the acute oral toxicity of both hybrid systems was assessed in mice to provide practical information for their pharmaceutical application.

2. Materials and Methods

2.1. Materials. Na^+-MMT with a CEC of 0.7–1.1 mequiv./g and AEA were supplied by Sigma-Aldrich (St. Louis, Mo, USA) and Sankyo (Tokyo, Japan), respectively. GSH and all the other reagents of high purity were purchased from Sigma-Aldrich.

2.2. Preparation of GSH-MMT Hybrids. GSH-MMT hybrid was prepared as follow; 10 g of Na^+-MMT was dispersed in 900 mL of deionized water and vigorously stirred for 4 h at room temperature. The various ratios of GSH compared with 10 g of MMT (1-, 2- and 3-fold of CEC) were dissolved in 100 mL of deionized water (pH value adjusted to 2.0 with HCl) and added to MMT suspension. The final pH of the GSH and MMT mixture solution was adjusted to 2.0 by addition of HCl solution. Thus, prepared suspension

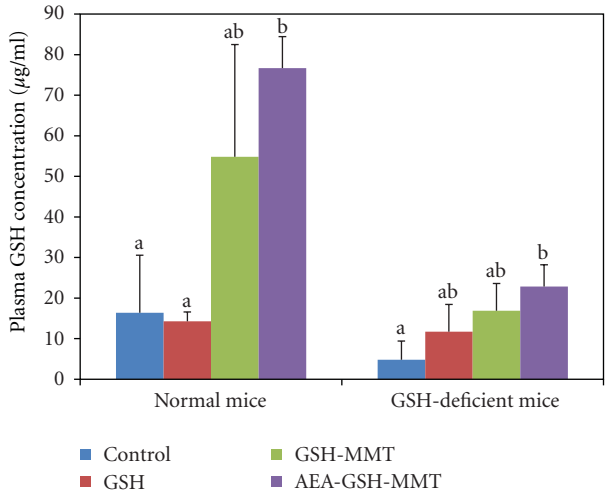

FIGURE 2: GSH concentration in the plasma at 1 h postoral administration of free GSH, GSH-MMT hybrid, or AEA-GSH-MMT hybrid in normal as well as GSH-deficient mice. Different letters indicate a significant difference based on ANOVA and Tukey's test ($P < 0.05$).

was stirred at room temperature overnight and finally the resulting product was freeze-dried. To obtain polymer coated GSH-MMT hybrid, the prepared GSH-MMT hybrid was redispersed in 800 mL of ethanol solution and 10 g of AEA in 100 mL of methylene chloride (MC) was then added. The final AEA-GSH-MMT hybrid was spray dried (EYLA spray dryer SD-1000, Tokyo, Japan) under the following conditions: atomizing pressure, 130 kPa; blower speed, 0.30 m^3/min; inlet temperature, 80°C; outlet temperature 40–50°C.

2.3. Characterization of GSH-MMT Hybrids. The prepared GSH-MMT hybrids were characterized by powder X-ray diffraction (PXRD) using a diffractometer (Rigaku D/MAX RINT 2200-Ultima+, Japan) with Ni-filtered CuKα radiation (λ = 1.5418 Å, voltage of 40 kV, a current of 30 mA, and a scanning rate of 2°/min). The morphology of the hybrids was observed by scanning electron microscopy (SEM; MIRA FE-SEM, Teskan).

2.4. Animal and Diets. Male ICR mice, aged 5.5 weeks and weighing 24 ± 1 g, were purchased from the G-Bio (Seoul, Republic of Korea). The animals were housed in plastic lab animal cages in a ventilated room. The room was maintained at 20 ± 2°C and 60 ± 10% relative humidity with a 12 h light/dark cycle. Water and commercial laboratory complete food for mice were available *ad libitum*. They were acclimated to this environment for 7 days before treatment. GSH-deficient mouse model was induced by pretreatment with the GSH synthesis inhibitor, L-buthionine-S, R-sulfoximine (BSO, 20 mM via drinking water), for 5 days [18]. All animal experiments were performed in compliance with the Animal and Ethnics Review Committee of the Seoul Women's University.

2.5. Plasma Concentration. The plasma concentration of GSH was analyzed after oral administration of GSH or the hybrids in normal and GSH-deficient mice, respectively. Each group of three mice was administrated via oral gavage with 100 mg/kg of free GSH or equivalent amount of the hybrids on the basis of GSH content from the hybrids. Another three mice group administered with 0.9% saline was used as a control group. The blood samples were collected via orbital sinus at 1 h postoral administration and then centrifuged at 3 000 rpm for 15 min at 4°C to obtain the plasma and stored at −70°C before analysis. The proteins in the plasma were precipitated by adding 4 volumes of acetonitrile, followed by vortexing for 20 sec and centrifuging at 10 000 rpm for 10 min at 4°C. The supernatant was then filtered by a nylon membrane with a pore size of 0.45 μm (Whatman, UK), and GSH concentration was then measured by high-performance liquid chromatography (HPLC) using an LC10-ADVP series (Shimadzu Co., Japan) on a Discovery RP-Amide 16 column (150 × 4.6 mm, 5 μm; Sigma, USA). The mobile phase was 50 mM $NaClO_4$ 0.1% H_3PO_4, and flow rate was set to 1 mL/min. Column temperature was maintained at 40°C, and detection of GSH was performed at 215 nm by UV detector [19].

2.6. Tissue Distribution. To evaluate delivery efficiency of GSH to organs, tissue samples such as brain, heart, kidney, liver, lung and intestine were collected at 1 h post-oral administration. The same doses used for plasma concentration measurement were orally administered to each group of three mice. 100 mg of each tissue were homogenized with the mixture of 3 mL 10 mM EDTA, 50 mM $NaClO_4$ and 0.1% H_3PO_4 buffer, followed by addition of 0.5% metaphosphoric acid for protein precipitation. The samples were vortexed for 20 sec, centrifuged at 10 000 rpm at 4°C and then analyzed by HPLC as described above.

2.7. Acute Toxicity. Acute oral toxicity of free GSH, GSH-MMT hybrid, and AEA-GSH-MMT hybrid was evaluated according to the OECD guideline 423. Prior to administration, food was withheld for 4 h, but water was available *ad libitum*. Three mice were orally administrated with four different concentrations of the samples (5, 50, 300, and 2000 mg/kg). Group of three mice, receiving identical volume of 0.9% saline, was served as a control. During 14 days, body weight change, symptoms, and mortality of mice treated with free GSH, GSH-MMT hybrid, or AEA-GSH-MMT hybrid were daily recorded.

2.8. Statistical Analysis. The data were expressed as means ± standard deviation. For statistical analysis, the experimental values were compared with their corresponding control ones. A one-way analysis of variance (ANOVA) in SAS software (Tukey's test, version 11.0) was used to illustrate the significant difference between the experimental group and the control. The statistical significance for all tests was set at $P < 0.05$.

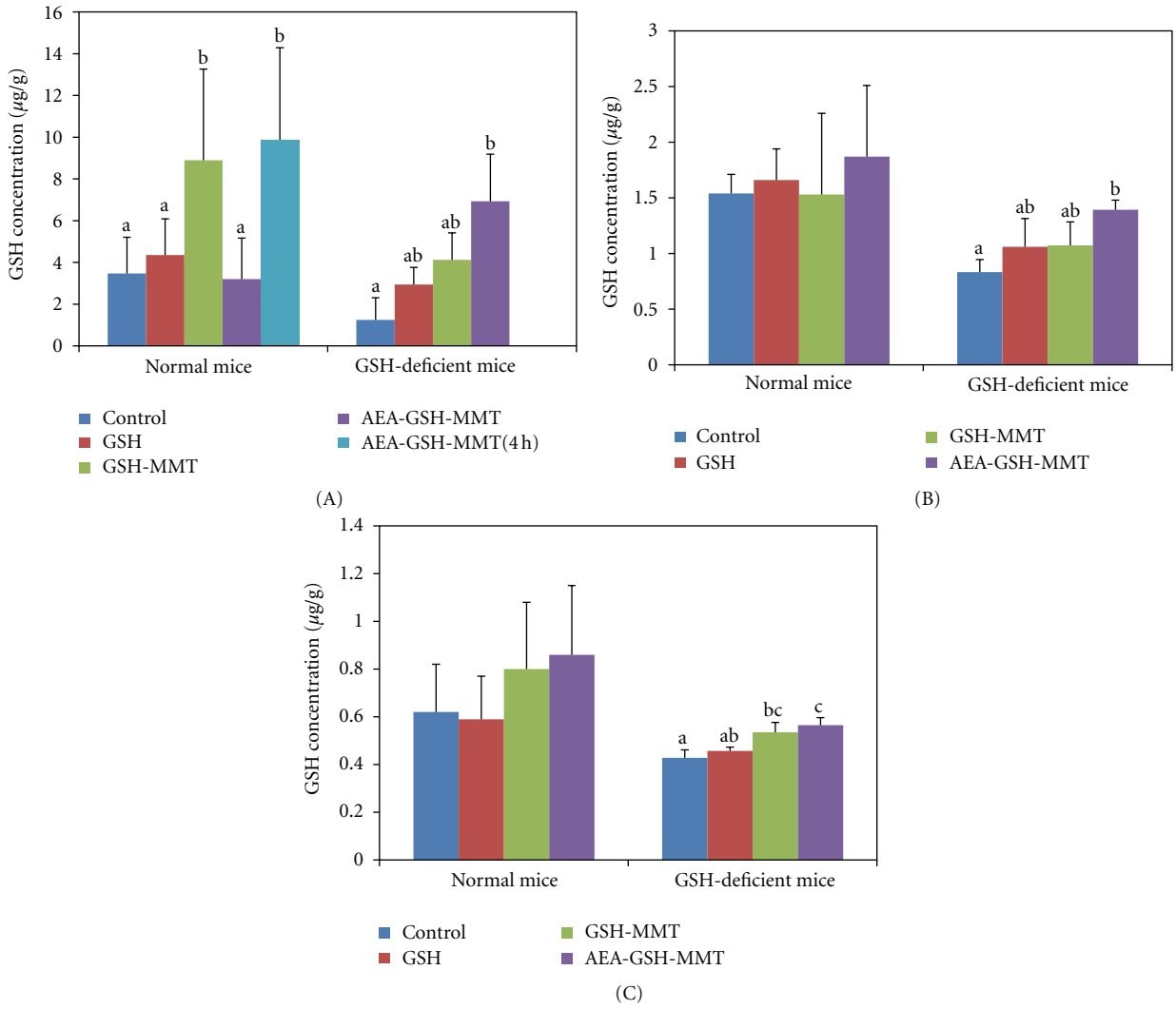

Figure 3: GSH concentration in the liver (A), heart (B), and kidney (C) at 1 h postoral administration of free GSH, GSH-MMT hybrid, or AEA-GSH-MMT hybrid in normal as well as GSH-deficient mice. Different letters indicate a significant difference based on ANOVA and the Tukey's test ($P < 0.05$).

3. Results and Discussions

3.1. Characterization. In order to synthesize GSH-MMT hybrid systems, we attempted to intercalate protonated GSH into the negatively charged Na^+-MMT layers at pH 2.0 by cation exchange reaction and optimized the synthetic condition by adding variouss ratio of GSH in comparison with MMT. Figure 1(A) showed the PXRD pattern of MMT and GSH-MMT hybrids, synthesized with 1- (CEC1-), 2- (CEC2-) and 3- (CEC3-) fold of CEC. The characteristic 2θ peaks for MMT, GSH-MMT hybrid (CEC1), GSH-MMT hybrid (CEC2), and GSH-MMT hybrid (CEC3) were found at 7.04°, 5.40°, 4.34°, and 4.24°, and d-spacing were calculated to be 12.54 Å, 16.35 Å, 20.34 Å and 20.82 Å, respectively, upon molecular size of interlayer GSH according to the Bragg's law. The peak shifting from higher diffraction angle to lower one is resulted from increased the d-spacing, indicating successful interaction of GSH into the interlayer spaces of MMT. In addition, the 2θ peak was not further shifted to lower one, and d-spacing did not remarkably increase even when CEC3 was added, suggesting that 2-fold of CEC was optimum to synthesize the hybrid system. Schematic diagram for pristine MMT and GSH-MMT hybrid showed that GSH was expected to be intercalated into MMT layers in a monomer form and stabilized by electrostatic interaction, on the basis of XRD pattern (Figure 1(A)). The hybrid was also coated with a basic polymer, AEA, for better stability *in vivo*, because positively charged AEA polymer under synthetic condition can further stabilize the hybrid by electrostatic interaction. SEM images of the hybrids showed different morphology between GSH-MMT and AEA-GSH-MMT hybrid systems (Figure 1(B)). The particle size of GSH-MMT hybrid was determined to be about 1 μm, probably resulted from the size of MMT itself [20]. On the other hand, the particle size of GSH-MMT hybrid further increased after polymer coating as shown in Figure 1(B)(b). This result suggests that

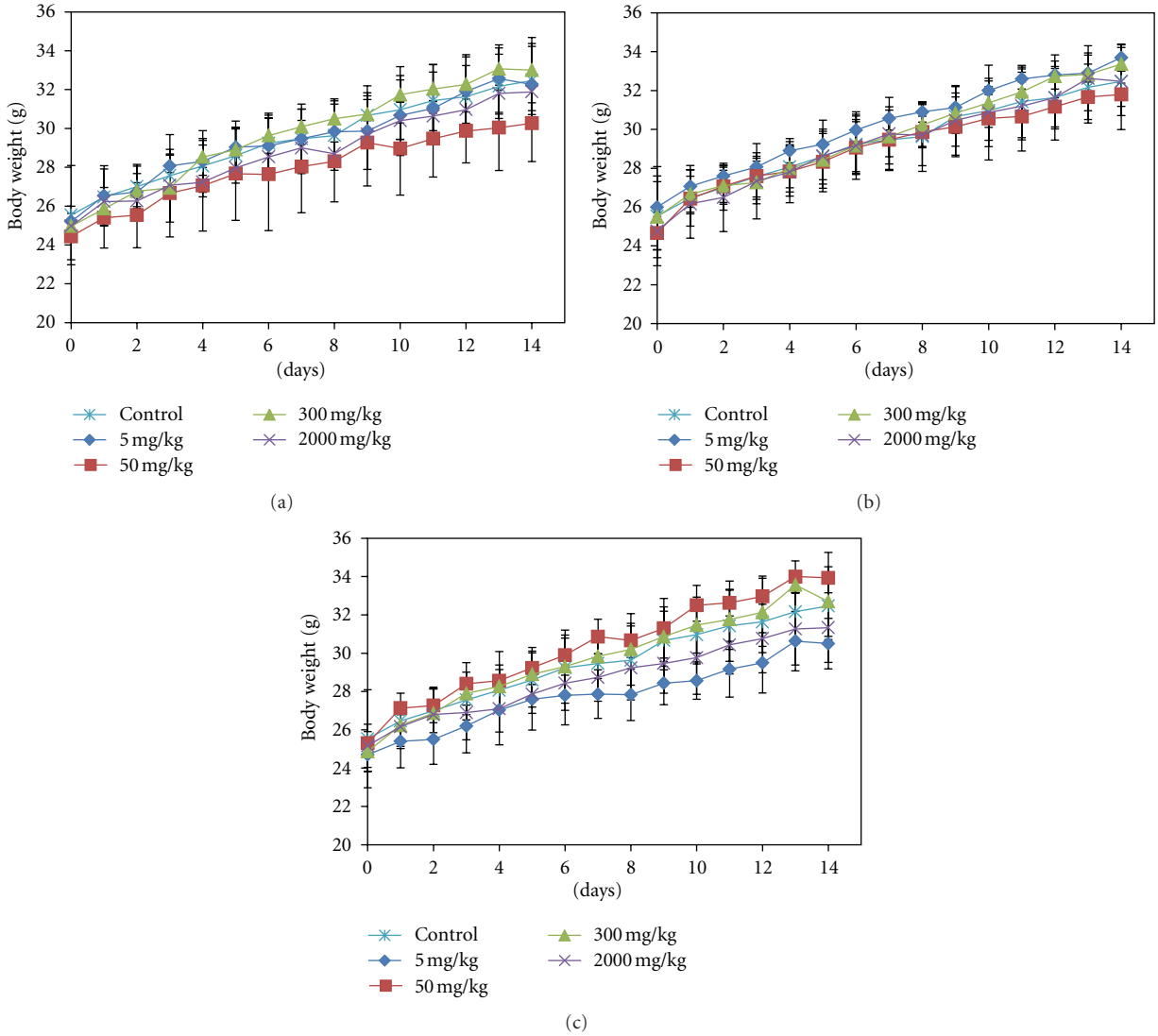

Figure 4: Change in body weight in mice treated with different doses of GSH (a), GSH-MMT hybrid (b), or AEA-GSH-MMT hybrid (c) during 14 days. Single-dose administration was performed by oral gavage. All treated groups showed statistically no significant differences from the control group ($P < 0.05$).

polymer AEA coating of GSH-MMT hybrid was successfully and uniformly performed.

3.2. Plasma Concentration. To evaluate absorption efficiency of both hybrid systems in GSH-deficient mouse model, mice were pretreated with the GSH synthesis inhibitor, L-BSO, via drinking water for 5 days. BSO is a well-known inhibitor for GSH synthesis by inhibiting specifically and irreversibly γ-glutamyl-cysteine synthetase (γ-GCS), the rate-limiting enzyme involved in GSH synthesis process [21]. After 1 h oral administration of free GSH and GSH-MMT hybrids in normal and GSH-deficient mice, respectively, the plasma samples were analyzed, since our previous study demonstrated that GSH concentration reached the highest level at 1 h after administration of the hybrids [17]. Figure 2 clearly demonstrated that GSH concentration in the plasma significantly decreased in GSH-deficient control mouse model compared with normal control group, confirming successful inhibition of GSH synthesis. Both hybrids significantly increased GSH level in the plasma in normal as well as in GSH-deficient mice. Interestingly, AEA-GSH-MMT hybrid greatly increased the plasma GSH level under both conditions (4.69-fold and 4.75-fold in normal and deficient mice, resp.), suggesting high absorption efficiency of the hybrid system. It is likely that high efficacy of AEA-GSH-MMT hybrid system *in vivo* is closely related to its high structural stability resulted from AEA coating.

3.3. Tissue Distribution. Several tissues such as brain, heart, kidney, liver, lung, and intestine were also collected after oral administration of the hybrids in normal as well as GSH-deficient mice to evaluate biodistribution and delivery

efficiency of the hybrids to organs. Figure 3 showed that GSH level significantly increased only in the liver when both hybrids were orally administered under normal condition. It is worth noting here that AEA-GSH-MMT hybrid increased GSH level in the liver after 4 h in comparison with GSH-MMT hybrid at 1 h after treatment (Figure 3(A)), which can be explained by controlled release property of the former due to AEA coating. Lower GSH level in GSH-deficient control mice than that in normal mice was observed in all the tissues, confirming successful induction of the deficient model. Whereas, GSH concentration remarkably increased in the liver, heart, and kidney in GSH-deficient mice, especially receiving AEA-GSH-MMT hybrid. Any significant difference in GSH level between treated and untreated control group was not found in the other organs (data not shown). This result clearly suggests that the hybrid systems enhanced GSH delivery efficiency to various organs and can be more effective under GSH-deficient condition. Therefore, we can expect enhanced pharmaceutical effect of the hybrid systems compared with free GSH intake alone.

3.4. Acute Toxicity. To ensure safety aspect of the hybrid systems and provide critical information about their toxicity potential, the acute oral toxicity of free GSH and GSH-MMT hybrids was evaluated in mice after single dose administration of four different doses (5, 50, 300, and 2000 mg/kg). Any remarkable abnormal behaviors, symptoms, and body weight loss were not observed in mice treated with free GSH or GSH-MMT hybrids during 14 days after administration (Figure 4). The LD_{50} values of free GSH and GSH-MMT hybrids, were estimated to be more than 2000 mg/kg on the basis of the fact that no mortality was found in all the mice treated with different doses. This result is in good agreement with our previous result, showing low acute oral toxicity of MMT delivery carrier *in vivo* [16]. Now, we are evaluating the morphological and histopathological changes to ascertain their toxicity potential.

4. Conclusion

In this study, we have successfully intercalated a powerful antioxidant, GSH into the interlayer spaces of MMT and obtained two different hybrid systems, GSH-MMT hybrid and AEA-GSH-MMT hybrid, respectively. The synthetic condition was further optimized by using different ratios of GSH compared with MMT. Both GSH-MMT and AEA-GSH-MMT hybrids significantly enhanced the absorption amount of GSH under both normal and GSH-deficient conditions as indicated by increased plasma GSH concentration. Tissue distribution study demonstrated that both hybrids increased GSH level only in the liver in normal mice, while high GSH concentration was found in the liver, heart, and kidney in GSH-deficient mouse model. Delivery efficiency of GSH to organs was more effective when AEA-GSH-MMT hybrid was orally administered, especially under GSH-deficient condition. Moreover, both the hybrid systems do not seem to induce acute oral toxicity. Therefore, all the results suggest that GSH-MMT hybrid systems will be promising candidates to enhance absorption and delivery efficiency of oral GSH, providing new insight into their pharmaceutical application in GSH-deficient patients.

Acknowledgments

This paper was supported by Basic Science Research Program through the National Research Foundation of Korea (NRF) funded by the Ministry of Education, Science and Technology (2011-0003755), and partly by National Research Foundation of Korea Grant funded by the Korean Government (SRC Program: 2012-0000650).

References

[1] H. Sies, "Glutathione and its role in cellular functions," *Free Radical Biology and Medicine*, vol. 27, no. 9-10, pp. 916–921, 1999.

[2] E. Brzezinska-Ślebodzinska, A. B. Ślebodzinski, B. Pietras, and G. Wieczorek, "Antioxidant effect of vitamin E and glutathione on lipid peroxidation in boar semen plasma," *Biological Trace Element Research*, vol. 47, no. 1–3, pp. 69–74, 1995.

[3] L. Milne, P. Nicotera, S. Orrenius, and M. J. Burkitt, "Effects of glutathione and chelating agents on copper-mediated DNA oxidation: pro-oxidant and antioxidant properties of glutathione," *Archives of Biochemistry and Biophysics*, vol. 304, no. 1, pp. 102–109, 1993.

[4] P. Li, Y. L. Yin, D. Li, W. S. Kim, and G. Wu, "Amino acids and immune function," *British Journal of Nutrition*, vol. 98, no. 2, pp. 237–252, 2007.

[5] I. A. Cotgreave and R. G. Gerdes, "Recent trends in glutathione biochemistry-glutathione-protein interactions: a molecular link between oxidative stress and cell proliferation?" *Biochemical and Biophysical Research Communications*, vol. 242, no. 1, pp. 1–9, 1998.

[6] W. Dröge, V. Hack, R. Breitkreutz et al., "Role of cysteine and glutathione in signal transduction, immunopathology and cachexia," *BioFactors*, vol. 8, no. 1-2, pp. 97–102, 1998.

[7] S. Gerald, S. Joel, T. Diane, and R. C. Susan, "The effectiveness of a mixture of β-carotene, α-tocopherol, glutathione, and ascorbic acid for cancer prevention," *Nutrition and Cancer*, vol. 20, no. 2, pp. 145–151, 1993.

[8] L. A. Herzenberg, S. C. De Rosa, J. G. Dubs et al., "Glutathione deficiency is associated with impaired survival in HIV disease," *Proceedings of the National Academy of Sciences of the United States of America*, vol. 94, no. 5, pp. 1967–1972, 1997.

[9] J. D. Peterson, L. A. Herzenberg, K. Vasquez, and C. Waltenbaugh, "Glutathione levels in antigen-presenting cells modulate Th1 versus Th2 response patterns," *Proceedings of the National Academy of Sciences of the United States of America*, vol. 95, no. 6, pp. 3071–3076, 1998.

[10] F. Jahoor, A. Jackson, B. Gazzard et al., "Erythrocyte glutathione deficiency in symptom-free HIV infection is associated with decreased synthesis rate," *American Journal of Physiology*, vol. 276, no. 1, pp. E205–E211, 1999.

[11] T. M. Hagen, G. T. Wierzbicka, B. B. Bowman, T. Y. Aw, and D. P. Jones, "Fate of dietary glutathione: disposition in the gastrointestinal tract," *American Journal of Physiology*, vol. 259, no. 4, pp. G530–G535, 1990.

[12] A. Witschi, S. Reddy, B. Stofer, and B. H. Lauterburg, "The systemic availability of oral glutathione," *European Journal of Clinical Pharmacology*, vol. 43, no. 6, pp. 667–669, 1992.

[13] M. E. Anderson, R. J. Bridges, and A. Meister, "Direct evidence for inter-organ transport of glutathione and that the non-filtration renal mechanism for glutathione utilization involves γ-glutamyl transpeptidase," *Biochemical and Biophysical Research Communications*, vol. 96, no. 2, pp. 848–853, 1980.

[14] T. Y. Aw, "Intestinal glutathione: determinant of mucosal peroxide transport, metabolism, and oxidative susceptibility," *Toxicology and Applied Pharmacology*, vol. 204, no. 3, pp. 320–328, 2005.

[15] A. Fudala, I. Palinko, and I.s Kiricsi, "Preparation and characterization of hybrid organic-inorganic composite materials using the amphoteric property of amino acids: amino acid intercalated layered double hydroxide and montmorillonite," *Inorganic Chemistry*, vol. 38, no. 21, pp. 4653–4658, 1999.

[16] M. Baek, J. A. Lee, and S. J. Choi, "Toxicological effects of cationic clays in vitro and in vivo," *Molecular & Cellular Toxicolgy*, vol. 8, no. 1, pp. 95–101, 2012.

[17] M. Baek, J. H. Choi, and S. J. Choi, "Montmorillonite intercalated with glutathione for antioxidant delivery: synthesis, characterization, and bioavailability evaluation," *International Journal of Pharmaceutics*, vol. 425, no. 1-2, pp. 29–34, 2012.

[18] T. Y. Aw, G. Wierzbicka, and D. P. Jones, "Oral glutathione increases tissue glutathione in vivo," *Chemico-Biological Interactions*, vol. 80, no. 1, pp. 89–97, 1991.

[19] Ö. Yilmaz, S. Keser, M. Tuzcu et al., "A practical HPLC method to measure reduced (GSH) and oxidized (GSSG) glutathione concentrations in animal tissues," *Journal of Animal and Veterinary Advances*, vol. 8, no. 2, pp. 343–347, 2009.

[20] A. Cadene, S. Durand-Vidal, P. Turq, and J. Brendle, "Study of individual Na-montmorillonite particles size, morphology, and apparent charge," *Journal of Colloid and Interface Science*, vol. 285, no. 2, pp. 719–730, 2005.

[21] T. Watanabe, H. Sagisaka, S. Arakawa et al., "A novel model of continuous depletion of glutathione in mice treated with L-Buthionine (S,R)-sulfoximine," *Journal of Toxicological Sciences*, vol. 28, no. 5, pp. 455–469, 2003.

Hindawi Publishing Corporation
Journal of Nanomaterials
Volume 2012, Article ID 631584, 7 pages
doi:10.1155/2012/631584

Research Article

Bifunctional Silica-Coated Superparamagnetic FePt Nanoparticles for Fluorescence/MR Dual Imaging

Syu-Ming Lai,[1] Tsiao-Yu Tsai,[1] Chia-Yen Hsu,[1] Jai-Lin Tsai,[2] Ming-Yuan Liao,[1] and Ping-Shan Lai[1]

[1] *Department of Chemistry, National Chung Hsing University, 250 Kuo Kuang Road, Taichung 402, Taiwan*
[2] *Department of Materials Science and Engineering, National Chung Hsing University, 250 Kuo Kuang Road, Taichung 402, Taiwan*

Correspondence should be addressed to Ping-Shan Lai, pslai@email.nchu.edu.tw

Received 14 January 2012; Revised 26 March 2012; Accepted 26 March 2012

Academic Editor: Krasimir Vasilev

Recently, superparamagnetic chemically disordered face-centered cubic (fcc) FePt nanoparticles have been demonstrated as superior negative contrast agents for magnetic resonance imaging (MRI). However, their low intracellular labeling efficiency has limited the potential usage and the nanotoxicity of the particles requires attention. We have developed fluorescein isothiocyanate-incorporated silica-coated FePt (FePt@SiO_2-FITC) nanoparticles that exhibited not only a significant T_1 and T_2 MR contrast abilities but also a fluorescent property without significant cytotoxicities. These results suggest that silica-coated superparamagnetic FePt nanoparticles are potential nanodevices for the combination of fluorescence and MRI contrast used for cancer diagnosis.

1. Introduction

Superparamagnetic iron oxide (SPIO) nanoparticles have demonstrated their practicability as MRI T_2-shortening agents for noninvasive cell labeling, drug delivery or tumor detections in clinical practice [1, 2]. However, low intracellular labeling efficiency and nanotoxicity of SPIO has limited their potential usage [3, 4]. Recently, bifunctional contrast agents for both optical and MR imaging have been developed to function as good imaging probes *in vitro* and *in vivo* [5–8] and the nanotoxicity of SPIO is suppressed by particular surface modification [9]. Thus, proper modifications of SPIO have been considered as a promising strategy to improve the aforementioned problems.

Long-range ordered $L1_0$ FePt films have been studied extensively and thought to be a promising candidate for ultrahigh-density magnetic recording media due to its high magnetocrystalline anisotropy (K_u). The magnetization thermal instability or superparamagnetic effect is delayed due to their very small critical grain size of around (3–5 nm). However, when FePt nanoparticles are disordered with face-centered cubic (fcc) structure, they exhibit superparamagnetic property under critical size. Superparamagnetic iron-platinum (FePt) nanoparticles, which show high saturation magnetization (M_S) compared to SPIO, are expected to be a high performance nanomagnet for magnetic medicine [10, 11]. In particular, the potential of FePt nanoparticles as an MRI contrast agent has been demonstrated [12]. Thus, the bifunctional contrast agent using superparamagnetic FePt nanoparticles seems to be a promising dual-modality biomedical detections material. In our strategy, silica was selected for surface coating of FePt nanoparticles to enhance the biocompatibility and easier modifications for bioconjugation or cell targeting [13]. Moreover, fluorescent dyes can be easily incorporated into a silica shell that provides a powerful tool for intracellular tracking [14]. Hence, the bifunctional fluorescein-isothiocyanate-(FITC-) incorporated silica-coated superparamagnetic FePt (FePt@SiO_2-FITC) nanoparticles were synthesized and their potential applications for dual fluorescent/magnetic imaging in this study were evaluated.

2. Experimental Procedure

2.1. Materials. For materials preparation, iron pentacarbonyl ($Fe(CO)_5$, 99.99%), platinum(II) acetylacetonate

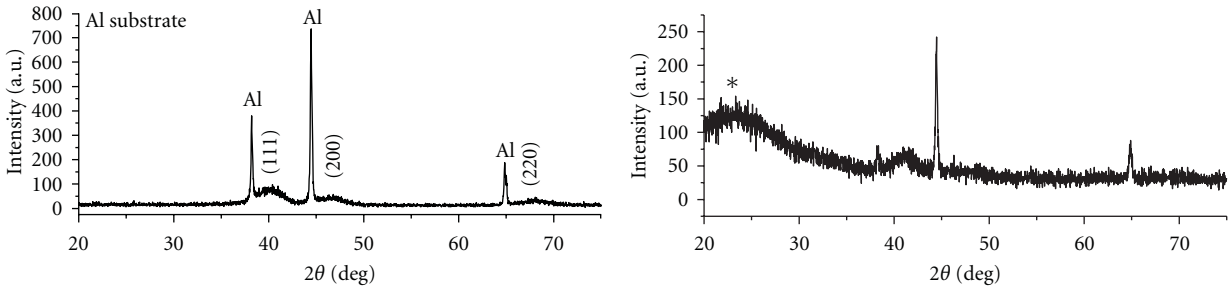

(a) FePt (b) FePt@SiO_2-FITC

Figure 1: XRD patterns of FePt and FePt@SiO_2-FITC nanoparticles.

($Pt(acac)_2$, 97%, 1,2-hexadecanediol, florescence isocyanate (FITC), 3-Aminopropyltrimethoxysilane (APTMS, 97%), Triton X100, hexanol, and benzyl ether were purchased from Sigma-Aldrich (St. Louis, MO, USA). Oleylamine (80–90%) was obtained from Acros (New Jersey, USA). Oleic acid and tetraethyl silicate (TEOS, 99.9%) were obtained from Showa (Tokyo, Japan). The ethanol (99.5%) and hexane were purchased from Echo in Taiwan. The solvents were all dehydrated prior to use.

For cell culture studies, sodium phosphate dibasic (Na_2HPO_4) and sodium chloride (NaCl) were obtained from Tedia (OH, USA). Potassium chloride (KCl), potassium dihydrogenphosphate (KH_2PO_4), and sodium bicarbonate ($NaHCO_3$) were obtained from Showa (Tokyo, Japan). Modified Eagle's Medium (MEM), fetal bovine serum (FBS), and 0.25% trypsin-EDTA were purchased from Gibco (Gibco-BRL, USA). The penicillin-streptomycin-neomycin solution and 10% formalin were purchased from Sigma-Aldrich (St. Louis, MO, USA). Double distilled water was used in all of the aqueous solutions.

2.2. Synthesis of FePt Nanoparticles. The synthesis of fcc FePt nanoparticles involving simultaneous chemical reduction of $Pt(acac)_2$ and $Fe(CO)_5$ by 1,2-hexadecanediol at high temperature was described as previous report [15]. Briefly, $Pt(acac)_2$ (0.48 mmol) was dissolved in 10 mL of benzyl ether and the solution was heated to 100°C under nitrogen atmosphere. The surfactants of oleylamine (0.5 mmol) and oleic acid (0.5 mmol) were added into the reaction and subsequently the $Fe(CO)_5$ (1 mmol) was injected. The mixture solution was then heated to 297°C under refluxing for 30 minutes. Finally, the reaction system was cooled down to room temperature and the FePt nanoparticles were purified using ethanol washing and then collected by centrifugation.

2.3. Synthesis of Silica-Coated FePt Nanoparticles. The bifunctional magnetic silica-coated FePt (FePt@SiO_2) nanoparticles were synthesized by a water-in-oil microemulsion method as previous reports [13, 16]. First, the *N*-1-(3-triethoxysilylpropyl)-*N*-fluoresceyl thiourea (FITC-APTMS) was prepared by stirring 5 mg FITC in 5 mL ethanolic APTMS solution (10 v/v%) for 24 hours. The monodisperse hydrophobic FePt nanoparticles were also redissolved in cyclohexane at room temperature and Triton X-100, hexanol and distilled water were added into the solution with stirring to generate a microemulsion. Then the TEOS, APTMS, and FITC-labeled APTMS were added into the system to form the functional silica shell structure. The sol-gel growth of silica was limited in the water domain in this w/o microemulsion. All procedures were carried out in subdued light. To remove free surfactants and unreacted chemicals, the as-synthesized silica-coated FePt nanoparticles solution was centrifuged and washed with ethanol and deionized water. All procedures were repeated twice and the final silica-coated FePt nanoparticles were stored in deionized water for following experiments.

These FePt@SiO_2-FITC nanoparticles were evaluated by the X-ray diffraction (XRD), transmission electron microscope (TEM), vibration sample magnetometer (VSM), fluorescence spectroscopy, T_2 enhancing relaxivity, and determinate the iron content of FePt@SiO_2-FITC nanoparticles by inductively coupled plasma atomic emission spectroscopy (ICP-AES).

2.4. Characterizations of FePt Nanoparticles and FePt@SiO_2-FITC Nanoparticles. The FePt nanoparticles were further characterized by XRD (Bruker MXP-III) with a 2.0 kW Cu tube and a Sol-X energy dispersive detector. The XRD sample was mounted with Vaseline on a glass substrate, and the data were collected from 20°–80° 2θ (step size = 0.6° and time per step = 1s) at room temperature.

The size and morphologies were observed under the TEM (JEM 1200, JEOL Ltd., Japan). Samples for TEM analysis were prepared as dilute dispersions in hexane/water with a small amount of surfactants. The size distributions were evaluated by dynamic light scattering (DLS, ZS-90, Malvern).

The magnetic properties and performance were characterized by VSM. Magnetization curves as a function of applied field were measured with fields up to 1.2 kOe at room temperatures. The relaxation times (T_1 and T_2) were measured by NMR (300 MHz, Varian) at room temperature. The iron concentrations of samples were determined by ICP-AES (ICAP 9000, Jarrell-Ash, USA). The MRI images were all taken by the clinical 3T MR scanner (Signa Excite 3 T, GE Healthcare, USA).

The cytotoxicity of FePt and FePt@SiO_2-FITC nanoparticles was evaluated by MTT assay using human cervical

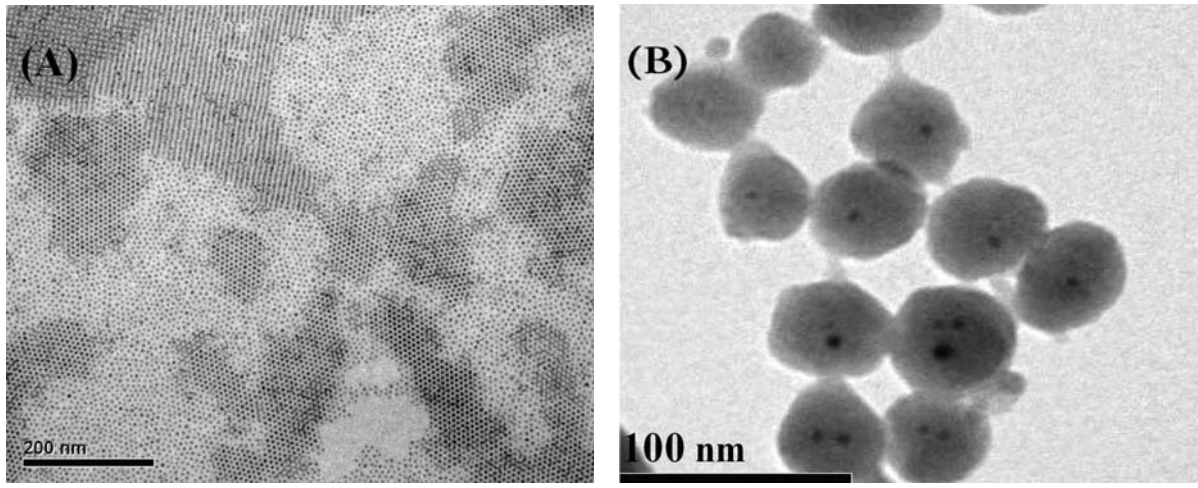

(a) (b)

Figure 2: The TEM images of (a) FePt and (b) FePt@SiO_2-FITC nanoparticles.

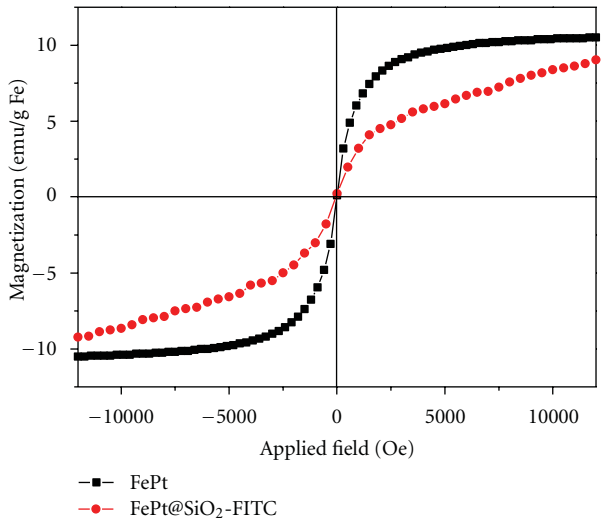

Figure 3: Room-temperature magnetization curves of FePt and FePt@SiO_2-FITC nanoparticles.

epithelioid carcinoma (HeLa) cells. The intracellular localization of FePt@SiO_2-FITC nanoparticles in HeLa cells was examined using a confocal microscope after costaining with LysoTracker Red (Invitrogen) as our previous report [17].

3. Results and Discussions

FePt nanoparticles were synthesized by heating the $Pt(acac)_2$ and $Fe(CO)_5$ precursors with the surfactants at 297°C for 30 minutes to form the black suspension. The as-synthesized FePt nanoparticles were washed and centrifuged for the following characterization and evaluations. Figure 1 showed the XRD patterns of oleic acid/oleylamine-capped FePt nanocrystals with or without the functionalized SiO_2 coating. It is known that the FePt nanoparticles were generated rapidly as the temperature rises from 250 to 297°C. Saita and Maenosono had also reported the effects of heating rate on the synthesized FePt nanoparticles [18]. Thus, we set the reaction temperature at 297°C for 30 min in this study to avoid formation of γ-Fe_2O_3 (or Fe_3O_4). As shown in Figure 1(a), the (111), (200), and (220) peaks of typical chemically disordered fcc-phase FePt crystallite without being annealed were evidently observed and there was no (311) peak observed around $2\theta = 35°$ [18–20]. These FePt nanocrystals were coated with SiO_2 using water-in-oil microemulsions method and NH_4OH was used to catalyze the decomposition of TEOS to silica over the course of 48 hrs. XRD patterns of FePt@SiO_2-FITC nanoparticles confirmed the existence of fcc-phase FePt after SiO_2 coating (Figure 1(b)). Due to the amorphous SiO_2 coating, the broaden peak was found in the low diffraction angle (indicated by *) [21]. It is noticed that the (111) FePt fundamental peak was shift slightly to the high angle. To prepare the FePt@SiO_2 and FePt@SiO_2-FITC nanoparticles, the multiple-surface modifications were carried out under air condition, and thus the surface oxidation of FePt might be occurred. In the XRD study, the shifted peak to high angle (from ~40° to ~41.7°) may be due to the coupling of FePt crystallite with the oxidized product on the FePt nanoparticle surface, in which the peak at about 41.7 is near to the reflection peak of FeO (200) at ~42° according to the assignment of JPCDS No. 86–2316 [22, 23]. Further investigations of FePt nanoparticles for structure changes are being undertaken at our lab.

Table 1: Longitudinal and transverse relaxivities and relaxivity ratios of FePt and FePt@SiO_2-FITC nanoparticles.

Material	r_1 ($s^{-1}mM^{-1}$)	r_2 ($s^{-1}mM^{-1}$)	r_2/r_1
FePt	5.7	396.1	69.5
FePt@SiO_2-FITC	6.8	102.3	15.0

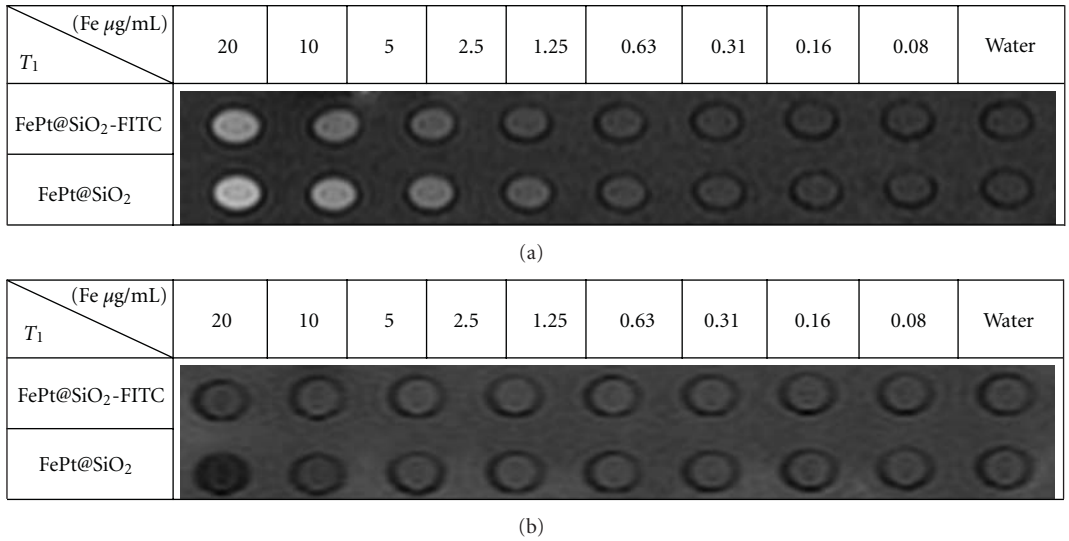

Figure 4: The MRI images of $FePt@SiO_2$ and $FePt@SiO_2$-FITC nanoparticles evaluated by clinical 3T MR scanner.

Figure 2 shows the TEM images of FePt and $FePt@SiO_2$-FITC nanoparticles and the sizes were analyzed by SigmaScan Pro software. The size of FePt nanoparticles was 4.59 ± 0.80 nm with sphere/cubic shape (Figure 2(a)). The $FePt@SiO_2$-FITC nanoparticles revealed 48.98 ± 6.41 nm thick silica structure that was coated around several FePt nanoparticles from TEM observation (Figure 2(b)). The polydispersity of $FePt@SiO_2$-FITC nanoparticles observed by DLS was 0.182.

The room-temperature magnetic hysteresis curves of FePt and $FePt@SiO_2$-FITC nanoparticles were all normalized to emu per gram of Fe content as shown in Figure 3. Clearly, the fcc-phase FePt nanoparticles sustain their superparamagnetic property in the silica composites at room temperature [20]. However, the lower and unsaturated magnetization of $FePt@SiO_2$-FITC nanoparticles observed under the applied field of 1.2 T may be due to the surface loose density of FePt component in the silanized particles or the surface dead layer around SiO_2 [24–26]. The significant difference in M_S among nanoparticles capped with varied ligands and the dead layer thickness have been estimated as previous report [27]. Thus, the electron donation from ligands to the Fe d band may reduce the magnetization. The possible FeO formation may also reduce Ms of nanoparticles.

The T_1 and T_2 values obtained from FePt or $FePt@SiO_2$-FITC nanoparticles dispersed in pure water are summarized in (Table S1 and Figure S1 in Supplementary Material available online at doi:10.1155/2012/631584) and the inverse relaxation times were almost linearly proportional to the concentration of nanoparticle similar to previous report [12]. Consequently, the r_1 (longitudinal relaxivities) and r_2 (transverse relaxivities) values of dispersed in pure water were determined to be 5.8 and 396.1 for FePt or 6.8 and $102.3\ s^{-1}\,mM^{-1}$ for $FePt@SiO_2$-FITC nanoparticles, respectively (Table 1). For a T_2 contrast agent, a higher r_2/r_1 ratio has a better contrast efficacy [28] and thus $FePt@SiO_2$-FITC nanoparticles with $r_2/r_1 = 15$ can be potentially used for MR contrast. The MRI images of $FePt@SiO_2$ and $FePt@SiO_2$-FITC nanoparticles were evaluated by clinical 3T MR scanner and the results were shown in Figure 4. Unexpectedly, $FePt@SiO_2$ and $FePt@SiO_2$-FITC nanoparticles revealed bright T_1-weighted imaging, whereas T_2-weighted imaging of both nanoparticles became dark as the Fe concentration increased. FePt nanoparticle has been demonstrated as potential T_2-weighted contrast agent for MR imaging due to its magnetization [29, 30]. For the T_1 contrast enhancement, it is possible that the generation of FeO surface coating on the FePt nanoparticle may provide additional assistance for the spin-lattice relaxation process.

The fluorescence spectrum of $FePt@SiO_2$-FITC nanoparticles was shown in Figure S1. Clearly, the property of FITC was observed in $FePt@SiO_2$-FITC nanoparticles which exhibited strong fluorescence at 535 nm with the excitation wavelength at 488 nm. Thus, $FePt@SiO_2$-FITC nanoparticles could be observed directly inside the cells by the florescence of the FITC. Figure 5 showed the intracellular localization of $FePt@SiO_2$-FITC nanoparticles in HeLa cells. After 12 hours incubation, the colocalization of fluorescence (Figure 5(c)) of $FePt@SiO_2$-FITC nanoparticles (Figure 5(a)) and LysoTracker (Figure 5(b)) was observed in HeLa cells. It is speculated that $FePt@SiO_2$-FITC nanoparticles were internalized into cells and entrapped presumably in the endosomes/lysosomes, as suggested by confocal microscopic observation. This result indicated that the $FePt@SiO_2$-FITC nanoparticles might be taken up by cells via endocytosis. The dose-dependent cytotoxicity of FePt and $FePt@SiO_2$-FITC in HeLa cells was demonstrated in Figure 6. No significant cytotoxicity was observed after 500 μM $FePt@SiO_2$-FITC nanoparticles incubation for 24 h or 72 h, whereas FePt nanoparticles induced cell toxicity at 500 μM for 72 h incubation (62% cell survival). Thus, the cytotoxicity of FePt nanoparticles was potentially suppressed with silica coating.

The introduction of APTMS and FITC-labeled APTMS in synthetic procedure of silica-coated nanoparticle not only

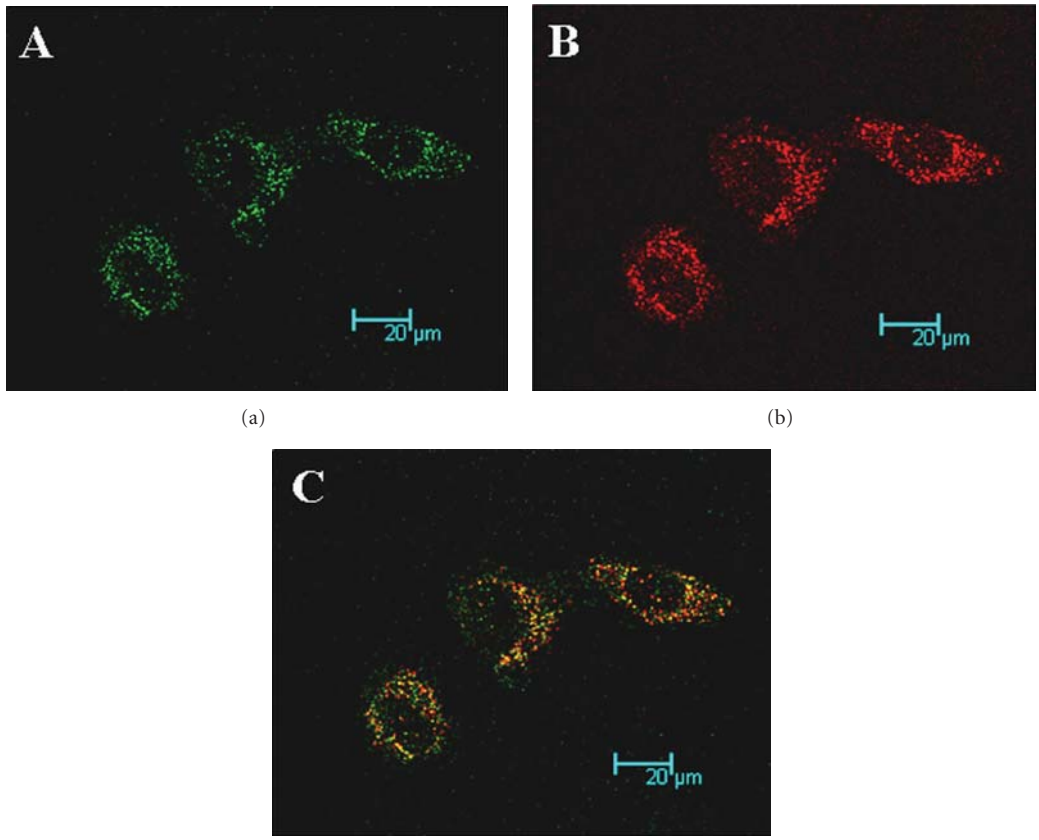

(a) (b)

(c)

Figure 5: Comparative intracellular localization of FePt@SiO_2-FITC nanoparticles with LysoTracker Red observed by confocal laser scanning microscopy.

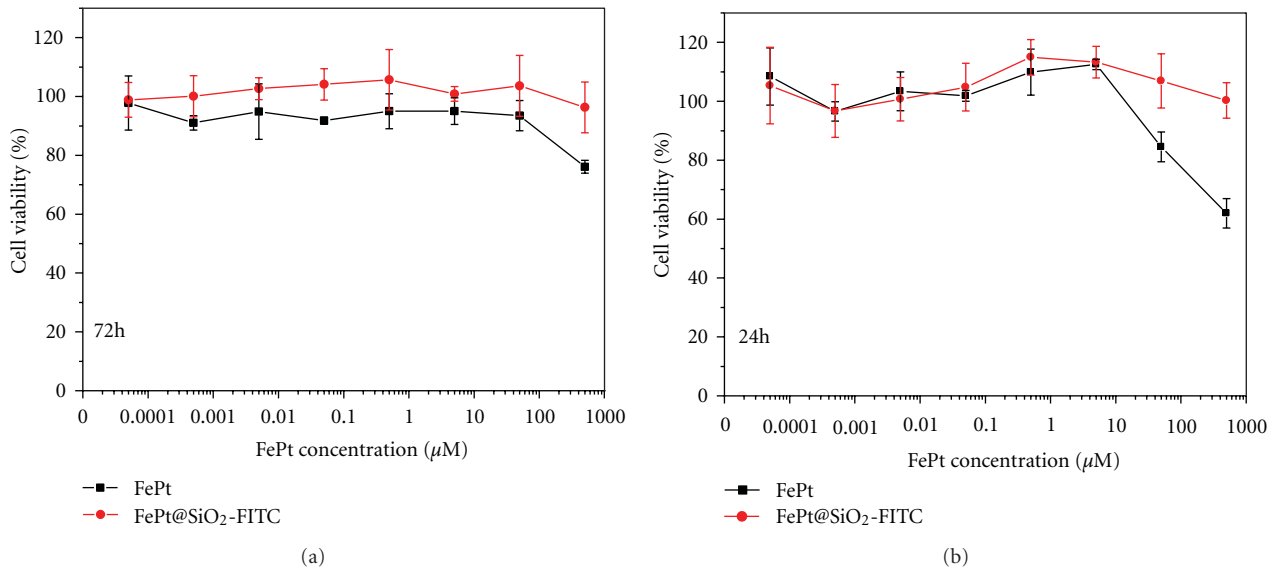

(a) (b)

Figure 6: Cytotoxicity of FePt and FePt@SiO_2-FITC nanoparticles. Cells were incubated for 24 h or 72 h at 37°C ($n = 4$).

provide the fluorescent property but produce the positive surface charge of FePt@SiO_2-FITC nanoparticles (Figure S2) that facilitate attachment and internalization of the particles [31]. Moreover, the amino groups of APTMS can be further conjugated using hydrophilic polyethylene glycol that results in steric hindrance to the phagocyte, system, and prolongation of blood circulation time [32]. Developing multiple imaging modalities in one nanoparticle is a promising field for biomedical applications. Chou et al. reported the dual modal biomedical imaging by using the FePt nanoparticles as simultaneous CT and MRI contrast agent [29]. Malvindi et al. also reported the dual mode imaging of the FePt-iron oxide and silica nanoparticles combination as the MRI and ultrasonography contrast agent [30]. These reports showed the advantages of these highly potential dual-mode imaging contrast agents for biomedical applications. Further investigations of FePt@SiO_2-FITC nanoparticles for simultaneous fluorescence/MR imaging *in vivo* are ongoing at our lab.

4. Conclusion

The longitudinal and transverse proton relaxation times obtained with silica-coated superparamagnetic FePt nanoparticles was measured. Unexpectedly, FePt@SiO_2 and FePt@SiO_2-FITC nanoparticles revealed bright T_1-weighted imaging, whereas T_2-weighted imaging of both nanoparticles became dark as the Fe concentration increased. Moreover, the surface coating using silica successfully suppressed the nanotoxicity of FePt. These results suggest that silica-coated superparamagnetic FePt nanoparticles are potential nanodevices for the combination of simultaneous fluorescence and MRI contrast for cancer diagnosis.

Acknowledgment

This research was supported by grants from Ministry of Education of the Republic of China under the ATU plan and National Science Council of the Republic of China (NSC 100-2218-E-002-002 and 100-2628-E-005-008-MY2).

References

[1] J. V. Frangioni, "New technologies for human cancer imaging," *Journal of Clinical Oncology*, vol. 26, no. 24, pp. 4012–4021, 2008.

[2] N. Nasongkla, E. Bey, J. Ren et al., "Multifunctional polymeric micelles as cancer-targeted, MRI-ultrasensitive drug delivery systems," *Nano Letters*, vol. 6, no. 11, pp. 2427–2430, 2006.

[3] N. Lewinski, V. Colvin, and R. Drezek, "Cytotoxicity of nanopartides," *Small*, vol. 4, no. 1, pp. 26–49, 2008.

[4] T. R. Pisanic, J. D. Blackwell, V. I. Shubayev, R. R. Fiñones, and S. Jin, "Nanotoxicity of iron oxide nanoparticle internalization in growing neurons," *Biomaterials*, vol. 28, no. 16, pp. 2572–2581, 2007.

[5] C. Tu, Y. Yang, and M. Gao, "Preparations of bifunctional polymeric beads simultaneously incorporated with fluorescent quantum dots and magnetic nanocrystals," *Nanotechnology*, vol. 19, no. 10, Article ID 105601, 2008.

[6] H. M. Liu, S. H. Wu, C. W. Lu et al., "Mesoporous silica nanoparticles improve magnetic labeling efficiency in human stem cells," *Small*, vol. 4, no. 5, pp. 619–626, 2008.

[7] W. J. M. Mulder, R. Koole, R. J. Brandwijk et al., "Quantum dots with a paramagnetic coating as a bimodal molecular imaging probe," *Nano Letters*, vol. 6, no. 1, pp. 1–6, 2006.

[8] C. Zhang and X. Xie, "Controllable assembly of hydrophobic superparamagnetic iron oxide nanoparticle with mPEG-PLA copolymer and its effect on MR transverse relaxation rate," *Journal of Nanomaterials*, vol. 2011, Article ID 152524, 7 pages, 2011.

[9] A. K. Gupta and M. Gupta, "Cytotoxicity suppression and cellular uptake enhancement of surface modified magnetic nanoparticles," *Biomaterials*, vol. 26, no. 13, pp. 1565–1573, 2005.

[10] S. Sun, C. B. Murray, D. Weller, L. Folks, and A. Moser, "Monodisperse FePt nanoparticles and ferromagnetic FePt nanocrystal superlattices," *Science*, vol. 287, no. 5460, pp. 1989–1992, 2000.

[11] S. Maenosono and S. Saita, "Theoretical assessment of FePt nanoparticles as heating elements for magnetic hyperthermia," *IEEE Transactions on Magnetics*, vol. 42, no. 6, pp. 1638–1642, 2006.

[12] S. Maenosono, T. Suzuki, and S. Saita, "Superparamagnetic FePt nanoparticles as excellent MRI contrast agents," *Journal of Magnetism and Magnetic Materials*, vol. 320, no. 9, pp. L79–L83, 2008.

[13] J. R. Skuza, R. A. Lukaszew, E. M. Dufresne et al., "Real time structural modification of epitaxial FePt thin films under x-ray rapid thermal annealing using undulator radiation," *Applied Physics Letters*, vol. 90, no. 25, Article ID 251901, 2007.

[14] L. Wang and W. Tan, "Multicolor FRET silica nanoparticles by single wavelength excitation," *Nano Letters*, vol. 6, no. 1, pp. 84–88, 2006.

[15] S. Sun, E. E. Fullerton, D. Weller, and C. B. Murray, "Compositionally controlled FePt nanoparticle materials," *IEEE Transactions on Magnetics*, vol. 37, no. 4, pp. 1239–1243, 2001.

[16] T. Tago, T. Hatsuta, K. Miyajima, M. Kishida, S. Tashiro, and K. Wakabayashi, "Novel synthesis of silica-coated ferrite nanoparticles prepared using water-in-oil microemulsion," *Journal of the American Ceramic Society*, vol. 85, no. 9, pp. 2188–2194, 2002.

[17] M. J. Shieh, C. L. Peng, P. J. Lou et al., "Non-toxic phototriggered gene transfection by PAMAM-porphyrin conjugates," *Journal of Controlled Release*, vol. 129, no. 3, pp. 200–206, 2008.

[18] S. Saita and S. Maenosono, "Formation mechanism of FePt nanoparticles synthesized via pyrolysis of iron(III) ethoxide and platinum(II) acetylacetonate," *Chemistry of Materials*, vol. 17, no. 26, pp. 6624–6634, 2005.

[19] H. L. Nguyen, L. E. M. Howard, G. W. Stinton et al., "Synthesis of size-controlled fcc and fct FePt nanoparticles," *Chemistry of Materials*, vol. 18, no. 26, pp. 6414–6424, 2006.

[20] L. Colak and G. C. Hadjipanayis, "Phase transformation in silica-coated FePt nanoparticles," *IEEE Transactions on Magnetics*, vol. 45, no. 10, pp. 4081–4084, 2009.

[21] G. Gupta, M. N. Patel, D. Ferrer et al., "Stable ordered FePt mesoporous silica catalysts with high loadings," *Chemistry of Materials*, vol. 20, no. 15, pp. 5005–5015, 2008.

[22] Y. Hou, Z. Xu, and S. Sun, "Controlled synthesis and chemical conversions of FeO nanoparticles," *Angewandte Chemie - International Edition*, vol. 46, no. 33, pp. 6329–6332, 2007.

[23] T. T. Trinh, D. Mott, N. T. K. Thanh, and S. Maenosono, "One-pot synthesis and characterization of well defined core-shell

structure of FePt@CdSe nanoparticles," *RSC Advances*, vol. 1, pp. 100–108, 2011.

[24] E. Kockrick, F. Schmidt, K. Gedrich et al., "Mesoporous ferromagnetic MPt@Silica/Carbon (M = Fe, Co, Ni) composites As advanced bifunctional catalysts," *Chemistry of Materials*, vol. 22, no. 5, pp. 1624–1632, 2010.

[25] P. J. Chen, S. H. Hu, C. S. Hsiao, Y. Y. Chen, D. M. Liu, and S. Y. Chen, "Multifunctional magnetically removable nanogated lids of Fe_3O_4-capped mesoporous silica nanoparticles for intracellular controlled release and MR imaging," *Journal of Materials Chemistry*, vol. 21, no. 8, pp. 2535–2543, 2011.

[26] P. E. Le Renard, R. Lortz, C. Senatore et al., "Magnetic and in vitro heating properties of implants formed in situ from injectable formulations and containing superparamagnetic iron oxide nanoparticles (SPIONs) embedded in silica microparticles for magnetically induced local hyperthermia," *Journal of Magnetism and Magnetic Materials*, vol. 323, no. 8, pp. 1054–1063, 2011.

[27] Y. Tanaka, S. Saita, and S. Maenosono, "Influence of surface ligands on saturation magnetization of FePt nanoparticles," *Applied Physics Letters*, vol. 92, no. 9, Article ID 093117, 2008.

[28] J. Qin, S. Laurent, Y. S. Jo et al., "A high-performance magnetic resonance imaging T_2 contrast agent," *Advanced Materials*, vol. 19, no. 14, pp. 1874–1878, 2007.

[29] S. W. Chou, Y. H. Shau, P. C. Wu, Y. S. Yang, D. B. Shieh, and C. C. Chen, "In vitro and in vivo studies of fept nanoparticles for dual modal CT/MRI molecular imaging," *Journal of the American Chemical Society*, vol. 132, no. 38, pp. 13270–13278, 2010.

[30] M. A. Malvindi, A. Greco, F. Conversano et al., "Magnetic/silica nanocomposites as dual-mode contrast agents for combined magnetic resonance imaging and ultrasonography," *Advanced Functional Materials*, vol. 21, no. 13, pp. 2548–2555, 2011.

[31] P. S. Lai, C. L. Pai, C. L. Peng, M. J. Shieh, K. Berg, and P. J. Lou, "Enhanced cytotoxicity of saporin by polyamidoamine dendrimer conjugation and photochemical internalization," *Journal of Biomedical Materials Research A*, vol. 87, no. 1, pp. 147–155, 2008.

[32] H. Otsuka, Y. Nagasaki, and K. Kataoka, "PEGylated nanoparticles for biological and pharmaceutical applications," *Advanced Drug Delivery Reviews*, vol. 55, no. 3, pp. 403–419, 2003.

Hindawi Publishing Corporation
Journal of Nanomaterials
Volume 2012, Article ID 190950, 12 pages
doi:10.1155/2012/190950

Research Article

In Vitro Degradation of PHBV Scaffolds and nHA/PHBV Composite Scaffolds Containing Hydroxyapatite Nanoparticles for Bone Tissue Engineering

Naznin Sultana[1,2] and Tareef Hayat Khan[3]

[1] *Department of Mechanical Engineering, The University of Hong Kong, Pokfulam Road, Hong Kong*
[2] *Medical Implant Technology Group (Mediteg), Department of Biomechanics and Biomedical Materials, FKBSK, Universiti Teknologi Malaysia, Johor, 81310 Johor Bahru, Malaysia*
[3] *Department of Architecture, FAB, Universiti Teknologi Malaysia, Johor, 81310 Johor Bahru, Malaysia*

Correspondence should be addressed to Naznin Sultana, naznin@biomedical.utm.my

Received 11 January 2012; Revised 2 April 2012; Accepted 3 April 2012

Academic Editor: Krasimir Vasilev

This paper investigated the long-term *in vitro* degradation properties of scaffolds based on biodegradable polymers and osteoconductive bioceramic/polymer composite materials for the application of bone tissue engineering. The three-dimensional porous scaffolds were fabricated using emulsion-freezing/freeze-drying technique using poly(hydroxybutyrate-co-hydroxyvalerate) (PHBV) which is a natural biodegradable and biocompatible polymer. Nanosized hydroxyapatite (nHA) particles were successfully incorporated into the PHBV scaffolds to render the scaffolds osteoconductive. The PHBV and nHA/PHBV scaffolds were systematically evaluated using various techniques in terms of mechanical strength, porosity, porous morphology, and *in vitro* degradation. PHBV and nHA/PHBV scaffolds degraded over time in phosphate-buffered saline at 37°C. PHBV polymer scaffolds exhibited slow molecular weight loss and weight loss in the *in vitro* physiological environment. Accelerated weight loss was observed in nHA incorporated PHBV composite scaffolds. An increasing trend of crystallinity was observed during the initial period of degradation time. The compressive properties decreased more than 40% after 5-month *in vitro* degradation. Together with interconnected pores, high porosity, suitable mechanical properties, and slow degradation profile obtained from long-term degradation studies, the PHBV scaffolds and osteoconductive nHA/PHBV composite scaffolds showed promises for bone tissue engineering application.

1. Introduction

Polymer-based composite scaffolds seem to have great potential in bone tissue-engineering. By selecting proper materials and fabrication technologies, good-quality scaffolds with consistent properties can be possible to fabricate [1]. There are some basic requirements that have been widely accepted for designing polymer scaffolds which can significantly affect the cell seeding and growth both *in vitro* and *in vivo* [2, 3]. The scaffolding materials should be biocompatible and biodegradable; the degradation products should be nontoxic and easily excreted by metabolic pathways. One of the key requirements is that the ideal scaffolding materials should be easy to fabricate into a desired shape, and they should have a controlled porous architecture to allow for cell infiltration, attachment, growth, tissue regeneration, and vascularization. The scaffolds should be mechanically strong to maintain their structural integrity during culture, and the ultimate mechanical properties of polymers at large deformations are important in selecting particular polymers for biomedical application.

Various biomaterials including biodegradable polymers, bioceramics, and biocomposites have been fabricated into scaffolds for the application of tissue regeneration. Poly(glycolic acid) (PGA), poly(lactic acid) (PLA), and their copolymers poly(lactic acid-co-glycolic acid) (PLGA) are

the most frequently used materials which already have been fabricated into scaffolds for cell transplantation and tissue-engineering [4, 5]. One of the materials of interest in tissue-engineering application is poly(hydroxybutyrate) (PHB) and its copolymer poly(hydroxybutyrate-co-hydroxyvalerate) (PHBV) which can be derived by microorganisms via fermentation [6]. These polymers are composed of hydroxybutyrate (HB) units with between 0 and 24% of hydroxyvalerate (HV) units appearing randomly throughout the polymer chain [7]. The chemical structure of PHBV is given by

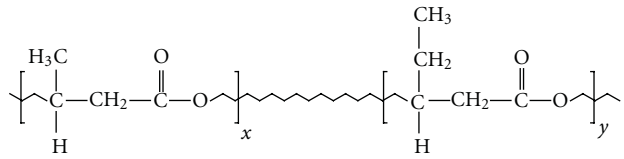

Poly(hydroxybutyrate-co-hydroxyvalerate)
(PHBV)

This polymer is degradable and piezoelectric (and thus might promote bone growth *in vivo*) and possesses extremely good biocompatibility [6, 8]. Together with highly biocompatibility, the copolymer PHBV has degradation times much longer than the other biocompatible polymers which will allow the scaffolds to maintain its mechanical integrity, until there is sufficient bone growth throughout the implant. PHBV copolymers have been found as minimal inflammatory in long-term studies of subcutaneous implants in mice and rats [9]. By considering these properties, PHBV copolymers may be a suitable candidate to support long-term bone regeneration [10]. The degradation products of PHB and PHBV polymers are the normal constituent of human blood, and hence they exert less inflammatory response to human body than other polymers [6, 11].

The uses of poly(hydroxyalkanoates) (PHA) could be extended considerably if a wider range of degradation profiles was available. The bone growth and healing can be stimulated theoretically as the polymer slowly degrades, by avoiding replacement operation. PHBV copolymers are also hydrolyzed in water with the normal universal acid-base catalysis for esters. At high pH, the rate of degradation is quite rapid, but the hydrolysis proceeds very slowly in neutral buffer at body temperature. Moreover, the experiments suggested that the rate of degradation of PHBV *in vivo* is significantly faster than the *in vitro* hydrolysis rate at the same temperature and pH [12]. Actually the nonspecific esterase and lysozyme enzymes secreted by the body's immune system catalyze the process. The variation of degradation rate of PHBV *in vivo* with the activity of the body's immune system thus is useful to explain some of the discrepancies in the literature of PHBV biodegradation. The range of biodeterioration of implanted films can be varied from very rapid to a modest but measurable resorption to virtually undetectable weight loss of fiber monofilament over an 18-months period. It was also reported that PHBV and that cell/PHBV constructs have the ability to produce neocartilage in a heterotopic site although the degradation rates of PHBV in different environments need more investigation [13].

It was reported that the *in vivo* and *in vitro* degradation of aliphatic polyesters was catalyzed by carboxyl end groups formed by chain cleavage, and the amorphous regions are preferentially degraded [14]. In general, the hydrolytic degradation of semicrystalline high molecular weight PLLA proceeds through random bulk hydrolysis in two distinct stages. The first stage is characterized by the preferential attack of the ester linkages in the more accessible amorphous regions, while the second stage is characterized by the attack of the less accessible crystalline regions [15]. It was reported that the cleavage of an ester bond of PLGA polymers yielded a carboxyl end group and a hydroxyl one, and thus formed carboxyl end groups were able to catalyze the hydrolysis of other ester bonds [14]. This phenomenon is called autocatalysis. Autocatalysis rate equation is applicable when the extent of reaction is slow or before the specimen experiences significant weight loss.

On the other hand, hydroxyapatite (HA) possesses osteoconductivity and is similar to the mineral component of natural bone. HA has been studied comprehensively. It is now widely used for bone tissue repair. Biodegradable composite scaffolds containing osteoconductive HA particles and biodegradable polymers are being explored [16, 17]. It was reported that by, incorporating nanosized HA particles in polymer scaffolds, the scaffolds should attain osteoconductive properties [18, 19]. These scaffolds will be promising in bone tissue-engineering application.

In this paper, firstly, the study of fabrication and evaluation of PHBV and HA/PHBV composite scaffolds was reported. Then the results of *in vitro* degradation of pure PHBV scaffold, and HA-incorporated PHBV scaffolds were discussed from the materials perspective. However, report on long-term degradation of PHBV scaffolds is rarely available. This paper reports and compares the long-term systematic investigations of hydrolytic degradation characteristics of the scaffolds produced by PHBV polymers and osteoconductive nHA/PHBV composites. By undertaking long-term investigations, important information had been achieved in the understanding of the hydrolytic degradation characteristics of the scaffolds, particularly the slow degradation mechanism of PHBV scaffolds, and degradation induced morphological and mechanical changes of HA/PHBV composite scaffolds for the application of bone tissue-engineering.

2. Materials of Methods

2.1. Materials. Poly(hydroxybutyrate-co-hydroxyvalerate) (PHBV) as powder form was purchased from *Tianan Biologic Material Ltd., Ningbo, China*. PHBV with 2.9% of 3-hydroxyvalerate content had the molecular weight 310,000 and purity 98.8%. These polymers were used without further purification. All the chemicals such as chloroform, acetic acid, and salts were analytical grade and were used as received. Water was ultra pure grade ($<18\,m\Omega$) supplied from a Mili-Q purification system. The HA nanoparticles used for composite scaffolds were produced in-house through a nanoemulsion process [20].

2.2. Fabrication and Characterization of Scaffolds. PHBV tissue-engineering scaffolds were fabricated using the emulsion freezing/freeze-drying technique described elsewhere [17, 18]. Briefly, PHBV was weighed accurately into a centrifuge tube, and then an accurately measured amount of chloroform was added to the tube to make a solution with a desired concentration of 2.5%–12.5% (w/v). To obtain a homogeneous polymer solution, the mixture was kept at 50°C in a water bath for five minutes and mixed thoroughly using a minishaker. The process was repeated for several times. After obtaining homogeneous solution, water phase was added. Homogenization at a fixed speed was performed in a homogenizer (Ultra-Turrax, T-25; IKA-WERKE). In order to fabricate scaffolds, 5 mL of PHBV emulsion was put into a glass vial (prewarmed to 50°C). The glass vial containing the mixture was then rapidly transferred into a freezer at a preset temperature (at −35°C) to solidify the emulsion. The solidified emulsion was maintained at that temperature for overnight. The frozen emulsion was then transferred into a freeze-drying vessel (LABCONCO-Freeze dry system, USA) at a preset temperature of −10°C. The samples were freeze-dried for at least 46 hrs to remove the solvent and water phase completely. The prepared scaffolds were placed in a vacuum desiccator at room temperature for storage and further removal of any residual solvent until characterization. The fabrication procedure of nHA/PHBV scaffolds was similar as PHBV scaffolds. In order to fabricate 10% HA-incorporated PHBV scaffold, 10% HA (w/w) relative to the total amount of polymer was dispersed in the polymer emulsion (0.1 g HA in 1 g PHBV) using the homogenizer. The other steps are similar as described above.

Using a scanning electron microscopy (SEM; Stereoscan 440, UK) at 12 kV, the pore structure and morphology of scaffolds were studied. The specimens were cut with a sharp razor blade after being frozen at −35°C for one day. Then they were coated with gold using a sputter coater (BAL-Tec, SCD 005; Sputter Coater). The coating time was 200 sec. Pore sizes and pore size distributions were determined using SEM micrographs of scaffolds. At least 40 pores were measured from SEM micrographs, and the average pore size was calculated. HA nanoparticles were also coated with gold. By using a field emission-scanning electron microscope (FE-SEM, LEO 1530, Germany), the morphology of dried nHA was examined. Energy-dispersive X-ray spectrometry (EDX, INCA 300, UK) was performed in order to determine the presence and distribution of HA nanoparticles in composite scaffolds.

Using a differential scanning calorimetry (DSC, Pyris 6, Perkin-Elmer, USA), the thermal properties of scaffolds were investigated. The degree of crystallinity, X_c, of scaffold samples was calculated with the use of DSC-melting curves of scaffolds. For composite scaffolds containing nHA, crystallinity is calculated using the equation given below [21]:

$$X_c(\%) = \frac{\Delta H_m/\varphi_{\mathrm{PHBV}}}{\Delta H_{m\,100\%}} \times 100\%, \tag{1}$$

where ΔH_m and $\Delta H_{m\,100\%}$ are the calculated enthalpy of polymer scaffolds and the theoretical enthalpy of melting for 100% crystalline PHBV polymer (114 J/g). The weight fraction of PHBV in the composite scaffolds is denoted by φ_{PHBV}. The skeletal density and the porosity of the scaffolds were measured according to liquid displacement method [22]. A scaffold sample of weight W was immersed in a graduated cylinder containing a known volume (V_1) of ethanol for 5 min. Then a series of brief evacuation-repressurization cycles with the aid of a vacuum oven (DZF 6020, China) was conducted to force the ethanol into the pores of the foam until no air bubbles were observed emerging from the foam. The total volume of ethanol and the ethanol-impregnated foam was then recorded as V_2. The ethanol-impregnated foam was removed from the cylinder, and the residual ethanol volume was recorded as V_3. The volume difference, $(V_2 - V_1)$, was the volume of the polymeric foam, and the quantity $(V_1 - V_3)$ was the volume of the ethanol held in the foam regarded as the void volume of the foam.

Thus the total volume of the scaffold is

$$V = V_2 - V_3. \tag{2}$$

Density of the foam is

$$d = \frac{w}{V_2 - V_3}. \tag{3}$$

Porosity is

$$\varepsilon = \frac{(V_1 - V_3)}{(V_2 - V_3)}. \tag{4}$$

Compressive mechanical properties of PHBV and PHBV-based scaffolds were determined at room temperature using an Instron mechanical tester (Instron 5848, USA) with a 100 N load cell and at a crosshead speed of 0.5 mm/min. The compressive modulus was calculated from the initial linear region of stress-strain curves.

2.3. In Vitro Degradation Study

2.3.1. Experimental Setup. In order to study the aqueous degradation of PHBV and 10 wt% nHA/PHBV scaffolds, selected samples fabricated from 10% (w/v) polymer solution were cut to the correct height (1.5 mm) and diameter (10 mm) with a sharp razor blade and weighed. Phosphate-buffered saline (PBS) was prepared by dissolving tablets of PBS (supplied by Zymed laboratories USA) with distilled water. The specimens were placed in sealable vials in 10 mL of PBS solution (pH 7.4). The samples were pressed under PBS by applying vacuum. Air trapped in pores was removed by venting with the aid of a vacuum oven. PBS solution was replaced with new solution each week. At regular intervals, samples from buffer were removed, extensively rinsed with distilled water and dried under vacuum at 37°C and weighed. The experiment was performed for a period of 11 months and according to ASTM F 1635-04a standard test method [23]. The test method is intended to help assess the biodegradation rates (i.e., the mass loss rate) and changes in material or structural properties.

2.3.2. Property Assessment

(1) Molecular Weight. Molecular weight was measured using a Zetasizer Nano series (Malvern 2000, Malvern Instruments Ltd., UK) which can perform molecular weight measurements using a process called static light scattering (SLS) which is a noninvasive technique used to characterise the molecules in a solution. Static light-scattering technique makes use of the time-averaged intensity of scattered light after the particles in a sample being illuminated by a light source such as laser. The initial molecular weight of the sample was measured. Samples were removed at each specified time period throughout the duration of the test, dried and tested for the molecular weight as above. The autocatalysis rate equation is given by

$$\ln M_{nt} = -kt + \ln M_{no}, \tag{5}$$

where, M_{nt} is the molecular weight after *in vitro* degradation at time t, M_{no} is the initial molecular weight, and k is the rate constant.

(2) Weight Loss. Three test samples were weighed prior to placement in the physiological solution. Upon completion of the specified time period, each sample was removed, gently rinsed with distilled water, and dried to a constant weight, and the weight loss was recorded. Weight loss during investigation was determined as

$$\text{Weight loss } (\%) = \frac{\left(W_i - W_f\right)}{W_i} \times 100, \tag{6}$$

where W_i and W_f are specimen weights before and after soaking in PBS.

(3) Water Uptake. In order to calculate water uptake, preweighed scaffolds specimens and thin films were removed periodically, washed with distilled water, blotted dry on filter paper in order to remove excess water, weighed, and returned to the PBS. The water uptake was calculated using the following equation:

$$\text{Water uptake } (\%) = \frac{(W_w - W_d)}{W_d} \times 100, \tag{7}$$

where W_d and W_w are specimen weights before and after soaking in PBS.

2.4. Characterization of Degraded Scaffolds. The compressive mechanical properties of the samples were determined prior to placement of the samples in the physiological solution (time zero). The samples were removed at each specified time period throughout the duration of the test and retest using the originally selected mechanical test methods and conditions. Crystallinities of as-fabricated and degraded scaffolds were also calculated as described earlier in Section 2.2. The morphologies of the as fabricated and degraded composite scaffolds were studied with a scanning electron microscopy (SEM; Stereoscan 440, Cambridge) at 12 kV as described in Section 2.2.

3. Results

3.1. Properties of PHBV and nHA/PHBV Scaffolds. It was observed that, using freeze-drying technique, PHBV and nHA/PHBV scaffolds of high porosity (low skeletal density) could be fabricated from polymer solutions of different polymer concentrations. It was also noticed that the skeletal density increased while porosity decreased with the increasing polymer solution concentration. The porosity and skeletal density of scaffolds prepared from 5% (w/v) PHBV solution were 88% and 0.1005 (g/cm^3), respectively, whereas the porosity and skeletal density of scaffolds prepared from 10% (w/v) PHBV solution were 78% and 0.2244 (g/cm^3), respectively. The porosity decreased to 75%, and skeletal density further increased to 0.2601 (g/cm^3) with the incorporation of 10 wt% HA (w/w) in 10% (w/v) PHBV solution. The effects of polymer concentration on the final microstructure, pore sizes and porosity were also investigated (Figure 1). The scaffolds fabricated from 5% (w/v) PHBV solution showed weak or low polymer interconnectivity Figures 1(a) and 1(b). On the other hand, the scaffolds produced from 10% (w/v) PHBV solution exhibited highly anisotropic array of open microtubule with stronger pore interconnectivity (Figures 1(c) and 1(d)). All the scaffolds exhibited open porous morphology. For the scaffolds fabricated from 10% (w/v) solution had uniform pore structures which had the pore sizes ranging from 70 to 600 μm with the average pore size of 297 μm. On the other hand, nHA/PHBV composite scaffolds had pore size range of 50–450 μm. The average pore size of nHA/PHBV composite scaffold was 210 μm.

Figure 2(a) shows the FE-SEM micrograph of nanosized HA. The HA nanoparticles had higher *in vitro* solubility under physiological conditions which suggested the higher bioresorbable nature [20]. The freeze-dried nHA powders used in this investigation consisted of tiny agglomerates of HA nanocrystallites. The particle size of the nHA powders was found to be in the range of 20–30 nm [20]. It was observed that at 10 wt % nHA concentration, nHA particles were distributed homogeneously within the pore walls of the scaffolds. No significant agglomeration of HA nanoparticles occurred within the pore walls. Figure 2(b) shows the nHA/PHBV scaffold with the nHA content of 10 wt%. The presence of nHA in polymer pore walls was confirmed by EDX spectrum and EDX analysis (Figure 2(c) and Table 1).

3.2. Effect of Polymer Concentration on Compressive Mechanical Properties. Figure 3(a) shows the typical compressive curves of the PHBV scaffolds made from the emulsion concentrations of 5%, 7.5%, 10%, and 12.5% (w/v). It can be observed from compressive curves that the compressive properties of the PHBV scaffolds increased with the increasing emulsion concentration. All the curves had three distinct regions consisting of initial linear region followed by a long plateau and then densification. The compressive modulus was calculated from initial linear region. The scaffolds of 7.5% (w/v) polymer solution had the compressive modulus of 1.1 ± 0.61 MPa in the 2.5%–7.5% strain range whereas the scaffolds of 12.5% (w/v) had the compressive modulus of 5.02 ± 1.03 MPa in the same strain range (Table 2). Figure 4

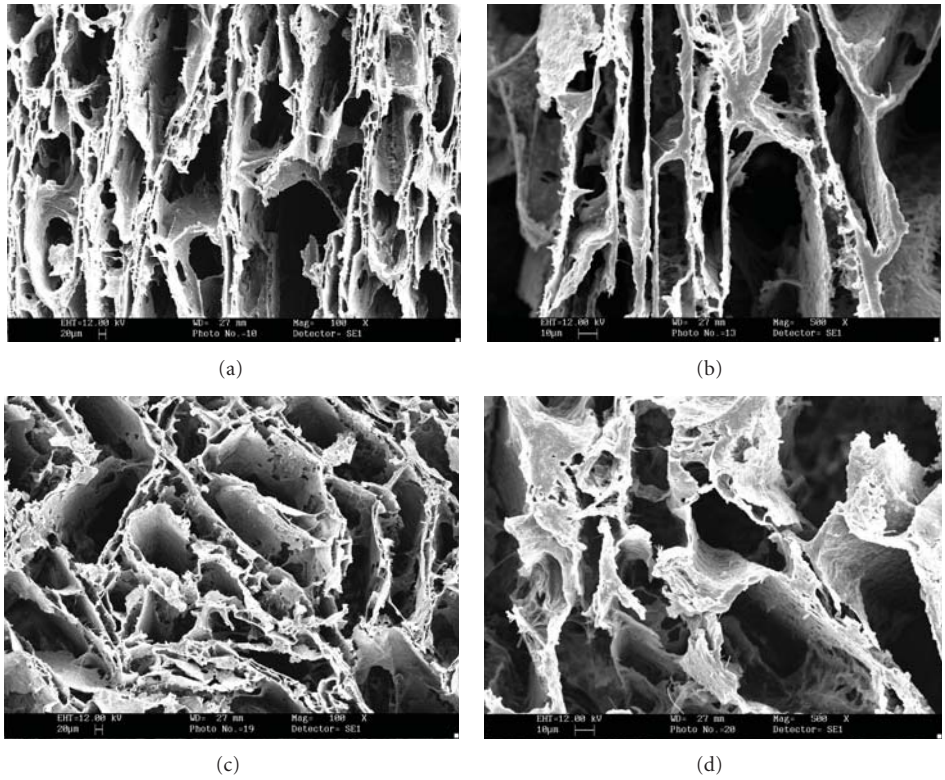

(a) (b) (c) (d)

Figure 1: SEM micrographs of PHBV scaffolds fabricated by emulsion freezing/freeze-drying technique from (a) and (b) 5% PHBV emulsion, and (c) and (d) 10% PHBV emulsion.

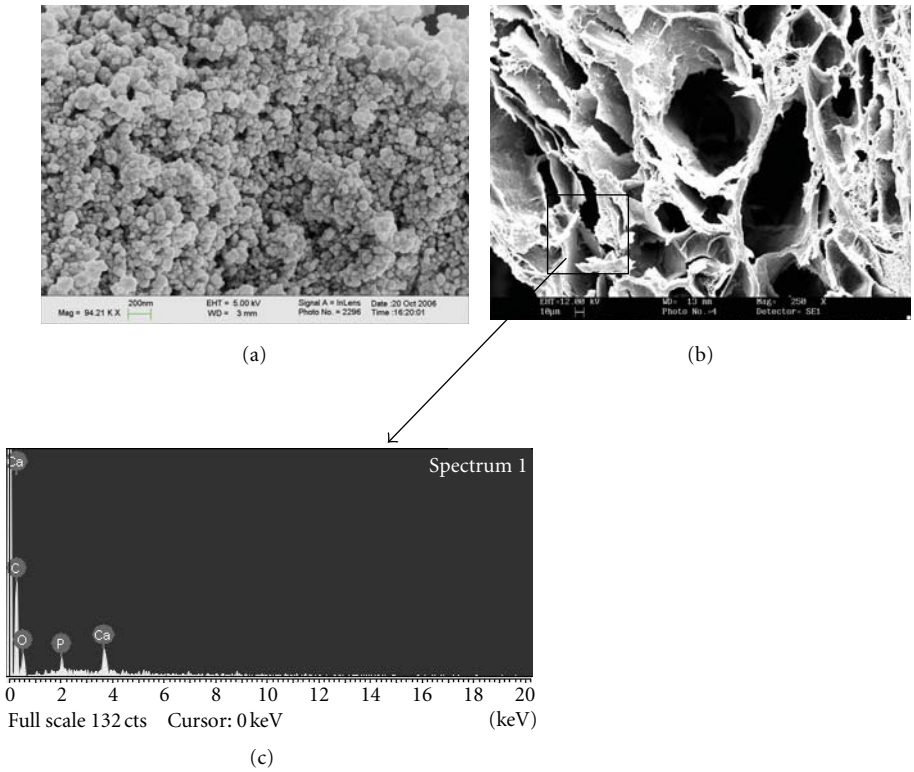

(a) (b) (c)

Figure 2: (a) FE-SEM micrograph of nanosized HA particles; (b) HA/PHBV composite scaffold containing 10% nHA; (c) an EDX spectrum confirming the presence of HA nanoparticles in HA/PHBV composite scaffold.

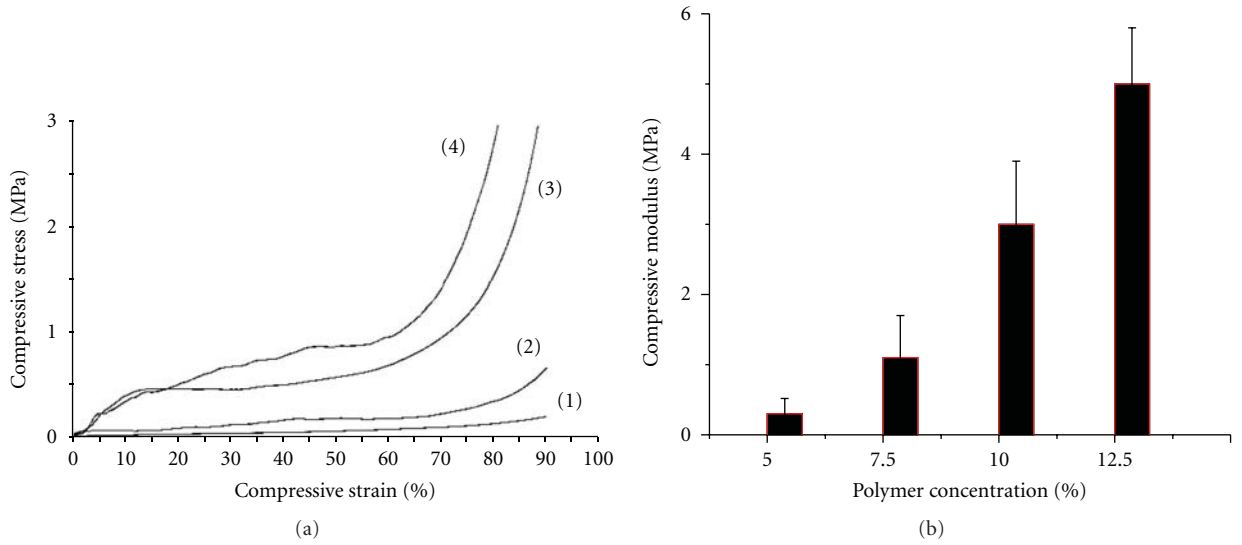

Figure 3: (a) Typical compressive curves of the PHBV scaffolds (1) 5%, (2) 7.5%, (3) 10%, and (4) 12.5% (w/v) polymer emulsions. (b) Compressive modulus of PHBV scaffolds with different polymer concentration.

Table 1: Elemental analysis of HA using EDX analysis of a HA/PHBV scaffold.

Element	Percentage of elements	
	Weight %	Atomic %
C	61.47	61.47
O	36.71	36.71
P	0.41	0.41
Ca	1.41	1.41

Table 2: Compressive modulus of PHBV scaffolds with different polymer concentration.

Polymer concentration	Compressive modulus (MPa)
5%	0.3 ± 0.22
7.5%	1.1 ± 0.61
10%	3.0 ± 0.9
12.5%	5.0 ± 0.8

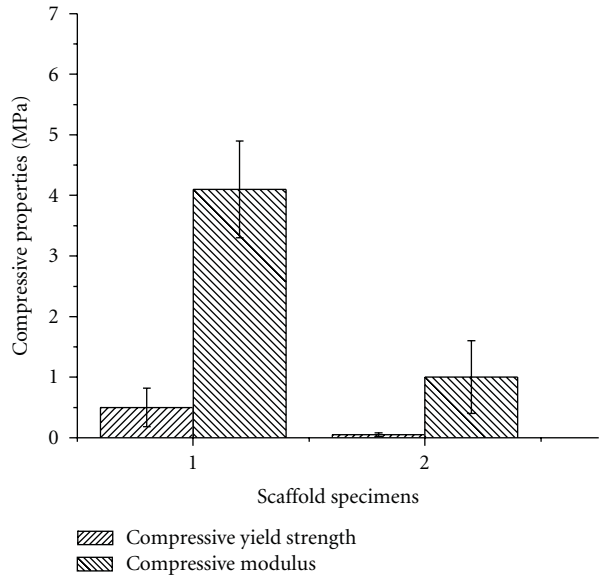

Figure 4: Effects of scaffold porosity on the compressive properties of the PHBV scaffolds: porosity (1) 77%, (2) 83%.

shows the effects of scaffold porosity on the compressive modulus of the PHBV scaffolds. It was found that the compressive modulus decreased with the increasing porosity (Table 3).

3.3. Water Uptake. Figure 5 shows the comparison of the water uptake curves between PHBV polymer scaffold and 10% nHA in PHBV composite scaffolds at 37°C. It was observed that the initial water uptake of HA-incorporated composite scaffold was much higher than that of polymer scaffold. Approximate equilibrium reached almost at the same immersion time for both of the scaffolds.

3.4. Molecular Weight Change of PHBV Scaffolds. Molecular weights of PHBV scaffolds immersed in the PBS solution at 37°C were measured at different time points and the results were shown in Figure 6(a). It was observed that the molecular weight dropped significantly from 24 weeks to 44 weeks after *in vitro* degradation. The average molecular weight of as-fabricated PHBV scaffold was 229 KDa. After the scaffold immersion in PBS for 12 weeks, 14 weeks, and 44 weeks, it decreased to 212 KDa, 194 KDa, and 121 KDa, respectively.

Figure 6(b) represents the plot of natural logarithm of molecular weights over degradation time for 44 weeks to fit the autocatalysis rate equation. As can be seen from Figure 6(b), the logarithm of molecular weight loss does not fall linearly over 44 weeks of time. But for the initial period

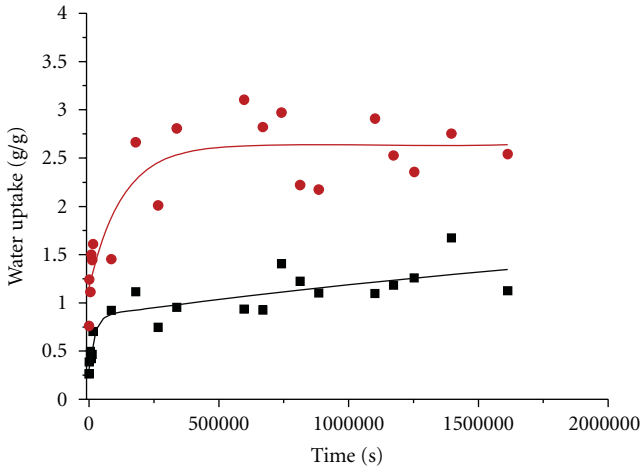

Figure 5: Comparison of water uptake between PHBV scaffolds (■) and 10% HA in PHBV composite scaffolds (•) at 37°C.

Table 3: Compressive properties of the PHBV scaffolds with different porosity.

Porosity	Compressive yield strength	Compressive modulus
77%	0.50 ± 0.31	4.1 ± 0.8
83%	0.052 ± 0.03	1.0 ± 0.6

up to 24 weeks, the decrease in molecular weight followed the linear trend (Figure 6(b), minigraph). Here the autocatalysis reaction model can be applied. The slope of the straight line or the rate constant was found to be 0.0067 week^{-1}. It can be concluded from this result that the reaction rate is comparatively slower.

3.5. Crystallinity Change. It was observed that after 5-week immersion in PBS, the crystallinity of pure PHBV scaffolds and 10% nHA/PHBV scaffolds increased by about 8% (Figure 7), which was due to the degradation of the amorphous part of the polymers. This degradation was a result of hydrolytic scission of polymer chains in the more susceptible amorphous part. Moreover, the presence of nHA could accelerate the scaffold degradation by the dissolution of nano-HA in the scaffold matrices.

3.6. Weight Loss. Figure 8(a) shows the effect of porosity on the weight loss of the scaffolds. It was observed that the scaffolds having higher porosity (88%) exhibited accelerated weight loss than that of lower porosity (78%). Figure 8(b) displays the weight loss of the scaffold specimens of PHBV (10% w/v) and the same composition containing 10% HA over 8 week period of time. After six weeks, the 10% nHA containing PHBV composite scaffold showed elevated weight loss (approx. 18%) than polymer scaffolds (<10%). Accelerated weight loss of nHA/PHBV composite scaffolds was due to dissolution of HA in the scaffolds matrix.

3.7. Changes of Compressive Mechanical Properties. Mechanical testing showed that compressive properties of PHBV scaffolds decreased considerably after 20-week immersion in PBS. Figure 9(a) shows the typical compressive stress-strain curves as fabricated, and Figure 9(b) shows the degraded PHBV scaffolds specimens fabricated from 10% (w/v) polymer emulsion. Compressive properties were determined from the initial linear part of the stress-strain curves. For each specimen compressive properties decreased more than 40% after *in vitro* degradation for 20 weeks at 37°C (Figure 9(c)).

3.8. Morphological and Microstructural Changes. Figures 10(a), 10(b), and 10(c) show the morphology of PHBV scaffolds after *in vitro* degradation in PBS at 37°C for 4 weeks and 44 weeks. After 44 weeks, large pores were observed in the PHBV scaffolds. Figures 10(d) and 10(e) show the morphological change of nHA/PHBV composite scaffolds containing 10% of HA after degradation tests. After 4 weeks in PBS, the pore distribution was found to be more irregular, and large pores were observed. After 44 weeks in PBS, major morphological changes were detected for composite scaffolds. After immersion in PBS, the pore walls were found to be collapsed in the composite scaffolds, which were not observed in the pure PHBV scaffolds.

4. Discussion

Polymer scaffolds prepared from the optimum parameters exhibited >70% porosity and better handling properties. The optimum parameters were polymer concentration, 10% (w/v); solvent to water phase ratio, 1 : 1 or the volume fraction of water phase $\phi = 0.5$; amount of HA, 10% (w/w); homogenizer speed, 17,500 rpm; freezer temperature, −35°C. The pore size ranged from several microns to few hundred microns, and they changed with the concentration of the polymer. Figure 1 shows the morphology of PHBV scaffolds of different concentrations. Anisotropic pore morphology with elongated pores and internal ladder-like microstructures in the pores of scaffolds were observed. The characteristic pore morphology obtained from emulsion freezing/freeze-drying technique can be explained by the phase separation and heat transfer mechanisms during freezing and solvent removal rate by freeze-drying processes. Incorporation of nHA did not significantly change the pore microstructures as observed in Figure 2.

The compressive stress-strain curves had the three regions as shown in Figure 3. It was found that they exhibit linear elasticity at low stresses followed by a long collapse plateau and a regime of densification in which the stress rises steeply. It was reported that cell wall bending of the scaffolds controls the initial linear elasticity of the scaffolds [24]. Collapse of the cells is the cause of the plateau region. The final region of rapidly increasing stress occurs when the cells have almost completely collapsed. In this region, opposing cell walls touch, further strain compresses the solid itself [18, 24]. Compressive modulus is the initial slope of the stress-strain curve. As the relative density increases, the cell walls thicken and the pore space shrinks. Increasing the relative density of the foam increases the modulus, raises the plateau

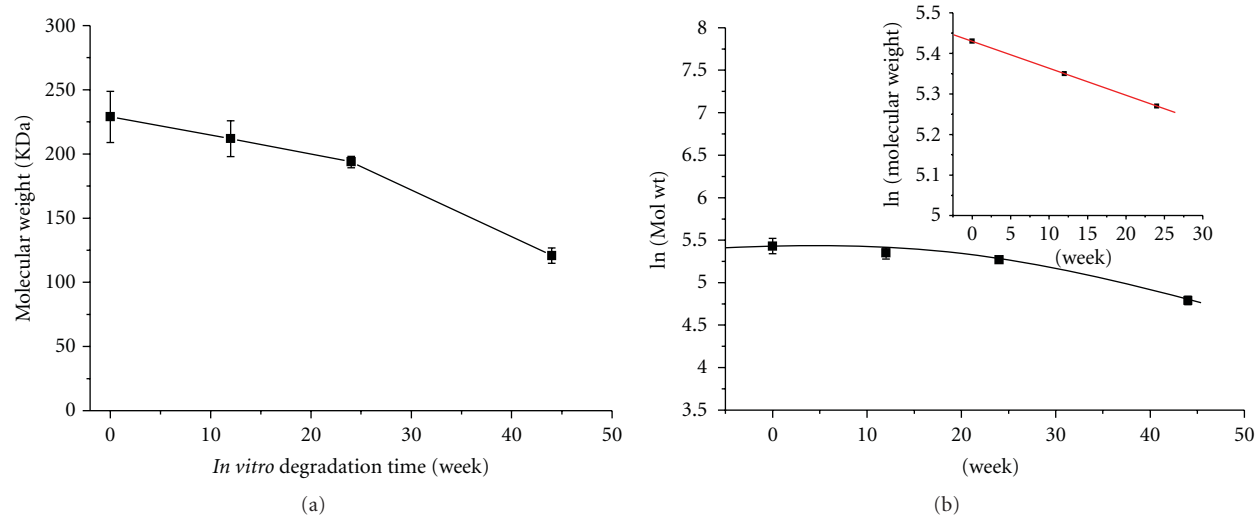

Figure 6: (a) Molecular weight (KDa) change with *in vitro* degradation time of PHBV scaffolds. (b) A plot of ln (molecular weight, KDa) with *in vitro* degradation of PHBV scaffolds for 44 weeks at 37°C; (minigraph) plot of ln (molecular weight, KDa) and degradation time (wk) at 37°C for 24 weeks.

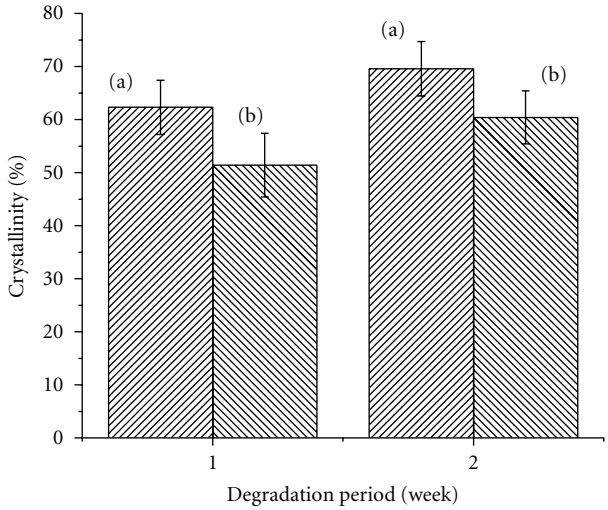

Figure 7: Crystallinity of (a) PHBV scaffolds and (b) 10% HA/PHBV scaffolds after (1) 0 week and (2) 5 weeks.

stress, and reduces the strain at which densification starts. For these reasons it was found that compressive modulus increases with increasing polymer/emulsion concentration or decreasing porosity (Figure 4).

The degradation mechanism and rate of biodegradable polymers can be affected by numerous factors. Among the factors which affect degradation are molecular weight, structure and content of comonomer unit, crystallinity, orientation, blending, porosity, pH, temperature, and catalytic molecules or ions [25]. It was also reported that when catalytic molecules or substances such as enzymes and alkalis are present in the degradation media or environment, the degradation of polymer-based materials proceeds via a surface erosion mechanism [25]. In the surface erosion mechanism, catalytic molecules or ions act only on the surface of materials and will not diffuse into the material. As a result, the material is eroded from the surface while the core part of the material remains unchanged. On the other hand, the degradation of biodegradable polymers takes place via a bulk erosion mechanism in the absence of catalytic molecules or ions as in a phosphate-buffered solution. It was also reported that the hydrolytic degradation mechanisms depend on the thickness of biodegradable materials, and the critical thickness above which the degradation mechanism changes from bulk erosion to surface erosion depends on the molecular structure of biodegradable or hydrolysable polymers [26]. A significant weight loss can be observed at an early stage of degradation for a surface erosion mechanism. On the other hand, the weight loss occurs only at a late stage of degradation for a bulk erosion mechanism when a large decrease in molecular weight takes place and when water soluble oligomers and monomers are formed. In order to trace bulk erosion, molecular weight change is most effective. On the other hand, it is quite ineffective in the case of surface erosion [25].

Figure 6(b) shows that the autocatalytic rate equation is not valid over 11 months of period. On the other hand, Figure 6(b) (mini-graph) shows the plot between ln (Molecular weight) for 24 weeks of *in vitro* degradation time. During this time period, the rate equation for autocatalysis was valid as it followed first order with the regression coefficient r^2 value being 0.99. The rate constant calculated from the slope was relatively small. It can demonstrate that the reaction proceeded slowly over this time period. It was reported that the reaction constant was 0.0584 week^{-1} for PLGA [14]. This value was significantly greater than the value calculated for PHBV scaffolds in this study which was 0.0067 week^{-1}. It has been reported that surface area and thickness of film have little effect on the rate of

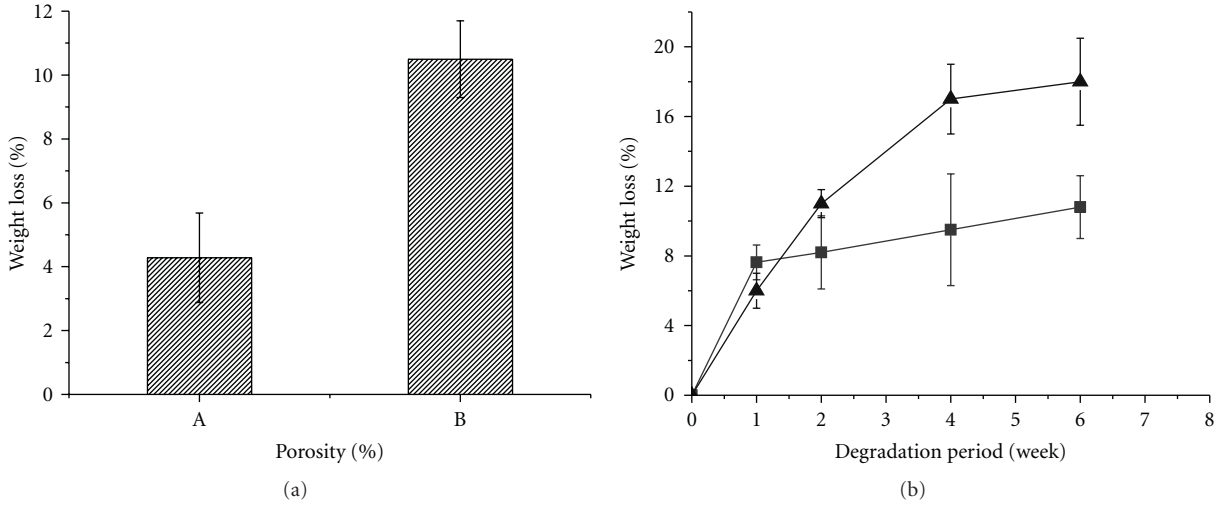

Figure 8: (a) Weight loss of PHBV scaffolds after *in vitro* degradation for 6 weeks: (A) 78% porosity; (B) 88% porosity. (b) Weight loss of PHBV scaffold (■) and HA/PHBV scaffold with 10% HA (▲) after *in vitro* degradation for 6 weeks.

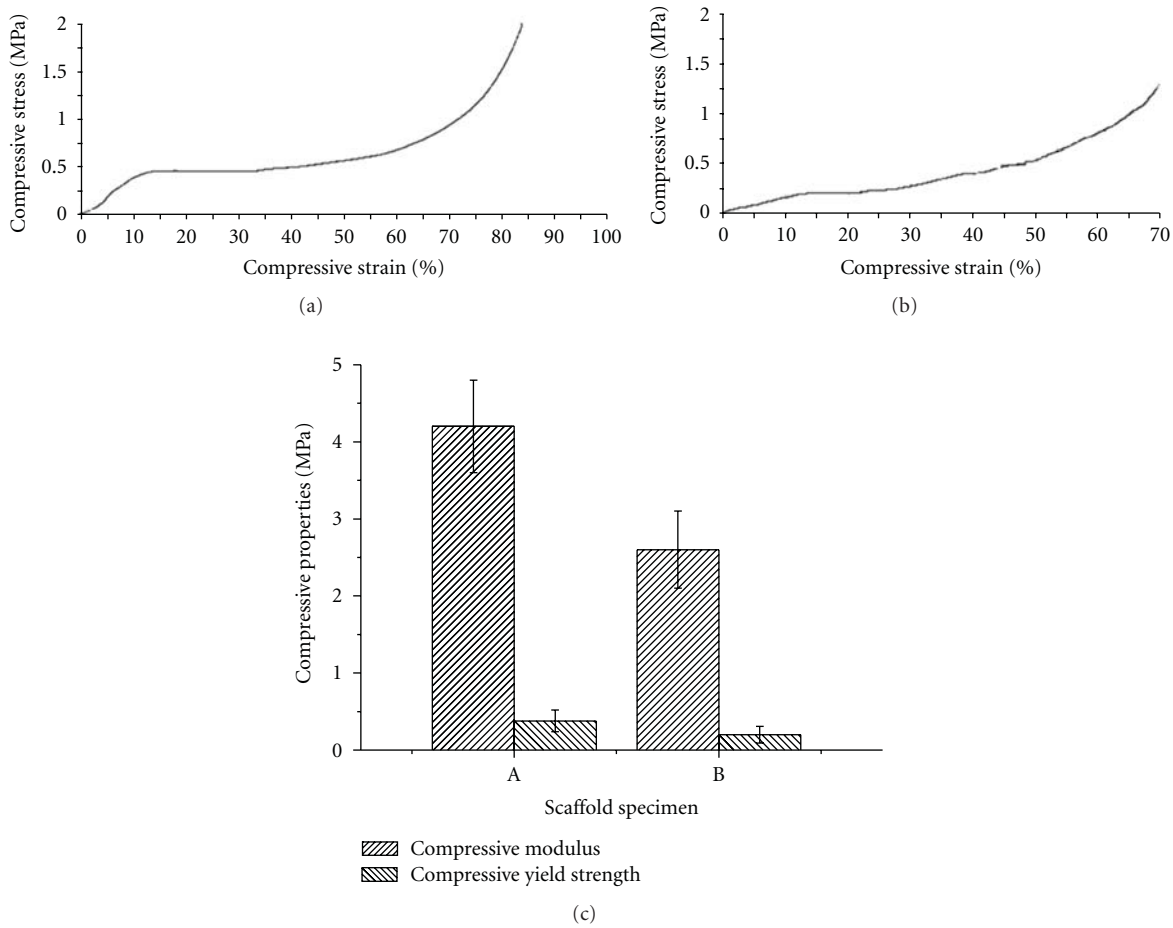

Figure 9: Comparison of compressive stress-strain curves for (a) as-fabricated and (b) a degraded (20 weeks) PHBV scaffold specimens fabricated from 10% (w/v) PHBV emulsion. (c) Compressive properties for an as-fabricated (A) and a degraded (20 weeks) (B) PHBV scaffold specimen.

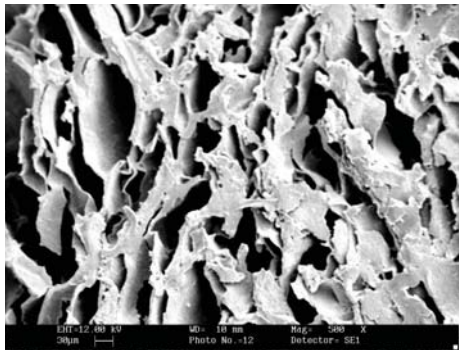

(a) *In vitro* degradation after 4 weeks

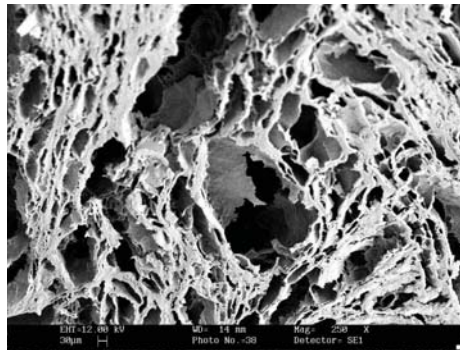

(b) *in vitro* degradation after 44 weeks

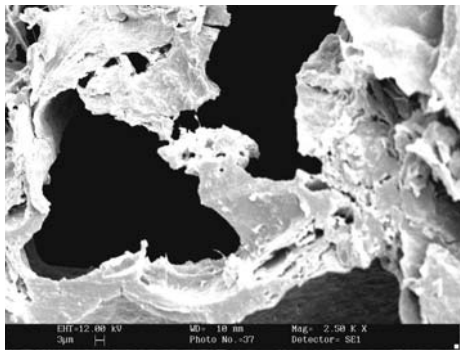

(c) *In vitro* degradation after 44 weeks (High magnification view)

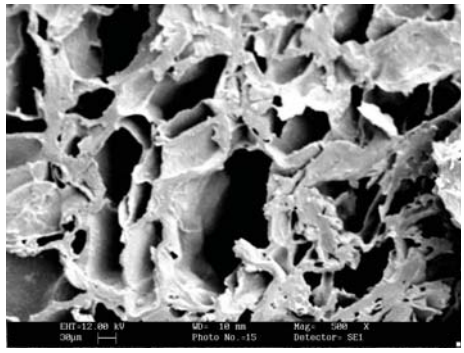

(d) *In vitro* degradation after 4 weeks

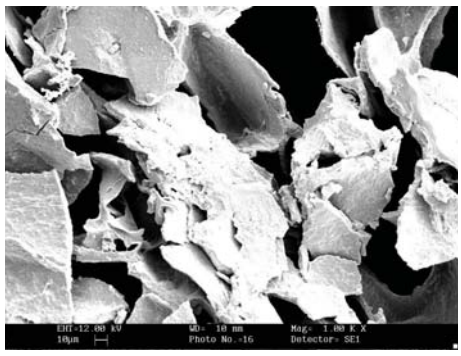

(e) *In vitro* degradation after 44 weeks

Figure 10: SEM micrographs of PHBV scaffolds after *in vitro* degradation in PBS at 37° (a, b, and c); SEM micrographs of HA/PHBV composite scaffolds: after *in vitro* degradation for 4 weeks (d) and 24 weeks (e) in PBS at 37°.

biodegradation of PHB or PHBV. The degree of crystallinity is the major factor which controls the hydrolysis rate [27].

The weight loss can be caused by physical disintegration and fragmentation of scaffolds. The hydrolytic scission of polymer backbone in the scaffolds gradually produces short-chain monomer molecules that absorb more water molecules from the aqueous medium. Figure 8(a) deals with the scaffolds prepared from 5% (w/v) and 10% emulsion concentration. As the scaffolds porosity increases with decreasing emulsion concentration, so it can be demonstrated that scaffolds weight loss increases with increasing porosity of the scaffolds. On the other hand, after certain period of time, the dissolution rate of nanosized HA may increase which can quicken the disintegration process (Figure 8(b)). For this reason, the weight loss of nHA-incorporated composite scaffolds was faster than PHBV scaffolds. Similar observations were obtained by several other research groups [8]. *In vitro* degradation experiment of phosphate glass-reinforced PHB-based degradable composites was studied in (PBS), and the results showed that the mass loss and mechanical property change could be closely correlated with the solubility rate of the reinforcing glass [8]. It was also demonstrated that the polymer was highly permeable.

Accelerated hydrolysis at elevated temperatures (55 and 70°C) was also investigated [28], and it was found that a homogeneous process was involved which had two stages. Above 60°C, there was no induction period, and the initial random scission of the ester groups occurred throughout

the polymer (amorphous and crystalline regions) which directed to a decrease in molecular weight but little change in the polydispersity and almost no bulk mass loss. As the scaffolds are intended to apply for biomedical application in the current study, experiments were conducted mainly on physiological temperature and condition.

It was established that the strength and stiffness of the materials reduced on *in vitro* environment exposure in PBS at 37°C for periods up to 4 months (Figure 9). The degradation rate was a function of composition and processing conditions, and the materials did not show any conclusive evidence of extensive structural breakdown *in vitro* during the study period. Major morphological changes were observed in composite scaffolds after the study period (Figures 10(d) and 10(e)). Fabrication, characterization, and *in vitro* degradation of composite scaffolds based on PHBV and bioactive glass (BG) were performed by another research group [29]. These results suggested that incorporation of BG into PHBV could improve the hydrophilicity of the composites, and the enhancement was dependent on the BG content. In the current study, the degradation assessment of the scaffolds was performed in PBS at 37°C, and the measurement of molecular weight loss of the PHBV scaffolds showed that the degradation rate is slow. The weight loss, crystallinity, and compressive mechanical properties of PHBV scaffolds were also monitored and compared with that of 10% nHA/PHBV composite scaffolds. The nanosized HA particles in the composite scaffolds accelerated the weight loss of the composite scaffolds due to dissolution of nHA particles and capillary water uptake through the interfaces of nHA particles. This process can increase the hydrolytic attack of the polymer matrix. The increasing trend of crystallinity of PHBV scaffolds and nHA/PHBV scaffolds was due to the degradation of the amorphous part of the polymers. This degradation was a result of hydrolytic scission of polymer chains in the more susceptible amorphous part of the scaffold matrix. The decrease in compressive properties can emphasize the fact that degradation proceeded with random cleavage of polymer chain backbone. The *in vitro* biological evaluation study was reported separately [19].

5. Conclusions

The scaffolds fabricated using emulsion freezing/freeze-drying technique exhibited the combined properties of high porosity, relatively low density, and optimum pore size distribution with good compressive mechanical properties. PHBV and nHA/PHBV scaffolds underwent hydrolytic degradation at 37°C. Mass losses, molecular weight loss of PHBV, decrease in compressive mechanical properties, increase in polymer crystallinity, and loss of structural integrity were observed during degradation. It was observed that autocatalytic rate equation can be applied for first 24 weeks of *in vitro* degradation. Successful fabrication of polymer and osteoconductive composite scaffolds with controlled porosity, pore size distribution together with slow and controlled degradation properties suggests great promise for the bone tissue-engineering applications.

Acknowledgments

N. Sultana thanks The University of Hong Kong (HKU) for providing her with a research studentship. This paper is a part of PhD thesis submitted to the University of Hong Kong by N. Sultana. Supervision of Professor Min Wang (HKU) is acknowledged. Assistance provided by Dr. Zhou Wenyou for the synthesis of HA is also acknowledged. This work was supported by a GRF grant (HKU 7182/05E) from the Research Grants Council of Hong Kong. N. Sultana and T. H. Khan also acknowledge the financial support provided by UTM research grant GUP Tier 2 (vote: Q.J130000.7136.03J35), (vote: Q.130000.7136.03J33), Ministry of Higher Education (MOHE) and RMC.

References

[1] L. G. Griffith and G. Naughton, "Tissue engineering—current challenges and expanding opportunities," *Science*, vol. 295, no. 5557, pp. 1009–1014, 2002.

[2] B. D. Ratner, *Biomaterials Science: An Introduction to Materials in Medicine*, Elsevier Academic Press, London, UK, 2nd edition, 2004.

[3] P. X. Ma, "Scaffolds for tissue fabrication," *Materials Today*, vol. 7, no. 5, pp. 30–40, 2004.

[4] K. U. Lewandrowski, *Tissue Engineering and Biodegradable Equivalents: Scientific and Clinical Applications*, Dekker, New York, NY, USA, 2002.

[5] J. B. Park and J. D. Bronzino, Eds., *Biomaterials: Principles and Applications*, CRC Press, Boca Raton, Fla, USA, 2003.

[6] P.A. Holmes, *Developments in Crystalline Polymers-2*, Edited by D. C. Basset, Elsevier Applied Science, London, UK, 1987.

[7] W. D. Luzier, "Materials derived from biomass/biodegradable materials," *Proceedings of the National Academy of Sciences of the United States of America*, vol. 89, no. 3, pp. 839–842, 1992.

[8] J. C. Knowles, G. W. Hastings, H. Ohta, S. Niwa, and N. Boeree, "Development of a degradable composite for orthopaedic use: in vivo biomechanical and histological evaluation of two bioactive degradable composites based on the polyhydroxybutyrate polymer," *Biomaterials*, vol. 13, no. 8, pp. 491–496, 1992.

[9] S. Gogolewski, M. Jovanovic, S. M. Perren, J. G. Dillon, and M. K. Hughes, "Tissue response and in vivo degradation of selected polyhydroxyacids: Polylactides (PLA), poly(3-hydroxybutyrate) (PHB), and poly(3- hydroxybutyrate-co-3-hydroxyvalerate) (PHB/VA)," *Journal of Biomedical Materials Research*, vol. 27, no. 9, pp. 1135–1148, 1993.

[10] A. Kumarasuriyar, R. A. Jackson, L. Grøndahl, M. Trau, V. Nurcombe, and S. M. Cool, "Poly(β-hydroxybutyrate-co-β-hydroxyvalerate) supports in vitro osteogenesis," *Tissue Engineering*, vol. 11, no. 7-8, pp. 1281–1295, 2005.

[11] C. Bastioli, *Handbook of Biodegradable Polymers*, Rapra Technology, Shrewsbury, UK, 2005.

[12] S. F. Williums and D. P. Martin, "Applications of PHAs in medicine and pharmacy," in *Biopolymers: Polyesters III*, Y. Doi and A. Steinbüchel, Eds., p. 91, Wiley-VCH, Weinheim, Germany, 2002.

[13] J. Liu, B. Zhao, Y. Zhang, Y. Lin, P. Hu, and C. Ye, "PHBV and predifferentiated human adipose-derived stem cells for cartilage tissue engineering," *Journal of Biomedical Materials Research. Part A*, vol. 94, no. 2, pp. 603–610, 2010.

[14] S. Li, "Degradation of biodegradable aliphatic polyesters," in *Scaffolding in Tissue Engineering*, P. X. Ma and J. Elisseeff, Eds., Taylor & Francis, 2006.

[15] N. A. Weir, F. J. Buchanan, J. F. Orr, and G. R. Dickson, "Degradation of poly-L-lactide. Part 1: in vitro and in vivo physiological temperature degradation," *Proceedings of the Institution of Mechanical Engineers, Part H*, vol. 218, no. 5, pp. 307–319, 2004.

[16] H. W. Tong, M. Wang, Z. Y. Li, and W. W. Lu, "Electrospinning, characterization and in vitro biological evaluation of nanocomposite fibers containing carbonated hydroxyapatite nanoparticles," *Biomedical Materials*, vol. 5, no. 5, Article ID 054111, 2010.

[17] N. Sultana and M. Wang, "PHBV/PLLA-based composite scaffolds containing nano-sized hydroxyapatite particles for bone tissue engineering," *Journal of Experimental Nanoscience*, vol. 3, no. 2, pp. 121–132, 2008.

[18] N. Sultana and M. Wang, "Fabrication of HA/PHBV composite scaffolds through the emulsion freezing/freeze-drying process and characterisation of the scaffolds," *Journal of Materials Science: Materials in Medicine*, vol. 19, no. 7, pp. 2555–2561, 2008.

[19] N. Sultana and M. Wang, "PHBV/PLLA-based composite scaffolds fabricated using an emulsion freezing/freeze-drying technique for bone tissue engineering: surface modification and in vitro biological evaluation," *Biofabrication*, vol. 4, no. 1, Article ID 015003, 2012.

[20] W. Y. Zhou, M. Wang, W. L. Cheung, B. C. Guo, and D. M. Jia, "Synthesis of carbonated hydroxyapatite nanospheres through nanoemulsion," *Journal of Materials Science: Materials in Medicine*, vol. 19, no. 1, pp. 103–110, 2008.

[21] J. F. Zhang and X. Sun, "Mechanical properties and crystallization behavior of poly(lactic acid) blended with dendritic hyperbranched polymer," *Polymer International*, vol. 53, no. 6, pp. 716–722, 2004.

[22] Y. Y. Hsu, J. D. Gresser, D. J. Trantolo, C. M. Lyons, P. R. J. Gangadharam, and D. L. Wise, "Effect of polymer foam morphology and density on kinetics of in vitro controlled release of isoniazid from compressed foam matrices," *Journal of Biomedical Materials Research*, vol. 35, no. 1, pp. 107–116, 1997.

[23] ASTM standard F 1635-04a, "Standard test method for in vitro degradation testing of hydrolytically degradable polymer resins and fabricated forms for surgical implants," ASTM International, West Conshohocken, Pa, USA, 2004.

[24] L. J. Gibson and M. F. Ashby, *Cellular Solids : Structure and Properties*, Cambridge Solid State Science Series, Cambridge University Press, Cambridge, UK, 2nd edition, 1997.

[25] H. Tsuji, *Degradation of Poly (lactide)—Based Biodegradable Materials*, Nova Science, New York, NU, USA, 2008.

[26] F. V. Burkersroda, L. Schedl, and A. Göpferich, "Why degradable polymers undergo surface erosion or bulk erosion," *Biomaterials*, vol. 23, no. 21, pp. 4221–4231, 2002.

[27] W. Amass, A. Amass, and B. Tighe, "A review of biodegradable polymers: uses, current developments in the synthesis and characterization of biodegradable polyesters, blends of biodegradable polymers and recent advances in biodegradation studies," *Polymer International*, vol. 47, no. 2, pp. 89–144, 1998.

[28] A. C. Albertsson, *Degradable Aliphatic Polyesters. Advances in Polymer Science*, Springer, Berlin, Germany, 2002.

[29] H. Li, R. Du, and J. Chang, "Fabrication, characterization, and in vitro degradation of composite scaffolds based on PHBV and bioactive glass," *Journal of Biomaterials Applications*, vol. 20, no. 2, pp. 137–155, 2005.

Hindawi Publishing Corporation
Journal of Nanomaterials
Volume 2012, Article ID 981670, 9 pages
doi:10.1155/2012/981670

Research Article

Novel Mannan-PEG-PE Modified Bioadhesive PLGA Nanoparticles for Targeted Gene Delivery

Guicun Wu,[1] Fang Zhou,[2] Linfu Ge,[2] Ximin Liu,[2] and Fansheng Kong[2]

[1] *Department of Hematology, Shandong Provincial Crops Hospital, Chinese People's Armed Forces, Jinan, China*
[2] *Department of Hematology, General Hospital of Jinan Command, PLA, Jinan, 250031, China*

Correspondence should be addressed to Fansheng Kong, kongfanshengphd@yahoo.com.cn

Received 22 December 2011; Accepted 30 March 2012

Academic Editor: Patricia Murray

Purpose. Biodegradable polymeric nanoparticles have been used frequently as gene delivery vehicles. The aim of this study is to modify bioadhesive PLGA nanoparticles with novel synthetic mannan-PEG-PE (MN-PEG-PE) to obtain active targeted gene delivery system. *Methods*. Mannan-PEG-PE ligands were synthesized and modified onto the NPs/pEGFP complexes. The modification rate was optimized, and the characteristics of the vehicle were evaluated. Then, the modified vectors were intravenous delivered to rats, and *in vivo* targeting behavior of MN-PEG-PE modified PLGA nanoparticles/pEGFP complexes (MN-PEG-PE-NPs/pEGFP) in liver macrophages was investigated. *Results*. MN-PEG-PE-NPs/pEGFP displayed remarkably higher transfection efficiencies than nonmodified NPs/pEGFP both *in vitro* and *in vivo*. *Conclusions*. Mannan containing targeting ligands could significantly improve the transfection efficiency of the carriers. MN-PEG-PE modified vectors very useful in targeted gene delivery.

1. Introduction

Nonviral pharmaceutical vectors, such as polymeric nanoparticles, liposomes, micelles, nanocapsules, solid lipid nanoparticles, niosomes, and other vectors, have been widely used for drug/gene delivery because they are less toxic, less immunogenic, and easy to be modified [1–5]. Biodegradable polymeric nanoparticles have been used frequently as gene delivery vehicles due to their extensive bioavailability, better encapsulation, high stability, and minimal toxicity [6, 7]. They can be tailor-made to achieve both controlled drug release and active targeting by tuning the polymer characteristics and shaping the surface through nanoengineering [8, 9]. A number of different polymers, both synthetic and natural, have been utilized in formulating biodegradable nanoparticles [10–14].

One of the most extensively investigated polymers for nanoparticles is the biodegradable and biocompatible poly (D,L-lactide-co-glycolide) (PLGA), which has been approved by the FDA for certain human clinical uses [15]. In our previous study, a novel mannan modified DNA loaded bioadhesive PLGA nanoparticles (MAN-DNA-NPs) were investigated for targeted gene delivery to the rats Kupffer cells (KCs) [16]. Bioadhesive PLGA nanoparticles were prepared and subsequently bound with pEGFP. Following the coupling of the mannan-based PE-grafted ligands (MAN-PE) with the DNA-NPs, the MAN-DNA-NPs were delivered intravenously to rats and achieved high *in vivo* transfection efficiency. So PLGA nanoparticles modified with mannan could be a promising carrier for gene delivery.

Poly(ethylene glycol) (PEG) modification of nanocarriers have emerged as common strategies to ensure stealth shielding and long-circulation and could also provide the nanocarriers active targeting properties by covalent attached with the wide assortment of targeting ligands by amide bonding or disulfide bridge formation [17]. A series of PEG containing ligands commonly named PEG-phosphatidylethanolamine (PEG-PE) conjugates were reported by Torchilin's group. They demonstrated that PEG-PE conjugates with various PEG lengths and terminal targeted moieties can provide extremely stable, long-circulating, and active-targeting nanocarriers spontaneously accumulate in specific sites [4, 18, 19]. Then PEG-PE was widely used in nanoparticulate formulations [20, 21]. After that, several ligands i.e. PEG-PE (TAT-PEG-PE for instant) were also applied for targeted delivery of drugs/genes [22–24].

In this study, a novel conjugated ligand mannan-PEG-PE (MN-PEG-PE) was synthesized, and MN-PEG-PE modified bioadhesive PLGA nanoparticles were investigated as active targeted gene delivery system using plasmid enhanced green fluorescent protein (pEGFP) as the model gene. The novel modified vectors were intravenous delivered to rats and *in vivo* targeting behavior of MN-PEG-PE modified PLGA nanoparticles/pEGFP complexes (MN-PEG-PE-NPs/pEGFP) in liver macrophages was investigated in comparison with non-modified NPs/pEGFP complexes and Lipofectamine 2000/pEGFP (Lipo/pEGFP) complexes.

2. Materials and Methods

2.1. Materials. Poly(D,L-lactic-*co*-glycolic) (PLGA, 50 : 50, Av. MW 25,000) was obtained from Shandong Institute of Medical Instrument (China). Butyl carbonyl (Boc)-NH-PEG_{2000}-COOH was purchased from Shanghai Yarebio Co., Ltd. (China). Mannan, L-α-phosphatidylethanolamine (PE), Concanavalin A (Con A), and MTT (3-[4,5-dimehyl-2-thiazolyl]-2,5-diphenyl-2H-tetrazolium bromide) were purchased from Sigma-Aldrich Co., Ltd. (USA). pEGFP-N1 was provided by Shandong University (China). Quant-iT PicoGreen dsDNA quantitation reagent and Lipofectamine 2000 were obtained from Invitrogen by Life Technologies (USA). All other chemicals were of analytical grade or higher.

2.2. Animals. Adult male Sprague Dawley rats (10 to 12 weeks old) were purchased from the Medical Animal Test Center of Shandong Province and housed under standard laboratory conditions. All animal experiments complied with the requirements of the National Act on the Use of Experimental Animals (People's Republic of China).

2.3. Synthesis of MN-PEG-PE Ligands. MN-PEG-PE ligands were synthesized as described in Figure 1. Boc-NH-PEG-COOH (100 mg) was dissolved with dimethyl sulfoxide (DMSO) and stirred with PE (36 mg) as a mixture. 1-[3-(dimethylamino)propyl]-3-ethylcarbodiimide (EDC·HCl) (72 mg) and triethylamine (TEA, 1 equivalent of EDC·HCl) were dissolved in DMSO and added dropwise into the mixture in an ice bath, stirred for 36 hours, then the concentrated hydrochloric acid was used to detach the Boc group, to produce NH_2-PEG-CO-NH-PE. Mannan (100 mg) was dissolved with sodium hydroxide (1 M, 1 mL) and stirred for 30 min for alkalinization, then chloroacetic acid (20%, 1 mL) was added into the solution and stirred in an oil bath (60°C) for 6 h. After that, hydrochloric acid (1 M) was added until pH 2-3 to complete the carboxymethylation of mannan [25]. Carboxymethylated mannan was then stirred with NH_2-PEG-CO-NH-PE in DMSO solution, and EDC·HCl mixed with TEA (1 equivalent of EDC·HCl, in DMSO) were added dropwise into the solution in an ice bath, stirred for 24 hours. DMSO was moved by rotary evaporation, and the product was dialyzed against *Milli-Q* water for 24 hours to finally form MN-PEG-PE. The structure of MN-PEG-PE was confirmed by IR and ^{1}H NMR spectroscopy. IR ν/cm^{-1}: 3517.3 (-NH-, -OH); 1820.4 (-C=O); 1667.9 (-HN-CO-); 1635.2 (-HN-CO-). ^{1}H NMR (DMSO-d6, 300 MHz) δ: 2.47 (CH_2CO), 3.26 (CH_2N) 6.05 (NH).

2.4. Preparation of pEGFP Loaded Bioadhesive PLGA Nanoparticles. Bioadhesive PLGA nanoparticles (NPs) were prepared following the methods described previously by our group [16]. Briefly, Carbopol 940 (CP) was dispersed in distilled water at room temperature and left overnight to swell. Required amount of 1 M NaOH was added to neutralize the dispersion until pH 7.0 was reached and diluted with distilled water to afford a 0.02% (w/v) CP solution. Bioadhesive PLGA nanoparticles were prepared under optimized conditions by a nanoprecipitation method (solvent displacement technique) [26, 27]. 50 mg of PLGA polymer was accurately weighted and dissolved in 3 mL acetone. The organic phase was added dropwise into the 0.02% CP solution being stirred at 600 rpm at room temperature. When complete evaporation of the organic solvent had occurred, the redundant stabilizers and the nanoparticles were separated by ultracentrifugation at 1000 g, 4°C for 20 min. The pellet was resuspended in Milli-Q water, washed three times, and filtered through a 0.45 μm membrane.

The reporter gene pEGFP was mixed with the PLGA nanoparticles by vortexing the nanoparticle suspension with a 1 mg/mL solution of DNA for 20 s. Incubation of the mixture for 30 min at RT facilitated the formation of the pEGFP-loaded PLGA nanoparticles (NPs/pEGFP) (Figure 2).

2.5. Modification of NPs/pEGFP with MN-PEG-PE. MN-PEG-PE modified NPs/pEGFP complexes (MN-PEG-PE-NPs/pEGFP) were produced by solvent diffusion method (Figure 2) [28, 29]. Briefly, MN-PEG-PE ligands were dissolved in 2 mL of phosphate buffered saline (PBS, pH 7.4). Then the solution was added dropwise into 10 mL of NPs/pEGFP complexes that was stirred at 600 rpm at RT leading to the immediate modification. Subsequently, free MN-PEG-PE was removed from modified NPs/pEGFP by gel chromatography using a Sephadex G-50 column (GE Healthcare, Sweden). The obtained complexes were resuspended in Milli-Q water, washed three times, and filtered through a membrane with 0.80 μm pore size to obtain MN-PEG-PE-NPs/pEGFP. To optimize the modification ratio, MN-PEG-PE ligands dissolved in PBS were designed at different weight rate to the NPs/pEGFP (w/w). The particle sizes and zeta potential of complexes were determined using a Zetasizer Nano-ZS instrument (Malvern Instruments, UK).

2.6. Determination of MN-PEG-PE Modification. To confirm the success of modification and determine the best ratio of MN-PEG-PE to NPs/pEGFP, several experiments were carried out.

2.6.1. Particle Sizes Determination and PicoGreen-Fluorometry Assay. During the modification procedure, MN-PEG-PE ligands were coated onto the NPs/pEGFP carriers due to the bioadhesive property of CP coated on the surface of the NPs. Theoretically, the more ligands modified onto the carriers, the better targeted delivery ability they will

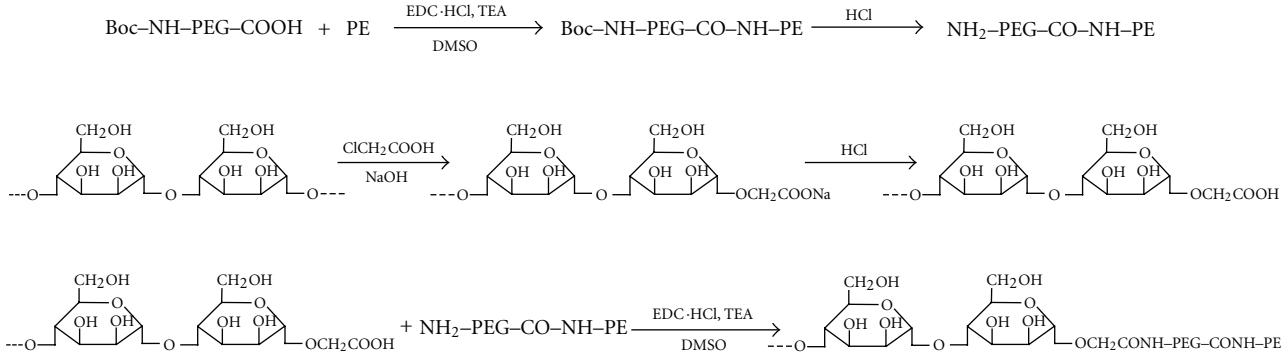

Figure 1: General reaction scheme for the synthesis of MN-PEG-PE.

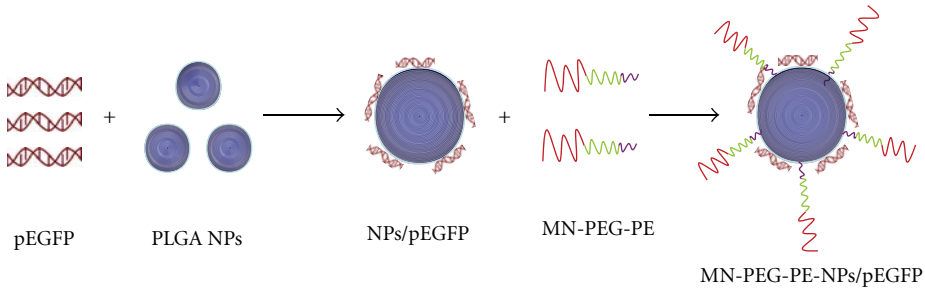

Figure 2: Preparation and modification of NPs-pEGFP complexes.

achieve. However, excessive modification could mask the surface change of the particle and cause the instability of the system. The complexes may disintegrate and pEGFP would detach from the vector and cause the notable decrease of the gene loading capacity, or the particles may aggregate and cause the mutation of particle size.

The particle sizes of the complexes at different ratios of MN-PEG-PE to NPs/pEGFP were detected to optimize the modification rate. The rates that obviously increase the particle sizes of the complexes are not suitable.

PicoGreen-fluorometry assay was used to further determine the appropriate modification rate of MN-PEG-PE ligands and also to quantitate the amount of pEGFP carried by the optimum modified NPs [30]. Different ratios of MN-PEG-PE to NPs/pEGFP were prepared and the pEGFP was isolated from the MN-PEG-PE- NPs/pEGFP by centrifugation at 1000 g, 4°C for 30 min. The concentration of pEGFP was determined by fluorescence, comparing with the supernatant from NPs. The amount of pEGFP loaded in the NPs was calculated according to the linear calibration curve of pEGFP.

2.6.2. Concanavalin A (Con A) Agglutination Study. Binding of the terminal α-mannose residues to Con A causes agglutination of the complexes in solution, resulting in an increase in turbidity [31]. Con A agglutination assay was performed to indentify the MN-PEG-PE ligands successfully modified onto the NPs/pEGFP surface. 100 μL of MN-PEG-PE-NPs/pEGFP complexes was added into 500 μL of Con A (1 mg/mL) in PBS (pH 7.4) with 5 mM of calcium chloride (CaCl2) and 5 mM of magnesium chloride (MgCl2). The increase in turbidity at 360 nm (OD360) was monitored.

2.7. Isolation and Culture of KCs. KCs were isolated from SD rats under pentobarbitone anaesthesia using the method described before [16]. Briefly, the rat's portal vein was cannulated and perfused with HBSS for 10 min, the liver was excised, and the perfusate was discarded. The liver was then perfused with 0.2% pronase, then with a recirculating solution of 0.05% pronase and 0.05% collagenase until the liver was digested. The liver was then cut into small pieces, suspended in the solution containing 0.02% pronase, 0.05% collagenase, and 0.005% DNase, and agitated. Following digestion, the liver homogenate was filtered through sterile gauze and centrifuged. The supernatant was removed and the pellet resuspended in Percoll gradient. Aliquots of this cell suspension were added to aliquots of Percoll gradient. These were carefully overlaid with HBSS and centrifuged. The nonparenchymal cell-enriched layer observed at the interface between the two layers was carefully harvested and diluted with HBSS. The suspension was then centrifuged to precipitate the KCs, which were then seeded into a 96-well microtiter plate in RPMI 1640 supplemented with 10% fetal bovine serum (FBS) and antibiotics. After incubation at 37°C for 2 h under 5% CO_2 atmosphere, the culture medium was replaced by 200 μL fresh RPMI 1640 to yield the purified KCs.

The isolated KCs were defined on the basis of the presence of phagocytosis of latex beads and positive immunostaining with antibody to the epitope ED2. With the above-mentioned method, about 8.28×10^7/rat liver KCs were

Table 1: Particle size and zeta potential of NPs.

Properties	Sample		
	NPs	NPs/pEGFP	MN-PEG-PE -NPs/pEGFP
Mean particle size (nm)	118.2 ± 3.4	149.5 ± 6.7	214.3 ± 8.3
Polydispersity index (PDI)	0.12 ± 0.06	0.21 ± 0.07	0.17 ± 0.08
Zeta potential (mV)	−28.36 ± 2.47	−36.17 ± 1.53	−20.28 ± 1.32

obtained; purity was about 91.8% (to 9.01×10^7/rat liver NPC). The isolated and purified rat KCs retained their *in vivo* morphological, biological, and immunological characteristics.

2.8. In Vitro Cytotoxicity Evaluation. The *in vitro* cytotoxicity of MN-PEG-PE-NPs/pEGFP in KCs was evaluated by MTT assay [32]. The KCs were incubated with MN-PEG-PE-NPs/pEGFP, unmodified NPs/pEGFP, and Lipo/pEGFP at various concentrations (10, 20, 50, 100, and 200 μg/mL) for 48 h at 37°C and 5% CO_2. The cell viability was then assessed by MTT assay. 5 mg/mL of MTT in PBS was then added to each well, and the plate was incubated for an additional 4 h at 37°C under the aforementioned 5% CO_2 atmosphere. Then the MTT containing medium was removed, and the crystals formed by living cells were dissolved in 100 μL DMSO. The absorbance at 570 nm was determined by a microplate reader. Untreated cells were taken as a control with 100% viability, and cells without the addition of MTT were used as a blank to calibrate the spectrophotometer to zero absorbance. The relative cell viability (%) compared to control cells was calculated using $(\text{Abs}_{\text{sample}}/\text{Abs}_{\text{control}}) \times 100$.

2.9. In Vitro Transfection Analysis. For transfection efficiency analysis, the KCs were seeded into 24-well plates at a density of 1×10^5cells/well in 1 mL of RPMI-1640 with 10% FBS. After about 24 h, the media were replaced with 400 μL transfection media containing MN-PEG-PE-NPs/pEGFP. Naked DNA, unmodified NPs/pEGFP, and Lipo/pEGFP were used as controls. The original incubation medium was replaced with 1 mL of complete medium after incubation at 37°C for 4 h under a 5% CO2 atmosphere. The cells were incubated and studied until 72 h after transfection. The fluorescent cells were observed using an inversion fluorescence microscope, at which time pictures were taken for the record.

2.10. In Vivo Gene Delivery. Adult male SD rats were divided into four groups (six rats in each group) and injected intravenously with 1 mL of MN-PEG-PE-NPs/pEGFP, NPs/pEGFP, Lipo/pEGFP, and naked pEGFP. At predetermined time intervals, the rats' KCs were isolated as described in Section 2.7. The cells were washed with 1 mL of PBS (100 g, 4°C for 5 min) and were detached with trypsin/EDTA. The supernatant was discarded and resuspended with 300 μL of PBS and added into the flow cytometry to determine the amount of KCs which has been successfully transfected.

2.11. Statistical Analysis. All studies were repeated three times, and all measurements were carried out in triplicate. Results were reported as means ± SD (SD = standard deviation). Statistical significance was analyzed using the Student's t-test. Differences between experimental groups were considered significant when the P value was less than 0.05 ($P < 0.05$).

3. Results

3.1. Characterization of pEGFP Loaded NPs. Mean particle size, polydispersity index (PDI), and zeta potential of NPs, NPs/pEGFP, and MN-PEG-PE-NPs/pEGFP were characterized and summarized in Table 1.

3.2. Optimization of the MN-PEG-PE Modification Rate. The particle sizes of the complexes at different ratios of MN-PEG-PE to NPs/pEGFP were detected and illustrated in Figure 3. With the increasing of the modification rate (from 5% to 20%), the particle size of NPs showed no obvious change (all around 210 mn). When the ratio of the ligands was increased to 35%, the particle size decreased to about 180mn, and then the size rose to 530 mn when the rate reached 45%.

PicoGreen-fluorometry assay was used to further determine the best modification rate of MN-PEG-PE ligands to the NPs/pEGFP carriers. Different ratios of MN-PEG-PE to NPs/pEGFP were prepared through the same method, and the amount of pEGFP was quantitated. Gene loading quantity(%)=(total amount of pEGFP − the amount of free pEGFP)/total amount of DNA × 100. The loading quantity of pEGFP loaded in the various modified NPs was calculated and displayed in Figure 4. Nonmodified NPs (0%) reach the gene loading quantity of 88.46%. With the increasing of the modification rate (from 5% to 20%), the loading amount of pEGFP showed no obvious change (all around 88%). When the ratio of the ligands was above 20%, the loading capacity was decreased, and observed only 36% gene carried at the ratio of 35%. Then the loading amount increased when the rate increased above 35%.

As the results proved clearly, the optimized rate of the MN-PEG-PE to NPs/pEGFP was 20%. This ratio was determined and used for the further experiments.

3.3. Determination of MN-PEG-PE Modification. Con A agglutination study was applied to further indentify the MN-PEG-PE ligands successfully modified onto the NPs/pEGFP surface. As stated above, the ratio of the MN-PEG-PE to NPs/pEGFP was 20% in this experiment and the following

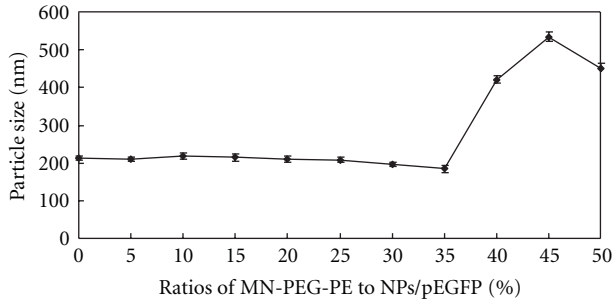

Figure 3: Optimization of MN-PEG-PE modification rate: Particle sizes determination.

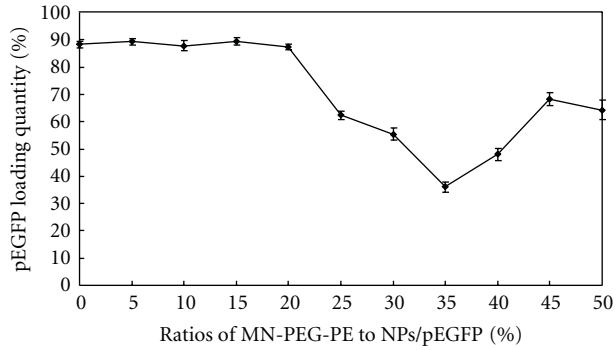

Figure 4: Optimization of MN-PEG-PE modification rate: Pico-Green-fluorometry assay.

investigation. The appearance in turbidity was monitored for 180 seconds (Figure 5).

MN-PEG-PE-NPs/pEGFP showed apparently increase in turbidity and reached 0.19 at the end of 180 s. NPs and NPs/pEGFP formulations appeared to show no significant increase in turbidity.

3.4. In Vitro Cytotoxicity Evaluation. *In vitro* cytotoxicity of MN-PEG-PE-NPs/pEGFP and non-modified NPs/pEGFP at various concentrations was evaluated by MTT assay. The cell viabilities of the NPs over the studied concentration range (10~200 μg/mL) were between 80% and 100% compared with controls (Figure 6). MN-PEG-PE-NPs/pEGFP exhibited no higher cytotoxicity than NPs/pEGFP and Lipo/pEGFP at all concentrations ($P > 0.05$).

3.5. In Vitro Transfection Analysis. The *in vitro* transfection efficiencies of MN-PEG-PE-NPs/pEGFP and NPs/pEGFP in KCs after 72 h of transfection were analyzed. Naked DNA was used as a negative control. When compared with naked DNA and NPs/pEGFP, MN-PEG-PE-NPs/pEGFP had higher transfection efficiency at different time intervals (Figure 7).

3.6. In Vivo Gene Delivery. After intravenous injection with 1 mL of MN-PEG-PE-NPs/pEGFP, NPs/pEGFP, and naked pEGFP, the rats were euthanized and the KCs were isolated at 48 h and 72 h. Flow cytometry was applied to quantitate the amount of cells which have been successfully transfected.

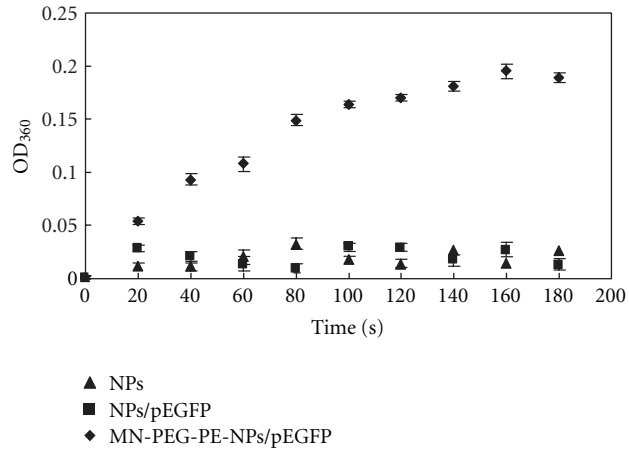

Figure 5: The turbidity of NPs, NPs/pEGFP, and MN-PEG-PE-NPs/pEGFP at different time intervals.

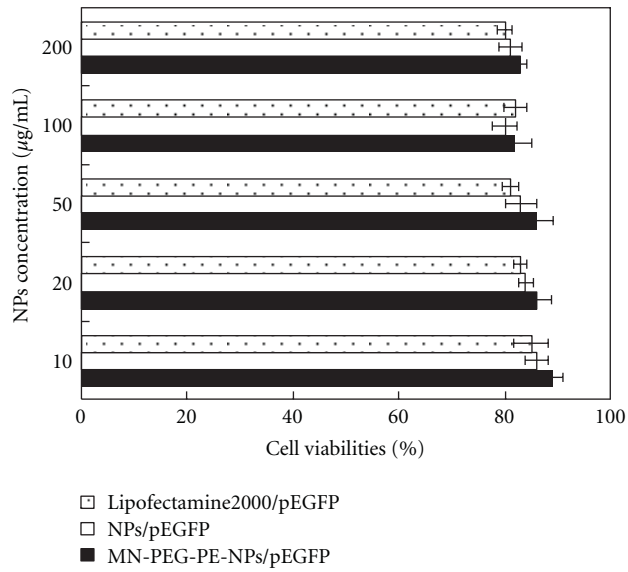

Figure 6: Cell viabilities of MN-PEG-PE-NPs/pEGFP and NPs/pEGFP.

As shown in Figure 8, MN-PEG-PE-NPs/pEGFP displayed a remarkably higher transfection efficiency than non-modified NPs/pEGFP ($P < 0.05$) and naked pEGFP ($P < 0.05$), especially at 72 h after transfection.

4. Discussion

Biodegradable polymeric nanoparticles have been used frequently as gene delivery vehicles because they can be tailor made and surface modified to achieve both controlled drug release and active targeting. In the present study, novel conjugated mannan containing ligand MN-PEG-PE was synthesized and MN-PEG-PE modified bioadhesive PLGA nanoparticles were investigated as active targeting gene delivery system.

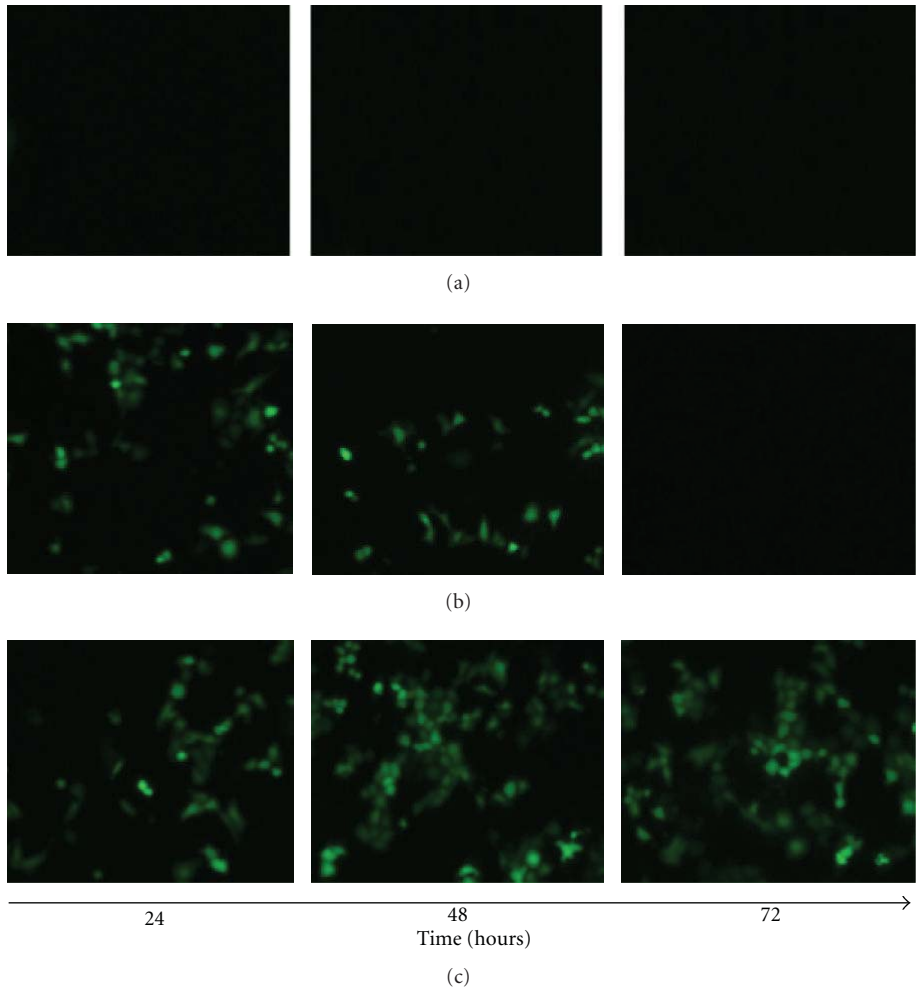

Figure 7: Fluorescent images of the KCs transfected with naked pEGFP (a), NPs/pEGFP (b), and MN-PEG-PE-NPs/pEGFP (c) at 24, 48, and 72 hours after transfection.

We began our investigation by synthesizing mannan containing PEG-PE ligand. Here, mannan is the target moiety which could bind to the mannose receptor (MR) in the macrophage, and PEG-PE is the spacer linked into the surface of NPs. It is reviewed that the length and flexibility of the spacer between the carbohydrate head group and nanocarrier surface mainly influence the target specificity and uptake of vectors by macrophages [33]. PEG-PE conjugates were reported, and TATp-PEG_{2000}-PE conjugates have been applied for the modification of nanocarriers to form active-targeting vectors [22], thus PEG_{2000}-PE was used at the anchor.

After the preparation of bioadhesive NPs and binding of NPs with pEGFP, MN-PEG-PE ligands were modified onto the NPs/pEGFP complexes by solvent diffusion method. The mannose group density is an important factor on the targeting efficiency [34] and vectors modified with higher content of sugar residues usually exhibit more efficient cellular recognition and internalization compare with lower sugar density. So theoretically, the more MN-PEG-PE ligands modified onto the carriers, the better targeted delivery ability they will achieve. However, excessive modification could mask the surface change of the particle and cause the instability of the system. The complexes may disintegrate, and pEGFP would detach from the vector and cause the notable decrease of the gene loading capacity, or the particles may aggregate and cause the mutation of particle size. Particle size measurement was applied, and particle sizes of the complexes at different ratios of MN-PEG-PE to NPs/pEGFP were detected (Figure 3). With the increasing of the modification rate (from 5% to 20%), the particle size of NPs showed no obvious change (all around 210 mn). When the ratio increased to 35%, the size decreased to about 180mn, which may be explained by the separation of pEGFP form the vectors. When the rates continue to rise, the size rose to above 500 nm. This could be the proof of the aggregation of the NPs. PicoGreen-fluorometry assay was used to further determine the appropriate modification rate of MN-PEG-PE ligands and also to quantitate the amount of pEGFP carried by the optimum modified NPs. With the increasing of the modification rate (from 5% to 20%), the loading amount of pEGFP showed no obvious change (all around 88%). When

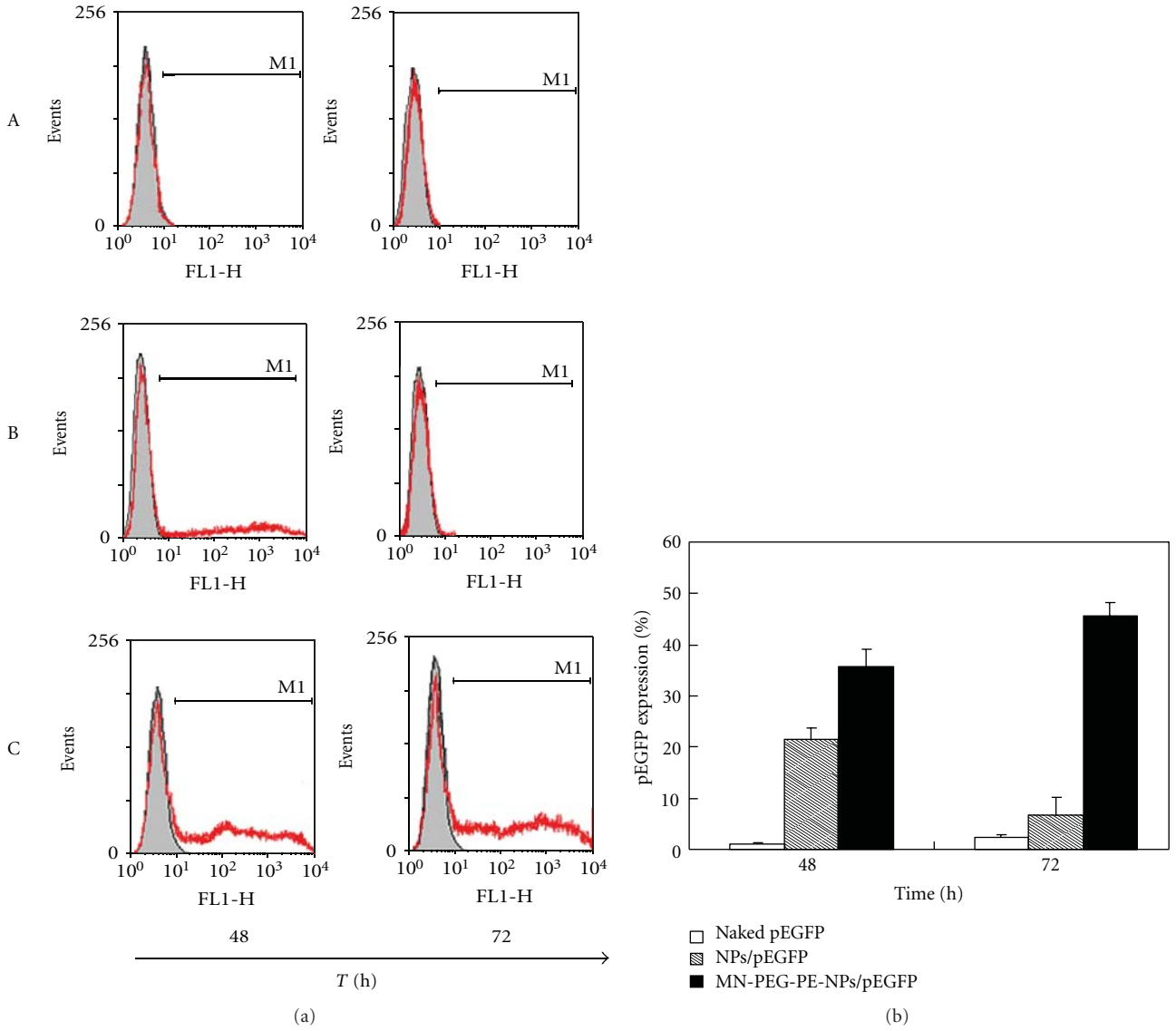

Figure 8: Flow cytometry analysis of KCs transfected by naked pEGFP (A), NPs/pEGFP (B) and MN-PEG-PE-NPs/pEGFP (C) *in vivo*.

the ratio of the ligands was above 20%, the loading capacity was decreased, and observed only 36% gene carried at the ratio of 35%. Then the loading amount increased when the rate increased above 35%. This could be explained by the aggregation of NPs reload with some of the pEGFP released form the NPs and caused the increase of loading amount to around 60%.

Con A was the first legume lectin recognized as one of the mannose-specific lectins and believed to play a role in recognition of mannose containing vectors [31, 35]. It was extensively used for the evaluating of glycoconjugates [36, 37]. Binding of the terminal α-mannose residues to Con A causes agglutination of the complexes in solution, resulting in an increase in turbidity. As shown in Figure 5, MN-PEG-PE-NPs/pEGFP showed apparent increase in turbidity and NPs and NPs/pEGFP formulations appeared to show no significant increase in turbidity. These could be the evidence of the success of mannan containing ligands modified onto the nanoparticle surface.

Targeting macrophages is one of the promising therapeutic ways to treat genetic metabolic diseases such as human immunodeficiency virus infection because macrophages play a major role in the immune response to foreign antigen [38]. KCs are liver-specific resident macrophages that play an integral part in the physiological homeostasis of the liver. They have significant roles in acute and chronic responses of the liver to bacterial and viral infections and toxic or carcinogenic attack as well as mediating hepatotoxicity [39]. In this study, rat KCs were isolated and used as model cells for *in vitro* cytotoxicity evaluation and transfection analysis. MN-PEG-PE-NPs/pEGFP exhibited no higher cytotoxicity than NPs/pEGFP and Lipo/pEGFP at all concentrations. When compared with naked DNA and NPs/pEGFP, MN-PEG-PE-NPs/pEGFP had higher transfection efficiency at

different time intervals. This may be explained by the active targeting mechanism mediated by sugar-lectin recognition. The MN-PEG-PE-NPs/pEGFP were more likely to bind to the KCs through the MR on the cells and delivered the DNA more easily into the cells to express EGFP. The cells exhibited better green fluorescence at 48 and 72 hours. So 48 h and 72 h were chosen as the time points for the *in vivo* gene delivery study.

The *in vivo* gene delivery and expression studies were applied in the animal models to test the gene delivery ability of the modified gene vectors. After intravenous injection, the rats were euthanized and the KCs were isolated at 48 h and analyzed with flow cytometer. MN-PEG-PE-NPs/pEGFP displayed higher transfection efficiency (36.07%) than non-modified NPs/pEGFP (21.73%) and naked pEGFP (0.82%) at 48 h and remarkably higher transfection efficiency (47.15%) than non-modified NPs/pEGFP (8.16%) and naked pEGFP (1.31%) at 72 h. These results could demonstrate, MN-PEG-PE modified NPs had the ability to target liver KCs, deliver more genes into the cells and display higher transfection efficiency. The higher transfection efficiency at 72 h after injection could also illustrate the controlled-release ability of the vehicles. These evidences could strongly support the active targeting ability of mannan containing PEG-PE modified bioadhesive PLGA nanoparticles, and the resulting vectors would be very useful in gene delivery both *in vitro* and *in vivo*.

5. Conclusions

In the present study, we further confirmed the observations of other laboratories and the researches of our group that mannose-mediated targeting can successfully deliver genes into MR expressing cells. This investigation could also demonstrate that having mannose containing targeting ligands, such as MN-PEG-PE in this research, in DNA loaded PLGA NPs could significantly improve the transfection efficiency. By carefully formulating the carriers with an optimal ratio of MN-PEG-PE, efficient gene expressions were achieved in rats' KCs both *in vitro* and *in vivo*. These evidences could strongly support the active targeting ability of mannan containing PEG-PE modified bioadhesive PLGA nanoparticles, and the resulting vectors would be very useful in gene delivery both *in vitro* and *in vivo*.

References

[1] H. Boulaiz, J. A. Marchal, J. Prados, C. Melguizo, and A. Aránega, "Non-viral and viral vectors for gene therapy," *Cellular and Molecular Biology*, vol. 51, no. 1, pp. 3–22, 2005.

[2] X. B. Zhao and R. J. Lee, "Tumor-selective targeted delivery of genes and antisense oligodeoxyribonucleotides via the folate receptor," *Advanced Drug Delivery Reviews*, vol. 56, no. 8, pp. 1193–1204, 2004.

[3] H. Atkinson and R. Chalmers, "Delivering the goods: viral and non-viral gene therapy systems and the inherent limits on cargo DNA and internal sequences," *Genetica*, vol. 138, no. 5, pp. 485–498, 2010.

[4] V. P. Torchilin, "Multifunctional nanocarriers," *Advanced Drug Delivery Reviews*, vol. 58, no. 14, pp. 1532–1555, 2006.

[5] S. D. Li and L. Huang, "Surface-modified LPD nanoparticles for tumor targeting," *Annals of the New York Academy of Sciences*, vol. 1082, pp. 1–8, 2006.

[6] A. Kumari, S. K. Yadav, and S. C. Yadav, "Biodegradable polymeric nanoparticles based drug delivery systems," *Colloids and Surfaces B*, vol. 75, no. 1, pp. 1–18, 2010.

[7] K. Chaturvedi, K. Ganguly, A. R. Kulkarni et al., "Cyclodextrin-based siRNA delivery nanocarriers: a state-of-the-art review," *Expert Opinion on Drug Delivery*, vol. 8, no. 11, pp. 1455–1468, 2011.

[8] W. E. Rudzinski and T. M. Aminabhavi, "Chitosan as a carrier for targeted delivery of small interfering RNA," *International Journal of Pharmaceutics*, vol. 399, no. 1-2, pp. 1–11, 2010.

[9] D. B. Shenoy and M. M. Amiji, "Poly(ethylene oxide)-modified poly(ε-caprolactone) nanoparticles for targeted delivery of tamoxifen in breast cancer," *International Journal of Pharmaceutics*, vol. 293, no. 1-2, pp. 261–270, 2005.

[10] R. C. Mundargi, V. R. Babu, V. Rangaswamy, P. Patel, and T. M. Aminabhavi, "Nano/micro technologies for delivering macromolecular therapeutics using poly(d,l-lactide-co-glycolide) and its derivatives," *Journal of Controlled Release*, vol. 125, no. 3, pp. 193–209, 2008.

[11] S. A. Agnihotri, N. N. Mallikarjuna, and T. M. Aminabhavi, "Recent advances on chitosan-based micro- and nanoparticles in drug delivery," *Journal of Controlled Release*, vol. 100, no. 1, pp. 5–28, 2004.

[12] S. M. Moghimi, A. C. Hunter, and J. C. Murray, "Long-circulating and target-specific nanoparticles: theory to practice," *Pharmacological Reviews*, vol. 53, no. 2, pp. 283–318, 2001.

[13] K. S. Soppimath, T. M. Aminabhavi, A. R. Kulkarni, and W. E. Rudzinski, "Biodegradable polymeric nanoparticles as drug delivery devices," *Journal of Controlled Release*, vol. 70, no. 1-2, pp. 1–20, 2001.

[14] J. Panyam and V. Labhasetwar, "Biodegradable nanoparticles for drug and gene delivery to cells and tissue," *Advanced Drug Delivery Reviews*, vol. 55, no. 3, pp. 329–347, 2003.

[15] W. Zou, C. Liu, Z. Chen, and N. Zhang, "Studies on bioadhesive PLGA nanoparticles: a promising gene delivery system for efficient gene therapy to lung cancer," *International Journal of Pharmaceutics*, vol. 370, no. 1-2, pp. 187–195, 2009.

[16] F. Zhou, F. Kong, L. Ge, X. Liu, and N. Huang, "Mannan-modified PLGA nanoparticles for targeted gene delivery," *International Journal of Photoenergy*, vol. 2012, Article ID 926754, 7 pages, 2012.

[17] L. E. Van Vlerken, T. K. Vyas, and M. M. Amiji, "Poly(ethylene glycol)-modified nanocarriers for tumor-targeted and intracellular delivery," *Pharmaceutical Research*, vol. 24, no. 8, pp. 1405–1414, 2007.

[18] V. P. Torchilin, "Micellar nanocarriers: pharmaceutical perspectives," *Pharmaceutical Research*, vol. 24, no. 1, pp. 1–16, 2007.

[19] A. N. Lukyanov, Z. Gao, L. Mazzola, and V. P. Torchilin, "Polyethylene glycol-diacyllipid micelles demonstrate increased acculumation in subcutaneous tumors in mice," *Pharmaceutical Research*, vol. 19, no. 10, pp. 1424–1429, 2002.

[20] V. P. Torchilin, "Recent advances with liposomes as pharmaceutical carriers," *Nature Reviews Drug Discovery*, vol. 4, no. 2, pp. 145–160, 2005.

[21] L. Yang, L. Wang, X. Q. Su et al., "Suppression of ovarian cancer growth via systemic administration with liposome-encapsulated adenovirus-encoding endostatin," *Cancer Gene Therapy*, vol. 17, no. 1, pp. 49–57, 2010.

[22] R. M. Sawant, J. P. Hurley, S. Salmaso et al., "'SMART' drug delivery systems: double-targeted pH-responsive pharmaceutical nanocarriers," *Bioconjugate Chemistry*, vol. 17, no. 4, pp. 943–949, 2006.

[23] J. A. Reddy, C. Abburi, H. Hofland et al., "Folate-targeted, cationic liposome-mediated gene transfer into disseminated peritoneal tumors," *Gene Therapy*, vol. 9, no. 22, pp. 1542–1560, 2002.

[24] O. Penate Medina, M. Haikola, M. Tahtinen et al., "Liposomal tumor targeting in drug delivery utilizing MMP-2- and MMP-9-binding ligands," *Journal of Drug Delivery*, vol. 2011, Article ID 160515, 9 pages, 2011.

[25] L. Yang, L. Cheng, Y. Wei, and L. Tian, "Synthesis of N-[2-(cholesteryloxycarbonylamino) ethyl] carbamoylmethylated mannan," *Journal of Sichuan University*, vol. 34, no. 4, pp. 730–732, 2003.

[26] S. J. Ahn, J. Costa, and J. R. Emanuel, "PicoGreen quantitation of DNA: effective evaluation of samples pre- or post-PCR," *Nucleic Acids Research*, vol. 24, no. 13, pp. 2623–2625, 1996.

[27] J. Ye, A. Wang, C. Liu, Z. Chen, and N. Zhang, "Anionic solid lipid nanoparticles supported on protamine/DNA complexes," *Nanotechnology*, vol. 19, no. 28, Article ID 285708, 2008.

[28] W. Wijagkanalan, S. Kawakami, M. Takenaga, R. Igarashi, F. Yamashita, and M. Hashida, "Efficient targeting to alveolar macrophages by intratracheal administration of mannosylated liposomes in rats," *Journal of Controlled Release*, vol. 125, no. 2, pp. 121–130, 2008.

[29] W. Yu, C. Liu, Y. Liu, N. Zhang, and W. Xu, "Mannan-modified solid lipid nanoparticles for targeted gene delivery to alveolar macrophages," *Pharmaceutical Research*, vol. 27, no. 8, pp. 1584–1596, 2010.

[30] N. Adjimatera, T. Kral, M. Hof, and I. S. Blagbrough, "Lipopolyamine-mediated single nanoparticle formation of calf thymus DNA analyzed by fluorescence correlation spectroscopy," *Pharmaceutical Research*, vol. 23, no. 7, pp. 1564–1573, 2006.

[31] A. Barre, Y. Bourne, E. J. M. Van Damme, W. J. Peumans, and P. Rougé, "Mannose-binding plant lectins: different structural scaffolds for a common sugar-recognition process," *Biochimie*, vol. 83, no. 7, pp. 645–651, 2001.

[32] Y. Gao, W. Gu, L. Chen, Z. Xu, and Y. Li, "A multifunctional nano device as non-viral vector for gene delivery: in vitro characteristics and transfection," *Journal of Controlled Release*, vol. 118, no. 3, pp. 381–388, 2007.

[33] W. Yu, N. Zhang, and C. Li, "Saccharide modified pharmaceutical nanocarriers for targeted drug and gene delivery," *Current Pharmaceutical Design*, vol. 15, no. 32, pp. 3826–3836, 2009.

[34] W. Yeeprae, S. Kawakami, F. Yamashita, and M. Hashida, "Effect of mannose density on mannose receptor-mediated cellular uptake of mannosylated O/W emulsions by macrophages," *Journal of Controlled Release*, vol. 114, no. 2, pp. 193–201, 2006.

[35] J. B. Summer and S. F. Howell, "The identification of the hemagglutinin of the jack bean with concanavalin A," *Journal of Bacteriology*, vol. 32, pp. 227–237, 1936.

[36] J. N. Kizhakkedathu, A. L. Creagh, R. A. Shenoi et al., "High molecular weight polyglycerol-based multivalent mannose conjugates," *Biomacromolecules*, vol. 11, no. 10, pp. 2567–2575, 2010.

[37] M. L. Wolfenden and M. J. Cloninger, "Mannose/glucose-functionalized dendrimers to investigate the predictable tunability of multivalent interactions," *Journal of the American Chemical Society*, vol. 127, no. 35, pp. 12168–12169, 2005.

[38] M. Yamada, M. Nishikawa, S. Kawakami et al., "Tissue and intrahepatic distribution and subcellular localization of a mannosylated lipoplex after intravenous administration in mice," *Journal of Controlled Release*, vol. 98, no. 1, pp. 157–167, 2004.

[39] H. Kitani, T. Takenouchi, M. Sato, M. Yoshioka, and N. Yamanaka, "A novel isolation method for macrophage-like cells from mixed primary cultures of adult rat liver cells," *Journal of Immunological Methods*, vol. 360, no. 1-2, pp. 47–55, 2010.

Hindawi Publishing Corporation
Journal of Nanomaterials
Volume 2012, Article ID 236953, 9 pages
doi:10.1155/2012/236953

Research Article

Nanopolymers Delivery of the Bone Morphogenetic Protein-4 Plasmid to Mesenchymal Stem Cells Promotes Articular Cartilage Repair In Vitro and In Vivo

Junjun Shi,[1] Xin Zhang,[1] Yanbin Pi,[1] Jingxian Zhu,[1] Chunyan Zhou,[2] and Yingfang Ao[1]

[1] *Institute of Sports Medicine, Peking University Third Hospital, Beijing 100191, China*
[2] *Department of Biochemistry and Molecular Biology, School of Basic Medical Sciences, Key Laboratory of Molecular Cardiovascular Sciences, Ministry of Education of China, Peking University, Beijing 100191, China*

Correspondence should be addressed to Chunyan Zhou, chunyanzhou@bjmu.edu.cn and Yingfang Ao, yingfang.ao@gmail.com

Received 21 March 2012; Accepted 1 April 2012

Academic Editor: Haifeng Chen

The clinical application of viral vectors for gene therapy is limited for biosafety consideration. In this study, to promote articular cartilage repair, poly (lactic-co glycolic acid) (PLGA) nanopolymers were used as non-viral vectors to transfect rabbit mesenchymal stem cells (MSCs) with the pDC316-BMP4-EGFP plasmid. The cytotoxicity and transfection efficiency in vitro were acceptable measuring by CCK-8 and flow cytometry. After transfection, Chondrogenic markers (mRNA of Col2a1, Sox9, Bmp4, and Agg) of experimental cells (MSCs being transfected with BMP-4 plasmid by PLGA nanopolymers) were increased more than those of control cells (MSCs being transfected with naked BMP-4 plasmid alone). In vivo study, twelve rabbits (24 knees) with large full thickness articular cartilage defects were randomly divided into the experimental group (MSCs being transfected with BMP-4 plasmid by PLGA nanopolymers) and the control group (MSCs being transfected with naked BMP-4 plasmid). The experimental group showed better regeneration than the control group 6 and 12 weeks postoperatively. Hyaline-like cartilage formed at week 12 in the experimental group, indicating the local delivery of BMP-4 plasmid to MSCs by PLGA nanopolymers improved articular cartilage repair significantly. PLGA nanopolymers could be a promising and effective non-viral vector for gene therapy in cartilage repair.

1. Introduction

Full-thickness articular cartilage defects in the knee are still a major problem in orthopedics because of the limited repair capacity of cartilage. These defects may result in pain, swelling, and hopping, and they may even progress to osteoarthritis. The prevalence of cartilage defects is reported to 60% in the knee arthroscopy patients worldwide [1]. Recent studies of cartilage repair have focused on tissue engineering and gene therapy.

Bone morphogenetic protein 4 (BMP-4) has attracted much attention in cartilage repair in recent years because it accelerates chondrogenesis, the deposition of both cartilage matrix and type II collagen, chondrocyte differentiation, matrix maturation, and cartilage regeneration in vitro and in vivo [2–5].

For gene delivery, viral vectors such as adenovirus and retrovirus have been frequently used and extensively investigated. But their clinical applications are limited for safety considerations. Though high transfection efficiency, these viral vectors pose the risk of recombining to regenerate wild-type, replication-competent strains and have, at some point, been associated with or caused death [6, 7]. Nonviral gene vectors such as lipoplexes, polyplexes, oligonucleotides and nanopolymers have attracted much attention recently [8]. With the rapid development of nanotechnology, there is increasing interest in nanopolymers for gene delivery because they have low immunogenicity, genotoxicity, oncogenicity and potential pathogenicity. These gene vectors are nontoxic and will not integrate into the host genome, thereby avoiding many of the risks of viral vectors. Many nanopolymers such as polyethyleneimine and poly (amido amine) dendrimers have been reported as gene delivery vectors [9–11].

However, few studies have reported on nonviral nanopolymers as gene vectors for cartilage repair.

Poly(lactic-co-glycolic acid) (PLGA) is biodegradable and has been approved by the Food and Drug Administration (FDA) for clinical applications. NanoFect (QIAGEN, Germany) is a commercial reagent based on modified PLGA nanotechnologies [12]. They are chemically synthesized, lipid-free, free of animal-derived components and lack endotoxins. They are composed of ultrasmall nanopolymers. They can form transfection complexes in the nanometer size range when mixed with DNA. In this study, we used this kind of commercial PLGA nanopolymers to deliver the BMP-4 plasmid DNA into MSCs to evaluate their effect both in vitro and in vivo.

2. Methods

2.1. Animals. Male Japanese White Rabbits (age 3-4 months, weight 3–3.5 kg) were obtained from the Animal Department of Peking University Health Science Center. All experiments were approved by the local Institutional Animal Care and Use Committee and complied with the Guide for the Care and Use of Laboratory Animals (1996).

2.2. Cell Isolation and Culture. The MSCs used in this study were isolated from the rabbit's femur bone marrow. Briefly, under sterile condition, femurs were excised. Bone marrow was flushed from the marrow cavity by PBS and was fractionated over a Ficoll-Paque (Dingguo, Beijing, China). Then the mononuclear cells were plated in 10 mm plates in Dulbecco's Modified Eagle Medium-(DMEM-) low glucose (GIBCO, Gaithersburg, USA) supplemented with 10% fetal bovine serum (HyClone, Logan, USA). The non-adherent cells were removed by changing the medium. The cultures were maintained at 37°C in a humidified incubator containing 5% CO_2 and the mediums were changed every 3 days.

2.3. Cell Surface Markers. CD44, CD90, CD14, and CD45 (antibodies from AbD Serotec, UK) on the surface of MSCs were analyzed by flow cytometry (FACS). Anti-mouse IgG1 was used as an isotype control.

After reached a confluence of 90%, the ADSCs were detached from the flasks by incubation with 0.2% trypsin for 30 seconds. ADSCs of 1×10^6 cells were suspended by 100 μL PBS with 10 μL labeled mAb specific for CD44 (MCA806G), CD90 (MCA47R), CD45 (MCA808G), or 10 μL conjugated mAb directed against CD14 (MCA2804C). After incubation, cells were washed three times with 2 mL PBS. Binding of the primary mAb was visualized using FITC-labeled secondary antibody (Zhongshan, Beijing, China) in a working dilution of 1 : 100. Mouse IgG1 (MCA1209C or MCA1209F) was used as an isotype control. All the antibodies were purchased from AbD Serotec (Oxford, UK). Finally, cells were washed with PBS and the membrane fluorescence was analyzed by flow cytometry analysis. The experiments were triplicated for verification.

2.4. Plasmid. Plasmid pDC316-BMP4-EGFP used in this study, containing the coding sequence of the enhanced Green Fluorescent Protein (EGFP) and BMP-4, was constructed by Vector Gene Technology Company (Beijing, China). DNA sequence encoding BMP-4 was generated from plasmid pAM/CAG-BMP4 (gift from Dr Yan CHAN, Hospital for Sick Children, University of Toronto, Ontario, Canada) by PCR and subcloned into the NotI-HindIII sites of the pDC316-mCMV-EGFP vector. The construct was verified by DNA sequencing.

In studies of in vivo, experimental cells (MSCs being transfected with BMP-4 plasmid by PLGA nanopolymers) and control cells (MSCs being transfected with naked BMP-4 plasmid alone) were both tested and compared with.

2.5. Cell Viability. Cell viability was measured by Cell Counting Kit-8 (CCK-8, Dojindo, Kumamoto, Japan) at 72 hours after transfection. MSCs were seeded in 96-well plates at 5×10^3 cells/100 μL medium per well and incubated for 24 hours to allow attachment. The transfection procedures were performed according to the instruction manual. BMP-4 plasmid DNA (0.25 μg) was condensed with different amounts of PLGA nanopolymers (NanoFect) (0.75 μL, 1 μL and 1.25 μL) giving rise to PLGA nanopolymers with PLGA nanopolymers/DNA (N/D; v/w) ratios of 3, 4, and 5, respectively. Then the nanopolymers/DNA complex was added to the experimental cells, while the BMP-4 naked plasmid DNA (0.25 μg) alone was added to the control cells per well. After 24 hours, 10 μL CCK-8 was added per well. The absorbance at 450 nm was measured using a microplate reader (BioRad, Tokyo, Japan) one hour later.

2.6. Transfection Efficiency. MSCs were seeded in 6-well plates at 3×10^5/2 mL medium per well and incubated for 24 hours to allow attachment. Then the BMP-4 plasmid (7.5 μg), being condensed with PLGA nanopolymers at N/D ratios of 3, 4 and 5 in 30 μL medium, was added to the experimental cells per well. The BMP-4 plasmid (7.5 μg) alone was added to the control cells per well. Transfection efficiency was evaluated by EGFP expressing using FACS 72 hours after transfection.

The best N/D ratio of 4, being determined from the cytotoxicity and transfection experiments, was used in subsequent experiments.

2.7. Immunofluorescence Analysis. After 72 hours of transfection, cells were fixed, perforated, and blocked by 1% BSA. BMP-4 antibody (sc-12721, Santa Cruz, CA, USA) was incubated at 1 : 50 for 2 hours, followed by incubation with a 1 : 100 TRITC-labeled secondary antibody (Zhongshan, Beijing, China) for 30 minutes. Nuclei were stained by Hoechst 33258 (blue, 1 : 1000, Invitrogen, CA, USA) for 15 minutes. The cells were observed under a laser confocal microscope.

2.8. Real-Time RT-PCR. After 3, 7, and 10 days of transfection, total RNA of MSCs was extracted and reverse transcribed to cDNA. Real-time RT-PCR was performed using SYBR Green Real-time PCR Master Mix (TOYOBO, Osaka, Japan) according to the manufacturer's instructions

by real-time RT-PCR instrument. The sequence of primers for GAPDH, type II collagen, and aggrecan had been previously described [13–15]: *GAPDH*: 5′-TCACCATCT-TCCAGGAGCGA-3′, 5′-CACAATGCCGAAGTGGTCGT-3′; type II collagen (*Col2a1*): 5′-AACACTGCCAACGTC-CAGAT-3′, 5′-CTGCAGCACGGTATAGGTGA-3′; Aggrecan (*Agg*): 5′-GCTACGGAGACAAGGATGAGTTC-3′, 5′-CGTAAAAGACCTCACCCTCCAT-3′; *Sox9*: 5′-AGTACC-CGCACCTGCACAAC-3′, 5′-CGCTTCTCGCTCTCGTTC-AG-3′; *Bmp4*: 5′-ATGTGACACGGTGGGAAACTTTC-3′, 5′-ACCTCAATGGCCAGCCCATA-3′. All gene expression was normalized to expression of the *GAPDH*. Data are presented in experimental cells as the fold change over the control cells. Three independent experiments were performed.

2.9. Scanning Electronic Microscopy (SEM) Observation of Scaffold. Cells after transfection 72 hours were seeded onto the PLLGA scaffold (Synthecon, Houston, USA) at a density of 1×10^6 cells/mL and cultured in medium for another 3 days. Then the MSCs-PLLGA composition was fixed immediately in 4 mL 2.5% glutaraldehyde at 4°C for 4 hours, dehydrated in ethanol, critical-point dried from liquid CO_2, coated with gold, and viewed with a scanning electron microscope (JEOL, JSM-5600LV, Tokyo, Japan).

2.10. Full-Thickness Articular Cartilage Defect Repair. After 12 rabbits were anesthetized intravenously with 2.5% pentobarbital sodium (1 mL/kg), full-thickness cylindrical cartilage defects (4.5 mm in diameter, 0.8 mm in depth) were created in the femoral trochlea of both knees of each rabbit using a corneal trephine under sterile condition. The two knees of each rabbit were randomly divided into experimental group or control group. The PLLGA scaffolds were made the same shape and size with the defect. The specific PLLGA scaffolds which were implanted for each group were prepared as follows: the experimental group, PLLGA scaffolds being seeded with experimental cells (MSCs being transfected with BMP-4 plasmid by PLGA nanopolymers 48 hours) and cultured for another one day; the control group, PLLGA scaffolds being seeded with control cells (MSCs being transfected with naked BMP-4 plasmid alone 48 hours) and being cultured for another one day. Incisions were closed in layers. The rabbits were kept in cages allowing full freedom of movement without immobilization. Every three rabbits in each group were sacrificed at 6 weeks and 12 weeks after surgery. One rabbit was sacrificed to observe the cells and the scaffold one week after surgery.

2.11. Macroscopic and Microscopic Observation. The distal femurs were removed and fixed in 4% paraformaldehyde (pH 7.4), decalcified in 10% EDTA (pH 7.2), and embedded in paraffin. Serial paraffin sections of 6 μm were cut along the maximum diameter of the repaired sites and stained with hematoxylin and eosin (HE) and with toluidine blue. Immunohistochemistry was performed with antibody for type II collagen (dilution 1 : 200, CP18, Calbiochem, CA, USA).

Table 1: Pineda cartilage repair score.

Characteristics	Score
Filling of defect	
125%	−1
100%	0
75%	1
50%	2
25%	3
0%	4
Reconstruction of osteochondral junction	
Yes	0
Almost	1
Not close	2
Matrix staining	
Normal	0
Reduced staining	1
Significantly reduced staining	2
Faint staining	3
No stain	4
Cell morphology	
Normal	0
Most hyaline and fibrocartilage	1
Mostly fibrocartilage	2
Some fibrocartilage, but mostly	3
Nonchondrocytic cells	4

A score of 0 indicates normal cartilage, with score of 12 indicating the most severe cartilage defects.

2.12. Histological Scores. The Pineda cartilage repair score was used to evaluate the results of the cartilage regeneration (Table 1). The score was ranged from 0 to 12. A score of 0 indicates normal cartilage, with higher scores indicating more severe cartilage defects. The samples were measured by two observers who were blinded to the group identities.

2.13. Statistical Analysis. All in vitro experiments were repeated three times. The data of Pineda scores were presented as medians ± interquartile range and analyzed with Mann-Whitney test. The data of others were presented as the means ± standard deviation and analyzed with ANOVA followed by post hoc Tukey's test. SPSS 17.0 was used for statistical analysis. Differences were considered to be statistically significant at $P < 0.05$.

3. Results

3.1. Surface Markers of MSCs. The MSCs surface markers were examined by FACS. MSCs were positive for the surface markers CD44 and CD90 (99.17% and 93.37%); negative for typical hematopoietic of CD14 and CD45, indicating that they were of mesenchymal origin (Figure 1(a)).

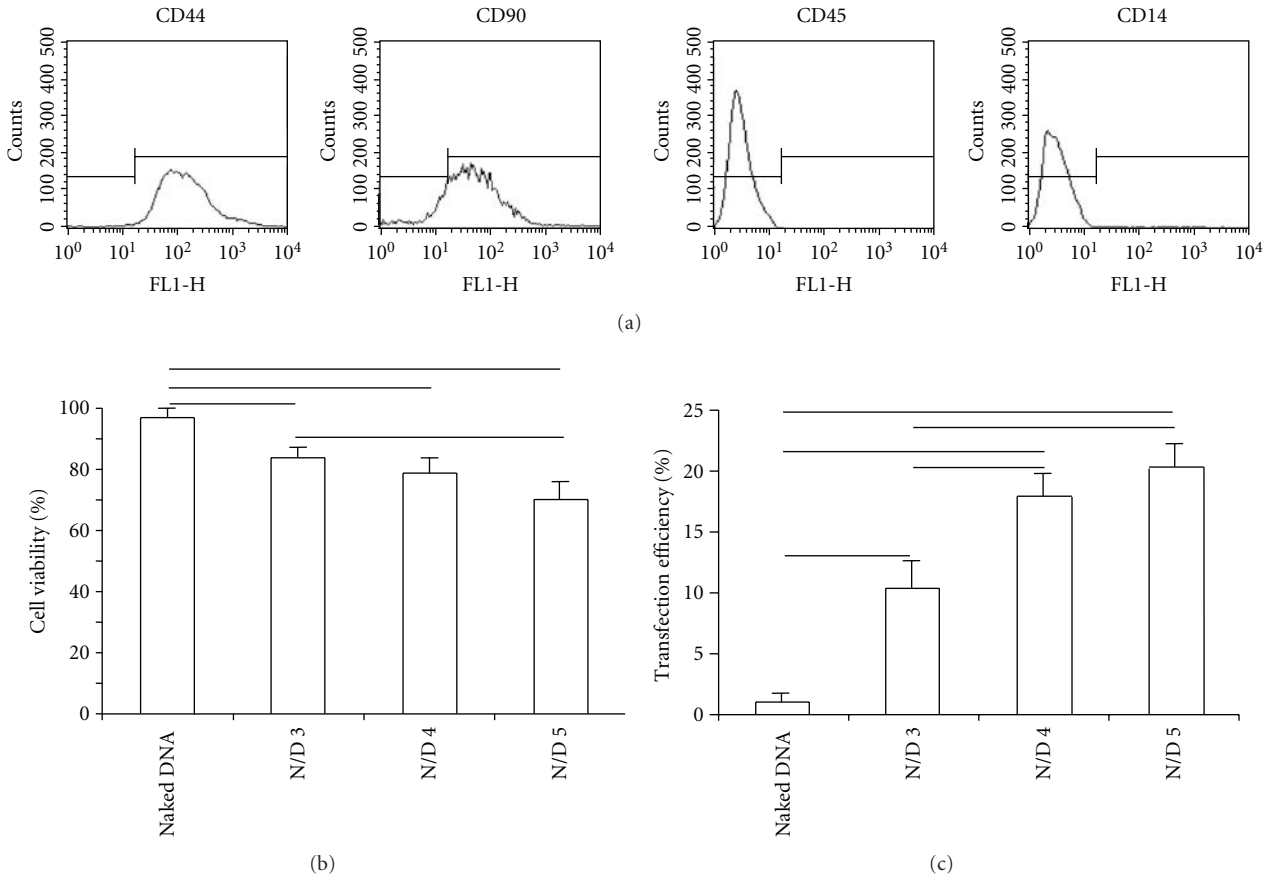

Figure 1: MSCs surface markers (a), cytotoxicity (b), and transfection efficiency (c) of PLGA nanopolymers. The mesenchymal-related antigens CD44 and CD90 were positive, but the hematopoietic-related antigens CD14 and CD45 were negative (a). The cell viability of the experimental cells (MSCs being transfected with BMP-4 plasmid by PLGA nanopolymers) significantly, decreased than that of the control cells (MSCs being transfected with naked BMP-4 plasmid alone) 72 hours after transfection. The cell viability was decreased with the N/D ratio increasing (b). The transfection efficiency of PLGA nanopolymers significantly increased than that of naked BMP-4 plasmid alone 72 hours after transfection, and was increased with the N/D ratio increasing (c). $^{*}P < 0.05$, $^{**}P < 0.01$.

3.2. Cytotoxicity and Transfection Efficiency. The cytotoxicity of the PLGA nanopolymers to MSCs was tested by CCK-8. Results showed an increasing trend of cytotoxicity with the increasing N/D ratio 72 hours after transfection. The BMP-4 plasmid was kept 0.25 μg constant per well in the 96-well plate. There were statistical differences between groups ($P < 0.01$). The cytotoxicity of the nanopolymers/DNA complex was significantly higher than that of the naked BMP-4 plasmid alone ($P < 0.05$). There was a statistically significant increase in cytotoxicity at N/D 5 than that at N/D 3 ($P < 0.05$), but the difference between N/D 3 and N/D 4 was not statistically significant, as well as between N/D 4 and N/D 5 ($P > 0.05$) (Figure 1(b)).

Transfection efficiency was analyzed for EGFP by FACS. Results showed an increasing trend of transfection efficiency with the increasing N/D ratio 72 hours after transfection. There were statistical differences between groups ($P < 0.01$). The transfection efficiency of the nanopolymers/DNA complex was significantly higher than that of naked BMP-4 plasmid alone ($P < 0.01$). The transfection efficiency of N/D 3 was statistically significant lower when than that of N/D 4 or N/D 5 ($P < 0.01$). There was a statistically significant increase in transfection efficiency at N/D 5 than at N/D 3 ($P < 0.05$), but the difference of the transfection efficiency between N/D 3 and N/D 4 was not statistically significant, as well as between N/D 4 and N/D 5 ($P > 0.05$) (Figure 1(c)).

3.3. BMP-4 Expression. Immunofluorescence was used to detect the BMP-4 expression after transfection. After 72 hours, both strong green fluorescence (EGFP) and red light (TRITC-labeled BMP-4 antibodies) were observed in the experimental cells, indicating EGFP and BMP-4 expression by a fluorescence microscope. However, EGFP and BMP-4 were not detected in the control cells (Figure 2(a)).

3.4. mRNA Expression. To detect the expression of chondrogenic markers, mRNA were measured by real-time RT-PCR. The mRNA levels of *Bmp4, Sox9, Agg*, and *Col2a1* in experimental cells were significantly upregulated than that in the experimental cells at each time point ($P < 0.05$). The expression of *Bmp4* mRNA remained constant at day 3 and day 7 ($P > 0.05$), then down-regulated at day 10 ($P < 0.05$). This indicated that the BMP-4 plasmid was

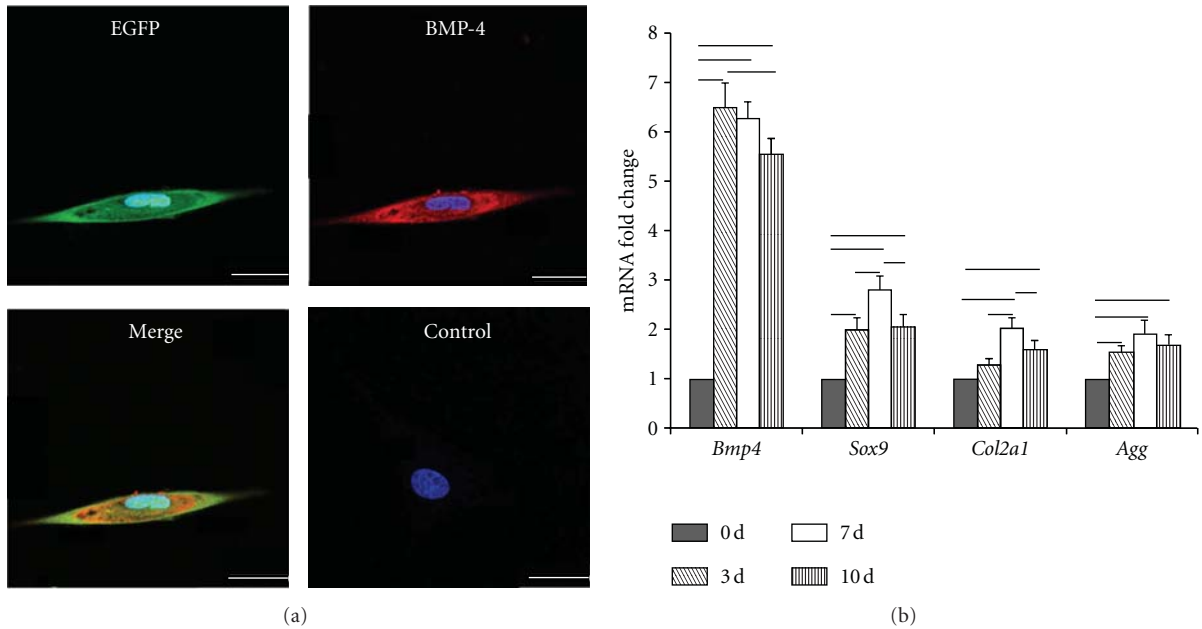

Figure 2: Immunofluorescence staining for BMP-4 (a) and the mRNA levels (b) of chondrogenic markers. EGFP (green) and BMP-4 (red) were expressed in the experimental cells (MSCs transfected with BMP-4 plasmid by PLGA nanopolymers). The control cells (MSCs being transfected with naked BMP-4 plasmid alone) showed no BMP-4 expression (a). The mRNA expressions of *Bmp4, Sox9, Col2a1*, and *Agg* in the experimental cells were upregulated in comparison with those of the control cells (b). $^{*}P < 0.05$, $^{**}P < 0.01$.

transfected successfully and the expression could last for at least 10 days. The peak levels of *Sox9, Agg*, and *Col2a1* mRNA were reached at day 7 after transfection and slowly decreased at day 10. This indicated the *Bmp4* overexpression resulted in the increasing of *Sox9, Agg*, and *Col2a1* mRNA (Figure 2(b)).

3.5. SEM Observation of Scaffold-Cell Constructs. MSCs after transfection three days were seeded into the PLLGA scaffold. The constructs were observed by SEM. MSCs were adhering to the scaffold and grew normally on the fibers of the scaffold (Figure 3).

3.6. Macroscopic Observations. No scaffold was dislodged from the defect site and no knee was infected after surgery. At week 6, the defects in the experimental group were filled with some white, semitransparent tissue newly formed cartilage. The thickness of the newly cartilage was a little thinner than that of the surrounding normal cartilage, but there were still concavity toward the center. The margins were clear and the surface was not as smooth as the normal cartilage (Figure 4(a)). In the control group, semitransparent tissue of the new cartilage filled the defect. The thickness was thinner than the adjacent normal cartilage. The surfaces were rough and the margin were sharply defined (Figure 4(b)).

At week 12, in the experimental group, the regenerative tissue became thicker and smoother. The margins of the defects were unclear. The boundaries between the normal cartilage and the regenerative tissue were hard to recognize (Figure 4(c)). In the control group, the regenerative tissue become thicker and smoother than those at week 6, but the centers were still a little thinner and uneven (Figure 4(d)).

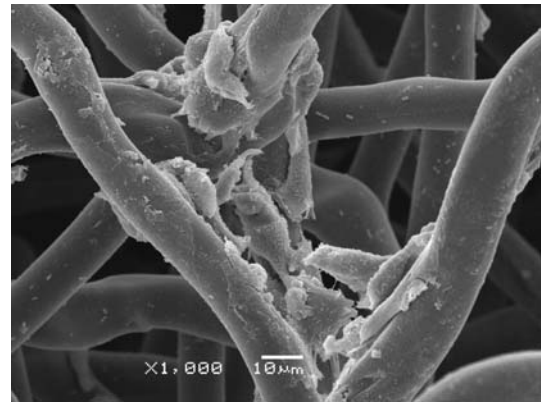

Figure 3: MSCs on PLLGA scaffolds. The MSCs adhered on the fibers of PLLGA scaffolds.

MSCs which were transfected with BMP-4 by PLGA nanopolymers stimulated articular cartilage regeneration more rapidly and effectively than the control ones.

3.7. Histological and Immunohistochemical Staining. At week 1, sections were stained with HE. The PLLGA scaffolds were not absorbed. The fibers of PLLGA scaffold could be identified. The cells existed in the pores between the fibers of the scaffold (Figure 5).

Histological and immunohistochemical staining were performed and the results further demonstrated that MSCs which were transfected with BMP-4 by PLGA nanopolymers promotes cartilage regeneration (Figure 4).

At week 6, in the experimental group, the surfaces were smooth with thinner regenerated cartilage layers than the

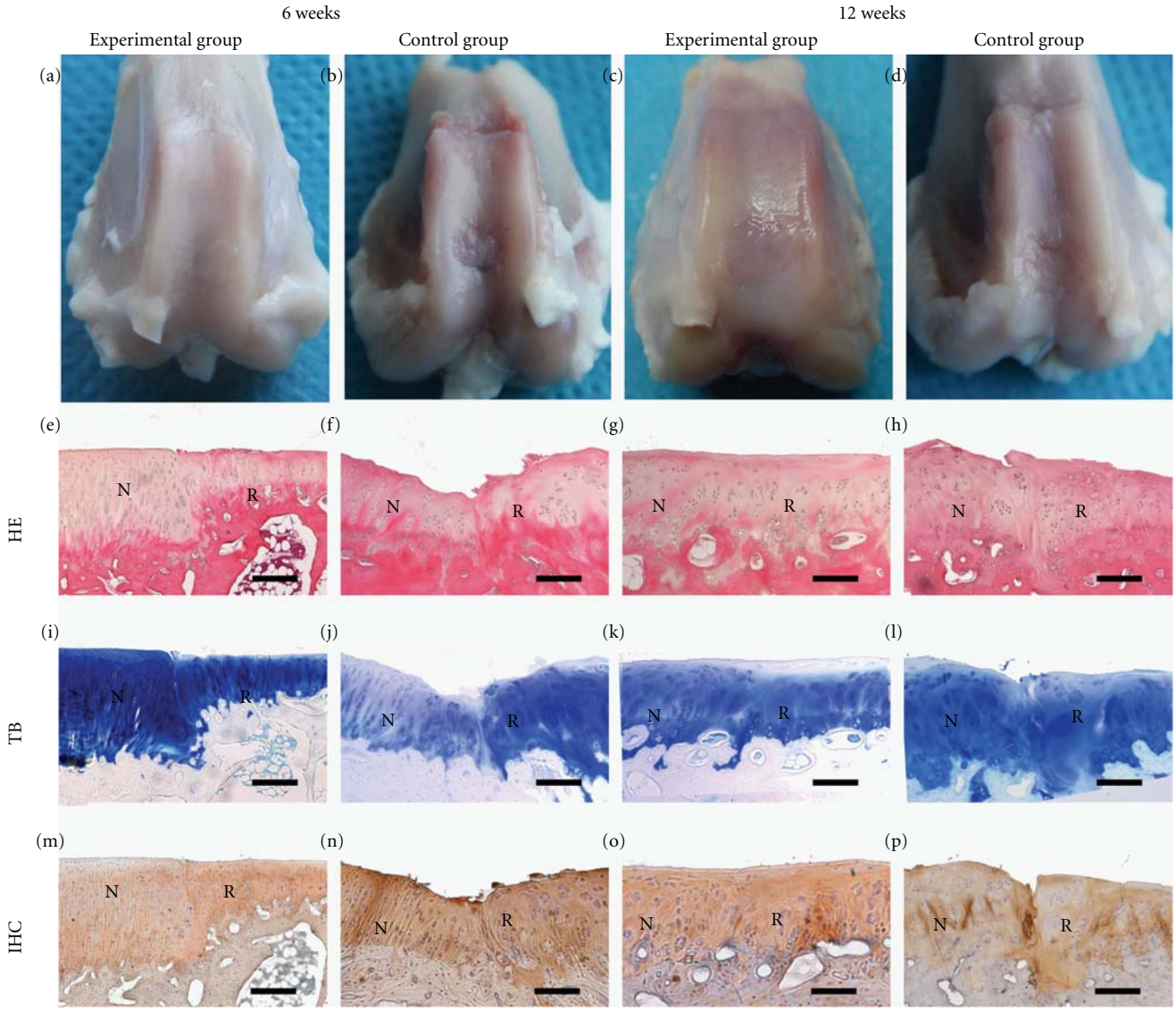

Figure 4: Macroscopic (a–d) and microscopic (e–p) observations of regenerated cartilage at week 6 and week 12. At week 6, in the experimental group, smooth semitransparent tissue newly tissues filled the defect, but there were still concavity toward the center. The new cartilages were stained positive with toluidine blue and collagen type II (a, e, i, m). In the control group, the thickness of the newly rough cartilage was thinner than normal cartilage. The junctions were obvious. Cells aligned areatus. Toluidine blue and collagen type II staining were positive (b, f, j, n). At week 12, the thickness of the regenerative tissue in the experimental group was similar to the adjacent normal cartilage. The surfaces were regular and mostly integrated with the hosts. Aggrecan and collagen type II deposited (c, g, k, o). In the control group, the thickness of the newly cartilage layer was thinner than that of the host. The surfaces were uneven and the margins could be distinguished easily. Cells aligned irregularly. The excellular matrices were also formed because of the positive staining of toluidine blue and collagen type II (d, h, l, p). The bar was 200 μm. N refers to normal cartilage, R refers to regenerative cartilage.

host cartilage. Cells aligned columnar, but few cartilage lacunae could be seen. The newly cartilages were stained positive with toluidine blue and collagen type II, indicating the extracellular matrix became formed (Figures 4(e), 4(i), and 4(m)). In the control group, the surfaces were uneven. The junctions were crimp and there was lack of thickness. Cells aligned areatus. Toluidine blue and collagen type II staining were positive in the new tissues (Figures 4(f), 4(j), and 4(n)).

At week 12, in the experimental group, the thickness was almost the same as that of the adjacent cartilage. The surfaces usually regular and mostly integrated with the host, but margins still could be identified. Toluidine blue and collagen type II staining were similar to the surrounding cartilages (Figures 4(g), 4(k), and 4(o)). In the control group, the thickness of the new cartilage layers were a little thinner than that of the hosts. The surfaces were uneven and the margins could be distinguished easily. The cells aligned irregularly. The excellular matrices were also formed because of the positive staining of toluidine blue and collagen type II (Figures 4(h), 4(l), and 4(p)).

3.8. Pineda Scores. Pineda cartilage repair score was used to evaluate the effect of cartilage repair. The scores of the

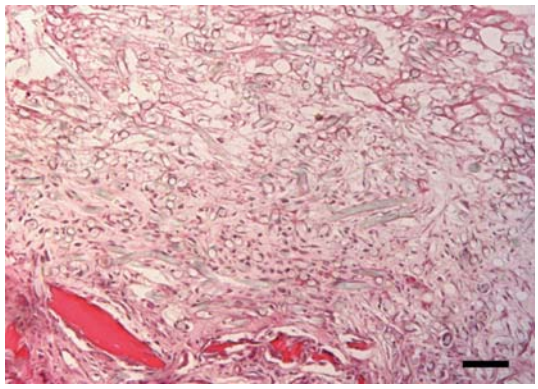

Figure 5: Microscopic observations (HE) of the PLLGA scaffold being implanted at week 1. The fibers of PLLGA scaffold could be identified. The cells existed in the pores between the fibers of the scaffold. The bar was 200 μm.

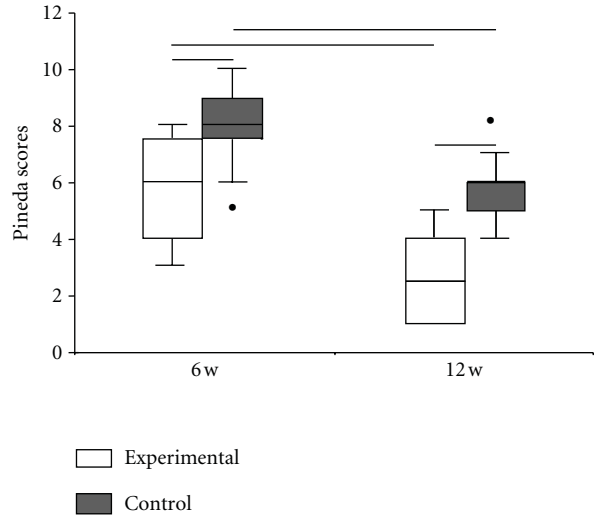

Figure 6: Pineda cartilage repair scores of the regenerative cartilage. Pineda cartilage repair score was used to evaluate the effect of cartilage repair. The scores of the experimental group were significant lower than that of the control group at either week 6 or week 12. We could also found the scores of both groups at week 12 were lower than that at week 6. $^{*}P < 0.05$, $^{**}P < 0.01$.

experimental group were significant lower than that of the control group at both week 6 (5.83 ± 1.85 versus 7.91 ± 1.48) and week 12 (1.85 ± 1.56 versus 5.75 ± 1.14) ($P < 0.05$). We could also find the scores of both groups at week 12 were lower than those at week 6 ($P < 0.05$) (Figure 6).

4. Discussion

The aim of this study was to optimize nanopolymers for transfection of rabbit MSCs. We isolated rabbit MSCs, detected their cell surface markers. Then we evaluated their cytotoxicity, transfection efficiency, and mRNA expression after transfection by PLGA nanopolymers in vitro. The cartilage repair effect of MSCs transfected with BMP-4 by PLGA nanopolymers was also evaluated in vivo. The results showed PLGA nanopolymers were safe and effective to deliver BMP-4 plasmid into MSCs and then the delivered plasmid could play its role on cartilage regeneration.

The transfection efficiency of viral vectors is significant, but the potential pathogenicity and oncogenicity could not be ignored. Nonviral methods are commonly less effective for gene transfer to MSCs [16]. Naked plasmid DNA has poor transfection efficiency because of their large size and hydrophilic nature due to negatively charged phosphate groups [17]. In addition, they are very susceptible to nuclease-mediated degradation [17]. Thus, nonviral vectors are favored. As nanotechnology advances rapidly, many types of nanoparticles have been used to deliver drugs, proteins and DNA into cells. NanoFect is a commercial nanovector. Report shows NanoFect transfection reagent is based on modified PLGA nanopolymers [12]. In our study, we select NanoFect as the gene vector because PLGA has been approved by the FDA for clinical use and commercial reagents are stable and feasible for experiments repeating. Studies have shown that betamethasone sodium phosphate contained in PLGA nanoparticles can be delivered to chondrocytes. The drug release from the nanopolymers is controlled by the molecular weight and the PLA/PGA ratio of the polymers, which allows the effective period of the DNA or protein to be adjusted [18]. Because its properties are known, PLGA can be modified to have various characteristics for different uses and to target different cells and tissues. There were few studies about PLGA nanopolymers in gene transfer to MSCs. Kim et al. use PEI-modified PLGA nanopolymers delivering SOX9 gene into human MSCs, showing satisfactory transfection efficiency at 99.38% 30 min to 4 hours after transfection [19]. Another relative study reported transfection efficiency of SOX9 gene into hMSCs with PEI-modified PLGA nanopolymers was 83% at two days after transfection [20]. The modification for NanoFect is not provided in the product instruction as a commercial secret. In our study, though the transfection efficiency we detected was not as high as these reports above 80%, it was similar to that of Lipofectamine 2000 with the similar experimental conditions which were reported about 5% ~ 19.60% [21, 22]. Since MSCs were cells of difficult transfection, this transfection efficiency about 20% was also acceptable. The difference between our study and the previous studies indicated surface modified was important for nanopolymers. Different modifications achieve notable results. Some more advance surface modification should be researched. Study also showed cytotoxicity lower than 10% after 72 hours [19]. Cytotoxicity of Lipofectamine 2000 was less than 20% [11, 21]. Results in this study showed the cytotoxicity was below 20% which was not so significant different from the reports.

Some study reports PLGA nanopolymers had little immunogenicity [23]. In our study, few inflammatory cells were observed in the experimental group in histological observations, demonstrating a low immunogenicity of the nanopolymers in vivo.

This study demonstrates that PLGA nanopolymers are able to deliver BMP-4 plasmid to MSCs effectively. The BMP-4 plays an important role in chondrogenesis, extracellular

matrix formation, and cartilage repair both in vitro and in vivo. The use of PLGA nanopolymers for gene delivery in cartilage repair has not been reported previously. BMP-4 has been the focus of much attention in recent years for its chondrogenic properties. Reports have shown that BMP-4 promotes chondrocyte differentiation, the extracellular matrix composition of cartilage, collage type II deposition, and cartilage regeneration [2–5]. Both BMP-4 protein and the BMP-4 plasmid transfected by viral vectors have been reported to stimulate chondrogenesis and repair cartilage defects [24, 25]. In the present study, BMP-4 expression in mRNA and protein level in MSCs was observed at both 72 hours and 10 days after transfection. Results indicated that the plasmid being delivered by nanopolymers could last for at least 10 days. The chondrogenesis of BMP-4 was proven both in vitro and in vivo. After transfection, the expression of *Bmp4* mRNA was upregulated and the secretion of BMP-4 protein was increased. Under the influence of BMP-4, the expression of the cartilage-specific markers *Col2a1*, *Agg* and *Sox9* was upregulated; the secretion of collagen type II was increased. In vivo, the chondrogenesis effect of BMP-4 was also played. MSCs were induced to differentiate into chondrocytes by BMP-4. Then they were induced to secrete collagen type II and glycosaminoglycan. In the cartilage repair models, the regenerated cartilage in the experimental group showed better regeneration than the cartilage in the control group with respect to thickness, surface smoothness, and integration with the surrounding normal cartilage at the same time point. In our in vivo study, hyaline cartilage was regenerated at week 12 in the experimental group.

In cartilage regeneration researches, MSCs are one of the most frequently used stem cells. MSCs are cells can be self-renewed and induced to terminally differentiate into osteoblasts, chondrocytes, and adipocytes either in vitro or in vivo. Their easy isolation and culture, as well as their high in vitro expansive potential, make these cells an attractive therapeutic tool for tissue engineering and promising candidates for gene. Their self-renewal and multiplex differentiation potential have been reported previously. Moreover, compared with direct transfer of gene vectors, engineering MSCs are associated with less immunologic interference [16]. What is more, MSCs also have the capacity of enhancing their therapeutic potential. One of the hypothetical mechanisms is the paracrine effect. In fact MSCs can recognize the location of injury, reach the site, and excrete several soluble factors to accelerate the healing process [26]. MSCs seeding in vivo can compensate for the insufficient cells in cartilage. Correspondingly, the cartilage defects are repaired much better and faster in the groups treated with MSCs. Crosstalk between extracellular components in the microenvironment and MSCs within the cartilage further contributes to the differentiation of stem cells into chondrocytes [27]. The surface marker expression of MSCs we detected is generally consistent with that reported in the literature.

We used PLLGA scaffolds as a temporary mechanical support for cartilage regeneration. PLLGA is approved by the FDA for clinical applications. PLGA scaffolds are used in popular in tissue engineering [28–30]. The scaffold we used is of three-dimensional structure with the appropriate size pores which could provide space for cell living. Moreover, the PLLGA scaffolds had degraded in 6 weeks without disturbing the remodeling of the regenerated tissue.

5. Conclusions

Nanopolymers are promising nonviral vector for gene delivery displaying acceptable cytotoxicity and transfection efficiency. We used it to deliver BMP-4 plasmid DNA to MSCs and BMP-4 exerted its chondrogenic effects on the MSCs. After transfection, the expression of *Sox9, Agg, and Col2a1* was upregulated and the collagen type II protein secretion was increased. MSCs transfected with BMP-4 plasmid using PLGA nanopolymers which were able to promote articular cartilage repair in vivo and to achieve hyaline-like cartilage regeneration in a short period. These findings suggest that BMP-4 plasmid transfection is a promising method for articular cartilage repair and that PLGA nanopolymers can serve as gene vectors for articular cartilage repair in vivo. This study provides an experimental basis for further clinical studies and applications.

Acknowledgments

This work was supported by the National Science and Technology Ministry of China (2007BAI04B09), the Program for Changjiang Scholars and Innovative Research Team in University (BMU2009129-112), and the Specialized Research Fund for the Doctoral Program of Higher Education (20100001110086).

References

[1] W. W. Curl, J. Krome, E. S. Gordon, J. Rushing, B. P. Smith, and G. G. Poehling, "Cartilage injuries: a review of 31,516 knee arthroscopies," *Arthroscopy*, vol. 13, no. 4, pp. 456–460, 1997.

[2] R. Kuroda, A. Usas, S. Kubo et al., "Cartilage repair using bone morphogenetic protein 4 and muscle-derived stem cells," *Arthritis and Rheumatism*, vol. 54, no. 2, pp. 433–442, 2006.

[3] N. Nakayama, D. Duryea, R. Manoukian, G. Chow, and C. Y. E. Han, "Microscopic cartilage formation with embryonic stem-cell-derived mesodermal progenitor cells," *Journal of Cell Science*, vol. 116, no. 10, pp. 2015–2028, 2003.

[4] J. Kramer, C. Hegert, K. Guan, A. M. Wobus, P. K. Müller, and J. Rohwedel, "Embryonic stem cell-derived chondrogenic differentiation in vitro: activation by BMP-2 and BMP-4," *Mechanisms of Development*, vol. 92, no. 2, pp. 193–205, 2000.

[5] X. Zhang, Z. Zheng, P. Liu et al., "The synergistic effects of microfracture, perforated decalcified cortical bone matrix and adenovirus-bone morphogenetic protein-4 in cartilage defect repair," *Biomaterials*, vol. 29, no. 35, pp. 4616–4629, 2008.

[6] S. Hacein-Bey-Abina, "*LMO2*-associated clonal T cell proliferation in two patients after gene therapy for SCID-X1," *Science*, vol. 302, no. 5644, pp. 415–419, 2003.

[7] T. Hollon, "Researchers and regulators reflect on first gene therapy death," *Nature Medicine*, vol. 6, no. 1, article 6, 2000.

[8] S. McLenachan, J. P. Sarsero, and P. A. Ioannou, "Flow-cytometric analysis of mouse embryonic stem cell lipofection using small and large DNA constructs," *Genomics*, vol. 89, no. 6, pp. 708–720, 2007.

[9] K. Kunath, A. Von Harpe, D. Fischer, and T. Kissel, "Galactose-PEI-DNA complexes for targeted gene delivery: degree of substitution affects complex size and transfection efficiency," *Journal of Controlled Release*, vol. 88, no. 1, pp. 159–172, 2003.

[10] M. Huang, C. W. Fong, E. Khor, and L. Y. Lim, "Transfection efficiency of chitosan vectors: effect of polymer molecular weight and degree of deacetylation," *Journal of Controlled Release*, vol. 106, no. 3, pp. 391–406, 2005.

[11] J. L. Santos, E. Oramas, A. P. Pêgo, P. L. Granja, and H. Tomás, "Osteogenic differentiation of mesenchymal stem cells using PAMAM dendrimers as gene delivery vectors," *Journal of Controlled Release*, vol. 134, no. 2, pp. 141–148, 2009.

[12] Telomolecular Corporation, "Pre-Effective Amendment to Registration of Securities by a Small-Business Issuer. Form SB-2. In SEC," 2007, http://www.secinfo.com/d199pj.u6.htm#1stPage.

[13] H. Park, J. S. Temenoff, Y. Tabata, A. I. Caplan, and A. G. Mikos, "Injectable biodegradable hydrogel composites for rabbit marrow mesenchymal stem cell and growth factor delivery for cartilage tissue engineering," *Biomaterials*, vol. 28, no. 21, pp. 3217–3227, 2007.

[14] P. J. Emans, F. Spaapen, D. A. M. Surtel et al., "A novel in vivo model to study endochondral bone formation; HIF-1α activation and BMP expression," *Bone*, vol. 40, no. 2, pp. 409–418, 2007.

[15] C. J. Bowman, K. J. Turner, M. Sar, N. J. Barlow, K. W. Gaido, and P. M. D. Foster, "Altered gene expression during rat Wolffian duct development following Di(n-Butyl) phthalate exposure," *Toxicological Sciences*, vol. 86, no. 1, pp. 161–174, 2005.

[16] A. Van Damme, T. Vanden Driessche, D. Collen, and M. K. Chuah, "Bone marrow stromal cells as targets for gene therapy," *Current Gene Therapy*, vol. 2, no. 2, pp. 195–209, 2002.

[17] M. S. Al-Dosari and X. Gao, "Nonviral gene delivery: principle, limitations, and recent Progress," *AAPS Journal*, vol. 11, no. 4, pp. 671–681, 2009.

[18] E. Horisawa, T. Hirota, S. Kawazoe et al., "Prolonged anti-inflammatory action of DL-lactide/glycolide copolymer nanospheres containing betamethasone sodium phosphate for an intra-articular delivery system in antigen-induced arthritic rabbit," *Pharmaceutical Research*, vol. 19, no. 4, pp. 403–410, 2002.

[19] J. H. Kim, J. S. Park, H. N. Yang et al., "The use of biodegradable PLGA nanoparticles to mediate SOX9 gene delivery in human mesenchymal stem cells (hMSCs) and induce chondrogenesis," *Biomaterials*, vol. 32, no. 1, pp. 268–278, 2011.

[20] J. S. Park, H. N. Yang, D. G. Woo et al., "Chondrogenesis of human mesenchymal stem cells mediated by the combination of SOX trio SOX5, 6, and 9 genes complexed with PEI-modified PLGA nanoparticles," *Biomaterials*, vol. 32, no. 14, pp. 3679–3688, 2011.

[21] Y. Gheisari, M. Soleimani, K. Azadmanesh, and S. Zeinali, "Multipotent mesenchymal stromal cells: optimization and comparison of five cationic polymer-based gene delivery methods," *Cytotherapy*, vol. 10, no. 8, pp. 815–823, 2008.

[22] F. Yang, J. J. Green, T. Dinio et al., "Gene delivery to human adult and embryonic cell-derived stem cells using biodegradable nanoparticulate polymeric vectors," *Gene Therapy*, vol. 16, no. 4, pp. 533–546, 2009.

[23] B. Semete, L. I. J. Booysen, L. Kalombo et al., "In vivo uptake and acute immune response to orally administered chitosan and PEG coated PLGA nanoparticles," *Toxicology and Applied Pharmacology*, vol. 249, no. 2, pp. 158–165, 2010.

[24] R. Kuroda, A. Usas, S. Kubo et al., "Cartilage repair using bone morphogenetic protein 4 and muscle-derived stem cells," *Arthritis and Rheumatism*, vol. 54, no. 2, pp. 433–442, 2006.

[25] Y. Jiang, L. K. Chen, D. C. Zhu et al., "The inductive effect of bone morphogenetic protein-4 on chondral-lineage differentiation and in situ cartilage repair," *Tissue Engineering*, vol. 16, no. 5, pp. 1621–1632, 2010.

[26] F. Tögel, Z. Hu, K. Weiss, J. Isaac, C. Lange, and C. Westenfelder, "Administered mesenchymal stem cells protect against ischemic acute renal failure through differentiation-independent mechanisms," *American Journal of Physiology*, vol. 289, no. 1, pp. F31–F42, 2005.

[27] F. Djouad, B. Delorme, M. Maurice et al., "Microenvironmental changes during differentiation of mesenchymal stem cells towards chondrocytes," *Arthritis Research and Therapy*, vol. 9, article R33, 2007.

[28] W. S. Koegler and L. G. Griffith, "Osteoblast response to PLGA tissue engineering scaffolds with PEO modified surface chemistries and demonstration of patterned cell response," *Biomaterials*, vol. 25, no. 14, pp. 2819–2830, 2004.

[29] E. Lieb, S. Milz, T. Vogel, M. Hacker, M. Dauner, and M. B. Schulz, "Effects of transforming growth factor β1 on bonelike tissue formation in three-dimensional cell culture: I. Culture conditions and tissue formation," *Tissue Engineering*, vol. 10, no. 9-10, pp. 1399–1413, 2004.

[30] E. Lieb, T. Vogel, S. Milz, M. Dauner, and M. B. Schulz, "Effects of transforming growth factor β1 on bonelike tissue formation in three-dimensional cell culture. II: osteoblastic differentiation," *Tissue Engineering*, vol. 10, no. 9-10, pp. 1414–1425, 2004.

Hindawi Publishing Corporation
Journal of Nanomaterials
Volume 2012, Article ID 315185, 19 pages
doi:10.1155/2012/315185

Review Article

Applications and Nanotoxicity of Carbon Nanotubes and Graphene in Biomedicine

Caitlin Fisher,[1,2] Amanda E. Rider,[1,2] Zhao Jun Han,[1,2] Shailesh Kumar,[1,2] Igor Levchenko,[1,2] and Kostya (Ken) Ostrikov[1,2]

[1] *Plasma Nanoscience Centre Australia (PNCA), CSIRO Materials Science and Engineering, P.O. Box 218, Lindfield, NSW 2070, Australia*
[2] *Plasma Nanoscience at Complex Systems, School of Physics, The University of Sydney, Sydney, NSW 2006, Australia*

Correspondence should be addressed to Zhao Jun Han, zhaojun.han@csiro.au

Received 7 March 2012; Accepted 29 March 2012

Academic Editor: Krasimir Vasilev

Owing to their unique mechanical, electrical, optical, and thermal properties, carbon nanostructures including carbon nanotubes and graphenes show great promise for advancing the fields of biology and medicine. Many reports have demonstrated the promise of these carbon nanostructures and their hybrid structures (composites with polymers, ceramics, and metal nanoparticles, etc.) for a variety of biomedical areas ranging from biosensing, drug delivery, and diagnostics, to cancer treatment, tissue engineering, and bioterrorism prevention. However, the issue of the safety and toxicity of these carbon nanostructures, which is vital to their use as diagnostic and therapeutic tools in biomedical fields, has not been completely resolved. This paper aims to provide a summary of the features of carbon nanotube and graphene-based materials and current research progress in biomedical applications. We also highlight the current opinions within the scientific community on the toxicity and safety of these carbon structures.

1. Introduction

Carbon nanotubes (CNTs) and graphene are very promising candidates to form the basis of new biological and medical devices. Carbon nanotubes can be thought of as rolled-up graphene sheets with no overlapping edges [1]. Their diameters typically vary from 1 to 100 nm and their lengths can be several orders of magnitude larger, up to millimeters, even centimeters long [2]. Various orientations of CNTs are shown in Figures 1(a)–1(c): randomly oriented, vertically aligned, and in a "dandelion-like" structure, respectively. The well-documented beneficial mechanical, electrical and chemical characteristics of CNTs and graphene [1, 3–7] as well as their ability to be hybridized with a wide range of organic and inorganic materials make them ideal candidates for many biomedical applications such as biosensing [8–12], tissue engineering [13–15], and drug delivery [16, 17].

In the past two decades, intense efforts have been directed at providing specificity, selectivity, reproducibility, and robustness to these carbon nanostructures in biologically relevant environments [18–22]. However, the issue of toxicity of CNTs and graphene in living biological systems, which is vital for the successful incorporation of these materials into functional biomedical devices, remains unsolved at macroscopic, cellular, and intracellular levels [23–25].

In this paper we will, in Section 2, discuss the role of CNTs in biosensing, tissue engineering, and drug delivery. Aspects of the toxicity of CNTs in living biological systems are then discussed in Section 3 and the emerging graphene-related biomedical applications and associated safety issues are briefly presented in Section 4. Finally, a summary of this work and an outlook for future research is provided.

2. Applications of Carbon Nanotubes in Biomedicine

Due to the chemical inertness of graphitic walls, functionalization of CNTs and graphene is often the key step required in

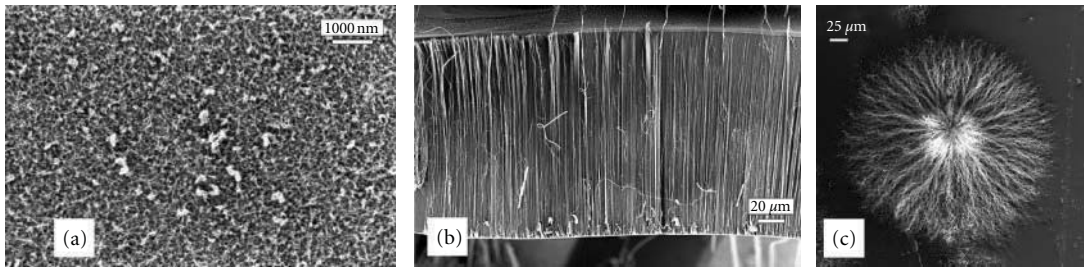

Figure 1: Various orientations of CNTs grown using chemical vapor deposition on Si substrates: (a) entangled, randomly orientated CNTs; (b) vertically aligned CNTs; (c) dense "dandelion-like" CNT structure grown using plasma-enhanced chemical vapor deposition on an etched, catalyst-free Si substrate. Details on the growth of similar structures can be found in [40].

any application of these materials. Let us first briefly consider the possible ways of performing such functionalization.

2.1. Functionalization of Carbon Nanotubes. Successful functionalization should maintain the integrity of CNT's mechanical, electrical, and chemical properties as well as the activity of the biological species being attached. In general, there are two CNT functionalization methods: covalent bonding and noncovalent wrapping [26–28].

Covalent bonding involves chemical attachment of the desirable species to the CNT [26], often at the tube ends or at defect sites [1, 29]. Oxidation processes are often used as a preparation step to create chemically active sites for covalent bonding [30]. These oxidation processes can be performed through wet chemical or dry plasma routes [30], amongst others. A variety of biological species have been covalently bonded to CNTs [26, 31, 32]. However, this often alters the intrinsic structure and properties of CNTs as well as the properties of attached biomolecules [33]. An example of a covalently functionalized CNT is shown in Figure 2(a), which shows a scanning electron microscope (SEM) image of multiwalled CNTs (MWCNTs) covalently functionalized with ferritin [34].

Noncovalent bonding, or physical adsorption, on the other hand, is the process of wrapping a species around the CNT walls [27]. This method is preferable to covalent bonding in many cases as it causes less structural damage to the CNT and the wrapped species, and the chemical environment required during fabrication is less harsh [28]. Over the years, the noncovalent wrapping of CNTs by polysaccharides [33], DNA [35, 36], proteins, polypeptides [37], and synthetic polymers has been widely reported.

The degree of CNT functionalization is commonly characterized by atomic force microscopy, Raman spectroscopy, SEM, transmission electron microscopy (TEM), ultraviolet-visible light spectroscopy, Fourier-transform infrared spectroscopy, thermal gravimetric analysis, and gel electrophoresis [38, 39]. The bioactivity of the attached biomolecules can be characterized by the immunochemical methods such as enzyme-linked immunosorbent assay (ELISA) [38]. It should be noted that whilst the bioactivity is strongly dependent on the bonding between the biomolecule and the CNT, the stoichiometry and the loading ratio are also important factors that must be considered [32].

2.2. Carbon Nanotubes for Biosensing. The incorporation of CNTs in biosensing devices has made a significant progress in the last decade [39]. By definition, a biosensor is an analytic device which consists of a receptor that interacts with the targeted analyte to be measured and a transducer (or detector) that transforms the signal from the interaction into a form that can be easily measured. The one-dimensional (1D) structure of CNTs allows signals to be transported in a confined space, making them extremely sensitive to electrical and chemical changes in their immediate environment [8]. There are generally two configurations of CNT-based biosensors: CNT field-effect transistors (CNT-FETs) [41, 42] and CNT electrochemical sensors [3, 43, 44]. Here, we concentrate on these two types of biosensors and provide details on the role of CNTs in these devices and the common approaches employed to improve their sensitivity.

Carbon nanotube FET biosensors have a current carrying channel connected to a source and a drain, which can be regulated by a gate voltage [3]. A typical CNT-FET setup is shown in Figure 2(b). The current carriers (electrons or holes) running through the channel are highly sensitive to changes in external electric fields and as such can be used to detect electrical signals produced by biological activity or biochemical interactions [45]. The conductive channel in CNT-FET devices can be either an individual semiconducting single-walled CNT (SWCNT) [46] or a randomly distributed bundle of CNTs [8]. The former was first introduced by Martel et al. [47] and has shown superior performance compared to traditional metal-oxide-semiconductor FETs (MOSFETs) [48]. Because of their high sensitivity, CNT-FET biosensors are well suited for the detection of very low analyte concentrations [8, 49]. For example, ultrasensitive detection of DNA at concentrations of 100 fM has been detected with SWCNT-FETs [35, 50].

Semiconducting SWCNTs are often used in FET biosensors as opposed to metallic SWCNTs since their conductivity can be gate-modulated by electrical changes in the external environment [49]. Various purification processes have been reported to separate metallic and semiconducting SWCNT mixtures, such as electrophoresis, centrifugation, chromatography, and solubilisation [55–57]. However, purification of semiconducting SWNTs can add considerable time and resources to the production process [56], and as

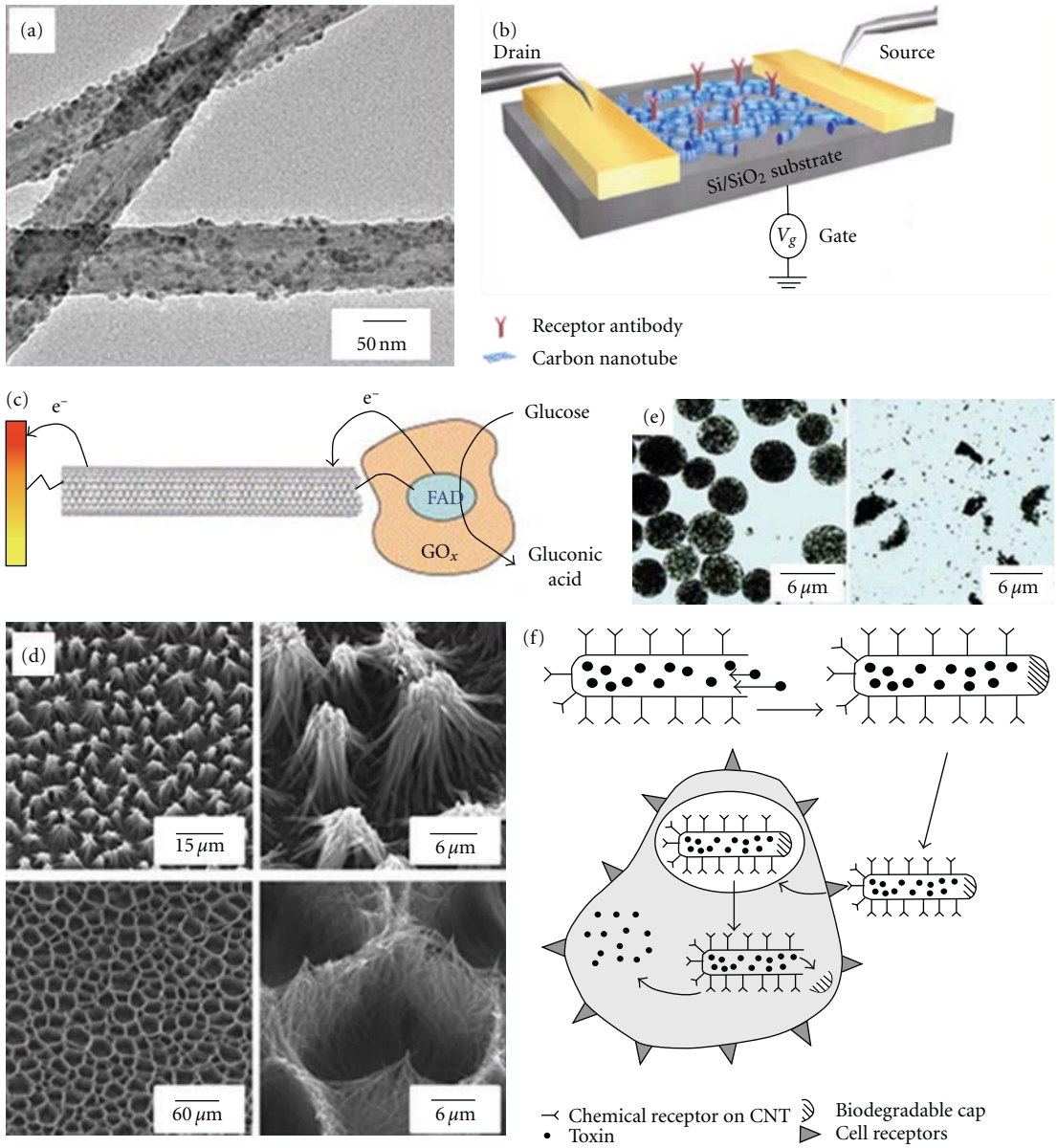

Figure 2: (a) Transmission electron microscopy image of ferritin-functionalized MWNT (reproduced with permission from [34]); (b) CNT-FET device for biosensing using antibody receptors (reproduced with permission from [22]); (c) Electrochemical sensor for glucose consisting of an Au electrode bonded to a CNT-GO_x which detects redox reactions between FAD and glucose (reproduced with permission from [51]); (d) "basket-like" periodic MWNT lattices into which mice fibroblast is to be implanted (reproduced with permission from [52]); (e) alginate-polylysinealginate microcapsule destruction by the photoacoustic effect by folate acid—functionalized SWNTs inside the cells (reproduced with permission from [53]); (f) loading and unloading of molecules inside CNTs for drug delivery; drugs are released when a CNT is uncapped within the cytoplasm of the cell (reproduced with permission from [54]).

such should be taken into account when considering the economic viability of CNT device fabrication.

Several approaches have been attempted to further amplify the signals and improve the specificity and sensitivity of CNT-FETs. One of these approaches is to bind specific receptor species, which can undergo selective interactions with the analyte, to the CNT channels. Many types of receptors have been successfully bound to functionalized CNT-FETs, such as aptamers [58], antibodies [59], sugars [60], DNA [50], and proteins [49, 61]. Furthermore, decorating the CNTs with conductive metal nanoparticles (typically Pt and Au) can also amplify the detection signals [62]. Rajesh et al. [63] demonstrated that the sensitivity of DNA detection was 2.5 times greater after the addition of ZnS nanoparticles into CNT-FETs.

Controlling the Schottky barrier effect is another common way to amplify detection in CNT-FETs. Changes in the conductivity of CNT-FETs are mostly due to gate coupling effects and the Schottky barrier effect. The Schottky barrier effect arises from differences between the work functions

of the CNT and the metal contacts [64] and is often hard to predict, and is therefore detrimental to the sensor's performance [8]. Methods such as coating the metal contacts with polymers have been used to minimize this effect and stabilize the response [64]. However, it should also be noted that one can actually amplify the CNT-FET signals for sensing applications by controlling the Schottky barrier effect [3, 65].

Real-time measurement is vital for the monitoring of dynamic systems and is a promising approach for applications in fields such as bioterrorism, food safety, drug testing, and on-the-spot medical diagnosis [65–67]. Carbon nanotube FET biosensors have also been used to monitor biological interactions in real time [8], including interactions involving DNA [35], proteins [64], immunoglobulin [58], morphine [45], and biological processes such as phagocytosis [62]. Again, decoration by metal nanoparticles can be used to improve the performance of CNT-FETs in real-time measurements, as has been demonstrated in the cases of glucose [35] and heroin [45].

On the other hand, CNT-based electrochemical biosensors have been used to detect chemical redox interactions [39, 68]. In this sensing mode the electrical properties and small size of each CNT is preferred, as it allows them to act as tiny electrodes with direct contact to biological systems. For example, a SWCNT with a diameter of 1 nm is comparable to the size of DNA and the active sites of proteins [69]. The 1D structure of CNTs also allows them to interact with one species at a time, ideal for single-species biodetection and biosensing [62, 70]. Carbon nanotube electrochemical biosensors have been used to detect DNA [68], glucose [71, 72], proteins [49], enzymes [72], RNA [73–75], H_2O_2 [76], and many other biomolecules. Analogous to the case of CNT-FET biosensors, functionalization of CNTs is important to increase the specificity of the electrochemical biosensors.

Figure 2(c) shows an example of an electrochemical biosensor, a gold electrode-CNT-glucose oxidase (GO_x) biosensor for detecting redox reactions between glucose (i.e., the analyte) and the redox active center of the GO_x, flavin adenine dinucleotide (FAD) [51]. The orientation of the CNTs on the electrode has been found to be important for sensing performance, with several studies showing that using aligned CNTs increased the sensitivity of the device [18, 69]. Other biosensors rely on an array of CNTs perpendicular to the electrode where the properties of the biosensor sensitivity are dependent on the spatial distribution and relative diameters of the CNTs in the array [50, 77]. Recently, spun CNT fibers have also been attached to electrodes for biosensing [78] and CNT fiber sensors have been reported to detect glucose with greater sensitivity than traditional Pt-Ir sensors [44].

Many different methods have been used to improve the sensitivity of CNT electrochemical biosensors. The most common way has been to combine metal nanoparticles with CNTs to increase the conductivity and redox activity of the sensor [64, 71, 72, 78]. Other methods include gas treatment [79], oxidation, and plasma etching [80, 81], which can add extra functional groups (e.g., –COOH, $–NH_2$) to the CNTs. These functional groups act as active reaction sites for analyte binding [82]. Lastly, optimizing the ratio of semiconducting and metallic CNTs can also improve the sensitivity [50] and even the response speed [78] of CNT electrochemical sensors. For example, it has been shown that biosensing devices using a mixture of metallic and semiconducting CNTs performed better than those using pure semiconducting CNTs alone [50].

Since many of these electrochemical biosensors are used in real biological environments, it is often necessary to prevent nonspecific binding of proteins, which can interfere with the measurements. Polymer coatings such as poly(ethylene glycol) (PEG) and poly(ethylene oxide) (PEO) are often used to reduce nonspecific binding [8, 49, 83, 84]. However, care must be taken to choose the correct polymer which does not distort the CNT and the biological receptor [36].

It should be noted that there are many nanostructures already used in biosensors, for example, Au nanoparticles [85]. Au nanoparticles are gold clusters ranging from 1 to 100 nm in diameter [86] and are easily functionalized with biomolecules such as DNA, enzymes, proteins, peptides, oligonucleotides, glucose, and RNA [85, 86]. Biosensing with Au nanoparticles is quite well established, especially by enhanced surface plasmon resonance [86] and enhanced Raman spectroscopy [86]. The toxicity of Au nanoparticles is currently deemed minimal compared to CNTs [85, 87]. The main advantage of using CNTs in biosensors instead of Au nanoparticles is that CNTs have many more parameters that can be varied, which potentially allows a wider variety of biosensors to be produced.

2.3. Carbon Nanotubes in Tissue Engineering. Tissue engineering aims to repair, regenerate, and replace diseased or damaged tissue. In tissue engineering, scaffolds are often used to promote cell adhesion, growth, differentiation, and proliferation in a three-dimensional (3D) matrix. These scaffolds also provide mechanical strength and add some degrees of control over location and orientation of the attached cells. Using CNTs as scaffolds has attracted great interest due to their mechanical strength [13], chemical stability [14], and biological inertness [52, 88]. Typically, carbon nanotubes are grown into a 3D porous structure, or else coat an existing 3D porous structure, for example, collagen [89] and then seeded with cells [90]. The cells are allowed to grow over the scaffold until they become self-supporting [90]. Carbon nanotube scaffolds can be fabricated into many different structures [91] with dimensions comparable to biological cellular scaffolds [88, 92], which allows them to support a wide range of biological species.

To promote cell growth and adhesion, CNTs are often functionalized with, for example, carboxyl groups, polymers, and sugars [13–15]. It has been shown that surface charge, functional groups, and hydrophilicity are important in determining cell adhesion and growth [93, 94]. For example, in a study by Zhang et al., hydrophilic, neutrally charged amylose-CNT hybrid matrices supported cell growth and proliferation as compared to chitosan-CNT, sodium alginate-CNT, or chitosan-sodium-alginate-CNTs [33].

The periodicity, size, and structure of the CNT scaffolds can also affect the cellular interactions with the scaffold [52, 95]. Vertically aligned MWCNTs can be fabricated into 3D scaffold matrices of periodic "basket-like" cavities, where the cavity size and density depend on the dimensions of the original array as shown in Figure 2(d) [52]. Mice fibroblast cell lines L929 were successfully cultured on these periodic matrices [52]. Patterns of CNTs can be fabricated by lithography and used to direct the growth of cells such as human mesenchymal stem cells (hMSCs) and neurons [96, 97]. In particular, hMSCs have been found to grow and differentiate well on 3D matrices of fibronectin (FN) functionalized CNTs [98], but their growth was inhibited when seeded on carboxylated CNT scaffolding [99]. The polarization of neurons is also extremely sensitive to their environment; hence CNTs could be used to direct neural connections and interactions, potentially for *in vivo* applications [100].

Apart from using CNTs solely to construct scaffolds, they can also be added to other scaffolding materials to produce heterostructures. For example, porous polymer composites can be produced by dispersing CNTs into PEG or poly(propylene fumarate) (PPF) [101–103]. The addition of CNTs allows the polymer composites to be electrically conductive, which is useful for stimulating cell growth [104]. These composites have generally been used to promote osteoblastic cell growth *in vitro* for bone regeneration research [104–107] and also for neural regeneration [108, 109]

We also note that another carbon nanostructure that has recently emerged as a potential scaffold material for tissue engineering is nanodiamond. For example, a monolayer of nanodiamonds has been shown to support neuronal cell growth [110]. Nanodiamond crystals range from 2 to 10 nm in diameter [111], are mechanically stable [110, 112], have a large surface area [112], and are nontoxic [111]. However, like the Au nanoparticles mentioned in Section 2.2, nanodiamonds have significantly fewer tunable characteristics compared to CNTs, thus offer fewer possibilities for tissue scaffold designs.

2.4. Carbon Nanotubes in Drug Delivery. In delivering drugs, the aim is to use a carrier molecule functionalized with a receptor to carry a drug around the body until it attaches to the problematic site, only then releasing the drug [113]. Receptor-functionalized CNTs have been suggested as targeted vehicles for drug delivery, where they are perceived to have several advantages. Firstly, the nanometer size of CNTs allows them to permeate into cellular membranes, making them ideal for inserting drugs directly into cells [16, 114, 115]. Secondly, each CNT can be functionalized to detect and interact with a single cell, improving the delivery efficiency and reducing the drug dosage [17, 116]. It has been demonstrated that 5 million species can be bonded to an 80 nm long CNT [54]. The combination of size and ease of functionalization allows CNT to deliver drugs to cells, such as neurons and cardiomyocytes, which are difficult to reach by traditional drug-delivery methods [117]. Lastly, drugs can be encapsulated into CNTs [54, 118–120], where release of the drug in the desired cell compartment requires the chemical disintegration of the CNT cap, as illustrated in Figure 2(f) [22]. Successful examples include anticancer drugs and IR-emitting molecules for direct heat treatment *in vivo* [121].

The CNT must have a drug-unloading mechanism for the drug delivery to function effectively [122]. Drug unloading from CNT carriers can by triggered by environmental changes, such as changes in temperature and pH [54]. For example, intracellular pH is lower than extracellular pH; and CNTs, which cross the membrane, can be activated to release their drug load and influence intracellular processes [123]. This allows gene delivery straight into the nuclei of cells, possible by "injection" of CNTs into cells [124]. Drugs may also be released by optical stimulation using near-infrared (700–1100 nm) wavelengths, which are not absorbed by most biological structures, in particular skin [125].

Apart from delivering specific drugs, CNTs can also be functionalized for therapeutic applications. For example, CNTs functionalized with folic acid can bind to cancer cells, which can be killed by using infrared radiation to induce vibration, that is, forming cellular "bombs" [53]. Similar research has been carried out in other studies [125–128]. Figure 2(e) includes two images showing folate-functionalized SWCNTs inside alginate-polylysine-alginate microcapsules [53]. The first image shows the microcapsules before IR irradiation and the second image shows the obliterated microcapsules after irradiation [53]. This specific targeting of cells reduces damage done to surrounding biological systems and is more effective at destroying malignant cells.

3. Nanotoxicity of Carbon Nanotubes

3.1. Background and Motivation. The diagnostic and therapeutic applications of CNT-based materials mentioned above will only be trialed clinically after detailed information on their environmental and health and safety effects in host biological systems is obtained [129–131]. A few preliminary tests have showed that CNTs are biologically benign to certain cells, tissues, and organs under limited conditions [132–134], while further studies have indicated that CNTs are potential hazards that can cause both acute and chronic adverse effects to many living systems [4, 24, 135]. Nevertheless, at this stage, it appears that the biological effects of CNTs are sample specific and must be assessed on a case-by-case basis. The nanotoxicity of CNTs, therefore, requires continuing and extensive investigations and, indeed, this will be required by regulatory bodies before CNTs can be used in clinical environments as functional biomaterials and biomedical devices.

Despite several years of research, definitive findings regarding the extent of toxicological risks arising from using nanotubes are far from complete. Continuing research is required to determine, for example, how CNTs enter cells, where CNTs are internalized, which the cytotoxic mechanisms are relevant, and how the nanotoxicity is affected by a variety of physicochemical characteristics, such as diameter, length, presence of impurities, surface functionalization, and surface wettability. In this section, we give a brief overview of the progress made to date on understanding

the nanotoxicity of CNTs, including the exposure, cellular uptake, subcellular localization, and intracellular trafficking, as well as mechanisms that may result in the mitigation and inhibition of nanotoxicity.

3.2. The Production of and Exposure to CNTs. Despite their relatively recent discovery [136], production of CNTs had already reached 4000 tons by 2010 and could exceed 12000 tons by 2015 [137]. Such large-scale production has inevitably led to exposure risks for both animals and human beings. The most common ways for CNTs to enter the host include inhalation, ingestion from food and water, and absorption through skin wounds or scars [138]. In laboratory-related exposure experiments, intravenous injection [4, 139, 140], intratracheal administration [141], and abdominal implantation [142], are often employed to study the nanotoxicity of CNTs in different organs including the lungs.

3.3. The Cellular Uptake of CNTs. The uptake of CNTs into cells plays a critical role in determining their cytotoxicity and genotoxicity. The outermost layer of the cell, the cellular membrane, consists of a phospholipid bilayer [129], which serves to segregate the subcellular compartments from the external medium, and to regular the transport of foreign materials, including CNTs, into cells [143].

Experimental results indicate that CNTs can be internalized by a variety of cells. Although systematic knowledge is still lacking, it is in general considered that there are two possible pathways for CNTs to cross the cellular membrane and enter cells [129]. One pathway is passive transport, which includes diffusion, membrane fusion, and direct pore transport [24, 144]. Individually dispersed CNTs in aqueous solutions have been experimentally demonstrated to be able to enter the cytoplasm of cells by directly crossing the membrane [145, 146], despite recent modeling showing that the energy cost of entering the cellular membrane via rupture and diffusion was high compared to that of the energy of thermal motion of CNTs [147].

A more common pathway for the cellular uptake of CNTs is active transport via *endocytosis*, which includes phagocytosis and pinocytosis [129, 143, 148]. Endocytosis involves the enclosing of foreign objects in vesicles or vacuoles pinched off from the cellular membrane. In general, long CNTs (>1 μm in length) were taken up by *phagocytosis*, which was mainly conducted by macrophages, monocytes, and neutrophils [143]. Shorter CNTs of length from a few to several hundred nanometers, on the other hand, were mainly internalized by *pinocytosis*, such as macropinocytosis, clathrin-mediated endocytosis, and caveolin-driven endocytosis [129, 143]. Endocytosis is an energy-dependent process, and the orientation of CNT entry can be controlled by the interplay between the tip recognition through receptor binding and the rotation driven by asymmetric elastic strain at the nanotube-phospholipid bilayer interface, as demonstrated recently by numerical modeling [149]. In the most common case, a near-perpendicular orientation resulted in a minimum energy barrier [147].

The exact cellular uptake pathway of CNTs is complex and depends on many experimental parameters, such as the size, length, hydrophobicity, surface chemistry, and the cell culture medium. For example, the uptake of functionalized SWCNTs in phagocytotic cells was found to occur via endocytosis if they were longer than 400 nm and via diffusion-controlled internalization if smaller than 400 nm [150]. Lee and Geckeler [129] have also shown that individual MWCNTs entered cells through direct penetration *in vitro*, whereas bundled MWCNTs entered via endocytosis.

Surface chemistry of SWCNTs also influences the cellular uptake pathway [151]. It was demonstrated that when SWCNTs were grafted with folate using PEGylation and linked by phospholipid bilayer, they could enter HeLa cells bound with the folate receptor (FR, a specific tumor marker) but not those without FR. Similarly, when SWCNTs were grafted with $\alpha_v\beta_3$, they could enter integrin- (a receptor of $\alpha_v\beta_3$) positive U87-MG cells but not integrin-negative cells [152]. If non-cell-targeting molecules were grafted, the entry mode of CNTs will depend on the properties of the conjugated molecules, for example, large molecules such as bovine serum albumin (BSA) enter cells only through endocytosis [152].

Additionally, the hydrophobic surface of CNTs can interact with components in cell growth medium and affect the cellular uptake. Serum proteins in the cell growth medium can bind to CNT walls through π-π interactions or electrostatic attractions, forming a protein coating [129]. The "screening effect" of such protein coatings, known as the "protein corona," allows functionalized CNTs to experience a similar cellular uptake pathway [129, 153].

Finally, the culture medium itself can affect the cellular uptake of CNTs. For example, single-walled CNTs grafted with fluorescein isothiocyamate (FITC) were found to be taken up by cells in a pH 5.8 medium, but the uptake was inhibited in a slightly alkaline medium (pH 7.2) [154]. It was suggested that under the alkaline condition, the anionic form of FITC could dominate the neutral form and hamper the cellular uptake of CNTs [154]. If properly exploited, this property may facilitate the removal of the internalized SWCNTs, though much more research is required.

3.4. Subcellular Localization and Intracellular Trafficking of CNTs. Once taken into the cell, CNTs are often localized in one of a number of different subcellular compartments, for example, cytoplasm, cytoskeleton, mitochondria, lysosomes, endoplasmic reticulum, vesicles, and nuclei and can be translocated between these compartments [143]. Because of their small size and the weak contrast between these cellular components and CNTs, it is often difficult to characterize the subcellular distribution of internalized CNTs. Over the years, techniques, such as confocal and fluorescent microscopy, TEM [4, 24], SEM with focused-ion beam (FIB) [155], Raman spectroscopy [4, 140], and laser and photobleaching [154], have been developed. For example, TEM is a very effective tool to see CNTs (and any other nanoparticles) inside frozen cells. It was utilized by Porter et al. [24] to show that SWCNTs were localized within lysosomes after 2 days,

whereas after 4 days, bundles of SWCNTs were localized in endosomes, translocated across the nuclear membrane, and localized within the nucleus.

One of the major findings made in recent years in this field is that the subcellular localization of CNTs depends on how CNTs enter the cells. When functionalized CNTs directly crossed the cell membrane, they were localized exclusively inside mitochondria, whereas if being endocytosized, they were located inside the lysosomes and phagososome [144, 148, 150]. Small CNTs that entered the cellular membrane through diffusion were found mainly in the cell cytoplasm [129, 150]. These preliminary findings have shed light on the selective translocation and localization of SWCNTs to desired subcellular components.

Figure 3 illustrates the main uptake pathways, the subcellular localization, and the intracellular trafficking of differently functionalized CNTs [129]. It is noted that the internalized CNTs may be translocated between different subcellular components through carrier-mediated transport [154]. For example, endocytosized MWCNTs accumulated in the endosomes could be transported to the endoplasmic reticulum, from which they translocated into the cytosol [148]. Intracellular trafficking can also be effectively controlled by attaching a suitable functional tag on the CNTs. For instance, FITC-SWCNTs were taken up in vacuoles through carrier-mediated transport, but when functionalized with an inhibitor of the carrier-mediated transport, they mostly accumulated in the cytoplasm [154]. Further trafficking of functionalized SWCNTs into nucleoplasm and the nucleus were also observed [129].

3.5. Nanotoxicity Mechanisms in the Lungs. One of the earliest concerns over the toxicity of CNTs arose from the similarity of their structure (i.e., a fibrous shape and a high aspect ratio) and biopersistence to asbestos, an infamous carcinogenic material known to cause mesothelioma [141, 156, 157]. Asbestos has a fibrous structure of 20 to several hundred nanometers in diameter. The toxicity of asbestos in the lungs is thought to be mediated through the generation of reactive oxygen species (ROS), which can induce the activation of antioxidant defenses, causing the release of proinflammatory and profibrotic cytokines from inflammatory and epithelial cells, and activation of the apoptotic (cell death) pathway [141, 158].

Carbon nanotubes in the lungs are often considered less toxic than asbestos [141]. However, many experiments have confirmed that they indeed show many asbestos-like behaviors, although it is still unknown if they can cause mesothelioma. The characteristics of cell deaths were observed when lung cells were exposed to CNTs [24]. When CNTs were inhaled, they were able to reach the subpleura and cause subpleural fibrosis in mice [135]. Chronic exposure to SWCNTs was also shown to cause the malignant transformation of human lung epithelial cells, which is evident for CNT-induced carcinogenesis [156].

Besides the ability to generate ROS in lung cells [4, 159], other cytotoxic mechanisms of CNTs also include blocking ion channels, regulating the intracellular calcium level, binding to subcellular organelles and proteins to stop their functions, and attacking the nucleus and damaging DNA, which can induce apoptosis or necrosis cell deaths and/or mutational cellular events [24, 160, 161]. These effects are in turn strongly influenced by the type, size, shape, surface chemistry, and the route of administration of CNTs [162].

The cytotoxic effect of size and shape of CNTs is best represented by their high aspect ratio, which results in incomplete phagocytosis by the mononuclear cells because the CNTs are too large [129]. This induced incomplete or frustrated phagocytosis can result in macrophage activation and granulomatous inflammation. In fact, it has been hypothesized that the failure of resident macrophages to clear CNTs is the main reason for the activation of proinflammatory pathways that induce lung fibrosis, lung cancer, and malignant mesothelioma [149]. In addition, the aggregation of CNTs by van der Waals' interactions could also affect profibrogenic cellular responses and contribute to the pulmonary toxicity of CNTs *in vivo* [141, 163].

In vivo studies using a mouse model also showed that the pathological origin of CNTs was dependent on the route of administration [164]. For the case of intratracheal instillation, the agglomerates of CNTs with different size and morphology were observed in bronchi of mice, which led to inflammation in 24 days. On the other hand, when CNTs were inhaled, aggregation of CNTs was observed on the lining wall of the bronchi but no inflammation was induced [164].

Surface wettability is another factor that affects the cytotoxicity of CNTs. When macrophages are in contact with hydrophilic CNTs, less inflammation was observed compared to those in contact with hydrophobic CNTs or titanium (a biocompatible metal) [165]. It was found that less proinflammatory cytokines (e.g., tumor necrosis factor-alpha, or TNF-alpha) and interleukin-6 (IL-6) were secreted from macrophages containing hydrophilic CNTs. As a result, hydrophobic CNTs are more toxic than their hydrophilic counterparts.

A final remark on the pulmonary toxicity of CNTs is that many nanoparticle impurities (e.g., Ni, Fe, and Co) carried by CNTs are highly toxic. Removing these nanoparticle impurities is necessary to show the intrinsic toxicity of CNTs [129, 135, 166]. However, conventional purification routes for removing these impurities may generate a high density of functional groups or defects on CNTs, which in turn influences the cytotoxicity. As demonstrated in a recent study, purified CNTs have been shown to have the strongest adverse effects among pristine CNTs, carbon graphite, active carbon, and carbon black.

3.6. Biodistribution and Nanotoxicity of CNTs in Other Organs. Many *in vivo* studies have shown that CNTs delivered to a specific area in the body are not confined to that area [139]. For example, intravenously injected CNTs were shown to be taken up both by the liver and the spleen and then excreted rapidly through the kidney [139, 140]. In contrast, SWCNTs injected into the bloodstream of mice persisted within liver and spleen macrophages (Kupffer cells) [4].

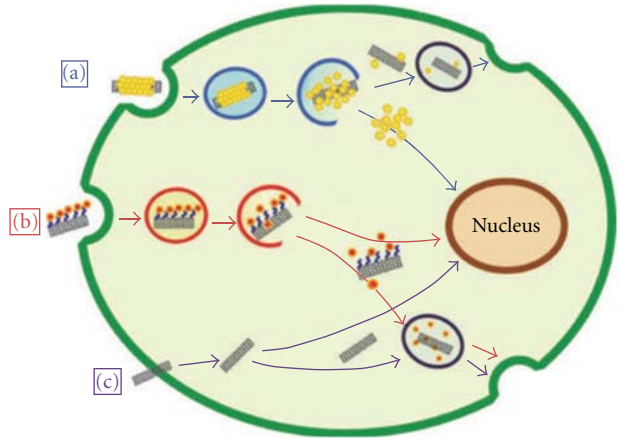

Figure 3: The cellular uptake pathways, subcellular localization and intracellular trafficking of differently functionalized CNTs. (a) Supermolecularly functionalized CNT via endocytosis, (b) covalently functionalized CNT bound with drugs via endocytosis, and (c) individual or specifically functionalized CNT via direct penetration (reproduced with permission from [130]).

Singh et al. [167] also reported that intravenously injected ammonia-functionalized SWCNTs were excreted mainly via the renal route without uptake in the liver and spleen in mice [167].

Because of the migration of CNTs in biological systems, their toxicity to a variety of other organs should also be tested. In many cases, macrophages, which form the first line of defense against foreign materials, will interact with the administrated CNTs [24]. This is why macrophages are one of the mostly studied cells in *in vitro* investigations of CNT toxicity. After CNTs have been ingested by macrophages, they can enter into the blood and lymph circulation at a later stage [24]. Carbon nanotubes can also be dispersed by mucins (glycosylated proteins produced by epithelial tissues) in certain cases and cleaned away in a physiological solution, before they can interact with cells [168].

The long-term accumulation of SWCNTs in organs was studied by Yang et al., who showed that no apoptosis was induced in the main organs [4]. On the other hand, a low percentage of early miscarriages and fetal malformations was observed in female mice exposed to pristine SWCNTs and ROS were detected in the placentas of malformed fetuses [169]. Carbon nanotubes could also induce actin (fibrous proteins that can form filaments and higher-order network structures of the cytoskeleton and that perform essential functions such as force generation, motility, and division) bundling and reduced cell proliferation, which may cause chronic changes to cellular functions [170]. Inhaled MWCNTs were also shown to be able to suppress the immune function of the spleen through the signals coming from the lungs of the exposed mice [171, 172].

3.7. The Mitigation and Inhibition of CNT Nanotoxicity. In attempting to fully utilize the excellent properties of CNTs without being hampered by their adverse effects, several strategies have been proposed to mitigate or inhibit the toxicity of CNTs. The most common method is through surface functionalization [129, 143]. Noncovalently PEGylated CNTs have been shown to be less toxic than oxidized and pristine CNTs [4, 140, 169]. Repeated administrations of carboxylated (CNT–COOH) and amine-CNTs (CNT–NH_2) in male mice caused only reversible testis damage with no effect on their fertility [173]. Other examples include cell-adhesion peptides bound MWCNTs, which did not interfere with neuronal functionality [174], and amine-functionalized SWCNTs, which even protected the neurons [96].

Another way to reduce the cytotoxicity is through the dispersion of CNTs in a biocompatible block copolymer [141, 175, 176]. *In vivo* experiments showed that SWCNTs functionalized with Pluronic polymers can be gradually cleared from the body by alveolar macrophages through mucociliary clearance, reducing risk of lung fibrosis [141]. Lastly, CNTs have been shown to be biodegradable to certain enzymes, such as plant peroxidases, where the degraded CNT fragments can then be effectively phagocytosized by surrounding cells [177, 178]. It has further been shown that the biodegraded CNT fragments, when aspirated into the lungs of mice, did not generate an inflammatory response [178].

4. Graphene: Biomedical Applications and Nanosafety

4.1. Introductory Remarks. Graphene, a 2D carbon nanomaterial with a honeycomb-like structure, has been the subject of a considerable interest after being the subject of the 2010 Nobel Prize for Physics. Its unique properties, including ballistic electron transport [179, 180] at room temperature, tunable band-gap (for few-layer graphene), high chemical and mechanical stability, low electrical noise, high thermal conductivity, and biocompatibility, have led it to be used in many advanced devices ranging from ultracapacitors to spintronic devices [181–186]. In line with the purpose of this paper, however, we will concentrate on the emerging biomedical-related applications of graphene

and its derivatives (i.e., pristine graphene, graphene oxide, metal nanoparticle decorated graphenes, vertical graphene nanosheets, and many other hybrid structures) in biosensors, biocompatible scaffolds, tumor treatment, and drug delivery. We will first present an overview of how and why graphene is used in these cutting edge applications, followed by a brief discussion of how to make graphene for these applications using plasma-based fabrication and other methods.

4.2. Graphene Biosensing and Biomedical Applications. As noted in Section 2, biosensors consist of two fundamental parts—a biomolecular recognition element (receptor) and a transducer. The former interacts with the analyte, whereas the latter processes the "sensed" information and translates it into a useable signal. Graphene is a particularly versatile material as it can play a role in both of these components, in plasmonic/optical- and electrical-based sensors. For example, the affinity of graphene for aromatic ring containing biomolecules has been utilized in the biomolecular recognition element in surface plasmon resonance (SPR) sensors. Wu et al. [189] demonstrated that a graphene-Au SPR biosensor, shown in Figure 4(d), was more sensitive than a conventional Au-only SPR biosensor due to (1) the greater adsorption efficiency of ring-based biomolecules on graphene and (2) increased sensitivity to refractive index (RI) changes (a 25% increase in sensitivity to RI change for 10 graphene layers compared to the Au only case). This affinity can also be used as the basis for graphene surface-enhanced Raman scattering (SERS) sensors [190]. Ling et al. [187] reported that using a graphene substrate resulted in a SERS enhancement (see Figures 4(a)–4(c)) of common SERS probes including Rhodamine 6G and crystal violet. This enhancement is chemical, rather than electromagnetic, in nature. Specifically, it is due to the π-π stacking that occurs when the ring-containing molecule aligns itself parallel to the graphene basal plane—this stacking means that charge transfer between graphene and the biomolecule occurs easily, resulting in a chemical SERS enhancements of around 2–17 times [187]. This chemical enhancement, however, is markedly less than the electromagnetic SERS enhancement achieved when Ag or Au nanostructures are used as SERS substrates, despite graphene's higher bioaffinity.

Vertical graphenes (such as those in Figures 5(a) and 5(b)) can, however, be used in combination with metal nanoparticles to make 3D metal-graphene nanohybrid SERS platforms. Rider et al. [188] presented a novel SERS substrate consisting of vertical graphenes decorated with Au nanoparticles (see Figures 5(d–g)). Using vertical, rather than horizontal, graphenes provides a markedly higher effective "bookshelf" like area to which Au nanoparticles can attach—a conservative estimate puts the bookshelf nanoparticle density as 224% greater than that for the "flat sensor area" [188]. This means that there is a much greater area to which analyte species can attach, compared to typical horizontal sensor architectures. Gold-decorated graphene composites have also been used in electrodes for electrochemical sensors, due to their high electrocatalytic activity and electrochemical stability [195]. In addition, making use of the high fluorescence quenching efficiency of graphene, Chang et al. [196] constructed a graphene fluorescence resonance energy transfer (FRET) aptasensor, with a reported thrombin detection limit two orders of magnitude lower than CNT-based FRET sensors.

Electrical sensors that have incorporated graphene include electrochemical-impedance based sensors [197], electrochemical sensors (in which graphene-related materials form the electrode) [198], and FET sensors [194, 199, 200]. Wan et al. [197] constructed immunosensors based on electrochemical impedance with reduced graphene sheets as electron conductors [197]. Ohno et al. [194, 201] showed that graphene FETs (such as those shown in Figure 5(f)) could be used for label-free biosensing—specifically, they demonstrated electrical detection (via a change in the drain current) of solution pH, protein adsorption and specific biomolecules (such as IgE). Zhang et al. noted that the hydrophobic interaction between certain proteins and chemically reduced graphene oxide is promising for protein immobilization and as a result could be used in a biosensor [202].

Aside from sensors, the biocompatibility and chemical inertness (the basal plane, not the edges, which are quite reactive) of graphene surfaces have led to their use as biocompatible scaffolds for the growth of human osteoblasts [203] as well as components in drug delivery and tumor treatment routes [193, 204–206]. Use of graphene oxide as a drug delivery vehicle for anticancer drug doxorubicin [207] is shown in Figure 5(e). Due to the strong optical absorbance of graphene nanosheets in the near infrared, they have been used as a crucial component in photothermal treatment [192, 208, 209] with reported efficient tumor ablation; this can be clearly seen in Figure 5(c), where the best tumor ablation was observed in mice treated with PEG-graphene nanosheets, indicated by the star [192]. The passage of single molecules through nanochannels or nanopores is important for many biological diagnosis processes [210] including DNA sequencing [211, 212]—nanopores in graphene have recently been used for single DNA molecule translocation [213].

Diagnostics and therapies do not exist in a vacuum, they are informed by each other—leading to mutual benefits—this is reflected in the emerging term "theranostics," focusing on individualized medical treatments [214]. This is an area in which graphene-related materials, as already indicated by Yang et al. [192, 215], can play a very important role as their properties lend them both to sensing and intervention/treatment methods.

4.3. Nanosafety and Nanotoxicity of Graphene. As mentioned in Section 3, for any biological-related application, particularly *in vivo* applications, great care must be taken to ensure that the toxicity of the nanomaterial is well characterized and understood. Whilst this has been extensively done for carbon nanotubes, markedly fewer studies [158, 216–222] are available for graphenes (e.g., an ISI Web of Knowledge topic search on 03/01/2012 gave 59 hits for "graphene" and "toxicity" compared to 1668 hits for "nanotube" and "toxicity"). There is even less consensus as to the sagacity of using this next-generation material as an integral component in *in vivo* applications. Zhang et al. [158] compared the

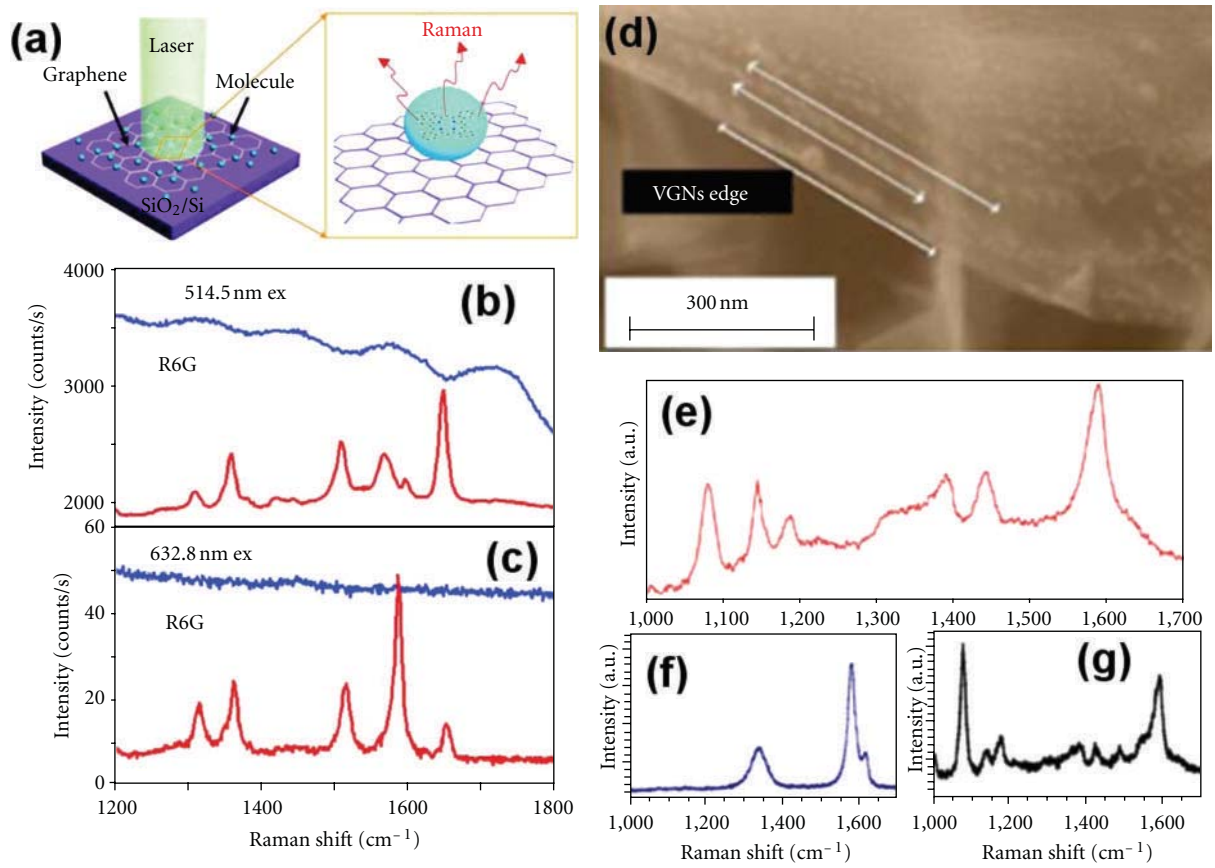

FIGURE 4: (a) Schematic of graphene as a SERS substrate. Graphene as a SERS substrate for Rhodamine 6G detection using (b) 514.4 nm laser and (c) 632.8 nm laser. The blue line is a SiO_2/Si substrate and the red line is graphene. Note that (a–c) reproduced with permission from [187]; (d) a quasi-linear arrangement of Au nanoparticles on vertical graphene nanosheets (VGNs); SERS spectra of 10^{-2} m 4-aminothiophenol on (e) Au-VGNs array, (f) VGNs only, and (g) Au nanoparticles only. Note that (d–g) reproduced with permission from [188].

cytotoxicity level of graphene to that of carbon nanotubes in the case of neuronal PC12 cells. They found that toxicity was shape and composition dependent, with graphene overall having a lower toxicity than CNTs; however the toxicity of graphene was curiously found to be inverse to concentration [223], with graphene exhibiting a higher toxicity than CNTs at low concentrations [223]. Studies on the uptake of PEG-coated graphene nanosheets in mice and subsequent photothermal treatment of cancerous tumors did not show any adverse toxic effects [192, 215]. In other studies, however, sharp graphene nanosheet edges [216] have been shown to cause considerable damage to the cell membrane of bacteria, although this antibacterial property has the potential to be useful. Moreover, hydrophilic carboxyl-functionalized graphenes have been shown to be able to be internalized in cells without any toxic effects, in contrast to hydrophobic pristine graphene [224]. The biocompatibility of graphene oxide has also been studied, with toxicity shown to be dose-dependent in both humans and animals [225], with little to no effect for low and medium doses in mice [225]. Graphene oxide nanosheets were demonstrated to be biocompatible with yeast cells [226]. With the wide range of morphologies, coatings, and hybrid structures available for graphenes, more detailed and longer-term studies are required before serious *in vivo* biomedical graphene applications are implemented.

4.4. Fabrication of Vertically Aligned Graphene Structures. Many different fabrication methods have been used to make graphene-related materials, from the first successful isolation via micromechanical cleavage [227], to chemical reduction of graphene oxide [228, 229], chemical vapour deposition (CVD) [230, 231], thermal decomposition of SiC [232], plasma nanofabrication techniques including plasma-enhanced CVD [233, 234] and arc discharges [235], as well as unzipping of CNTs via a variety of methods (e.g., chemical treatment, plasma etching) [236, 237]. For a detailed description of the relative merits of these fabrication methods, we refer the interested reader to two comprehensive reviews [238, 239]. As noted in Section 4.2, vertically aligned graphene structures have beneficial properties for sensing and other biomedical devices. However, so far there have been limited successes in fabricating these structures. In particular, plasma-based self-organization [240] is a promising way to grow catalyst-free, high-quality vertical graphenes

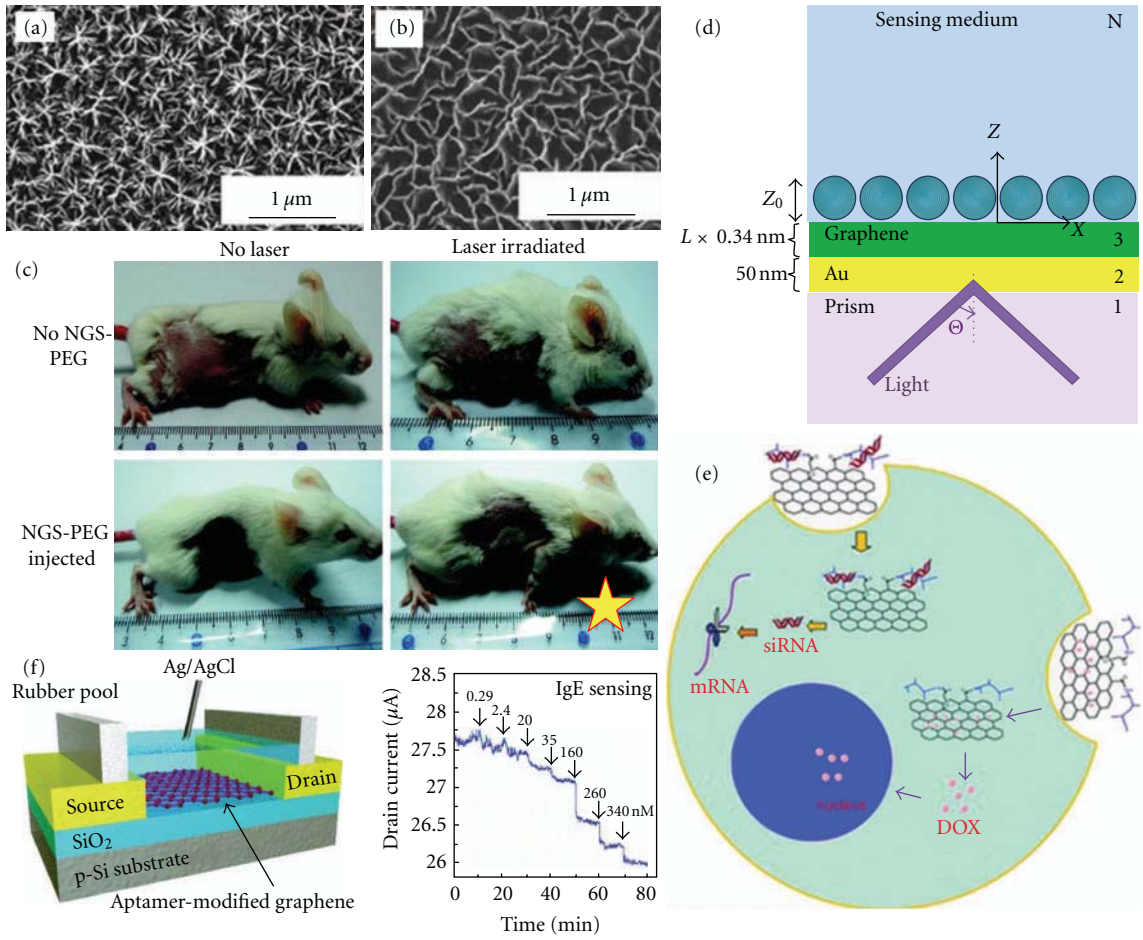

FIGURE 5: (a, b) Turnstile-like VGNs and maze-like VGNs, respectively. Reproduced with permission from [191]; (c) efficient tumor ablation in mice using PEG-graphene nanosheets where the best tumor ablation occurred in the mice injected with PEG-graphene nanosheets and laser treated (indicated by the yellow star). Reproduced with permission from [192]; (d) graphene as a biomolecular recognition element in SPR sensor. Reproduced with permission from [189]; (e) use of graphene oxide as a drug delivery vehicle for anticancer drug DOX. Reproduced with permission from [193]; (f) use of graphene in FRET-based sensor, specifically for detecting IgE; reproduced with permission from [194].

[191, 241]. Papers by Seo and Kumar et al. [20, 191, 241] have shown that it is possible to grow graphene nanosheets with a variety of morphologies (e.g., unidirectional, or see Figure 5(a) for turnstile and Figure 5(b) for maze-like) with different optoelectronic properties by modifying the plasma parameters such as gas composition and the degree of ionization. Plasma-based fabrication routes reduce human exposure to any hazardous byproducts since the growth is conducted under vacuum. Moreover, the nanostructures are typically surface-bound, which means they are less likely to be ingested or inhaled, as discussed for CNTs in Section 3 [131].

5. Summary and Outlook

In this paper, we have discussed the promising future of incorporating CNTs into the field of biomedicine, specifically their current roles in biosensing, drug delivery, and tissue engineering. The benefits of CNTs were presented, together with potential nanotoxicity and harmful effects of CNTs, on biological systems. Also discussed were the potential uses for graphene for similar biomedical applications as well as the problems associated with graphene's toxicity and safety. There are many challenges ahead that must be addressed before CNTs and graphene can be successfully integrated into biomedical devices and technology. The main advances required, in our opinions, include the following.

(i) Advanced techniques and facile methods are needed to increase the sensitivity of CNT biosensors towards single-molecule detection.

(ii) More efficient loading and unloading methods for drug delivery would refine overall performance of CNTs as carriers.

(iii) Further research is required into various CNT hybrid scaffolds to promote cell adhesion, growth, differentiation, and proliferation.

(iv) More specialized coatings and CNT-functionalization to minimize nonspecific bonding are needed.

(v) Protocols and further experiments should be conducted to determine the exact nature of the nanotoxicity of CNT-based and graphene-based materials.

(vi) Innovative ideas and further experiments are needed to further develop the use of graphene in advanced biomedical applications.

(vii) Innovative solutions are required to reduce fabrication and running costs of CNT and graphene biomedical devices to make them economically viable.

The long-term goals associated with incorporating CNTs and graphene into biomedical technology suggest that further research is required before these carbon nanostructured devices reach sufficient performance standards.

Authors' Contribution

C. Fisher, A. Rider, and Z. Han contributed equally to this work.

Acknowledgments

The authors would like to thank Q. Cheng, S. Yick, T. van der Laan, D. H. Seo, and W. Yan for insightful discussion. C. Fisher acknowledges the CSIRO OCE Honors Scholarship for Electroactive Biomaterials, A. Rider and Z. Han acknowledge the CSIRO OCE Postdoctoral Fellowship and support from the CSIRO Sensors and Sensor Network TCP. This work is supported by the Australian Research Council (ARC) and CSIRO's OCE Science Leadership Program.

References

[1] M. S. Dresselhaus, G. Dresselhaus, J. C. Charlier, and E. Hernández, "Electronic, thermal and mechanical properties of carbon nanotubes," *Philosophical Transactions of the Royal Society A*, vol. 362, no. 1823, pp. 2065–2098, 2004.

[2] S. Chakrabarti, H. Kume, L. Pan, T. Nagasaka, and Y. Nakayama, "Number of walls controlled synthesis of millimeter-long vertically aligned brushlike carbon nanotubes," *Journal of Physical Chemistry C*, vol. 111, no. 5, pp. 1929–1934, 2007.

[3] S. N. Kim, J. F. Rusling, and F. Papadimitrakopoulos, "Carbon nanotubes for electronic and electrochemical detection of biomolecules," *Advanced Materials*, vol. 19, no. 20, pp. 3214–3228, 2007.

[4] S. T. Yang, X. Wang, G. Jia et al., "Long-term accumulation and low toxicity of single-walled carbon nanotubes in intravenously exposed mice," *Toxicology Letters*, vol. 181, no. 3, pp. 182–189, 2008.

[5] C. Fisher, Z. J. Han, I. Levchenko, and K. Ostrikov, "Control of dense carbon nanotube arrays via hierarchical multilayer catalyst," *Applied Physics Letters*, vol. 99, no. 14, Article ID 143104, 2011.

[6] Z. J. Han, I. Levchenko, S. Yick, and K. Ostrikov, "3-Orders-of-magnitude density control of single-walled carbon nanotube networks by maximizing catalyst activation and dosing carbon supply," *Nanoscale*, vol. 3, no. 11, pp. 4848–4853, 2011.

[7] Z. J. Han, S. Yick, I. Levchenko et al., "Controlled synthesis of a large fraction of metallic single-walled carbon nanotube and semiconducting carbon nanowire networks," *Nanoscale*, vol. 3, no. 8, pp. 3214–3220, 2011.

[8] G. Gruner, "Carbon nanotube transistors for biosensing applications," *Analytical and Bioanalytical Chemistry*, vol. 384, no. 2, pp. 322–335, 2006.

[9] M. O'Connor, N. K. Sang, A. J. Killard et al., "Mediated amperometric immunosensing using single walled carbon nanotube forests," *Analyst*, vol. 129, no. 12, pp. 1176–1180, 2004.

[10] M. Pumera, "The electrochemistry of carbon nanotubes: fundamentals and applications," *Chemistry*, vol. 15, no. 20, pp. 4970–4978, 2009.

[11] V. Vamvakaki, M. Fouskaki, and N. Chaniotakis, "Electrochemical biosensing systems based on carbon nanotubes and carbon nanofibers," *Analytical Letters*, vol. 40, no. 12, pp. 2271–2287, 2007.

[12] A. Merkoçi, "Carbon nanotubes in analytical sciences," *Microchimica Acta*, vol. 152, no. 3-4, pp. 157–174, 2006.

[13] B. S. Harrison and A. Atala, "Carbon nanotube applications for tissue engineering," *Biomaterials*, vol. 28, no. 2, pp. 344–353, 2007.

[14] L. Zhang and T. J. Webster, "Nanotechnology and nanomaterials: promises for improved tissue regeneration," *Nano Today*, vol. 4, no. 1, pp. 66–80, 2009.

[15] T. Dvir, B. P. Timko, D. S. Kohane, and R. Langer, "Nanotechnological strategies for engineering complex tissues," *Nature Nanotechnology*, vol. 6, no. 1, pp. 13–22, 2011.

[16] O. C. Farokhzad and R. Langer, "Impact of nanotechnology on drug delivery," *ACS Nano*, vol. 3, no. 1, pp. 16–20, 2009.

[17] A. Bianco, K. Kostarelos, and M. Prato, "Applications of carbon nanotubes in drug delivery," *Current Opinion in Chemical Biology*, vol. 9, no. 6, pp. 674–679, 2005.

[18] Y. Lin, F. Lu, Y. Tu, and Z. Ren, "Glucose biosensors based on carbon nanotube nanoelectrode ensembles," *Nano Letters*, vol. 4, no. 2, pp. 191–195, 2004.

[19] L. Lacerda, A. Bianco, M. Prato, and K. Kostarelos, "Carbon nanotubes as nanomedicines: from toxicology to pharmacology," *Advanced Drug Delivery Reviews*, vol. 58, no. 14, pp. 1460–1470, 2006.

[20] S. Kumar and K. Ostrikov, "Unidirectional arrays of vertically standing graphenes in reactive plasmas," *Nanoscale*, vol. 3, no. 10, pp. 4296–4300, 2011.

[21] M. Bottini, N. Rosato, and N. Bottini, "PEG-modified carbon nanotubes in biomedicine: current status and challenges ahead," *Biomacromolecules*, vol. 12, no. 10, pp. 3381–3393, 2011.

[22] D. W. H. Fam, A. Palaniappan, A. I. Y. Tok, B. Liedberg, and S. M. Moochhala, "A review on technological aspects influencing commercialization of carbon nanotube sensors," *Sensors and Actuators B*, vol. 157, no. 1, pp. 1–7, 2011.

[23] C. W. Lam, J. T. James, R. McCluskey, S. Arepalli, and R. L. Hunter, "A review of carbon nanotube toxicity and assessment of potential occupational and environmental health risks," *Critical Reviews in Toxicology*, vol. 36, no. 3, pp. 189–217, 2006.

[24] A. E. Porter, M. Gass, K. Muller, J. N. Skepper, P. A. Midgley, and M. Welland, "Direct imaging of single-walled carbon nanotubes in cells," *Nature Nanotechnology*, vol. 2, no. 11, pp. 713–717, 2007.

[25] C. P. Firme and P. R. Bandaru, "Toxicity issues in the application of carbon nanotubes to biological systems," *Nanomedicine: Nanotechnology, Biology, and Medicine*, vol. 6, no. 2, pp. 245–256, 2010.

[26] X. Peng and S. S. Wong, "Functional covalent chemistry of carbon nanotube surfaces," *Advanced Materials*, vol. 21, no. 6, pp. 625–642, 2009.

[27] M. Shim, N. W. S. Kam, R. J. Chen, Y. Li, and H. Dai, "Functionalization of carbon nanotubes for biocompatibility and biomolecular recognition," *Nano Letters*, vol. 2, no. 4, pp. 285–288, 2002.

[28] C. Y. Hu, Y. J. Xu, S. W. Duo, R. F. Zhang, and M. S. Li, "Non-covalent functionalization of carbon nanotubes with surfactants and polymers," *Journal of the Chinese Chemical Society*, vol. 56, no. 2, pp. 234–239, 2009.

[29] J. N. Coleman, U. Khan, W. J. Blau, and Y. K. Gun'ko, "Small but strong: a review of the mechanical properties of carbon nanotube-polymer composites," *Carbon*, vol. 44, no. 9, pp. 1624–1652, 2006.

[30] N. Karousis, N. Tagmatarchis, and D. Tasis, "Current progress on the chemical modification of carbon nanotubes," *Chemical Reviews*, vol. 110, no. 9, pp. 5366–5397, 2010.

[31] W. Huang, S. Taylor, K. Fu et al., "Attaching proteins to carbon nanotubes via diimide-activated amidation," *Nano Letters*, vol. 2, no. 4, pp. 311–314, 2002.

[32] S. S. Karajanagi, A. A. Vertegel, R. S. Kane, and J. S. Dordick, "Structure and function of enzymes adsorbed onto single-walled carbon nanotubes," *Langmuir*, vol. 20, no. 26, pp. 11594–11599, 2004.

[33] X. Zhang, L. Meng, and Q. Lu, "Cell behaviors on polysaccharide-wrapped single-wall carbon nanotubes: a quantitative study of the surface properties of biomimetic nanofibrous scaffolds," *ACS Nano*, vol. 3, no. 10, pp. 3200–3206, 2009.

[34] K. Jiang, L. S. Schadler, R. W. Siegel, X. Zhang, H. Zhang, and M. Terrones, "Protein immobilization on carbon nanotubes via a two-step process of diimide-activated amidation," *Journal of Materials Chemistry*, vol. 14, no. 1, pp. 37–39, 2004.

[35] J. W. Ko, J. M. Woo, A. Jinhong et al., "Multi-order dynamic range DNA sensor using a gold decorated SWCNT random network," *ACS Nano*, vol. 5, no. 6, pp. 4365–4372, 2011.

[36] Y. Weizmann, D. M. Chenoweth, and T. M. Swager, "Addressable terminally linked DNA-CNT nanowires," *Journal of the American Chemical Society*, vol. 132, no. 40, pp. 14009–14011, 2010.

[37] K. A. Williams, P. T. M. Veenhuizen, B. G. De la Torre, R. Eritja, and C. Dekker, "Nanotechnology: carbon nanotubes with DNA recognition," *Nature*, vol. 420, no. 6917, p. 761, 2002.

[38] W. Huang, S. Taylor, K. Fu et al., "Attaching proteins to carbon nanotubes via diimide-activated amidation," *Nano Letters*, vol. 2, no. 4, pp. 311–314, 2002.

[39] W. Yang, P. Thordarson, J. J. Gooding, S. P. Ringer, and F. Braet, "Carbon nanotubes for biological and biomedical applications," *Nanotechnology*, vol. 18, no. 41, Article ID 412001, 2007.

[40] S. Kumar, I. Levchenko, K. Ostrikov, and J. A. McLaughlin, "Plasma-enabled, catalyst-free growth of carbon nanotubes on mechanically-written Si features with arbitrary shape," *Carbon*, vol. 50, no. 1, pp. 325–329, 2012.

[41] X. Guo, L. Huang, S. O'Brien, P. Kim, and C. Nuckolls, "Directing and sensing changes in molecular conformation on individual carbon nanotube field effect transistors," *Journal of the American Chemical Society*, vol. 127, no. 43, pp. 15045–15047, 2005.

[42] Z. Kuang, S. N. Kim, W. J. Crookes-Goodson, B. L. Farmer, and R. R. Naik, "Biomimetic chemosensor: designing peptide recognition elements for surface functionalization of carbon nanotube field effect transistors," *ACS Nano*, vol. 4, no. 1, pp. 452–458, 2010.

[43] X. Yu, D. Chattopadhyay, I. Galeska, F. Papadimitrakopoulos, and J. F. Rusling, "Peroxidase activity of enzymes bound to the ends of single-wall carbon nanotube forest electrodes," *Electrochemistry Communications*, vol. 5, no. 5, pp. 408–411, 2003.

[44] Z. Zhu, W. Song, K. Burugapalli, F. Moussy, Y. L. Li, and X. H. Zhong, "Nano-yarn carbon nanotube fiber based enzymatic glucose biosensor," *Nanotechnology*, vol. 21, no. 16, Article ID 165501, 2010.

[45] S. G. Mhaisalkar, J. N. Tey, S. Gandhi et al., "Direct detection of heroin metabolites using a competitive immunoassay based on a carbon-nanotube liquid-gated field-effect transistor," *Small*, vol. 6, no. 9, pp. 993–998, 2010.

[46] D. W. H. Fam and A. I. Y. Tok, "Mono-distributed single-walled carbon nanotube channel in field effect transistors (FETs) using electrostatic atomization deposition," *Journal of Colloid and Interface Science*, vol. 338, no. 1, pp. 266–269, 2009.

[47] R. Martel, T. Schmidt, H. R. Shea, T. Hertel, and P. Avouris, "Single- and multi-wall carbon nanotube field-effect transistors," *Applied Physics Letters*, vol. 73, no. 17, pp. 2447–2449, 1998.

[48] S. Roy and Z. Gao, "Nanostructure-based electrical biosensors," *Nano Today*, vol. 4, no. 4, pp. 318–334, 2009.

[49] R. J. Chen, S. Bangsaruntip, K. A. Drouvalakis et al., "Non-covalent functionalization of carbon nanotubes for highly specific electronic biosensors," *Proceedings of the National Academy of Sciences of the United States of America*, vol. 100, no. 9, pp. 4984–4989, 2003.

[50] D. Fu, H. Okimoto, C. W. Lee et al., "Ultrasensitive detection of DNA molecules with high on/off single-walled carbon nanotube network," *Advanced Materials*, vol. 22, no. 43, pp. 4867–4871, 2010.

[51] A. Merkoçi, M. Pumera, X. Llopis, B. Pérez, M. Del Valle, and S. Alegret, "New materials for electrochemical sensing VI: carbon nanotubes," *TrAC—Trends in Analytical Chemistry*, vol. 24, no. 9, pp. 826–838, 2005.

[52] M. A. Correa-Duarte, N. Wagner, J. Rojas-Chapana, C. Morsczeck, M. Thie, and M. Giersig, "Fabrication and biocompatibility of carbon nanotube-based 3D networks as scaffolds for cell seeding and growth," *Nano Letters*, vol. 4, no. 11, pp. 2233–2236, 2004.

[53] B. Kang, D. Yu, Y. Dai, S. Chang, D. Chen, and Y. Ding, "Cancer-cell targeting and photoacoustic therapy using carbon nanotubes as "bomb" agents," *Small*, vol. 5, no. 11, pp. 1292–1301, 2009.

[54] T. A. Hilder and J. M. Hill, "Encapsulation of the anticancer drug cisplatin into nanotubes," in *International Conference on Nanoscience and Nanotechnology (ICONN '08)*, pp. 109–112, February 2008.

[55] N. Komatsu and F. Wang, "A comprehensive review on separation methods and techniques for single-walled carbon nanotubes," *Materials*, vol. 3, no. 7, pp. 3818–3844, 2010.

[56] R. Krupke, F. Hennrich, H. V. Löhneysen, and M. M. Kappes, "Separation of metallic from semiconducting single-walled carbon nanotubes," *Science*, vol. 301, no. 5631, pp. 344–347, 2003.

[57] P. Łukaszczuk, E. Borowiak-Paleń, M. H. Rümmeli, and R. J. Kaleńczuk, "Gel-based separation of single-walled carbon nanotubes for metallic and semiconducting fractions," *Materials Research Bulletin*, vol. 46, no. 10, pp. 1535–1539, 2011.

[58] K. Maehashi, T. Katsura, K. Kerman, Y. Takamura, K. Matsumoto, and E. Tamiya, "Label-free protein biosensor based on aptamer-modified carbon nanotube field-effect transistors," *Analytical Chemistry*, vol. 79, no. 2, pp. 782–787, 2007.

[59] K. Bradley, M. Briman, A. Star, and G. Gruner, "Charge transfer from adsorbed proteins," *Nano Letters*, vol. 4, no. 2, pp. 253–256, 2004.

[60] L. N. Cella, W. Chen, N. V. Myung, and A. Mulchandani, "Single-walled carbon nanotube-based chemiresistive affinity biosensors for small molecules: ultrasensitive glucose detection," *Journal of the American Chemical Society*, vol. 132, no. 14, pp. 5024–5026, 2010.

[61] R. J. Chen, H. C. Choi, S. Bangsaruntip et al., "An investigation of the mechanisms of electronic sensing of protein adsorption on carbon nanotube devices," *Journal of the American Chemical Society*, vol. 126, no. 5, pp. 1563–1568, 2004.

[62] I. Heller, W. T. T. Small, S. G. Lemay, and C. Dekker, "Probing macrophage activity with carbon-nanotube sensors," *Small*, vol. 5, no. 22, pp. 2528–2532, 2009.

[63] Rajesh, B. K. Das, S. Srinives, and A. Mulchandani, "ZnS nanocrystals decorated single-walled carbon nanotube based chemiresistive label-free DNA sensor," *Applied Physics Letters*, vol. 98, no. 1, Article ID 013701, 2011.

[64] I. Heller, A. M. Janssens, J. Männik, E. D. Minot, S. G. Lemay, and C. Dekker, "Identifying the mechanism of biosensing with carbon nanotube transistors," *Nano Letters*, vol. 8, no. 2, pp. 591–595, 2008.

[65] F. N. Ishikawa, B. Stauffer, D. A. Caron, and C. Zhou, "Rapid and label-free cell detection by metal-cluster-decorated carbon nanotube biosensors," *Biosensors and Bioelectronics*, vol. 24, no. 10, pp. 2967–2972, 2009.

[66] T. H. Kim, S. H. Lee, J. Lee et al., "Single-carbon-atomic-resolution detection of odorant molecules using a human olfactory receptor-based bioelectronic nose," *Advanced Materials*, vol. 21, no. 1, pp. 91–94, 2009.

[67] G. Peng, E. Track, and H. Haick, "Detecting simulated patterns of lung cancer biomarkers by random network of single-walled carbon nanotubes coated with nonpolymeric organic materials," *Nano Letters*, vol. 8, no. 11, pp. 3631–3635, 2008.

[68] H. Wang, R. Yang, L. Yang, and W. Tan, "Nucleic acid conjugated nanomaterials for enhanced molecular recognition," *ACS Nano*, vol. 3, no. 9, pp. 2451–2460, 2009.

[69] J. J. Gooding, R. Wibowo, J. Liu et al., "Protein electrochemistry using aligned carbon nanotube arrays," *Journal of the American Chemical Society*, vol. 125, no. 30, pp. 9006–9007, 2003.

[70] H. Jin, D. A. Heller, M. Kalbacova et al., "Detection of single-molecule H_2O_2 signalling from epidermal growth factor receptor using fluorescent single-walled carbon nanotubes," *Nature Nanotechnology*, vol. 5, no. 4, pp. 302–309, 2010.

[71] X. B. Yan, X. J. Chen, B. K. Tay, and K. A. Khor, "Transparent and flexible glucose biosensor via layer-by-layer assembly of multi-wall carbon nanotubes and glucose oxidase," *Electrochemistry Communications*, vol. 9, no. 6, pp. 1269–1275, 2007.

[72] R. Cui, H. Huang, Z. Yin, D. Gao, and J. J. Zhu, "Horseradish peroxidase-functionalized gold nanoparticle label for amplified immunoanalysis based on gold nanoparticles/carbon nanotubes hybrids modified biosensor," *Biosensors and Bioelectronics*, vol. 23, no. 11, pp. 1666–1673, 2008.

[73] T. Dastagir, E. S. Forzani, R. Zhang et al., "Electrical detection of hepatitis C virus RNA on single wall carbon nanotube-field effect transistors," *Analyst*, vol. 132, no. 8, pp. 738–740, 2007.

[74] X. Tang, S. Bansaruntip, N. Nakayama, E. Yenilmez, Y. I. Chang, and Q. Wang, "Carbon nanotube DNA sensor and sensing mechanism," *Nano Letters*, vol. 6, no. 8, pp. 1632–1636, 2006.

[75] H. M. So, D. W. Park, E. K. Jeon et al., "Detection and titer estimation of Escherichia coli using aptamer-functionalized single-walled carbon-nanotube field-effect transistors," *Small*, vol. 4, no. 2, pp. 197–201, 2008.

[76] E. Nossol and A. J. G. Zarbin, "A simple and innovative route to prepare a novel carbon nanotube/prussian blue electrode and its utilization as a highly sensitive H_2O_2 amperometric sensor," *Advanced Functional Materials*, vol. 19, no. 24, pp. 3980–3986, 2009.

[77] F. N. Ishikawa, M. Curreli, C. A. Olson et al., "Importance of controlling nanotube density for highly sensitive and reliable biosensors functional in physiological conditions," *ACS Nano*, vol. 4, no. 11, pp. 6914–6922, 2010.

[78] J. Wang, "Electrochemical glucose biosensors," *Chemical Reviews*, vol. 108, no. 2, pp. 814–825, 2008.

[79] X. Xu, S. Jiang, Z. Hu, and S. Liu, "Nitrogen-doped carbon nanotubes: high electrocatalytic activity toward the oxidation of hydrogen peroxide and its application for biosensing," *ACS Nano*, vol. 4, no. 7, pp. 4292–4298, 2010.

[80] C. Fernández-Sánchez, E. Pellicer, J. Orozco, C. Jiménez-Jorquera, L. M. Lechuga, and E. Mendoza, "Plasma-activated multi-walled carbon nanotube-polystyrene composite substrates for biosensing," *Nanotechnology*, vol. 20, no. 33, Article ID 335501, 2009.

[81] Z. Wu, Y. Xu, X. Zhang, G. Shen, and R. Yu, "Microwave plasma treated carbon nanotubes and their electrochemical biosensing application," *Talanta*, vol. 72, no. 4, pp. 1336–1341, 2007.

[82] K. Jiang, A. Eitan, L. S. Schadler et al., "Selective attachment of gold nanoparticles to nitrogen-doped carbon nanotubes," *Nano Letters*, vol. 3, no. 3, pp. 275–277, 2003.

[83] S. Srivastava and J. LaBaer, "Nanotubes light up protein arrays," *Nature Biotechnology*, vol. 26, no. 11, pp. 1244–1246, 2008.

[84] A. Star, J. C. P. Gabriel, K. Bradley, and G. Grüner, "Electronic detection of specific protein binding using nanotube FET devices," *Nano Letters*, vol. 3, no. 4, pp. 459–463, 2003.

[85] P. Ghosh, G. Han, M. De, C. K. Kim, and V. M. Rotello, "Gold nanoparticles in delivery applications," *Advanced Drug Delivery Reviews*, vol. 60, no. 11, pp. 1307–1315, 2008.

[86] S. Zeng, K. T. Yong, I. Roy, X. Q. Dinh, X. Yu, and F. Luan, "A review on functionalized gold nanoparticles for biosensing applications," *Plasmonics*, vol. 6, no. 3, pp. 491–506, 2011.

[87] E. Boisselier and D. Astruc, "Gold nanoparticles in nanomedicine: preparations, imaging, diagnostics, therapies and toxicity," *Chemical Society Reviews*, vol. 38, no. 6, pp. 1759–1782, 2009.

[88] H. L. Hsu, L. J. Teng, Y. C. Chen et al., "Flexible UV-ozone-modified carbon nanotube electrodes for neuronal recording," *Advanced Materials*, vol. 22, no. 19, pp. 2177–2181, 2010.

[89] E. Hirata, M. Uo, H. Takita, T. Akasaka, F. Watari, and A. Yokoyama, "Multiwalled carbon nanotube-coating of 3D

collagen scaffolds for bone tissue engineering," *Carbon*, vol. 49, no. 10, pp. 3284–3291, 2011.

[90] J. V. Veetil and K. Ye, "Tailored carbon nanotubes for tissue engineering applications," *Biotechnology Progress*, vol. 25, no. 3, pp. 709–721, 2009.

[91] S. Y. Park, D. S. Choi, H. J. Jin et al., "Polarization-controlled differentiation of human neural stem cells using synergistic cues from the patterns of carbon nanotube monolayer coating," *ACS Nano*, vol. 5, no. 6, pp. 4704–4711, 2011.

[92] M. Endo, S. Koyama, Y. Matsuda, T. Hayashi, and Y. A. Kim, "Thrombogenicity and blood coagulation of a microcatheter prepared from carbon nanotube-Nylon-based composite," *Nano Letters*, vol. 5, no. 1, pp. 101–105, 2005.

[93] H. Fan, P. Chen, R. Qi et al., "Greatly improved blood compatibility by microscopic multiscale design of surface architectures," *Small*, vol. 5, no. 19, pp. 2144–2148, 2009.

[94] W. Tutak, M. Chhowalla, and F. Sesti, "The chemical and physical characteristics of single-walled carbon nanotube film impact on osteoblastic cell response," *Nanotechnology*, vol. 21, no. 31, Article ID 315102, 2010.

[95] N. A. Kotov, B. S. Shim, and J. Zhu, "Carbon nanotubes composites made by the layer-by-layer assembly: from ultrastrong materials to solar cells and devices for neural interface," *Abstracts of Papers of the American Chemical Society*, vol. 237, 2009.

[96] H. J. Lee, J. Park, O. J. Yoon et al., "Amine-modified single-walled carbon nanotubes protect neurons from injury in a rat stroke model," *Nature Nanotechnology*, vol. 6, no. 2, pp. 121–125, 2011.

[97] M. P. Mattson, R. C. Haddon, and A. M. Rao, "Molecular functionalization of carbon nanotubes and use as substrates for neuronal growth," *Journal of Molecular Neuroscience*, vol. 14, no. 3, pp. 175–182, 2000.

[98] S. Namgung, T. Kim, K. Y. Baik, M. Lee, J. M. Nam, and S. Hong, "Fibronectin-carbon-nanotube hybrid nanostructures for controlled cell growth," *Small*, vol. 7, no. 1, pp. 56–61, 2011.

[99] D. Liu, C. Yi, D. Zhang, J. Zhang, and M. Yang, "Inhibition of proliferation and differentiation of mesenchymal stem cells by carboxylated carbon nanotubes," *ACS Nano*, vol. 4, no. 4, pp. 2185–2195, 2010.

[100] H. Hu, Y. Ni, V. Montana, R. C. Haddon, and V. Parpura, "Chemically functionalized carbon nanotubes as substrates for neuronal growth," *Nano Letters*, vol. 4, no. 3, pp. 507–511, 2004.

[101] X. Shi, J. L. Hudson, P. P. Spicer, J. M. Tour, R. Krishnamoorti, and A. G. Mikos, "Injectable nanocomposites of single-walled carbon nanotubes and biodegradable polymers for bone tissue engineering," *Biomacromolecules*, vol. 7, no. 7, pp. 2237–2242, 2006.

[102] T. R. Nayak, L. Jian, L. C. Phua, H. K. Ho, Y. Ren, and G. Pastorin, "Thin films of functionalized multiwalled carbon nanotubes as suitable scaffold materials for stem cells proliferation and bone formation," *ACS Nano*, vol. 4, no. 12, pp. 7717–7725, 2010.

[103] A. Eitan, K. Jiang, D. Dukes, R. Andrews, and L. S. Schadler, "Surface modification of multiwalled carbon nanotubes: toward the tailoring of the interface in polymer composites," *Chemistry of Materials*, vol. 15, no. 16, pp. 3198–3201, 2003.

[104] M. Vila, J. L. Hueso, M. Manzano et al., "Carbon nanotubes—mesoporous silica composites as controllable biomaterials," *Journal of Materials Chemistry*, vol. 19, no. 41, pp. 7745–7752, 2009.

[105] B. Sitharaman, X. Shi, X. F. Walboomers et al., "In vivo biocompatibility of ultra-short single-walled carbon nanotube/biodegradable polymer nanocomposites for bone tissue engineering," *Bone*, vol. 43, no. 2, pp. 362–370, 2008.

[106] S. Giannona, I. Firkowska, J. Rojas-Chapana, and M. Giersig, "Vertically aligned carbon nanotubes as cytocompatible material for enhanced adhesion and proliferation of osteoblast-like cells," *Journal of Nanoscience and Nanotechnology*, vol. 7, no. 4-5, pp. 1679–1683, 2007.

[107] Z. J. Han, K. Ostrikov, C. M. Tan, B. K. Tay, and S. A. F. Peel, "Effect of hydrophilicity of carbon nanotube arrays on the release rate and activity of recombinant human bone morphogenetic protein-2," *Nanotechnology*, vol. 22, no. 29, Article ID 295712, 2011.

[108] M. A. Shokrgozar, F. Mottaghitalab, V. Mottaghitalab, and M. Farokhi, "Fabrication of porous chitosan/poly(vinyl alcohol) reinforced single-walled carbon nanotube nanocomposites for neural tissue engineering.," *Journal of biomedical nanotechnology*, vol. 7, no. 2, pp. 276–284, 2011.

[109] H. J. Lee, O. J. Yoon, D. H. Kim et al., "Neurite outgrowth on nanocomposite scaffolds synthesized from PLGA and carboxylated carbon nanotubes," *Advanced Engineering Materials*, vol. 11, no. 12, pp. B261–B266, 2009.

[110] V. N. Mochalin, O. Shenderova, D. Ho, and Y. Gogotsi, "The properties and applications of nanodiamonds," *Nature Nanotechnology*, vol. 7, no. 1, pp. 11–23, 2012.

[111] A. M. Schrand, H. Huang, C. Carlson et al., "Are diamond nanoparticles cytotoxic?" *Journal of Physical Chemistry B*, vol. 111, no. 1, pp. 2–7, 2007.

[112] V. N. Khabashesku, J. L. Margrave, and E. V. Barrera, "Functionalized carbon nanotubes and nanodiamonds for engineering and biomedical applications," *Diamond and Related Materials*, vol. 14, no. 3–7, pp. 859–866, 2005.

[113] W. Wu, R. Li, X. Bian et al., "Covalently combining carbon nanotubes with anticancer agent: preparation and antitumor activity," *ACS Nano*, vol. 3, no. 9, pp. 2740–2750, 2009.

[114] J. Chen, S. Chen, X. Zhao, L. V. Kuznetsova, S. S. Wong, and I. Ojima, "Functionalized single-walled carbon nanotubes as rationally designed vehicles for tumor-targeted drug delivery," *Journal of the American Chemical Society*, vol. 130, no. 49, pp. 16778–16785, 2008.

[115] J. Rojas-Chapana, J. Troszczynska, I. Firkowska, C. Morsczeck, and M. Giersig, "Multi-walled carbon nanotubes for plasmid delivery into Escherichia coli cells," *Lab on a Chip*, vol. 5, no. 5, pp. 536–539, 2005.

[116] C. R. Martin and P. Kohli, "The emerging field of nanotube biotechnology," *Nature Reviews Drug Discovery*, vol. 2, no. 1, pp. 29–37, 2003.

[117] M. S. Ladeira, V. A. Andrade, E. R. M. Gomes et al., "Highly efficient siRNA delivery system into human and murine cells using single-wall carbon nanotubes," *Nanotechnology*, vol. 21, no. 38, Article ID 385101, 2010.

[118] S. J. Son, X. Bai, and S. B. Lee, "Inorganic hollow nanoparticles and nanotubes in nanomedicine. Part 1. Drug/gene delivery applications," *Drug Discovery Today*, vol. 12, no. 15-16, pp. 650–656, 2007.

[119] R. Prakash, S. Washburn, R. Superfine, R. E. Cheney, and M. R. Falvo, "Visualization of individual carbon nanotubes with fluorescence microscopy using conventional fluorophores," *Applied Physics Letters*, vol. 83, no. 6, pp. 1219–1221, 2003.

[120] M. Ritschel, A. Leonhardt, D. Elefant, S. Oswald, and B. Büchner, "Rhenium-catalyzed growth carbon nanotubes," *Journal of Physical Chemistry C*, vol. 111, no. 24, pp. 8414–8417, 2007.

[121] R. Klingeler, S. Hampel, and B. Büchner, "Carbon nanotube based biomedical agents for heating, temperature sensoring and drug delivery," *International Journal of Hyperthermia*, vol. 24, no. 6, pp. 496–505, 2008.

[122] T. A. Hilder and J. M. Hill, "Modeling the loading and unloading of drugs into nanotubes," *Small*, vol. 5, no. 3, pp. 300–308, 2009.

[123] Q. Mu, D. L. Broughton, and B. Yan, "Endosomal leakage and nuclear translocation of multiwalled carbon nanotubes: developing a model for cell uptake," *Nano Letters*, vol. 9, no. 12, pp. 4370–4375, 2009.

[124] A. Nunes, N. Amsharov, C. Guo et al., "Hybrid polymer-grafted multiwalled carbon nanotubes for in vitro gene delivery," *Small*, vol. 6, no. 20, pp. 2281–2291, 2010.

[125] H. K. Moon, S. H. Lee, and H. C. Choi, "In vivo near-infrared mediated tumor destruction by photothermal effect of carbon nanotubes," *ACS Nano*, vol. 3, no. 11, pp. 3707–3713, 2009.

[126] A. Joshi, S. Punyani, S. S. Bale, H. Yang, T. Borca-Tasciuc, and R. S. Kane, "Nanotube-assisted protein deactivation," *Nature Nanotechnology*, vol. 3, no. 1, pp. 41–45, 2008.

[127] S. Ghosh, S. Dutta, E. Gomes et al., "Increased heating efficiency and selective thermal ablation of malignant tissue with DNA-encased multiwalled carbon nanotubes," *ACS Nano*, vol. 3, no. 9, pp. 2667–2673, 2009.

[128] B. Kang, Y. Dai, S. Chang, and D. Chen, "Explosion of single-walled carbon nanotubes in suspension induced by a large photoacoustic effect," *Carbon*, vol. 46, no. 6, pp. 978–981, 2008.

[129] Y. Lee and K. E. Geckeler, "Carbon nanotubes in the biological interphase: the relevance of noncovalence," *Advanced Materials*, vol. 22, no. 36, pp. 4076–4083, 2010.

[130] P. Ghafari, C. H. St-Denis, M. E. Power et al., "Impact of carbon nanotubes on the ingestion and digestion of bacteria by ciliated protozoa," *Nature Nanotechnology*, vol. 3, no. 6, pp. 347–351, 2008.

[131] Z. J. Han, I. Levchenko, S. Kumar et al., "Plasma nanofabrication and nanomaterials safety," *Journal of Physics D*, vol. 44, no. 17, Article ID 174019, 2011.

[132] A. Huczko, "Synthesis of aligned carbon nanotubes," *Applied Physics A*, vol. 74, no. 5, pp. 617–638, 2002.

[133] D. Elgrabli, M. Floriani, S. Abella-Gallart et al., "Biodistribution and clearance of instilled carbon nanotubes in rat lung," *Particle and Fibre Toxicology*, vol. 5, article no. 20, 2008.

[134] Y. Usui, K. Aoki, N. Narita et al., "Carbon nanotubes with high bone-tissue compatibility and bone-formation acceleration effects," *Small*, vol. 4, no. 2, pp. 240–246, 2008.

[135] J. P. Ryman-Rasmussen, M. F. Cesta, A. R. Brody et al., "Inhaled carbon nanotubes reach the subpleural tissue in mice," *Nature Nanotechnology*, vol. 4, no. 11, pp. 747–751, 2009.

[136] S. Iijima, "Helical microtubules of graphitic carbon," *Nature*, vol. 354, no. 6348, pp. 56–58, 1991.

[137] Innovative Research and Products Incorporated, "Production and applications of carbon nanotubes, carbon nanofibres, fullerenes, graphene and nanodiamonds: a global technology survey and market analysis," 2011, http://www.innoresearch.net/report_summary.aspx?id=77&pg531&rcd=et-113&pd=2/1/2011.

[138] C. Buzea, I. I. Pacheco, and K. Robbie, "Nanomaterials and nanoparticles: sources and toxicity," *Biointerphases*, vol. 2, no. 4, pp. MR17–MR71, 2007.

[139] X. Deng, G. Jia, H. Wang et al., "Translocation and fate of multi-walled carbon nanotubes in vivo," *Carbon*, vol. 45, no. 7, pp. 1419–1424, 2007.

[140] M. L. Schipper, N. Nakayama-Ratchford, C. R. Davis et al., "A pilot toxicology study of single-walled carbon nanotubes in a small sample of mice," *Nature Nanotechnology*, vol. 3, no. 4, pp. 216–221, 2008.

[141] G. M. Mutlu, G. R. S. Budinger, A. A. Green et al., "Biocompatible nanoscale dispersion of single-walled carbon nanotubes minimizes in vivo pulmonary toxicity," *Nano Letters*, vol. 10, no. 5, pp. 1664–1670, 2010.

[142] C. A. Poland, R. Duffin, I. Kinloch et al., "Carbon nanotubes introduced into the abdominal cavity of mice show asbestos-like pathogenicity in a pilot study," *Nature Nanotechnology*, vol. 3, no. 7, pp. 423–428, 2008.

[143] F. Zhao, Y. Zhao, Y. Liu, X. Chang, C. Chen, and Y. Zhao, "Cellular uptake, intracellular trafficking, and cytotoxicity of nanomaterials," *Small*, vol. 7, no. 10, pp. 1322–1337, 2011.

[144] F. Zhou, D. Xing, B. Wu, S. Wu, Z. Ou, and W. R. Chen, "New insights of transmembranal mechanism and subcellular localization of noncovalently modified single-walled carbon nanotubes," *Nano Letters*, vol. 10, no. 5, pp. 1677–1681, 2010.

[145] D. Pantarotto, J. P. Briand, M. Prato, and A. Bianco, "Translocation of bioactive peptides across cell membranes by carbon nanotubes," *Chemical Communications*, vol. 10, no. 1, pp. 16–17, 2004.

[146] S. Liu, L. Wei, L. Hao et al., "Sharper and faster "Nano darts" kill more bacteria: a study of antibacterial activity of individually dispersed pristine single-walled carbon nanotube," *ACS Nano*, vol. 3, no. 12, pp. 3891–3902, 2009.

[147] S. Pogodin and V. A. Baulin, "Can a carbon nanotube pierce through a phospholipid bilayer?" *ACS Nano*, vol. 4, no. 9, pp. 5293–5300, 2010.

[148] M. Wang, S. Yu, C. Wang, and J. Kong, "Tracking the endocytic pathway of recombinant protein toxin delivered by multiwalled carbon nanotubes," *ACS Nano*, vol. 4, no. 11, pp. 6483–6490, 2010.

[149] X. Shi, A. Von Dem Bussche, R. H. Hurt, A. B. Kane, and H. Gao, "Cell entry of one-dimensional nanomaterials occurs by tip recognition and rotation," *Nature Nanotechnology*, vol. 6, no. 11, pp. 714–719, 2011.

[150] A. Antonelli, S. Serafini, M. Menotta et al., "Improved cellular uptake of functionalized single-walled carbon nanotubes," *Nanotechnology*, vol. 21, no. 42, Article ID 425101, 2010.

[151] Q. Mu, D. L. Broughton, and B. Yan, "Endosomal leakage and nuclear translocation of multiwalled carbon nanotubes: developing a model for cell uptake," *Nano Letters*, vol. 9, no. 12, pp. 4370–4375, 2009.

[152] F. Zhou, D. Xing, B. Wu, S. Wu, Z. Ou, and W. R. Chen, "New insights of transmembranal mechanism and subcellular localization of noncovalently modified single-walled carbon nanotubes," *Nano Letters*, vol. 10, no. 5, pp. 1677–1681, 2010.

[153] K. Kostarelos, L. Lacerda, G. Pastorin et al., "Cellular uptake of functionalized carbon nanotubes is independent of functional group and cell type," *Nature Nanotechnology*, vol. 2, no. 2, pp. 108–113, 2007.

[154] M. F. Serag, N. Kaji, E. Venturelli et al., "Functional platform for controlled subcellular distribution of carbon nanotubes," *ACS Nano*, vol. 5, no. 11, pp. 9264–9270, 2011.

[155] Y. Yao, L. K. L. Falk, R. E. Morjan, O. A. Nerushev, and E. E. B. Campbell, "Cross-sectional TEM investigation of nickel-catalysed carbon nanotube films grown by plasma-enhanced CVD," *Journal of Microscopy*, vol. 219, no. 2, pp. 69–75, 2005.

[156] L. Wang, S. Luanpitpong, V. Castranova et al., "Carbon nanotubes induce malignant transformation and tumorigenesis of human lung epithelial cells," *Nano Letters*, vol. 11, no. 7, pp. 2796–2803, 2011.

[157] M. J. Osmond-McLeod, C. A. Poland, F. Murphy et al., "Durability and inflammogenic impact of carbon nanotubes compared with asbestos fibres," *Particle and Fibre Toxicology*, vol. 8, article no. 15, 2011.

[158] Y. Zhang, S. F. Ali, E. Dervishi et al., "Cytotoxicity effects of graphene and single-wall carbon nanotubes in neural phaeochromocytoma-derived pc12 cells," *ACS Nano*, vol. 4, no. 6, pp. 3181–3186, 2010.

[159] J. Palomäki, E. Välimäki, J. Sund et al., "Long, needle-like carbon nanotubes and asbestos activate the NLRP3 inflammasome through a similar mechanism," *ACS Nano*, vol. 5, no. 9, pp. 6861–6870, 2011.

[160] N. M. Schaeublin, L. K. Braydich-Stolle, A. M. Schrand et al., "Surface charge of gold nanoparticles mediates mechanism of toxicity," *Nanoscale*, vol. 3, no. 2, pp. 410–420, 2011.

[161] J. Muller, I. Decordier, P. H. Hoet et al., "Clastogenic and aneugenic effects of multi-wall carbon nanotubes in epithelial cells," *Carcinogenesis*, vol. 29, no. 2, pp. 427–433, 2008.

[162] K. Kostarelos, A. Bianco, and M. Prato, "Promises, facts and challenges for carbon nanotubes in imaging and therapeutics," *Nature Nanotechnology*, vol. 4, no. 10, pp. 627–633, 2009.

[163] X. Wang, T. Xia, S. Addo Ntim et al., "Dispersal state of multiwalled carbon nanotubes elicits profibrogenic cellular responses that correlate with fibrogenesis biomarkers and fibrosis in the murine lung," *ACS Nano*, vol. 5, no. 12, pp. 9772–9787, 2011.

[164] J. G. Li, W. X. Li, J. Y. Xu et al., "Comparative study of pathological lesions induced by multiwalled carbon nanotubes in lungs of mice by intratracheal instillation and inhalation," *Environmental Toxicology*, vol. 22, no. 4, pp. 415–421, 2007.

[165] Y. W. Chun, W. Wang, J. Choi et al., "Control of macrophage responses on hydrophobic and hydrophilic carbon nanostructures," *Carbon*, vol. 49, no. 6, pp. 2092–2103, 2011.

[166] G. Cellot, L. Ballerini, M. Prato, and A. Bianco, "Neurons are able to internalize soluble carbon nanotubes: new opportunities or old risks?" *Small*, vol. 6, no. 23, pp. 2630–2633, 2010.

[167] R. Singh, D. Pantarotto, L. Lacerda et al., "Tissue biodistribution and blood clearance rates of intravenously administered carbon nanotube radiotracers," *Proceedings of the National Academy of Sciences of the United States of America*, vol. 103, no. 9, pp. 3357–3362, 2006.

[168] B. Belgorodsky, E. Drug, L. Fadeev, N. Hendler, E. Mentovich, and M. Gozin, "Mucin complexes of nanomaterials: first biochemical encounter," *Small*, vol. 6, no. 2, pp. 262–269, 2010.

[169] A. Pietroiusti, M. Massimiani, I. Fenoglio et al., "Low doses of pristine and oxidized single-wall carbon nanotubes affect mammalian embryonic development," *ACS Nano*, vol. 5, no. 6, pp. 4624–4633, 2011.

[170] B. D. Holt, P. A. Short, A. D. Rape, Y. L. Wang, M. F. Islam, and K. N. Dahl, "Carbon nanotubes reorganize actin structures in cells and ex Vivo," *ACS Nano*, vol. 4, no. 8, pp. 4872–4878, 2010.

[171] L. A. Mitchell, J. Gao, R. V. Wal, A. Gigliotti, S. W. Burchiel, and J. D. McDonald, "Pulmonary and systemic immune response to inhaled multiwalled carbon nanotubes," *Toxicological Sciences*, vol. 100, no. 1, pp. 203–214, 2007.

[172] L. A. Mitchell, F. T. Lauer, S. W. Burchiel, and J. D. McDonald, "Mechanisms for how inhaled multiwalled carbon nanotubes suppress systemic immune function in mice," *Nature Nanotechnology*, vol. 4, no. 7, pp. 451–456, 2009.

[173] Y. Bai, Y. Zhang, J. Zhang et al., "Repeated administrations of carbon nanotubes in male mice cause reversible testis damage without affecting fertility," *Nature Nanotechnology*, vol. 5, no. 9, pp. 683–689, 2010.

[174] C. Gaillard, G. Celiot, S. Li et al., "Carbon nanotubes carrying cell-adhesion peptides do not interfere with neuronal functionality," *Advanced Materials*, vol. 21, no. 28, pp. 2903–2908, 2009.

[175] E. B. Malarkey, R. C. Reyes, B. Zhao, R. C. Haddon, and V. Parpura, "Water soluble single-walled carbon nanotubes inhibit stimulated endocytosis in neurons," *Nano Letters*, vol. 8, no. 10, pp. 3538–3542, 2008.

[176] X. Shi, B. Sitharaman, Q. P. Pham et al., "In vitro cytotoxicity of single-walled carbon nanotube/biodegradable polymer nanocomposites," *Journal of Biomedical Materials Research A*, vol. 86, no. 3, pp. 813–823, 2008.

[177] B. L. Allen, P. D. Kichambare, P. Gou et al., "Biodegradation of single-walled carbon nanotubes through enzymatic catalysis," *Nano Letters*, vol. 8, no. 11, pp. 3899–3903, 2008.

[178] V. E. Kagan, N. V. Konduru, W. Feng et al., "Carbon nanotubes degraded by neutrophil myeloperoxidase induce less pulmonary inflammation," *Nature Nanotechnology*, vol. 5, no. 5, pp. 354–359, 2010.

[179] S. V. Morozov, K. S. Novoselov, and A. K. Geim, "Electron transport in graphene," *Physics-Uspekhi*, vol. 51, no. 7, pp. 727–748, 2008.

[180] B. Rosenstein, M. Lewkowicz, H. C. Kao, and Y. Korniyenko, "Ballistic transport in graphene beyond linear response," *Physical Review B*, vol. 81, no. 4, Article ID 041416, 2010.

[181] C. Liu, Z. Yu, D. Neff, A. Zhamu, and B. Z. Jang, "Graphene-based supercapacitor with an ultrahigh energy density," *Nano Letters*, vol. 10, no. 12, pp. 4863–4868, 2010.

[182] B. Chitara, L. S. Panchakarla, S. B. Krupanidhi, and C. N. R. Rao, "Infrared photodetectors based on reduced graphene oxide and graphene nanoribbons," *Advanced Materials*, vol. 23, no. 45, pp. 5419–5424, 2011.

[183] Q. Zeng, J. Cheng, L. Tang et al., "Self-assembled graphene-enzyme hierarchical nanostructures for electrochemical biosensing," *Advanced Functional Materials*, vol. 20, no. 19, pp. 3366–3372, 2010.

[184] S. K. Saha, M. Baskey, and D. Majumdar, "Graphene quantum sheets: a new material for spintronic applications," *Advanced Materials*, vol. 22, no. 48, pp. 5531–5536, 2010.

[185] J. R. Miller, R. A. Outlaw, and B. C. Holloway, "Graphene double-layer capacitor with ac line-filtering performance," *Science*, vol. 329, no. 5999, pp. 1637–1639, 2010.

[186] M. S. Lundstrom, "Graphene: the long and winding road," *Nature Materials*, vol. 10, no. 8, pp. 566–567, 2011.

[187] X. Ling, L. Xie, Y. Fang et al., "Can graphene be used as a substrate for Raman enhancement?" *Nano Letters*, vol. 10, no. 2, pp. 553–561, 2010.

[188] A. E. Rider, S. Kumar, S. A. Furman, and K. K. Ostrikov, "Self-organized Au nanoarrays on vertical graphenes: an advanced three-dimensional sensing platform," *Chemical Communications*, vol. 48, no. 21, pp. 2659–2661, 2012.

[189] L. Wu, H. S. Chu, W. S. Koh, and E. P. Li, "Highly sensitive graphene biosensors based on surface plasmon resonance.," *Optics express*, vol. 18, no. 14, pp. 14395–14400, 2010.

[190] X. Ling and J. Zhang, "Interference phenomenon in graphene-enhanced Raman scattering," *Journal of Physical Chemistry C*, vol. 115, no. 6, pp. 2835–2840, 2011.

[191] D. H. Seo, S. Kumar, and K. Ostrikov, "Control of morphology and electrical properties of self-organized graphenes in a plasma," *Carbon*, vol. 49, no. 13, pp. 4331–4339, 2011.

[192] K. Yang, S. Zhang, G. Zhang, X. Sun, S. T. Lee, and Z. Liu, "Graphene in mice: ultrahigh in vivo tumor uptake and efficient photothermal therapy," *Nano Letters*, vol. 10, no. 9, pp. 3318–3323, 2010.

[193] L. Zhang, Z. Lu, Q. Zhao, J. Huang, H. Shen, and Z. Zhang, "Enhanced chemotherapy efficacy by sequential delivery of siRNA and anticancer drugs using PEI-grafted graphene oxide," *Small*, vol. 7, no. 4, pp. 460–464, 2011.

[194] Y. Ohno, K. Maehashi, and K. Matsumoto, "Label-free biosensors based on aptamer-modified graphene field-effect transistors," *Journal of the American Chemical Society*, vol. 132, no. 51, pp. 18012–18013, 2010.

[195] W. Hong, H. Bai, Y. Xu, Z. Yao, Z. Gu, and G. Shi, "Preparation of gold nanoparticle/graphene composites with controlled weight contents and their application in biosensors," *Journal of Physical Chemistry C*, vol. 114, no. 4, pp. 1822–1826, 2010.

[196] H. Chang, L. Tang, Y. Wang, J. Jiang, and J. Li, "Graphene fluorescence resonance energy transfer aptasensor for the thrombin detection," *Analytical Chemistry*, vol. 82, no. 6, pp. 2341–2346, 2010.

[197] Y. Wan, Z. Lin, D. Zhang, Y. Wang, and B. Hou, "Impedimetric immunosensor doped with reduced graphene sheets fabricated by controllable electrodeposition for the non-labelled detection of bacteria," *Biosensors and Bioelectronics*, vol. 26, no. 5, pp. 1959–1964, 2011.

[198] T. Kuila, S. Bose, P. Khanra, A. K. Mishra, N. H. Kim, and J. H. Lee, "Recent advances in graphene-based biosensors," *Biosensors and Bioelectronics*, vol. 26, no. 12, pp. 4637–4648, 2011.

[199] Y. A. Akimov, K. Ostrikov, and E. P. Li, "Surface plasmon enhancement of optical absorption in thin-film silicon solar cells," *Plasmonics*, vol. 4, no. 2, pp. 107–113, 2009.

[200] I. Heller, S. Chatoor, J. Männik, M. A. G. Zevenbergen, C. Dekker, and S. G. Lemay, "Influence of electrolyte composition on liquid-gated carbon nanotube and graphene transistors," *Journal of the American Chemical Society*, vol. 132, no. 48, pp. 17149–17156, 2010.

[201] H. Ohno, D. Takagi, K. Yamada, S. Chiashi, A. Tokura, and Y. Homma, "Growth of vertically aligned single-walled carbon nanotubes on alumina and sapphire substrates," *Japanese Journal of Applied Physics*, vol. 47, no. 4, pp. 1956–1960, 2008.

[202] Y. Zhang, J. Zhang, X. Huang, X. Zhou, H. Wu, and S. Guo, "Assembly of graphene oxide-enzyme conjugates through hydrophobic interaction," *Small*, vol. 8, no. 1, pp. 154–159, 2012.

[203] J. S. Czarnecki, K. Lafdi, and P. A. Tsonis, "A novel approach to control growth, orientation, and shape of human osteoblasts," *Tissue Engineering A*, vol. 14, no. 2, pp. 255–265, 2008.

[204] H. Pandey, V. Parashar, R. Parashar, R. Prakash, P. W. Ramteke, and A. C. Pandey, "Controlled drug release characteristics and enhanced antibacterial effect of graphene nanosheets containing gentamicin sulfate," *Nanoscale*, vol. 3, no. 10, pp. 4104–4108, 2011.

[205] V. K. Rana, M. C. Choi, J. Y. Kong et al., "Synthesis and drug-delivery behavior of chitosan-functionalized graphene oxide hybrid nanosheets," *Macromolecular Materials and Engineering*, vol. 296, no. 2, pp. 131–140, 2011.

[206] X. M. Sun, Z. Liu, K. Welsher et al., "Nano-graphene oxide for cellular imaging and drug delivery," *Nano Research*, vol. 1, no. 3, pp. 203–212, 2008.

[207] L. Zhang, J. Xia, Q. Zhao, L. Liu, and Z. Zhang, "Functional graphene oxide as a nanocarrier for controlled loading and targeted delivery of mixed anticancer drugs," *Small*, vol. 6, no. 4, pp. 537–544, 2010.

[208] W. Zhang, Z. Guo, D. Huang, Z. Liu, X. Guo, and H. Zhong, "Synergistic effect of chemo-photothermal therapy using PEGylated graphene oxide," *Biomaterials*, vol. 32, no. 33, pp. 8555–8561, 2011.

[209] B. Tian, C. Wang, S. Zhang, L. Feng, and Z. Liu, "Photothermally enhanced photodynamic therapy delivered by nano-graphene oxide," *ACS Nano*, vol. 5, no. 9, pp. 7000–7009, 2011.

[210] C. Dekker, "Solid-state nanopores," *Nature Nanotechnology*, vol. 2, no. 4, pp. 209–215, 2007.

[211] S. K. Min, W. Y. Kim, Y. Cho, and K. S. Kim, "Fast DNA sequencing with a graphene-based nanochannel device," *Nature Nanotechnology*, vol. 6, no. 3, pp. 162–165, 2011.

[212] Y. Cho, S. K. Min, W. Y. Kim, and K. S. Kim, "The origin of dips for the graphene-based DNA sequencing device," *Physical Chemistry Chemical Physics*, vol. 13, no. 32, pp. 14293–14296, 2011.

[213] C. A. Merchant, K. Healy, M. Wanunu et al., "DNA translocation through graphene nanopores," *Nano Letters*, vol. 10, no. 8, pp. 2915–2921, 2010.

[214] S. S. Kelkar and T. M. Reineke, "Theranostics: combining imaging and therapy," *Bioconjugate Chemistry*, vol. 22, no. 10, pp. 1879–1903, 2011.

[215] K. Yang, J. Wan, S. Zhang, Y. Zhang, S. T. Lee, and Z. Liu, "In vivo pharmacokinetics, long-term biodistribution, and toxicology of pegylated graphene in mice," *ACS Nano*, vol. 5, no. 1, pp. 516–522, 2011.

[216] O. Akhavan and E. Ghaderi, "Toxicity of graphene and graphene oxide nanowalls against bacteria," *ACS Nano*, vol. 4, no. 10, pp. 5731–5736, 2010.

[217] Y. Chang, S. T. Yang, J. H. Liu et al., "In vitro toxicity evaluation of graphene oxide on A549 cells," *Toxicology Letters*, vol. 200, no. 3, pp. 201–210, 2011.

[218] K. M. Garza, K. F. Soto, and L. E. Murr, "Cytotoxicity and reactive oxygen species generation from aggregated carbon and carbonaceous nanoparticulate materials," *International Journal of Nanomedicine*, vol. 3, no. 1, pp. 83–94, 2008.

[219] K.-H. Liao, Y. S. Lin, C. W. MacOsko, and C. L. Haynes, "Cytotoxicity of graphene oxide and graphene in human erythrocytes and skin fibroblasts," *ACS Applied Materials and Interfaces*, vol. 3, no. 7, pp. 2607–2615, 2011.

[220] M. Pumera, "Graphene in biosensing," *Materials Today*, vol. 14, no. 7-8, pp. 308–315, 2011.

[221] S. K. Singh, M. K. Singh, M. K. Nayak, S. Kumari, J. J. Grácio, and D. Dash, "Characterization of graphene oxide by flow cytometry and assessment of its cellular toxicity.," *Journal of biomedical nanotechnology*, vol. 7, no. 1, pp. 30–31, 2011.

[222] X. Zhang, J. Yin, C. Peng et al., "Distribution and biocompatibility studies of graphene oxide in mice after intravenous administration," *Carbon*, vol. 49, no. 3, pp. 986–995, 2011.

[223] L. Yan, F. Zhao, S. Li, Z. Hu, and Y. Zhao, "Low-toxic and safe nanomaterials by surface-chemical design, carbon nanotubes, fullerenes, metallofullerenes, and graphenes," *Nanoscale*, vol. 3, no. 2, pp. 362–382, 2011.

[224] A. Sasidharan, L. S. Panchakarla, P. Chandran et al., "Differential nano-bio interactions and toxicity effects of pristine versus functionalized graphene.," *Nanoscale*, vol. 3, no. 6, pp. 2461–2464, 2011.

[225] K. Wang, J. Ruan, H. Song et al., "Biocompatibility of graphene oxide," *Nanoscale Research Letters*, vol. 6, no. 1, pp. 1–8, 2011.

[226] S. H. Yang, T. Lee, E. Seo, E. H. Ko, I. S. Choi, and B.-S. Kim, "Interfacing living yeast cells with graphene oxide nanosheaths," *Macromolecular Bioscience*, vol. 12, no. 1, pp. 61–66, 2012.

[227] K. S. Novoselov, A. K. Geim, S. V. Morozov et al., "Electric field in atomically thin carbon films," *Science*, vol. 306, no. 5696, pp. 666–669, 2004.

[228] K. Liu, J. J. Zhang, F. F. Cheng, T. T. Zheng, C. Wang, and J. J. Zhu, "Green and facile synthesis of highly biocompatible graphene nanosheets and its application for cellular imaging and drug delivery," *Journal of Materials Chemistry*, vol. 21, no. 32, pp. 12034–12040, 2011.

[229] S. Alwarappan, A. Erdem, C. Liu, and C. Z. Li, "Probing the electrochemical properties of graphene nanosheets for biosensing applications," *Journal of Physical Chemistry C*, vol. 113, no. 20, pp. 8853–8857, 2009.

[230] A. N. Obraztsov, E. A. Obraztsova, A. V. Tyurnina, and A. A. Zolotukhin, "Chemical vapor deposition of thin graphite films of nanometer thickness," *Carbon*, vol. 45, no. 10, pp. 2017–2021, 2007.

[231] Q. Yu, J. Lian, S. Siriponglert, H. Li, Y. P. Chen, and S. S. Pei, "Graphene segregated on Ni surfaces and transferred to insulators," *Applied Physics Letters*, vol. 93, no. 11, Article ID 113103, 2008.

[232] Y. Q. Wu, P. D. Ye, M. A. Capano et al., "Top-gated graphene field-effect-transistors formed by decomposition of SiC," *Applied Physics Letters*, vol. 92, no. 9, Article ID 092102, 2008.

[233] A. N. Obraztsov, A. A. Zolotukhin, A. O. Ustinov, A. P. Volkov, Y. Svirko, and K. Jefimovs, "DC discharge plasma studies for nanostructured carbon CVD," *Diamond and Related Materials*, vol. 12, no. 3–7, pp. 917–920, 2003.

[234] M. Zhu, J. Wang, B. C. Holloway et al., "A mechanism for carbon nanosheet formation," *Carbon*, vol. 45, no. 11, pp. 2229–2234, 2007.

[235] K. S. Subrahmanyam, L. S. Panchakarla, A. Govindaraj, and C. N. R. Rao, "Simple method of preparing graphene flakes by an arc-discharge method," *Journal of Physical Chemistry C*, vol. 113, no. 11, pp. 4257–4259, 2009.

[236] L. Jiao, L. Zhang, X. Wang, G. Diankov, and H. Dai, "Narrow graphene nanoribbons from carbon nanotubes," *Nature*, vol. 458, no. 7240, pp. 877–880, 2009.

[237] D. V. Kosynkin, A. L. Higginbotham, A. Sinitskii et al., "Longitudinal unzipping of carbon nanotubes to form graphene nanoribbons," *Nature*, vol. 458, no. 7240, pp. 872–876, 2009.

[238] W. Choi, I. Lahiri, R. Seelaboyina, and Y. S. Kang, "Synthesis of graphene and its applications: a review," *Critical Reviews in Solid State and Materials Sciences*, vol. 35, no. 1, pp. 52–71, 2010.

[239] H. Jiang, "Chemical preparation of graphene-based nanomaterials and their applications in chemical and biological sensors," *Small*, vol. 7, no. 17, pp. 2413–2427, 2011.

[240] A. E. Rider and K. Ostrikov, "Assembly and self-organization of nanomaterials," in *Plasma Processing of Nanomaterials*, R. M. Sankaran, Ed., pp. 371–392, CRC Press, Boca Raton, Fla, USA, 2011.

[241] D. H. Seo, S. Kumar, and K. Ostrikov, "Thinning vertical graphenes, tuning electrical response: from semiconducting to metallic," *Journal of Materials Chemistry*, vol. 21, no. 41, pp. 16339–16343, 2011.

Hindawi Publishing Corporation
Journal of Nanomaterials
Volume 2012, Article ID 867036, 5 pages
doi:10.1155/2012/867036

Research Article

Enhancement of Radiotherapeutic Efficacy by Paclitaxel-Loaded pH-Sensitive Block Copolymer Micelles

Joohee Jung,[1,2] Min Sang Kim,[3] Sung-Jin Park,[1,4] Hye Kyung Chung,[5] Jinhyang Choi,[1] Jaesook Park,[1] Dong-Hoon Jin,[1] Si Yeol Song,[1,6] Heon Joo Park,[7] Doo Sung Lee,[3] Seong-Yun Jeong,[1] and Eun Kyung Choi[1,5,6]

[1] *Institute for Innovative Cancer Research, Asan Medical Center, University of Ulsan College of Medicine, Seoul 138-736, Republic of Korea*
[2] *College of Pharmacy, Duksung Women's University, Seoul 132-714, Republic of Korea*
[3] *Theranostic Macromolecular Research Center, Department of Polymer Science and Engineering, Sungkyunkwan University, Suwon 440-746, Republic of Korea*
[4] *Laboratory of Bioimaging Probe Development, Singapore Bioimaging Consortium, Singapore 138667*
[5] *Center for Development and Commercialization of Anti-Cancer Therapeutics, Asan Medical Center, Seoul 138-736, Republic of Korea*
[6] *Department of Radiation Oncology, Asan Medical Center, University of Ulsan College of Medicine, Seoul 138-736, Republic of Korea*
[7] *Department of Microbiology, College of Medicine, Inha University, Inchon 400-712, Republic of Korea*

Correspondence should be addressed to
Seong-Yun Jeong, syj@amc.seoul.kr and Eun Kyung Choi, ekchoi@amc.seoul.kr

Received 13 February 2012; Accepted 31 March 2012

Academic Editor: Haifeng Chen

Radiotherapy (RT) is a major modality for cancer treatment, but its efficacy is often compromised by the resistance caused by tumor-specific microenvironment including acidosis and hypoxia. For an effective RT, concurrent administration of radiosensitizer with RT has been emphasized. However, most anticancer agents enhancing radiotherapeutic efficacy have obstacles such as poor solubility and severe toxicity. Paclitaxel (PTX), a well-known radiosensitizer, is insoluble in water and needs toxic solvent like Cremophor EL. Nanomaterials in drug delivery systems have been utilized for improving the drawbacks of anti-cancer drugs. Solubilization, tumor accumulation, and toxicity attenuation of drug by nanomaterials are suitable for enhancement of radiotherapeutic efficacy. In this study, PTX was incorporated into pH-sensitive block copolymer micelle (psm-PTX), polyethylene glycol-graft-poly(β-amino ester), and preclinically evaluated for its effect on RT. The size of psm-PTX was 125.7 ± 4.4 nm at pH 7.4. psm-PTX released PTX rapidly in the acidic condition (pH 6.5), while it was reasonably stable in the physiologic condition (pH 7.4). The clonogenic assay showed that psm-PTX greatly sensitized human non-small-cell lung cancer A549 cells to radiation. In the xenograft tumor model, the combination of psm-PTX and radiation significantly delayed the tumor growth. These results demonstrated the feasibility of psm-PTX to enhance the chemoradiotherapeutic efficacy.

1. Introduction

Radiotherapy (RT) is a major treatment for many cancers, especially non-small-cell lung cancer (NSCLC), but the overall cure rate and survival rate remain low because of radioresistance by proficient repair of radiation damage, accelerated cell repopulation, hypoxia, various molecular inhibitors of cell death, and so on [1]. To increase tumor control, concurrent administration of radiosensitizer with RT has been a common treatment regimen [2]. Most radiosensitizers are mainly anticancer agents. One of well known radiosensitizers is paclitaxel (PTX), which is being widely studied for clinical trials [3]. However, PTX needs toxic solvent such as Cremophor EL for clinical application due to its insolubility and has toxicities such as neutropenia, peripheral sensory neuropathy, dermatitis, and hypersensitivity reaction. Thus, there has been passionate interest in developing alternative formulation of PTX.

Nanomaterials in drug delivery systems (DDSs) have been playing a key role in the medical field, especially anticancer therapy. Nanomaterials such as polymeric nanoparticles and micelles are associated with solubilization of low-solubility drugs. PTX-loaded NK105 micellar nanoparticles, Abraxane (PTX-loaded albumin particle), Xyota (polymer-conjugated PTX), and Tocosol (tocophenol-based PTX), improve the low solubility of PTX. They are being evaluated in preclinical and clinical studies [4, 5]. Furthermore, these nanomaterials are suitable for drug accumulation in tumor by the enhanced permeability and retention (EPR) effect. Recently many efforts have been dedicated to study modified nanomaterials with tumor cell targeting moieties or tumor environmental sensitivity (temperature, pH, and enzyme activity). These properties control cell selectivity, cellular uptake, and drug release. Among them, tumor acidity, slightly a low extracellular pH (~6.8) [6], is exploited for DDS. pH-sensitive nanomaterials are suited for controlled drug release by the normal/cancer cells microenvironmental difference. pH-sensitive drug carriers have been developed to include liposome, micelles, dendrimers, and drug-polymer conjugates [7–9]. In our previous study, methyl ether poly(ethylene glycol)-poly(β-amino ester) polymeric micelles (MPEG-PM) was synthesized and evaluated as a PTX-loaded smart carrier *in vitro* [10]. Moreover, camptothecin-incorporated MPEG-PM was reported for cancer therapeutic efficacy [11]. Herein, we evaluated PTX-loaded pH-sensitive micelle (psm-PTX) as a radiosensitizer for chemoradiotherapy in NSCLC both *in vitro* and *in vivo*.

2. Materials and Methods

2.1. Preparing psm-PTX. pH-sensitive block copolymer micelle (psm), of which M_n is 13,000 g·mol^{-1} and which contains 4 mol-% PEG, was obtained according to the previous study [12]. PTX was conjugated with psm using anhydrous dichloromethane as reported previously [13]. The size distribution of psm-PTX was measured by dynamic light scattering (DLS) at 25°C.

2.2. PTX Release from psm-PTX In Vitro. To determine the release of PTX depending on pH, psm-PTX (1 mg/mL) solution at pH 6.0–8.0 was prepared. The pH of psm-PTX was adjusted stepwise with NaOH solution and immediately filtered. To measure the release of PTX depending on time, 1 mg/mL of psm-PTX was loaded to a dialysis membrane (MWCO, 3500) and immersed in 20 mL of the medium at 37°C. At predetermined time intervals, the medium was withdrawn. The concentration of PTX was measured by HPLC as described in the previous study [12]. Briefly, the mobile phase was changed linearly from acetonitrile-water (50 : 50 v/v) to acetonitrile-water (90 : 10 v/v), and a C-18 reverse-phase column was used. The flow rate was 0.5 mL/min.

2.3. Clonogenic Assay. Human lung adenocarcinoma A549 cells purchased from the American Type Culture Collection (ATCC) were maintained in Dulbecco's modified Eagle's medium (DMEM; Invitrogen, Carlsbad, CA) supplemented with 10% fetal bovine serum (Invitrogen) and 1% penicillin/streptomycin under a humidified atmosphere of 5% CO_2 at 37°C. A549 cells were seeded from 100 to 1,000 cells/well in 6-well plate and treated with PTX or psm-PTX (0.2 nM as PTX). PTX was dissolved by 50% Cremophor EL/ethanol and diluted one-fifth by phosphate-buffered saline (pH 7.4) before use. After 2 h, A549 cells were irradiated at 2 Gy using a 6 MV photon beam linear accelerator (CL/1800, Varian Medical System, Palo Alto, CA). The cells were incubated for 11 days to allow colony formation. The colonies composing of over 50 cells were counted, and the survival fraction was calculated as in the previously study [14]. Plating efficiency was defined from nonirradiated cells as (mean colonies counted)/(cells plated). Survival fraction was calculated as (mean colonies counted)/[(cells plated) × (plating efficiency)].

2.4. Tumor Growth Delay. All experiments were performed following the protocol approved by the Institutional Animal Care and Use Committee of ASAN Institute for Life Science. A549 cells (5×10^5 cells) were implanted subcutaneously into the right hind leg of five-week-old male BALB/c nude mice weighing about 20 g (Japan SLC, Shizuoka, Japan), as previously described [15]. When the tumors grew to about 100 mm^3, the mice were randomized and divided into the experimental groups ($n = 5$/group). The mice were intravenously injected with 10 mg/kg of psm-PTX (as at a concentration of PTX) or equal amount of psm (300 mg/kg) without PTX as a control. After 2 h, tumors were irradiated to 5 Gy. The tumor volume was calculated by the following formula: V = (longest dimension) × (shortest dimension)^2 × 0.5.

3. Results and Discussions

3.1. Characterization of psm-PTX. For pH-sensitivity and hydrophilic block, psm consisted of poly(β-amino ester) and PEG (Figure 1(a)). Molecular weight of PEG was 2,000, which was known to be degradable without toxicity [16, 17]. Furthermore, the micellization/demicellization transition of psm was reported at the sharp pH transition between 6.4 and 6.8 in previous work [11]. PTX was easily loaded into psm without an organic solvent. Loading efficiency of PTX was 48%, and loading amount was 2.3% (w/w). Lyophilized psm-PTX was reconstructed by sterilized water for the evaluation of psm-PTX. As a result, psm-PTX improved the water solubility of PTX by hydrophilic block, suggesting it excluded cremophor EL-induced toxicity. The size of psm-PTX was determined as 125.7 ± 4.4 nm at pH 7.4 by DLS, while psm was 27.7 ± 1.2 nm (Figure 1(b)). The encapsulation of PTX in psm expanded the size of polymeric micelles. These results suggested that the properties of psm-PTX (its size, solubility, and pH sensitivity) could play a smart carrier role in chemotherapy.

3.2. pH-Dependent Drug Release of psm-PTX. psm-PTX was investigated for controlled drug release. psm-PTX showed

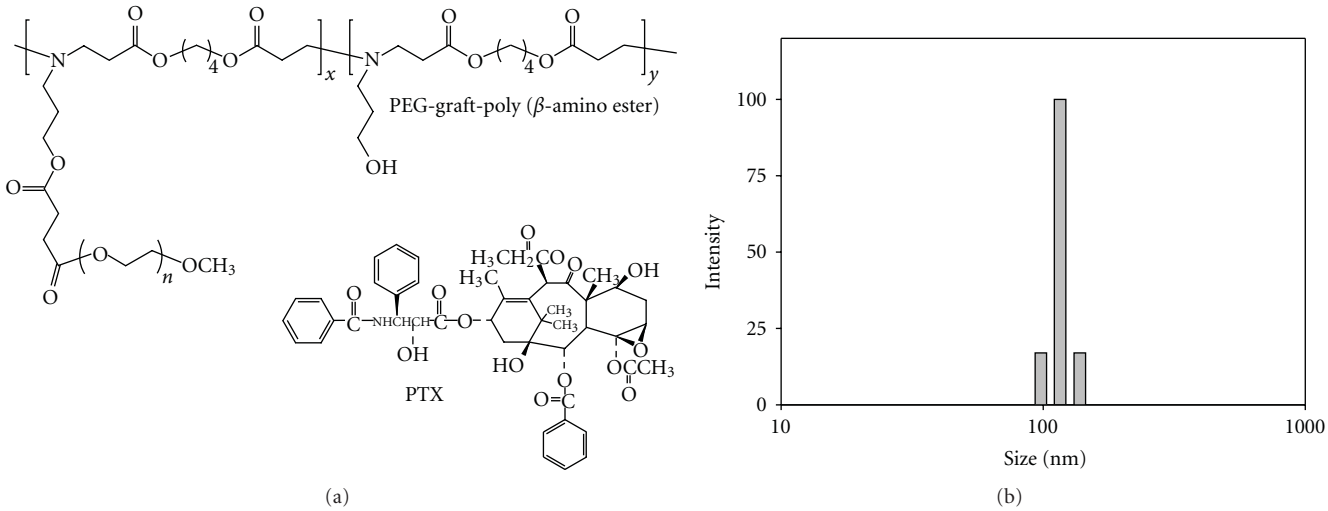

Figure 1: Composition (a) and size (b) of psm-PTX.

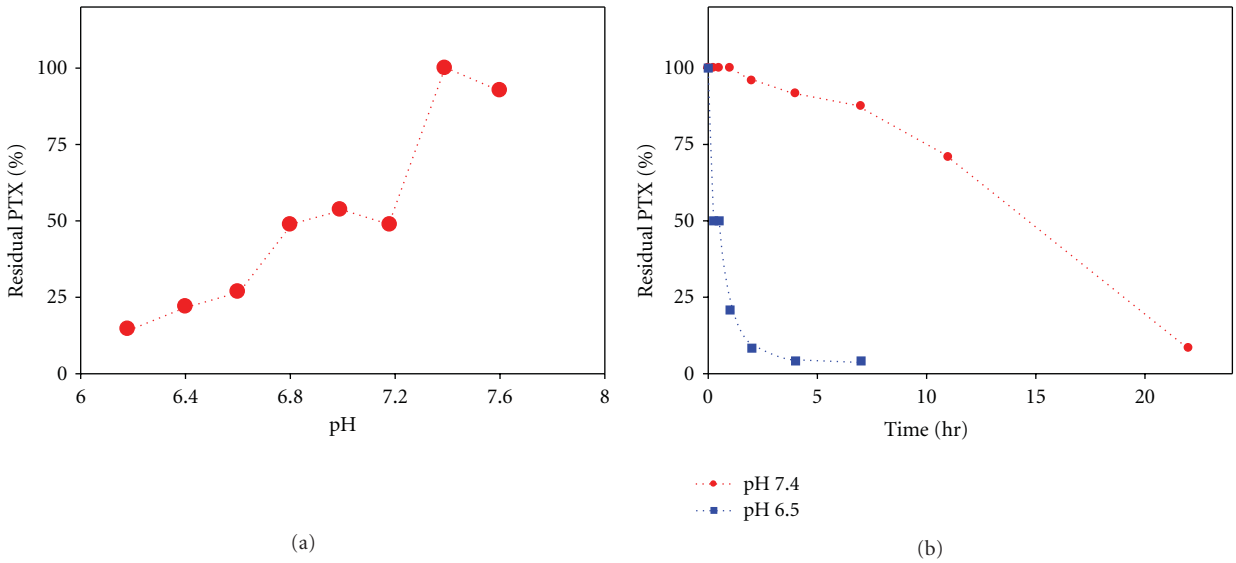

Figure 2: *In vitro* release of PTX from psm-PTX. (a) pH-dependent PTX release. psm-PTX (25 μg/ml as PTX) was immediately filtered after titration. (b) Time-dependent PTX release. psm-PTX (25 μg/ml as PTX) was filtered after incubation at 37°C. PTX was analyzed by HPLC as described in Section 2.

a pH-dependent drug release according to the different pH conditions (Figure 2(a)). Below pH 6.8, PTX was dramatically released over 50% from psm-PTX. Moreover, 50% of PTX in psm-PTX was rapidly released PTX within 30 min and then psm-PTX remained less 10% PTX at 4 h under the pH 6.5 condition, indicating that psm-PTX was demicellized at the acidic pH (Figure 2(b)). The results suggested that psm-PTX could trigger the PTX release at tumor site due to the acidic environment of the tumor site. On the other hand, psm-PTX was stable and slowly released for 12 h at 37°C in pH 7.4 (Figure 2(b)), suggesting that psm-PTX preserved PTX during systemic circulation. However, residual PTX did not remain for a day at normal pH, and thus the modified formulation of psm-PTX is being studied for a long circulation.

3.3. Radiosensitizing Effect of psm-PTX in A549 Human Lung Cancer Cells. The radiosensitizing effect of psm-PTX was evaluated on A549 cells by clonogenic assay (Figure 3). Survival fraction of psm did not differ from control at any pH. Survival fraction of PTX was similar to that of ionizing radiation (IR, 2 Gy), and the combination of PTX with IR showed the expectative sensitizing effect. Importantly, psm-PTX showed greatly lower survival fraction than PTX, suggesting that psm-PTX was uptaken rapidly into cells and

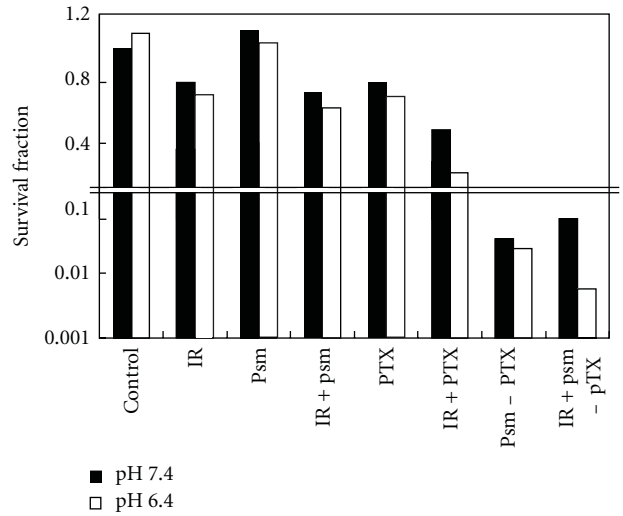

Figure 3: *In vitro* radiosensitizing effect of psm-PTX. A549 cells were treated with PTX or psm-PTX (0.2 nM as PTX) for 2 h and irradiated at 2 Gy. After 11 days, colony was counted and survival fraction was calculated.

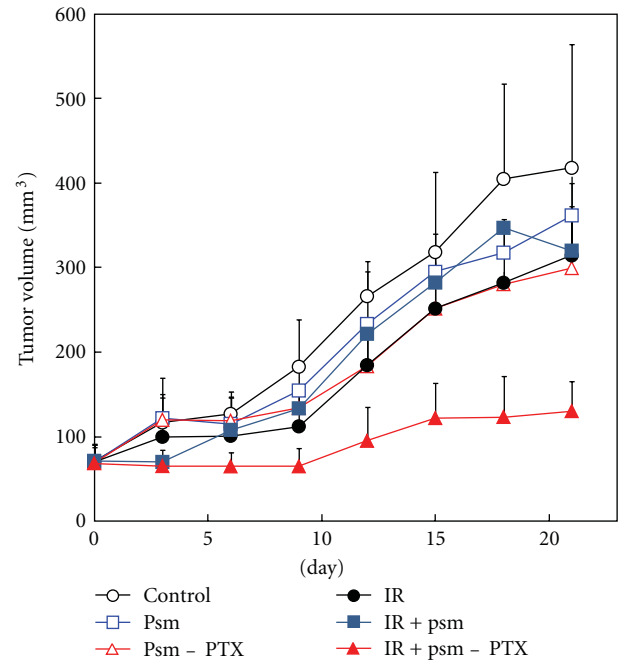

Figure 4: *In vivo* tumor growth delay of psm-PTX. Mice bearing A549-derived tumor were treated with PTX or psm-PTX (10 mg/kg as PTX) and irradiated at 5 Gy after 2 h. Tumor size was measured every 3 days and tumor volume was calculated as in Section 2. Data present mean ± standard deviation (*, $P < 0.05$, t-test).

internalized psm-PTX was demicellized by the endosomal acid pH (below pH 6.5). Especially, the combination of psm-PTX with IR showed more cytotoxicity than psm-PTX or IR in the low acidic pH environment (pH 6.5). These results showed that psm-PTX had a potential to exert an enhanced radiosensitization effect at the acidic pH condition.

3.4. In Vivo Tumor Growth Delay of the Combination of psm-PTX with IR. The acidic environment of the tumor is an important property for active targeting. In the previous study, the tumor growth delay of anticancer drug was enhanced by using camptothecin- (CPT-) loaded pH-responsive polymeric micelles (CPT-pH-PMs) [11]. In this study, the radiotherapeutic efficacy of psm-PTX was evaluated in mice bearing A549-derived tumor. The psm-PTX was administered by intravenous injection via tail vein. As shown in Figure 4, psm-PTX-treated group showed similar tumor growth to IR-treated group. The combination of psm-PTX with IR significantly enhanced the radiotherapeutic efficacy. At 21 days after administration, psm-PTX, IR, and the combination of psm-PTX with IR suppressed the tumor size by 71%, 75%, and 31%, respectively. During this examination, the change of body weight was not shown in any group. The results indicated that psm-PTX as a radiosensitizer was able to be utilized for chemoradiotherapy.

Chemoradiotherapy is a standard treatment regimen for various cancers. In addition, nanomaterials as drug carriers induce the enhancement of therapeutic efficacy as well as the attenuation of toxicity. Abraxane, approved by US Food and Drug Administration, was also reported to improve radiotherapy [18]. Although several pH-responding carriers containing PTX have been reported for chemotherapeutics, an utilization of pH-responding carrier as radiosensitizer has not been reported. Therefore, we aimed to apply psm-PTX, a smart carrier responding the tumor-specific microenvironment such as low pH, to improve radiotherapeutic efficacy. The results of this study demonstrated the feasibility of psm-PTX to enhance the chemoradiotherapeutic efficacy. Inasmuch as this study was designed primarily for the enhancement of concurrent chemoradiotherapy, we have focused on the radiosensitization effect in the presence of psm-PTX during radiation. Although we have not evaluated the effect of psm-PTX on a sequential chemoradiotherapy in which chemotherapy and RT are separately given to tumor, further investigation to confirm the efficacy of psm-PTX on sequential chemoradiotherapy is clearly warranted. This study suggests that psm-PTX as a radiosensitizer would be a potential candidate for clinical chemoradiotherapy trials.

Acknowledgments

This work was supported by a grant from the Korean Health Technology R&D Project, Ministry for Health and Welfare, Republic of Korea (A062254 and A102059), the Nuclear R&D program through the Korea Science and Engineering Foundation funded by the Ministry of Education, Science and Technology of Korea (2008-03876), the Basic Science Research Program through the National Research Foundation of Korea (NRF) funded by the Ministry of Education, Science and Technology (KRF-2008-313E00444), and a grant from ASAN Institute for Life Science, Seoul, Republic of Korea (2010-445). D. S. Lee. would like to thank the support by the Basic Science Research Program through a National Research Foundation of Korea grant funded by the Korean Government (MEST) (2010-0027955).

References

[1] W. T. Sause, C. Scott, S. Taylor et al., "Radiation Therapy Oncology Group (RTOG) 88-08 and Eastern Cooperative Oncology Group (ECOG) 4588: preliminary results of a phase III trial in regionally advanced, unresectable non-small-cell lung cancer," *Journal of the National Cancer Institute*, vol. 87, no. 3, pp. 198–205, 1995.

[2] O. Caffo, "Radiosensitization with chemotherapeutic agents," *Lung Cancer*, vol. 34, no. 4, supplement, pp. 81–90, 2001.

[3] D. L. Carter, D. Garfield, J. Hathorn et al., "A randomized phase III trial of combined paclitaxel, carboplatin, and radiation therapy followed by weekly paclitaxel or observation for patients with locally advanced inoperable non-small-cell lung cancer," *Clinical Lung Cancer*, vol. 13, no. 3, pp. 205–213, 2012.

[4] Y. Matsumura and K. Kataoka, "Preclinical and clinical studies of anticancer agent-incorporating polymer micelles," *Cancer Science*, vol. 100, no. 4, pp. 572–579, 2009.

[5] J. B. Bulitta, P. Zhao, R. D. Arnold et al., "Mechanistic population pharmacokinetics of total and unbound paclitaxel for a new nanodroplet formulation versus Taxol in cancer patients," *Cancer Chemotherapy and Pharmacology*, vol. 63, no. 6, pp. 1049–1063, 2009.

[6] M. Stubbs, P. M. J. McSheehy, J. R. Griffiths, and C. L. Bashford, "Causes and consequences of tumour acidity and implications for treatment," *Molecular Medicine Today*, vol. 6, no. 1, pp. 15–19, 2000.

[7] S. Salmaso, S. Bersani, M. Pirazzini, and P. Caliceti, "PH-sensitive PEG-based micelles for tumor targeting," *Journal of Drug Targeting*, vol. 19, no. 4, pp. 303–313, 2011.

[8] D. Chen, X. Jiang, J. Liu, X. Jin, C. Zhang, and Q. Ping, "In vivo evaluation of novel pH-sensitive mPEG-Hz-chol conjugate in liposomes: pharmacokinetics, tissue distribution, efficacy assessment," *Artificial Cells, Blood Substitutes, and Biotechnology*, vol. 38, no. 3, pp. 136–142, 2010.

[9] J. K. Kim, V. K. Garripelli, U. H. Jeong, J. S. Park, M. A. Repka, and S. Jo, "Novel pH-sensitive polyacetal-based block copolymers for controlled drug delivery," *International Journal of Pharmaceutics*, vol. 401, no. 1-2, pp. 79–86, 2010.

[10] M. S. Kim and D. S. Lee, "In vitro degradability and stability of hydrophobically modified pH-sensitive micelles using MPEG-grafted poly(β-amino ester) for efficient encapsulation of paclitaxel," *Journal of Applied Polymer Science*, vol. 118, no. 6, pp. 3431–3438, 2010.

[11] K. H. Min, J. H. Kim, S. M. Bae et al., "Tumoral acidic pH-responsive MPEG-poly(β-amino ester) polymeric micelles for cancer targeting therapy," *Journal of Controlled Release*, vol. 144, no. 2, pp. 259–266, 2010.

[12] W. S. Shim, S. W. Kim, E. K. Choi, H. J. Park, J. S. Kim, and D. S. Lee, "Novel pH sensitive block copolymer micelles for solvent free drug loading," *Macromolecular Bioscience*, vol. 6, no. 2, pp. 179–186, 2006.

[13] M. S. Kim, G. H. Gao, S. W. Kang, and D. S. Lee, "Evaluation of pH-Sensitive poly(β-amino ester)-graft-poly(ethylene glycol) and its usefulness as a pH-Sensor and protein carrier," *Macromolecular Bioscience*, vol. 11, no. 7, pp. 946–951, 2011.

[14] J. Jung, E.-J. Kim, H. K. Chung, H. J. Park, S.-Y. Jeong, and E. K. Choi, "c-Myc down-regulation is involved in proteasome inhibitor-mediated enhancement of radiotherapeutic efficacy in non-small cell lung cancer," *International Journal of Oncology*, vol. 40, no. 2, pp. 385–390, 2012.

[15] S. Y. Jeong, S. J. Park, S. M. Yoon et al., "Systemic delivery and preclinical evaluation of Au nanoparticle containing β-lapachone for radiosensitization," *Journal of Controlled Release*, vol. 139, no. 3, pp. 239–245, 2009.

[16] O. Biondi, S. Motta, and P. Mosesso, "Low molecular weight polyethylene glycol induces chromosome aberrations in Chinese hamster cells cultured in vitro," *Mutagenesis*, vol. 17, no. 3, pp. 261–264, 2002.

[17] A. D. Mitchell, A. E. Auletta, D. Clive, P. E. Kirby, M. M. Moore, and B. C. Myhr, "The L5178Y/tk(+/−) mouse lymphoma specific gene and chromosomal mutations assay: a phase III report of the U.S. environmental protection agency Gene-Tox program," *Mutation Research*, vol. 394, no. 1–3, pp. 177–303, 1997.

[18] N. Wiedenmann, D. Valdecanas, N. Hunter et al., "130-nm albumin—bound paclitaxel enhances tumor radiocurability and therapeutic gain," *Clinical Cancer Research*, vol. 13, no. 6, pp. 1868–1874, 2007.

Hindawi Publishing Corporation
Journal of Nanomaterials
Volume 2012, Article ID 674145, 9 pages
doi:10.1155/2012/674145

Research Article

Antibacterial Properties of Silver-Loaded Plasma Polymer Coatings

Lydie Ploux,[1] Mihaela Mateescu,[1] Karine Anselme,[1] and Krasimir Vasilev[2]

[1] *Institut de Science des Matériaux de Mulhouse, CNRS LRC 7228, 15 rue Jean Starcky, BP2488, 68057 Mulhouse Cedex, France*
[2] *Mawson Institute and School of Advanced Manufacturing, University of South Australia, Mawson Lakes Campus, Mawson Lakes, SA 5099, Australia*

Correspondence should be addressed to Lydie Ploux, lydie.ploux@uha.fr

Received 8 February 2012; Accepted 22 March 2012

Academic Editor: Haifeng Chen

In a previous paper, we proposed new silver nanoparticles (SNPs) based antibacterial coatings able to protect eukaryotic cells from SNPs related toxic effects, while preserving antibacterial efficiency. A SNPs containing n-heptylamine (HA) polymer matrix was deposited by plasma polymerization and coated by a second HA layer. In this paper, we elucidate the antibacterial action of these new coatings. We demonstrated that SNPs-loaded material can be covered by thin HA polymer layer without losing the antibacterial activity to planktonic bacteria living in the near surroundings of the material. SNPs-containing materials also revealed antibacterial effect on adhered bacteria. Adhered bacteria number was significantly reduced compared to pure HA plasma polymer and the physiology of the bacteria was affected. The number of adhered bacteria directly decreased with thickness of the second HA layer. Surprisingly, the quantity of cultivable bacteria harvested by transfer to nutritive agar decreased not only with the presence of SNPs, but also in relation to the covering HA layer thickness, that is, oppositely to the increase in adhered bacteria number. Two hypotheses are proposed for this surprising result (stronger attachment or weaker vitality), which raises the question of the diverse potential ways of action of SNPs entrapped in a polymer matrix.

1. Introduction

Biofilms are a common cause for biomaterials-related infections [1, 2], often leading to implant failure and removal [3–5]. Extensive research efforts in the fields of microbiology, chemistry, and material science have focussed on understanding bacteria-material surface interactions [6] and developing novel materials which are able to resist and fight against bacterial adhesion and biofilm formation [7]. The release of antibacterial agent from coatings or materials is one of the most promising solutions and many original so-called drug delivery systems have been reported in the literature [8–11]. This strategy has advantages to surface-immobilized antibacterial agents, because it acts on both adhered bacteria and planktonic bacteria living in the near surroundings. However, health risks related to the release of bioactive drug in the patient body remain an important cause of anxiety for both medical and general public.

Amongst many antibacterial agents, silver is probably the most famous. It has been known since the ancient times for its antibacterial properties and silver-based compounds have been used extensively in many applications [12, 13]. After being neglected in the second 20th century part, the increased occurrence of antibiotics-resistant bacteria in infections has made silver popular again, especially for creating new antibacterial coatings and materials [5, 14–18]. In its ionic form (Ag^+), silver is known to exhibit a strong toxicity to a wide range of microorganisms while the risk of bacterial resistance to silver is usually considered to be lower than to antibiotics. Ag^+ ions disturb biological functions such as permeability and respiration by interacting with the bacterial membrane. In addition, Ag^+ ions can penetrate inside the cell where they cause damage by binding with enzymes and DNA [13, 19, 20]. Silver nanoparticles (SNPs) also exhibit antibacterial properties via bacterial inactivation and growth inhibition [21, 22] but the mechanism of action is not yet completely understood [23].

Toxicity of silver ions to human cells is low and relatively high levels (2.89 g on silver-coated megaprostheses) have been used in patients without leading to any argyrosis and

toxic side effects [24]. In addition, when embedded in a coating like a polymer matrix, SNPs cannot be released in the material surroundings. Rather, antibacterial properties are due to the release of silver ions resulting from the oxidation of embedded SNPs [25, 26]. However, the potential toxicity of biomaterials containing silver in any form and in particular when used as nanoparticles remains a current question [27]. Therefore, protecting eukaryotic cells from direct contact with SNPs, even immobilized in coating, is a relevant challenge.

Recently, we demonstrated that it is possible to preserve antibacterial efficiency (*Staphylococcus epidermidis*) of a coating embedding SNPs, while protecting eukaryotic cells (SaOS2 osteoblastic cells) from the toxic effects due to direct contact with the embedded SNPs, [28]. This new coating was based on one matrix of n-heptylamine (HA) polymer, deposited by plasma polymerization, embedding SNPs. A second HA layer, covering the SNPs-containing matrix, protected eukaryotic cells from direct contact with the nanoparticles embedded in the matrix surface. In the present study, we aim to fully unravel the antibacterial action of these coatings. We focus on diverse aspects of antibacterial properties by considering effects on planktonic, that is, free living bacteria, adhered bacteria, and physiological state of planktonic and adhered bacteria. Three different thicknesses (6 nm, 12 nm, and 18 nm) of covering HA layer were considered, aiming at better understanding the role of the second layer in the preservation or the degradation of antibacterial properties.

2. Materials and Methods

2.1. Material Preparation. Material design (Figure 1(b)) and processing were described elsewhere [28]. Briefly, a 100 nm thick n-heptylamine (HA) plasma polymer film was deposited on clean glass slide of around 1 cm × 1 cm. The film was loaded with silver ions by immersion in $AgNO_3$, which were subsequently reduced to silver nanoparticles by immersion in $NaBH_4$. A second HA plasma polymer film was deposited on top of the SNPs-loaded film. In the present work, three different thicknesses of the second layer of 6 nm, 12 nm, and 18 nm were considered. Two additional materials were used as a negative (HA film without loaded SNPs) and a positive control (SNPs loaded HA film without second layer). The samples used in the present work thus presented five types of architecture that are called as the following in the present paper: "Negative Control": Clean glass slide + 100 nm HA; "Positive Control": Clean glass slide + HA + SNPs; "6 nm": Clean glass slide + HA + SNPs + 6 nm HA; "12 nm": Clean glass slide + HA + SNPs + 12 nm HA; "18 nm": Clean glass slide + HA + SNPs + 18 nm HA. Negative Control was regarded as the reference surface for evaluating the SNPs-related antibacterial efficiencies. Before use for microbiological investigation, samples were sterilized by UV (254 nm wave length) during 7 minutes at 2 cm from the lamp. Characterisation and details of the different types of material were reported elsewhere [28]. The release kinetics of silver ions from the films was shown to be a function of the thickness of the second HA layer (Figure 1(a)).

2.2. Bacterial Culture. Microbiological investigation was conducted with *Escherichia coli* (*E. coli*) that are among bacteria the most frequently implicated in infections on implants. *E. coli* MG1655 (PHL628 [29]) known to produce curli and exocellular polymeric substances (EPSs) and to attach to abiotic surfaces was used. Bacteria were cultivated in a selective medium at 30°C. Prior to each experiment, bacteria stored at −80°C were spread on a Luria-Bertani (LB) nutritive medium agar plate and grown about 24 hours. Selective nutritive medium (M63G, pH 6.8 [29]) was then inoculated with one bacterial colony and let overnight at 30°C. This culture was used to inoculate a second preculture (10% vol. of first preculture) which was grown for about 4 h before inoculating the culture (10% vol. of second preculture) finally used for experiments (containing about 5×10^6 bacteria/mL corresponding to an absorbance at 600 nm of 0.01, measured by UV spectrophotometry ($Abs_{600\,nm}$)).

2.3. Antibacterial Efficiency Analyses

2.3.1. Antibacterial Efficiency in the Material Surroundings: Supernatant Analysis. This test aims at evaluating the capacity of the entrapped SNPs to inhibit bacterial growth in the surrounding aqueous medium. Each sterilized material sample was placed in a Petri dish with the polymer face up. 3 mL of bacteria suspension prepared as described above were inoculated and cultured at 30°C in contact with the sample. After 2 hours of culture, 2.5 mL of supernatant were harvested from the dish and replaced by 2.5 mL of NaCl solution (9 g/L in water). This process was repeated 3 times, leading to the following harvested solutions Initial supernatant, 1st rinsing, 2nd rinsing, 3rd rinsing, 4th rinsing. The sufficient efficiency of 4 rinsing steps for harvesting all free living, that is, nonattached bacteria, was stated by a preliminary experiment (data not shown). Care has been taken that the samples remained in immersion for avoiding any supplementary cleaning through dewetting phenomena. Bacteria content of each harvested solution was assessed by absorbance measurement at 600 nm with a UV-spectrophotometer ($Abs_{600\,nm}$). $Abs_{600\,nm}$ values were transformed in planktonic bacteria amount by using an "$Abs_{600\,nm}$" versus "planktonic bacteria amount" calibration curve that was previously established by measuring the $Abs_{600\,nm}$ values of several dilutions of bacterial suspensions (data not shown). Planktonic bacteria amounts of initial supernatant and rinsing solutions were summed for each sample type in order to assess planktonic bacteria growth. Experiment for characterising antibacterial effect in supernatant was run 5 times.

2.3.2. Antibacterial Efficiency in the Material Surroundings: "Diffusion" Test. This test aims at evaluating the capacity of the entrapped SNPs to inhibit bacterial growth in the close surroundings of the substrate. 100 μL of a fresh bacterial suspension was spread on an LB agar plate in order to form a thin bacterial film. Sterilized material sample was placed in contact with this previously homogenously inoculated agar plate (sample top side in contact with agar). After overnight incubation at 30°C, the inhibition area that potentially

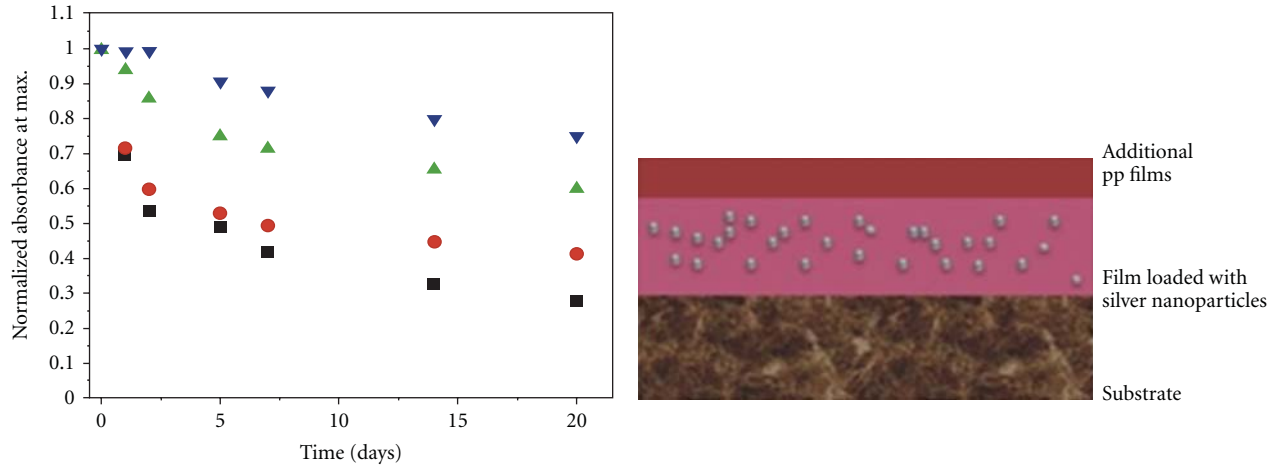

(a) (b)

Figure 1: Control over the release of silver ions. Control over release of silver was achieved by depositing an additional layer of HA pp film on top of the silver nanoparticles loaded films (b). The graph on the left shows the kinetic of release of silver ions from the films over 20-day immersion in PBS. Black squares—silver-loaded films as prepared; red circles—after deposition of 6 nm film of HA; green triangles—after deposition of 12 nm film of HA; blue triangles—after deposition of 18 nm film of HA (reprinted with permission from [28], Copyright 2010 American Chemical Society).

appeared around the sample was measured. The inhibition area border was approximated by both a round and a square zone (Figure 2(a)). Final value was obtained by averaging results of round zone and square zone approximations and subsequent subtraction of the sample area. "Diffusion" test experiment was run 3 times.

2.3.3. Antibacterial Efficiency at the Material Surface: Direct Observation under Fluorescence Confocal Microscope. This test aims at evaluating the capacity of the entrapped SNPs to inhibit the short-time colonisation of the material surface by bacteria. Each sterilized material sample was placed in a Petri dish with the polymer face up and treated as already describes above (Section 2.3.1). Finally, the last 4th rinsing solution was replaced by 2 mL of fresh NaCl solution without creation of any air-material interface. Bacteria attached on the material sample were observed to be immersed in the NaCl solution for keeping bacteria in physiological conditions. The upright Confocal Laser Scanning Microscopy (CLSM) (Carl Zeiss, LSM700) used for the observation was equipped with a long working distance objective (LD EC Epiplan Neofluar 50x/0.55 DIC M27). All CLSM observations were done in reflection mode, without any bacteria staining. Quantity of adherent bacteria was measured using ImageJ software [30]. Experiment for characterising antibacterial effect at the material surface was run 2 times.

2.3.4. Antibacterial Efficiency at the Material Surface: "Print" Test. This test aims at evaluating the proliferation capacity of bacteria adhered at the surface of the material samples. Each sterilized material sample was placed in a Petri dish with the polymer face up and treated as already described above (Section 2.3.1). After complete rinsing, the sample was taken out and its topside was slightly pressed for 5 sec on LB agar plate. Sample was then taken off and the Petri dish was incubated for 16 h at 30°C. The efficiency of bacteria transfer from material sample onto the LB-agar plate was supposed not to vary from a type of material to another. The proliferation capacity of bacteria initially adhered on the material was estimated as the capacity of the transferred bacteria to form colonies on the LB agar plates, which was assessed by measuring rate of sample surface covered by bacteria colonies. Measurement was performed by using image analysis with ImageJ software. "Print" test experiment was run 5 times.

3. Results and Discussion

For each material type, planktonic bacteria amounts corresponding to the initial supernatant and the four rinsing solutions were summed for assessing bacteria growth in the liquid surrounding material samples (Figure 3). The corresponding bacterial growth inhibition rates, that were calculated with HA material as a reference, are given in Table 1. The significantly ($P < 0.001$) smaller planktonic bacteria amounts measured for all materials that contained SNPs (in comparison with HA material) clearly indicated that the growth of bacteria in medium was affected by the presence of SNPs in the materials. Since, as previously demonstrated [28], SNPs do not release from the materials used in this study, this antibacterial effect must be attributed to silver ions (Ag^+) that were released in the surrounding liquid. Ag^+ ions are formed by oxidation of SNPs after contact with the surrounding aqueous medium, either at the material-liquid interface for SNPs exposed at the polymer matrix surface or after water uptake by the polymer matrix as already reported by other authors [25, 31]. In the last case, the nanoporous morphology structure of HA enables Ag^+ to diffuse through and to be released from the polymer matrix [28]. Accordingly, the HA polymer covering layer does not

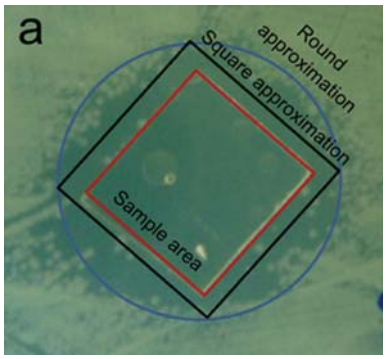

(a)

(b)

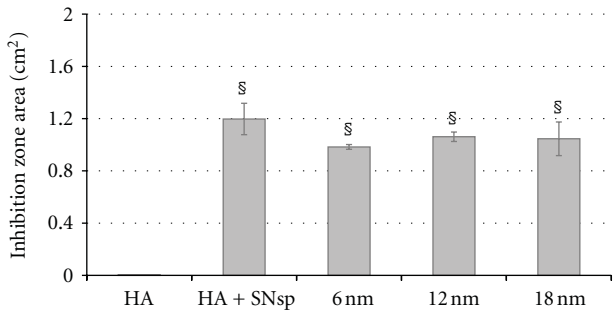

(c)

Figure 2: (a) Approximation of the inhibition area border by a round or square zone. (b) Example of the inhibition area observed around the HA film ("HA"), loaded with SNPs ("HA + SNPs"), and recovered by a second HA layer of 6 nm ("6 nm"), 12 nm ("12 nm"), and 18 nm ("18 nm") of thickness (2 different samples were placed on each plate). (c) Quantitative results of the diffusion test on LB agar plates for the 5 different types of material. § symbol indicates significant difference compared to HA ($P < 0.01$).

significantly affect the release of Ag^+, which is in accordance with its suitability for Ag^+ diffusion. In addition, no significant difference in the quantity of planktonic bacteria was observed between the 4 SNPs-loaded materials. This further demonstrates that the second HA layer covering SNPs does not reduce the antibacterial activity on planktonic bacteria, that is, the antibacterial activity due to Ag^+ ions released in material surroundings. Finally, the antibacterial effect of SNPs-containing materials on planktonic bacteria can be attributed to inhibition of bacteria proliferation and death of

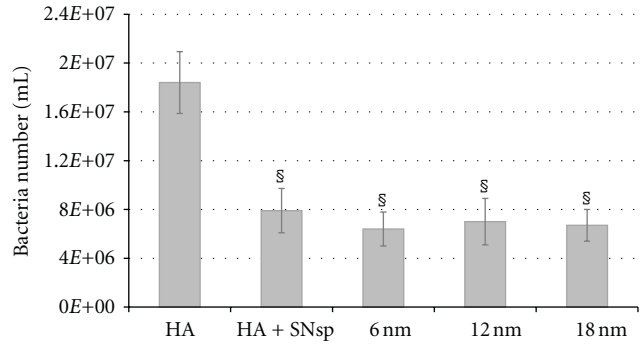

Figure 3: Amount of planktonic bacteria after 2 hours of culture in the surroundings of the following samples: HA film ("HA"), loaded with SNPs ("HA + SNPs"), and recovered by a second HA layer of 6 nm ("6 nm"), 12 nm ("12 nm"), and 18 nm ("18 nm") of thickness. Values were obtained by summing planktonic bacteria amount measured in the initial supernatants and the corresponding 4 rinsing solutions. § symbol indicates significant difference compared to HA ($P < 0.001$).

Table 1: Rates of bacteria growth inhibition, calculated with Negative Control as the reference.

Material sample type	Negative Control	Positive Control	6 nm	12 nm	18 nm
Inhibition rate	Reference	57%	65%	62%	64%
Standard Deviation		5%	5%	8%	4%

some bacteria. It is probable that, as proposed in the literature [19–21], both phenomena act together to disturb the growth of the planktonic population of bacteria.

Diffusion assays on nutritive agar plates confirmed the antibacterial effect resulting from loading of HA materials with SNPs. Images representative of the assays (Figure 2(b)) show the presence of bacterial growth inhibition zones (IZs) around the materials that were loaded with SNPs and the absence of this area for the SNPs-free HA polymer sample. This confirms that HA film does not release a substance able to inhibit *E. coli* growth which states that antibacterial effect revealed by all SNPs-containing materials is related to the presence of SNPs. In addition, IZ areas measurements (Figure 2(c)) show that HA + SNPs material led to an insignificantly wider IZ than SNPs-containing materials covered with a second HA layer. This highlights that the antibacterial effect due to Ag^+ released from embedded SNPs is possible even in the presence of an HA covering layer potentially as thick as 18 nm. Nevertheless, Ag^+ diffusion through the second HA layer may slightly slow Ag^+ release in the aqueous medium surrounding materials.

Contrary to the antibacterial effect that was demonstrated for bacteria present in the surroundings of materials, the effect on bacteria adhered on the material surface was significantly dependent on the thickness of the covering HA layer. Through CLSM observation of adhered bacteria and subsequent micrograph analysis with ImageJ software, the number

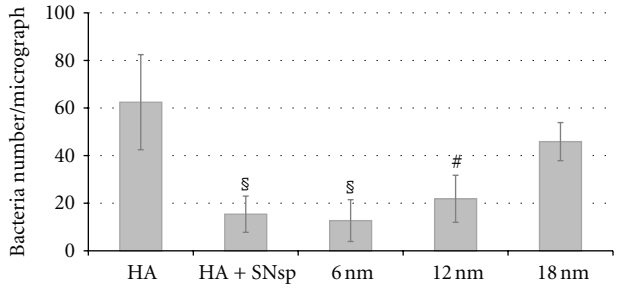

Figure 4: Number of *E. coli* adhered after 2 h of growth on HA film ("HA"), loaded with SNPs ("HA + SNPs"), and recovered by a second HA layer of 6 nm ("6 nm"), 12 nm ("12 nm"), and 18 nm ("18 nm") of thickness. Results were obtained by analysing CLSM micrographs with ImageJ software. § and # symbols indicate significant difference compared to HA ($P < 0.005$ and $P < 0.05$ resp.).

of bacteria adhered on the top of the HA + SNPs material surface was shown, as expected, to be dramatically less ($P > 0.005$) than on HA material (Figure 4). Compared to HA, the number of adhered bacteria was also reduced on SNPs-loaded films with a second HA layer. Nevertheless, this reduction was less marked on 12 nm material samples ($P > 0.05$) than on 6 nm material samples ($P > 0.005$) and still decreased on 18 nm material samples (nonsignificant difference between 18 nm and HA material samples). These results demonstrate that SNPs-containing materials result in a reduction of bacterial colonisation compared to SNPs-free HA. Nevertheless, the additional HA layers used to cover SNPs seem to limit the reduction of the antibacterial efficiency on adhered bacteria: increasing the layer thickness results in decreasing the SNPs-related effect on adhered bacteria.

Since planktonic bacteria were shown not to be differently affected by Ag^+ according to the thickness of the second HA layer, differences in Ag^+ release in aqueous medium due to different thickness of second layer might be too low to result in significant differences in the antibacterial effect on adhered bacteria. Hence, antibacterial effect on adhered bacteria must be attributed to a direct contact between cells and the SNPs-containing material, maybe due to Ag^+ accumulated at the material surface before final release. Assuming that HA polymer is a more favourable substrate for bacteria to adhere than SNPs and since the second HA layer is a thin, noncontinuous film presenting pores opened on the subjacent SNPs deposit, increasing the HA layer thickness increases the quantity of favorable sites for bacterial adhesion. Consequently, it is preferable that the second HA layer is as thin as possible to maintain a significant protective effect of the material on bacterial colonisation.

Bacterial physiology was also affected by the presence of SNPs in the materials. As shown by the micrographs realised with CLSM (Figure 5), bacteria that adhered on SNPs-free HA material presented a typical bacillus shape while, on SNPs-containing materials, bacterial morphology was modified: cells were shorter in length and had rounded shape. This change of the morphology of *E. coli* suggested that bacteria were unable to grow and proliferate, which is supported by the absence of divided cells on the SNPs-loaded surfaces. Such nongrowing state, that is known as one of the most common strategies used by bacteria to resist against antibacterial agents [32], can be here attributed to the presence of SNPs. However, it is difficult to distinguish between the potential roles of free Ag^+, Ag^+ accumulated at the material surface, or SNPs accessible at the material surface.

To further assess the capacity for proliferation of adhered bacteria, an original method was developed: through a so-called "print test," bacteria adhered on the diverse materials were transferred to agar nutritive medium and areas covered by the colonies formed by the transferred bacteria were measured as an indication of bacteria vitality. Surprisingly, areas covered by bacterial colonies decreased according to the HA > HA + SNPs > 6 nm > 12 nm > 18 nm ranking, as shown in Figure 6. The result demonstrated above (Figure 4), that is, the increase of adhered bacteria amount with the thickness of the HA layer covering SNPs, rather led to expect a decrease of the covered area following the HA > 18 nm > 12 nm > 6 nm > HA + SNPs ranking. In other words, the results of the present study showed that the thickest covering HA layer presents the highest amount of attached cells, yet the smallest amount of cultivable, harvested cells. The difference of cultivable bacteria harvested by printing with HA samples and 18 nm covered SNPs samples (that showed similar numbers of adhered bacteria) may be attributed to the loss of cultivability of the adhered bacteria due to the silver-related toxic surroundings [5]. However, the cause of the decrease in adhered bacteria cultivability with the increase of the second HA layer thickness despite an oppositely increase in bacteria amount adhered on the surface is not obvious. We propose two hypotheses for explaining this phenomenon.

(i) The characteristics of the silver species present at the SNPs-containing material surface may be changed by plasma treatment leading to modify antibacterial efficiency. Quantity of Ag^+ or SNPs, charge of SNPs, shape of SNPs, and so forth may be concerned. One possible scenario is that Ag^+ that may remain in the material in an unreduced state (despite the $NaBH_4$-based reduction process) may be reduced by plasma, thus leading to create new SNPs during the time of deposition of the second HA layer. Without or with noncontinuous second HA layer, Ag^+ that remained unreduced in the material may be eliminated soon after the coating elaboration. On the contrary, SNPs that may have been reduced under plasma may accumulate in the second HA layer surface and create a reservoir for further, slower release of more Ag^+ [25, 33] in the close surroundings of the second layer. Hence, the contact-related antibacterial effect may be enhanced. Therefore, surfaces covered with thicker HA layer may present bacteria with less viability and cultivability, yet in higher number as mentioned above. In this scenario, the use of 18 nm thick covering HA layer should be preferred for enhancing the contact-related antibacterial effect, while protecting

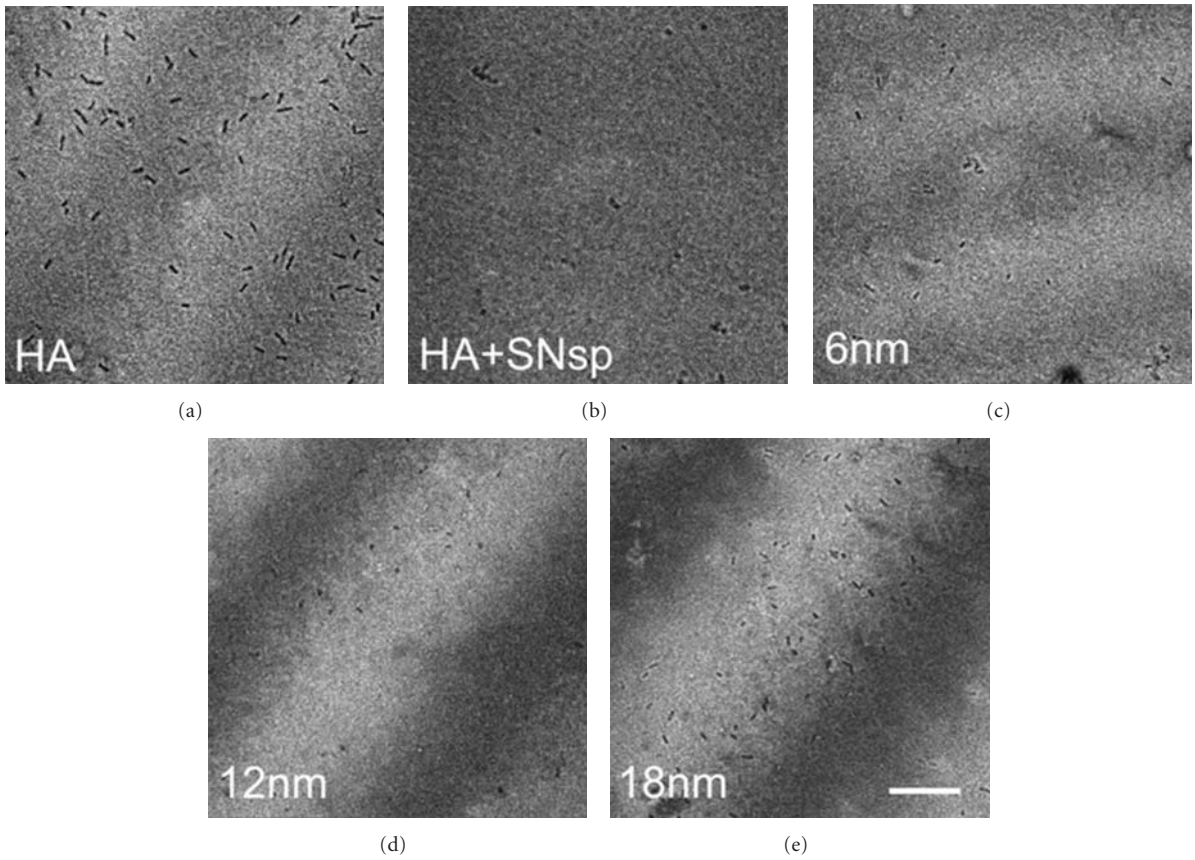

Figure 5: CSLM micrographs of *E. coli* adhered after 2 h of growth on HA film ("HA"), loaded with SNPs ("HA + SNPs"), and recovered by a second HA layer of 6 nm ("6 nm"), 12 nm ("12 nm"), and 18 nm ("18 nm") of thickness (Scale bar 20 μm).

eukaryotic cells from contact-related toxic effect of silver (as demonstrated elsewhere [28]).

(ii) Adhesion forces between bacteria and surface may be stronger on HA than on SNPs-containing material surfaces. Obviously, more bacteria should be harvested by printing when adhesion forces are smaller. Therefore, thicker, then larger covering with HA polymer of the SNPs deposit may result in larger retention of bacteria on the surface, leading to fewer bacteria that could be "printed" on the LB-agar plate. Comparing the ratio between the numbers of bacteria adhered on 18 nm material and HA + SNPs material (3 ± 2) and the ratio between the covered surfaces on 18 nm material (supposed to be recovered by a continuous layer of HA) and HA + SNPs material (0.5 ± 0.3), it is possible to estimate the ratio of bacterial adhesion strength between SNPs layer and HA layer at a value of 1/6. If confirmed, this difference in adhesion strength may be a crucial indication for the elaboration of new antibacterial coatings based on the use of SNPs. In this scenario, the use of intermediate thickness of covering HA layer should be preferred for limiting the surface of HA polymer available for contact with bacteria, while preserving protective effect for eukaryotic cells.

Further investigations must be realized to distinguish between both effects, using fluorescence staining specific for bacterial bioactivity (viability and respiratory activity) to determine if bacteria metabolism is more affected on HA covered than on nude SNPs-containing materials. Additionally, force measurements (by AFM, e.g.) may allow to determine the bacterial adhesion strength ratio between HA and SNPs materials. Nevertheless, these unexpected results already allow to raise a new question about the antibacterial action of SNPs-containing materials and the methodology used to prove antibacterial efficiency. Whether the few quantity of agar transferred bacteria is due to low cultivability or high adhesion to HA material, antibacterial efficiency appears to be more complex as a simple action of Ag^+ released in the material surroundings. Ag^+ accumulation at the material surface and adhesion strength between bacteria and the SNPs-containing material surface may also play a crucial role in the success of an antibacterial material strategy.

4. Conclusion

We demonstrated here that SNPs-loaded material can be covered by thin HA polymer layer without losing the antibacterial activity on planktonic bacteria living in the near (liquid or semisolid) surroundings of the material. This activity was

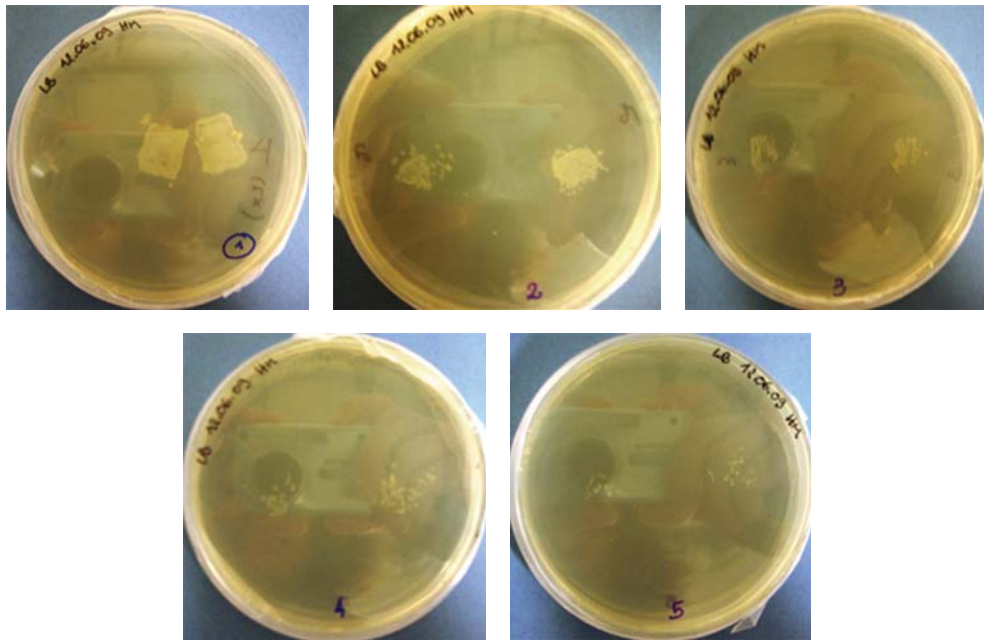

(a)

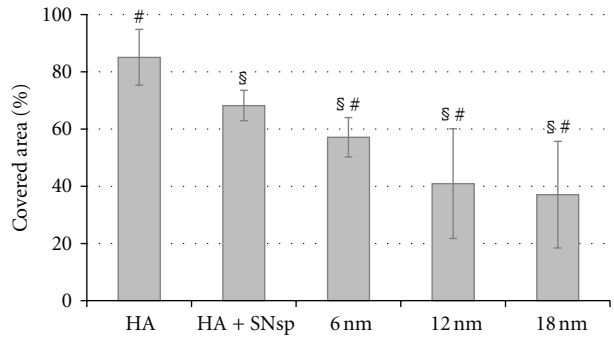

(b)

Figure 6: (a) Example of bacteria colonization after "print test" of the HA film ("HA"), loaded with SNPs ("HA + SNPs"), and recovered by a second HA layer of 6 nm ("6 nm"), 12 nm ("12 nm"), and 18 nm ("18 nm") of thickness (2 different samples were placed on each plate). (b) Rates of the print surfaces covered by bacteria colonies. Measurement was performed by image analysis using ImageJ software. § and # symbols indicate significant difference compared to HA ($P < 0.005$) and HA + SNPs ($P < 0.05$) respectively.

maintained even with 18 nm thick HA layer covering SNPs-containing material. SNPs-containing materials also revealed an antibacterial effect on adhered bacteria. In general, adhered bacteria number was significantly less than on HA material and adhered bacteria physiology was affected on SNPs-containing HA materials. According to the thickness of the second HA layer, differences in adhered bacteria number were shown, indicating that antibacterial efficiency on adhered bacteria was not only due to indirect effect of released silver ions but was also the result of direct bacteria-surface contact. More precisely, the number of adhered bacteria decreased with the thickness of the second HA layer. Surprisingly, the quantity of cultivable bacteria harvested by transfer to nutritive agar decreased not only according to the presence of SNPs in the material coating, but also in relation with covering HA layer thickness, that is, oppositely to the increase in the number of adhered bacteria. We proposed two hypotheses to explain this surprising result. The first one suggests an enhancement of the SNPs-containing materials activity through plasma-induced modifications (increase of SNPs quantity, size or shape modification, e.g.). The second one suggests the existence of differences in the strength of bacterial adhesion to material surface depending on the fraction of the material surface covered by HA or SNPs. Bacteria observation under confocal microscope qualitatively demonstrated that the physiology of adhered bacteria was affected by the presence of SNPs, but failed to highlight any differences in physiology between SNPs-containing materials. These results raise the question of the diverse potential ways of action of SNPs entrapped in a polymer matrix, which we highlighted for the first time in this study. Further investigations are needed to conclude whether the small quantity

of cultivable bacteria harvested by printing from HA-covered SNPs-containing materials is due to stronger attachment or to weaker vitality.

Acknowledgments

The authors thank the French Centre National de la Recherche Scientifique (CNRS) and Australian Research Council (ARC) (Fellowship FT100100292) for financial support.

References

[1] J. W. Costerton, P. S. Stewart, and E. P. Greenberg, "Bacterial biofilms: a common cause of persistent infections," *Science*, vol. 284, no. 5418, pp. 1318–1322, 1999.

[2] R. O. Darouiche, "Treatment of infections associated with surgical implants," *The New England Journal of Medicine*, vol. 350, no. 14, pp. 1422–1429, 2004.

[3] C. A. Fux, J. W. Costerton, P. S. Stewart, and P. Stoodley, "Survival strategies of infectious biofilms," *Trends in Microbiology*, vol. 13, no. 1, pp. 34–40, 2005.

[4] B. Gottenbos, H. J. Busscher, H. C. Van Der Mei, and P. Nieuwenhuis, "Pathogenesis and prevention of biomaterial centered infections," *Journal of Materials Science*, vol. 13, no. 8, pp. 717–722, 2002.

[5] J. Hardes, C. Von Eiff, A. Streitbuerger et al., "Reduction of periprosthetic infection with silver-coated megaprostheses in patients with bone sarcoma," *Journal of Surgical Oncology*, vol. 101, no. 5, pp. 389–395, 2010.

[6] L. Ploux, A. Ponche, and K. Anselme, "Bacteria/material interfaces: role of the material and cell wall properties," *Journal of Adhesion Science and Technology*, vol. 24, no. 13-14, pp. 2165–2201, 2010.

[7] K. Vasilev, J. Cook, and H. J. Griesser, "Antibacterial surfaces for biomedical devices," *Expert Review of Medical Devices*, vol. 6, no. 5, pp. 553–567, 2009.

[8] M. Zilberman and J. J. Elsner, "Antibiotic-eluting medical devices for various applications," *Journal of Controlled Release*, vol. 130, no. 3, pp. 202–215, 2008.

[9] R. M. Joyce-Wöhrmann and H. Münstedt, "Determination of the silver ion release from polyurethanes enriched with silver," *Infections*, vol. 27, supplement 1, pp. S46–S48, 1999.

[10] L. Rojo, J. M. Barcenilla, B. Vázquez, R. González, and J. San Román, "Intrinsically antibacterial materials based on polymeric derivatives of eugenol for biomedical applications," *Biomacromolecules*, vol. 9, no. 9, pp. 2530–2535, 2008.

[11] S. Simovic, D. Losic, and K. Vasilev, "Controlled drug release from porous materials by plasma polymer deposition," *Chemical Communications*, vol. 46, no. 8, pp. 1317–1319, 2010.

[12] H. J. Klasen, "A historical review of the use of silver in the treatment of burns. II. Renewed interest for silver," *Burns*, vol. 26, no. 2, pp. 131–138, 2000.

[13] J. M. Schierholz, L. J. Lucas, A. Rump, and G. Pulverer, "Efficacy of silver-coated medical devices," *Journal of Hospital Infection*, vol. 40, no. 4, pp. 257–262, 1998.

[14] A. Airoudj, E. Kulaga, V. Roucoules, and L. Ploux, "Mechanically switchable biocide plasma-polymer coatings for biomaterials," *Advanced Engineering Materials*, vol. 13, no. 10, pp. B360–B368, 2011.

[15] M. Ramstedt, B. Ekstrand-Hammarström, A. V. Shchukarev et al., "Bacterial and mammalian cell response to poly(3-sulfopropyl methacrylate) brushes loaded with silver halide salts," *Biomaterials*, vol. 30, no. 8, pp. 1524–1531, 2009.

[16] A. Coughlan, D. Boyd, C. W. I. Douglas, and M. R. Towler, "Antibacterial coatings for medical devices based on glass polyalkenoate cement chemistry," *Journal of Materials Science*, vol. 19, no. 12, pp. 3555–3560, 2008.

[17] M. Malcher, D. Volodkin, B. Heurtault et al., "Embedded silver ions-containing liposomes in polyelectrolyte multilayers: cargos films for antibacterial agents," *Langmuir*, vol. 24, no. 18, pp. 10209–10215, 2008.

[18] K. Vasilev, V. R. Sah, R. V. Goreham, C. Ndi, R. D. Short, and H. J. Griesser, "Antibacterial surfaces by adsorptive binding of polyvinyl-sulphonate- stabilized silver nanoparticles," *Nanotechnology*, vol. 21, no. 21, Article ID 215102, 2010.

[19] Q. L. Feng, J. Wu, G. Q. Chen, F. Z. Cui, T. N. Kim, and J. O. Kim, "A mechanistic study of the antibacterial effect of silver ions on *Escherichia coli* and *Staphylococcus aureus*," *Journal of Biomedical Material Research A*, vol. 52, no. 4, pp. 662–668, 2000.

[20] W. K. Jung, H. C. Koo, K. W. Kim, S. Shin, S. H. Kim, and Y. H. Park, "Antibacterial activity and mechanism of action of the silver ion in *Staphylococcus aureus* and *Escherichia coli*," *Applied and Environmental Microbiology*, vol. 74, no. 7, pp. 2171–2178, 2008.

[21] I. Sondi and B. Salopek-Sondi, "Silver nanoparticles as antimicrobial agent: a case study on *E. coli* as a model for gram-negative bacteria," *Journal of Colloid and Interface Science*, vol. 275, no. 1, pp. 177–182, 2004.

[22] J. S. Kim, E. Kuk, K. N. Yu et al., "Antimicrobial effects of silver nanoparticles," *Nanomedicine*, vol. 3, no. 1, pp. 95–101, 2007.

[23] S. Pal, Y. K. Tak, and J. M. Song, "Does the antibacterial activity of silver nanoparticles depend on the shape of the nanoparticle? A study of the gram-negative bacterium *Escherichia coli*," *Applied and Environmental Microbiology*, vol. 73, no. 6, pp. 1712–1720, 2007.

[24] J. Hardes, H. Ahrens, C. Gebert et al., "Lack of toxicological side-effects in silver-coated megaprostheses in humans," *Biomaterials*, vol. 28, no. 18, pp. 2869–2875, 2007.

[25] R. Kumar and H. Münstedt, "Silver ion release from antimicrobial polyamide/silver composites," *Biomaterials*, vol. 26, no. 14, pp. 2081–2088, 2005.

[26] D. R. Monteiro, L. F. Gorup, A. S. Takamiya, A. C. Ruvollo-Filho, E. R. D. Camargo, and D. B. Barbosa, "The growing importance of materials that prevent microbial adhesion: antimicrobial effect of medical devices containing silver," *International Journal of Antimicrobial Agents*, vol. 34, no. 2, pp. 103–110, 2009.

[27] M. V .D. Z. Park, A. M. Neigh, J. P. Vermeulen et al., "The effect of particle size on the cytotoxicity, inflammation, developmental toxicity and genotoxicity of silver nanoparticles," *Biomaterials*, vol. 32, no. 36, pp. 9810–9817, 2011.

[28] K. Vasilev, V. Sah, K. Anselme et al., "Tunable antibacterial coatings that support mammalian cell growth," *Nanoletters*, vol. 10, no. 1, pp. 202–207, 2010.

[29] O. Vidal, R. Longin, C. Prigent-Combaret, C. Dorel, M. Hooreman, and P. Lejeune, "Isolation of an *Escherichia coli* K-12 mutant strain able to form biofilms on inert surfaces: involvement of a new ompR allele that increases curli expression," *Journal of Bacteriology*, vol. 180, no. 9, pp. 2442–2449, 1998.

[30] W. Rasband, *ImageJ*, U. S. National Institutes of Health, Bethesda, Md, USA, 1997.

[31] E. Körner, M. H. Aguirre, G. Fortunato, A. Ritter, J. Rühe, and D. Hegemann, "Formation and distribution of silver nanoparticles in a functional plasma polymer matrix and related Ag^+ release properties," *Plasma Processes and Polymers*, vol. 7, no. 7, pp. 619–625, 2010.

[32] K. Lewis, "Riddle of biofilm resistance," *Antimicrobial Agents and Chemotherapy*, vol. 45, no. 4, pp. 999–1007, 2001.
[33] C. Damm, H. Münstedt, A. Rösch et al., "The antimicrobial efficacy of polyamide 6/silver-nano- and microcomposites," *Materials Chemistry and Physics*, vol. 108, no. 1, pp. 61–66, 2008.

Hindawi Publishing Corporation
Journal of Nanomaterials
Volume 2012, Article ID 480626, 5 pages
doi:10.1155/2012/480626

Research Article

Magnetic Nanoparticle Hyperthermia Using Pluronic-Coated Fe_3O_4 Nanoparticles: An *In Vitro* Study

Asahi Tomitaka,[1] Tsutomu Yamada,[2] and Yasushi Takemura[2]

[1] *Institute of Frontier Medical Sciences, Kyoto University, 53 Kawara-cho Shogoin, Sakyo-ku, Kyoto 606-8507, Japan*
[2] *Department of Electrical and Computer Engineering, Yokohama National University, 79-5 Tokiwadai, Hodogaya-ku, Yokohama 240-8501, Japan*

Correspondence should be addressed to Asahi Tomitaka, setougoasahix@gmail.com

Received 13 January 2012; Accepted 16 March 2012

Academic Editor: Krasimir Vasilev

Magnetic nanoparticles are promising materials for hyperthermia treatment. The temperature rise under ac magnetic field, cytotoxicity, and *in vitro* hyperthermia effect of Fe_3O_4 nanoparticles coated with Pluronic f-127 were evaluated in this paper. The Pluronic-coated Fe_3O_4 nanoparticles exhibited no cytotoxic effect on HeLa cells. The optimal magnetic field of Pluronic-coated Fe_3O_4 nanoparticles was 16 kA/m (200 Oe) at the field strength of 210 kHz. Appropriate temperature rise significantly reduced the viability of HeLa cells and induced apoptosis.

1. Introduction

Hyperthermia is a cancer therapy; that is, increasing the temperature of the body or a particular region at temperature higher than 42°C. This hyperthermia treatment has great advantages of being less risky to the body, causing less side effects and providing the possibility of repeating treatment compared to traditional cancer treatment, such as surgical operation, chemotherapy, and radiation therapy. Dewey et al. reported the thermal sensitivity of Chinese hamster ovary (CHO) cells in 1977 [1]. The cells heated at more than 42.5°C greatly reduced their viability according to the temperature.

Magnetic nanoparticles have attracted attention as various biomedical applications including contrast agent for magnetic resonance imaging (MRI), carrier of drug delivery system, and the heat source for hyperthermia [2]. They possess unique properties such as magnetic transportation, magnetic isolation, and self-heating in an ac magnetic field. The magnetic nanoparticles can be injected intravenously and transferred to specific parts of the body with EPR (enhanced permeation and retention) effect and a magnetic field. The tumor is then treated with the heat, which is generated by the magnetic nanoparticles under an external ac magnetic field. Magnetic nanoparticle hyperthermia has great advantages of local treatment with specific targeting and combination therapy with drug delivery system. The temperature of magnetic nanoparticles is controlled by the strength and frequency of the external magnetic field.

In order to apply magnetic nanoparticles for bioapplications, it is significant to keep their biocompatibility and avoid the aggregation of each nanoparticle for the EPR effect and to reduce the chance of obstruction of blood capillaries. We have previously reported the magnetic properties and heat dissipation of Fe_3O_4 nanoparticles coated with polyethylenimine (PEI), oleic acid, and Pluronic F-127 [3]. The Pluronic-coated Fe_3O_4 nanoparticles, the heat dissipation of which was not related to surrounding viscosity and known as biocompatible material, will be suitable for a heat source of hyperthermia. Pluronic is a water-soluble triblock copolymer composed of a hydrophobic central segment of poly(propylene oxide) (PO) flanked by two hydrophilic segments of poly(ethylene oxide) (EO). Pluronic can be represented as EOa-POb-EOa, where a and b are the number of ethylene oxide and propylene oxide units, respectively. Pluronic F-127 contains 200.45 EO units (a = 100) and 65.17 PO units (b = 65) with a molecular weight

of 12,600 Da [4]. In this study, the efficacy of hyperthermia treatment using Pluronic-coated Fe_3O_4 nanoparticles was evaluated.

2. Experiments

2.1. Surface Coating. Fe_3O_4 nanoparticles (particle size of 20–30 nm) were used as samples (Nanostructured & Amorphous Materials, Inc.). The Fe_3O_4 nanoparticles were dispersed in a solution containing 100 mL of 1 mg/mL oleic acid (Nacalai Tesque) and 25 mL of ammonia solution by ultrasonication. This solution was then heated below the boiling point with vigorous stirring at 1,200 rpm for 90 min. The solution was then washed with ethanol four times by magnetic decantation to remove the excess oleic acid, and the sediment was then dried. The dried powders were redispersed in a solution containing 100 mL of Pluronic F-127 with vigorous stirring at 1,200 rpm for 4 h at room temperature. The solution was purified by centrifugation at 3,000 rpm for 15 min. The supernatant was then centrifuged at 10,000 g for 30 min. Finally, the precipitate was collected.

2.2. Heat Dissipation. The temperature rise of Pluronic-coated Fe_3O_4 nanoparticles was measured by applying an ac magnetic field of 4.0–20 kA/m (50–250 Oe) at a frequency of 210 kHz. The samples were dispersed in water. The weight concentrations of these samples were 3 mg/mL. The temperature rise of each sample was measured by optical fiber thermometer.

2.3. Cytotoxicity. A cytotoxicity study of Pluronic-coated Fe_3O_4 nanoparticles was conducted on human cervical carcinoma cells (HeLa cells). HeLa cells were cultured in Dulbecco's modified eagle medium (DMEM; GIBCO) with 10% fetal bovine serum (Equitec-bio, Inc.) and 1% penicillin streptomycin (GIBCO); they were incubated at 37°C in 5% CO_2 atmosphere. HeLa cells were seeded at a density of 2×10^4 cells/well in 24-well plates and incubated at 37°C in a 5% CO_2 atmosphere. After 24 h of incubation, HeLa cells were exposed to 10–500 μg/mL of each nanoparticle dispersed in the medium. The HeLa cells were observed for 3 days after exposure to the nanoparticles. The medium was removed and the nanoparticles were washed with phosphate-buffered saline (PBS). Then the cells were trypsinized and the number of the living cells was counted using Burker-Turk hemocytometer.

2.4. In Vitro Hyperthermia. HeLa cells were subjected to hyperthermia treatment using Pluronic-coated Fe_3O_4 nanoparticles (20–30 nm). HeLa cells were seeded at a density of 5×10^5 cells/well in 30 mmφ dishes and incubated at 37°C in 5% CO_2 atmosphere. After 24 h of incubation, the HeLa cells were exposed to 500 μg/mL of Pluronic-coated Fe_3O_4 nanoparticles dispersed in a medium. Next, the HeLa cells were exposed to an ac magnetic field of 16 kA/m (200 Oe) and 20 kA/m (250 Oe) at 210 kHz for a period of 15–60 min. After the hyperthermia treatment, the medium containing the magnetic nanoparticles was washed with phosphate-buffered saline (PBS) and fresh medium was added. After 24 h of incubation, the cells were trypsinized and the number of the living and dead cells was counted using the Burker-Turk hemocytometer. The viability of the cells was evaluated by the trypan blue method. The viability was calculated by the following equation:

$$\text{Viability } [\%] = \frac{\text{number of living cells [cells]}}{\text{total number of cells [cells]}}. \quad (1)$$

2.5. Apoptosis. After the hyperthermia treatment, the medium containing magnetic nanoparticles was washed with phosphate-buffered saline (PBS) and a fresh medium was added. After 24 h of incubation, the cells were trypsinized and the number of the cells treated under each condition was fixed at the same density. Then, mitochondrial membrane potential and activation of caspase 3 were measured using the Dual Sensor: MitoCasp (Cell Technology Inc.,) and Caspase-Glo 3/7 Assay (Promega), respectively, according to the manufacturers' protocol. The mitochondrial membrane potential dye contains a cationic mitochondrial dye that accumulates in intact mitochondria to emit red fluorescence. Caspase-Glo 3/7 Assay uses a proluminescent substrate containing a DEVD sequence, which is recognized and activated by caspase 3 and caspase 7, and the luminescence signal is proportional to the net activation of caspase 3 and caspase 7.

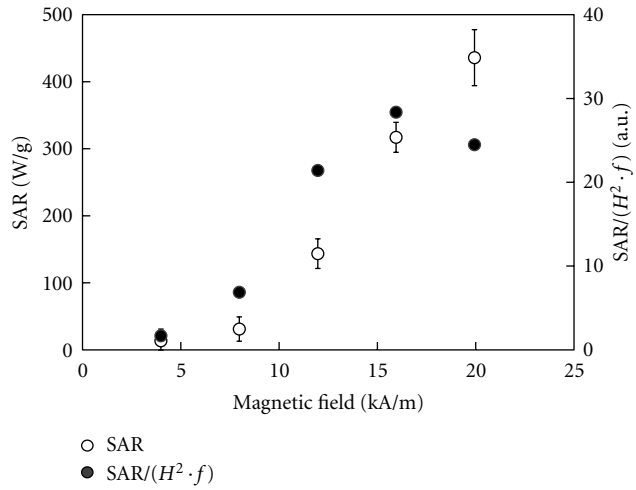

Figure 1: Dependence of magnetic field strength on specific absorption rate (SAR) of Pluronic-coated magnetic nanoparticles (open circles). Energy efficiency of applied magnetic field to generate self-heating (closed circles). The temperature rise was divided by $H^2 \times f$, where H and f are the amplitude and frequency of applied ac magnetic field, respectively. The ac field frequency was 210 kHz, and the amplitude was varied from 4 to 20 kA/m (50 to 250 Oe).

3. Results and Discussion

3.1. Surface Coating. Morphology and hydrodynamic particle size of the Pluronic-coated Fe_3O_4 nanoparticles have been

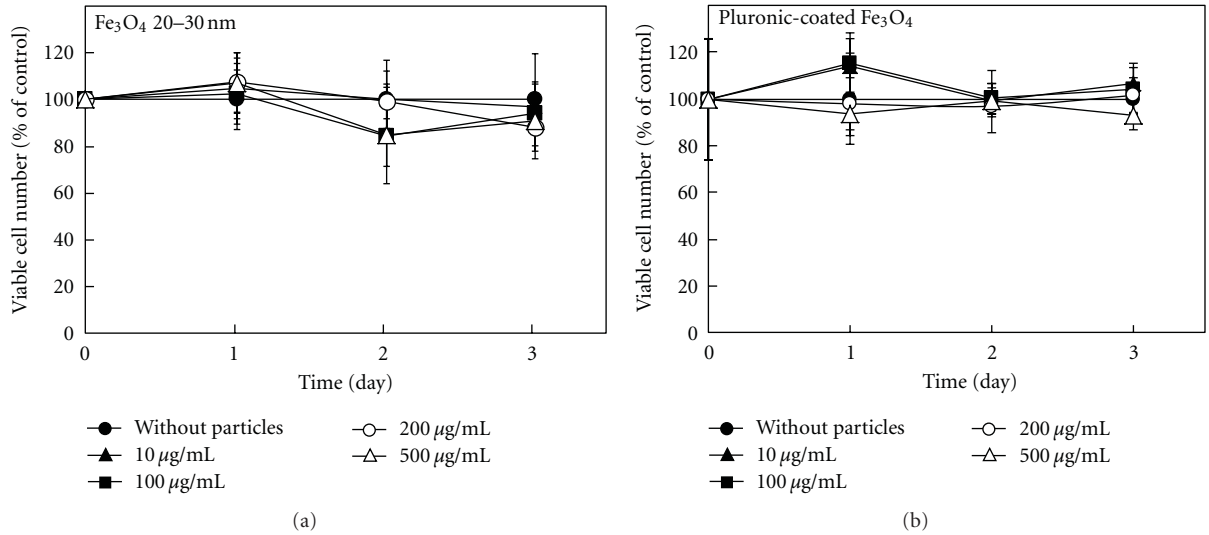

Figure 2: Viable cell number of the HeLa cells treated with Fe_3O_4 nanoparticles and without nanoparticles at concentration of 10–500 μg/mL. (a) uncoated, (b) Pluronic-coated Fe_3O_4 nanoparticles.

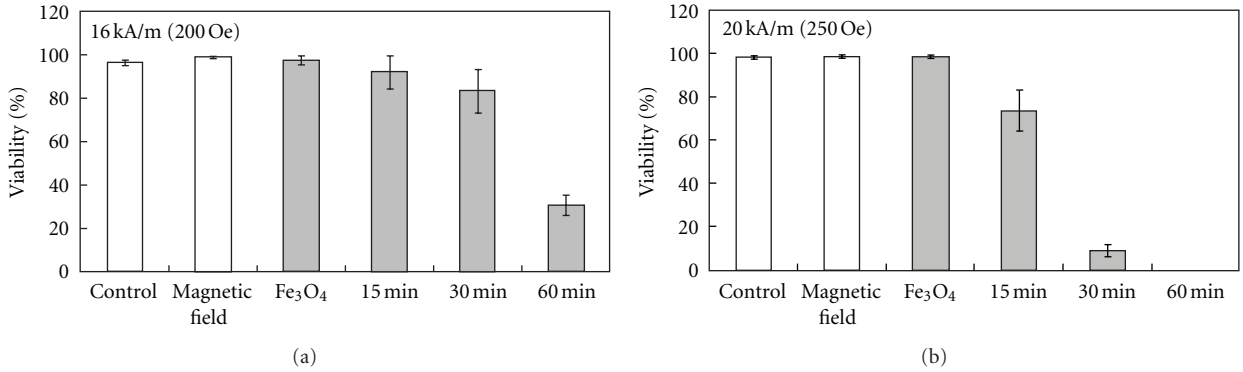

Figure 3: Viability of HeLa cells treated with hyperthermia treatment using the Pluronic-coated Fe_3O_4 nanoparticles at the field strength of (a) 16 kA/m (200 Oe) and (b) 20 kA/m (250 Oe) for 15, 30, and 60 min. $^*P < 0.05$, $^{**}P < 0.01$, $n = 3$.

reported previously [3]. The hydrodynamic particle size of the Pluronic-coated Fe_3O_4 nanoparticles was 181 nm. The uncoated magnetic nanoparticles formed large clusters with hydrodynamic sizes in the order of tens of micrometers.

3.2. Heat Dissipation. Temperature rise of the Pluronic-coated Fe_3O_4 nanoparticles under an ac magnetic field was measured. The magnetic field strength was fixed at 16 kA/m (200 Oe) and 20 kA/m (250 Oe), and frequency was 210 kHz. The temperature reached at 45°C and 51°C within 30 min under ac magnetic fields of 16 kA/m (200 Oe) and 20 kA/m (250 Oe), respectively. Figure 1 shows the specific absorption rate (SAR) of Pluronic-coated Fe_3O_4 nanoparticles and the efficiency of applied energy to generate self-heating. The ability of heat dissipation of magnetic nanoparticles is usually described as the specific absorption rate (SAR). The SAR values (W/g) were calculated by the following equation:

$$\mathrm{SAR} = C\frac{\Delta T}{\Delta t}\frac{1}{m}, \tag{2}$$

where C is the specific heat capacity, m the weight of the sample, and $\Delta T/\Delta t$ the initial slope of the time-dependent temperature rise. The specific heat capacity of the sample is almost that of water $C \approx C_{\mathrm{water}} = 4.18\,\mathrm{Jg}^{-1}\,\mathrm{K}^{-1}$.

The efficiency of applied energy was determined by the temperature rise divided by $H^2 \times f$, where H and f are the amplitude and frequency of applied ac magnetic field. The energy applied to generate a magnetic field is proportional to the product of H^2 and f. Figure 1 shows that the optimum field strength to generate heat was 16 kA/m (200 Oe) at a frequency of 210 kHz for the Pluronic-coated Fe_3O_4 nanoparticles. Therefore, the magnetic field strength of 16 kA/m (200 Oe) will be suitable for hyperthermia treatment using the Pluronic-coated Fe_3O_4 nanoparticles.

3.3. Cytotoxicity. The viable cell number of the HeLa cells exposed to the uncoated and Pluronic-coated Fe_3O_4 nanoparticles is shown in Figure 2. The HeLa cells exposed to the uncoated Fe_3O_4 nanoparticles exhibited a viable cell number of higher than 84%. Fe_3O_4 nanoparticles are widely

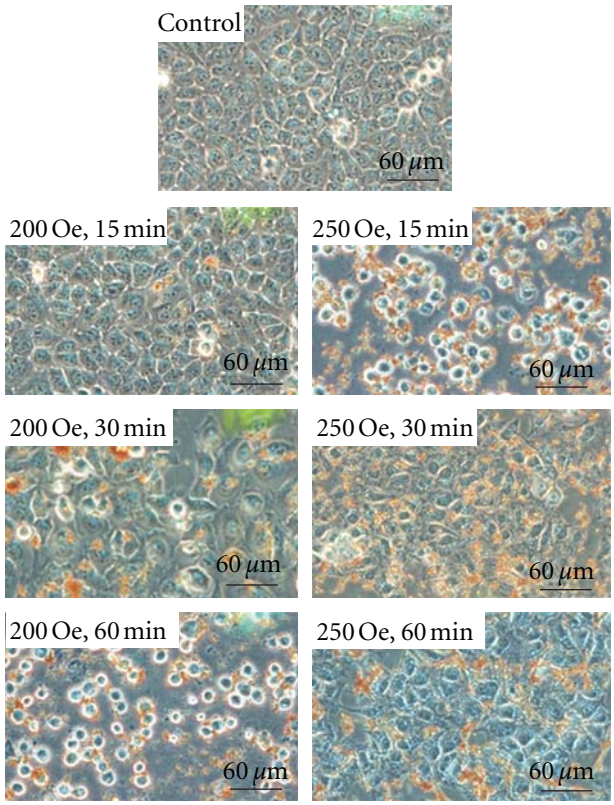

Figure 4: Morphology of HeLa cells treated with hyperthermia treatment using Pluronic-coated Fe_3O_4 nanoparticles at the field strength of 16 kA/m (200 Oe) and 20 kA/m (250 Oe) for 15, 30, and 60 min.

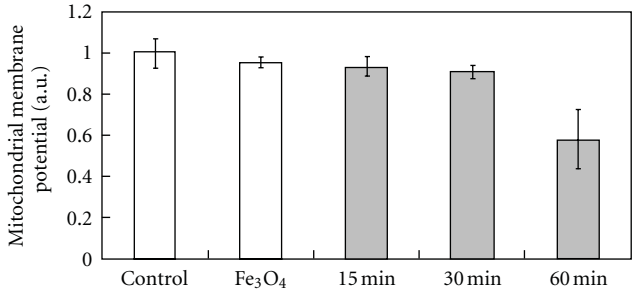

Figure 5: Mitochondrial membrane of the HeLa cells treated with hyperthermia using the Pluronic-coated Fe_3O_4 nanoparticles at the field strength of 16 kA/m (200 Oe) for 15, 30, and 60 min. They are normalized to untreated control cells.

accepted as biocompatible materials, but the cytotoxicity of nanoparticles is not fully understood. The viability reduction of cells exposed to uncoated Fe_3O_4 nanoparticles has been reported, while no cytotoxicity was found with the exposure of Fe_3O_4 nanoparticles coated with biocompatible substances [5, 6]. On the other hand, no significant difference in the cytotoxicity of uncoated nanoparticles between coated Fe_3O_4 nanoparticles has been reported [7]. These differences in cytotoxicity may be due to the use of different cell lines and particle size.

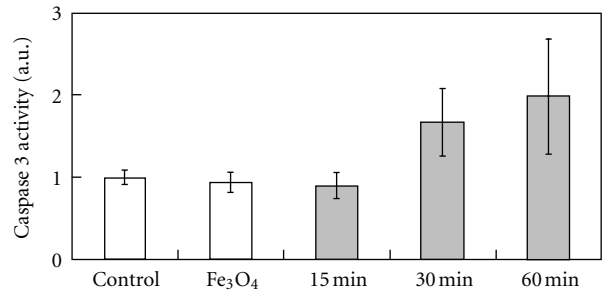

Figure 6: Caspase 3 activity of the HeLa cells treated with hyperthermia using the Pluronic-coated Fe_3O_4 nanoparticles at the field strength of 16 kA/m (200 Oe) for 15, 30, and 60 min. They are normalized to untreated control cells.

No cytotoxic effect was observed for the HeLa cells exposed to the Pluronic-coated Fe_3O_4 nanoparticles even at the concentration of 500 μg/mL. Pluronics have attracted attention for use in drug delivery systems because of their biocompatibility [8, 9] and long blood-circulation time [10, 11]. Our results corresponded to these reports.

3.4. In Vitro Hyperthermia. Viability and morphology of HeLa cells treated with magnetic nanoparticle hyperthermia are shown in Figures 3 and 4, respectively. The viability of HeLa cells treated with hyperthermia at the field strength of 16 kA/m (200 Oe) for 15 min, 30 min, and 60 min was 90%, 83%, and 46%, respectively. Hyperthermia treatment significantly reduced the viability of the HeLa cells. The HeLa cells were observed to shrink with hyperthermia treatment for 30 min and 60 min. Lower viability was observed for the HeLa cells treated at the field strength of 20 kA/m (250 Oe). The viability of HeLa cells treated for 15 min, 30 min, and 60 min was 74%, 9%, and 0%, respectively. HeLa cells exposed to the magnetic field for more than 30 min did not shrink.

3.5. Apoptosis. Mitochondrial membrane potential and caspase 3 activity normalized in untreated control cells are shown in Figures 5 and 6, respectively. In Figure 5, a clear collapse of the mitochondrial membrane potential is observed in the case of hyperthermia treatment for 60 min. Figure 6 shows that caspase 3 activity increased in HeLa cells treated for 30 min and 60 min.

Apoptosis can be triggered by various stimuli such as UV radiation, chemotherapy, and heat. An apoptotic cell changes its morphology. The cell shrinks, its chromatin condenses, and fragmentation of nucleus occurs [12]. There are two main apoptotic pathways: the extrinsic (death receptor) pathway and the intrinsic (mitochondrial) pathway. Mitochondrial permeability transition is an important step in the induction of the intrinsic apoptosis pathway. During this process, the mitochondrial membrane potential collapses. Activation of caspase 3 is a downstream effector of the apoptotic pathway. These results indicate that hyperthermia treatment using the Pluronic-coated Fe_3O_4 nanoparticles mediates apoptosis through the mitochondrial pathway.

Hyperthermia treatment is suitable for inducing both necrosis and apoptosis depending on the temperature. Cells heated at temperatures in the range of 41°C to 47°C begin to show signs of apoptosis, whereas increasing temperatures (above 50°C) are associated with decreased apoptosis and increased necrosis [13]. Our results confirm that apoptosis is induced by thermal treatment at 45°C. HeLa cells heated at 45°C showed shrinkage, although those heated at 51°C did not show shrinkage (Figure 4). Hyperthermia treatment at a higher temperature might induce necrosis instead of apoptosis.

4. Conclusion

The temperature rise under ac magnetic field, cytotoxicity, and *in vitro* hyperthermia effect of Pluronic-coated Fe_3O_4 nanoparticles was evaluated in this study. Appropriate temperature rise was achieved under an ac magnetic field of 16 kA/m (200 Oe) and 20 kA/m (250 Oe) at 210 kHz. No cytotoxic effect was observed on the HeLa cells. *In vitro* hyperthermia treatment using Pluronic-coated Fe_3O_4 nanoparticles significantly reduced the viability of HeLa cancer cells. The collapse of mitochondria membrane potential and caspase 3 activity were observed. Hyperthermia using the Pluronic-coated Fe_3O_4 nanoparticles induced cell death related to apoptosis through mitochondrial pathway.

Acknowledgment

This paper was supported by a Grant-in-Aid for JSPS Fellows.

References

[1] W. C. Dewey, L. E. Hopwood, S. A. Sapareto, and L. E. Gerweck, "Cellular responses to combinations of hyperthermia and radiation," *Radiology*, vol. 123, no. 2, pp. 463–474, 1977.

[2] M. Arruebo, R. Fernandez-Pacheco, M. R. Ibarra, and J. Santamaria, "Magnetic nanoparticles for drug delivery," *Nanotoday*, vol. 2, pp. 22–32, 2007.

[3] A. Tomitaka, K. Ueda, T. Yamada, and Y. Takemura, "Heat dissipation and magnetic properties of surface-coated Fe_3O_4 nanoparticlesfor biomedical applications," *Journal of Magnetism and Magnetic Materials*. In press.

[4] T. K. Jain, S. P. Foy, B. Erokwu, S. Dimitrijevic, C. A. Flask, and V. Labhasetwar, "Magnetic resonance imaging of multifunctional pluronic stabilized iron-oxide nanoparticles in tumor-bearing mice," *Biomaterials*, vol. 30, no. 35, pp. 6748–6756, 2009.

[5] A. K. Gupta and M. Gupta, "Cytotoxicity suppression and cellular uptake enhancement of surface modified magnetic nanoparticles," *Biomaterials*, vol. 26, no. 13, pp. 1565–1573, 2005.

[6] M. Kim, J. Jung, J. Lee, K. Na, S. Park, and J. Hyun, "Amphiphilic comblike polymers enhance the colloidal stability of Fe_3O_4 nanoparticles," *Colloids and Surfaces B*, vol. 76, no. 1, pp. 236–240, 2010.

[7] D. H. Kim, K. N. Kim, K. M. Kim, and Y. K. Lee, "Targeting to carcinoma cells with chitosan- and starch-coated magnetic nanoparticles for magnetic hyperthermia," *Journal of Biomedical Materials Research. Part A*, vol. 88, no. 1, pp. 1–11, 2009.

[8] J. Qin, S. Laurent, Y. S. Jo et al., "A high-performance magnetic resonance imaging T_2 contrast agent," *Advanced Materials*, vol. 19, no. 14, pp. 1874–1878, 2007.

[9] J. Y. Kim, W. I. Choi, Y. H. Kim et al., "In-vivo tumor targeting of pluronic-based nano-carriers," *Journal of Controlled Release*, vol. 147, no. 1, pp. 109–117, 2010.

[10] M. A. Morales, T. K. Jain, V. Labhasetwar, and D. L. Leslie-Pelecky, "Magnetic studies of iron oxide nanoparticles coated with oleic acid and Pluronic block copolymer," *Journal of Applied Physics*, vol. 97, no. 10, Article ID 10Q905, pp. 1–3, 2005.

[11] T. K. Jain, J. Richey, M. Strand, D. L. Leslie-Pelecky, C. A. Flask, and V. Labhasetwar, "Magnetic nanoparticles with dual functional properties: drug delivery and magnetic resonance imaging," *Biomaterials*, vol. 29, no. 29, pp. 4012–4021, 2008.

[12] A. Gewies, "Introduction to Apoptosis," *ApoReview*, pp. 1–26, 2003.

[13] P. Cherukuri, E. S. Glazer, and S. A. Curley, "Targeted hyperthermia using metal nanoparticles," *Advanced Drug Delivery Reviews*, vol. 62, no. 3, pp. 339–345, 2010.

Hindawi Publishing Corporation
Journal of Nanomaterials
Volume 2012, Article ID 731382, 8 pages
doi:10.1155/2012/731382

Research Article

Electrospun Borneol-PVP Nanocomposites

Xiao-Yan Li, Xia Wang, Deng-Guang Yu, Shuai Ye, Qi-Kun Kuang, Qing-Wen Yi, and Xin-Zhe Yao

School of Materials Science and Engineering, University of Shanghai for Science and Technology, Shanghai 200093, China

Correspondence should be addressed to Xiao-Yan Li, lixiaoyan@usst.edu.cn and Deng-Guang Yu, ydg017@usst.edu.cn

Received 13 January 2012; Accepted 5 March 2012

Academic Editor: Haifeng Chen

The present work investigates the validity of electrospun borneol-polyvinylpyrrolidone (PVP) nanocomposites in enhancing drug dissolution rates and improving drug physical stability. Based on hydrogen bonding interactions and *via* an electrospinning process, borneol and PVP can form stable nanofiber-based composites. FESEM observations demonstrate that composite nanofibers with uniform structure could be generated with a high content of borneol up to 33.3% (w/w). Borneol is well distributed in the PVP matrix molecularly to form the amorphous composites, as verified by DSC and XRD results. The composites can both enhance the dissolution profiles of borneol and increase its physical stability against sublimation for long-time storage by immobilization of borneol molecules with PVP. The incorporation of borneol in the PVP matrix weakens the tensile properties of nanofibers, and the mechanism is discussed. Electrospun nanocomposites can be alternative candidates for developing novel nano-drug delivery systems with high performance.

1. Introduction

Electrospinning is a popular procedure in scientific researches due to the ease of implementation, the cost-effectiveness of the process, and the unique properties and potential applications of the resultant nanofibers [1–4]. It has a strong capability of producing nanofibers of polymers and some small molecules such as phospholipids and cyclodextrin, of giving the nanofibers with secondary structural characteristics by copying the spinnerets such as coaxial and side-by-side, and of generating polymer-based composites through the interactions between the filament-forming polymer matrix and the functional ingredients [5–9].

Nanocomposites have drawn considerable attentions because of the ability to produce high-performance materials with enhanced or novel properties [10, 11]. As a simple one-step top-down process for preparing one-dimensional (1D) nanofibers, electrospinning exhibits great capability in preparing nanoscale polymer composites owing to the tremendous rapid drying process, often in a time scale of 10^{-2} s [12–16]. It has been demonstrated that electrospun nanofiber composites can enhance the functions of active ingredients and even achieve new functions by taking advantages of their unique properties, such as continuous three-dimensional web structure, thin diameter, large surface area, and high porosity [17–19].

Borneol, a compound derived from *ryobalanops aromatica* (a tree that belongs to the teak family), is a common ingredient in many traditional Chinese herbal formulas. Borneol has a wide range of uses. It aids the digestive system by stimulating the production of gastric juices; tones the heart and improves circulation, treats bronchitis, coughs and colds, can relieve pain caused by rheumatic diseases and sprains, reduces swelling, relives stress, and can be used as a tonic to promote relaxation and reduce exhaustion. In some parts of the world, it is even used as an insect repellant. However, borneol has very poor water solubility, poor physical stability due to easy sublimation, and side effect of resulting in irritation [20–22].

Based on above-mentioned knowledge, we presently investigate that electrospinning is exploited to prepare composites of borneol and hydrophilic excipients in the form of nanofibers. Polyvinylpyrrolidone was selected as the filament-forming matrix because it has been broadly reported to

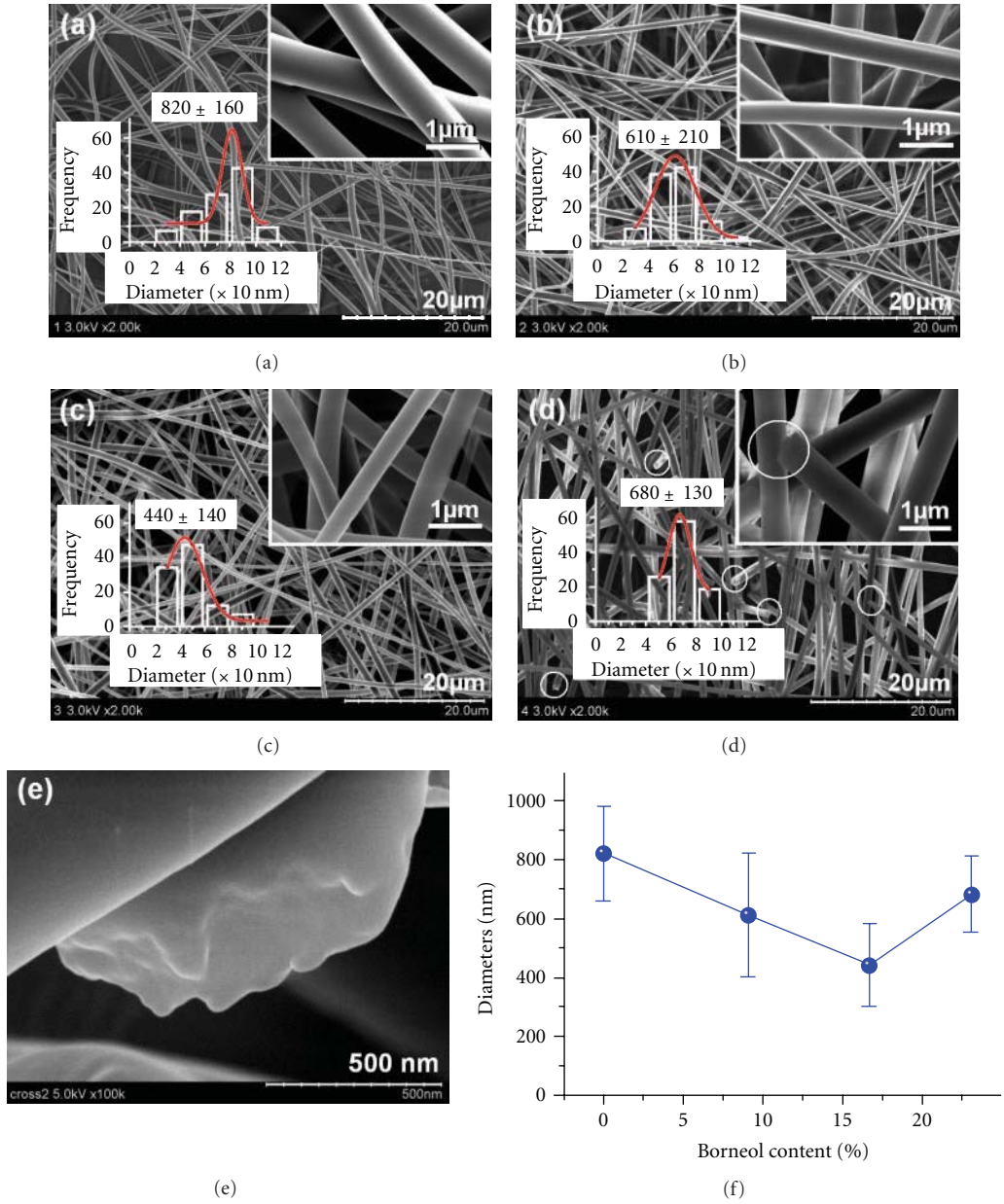

(a) (b) (c) (d) (e) (f)

Figure 1: FESEM images: (a)–(d) surface morphology of the composite nanofibers F0, F1, F2, and F3, respectively; (e) cross-section of the composite nanofibers F3; (f) relationship between fiber diameter and borneol content.

be used for enhancing solubility of a wide variety of poorly water-soluble drug and it has good electrospinnability in a series of typical organic solvents such as methanol, ethanol, chloroform, and N, N-dimethylacetamide [23–26].

2. Experimental

2.1. Materials. Borneol (purity over 95%) was purchased from Shanghai Winherb Medical S & T Development Co., Ltd (Shanghai, China). Polyvinylpyrrolidone K60 (PVP K60, $M = 360,000$) was obtained from the Shanghai Yunhong Pharmaceutical Aids and Technology Co., Ltd. (Shanghai, China). Anhydrous ethanol was provided by the Sinopharm Chemical Reagent Co., Ltd. All other chemicals used were analytical grade, and ultra-high-quality water was used.

2.2. Preparation

Preparation of Spinning Solutions. Borneol and the polymer PVP K60 were dissolved in ethanol in turn at the ambient temperature 21°C. The concentration of PVP was fixed at 10 (w/v)%. Four types of spinning solution with varied concentrations of borneol 0, 1 (w/v)%, 2 (w/v)%, and 5 (w/v)% (Table 1) were prepared, and the composite nanofiber mats

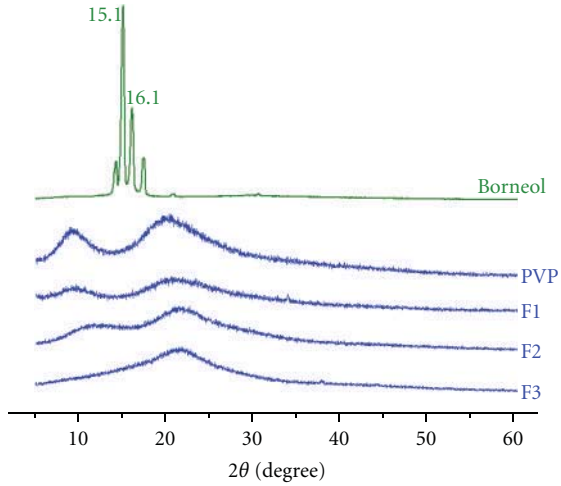

Figure 2: X-ray diffraction patterns of the components (borneol and PVP) and their nanofibers with different ratio of borneol to PVP.

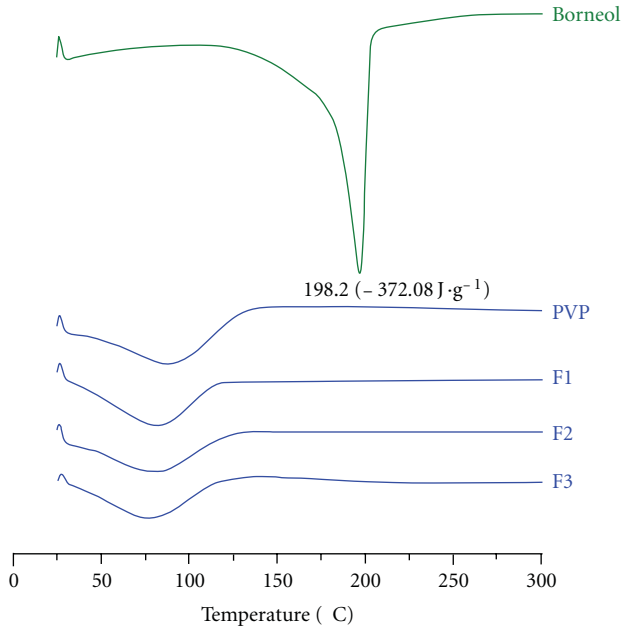

Figure 3: DSC thermograms of the components (borneol and PVP) and their nanofibers with different ratio of borneol to PVP.

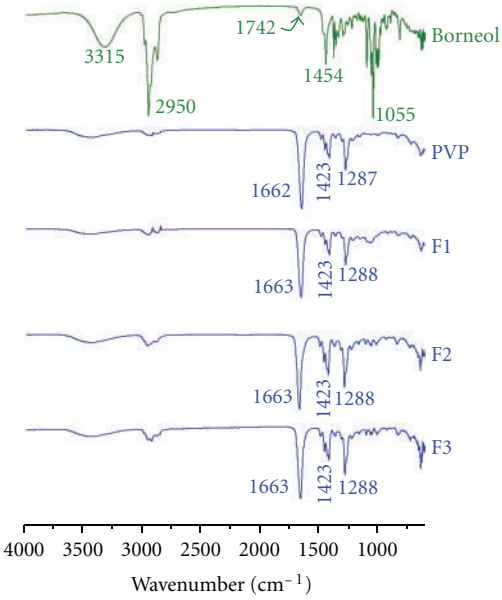

Figure 4: ATR-FTIR spectra of the components (borneol and PVP) and their nanofibers with different ratio of borneol to PVP.

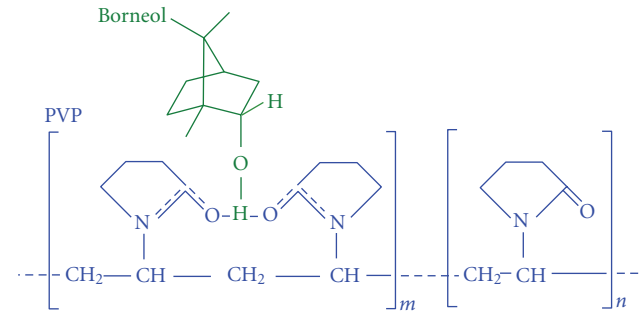

Figure 5: Molecular structures of the components (borneol and PVP) and the hydrogen bonding between them.

were denoted as F0, F1, F2, and F3, respectively. Mechanical stirring was applied for 1 h to obtain homogeneous co-dissolved spinning solutions. The solutions were degassed with a SK5200H ultrasonator (350W, Shanghai Jinghong Instrument Co., Ltd. Shanghai, China) for 10 minutes before electrospinning.

Electrospinning Process. A high-voltage power supply (Shanghai Sute Electrical CO., Ltd., Shanghai, China) was used to provide high voltages in the range of 0–60 kV. To avoid carrying any air bubbles, spinning solutions were carefully loaded in a 10 mL syringe to which a stainless steel capillary metal-hub needle was attached. The inside diameter of the metal needle was 0.5 mm. The positive electrode of the high-voltage power supply was connected to the needle tip and the grounded electrode was linked to a metal collector wrapped with aluminum foil.

The electrospinning process was carried out under ambient conditions (21 ± 2°C and relative humidity 61 ± 3%). A fixed electrical potential of 12 kV was applied across a fixed distance of 15 cm between the tip, and the collector. The feed rate of solutions was controlled at 2.0 mL·h^{-1} by means of a single syringe pump (KDS100, Cole-Parmer, Vernon Hills, IL, USA).

2.3. Characterization. The morphology of the surface, cross-sections of the nanofiber mats, and the casting films were assessed using a S-4800 field emission scanning electron microscope (FESEM) (Hitachi, Japan). The average fiber diameter was determined by measuring diameters of fibers at over 100 points from FESEM images using NIH Image J software (National Institutes of Health).

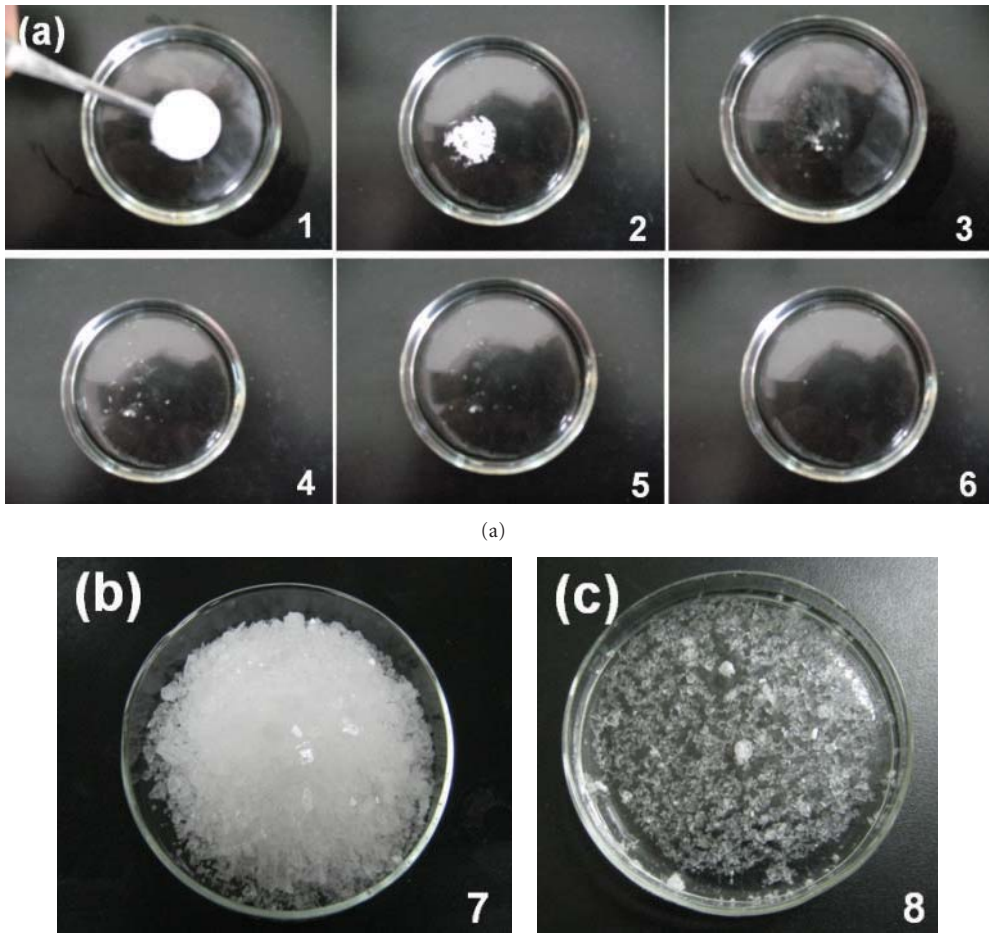

Figure 6: Dissolving tests: (a) photographs of the disintegrating process of F3, the fast-dissolving process of F3 is shown in sequence from 1 to 6; (b) pure borneol particle; (c) the dissolving status of borneol.

Table 1: Preparation conditions for the borneol-PVP nanocomposites.

	F0	F1	F2	F3
C_{PVP}[a] (w/v%)		10		
C_b[b] (w/v%)	0	1	2	5
P_b[c] (w/w%)	0	9.1	16.7	33.3

[a] C_{PVP}: concentration of PVP in spinning solutions.
[b] C_b: concentration of borneol in spinning solutions.
[c] P_b: percentage borneol in the nanofibers, $P_b = C_b/(C_{PVP} + C_b) \times 100\%$.

The differential scanning calorimetry (DSC) analyses were carried out using an MDSC 2910 differential scanning calorimeter (TA Instruments Co., USA). Sealed samples were heated at $10^\circ C \cdot min^{-1}$ from 21 to 300°C. The nitrogen gas flow rate was $40\,mL \cdot min^{-1}$.

X-ray diffraction analyses (XRD) were obtained on a D/Max-BR diffractometer (Rigaku, Japan) with Cu Kα radiation in the 2θ range of 5–60° at 40 mV and 300 mA.

Attenuated total reflectance Fourier transform infrared (ATR-FTIR) analysis was carried out on a Nicolet-Nexus 670 FTIR spectrometer (Nicolet Instrument Corporation, Madison, USA) over the range 500–4000 cm^{-1} and a resolution of 2 cm^{-1}.

2.4. Properties of the Borneol-PVP Nanofiber Mats. To determine the effect of composites in improving borneol physical stability, a comparison study was conducted. 50 mg of borneol particles (pulverized to pass through a 125 μm mesh sieve) fiber mats containing 50 mg borneol (i.e., 550 mg fibers F1, 300 mg fibers F2 and 150 mg fibers F3) were placed on the petri dishes in the atmosphere. Their weights were measured every 24 h.

A petri dish of water was used to demonstrate the speed of the dissolving process of the borneol-PVP nanofiber mats. The dissolving processes were recorded at 30 frames per second with a digital video recorder (Canon PowerShot A490, Tokyo, Japan).

Tensile tests were measured according to ASTM D882 using a universal testing machine (Instron5566, Instron, Canton, MA). All samples were cut to the standard dumbbell shape, conditioned overnight (21 ± 1°C, relative humidity of 65 ± 2%) before testing.

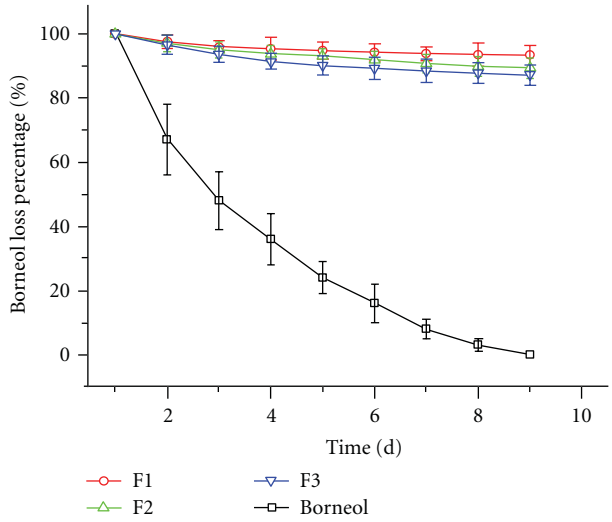

FIGURE 7: Weight loss of pure borneol and their nanofibers with different ratio of borneol to PVP in the atmosphere.

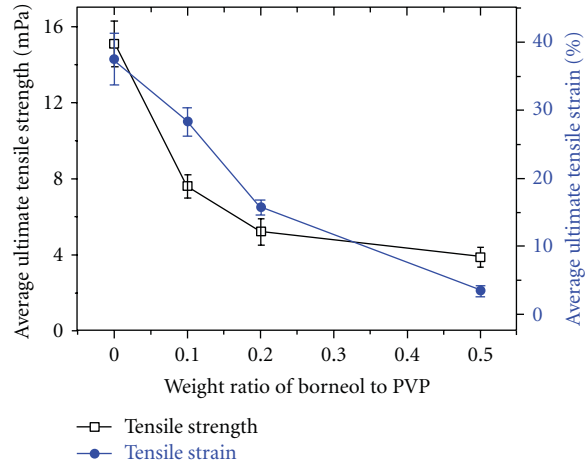

FIGURE 8: Tensile properties of electrospun borneol-PVP nanocomposite fibers with different ratio of borneol to PVP.

3. Results and Discussion

3.1. Morphology. Figures 1(a)–1(d) show FESEM images of PVP nanofibers with a content of borneol at 0% (F0), 9.1% (F1), 16.7% (F2), and 33.3% (F3) (w/v), respectively. All the four types of nanofibers have uniform structures without beads-on-a-string morphology, they had smooth surfaces, and the matrix was free of any separating particles. However, the fibers F3 were very crisp, as verified by circle in Figure 1(d) in which the cross-sections of nanofibers should be generated during the sampling process.

Figure 1(e) shows FESEM images of the cross-section of the composite nanofibers F3. It is clear that there are no apparent particles within them, indicating that no phase separating had occurred during electrospinning. This also suggests that borneol molecules are uniformly distributed throughout the PVP matrix.

As the concentrations of borneol increased, the average diameters of the nanofibers gradually decreased (F0 to F1 and F2). The addition of borneol in PVP solutions can increase their conductivities and thereby enhanced the electrical drawing effects on the jet fluids, resulting thinner nanofibers [12]. However, when the drug loading was further increased, the average diameters of nanofibers F3 increased (F3). As the concentration of borneol further increased, the solution viscosity also increased, and this counteracted the influence of conductivity increases and gradually had a greater influence on nanofiber diameter compared to electrical forces [27]. The relationship between fiber diameter and borneol content is shown in Figure 1(f).

3.2. Physical Status of the Components in the Electrospun Fibers. DSC and XRD tests were undertaken to determine the physical status of borneol in the composite nanofibers. As shown in Figure 2, the presence of distinct peaks in the XRD patterns indicated that borneol was present as crystalline materials with characteristic diffraction peaks at 15.1° and 16.1°. The PVP diffraction exhibits a diffused background pattern with two diffraction halos indicating that the polymer is amorphous. In respect to the composite nanofibers F1 to F3, the characteristic peaks of borneol were absent. This suggests that borneol were no longer present as crystalline material, but was converted into an amorphous state.

The DSC thermograms are shown in Figure 3, and the DSC curve of pure borneol exhibited a single endothermic response corresponding to melting points of 198.2°C ($-372.08\ J \cdot g^{-1}$). As an amorphous polymer PVP K60 did not show any fusion peaks or phase transitions, apart from a broad endotherm, this being due to dehydration, which lies between 80 and 120°C and with a peak at 85°C. DSC thermograms of the composite nanofibers did not show any melting peaks of borneol. All the borneol-PVP composite nanofibers had a broad endotherm ranging from about 60 to 100°C. The results form DSC and XRD similarly demonstrated that borneol was no longer present as a crystalline material but had been converted into amorphous composites with matrix PVP.

3.3. The Secondary Interactions among the Components. The compatibility among the components is essential for producing high quality and the stability of the composite nanofibers. Often the second-order interactions such as hydrogen bonding, electrostatic interactions, and hydrophobic interactions would improve their compatibility [12]. Each borneol molecule has one –OH group whereas PVP molecules have numerous –C=O groups. So they can form composites with borneol acting as proton donors and PVP molecules acting as proton receptors.

This can be as verified by the ATR-FTIR spectra in which sharp peaks were visible for pure crystalline borneol at 2950, 1454, and 1055 cm^{-1} (Figure 4). However, all the peaks for borneol disappeared in the composite nanofibers when samples were run in the ATR-FTIR spectra, jointly demonstrating that hydrogen bonding occurred (Figure 5).

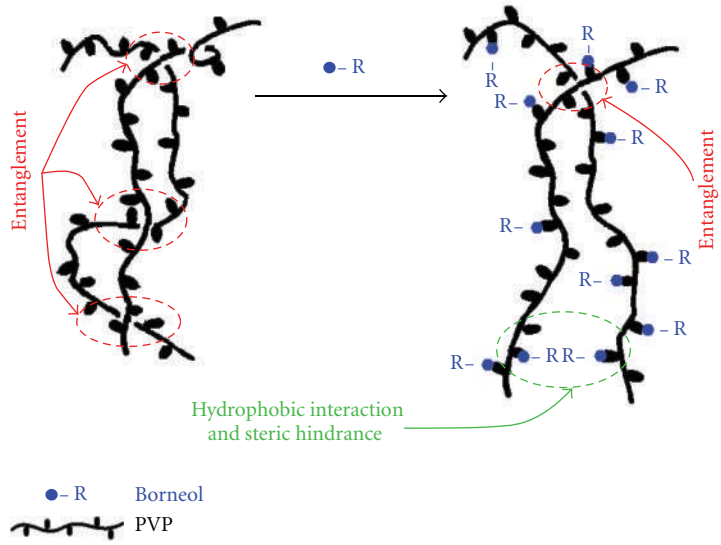

Figure 9: Influence of borneol on the properties of PVP matrix nanofibers.

By the way, there is a tiny peak of 1742 cm^{-1} in spectra of borneol in Figure 4, reflecting that some borneol had been oxidized to camphor.

Electrospinning is not only a useful tool for fabricating 1D polymer nanofibers, but also an excellent process for generating composites with the functional gradients dispersing on the filament-forming polymer matrix molecularly [7, 28]. Here, PVP can provide functional groups for "anchoring" borneol to amorphize them during the fast drying electrospinning process. Only the rapid evaporation of the solvent and the favorable interactions between the ingredients that resulted in the nanofiber composites, in which borneol molecules were distributed through the PVP matrix with their physical state in the liquid solutions to be propagated into the solid nanofibers and lose the original crystal state as pure materials.

Discs with a diameter of 16 cm were cut from the composite nanofiber mats F0 to F3 for fast dissolving tests. Pure borneol particles were used as controls. Shown in Figure 6(a) is a typical disintegrating process of nanofiber F3, and Figures 6(b) and 6(c) show the borneol particles and their insolubility in water. The dissolution of F3 cost 14.5 ± 2.4 s ($n = 6$). The average disappearance times for nanofiber mats F0 to F2 in water were 13.8 ± 1.2 s, 14.3 ± 2.2 s, and 14.3 ± 2.6 s, respectively. The disintegrating times were not significantly different statistically ($P > 0.05$, paired t-test) between the pure PVP nanofibers and the borneol-contained nanofibers, suggesting that the poorly water-soluble borneol can be "led" to quickly dissolve by hydrophilic PVP molecules through their composites. The 3D continuous web structure, the big surface resulting from the small diameter of nanofibers, and the amorphous status of borneol in the PVP matrix synergistically acted to promote the fast dissolution of borneol.

Shown in Figure 7 is the weight loss of the borneol particles and its electrospun composites. The 50 mg borneol particle totally disappeared in the ninth day, whereas all the composites still immobilized over 92% of the contained borneol. The hydrogen bonding between PVP and borneol effectively kept the drug from sublimation from the composites, demonstrating that the nanofiber mats could greatly increase borneol physical stability.

The ultimate tensile strength and tensile strain for all the electrospun borneol/PVP nanofibrous membranes with various borneol contents were tested and summarized (Figure 8). This process characterises the relationship between the average ultimate tensile strength, average ultimate tensile strain, and borneol content. The neat PVP nanofibers showed highest tensile strain. Increasing the weight ratio of borneol showed a decrease in the average tensile strength.

PVP is a linear polymer and has good electrospinnability. When borneol is added to PVP solutions, it is able to interact with PVP molecules through hydrogen bonding. The PVP and borneol molecules together are likely to behave like branched polymers the hydrophobic interactions and stereic hindrance resulting from the branched-borneol would change the nanofibers' matrix PVP chain conformation and PVP-PVP molecular interactions and so decreasing their direct entanglements (Figure 9).

Thus, the presence of borneol affects the stiffness of the PVP main chains and distributes the stretching properties in the chains of PVP, and the disturbance was more significant with the higher addition percentage of borneol, resulting in the obvious decrease of the average tensile strength and strain of borneol-PVP composite nanofiber mats. These results confirm observation obtained from FESEM and also the results of FT-IR studies.

4. Conclusions

With hydrophilic polymer PVP as the filament-firming matrix, several borneol-PVP nanocomposites with varied drug content have been successfully prepared using a single

fluid electrospinning process. FESEM observations demonstrate that composite nanofibers with uniform structure could be generated with a high content of borneol up to 33.3% (w/w). Borneol was well distributed in the PVP matrix molecularly to form the amorphous composites, as verified by DSC and XRD results. The composites effectively enhanced the dissolution profiles of borneol within a time period of 15 s and they were also able to increase borneol physical stability against sublimation for long-time storage by immobilization of borneol molecules with PVP through hydrogen bonding. The incorporation of borneol in the PVP matrix weakens the tensile properties of nanofibers. The present strategy shows an avenue that a wide variety of volatile functional active pharmaceutical ingredients (no matter liquid or solid substance) can be immobilized using electrospun nanofibers for easy development of novel nanodosage form.

Acknowledgments

This work was supported by the scientific starting funds for young teachers of the University of Shanghai for Science and Technology (no. 10-00-310-001), Zwick/Roell innovation project of college student fund, and Grant 10JC1411700 from the Science and Technology Commission of Shanghai Municipality.

References

[1] T. Lin and X. Wang, *Encyclopedia of Nanoscience and Nanotechnology*, edited by H. S. Nalwa, American Scientific, Los Angeles, Calif, USA, 2nd edition, 2011.

[2] L. Ji, Z. Lin, A. Medford, and X. Zhang, "In-situ encapsulation of nickel particles in electrospun carbon nanofibers and the resultant electrochemical performance," *Chemistry A*, vol. 15, no. 41, pp. 10718–10722, 2009.

[3] H. Niu, J. Zhang, Z. Xie, X. Wang, and T. Lin, "Preparation, structure and supercapacitance of bonded carbon nanofiber electrode materials," *Carbon*, vol. 49, no. 7, pp. 2380–2388, 2011.

[4] X. Wang, H. Niu, X. Wang, and T. Lin, "Needleless electrospinning of fine and uniform nanofibers using spiral coil spinnerets," *Journal of Nanomaterials*, vol. 2012, Article ID 785920, 9 pages, 2012.

[5] D. G. Yu, C. Branford-White, G. R. Williams et al., "Self-assembled liposomes from amphiphilic electrospun nanofibers," *Soft Matter*, vol. 7, pp. 8239–8246, 2011.

[6] D. G. Yu, C. Branford-White, S. W. A. Bligh, K. White, N. P. Chatterton, and L. M. Zhu, "Improving polymer nanofiber quality using a modified co-axial electrospinning process," *Macromolecular Rapid Communications*, vol. 32, no. 9-10, pp. 744–750, 2011.

[7] D. G. Yu, L. M. Zhu, C. Branford-White et al., "Solid dispersions in the form of electrospun core-sheath nanofibers," *International Journal of Nanomedicine*, vol. 6, pp. 3271–3280, 2011.

[8] D. G. Yu, P. Lu, C. Branford-White, J. H. Yang, and X. Wang, "Polyacrylonitrile nanofibers prepared using co-axial electrospinning with LiCl solution as sheath fluid," *Nanotechnology*, vol. 22, Article ID 435301, 7 pages, 2011.

[9] D. G. Yu, K. White, J. H. Yang, X. Wang, W. Qian, and Y. Li, "PVP nanofibers prepared using co-axial electrospinning with salt solution as sheath fluid," *Materials Letter*, vol. 67, pp. 78–80, 2012.

[10] X. Lu, C. Wang, and Y. Wei, "One-dimensional composite nanomaterials: synthesis by electrospinning and their applications," *Small*, vol. 5, no. 21, pp. 2349–2370, 2009.

[11] Y. Dou, K. Lin, and J. Chang, "Polymer nanocomposites with controllable distribution and arrangement of inorganic nanocomponents," *Nanoscale*, vol. 3, no. 4, pp. 1508–1511, 2011.

[12] D. G. Yu, L. D. Gao, K. White, C. Branford-White, W. Y. Lu, and L. M. Zhu, "Multicomponent amorphous nanofibers electrospun from hot aqueous solutions of a poorly soluble drug," *Pharmaceutical Research*, vol. 27, no. 11, pp. 2466–2477, 2010.

[13] L. Ji, Z. Lin, M. Alcoutlabi, and X. Zhang, "Recent developments in nanostructured anode materials for rechargeable lithium-ion batteries," *Energy and Environmental Science*, vol. 4, no. 8, pp. 2682–2699, 2011.

[14] Z. Dong, S. J. Kennedy, and Y. Wu, "Electrospinning materials for energy-related applications and devices," *Journal of Power Sources*, vol. 196, no. 11, pp. 4886–4904, 2011.

[15] X. Zhang, L. Ji, O. Toprakci, and M. Alcoutlabi, "Electrospun nanofiber-based anodes, cathodes, and separators for advanced lithium-ion batteries," *Polymer Reviews*, vol. 51, pp. 239–264, 2011.

[16] L. Ji, Z. Lin, B. Guo, A. J. Medford, and X. Zhang, "Assembly of carbon-SnO_2 core-sheath composite nanofibers for superior lithium storage," *Chemistry A*, vol. 16, no. 38, pp. 11543–11548, 2010.

[17] C. Huang, S. J. Soenen, J. Rejman et al., "Stimuli-responsive electrospun fibers and their applications," *Chemical Society Reviews*, vol. 40, no. 5, pp. 2417–2434, 2011.

[18] X. Fang, H. Ma, S. Xiao et al., "Facile immobilization of gold nanoparticles into electrospun polyethyleneimine/polyvinyl alcohol nanofibers for catalytic applications," *Journal of Materials Chemistry*, vol. 21, no. 12, pp. 4493–4501, 2011.

[19] D. G. Yu, L. M. Zhu, S. W. A. Bligh, C. Branford-White, and K. White, "Coaxial electrospinning with organic solvent for controlling the size of self-assembled nanoparticles," *Chemical Communications*, vol. 47, no. 4, pp. 1216–1218, 2011.

[20] Anonymity, 2011, http://acupuncturetoday.com/herbcentral/borneol.php.

[21] J. Pitha and T. Hoshino, "Effects of ethanol on formation of inclusion complexes of hydroxypropylcyclodextrins with testosterone or with methyl orange," *International Journal of Pharmaceutics*, vol. 80, no. 2-3, pp. 243–251, 1992.

[22] T. Loftsson and M. E. Brewster, "Pharmaceutical applications of cyclodextrins. 1. Drug solubilization and stabilization," *Journal of Pharmaceutical Sciences*, vol. 85, no. 10, pp. 1017–1025, 1996.

[23] D. G. Yu, N. P. Chatterton, J. H. Yang, X. Wang, and Y. Z. Liao, "Co-axial electrospinning with Triton X-100 solutions as sheath fluids for preparing PANnanofibers," *Macromolecule and Materials Engineering*. In press.

[24] J. M. Yang and D. G. Yu, "Co-axial electrospinning with sodium thiocyanate solution for preparing polyacrylonitrile nanofibers," *Journal of Polymer Research*, vol. 19, article 9789, 7 pages, 2011.

[25] D. G. Yu, G. R. Williams, L. D. Gao, S. W. A. Bligh, J. H. Yang, and X. Wang, "Polyacrylonitrile nanofibers prepared by co-axial electrospinning with a surfactant solution," *Colloids and Surface Part A*, vol. 396, pp. 161–168, 2012.

[26] D. G. Yu, C. Branford-White, N. P. Chatterton et al., "Electrospinning of concentrated polymer solutions," *Macromolecules*, vol. 43, no. 24, pp. 10743–10746, 2010.

[27] X. X. Shen, D. G. Yu, L. M. Zhu, C. Branford-White, K. White, and N. P. Chatterton, "Electrospun diclofenac sodium loaded Eudragit L100-55 nanofibers for colon-targeted drug delivery," *International Journal of Pharmaceutics*, vol. 408, no. 1-2, pp. 200–207, 2011.

[28] D. G. Yu, X. X. Shen, C. Branford-White, K. White, L. M. Zhu, and S. W. A. Bligh, "Oral fast-dissolving drug delivery membranes prepared from electrospun polyvinylpyrrolidone ultrafine fibers," *Nanotechnology*, vol. 20, no. 5, Article ID 055104, 9 pages, 2009.

Hindawi Publishing Corporation
Journal of Nanomaterials
Volume 2012, Article ID 839053, 7 pages
doi:10.1155/2012/839053

Research Article

Gradient Technology for High-Throughput Screening of Interactions between Cells and Nanostructured Materials

Andrew Michelmore,[1] Lauren Clements,[2] David A. Steele,[1] Nicolas H. Voelcker,[2] and Endre J. Szili[1]

[1] *Mawson Institute, University of South Australia, Mawson Lakes, SA 5095, Australia*
[2] *School of Chemical and Physical Sciences, Flinders University, Bedford Park, SA 5042, Australia*

Correspondence should be addressed to Andrew Michelmore, andrew.michelmore@unisa.edu.au

Received 28 November 2011; Accepted 21 February 2012

Academic Editor: Krasimir Vasilev

We present a novel substrate suitable for the high-throughput analysis of cell response to variations in surface chemistry and nanotopography. Electrochemical etching was used to produce silicon wafers with nanopores between 10 and 100 nm in diameter. Over this substrate and flat silicon wafers, a gradient film ranging from hydrocarbon to carboxylic acid plasma polymer was deposited, with the concentration of surface carboxylic acid groups varying between 0.7 and 3% as measured by XPS. MG63 osteoblast-like cells were then cultured on these substrates and showed greatest cell spreading and adhesion onto porous silicon with a carboxylic acid group concentration between 2-3%. This method has great potential for high-throughput screening of cell-material interaction with particular relevance to tissue engineering.

1. Introduction

There are approximately 500,000 bone graft procedures performed in the US alone each year [1]. At an average of around $35,000 USA [2], this represents a significant cost per graft. The majority of bone graft procedures use allograft or autograft bone tissues, which can be painful and also have limitations with incompatibility and disease transmission. An alternative approach is the use of engineered bone tissue scaffolds [3]. It has been shown for different cell-types that surface topography can have a major affect on the way cells adhere and proliferate on surfaces [4–8]. It has been hypothesised that the architecture of the cell membrane can change in response to topographical features at the nanoscale, which, in turn, can maximise the cell's attachment to the surface [9, 10]. As cells adhere to their growing surface, stresses are imparted to their cytoskeletal wall, which impacts on their focal adhesion. Although this phenomenon is still not completely understood, it is known that ideally the surface nanotopography should be tuned for each cell type to achieve optimal cell adhesion on synthetic materials.

Ideally, the scaffold should mimic the physical and chemical environment of natural bone tissue, which is mainly composed of a porous hydroxyapatite (HA) and collagen I matrix, to promote optimal osteoblast (bone producing cell) activity leading to bone mineral synthesis/precipitation and integration with the surrounding bone tissue. Nanotextured surfaces have been shown to regulate osteoblast cell growth structure and function [11] and have been used to maintain stem-cell pluripotency and growth [12]. These surfaces typically mimic the structure of extracellular matrix proteins and the basement membrane (10–300 nm) and hydroxyapatite crystals (4 nm) [13].

Surface chemistry also plays an important role in regulating osteoblast cellular activity. For example, attachment of osteoblast cells can be controlled by negatively charged surface functional groups [14]. However, the analysis of both nanotopography and surface chemistry in the development of bone engineered tissue scaffolds is both costly and time consuming, limiting the combinations of topography/chemistry that can be analysed. Thin film chemical gradients can be used to investigate cell behaviour [15] whilst maintaining the nanotopography of the surface if the film is thin enough [16].

One method for coating substrates with thin film coatings with functionalised chemistry is plasma polymerisation

[17]. In this method, a vapour of monomer molecules are electrically excited to form a plasma phase; components of the plasma phase (ions, radicals, and neutrals) then may oligomerise and deposit on any substrate placed in contact with the plasma [18–20]. Through the use of low power and low pressure, functional groups in the monomer may be retained in the final deposited film, for example, carboxylic acid groups from acrylic acid [21]. This method has many advantages over other thin-film coating technologies: the requirements for surface preparation are not stringent, the method relies on an environmentally friendly, solvent-free process conducted at ambient temperature. Furthermore, the plasma deposit forms a pinhole-free, conformal film over the substrate. Plasma polymerisation has been successfully applied to substrates such as 3D scaffolds [22] and microparticles [23]. Gradients of chemical functionality have also been fabricated using this method [24] and can be tailored for investigations into cell behaviour [16, 25].

In this paper, a high-throughput platform is demonstrated for analysing cell response to surface chemistry on anodised porous silicon. Gradients of carboxylic acid functional groups were plasma polymerised onto flat and porous silicon with controlled pore geometries between 10 nm and 100 nm. Following surface characterisation by means of both XPS and AFM, we examined the growth of MG63 osteoblasts on the functionalised nanostructured surfaces.

2. Experimental

2.1. Materials. 1,7-octadiene and propionic acid (>98%) were purchased from Sigma-Aldrich and used as received. P^+-type silicon wafers were purchased from Virginia Semiconductors (1–5 Ωcm resistivity (100) orientated, boron doped).

2.2. Porous Silicon Preparation. Porous silicon substrates were prepared by the electrochemical anodisation of p^+-type silicon [26]. Anodisation was carried out by placing a platinum (Pt) electrode parallel to and ∼5 mm from the silicon surface in a circular Teflon well. Hydrofluoric acid (HF) electrolyte solutions were prepared using 49% aqueous HF and 100% ethanol as a surfactant. A 1 : 1 HF/ethanol solution was used, applying a current density of 28 mA cm^{-2} for 4 min. Following anodisation, samples were rinsed with ethanol, methanol, acetone, and dichloromethane and subsequently dried under a stream of nitrogen gas.

2.3. Plasma Polymer Deposition. Plasma polymer gradients were deposited onto flat and porous silicon wafers using a previously described method [24]. Briefly, the silicon samples were placed under a mask with a 1 mm slot. Initially the slot was placed at one end of the porous silicon, a needle valve was opened to allow 1,7-octadiene to flow into the chamber at 1 sccm, and the plasma was ignited at 15 W. After 1 min deposition, the mask was moved 0.25 mm by an electric motor and the valve was closed slightly to decrease the flow of the monomer into the chamber and at the same time another valve opened slightly to allow propionic acid vapour into the chamber. This process was continued until the end of the silicon sample was reached (14 mm) at which point the valve connected to the 1,7-octadiene flask was completely closed and only propionic acid vapour was flowing into the chamber at 1 sccm.

Table 1: Peak assignments for XPS analysis of the C1s coreline peaks.

Functional group	Peak position (eV)
C–C/C–H	285
C–O	286.5
C=O	287.9
COOH/R	289.2
C*–COOH/R	285.7

2.4. X-Ray Photoelectron Spectroscopy. The chemical composition of the plasma polymer deposit was analysed by X-ray photoelectron spectroscopy (XPS) using a SPECS SAGE XPS system with a Phoibos 150 hemispherical analyser at a take-off angle of 90° and an MCD-9 detector. The analysis area was circular with a diameter of 0.5 mm. All the results presented here correspond to the use of the Mg Kα ($h\nu$ = 1253.6 eV), operated at 10 kV and 20 mA (200 W). The background pressure was 2×10^{-6} Pa. A pass energy of 100 eV and kinetic energy steps of 0.5 eV were used to obtain wide scan survey spectra, while 20 eV pass energy and energy steps of 0.1 eV were used for the high-resolution spectra of the C1s coreline peaks. Survey and C1s spectra were collected at 1 mm intervals.

Spectra were analysed using CasaXPS (Neil Fairley, UK). A linear background was applied to the C1s coreline spectra, and synthetic peaks were applied following Beamson and Briggs [27] as outlined in Table 1. The lineshape and full-width-at-half-maximum of the synthetic peaks were kept constant at GL(30) (30% Lorentzian, 70% Gaussian) and 1.7 eV, respectively. Spectra were charge corrected with respect to the aliphatic carbon peak at 285.0 eV.

2.5. Atomic Force Microscopy. An NT-MDT NTEGRA SPM with a 100 μm piezo scanner was used to measure the topography of the substrates in noncontact mode. Silicon nitride NT-MDT NSG03 gold-coated tips were used and had a resonance frequency between 65 and 90 kHz, and a tip radius of less than 10 nm. The amplitude of oscillation was 10 nm and all experiments were performed at a scan rate of 1 Hz. The scanner was calibrated in the x, y, and z directions using 1.5 μm grids with a height of 22 nm.

2.6. MG63 Osteoblast-Like Cell Culture. Immortalised MG63 osteoblast-like cells, derived from an osteosarcoma of human bone with a fibroblast morphology and adherent growth properties, were cultured in Dulbecco's modified Eagle's medium (DMEM) supplemented with 10% (v/v) newborn calf serum, 100 units of penicillin, and 100 μg of streptomycin under typical cell culture conditions (37°C in a humidified 5% CO_2 atmosphere). The cells were dislodged from

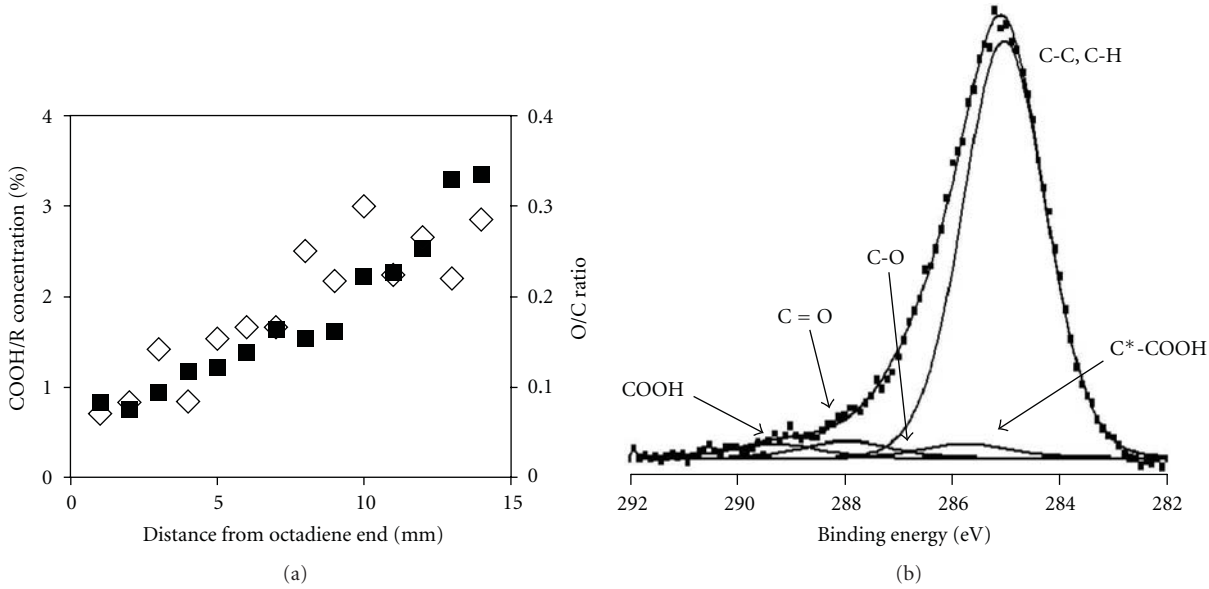

FIGURE 1: (a) Concentration of COOH/R groups from the C1s coreline XP spectra (◊) and the O/C ratio across a silicon substrate coated with a plasma polymer gradient (■). (b) High-resolution scan of the C1s coreline peak at the carboxylic acid rich end of the plasma polymer gradient. The carboxylic acid peak occurs at 289.2 eV.

the flasks for passaging and transferred to the test samples with the aid of trypsin. The dilution of cells seeded onto each test sample is given in each figure caption. All cell culture reagents were purchased from Sigma.

2.7. Cell Staining. Cell nuclei were stained with 2 mL of 0.1 mg/mL Hoechst 33342 dye (Invitrogen) prepared in PBS (pH 7.4) for 30 min. Cell membranes were stained using 2 mL of 100 μM of $DiOC_5(3)$ (Invitrogen). The samples containing the stained cells were then washed twice with 2 mL of PBS. The cells were then fixed with 1 mL of formaldehyde (Sigma) and rinsed in Milli-Q water.

2.8. Fluorescence Microscopy. Fluorescence microscopy was carried out using a TE2000 Nikon inverted microscope equipped with a 4x objective for cell nuclei (Hoechst 33342 stained cells) imaging and through a 20x objective for cell membrane ($DiOC_5(3)$ stained cells) imaging. Images of Hoechst 33342 were captured through a Nikon filter with 381–392 nm excitation and 415–570 nm emission, and for $DiOC_5(3)$, through a Nikon filter with 455–485 nm excitation and 500–545 nm emission. Images were recorded with a Nikon DXM1200C digital camera and processed using NIS-Elements Basic Research v2.2 software.

3. Results

3.1. Surface Characterisation. The surfaces were coated with a chemical gradient ranging from 1,7-octadiene plasma polymer to propionic acid plasma polymer extending over a distance of 14 mm as shown in Figure 1. The concentration of COOH/R groups increased from 0.7% at one end to 3.0% at the other of the gradient. The O/C ratio increased from 0.07 to 0.34 indicating an increasing degree of oxygen incorporation into the plasma polymer film towards the propionic acid end, consistent with the increasing concentration of COOH/R groups.

Survey spectra were performed at all points along the gradient and showed minor peaks for Si 2s and Si 2p. This showed that the plasma polymer layer thickness was less than the sampling depth of XPS, at around 10 nm [28]. This was confirmed by AFM images of points along the gradient, shown in Figure 2. The RMS surface roughness of flat silicon was measured to be less than 0.2 nm, with a maximum peak-peak of less than 1 nm. As expected, the RMS roughness was higher on porous silicon at 0.6 nm, and the maximum peak-peak was also higher at 6 nm. The roughness of the flat and porous silicon surfaces remained unchanged after deposition of the plasma polymer gradient, indicating that the coating was thin and had conformed to the underlying substrate topography.

3.2. Cell Adhesion and Spreading. After incubation with MG63 osteoblast-like cells for 4 h, the cell nuclei and membrane were stained with Hoechst 33342 and $DiOC_5(3)$, respectively. As shown in Figure 3, the cells attached relatively homogeneously to the chemical gradient surface for both flat and porous silicon, with a slightly higher density on porous silicon. This is also shown quantitatively in Figure 4, where after 4 h of incubation, the cell density was relatively constant across the gradient at an average of 1.5×10^5 cells/cm^2 for porous silicon, and 8×10^4 cells/cm^2 for flat silicon. However, the level of cell spreading was observed to be different across the substrates. At positions 10 and 11 mm (Figure 5), corresponding to a carboxylic acid concentration of 2-3%, a greater degree of cells spread compared to cells

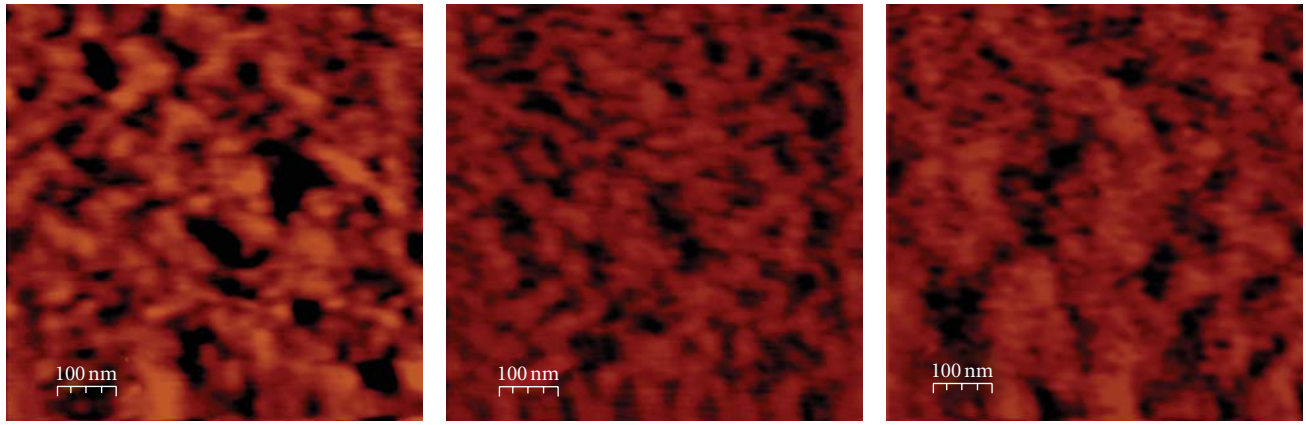

(a) (b) (c)

Figure 2: AFM height images of porous silicon coated with a plasma polymer gradient. (a) Hydrocarbon end (position 1 mm). (b) Hydrocarbon/carboxylic acid combined (position 7 mm) and (c) carboxylic acid end (position 13 mm).

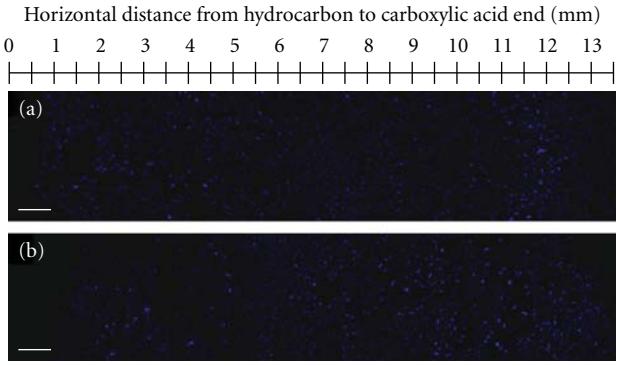

Figure 3: Fluorescence micrographs of Hoechst 33342 stained MG63 osteoblast-like cells on plasma polymer chemical gradients of carboxylic acid deposited onto (a) a flat silicon wafer and (b) a porous silicon wafer. Images were recorded after 4 h of incubation with 7.7×10^4 cells/mL. Scale bar = 500 μm.

attached to the substrate outside of this region. Outside of these regions, the cells were rounded and exhibited very little spreading. The attachment of cells is mediated by an intermediate complex proteinaceous layer, which quickly adsorbs to the material (in this case the plasma polymer) before cells reach the surface. It is well known that many of the proteins found in the serum supplement of the cell culture medium contain cell adhesion motifs, such as the arginine-glycine-aspartate (RGD) amino acid sequence, which interact with cell surface receptors to facilitate cell attachment. We hypothesise that the strength of protein adsorption was much greater at the hydrophobic (hydrocarbon-rich) end of the chemical gradient compared to the relatively weak interactions at the hydrophilic (carboxylic acid-rich) end. The strong interactions between the protein and the hydrophobic polymer surface may have induced protein denaturation or conformational changes rendering the cell adhesion motif of the proteins inaccessible to the cell surface receptors. In addition, we also note that surface topography significantly influenced the attachment and growth of the cells. Cell spreading was enhanced on the plasma polymer film coated on the nanostructured porous silicon wafer compared to the flat silicon wafer. In Figures 5(a)–5(d), the cells were rounded and showed some degree of spreading on flat silicon. For images (e)–(h) on porous silicon however, the cells were more elongated and showed a higher degree of spreading.

After a further 20 h of incubation, the substrates were washed to remove rounded and loosely bound cells from the substrate surface. At the hydrocarbon-rich end of the gradient, most of the cells were easily removed from both flat and porous silicon wafers. However, in the region with 2-3% carboxylic acid groups, many cells remained on the surface, resulting in a gradient of cell density as shown in Figure 6. As shown in Figure 4, the cell density was higher on porous silicon compared to flat silicon. The maximum cell density of approximately 5×10^5 cells/cm^2 occurred at position 11 mm, corresponding to a carboxylic acid concentration of 2.6%.

4. Discussion

4.1. Topography. It has previously been shown that topography on the nanoscale can affect cellular attachment. For example, Suh et al. [29] showed that micron-scale pits in titanium substrates enhanced early osteoblast attachment and proliferation. Substrates with smaller pores have also been studied [7]. Pores approximately 170 nm in diameter and 14 nm deep doubled cell adhesion of osteoblast cells compared to flat surfaces, but larger and deeper pores exhibited less of an effect. The results presented here show an increase in osteoblast attachment on porous silicon substrates compared to flat substrates, in agreement with these previous studies.

These results indicate that surface roughness and nanotopography can promote cell adhesion and growth. There is probably a value of surface roughness that is ideal for promoting cell adhesion. Determining this ideal level using standard techniques would involve preparing a large number of samples. An alternate approach has been demonstrated by others, where cells were cultured on porosity gradients

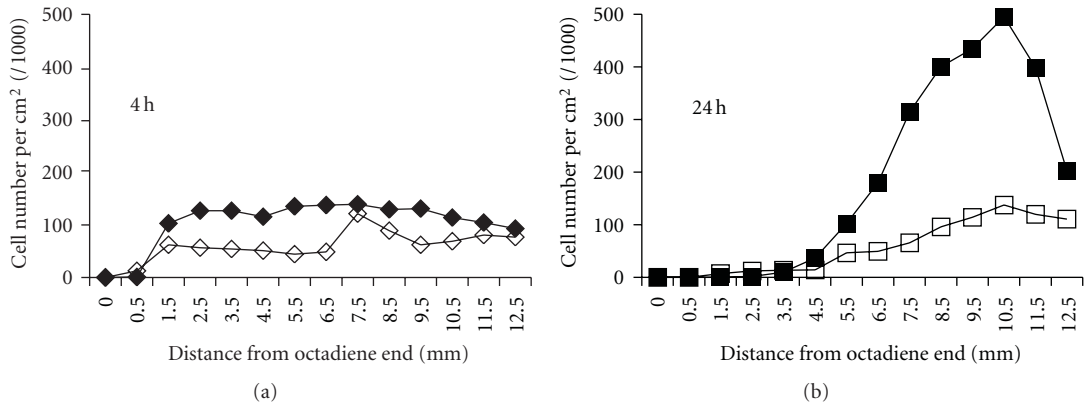

FIGURE 4: Cell density on flat (open symbols) and porous silicon (closed symbols) after 4 h incubation (a) and 24 h incubation (b).

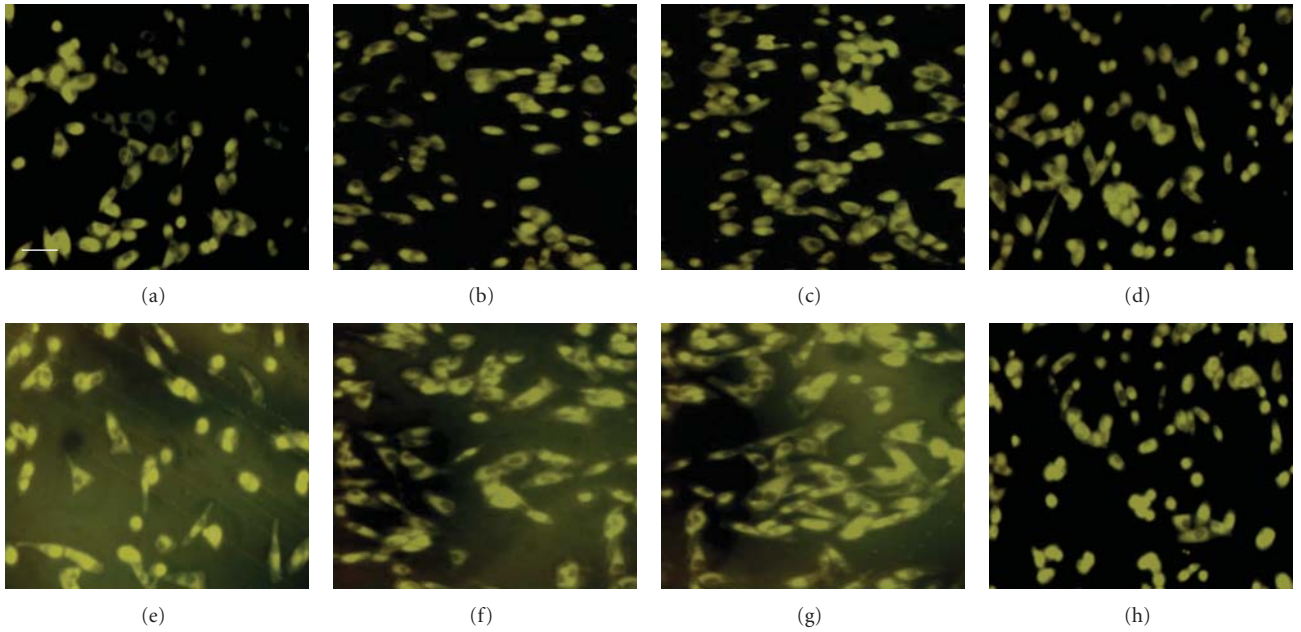

FIGURE 5: Fluorescence micrographs of $DiOC_5(3)$ (membrane) stained MG63 osteoblast-like cells grown on a plasma polymer film coated onto flat silicon (a–d) and porous silicon (e–h). Images were recorded after 4 h of incubation with 7.7×10^4 cells/mL. Distances from the hydrocarbon end were 1 mm (a + e), 10 mm (b + f) 11 mm (c + g), and 13 mm (d + h). Scale bar = 100 μm.

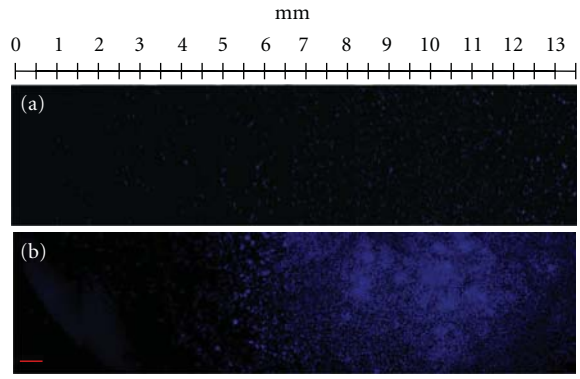

FIGURE 6: Fluorescence micrograph of Hoechst 33342 stained MG63 osteoblast-like cells on plasma polymer chemical gradients on flat silicon (a) and porous silicon (b). Images were recorded after 24 h of incubation with 7.7×10^4 cells/mL and subsequent washing to remove loosely bound cells. Scale bar = 500 μm.

[30]. Pores were produced ranging from 5 nm up to 3 μm in a continuous gradient, and following culturing, differences in cell morphology and density were observed. For neuroblastoma cells, a minimum in the cell density and spreading was observed for pores around 100 nm, while 1–3 μm pores showed a modest increase in cell spreading compared to flat silicon. These results demonstrate the utility of this method to quickly and simply study the effect of nanotopography on cell behaviour.

4.2. Chemistry. Surface chemical gradients of plasma polymers have also been utilised in previous studies to measure cell behaviour. For example, the surface density of carboxylic acid groups has been used to control the ability of mouse embryonic stem cells to attach to, and spread on, plasma-polymer-coated glass coverslips [31]. It was found that increasing the COOH surface concentration resulted in greater cell attachment, but the pluripotency of the cells, the potential of a stem cell to differentiate into different cell types, was diminished if the cells were able to spread beyond 140 μm^2.

Cellular attachment of osteoblast cells has also been shown to be extremely sensitive to even small changes in the concentration of negatively charged carboxylic acid groups on substrates, probably due to amphoteric interactions between the polymer chains on the surface and the cell membrane [32]. Daw et al. [14] utilised chemical gradients to measure the effect of carboxylic acid surface functionality on the attachment of osteoblast-like cells. Their study showed cell attachment increased by approximately 200% with a surface carboxylic acid concentration of just 0.5%. A maximum level in cell attachment was observed at a surface concentration of ~3% carboxylic acid groups, after which the number of attached cells decreased and returned to "pure hydrocarbon" baseline levels at ~5%. This is in excellent agreement with results presented here, which show a maximum level of cell attachment at a surface concentration of ~2-3% carboxylic acid groups.

4.3. Potential for 2D Gradients. As discussed above, both surface chemistry and topography have been independently shown to influence cell behaviour and interactions. Gradients of surface chemistry and topography have separately been used to measure their effect on cells in a one-step process. The results reported here, open the possibility of developing a 2D gradient of topography and surface chemistry, with the gradients oriented orthogonally to each other [33, 34]. It should be noted that the topographical features fabricated here and in other studies [7, 12, 30] consist of pits or holes. Another approach is to use a chemical gradient to adhere nanoparticles to a surface in a gradient fashion [16]. These nanoparticle density gradients could then be coated with a second chemical gradient to produce a similar 2D gradient, but with "pillars" rather than holes. This method may be advantageous as the size of the topographical features can be controlled by selecting the size of the nanoparticles. Such surfaces could be used as a method of screening osteoblast cells for bone graft procedures.

5. Conclusions

This study has shown that both surface chemistry and surface topography affect the adhesion and spreading of osteoblast-like cells. A greater degree of cell spreading was observed on surfaces with nanoscale pores compared to flat surfaces. Also, surfaces with a surface concentration of 2-3% carboxylic acid groups were shown to be optimal for cell adhesion and spreading. The use of gradient materials here has demonstrated the possibility of high-throughput screening of mammalian cells interacting with biomaterial surfaces, which is critically relevant to the effort of developing new generation bone-tissue engineering scaffolds. Therefore, plasma polymerised functional chemical gradients on porous silicon substrates show great promise as high-throughput diagnostic tools for analysis of cell and biomaterial interactions.

References

[1] B. Stevens, Y. Yang, A. Mohandas, B. Stucker, and K. T. Nguyen, "A review of materials, fabrication methods, and strategies used to enhance bone regeneration in engineered bone tissues," *Journal of Biomedical Materials Research B*, vol. 85, no. 2, pp. 573–582, 2008.

[2] S. D. Glassman, L. Y. Carreon, M. J. Campbell et al., "The perioperative cost of Infuse bone graft in posterolateral lumbar spine fusion," *Spine Journal*, vol. 8, no. 3, pp. 443–448, 2008.

[3] C. Laurencin, Y. Khan, and S. F. El-Amin, "Bone graft substitutes," *Expert Review of Medical Devices*, vol. 3, no. 1, pp. 49–57, 2006.

[4] P. Linez-Bataillon, F. Monchau, M. Bigerelle, and H. F. Hildebrand, "In vitro MC3T3 osteoblast adhesion with respect to surface roughness of Ti6Al4V substrates," *Biomolecular Engineering*, vol. 19, no. 2–6, pp. 133–141, 2002.

[5] L. A. Cyster, K. G. Parker, T. L. Parker, and D. M. Grant, "The effect of surface chemistry and nanotopography of titanium nitride (TiN) films on primary hippocampal neurones," *Biomaterials*, vol. 25, no. 1, pp. 97–107, 2004.

[6] Y. F. Chou, W. Huang, J. C. Y. Dunn, T. A. Miller, and B. M. Wu, "The effect of biomimetic apatite structure on osteoblast viability, proliferation, and gene expression," *Biomaterials*, vol. 26, no. 3, pp. 285–295, 2005.

[7] J. Y. Lim, A. D. Dreiss, Z. Zhou et al., "The regulation of integrin-mediated osteoblast focal adhesion and focal adhesion kinase expression by nanoscale topography," *Biomaterials*, vol. 28, no. 10, pp. 1787–1797, 2007.

[8] T. P. Kunzler, T. Drobek, M. Schuler, and N. D. Spencer, "Systematic study of osteoblast and fibroblast response to roughness by means of surface-morphology gradients," *Biomaterials*, vol. 28, no. 13, pp. 2175–2182, 2007.

[9] E. K. F. Yim, E. M. Darling, K. Kulangara, F. Guilak, and K. W. Leong, "Nanotopography-induced changes in focal adhesions, cytoskeletal organization, and mechanical properties of human mesenchymal stem cells," *Biomaterials*, vol. 31, no. 6, pp. 1299–1306, 2010.

[10] T. P. Kunzler, C. Huwiler, T. Drobek, J. Vörös, and N. D. Spencer, "Systematic study of osteoblast response to nanotopography by means of nanoparticle-density gradients," *Biomaterials*, vol. 28, no. 33, pp. 5000–5006, 2007.

[11] G. Mendonça, D. B. S. Mendonça, F. J. L. Aragão, and L. F. Cooper, "Advancing dental implant surface technology—from

micron- to nanotopography," *Biomaterials*, vol. 29, no. 28, pp. 3822–3835, 2008.

[12] R. J. McMurray, N. Gadegaard, P. M. Tsimbouri et al., "Nanoscale surfaces for the long-term maintenance of mesenchymal stem cell phenotype and multipotency," *Nature Materials*, vol. 10, no. 8, pp. 637–644, 2011.

[13] M. M. Stevens and J. H. George, "Exploring and engineering the cell surface interface," *Science*, vol. 310, no. 5751, pp. 1135–1138, 2005.

[14] R. Daw, S. Candan, A. J. Beck et al., "Plasma copolymer surfaces of acrylic acid/1,7 octadiene: surface characterisation and the attachment of ROS 17/2.8 osteoblast-like cells," *Biomaterials*, vol. 19, no. 19, pp. 1717–1725, 1998.

[15] M. Arnold, V. C. Hirschfeld-Warneken, T. Lohmüller et al., "Induction of cell polarization and migration by a gradient of nanoscale variations in adhesive ligand spacing," *Nano Letters*, vol. 8, no. 7, pp. 2063–2069, 2008.

[16] R. V. Goreham, R. D. Short, and K. Vasilev, "Method for the generation of surface-bound nanoparticle density gradients," *Journal of Physical Chemistry C*, vol. 115, no. 8, pp. 3429–3433, 2011.

[17] T. Willliams and M. W. Hayes, "Polymerization in a glow discharge," *Nature*, vol. 209, no. 5025, pp. 769–773, 1966.

[18] H. Yasuda, *Plasma Polymerisation*, Academic Press, New York, NY, USA, 1985.

[19] M. A. Lieberman and A. J. Lichtenberg, *Principles of Plasma Discharges and Materials Processing*, John Wiley and Sons, Chicester, UK, 1994.

[20] H. Biederman, *Plasma Polymer Films*, Imperial College Press, London, UK, 2004.

[21] A. J. Beck, F. R. Jones, and R. D. Short, "Plasma copolymerization as a route to the fabrication of new surfaces with controlled amounts of specific chemical functionality," *Polymer*, vol. 37, no. 24, pp. 5537–5539, 1996.

[22] J. J. A. Barry, D. Howard, K. M. Shakesheff, S. M. Howdle, and M. R. Alexander, "Using a core-sheath distribution of surface chemistry through 3D tissue engineering scaffolds to control cell ingress," *Advanced Materials*, vol. 18, no. 11, pp. 1406–1410, 2006.

[23] J. Cho, F. S. Denes, and R. B. Timmons, "Plasma processing approach to molecular surface tailoring of nanoparticles: improved photocatalytic activity of TiO_2," *Chemistry of Materials*, vol. 18, no. 13, pp. 2989–2996, 2006.

[24] J. D. Whittle, D. Barton, M. R. Alexander, and R. D. Short, "A method for the deposition of controllable chemical gradients," *Chemical Communications*, vol. 9, no. 14, pp. 1766–1767, 2003.

[25] K. Vasilev, Z. Poh, K. Kant, J. Chan, A. Michelmore, and D. Losic, "Tailoring the surface functionalities of titania nanotube arrays," *Biomaterials*, vol. 31, no. 3, pp. 532–540, 2010.

[26] L. R. Clements, P.-Y. Wang, F. Harding, W.-B. Tsai, H. Thissen, and N. H. Voelcker, "Mesenchymal stem cell attachment to peptide density gradients on porous silicon generated by electrografting," *Physica Status Solidi A*, vol. 208, no. 6, pp. 1440–1445, 2011.

[27] G. Beamson and D. Briggs, *High Resolution XPS of Organic Polymers: The Scienta ESCA300 Database*, John Wiley and Sons, Chicester, UK, 1992.

[28] D. Briggs, *Surface Analysis of Polymers by XPS and Static SIMS*, Cambridge Univeristy Press, Cambridge, UK, 1998.

[29] J. Y. Suh, B. C. Jang, X. Zhu, J. L. Ong, and K. Kim, "Effect of hydrothermally treated anodic oxide films on osteoblast attachment and proliferation," *Biomaterials*, vol. 24, no. 2, pp. 347–355, 2003.

[30] Y. L. Khung, G. Barritt, and N. H. Voelcker, "Using continuous porous silicon gradients to study the influence of surface topography on the behaviour of neuroblastoma cells," *Experimental Cell Research*, vol. 314, no. 4, pp. 789–800, 2008.

[31] N. Wells, M. A. Baxter, J. E. Turnbull et al., "The geometric control of E14 and R1 mouse embryonic stem cell pluripotency by plasma polymer surface chemical gradients," *Biomaterials*, vol. 30, no. 6, pp. 1066–1070, 2009.

[32] N. G. Maroudas, "Adhesion and spreading of cells on charged surfaces," *Journal of Theoretical Biology*, vol. 49, no. 2, pp. 417–424, 1975.

[33] J. Zhang and Y. Han, "A topography/chemical composition gradient polystyrene surface: toward the investigation of the relationship between surface wettability and surface structure and chemical composition," *Langmuir*, vol. 24, no. 3, pp. 796–801, 2008.

[34] J. Yang, F. R. A. J. Rose, N. Gadegaard, and M. R. Alexander, "A high-throughput assay of cell-surface interactions using topographical and chemical gradients," *Advanced Materials*, vol. 21, no. 3, pp. 300–304, 2009.

Hindawi Publishing Corporation
Journal of Nanomaterials
Volume 2012, Article ID 891318, 7 pages
doi:10.1155/2012/891318

Research Article

Nanoparticles in Cancer Imaging and Therapy

Leon Smith,[1] Zdenka Kuncic,[1] Kostya (Ken) Ostrikov,[1,2] and Shailesh Kumar[2]

[1] *Institute of Medical Physics, School of Physics, The University of Sydney, Sydney, N.S.W 2006, Australia*
[2] *Plasma Nanoscience Centre Australia (PNCA), CSIRO Materials Science and Engineering, P.O. Box 218, Lindfield, N.S.W 2070, Australia*

Correspondence should be addressed to Zdenka Kuncic, zdenka.kuncic@sydney.edu.au

Received 10 February 2012; Accepted 3 March 2012

Academic Editor: Krasimir Vasilev

Nanoparticle contrast agents offer the potential to significantly improve existing methods of cancer diagnosis and treatment. Advantages include biocompatibility, selective accumulation in tumor cells, and reduced toxicity. Considerable research is underway into the use of nanoparticles as enhancement agents for radiation therapy and photodynamic therapy, where they may be used to deliver treatment agents, produce localized enhancements in radiation dose and selectively target tumor cells for localized damage. This paper reviews the current status of nanoparticles for cancer treatment and presents preliminary results of a pilot study investigating titanium dioxide nanoparticles for dual-mode enhancement of computed tomography (CT) imaging and kilovoltage radiation therapy. Although titanium dioxide produced noticeable image contrast enhancement in the CT scans, more sensitive detectors are needed to determine whether the nanoparticles can also produce localized dose enhancement for targeted radiation therapy.

1. Introduction

Contrast agents are now standard practice in the field of medical imaging, where they are used to enhance image contrast and improve the visibility of features that would otherwise be difficult to detect [1]. Nanoparticle agents continue to receive considerable attention in this field for their potential as contrast agents [2], offering the advantage of greater biocompatibility and reduced toxicity compared to more conventional chemical agents [3]. Present nanoparticles under development for this role include gold nanoparticles for X-ray contrast enhancement [3], magnetic nanoparticles for MRI enhancement [4], and even hybrid nanoparticles containing iron oxide and gold in a polymer coating, which serve as contrast agents for both CT and MRI [5].

In addition to imaging, nanoparticle agents are also being investigated for potential applications to cancer *therapy* [6–8], where they offer similar advantages over other contrast agents as they do in imaging, coupled with the potential for designing nanoparticles that can selectively accumulate in cancer cells, providing "targeted" treatments that may not be possible with conventional techniques [7]. Indeed, nanoparticles have proven their use as a general platform for targeted drug delivery, owing to the ability for tethered functionality such as an antibody agent or quantum dot fluorescent reporter to enhance delivery of chemotherapeutic agents [9] (Figure 1). There is now also growing interest in the use of nanoparticles as enhancement agents in cancer radiation therapy and photodynamic therapy to improve patient outcomes and reduce side effects. As an increasing number of cancer patients are treated with radiotherapy, there is potential for a much wider impact of nanoparticle-enhanced radiotherapy.

In this paper, we review the current status of nanoparticle enhancement agents for radiation therapy and photodynamic therapy. In addition, we present preliminary results for a pilot study investigating the use of titanium dioxide nanoparticles as possible dual-mode enhancement agents for computed tomography (CT) imaging and radiation therapy.

2. Contrast-Enhanced Radiation Therapy with Nanoparticles

There has been considerable investigation into the potential of traditional imaging contrast agents, such as iodine, for

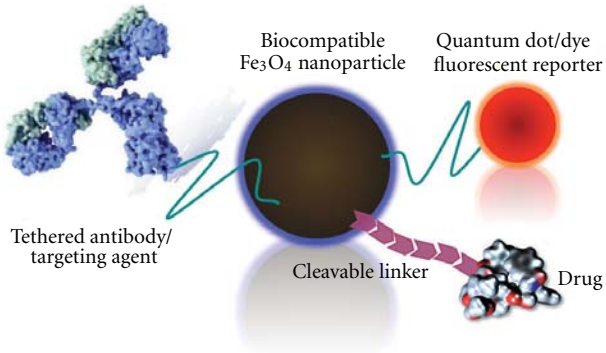

Figure 1: Schematic of an iron-based nanoparticle showing multifunctionality for image contrast and targeted drug delivery. (With kind permission from A. L. Yuen, School of Chemistry, University of Sydney.)

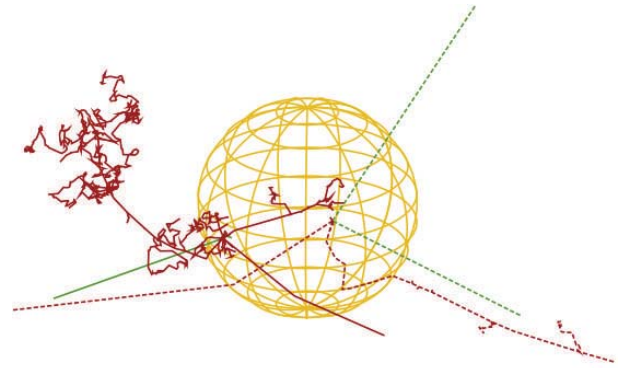

Figure 2: Monte Carlo visualization of the interaction of a low-energy photon (green lines) with a 20 nm gold nanoparticle (yellow sphere), showing electron tracks (red) associated with ionization events. Solid and dashed lines correspond to events outside and inside the nanoparticle, respectively. (Reprinted by permission from Macmillan Publishers Ltd: Scientific Reports [22], copyright 2011.)

applications to radiation therapy cancer treatment [10–13]. During radiation therapy, ionising radiation is delivered to the tumor, causing damage to the tumor cells' DNA and other biological molecules, resulting in the death of the cell. Experiments on mice bearing Ehrlich ascites carcinoma treated with iodine contrast agents have shown complete regression in up to 80% of mice tested [10].

An inherent limitation of radiation therapy is the unavoidable radiation dose delivered to healthy tissue surrounding the tumor being treated. For some tumors, this has limited the use of radiotherapy as the necessary dose to destroy the tumor will also cause unacceptable damage to nearby healthy tissue [14]. Contrast-enhanced radiotherapy (CERT) [6] involves the administration of high-Z (i.e., high atomic number) contrast agents to the target volume and irradiation with kilovoltage X-rays. As high-Z materials have different absorption properties from surrounding tissue, their presence can modify the distribution in absorbed dose; in particular, a localized dose enhancement can be obtained in regions where the contrast agent is present without affecting healthy tissue [11, 12]. As this difference in photoabsorption properties is most pronounced at kilovoltage energies [6, 15], kilovoltage X-rays are generally considered to be the optimum energy range for CERT [12], but several studies have also investigated contrast enhancement using X-rays in the megavoltage energy range produced by medical linear accelerators [16, 17].

In recent years, studies into potential radiotherapy contrast agents have often focused on gold nanoparticles [16–21]. Gold nanoparticles have a number of useful properties that make them highly attractive contrast agents for cancer therapy, particularly their high-Z and biocompatibility [21, 22]. Monte Carlo simulations of interactions between the radiation treatment beam and individual nanoparticles indicate that the presence of a gold nanoparticle can increase secondary electron production from a 50 kV X-ray beam by up to a factor of 2000 compared to a similar volume of water [23] (Figure 2). Nanoparticles smaller than 100 nm can also cross human cell membranes and preferentially accumulate in cancer cells [24]. Recent studies have found that gold nanoparticles in conjunction with kilovoltage radiotherapy can increase the one-year survival rate of mice with EMT-6 mammary tumors to 86%, compared to 20% with radiotherapy alone [19].

It has been observed that gold nanoparticles appear to cause clinically relevant increases in cell killing rates at concentrations well below those predicted by Monte Carlo simulations [22, 25]. Although the simulations predict that cell killing effects should become noticeable only at nanoparticle concentrations on the order of 1%, they have been observed at concentrations orders of lower magnitude [22]. It has been speculated that this discrepancy is due to the Monte Carlo averaging of the effects of the nanoparticles over macroscopic volumes, thereby ignoring nanoscale inheterogeneities in dose distribution in the vicinity of each nanoparticle [22, 23]. Simulating these inheterogeneities and their corresponding biological effects predicts cell killing at concentrations closer to those reported in experimental studies [22].

An additional factor that is relevant to the effects of nanoparticles on cell killing is their radiosensitization properties. There is increasing evidence that gold nanoparticles, while biocompatible, are not necessarily biologically *inert* [25], which influences their effects on cells during cancer therapy. Gold nanoparticles have also demonstrated the capacity to form radiosensitized DNA molecules in cells they affect, making them more susceptible to radiation whilst simultaneously increasing localised dose near the target [21]. One consequence of these biological effects is that gold nanoparticles appear to demonstrate considerably greater cell killing effects in some cell lines as compared to others [25], which should be taken into consideration in future studies.

3. Nanoparticles in Photodynamic Cancer Therapy

Photodynamic therapy (PDT) is a treatment modality which involves administering a photosensitive agent and

illuminating the target area to activate the agent [26, 27]. In cancer therapy, existing PDT agents react upon photostimulation to produce cytotoxic oxygen species, killing the target cell [27, 28]. Some of the advantages of PDT include its localized effects, reduced cost, and the fact that it is largely an outpatient therapy [27]. Interestingly, it can also induce immune responses even against tumors that are not particularly immunogenic [7]. One of its primary limitations, however, is the limited penetration depth of visible, infrared, and UV radiation into the patient [27–29] and the lack of effective dosimetry techniques for PDT, making it difficult for dose distributions in the treatment volume to be accurately measured [30].

As of 2010, only three classes of photosensitisers for PDT had entered clinical use for cancer therapy [28, 30], all of them chemical products rather than nanoparticles. However, a myriad of nanoparticle PDT agents are presented in various stages of development and show promise against a wide range of cancers. These nanoparticles can be separated into "passive" nanoparticles, which carry photosensitive agents, and "active" particles, which are themselves involved in the photostimulation process [7].

3.1. Passive Nanoparticles. A wide range of materials are in use for passive nanoparticles, including gold [31], polyacrylamide [32], silica [33], and biodegradable polymers [7]. One of their primary advantages over unencapsulated photosensitizers is their ability to preferentially accumulate in target cells [7, 33], which is of particular use given that most photosensitizers described so far in the literature have a low solubility in water and tend to accumulate in blood cells rather than tumors. This allows similar therapeutic effects to be achieved with lower doses of conventional photosensitizers such as hypericin, limiting their side effects [34]. Encapsulating potentially toxic photosensitizers inside nanoparticles is another possibility, enabling their use in patients when this might not otherwise be possible [7]. One issue that must be considered in passive photodynamic nanoparticles is the optimum drug concentration within the nanoparticle to achieve maximum therapeutic effect, as excessive drug loading can reduce the overall effect of the nanoparticles [34].

There is increasing presence in the literature of biodegradable passive nanoparticles for photodynamic therapy, typically made from polylactic acid or poly(lactic-co-glycolic acid) [7]. These nanoparticles can selectively deliver photosensitizers to target cells and then break down inside the cell, releasing the photosensitizer into target cells. This approach has seen impressive results in mouse models; in a study involving the administration of the photosensitizer hexadecafluoro zinc phthalocyanine to EMT-6 mammary tumors in mice, encapsulation of the photosensitizer in polylactic acid nanoparticles resulted in 100% of tested mice achieving tumor regression, compared with only 60% of mice administered the free drug [35]. Nanoparticle encapsulation of Indocyanine green, recently evaluated as a possible photosensitizer, was observed to increase organ deposition to the photosensitizer to levels 2–8 times that for the free drug [36]. Other photosensitizers which have observed beneficial results from encapsulation in biodegradable nanoparticles include hypericin [34] and zinc (II) phthalocyanine [37].

3.2. Active Nanoparticles. A rare example of nanoparticles that can act as a photosensitizer on their own are titanium dioxide (TiO_2) nanoparticles, which are receiving considerable attention as TiO_2 is a known photocatalyst and reacts with water to produce oxidizing free radicals when exposed to UV light [38], which can result in localized damage to nearby cells [38–40]. Recent *in vitro* studies on glioma cells have demonstrated the potential of such nanoparticles for photodynamic therapy [39]. A similar effect has recently been produced in TiO_2 nanoparticles with ultrasonic stimulation, which is able to kill nanoparticle-impregnated glioma cells when exposed to ultrasound in a similar manner to UV-stimulated nanoparticles [29]. TiO_2 nanoparticles are also essentially non toxic [41–43] and hence show considerable promise as cancer therapy agents. Other nanoparticles that have recently been shown to demonstrate photosensitizer effects include porous silicon and carbon-60 buckyballs [8, 44].

Other active nanoparticles generally serve to enhance the photodynamic process and are still used in conjunction with a photosensitizer. The aim of these nanoparticles is usually to generate light at frequencies useful for photodynamic therapy in regions deeper inside the patient, sidestepping the issue of the limited penetration hampering photodynamic therapy at non superficial depths. The majority of studies in this area has focused on "upconverting" nanoparticles, which convert low-frequency near infrared radiation (NIR) into frequencies usable for existing photosensitizers [7]. As well as penetrating further into the patient, NIR is also less damaging to the patient.

The most popular upconverting material for such nanoparticles at present is sodium yttrium fluoride doped with erbium and yttrium ions with a poly(ethylene imine) coat, forming PEI/$NaYF_4$: Yb^{3+}, E^{r3+} nanoparticles [7, 27]. Proof-of-concept studies in rats have confirmed that these upconverting nanoparticles can activate zinc phthalocyanine photosensitisers in rats, with resultant therapeutic effects, upon stimulation with NIR radiation well outside the absorption spectrum of the photosensitizer [27]. Upconverting nanoparticles, their photosensitizer, and a biocompatible layer may be combined into "composite nanoparticles," which can produce millimolar quantities of cytotoxic radicals upon illumination with NIR [45]. The upconverting phosophor used in these nanoparticles may also be activated with X-ray radiation, which would completely eliminate the depth limitations of photodynamic therapy, at the expense of increased healthy tissue damage [45].

4. Nanoparticles for Dual-Mode Imaging and Therapy?

One area that remains relatively unexplored is the concept of agents for dual-mode image contrast and therapy enhancement. The concept of dual-mode enhancement agents has

been tested using traditional non-nanoparticle image contrast agents, such as iodine, for radiotherapy enhancement applications [11–13]. As iodine is routinely used as an image contrast agent for CT scans [46], a conventional CT scanner could in principle be used to simultaneously monitor tumor progression and iodine uptake.

For nanoparticle-based enhancement agents, progress remains limited, although initial studies combining MRI enhancement and photodynamic therapy have recently appeared in the literature [47, 48]. If nanoparticles for radiotherapy using ionizing radiation were developed, however, it would be desirable to detect them on CT scanners instead. CT scanners are the standard imaging technique for diagnosis and treatment planning in virtually all cancer centres [49] and are increasingly replacing traditional simulator units for radiotherapy treatment planning. It is even possible to modify a conventional CT scanner to deliver therapeutic X-ray doses using iodine CERT [12, 50]. This treatment modality produces dose distributions similar to those obtained with 10 MV megavoltage therapy [12] and enables combined imaging, simulation, and treatment with the same machine. A similar option for more sophisticated contrast agents such as TiO_2 would be highly desirable and deserves investigation.

4.1. A Pilot Study with TiO_2 Nanoparticles. We conducted a pilot study investigating the potential of TiO_2 nanoparticles as a potential contrast agent for dual-mode imaging and therapy. We measured the effects of each of these agents on dose delivered by a kilovoltage X-ray therapy unit and imaged nanoparticle-impregnated volumes with a clinical CT scanner to determine their image contrast properties.

4.1.1. Methodology. In this study, rutile phase TiO_2 nanoparticles, with a diameter of 2-3 nm, were used. The concentration of these solutions ranged from 0 to 0.231 g/mL. The nanoparticles were fabricated using a DC magnetron-assisted sputtering deposition system. Ultra-high-purity argon and oxygen (both of purity greater than 99.99%) were used as the sputtering and reactive gases, respectively. The deposition process was carried out on ultrasonically cleaned silicon wafers.

To evaluate their imaging capabilities, the nanoparticle solutions were placed in a cylindrical plastic vial at a depth of 1.5 cm. These vials were imaged using a Toshiba Aquilion wide-bore CT scanner. The CT numbers of each vial in Hounsfield Units (the standard units used in CT scans [45]) of each vial were plotted against concentration and a linear fit was produced.

To evaluate their dose enhancement capabilities, the solutions were irradiated on a Pantak Therapax DXT 300 kVp X-ray unit. The solutions were placed in plastic containers on the surface of an RMI solid-water phantom, such that the nanoparticle solution had a thickness of 0.5 cm. Pieces of radiation-sensitive EBT2 radiochromic film were placed on the surface of the solution, such that the active layer was facing the radiation source. The film was then irradiated with a dose of 1.00 Gy at the surface. The dose recorded by each film piece was plotted against nanoparticle concentration to determine if the presence of the nanoparticles produced a dose enhancement. The dose values were normalized with respect to the dose recorded for the solution containing no nanoparticles.

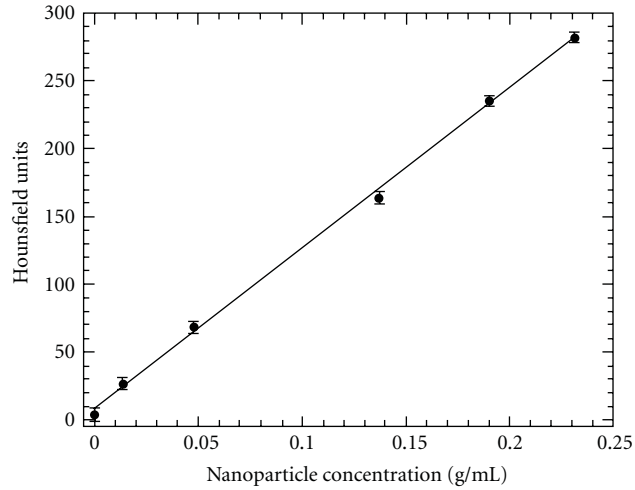

Figure 3: CT numbers of titanium dioxide nanoparticle solutions as a function of concentration (symbols, with error bars) and a linear best fit.

4.1.2. Results. The CT numbers of the scanned nanoparticle concentrations are shown in Figure 3. A sample scan is shown in Figure 4. The CT numbers of the nanoparticle solutions increase approximately linearly with nanoparticle concentration, ranging from 0 ± 5 HU (no nanoparticles) to 281.5 ± 4 HU (0.231 g/mL). The uncertainty in each measurement (given by the standard deviation of the Hounsfield unit measurements) is within 5 HU for each measurement. A nanoparticle concentration of 0.015 g/mL gives a reading of 26.6 ± 4 HU, which is greater than the typical noise value of about 5 HU reported on most CT scanners [46]. These results indicate that even at low concentrations, the presence of TiO_2 nanoparticles produces detectable changes in the CT numbers of scanned media which are detectable on a conventional medical CT scanner.

The surface doses recorded by the EBT2 film pieces as a function of nanoparticle concentration are shown in Figures 5 and 6. For both energies, no enhancement effects in surface dose are observed. In both cases, the dose measured in the solution containing no nanoparticles is the highest measured. The dose measured at 50 kVp decays approximately monotonically with nanoparticle concentration. For the 125 kVp beam energy, the fluctuations observed in the dose measurements for all nanoparticle concentrations are within the 4% calculated uncertainty. None of these values are more than 97% of the dose measured for the vial containing no nanoparticles. It is possible that the reduction in surface dose at higher nanoparticle concentrations is due to absorption of backscattered radiation near the surface by the nanoparticle solutions, with no corresponding dose enhancement to compensate for this. As such, it can be

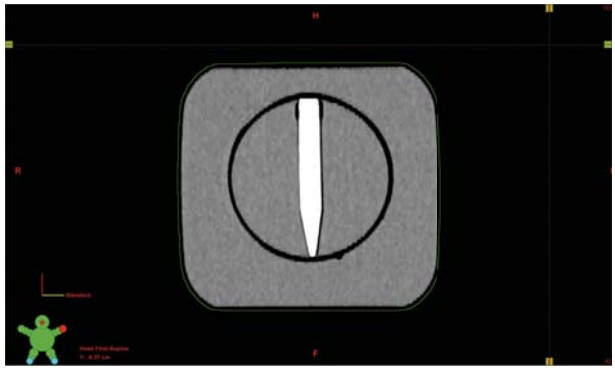

Figure 4: Sample coronal CT scan of a nanoparticle-containing vial. The nanoparticle solution (of high attenuation) appears as white, whereas the plastic frame containing the vial (of low attenuation) appears black.

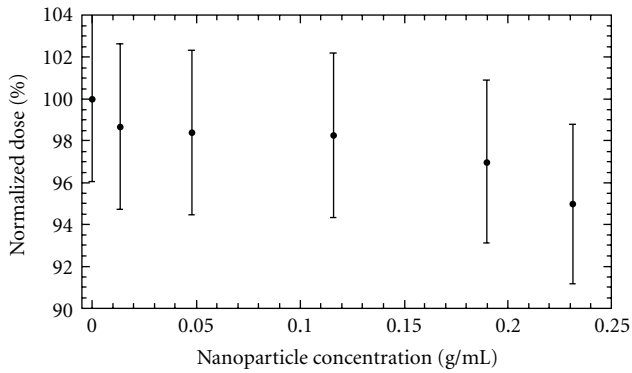

Figure 5: Normalized surface dose recorded for the 50 kVp radiation beam as a function of nanoparticle concentration.

concluded that a therapeutic enhancement in surface dose is not observable using TiO_2 nanoparticles of the phase and concentrations investigated in this study, to within the sensitivity limits of the film dosimetry technique that was used.

5. Conclusion

Nanoparticles offer enormous potential for improving cancer imaging and treatment. With demonstrated success in existing diagnostic imaging and drug delivery techniques, there is now growing interest in the potential applications to radiation therapy and photodynamic therapy. Several classes of nanoparticles are presently under development for both of these techniques and are likely to enable significant improvements to the efficacy of existing cancer therapy regimes in the foreseeable future. We reviewed the current status of nanoparticle agents for cancer therapy. Preliminary results for titanium dioxide nanoparticles as potential dual-mode imaging and therapy enhancement agents indicate they are a promising candidate for image contrast in computed tomography. However, more comprehensive studies are needed, with more sensitive detection techniques, to determine whether they may also serve to enhance radiation dose for targeted cancer radiotherapy applications.

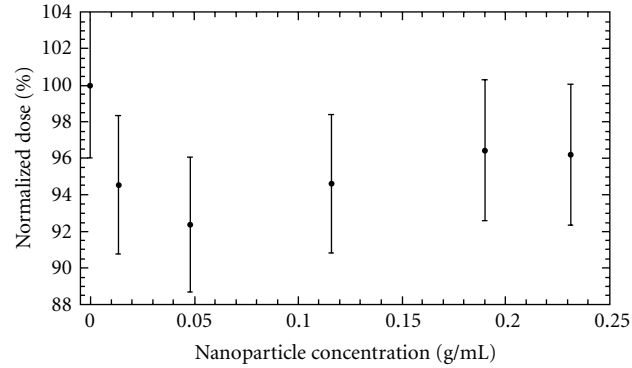

Figure 6: Normalized surface dose recorded for the 125 kVp radiation beam as a function of nanoparticle concentration.

Acknowledgments

L. Smith acknowledges support from a CSIRO Scholarship. The authors wish to acknowledge Royal Prince Alfred Hospital, Sydney, Australia, for access to clinical facilities and also wish to thank A. L. Yuen at the School of Chemistry, University of Sydney, for providing Figure 1. This work is supported by the Australian Research Council (ARC) and CSIRO's OCE Science Leadership Program.

References

[1] P. Suetens, *Fundamentals of Medical Imaging*, Cambridge University Press, New York, NY, USA, 2nd edition, 2009.

[2] P. Jackson, S. Periasamy, V. Bansal, and M. Geso, "Evaluation of the effects of gold nanoparticle shape and size on contrast enhancement in radiological imaging," *Australasian Physical and Engineering Sciences in Medicine*, vol. 34, no. 2, pp. 243–249, 2011.

[3] J. F. Hainfeld, D. N. Slatkin, T. M. Focella, and H. M. Smilowitz, "Gold nanoparticles: a new X-ray contrast agent," *British Journal of Radiology*, vol. 79, no. 939, pp. 248–253, 2006.

[4] C. Fang and M. Zhang, "Multifunctional magnetic nanoparticles for medical imaging applications," *Journal of Materials Chemistry*, vol. 19, no. 35, pp. 6258–6266, 2009.

[5] D. Kim, M. K. Yu, T. S. Lee, J. J. Park, Y. Y. Jeong, and S. Jon, "Amphiphilic polymer-coated hybrid nanoparticles as CT/MRI dual contrast agents," *Nanotechnology*, vol. 22, no. 15, Article ID 155101, 2011.

[6] H. M. Garnica-Garza, "Contrast-enhanced radiotherapy: feasibility and characteristics of the physical absorbed dose distribution for deep-seated tumors," *Physics in Medicine and Biology*, vol. 54, no. 18, pp. 5411–5425, 2009.

[7] D. K. Chatterjee, L. S. Fong, and Y. Zhang, "Nanoparticles in photodynamic therapy: an emerging paradigm," *Advanced Drug Delivery Reviews*, vol. 60, no. 15, pp. 1627–1637, 2008.

[8] B. C. Wilson and M. S. Patterson, "The physics, biophysics and technology of photodynamic therapy," *Physics in Medicine and Biology*, vol. 53, no. 9, pp. R61–R109, 2008.

[9] A. K. L. Yuen, G. A. Hutton, A. F. Masters, and T. Maschmeyer, "The interplay of catechol ligands with nanoparticulate iron oxides," *Dalton Transactions*, vol. 41, no. 9, pp. 2545–2559, 2012.

[10] R. S. Mello, H. Callison, J. Winter, A. R. Kagan, and A. Norman, "Radiation dose enhancement in tumors with iodine," *Medical Physics*, vol. 10, no. 1, pp. 75–78, 1983.

[11] A. V. Mesa, A. Norman, T. D. Solberg, J. J. Demarco, and J. B. Smathers, "Dose distributions using kilovoltage X-rays and dose enhancement from iodine contrast agents," *Physics in Medicine and Biology*, vol. 44, no. 8, pp. 1955–1968, 1999.

[12] J. H. Rose, A. Norman, and M. Ingram, "First experience with radiation therapy of small brain tumors delivered by a computerized tomography scanner," *International Journal of Radiation Oncology Biology Physics*, vol. 30, pp. 1127–1132, 1994.

[13] F. Verhaegen, B. Reniers, F. Deblois, S. Devic, J. Seuntjens, and D. Hristov, "Dosimetric and microdosimetric study of contrast-enhanced radiotherapy with kilovolt x-rays," *Physics in Medicine and Biology*, vol. 50, no. 15, pp. 3555–3569, 2005.

[14] A. R. Kagan, R. J. Steckel, P. Cancilla, G. Juillard, and T. Patin, "The pathogenesis of brain necrosis: time and dose parameters," *International Journal of Radiation Oncology Biology Physics*, vol. 1, no. 7-8, pp. 729–732, 1976.

[15] S. J. McMahon, M. H. Mendenhall, S. Jain, and F. Currell, "Radiotherapy in the presence of contrast agents: a general figure of merit and its application to gold nanoparticles," *Physics in Medicine and Biology*, vol. 53, no. 20, pp. 5635–5651, 2008.

[16] R. I. Berbecoa, W. Ngwaa, and M. Makrigiorgosa, "Localized dose enhancement to tumor blood vessel endothelial cells via targeted gold nanoparticles: new potential for external beam radiotherapy," *International Journal of Radiation Oncology Biology Physics*, vol. 78, pp. S649–S650, 2010.

[17] D. B. Chithrani, S. Jelveh, F. Jalali et al., "Gold nanoparticles as radiation sensitizers in cancer therapy," *Radiation Research*, vol. 173, no. 6, pp. 719–728, 2010.

[18] J. F. Hainfeld, F. A. Dilmanian, D. N. Slatkin, and H. M. Smilowitz, "Radiotherapy enhancement with gold nanoparticles," *The Journal of Pharmacy and Pharmacology*, vol. 60, no. 8, pp. 977–985, 2008.

[19] J. F. Hainfeld, D. N. Slatkin, and H. M. Smilowitz, "The use of gold nanoparticles to enhance radiotherapy in mice," *Physics in Medicine and Biology*, vol. 49, no. 18, pp. N309–N315, 2004.

[20] Y. Zheng, P. Cloutier, D. J. Hunting, and L. Sanche, "Radiosensitization by gold nanoparticles: comparison of DNA damage induced by low and high-energy electrons," *Journal of Biomedical Nanotechnology*, vol. 4, no. 4, pp. 469–473, 2008.

[21] S. Bhattacharyya, R. A. Kudgus, R. Bhattacharya, and P. Mukherjee, "Inorganic nanoparticles in cancer therapy," *Pharmaceutical Research*, vol. 28, no. 2, pp. 237–259, 2011.

[22] S. J. McMahon, W. B. Hyland, M. F. Muir et al., "Biological consequences of nanoscale energy deposition near irradiated heavy atom nanoparticles," *Scientific Reports*, vol. 1, article 18, 2011.

[23] M. K. K. Leung, J. C. L. Chow, B. D. Chithrani, M. J. G. Lee, B. Oms, and D. A. Jaffray, "Irradiation of gold nanoparticles by X-rays: Monte Carlo simulation of dose enhancements and the spatial properties of the secondary electrons production," *Medical Physics*, vol. 38, no. 2, pp. 624–631, 2011.

[24] A. Anshup, J. S. Venkataraman, C. Subramaniam et al., "Growth of gold nanoparticles in human cells," *Langmuir*, vol. 21, no. 25, pp. 11562–11567, 2005.

[25] S. Jain, J. A. Coulter, A. R. Hounsell et al., "Cell-Specific Radiosensitization by gold nanoparticles at megavoltage radiation energies," *International Journal of Radiation Oncology Biology Physics*, vol. 79, no. 2, pp. 531–539, 2011.

[26] M. Triesscheijn, P. Baas, J. H. M. Schellens, and F. A. Stewart, "Photodynamic therapy in oncology," *Oncologist*, vol. 11, no. 9, pp. 1034–1044, 2006.

[27] D. K. Chatterjee and Z. Yong, "Upconverting nanoparticles as nanotransducers for photodynamic therapy in cancer cells," *Nanomedicine*, vol. 3, no. 1, pp. 73–82, 2008.

[28] R. R. Allison, V. S. Bagnato, and C. H. Sibata, "Future of oncologic photodynamic therapy," *Future Oncology*, vol. 6, no. 6, pp. 929–940, 2010.

[29] S. Yamaguchi, H. Kobayashi, T. Narita et al., "Sonodynamic therapy using water-dispersed TiO_2-polyethylene glycol compound on glioma cells: comparison of cytotoxic mechanism with photodynamic therapy," *Ultrasonics Sonochemistry*, vol. 18, no. 5, pp. 1197–1204, 2011.

[30] R. R. Allison, G. H. Downie, R. Cuenca, X.-H. Hu, C. J. H. Childs, and C. H. Sibata, "Photosensitizers in clinical PDT," *Photodiagnosis and Photodynamic Therapy*, vol. 1, no. 1, pp. 27–42, 2004.

[31] M. K. K. Oo, *Multifunctional Gold Nanoparticles For Photodynamic Therapy of Cancer*, Stevens Institute of Technology, Hoboken, NJ, USA, 2010.

[32] M. Kuruppuarachchi, H. Savoie, A. Lowry, C. Alonso, and R. W. Boyle, "Polyacrylamide nanoparticles as a delivery system in photodynamic therapy," *Molecular Pharmaceutics*, vol. 8, no. 3, pp. 920–931, 2011.

[33] P. Couleaud, V. Morosini, C. Frochot, S. Richeter, L. Raehm, and J.-O. Durand, "Silica-based nanoparticles for photodynamic therapy applications," *Nanoscale*, vol. 2, no. 7, pp. 1083–1095, 2010.

[34] M. Zeisser-Labouebe, N. Lange, R. Gurny, and F. Delie, "Hypericin-loaded nanoparticles for the photodynamic treatment of ovarian cancer," *International Journal of Pharmaceutics*, vol. 326, no. 1-2, pp. 174–181, 2006.

[35] E. Allemann, N. Brasseur, O. Benrezzak et al., "PEG-coated poly(lactic acid) nanoparticles for the delivery of hexadecafluoro zinc phthalocyanine to EMT-6 mouse mammary tumours," *The Journal of Pharmacy and Pharmacology*, vol. 47, no. 5, pp. 382–387, 1995.

[36] V. Saxena, M. Sadoqi, and J. Shao, "Polymeric nanoparticulate delivery system for indocyanine green: biodistribution in healthy mice," *International Journal of Pharmaceutics*, vol. 308, no. 1-2, pp. 200–204, 2006.

[37] E. Ricci-Junior and J. M. Marchetti, "Zinc(II) phthalocyanine loaded PLGA nanoparticles for photodynamic therapy use," *International Journal of Pharmaceutics*, vol. 310, no. 1-2, pp. 187–195, 2006.

[38] L. Liu, P. Miao, Y. Xu, Z. Tian, Z. Zou, and G. Li, "Study of Pt/Tio_2 nanocomposite for cancer-cell treatment," *Journal of Photochemistry and Photobiology B*, vol. 98, no. 3, pp. 207–210, 2010.

[39] S. Yamaguchi, H. Kobayashi, T. Narita et al., "Novel photodynamic therapy using water-dispersed TiO_2 polyethylene glycol compound: evaluation of antitumor effect on glioma cells and spheroids in vitro," *Photochemistry and Photobiology*, vol. 86, no. 4, pp. 964–971, 2010.

[40] A. Janczyk, A. Wolnicka-Głubisz, K. Urbanska, H. Kisch, G. Stochel, and W. Macyk, "Photodynamic activity of platinum(IV) chloride surface-modified TiO_2 irradiated with visible light," *Free Radical Biology and Medicine*, vol. 44, no. 6, pp. 1120–1130, 2008.

[41] E. Fabian, R. Landsiedel, L. Ma-Hock, K. Wiench, W. Wohlleben, and B. van Ravenzwaay, "Tissue distribution and toxicity of intravenously administered titanium dioxide nanoparticles in rats," *Archives of Toxicology*, vol. 82, no. 3, pp. 151–157, 2008.

[42] B. K. Bernard, M. R. Osheroff, A. Hofmann, and J. H. Mennear, "Toxicology and carcinogenesis studies of dietary titanium dioxide-coated mica in male and female Fischer 344 rats," *Journal of Toxicology and Environmental Health*, vol. 29, no. 4, pp. 417–429, 1990.

[43] F. Bischoff and G. Bryson, "Tissue reaction to and fate of parenterally administered titanium dioxide. I. The intraperitoneal site in male Marsh-Buffalo mice," *Research Communications in Chemical Pathology and Pharmacology*, vol. 38, no. 2, pp. 279–290, 1982.

[44] C. Yu, T. Canteenwala, M. E. El-Khouly et al., "Efficiency of singlet oxygen production from self-assembled nanospheres of molecular micelle-like photosensitizers FC_4S," *Journal of Materials Chemistry*, vol. 15, no. 18, pp. 1857–1864, 2005.

[45] B. Ungun, R. K. Prud'homme, S. J. Budijono et al., "Nanofabricated upconversion nanoparticles for photodynamic therapy," *Optics Express*, vol. 17, no. 1, pp. 80–86, 2009.

[46] C. Guy and D. Ffytche, *An Introduction to The Principles of Medical Imaging*, Imperial College Press, London, UK, 2005.

[47] T. D. Schladt, K. Schneider, M. I. Shukoor et al., "Highly soluble multifunctional MnO nanoparticles for simultaneous optical and MRI imaging and cancer treatment using photodynamic therapy," *Journal of Materials Chemistry*, vol. 20, no. 38, pp. 8297–8304, 2010.

[48] W.-Y. Huang and J. J. Davis, "Multimodality and nanoparticles in medical imaging," *Dalton Transactions*, vol. 40, no. 23, pp. 6087–6103, 2011.

[49] E. B. Podgorsak, *Radiation Oncology Physics: A Handbook for Teachers and Students*, IAEA, Vienna, Austria, 2005.

[50] B.-J. Schultz, P. Wust, L. Ludemann, G. Jost, and H. Pietsch, "Monte Carlo simulation of contrast-enhanced whole brain radiotherapy on a CT scanner," *Medical Physics*, vol. 38, no. 8, pp. 4672–4680, 2011.